Cumhuriyet Science Journal
Faculty of Science, Cumhuriyet University
58140 - Sivas - Türkiye
Phone: +90(346) 487 13 72
Fax: +90(346) 219 11 86
e-mail: csj@cumhuriyet.edu.tr
http://csj.cumhuriyet.edu.tr/en
http://dergipark.org.tr/en/pub/csj

Cumhuriyet Science Journal Vol: 44 No: 2 Year 2023

Sivas Cumhuriyet University

ISSN : 2680-2587
e-ISSN : 246-2587X
dergipark.org.tr/tr/pub/csj
e-mail: csj@cumhuriyet.edu.tr

Cumhuriyet Science Journal

Cumhuriyet Science Journal (CSJ) is an official publication of Sivas Cumhuriyet University, Science Faculty. The high quality research papers related to the natural sciences are published as online four times a year. CSJ is an open access, free of charge journal and all articles in CSJ have undergone peer review and upon acceptance are immediately and permanently free for everyone to read and download.

Volume: 44 Number: 2 Year: 2023

ISSN: 2587-2680
e-ISSN: 2587-246X
Period: Quarterly
Founded: 2002
Publisher: Sivas Cumhuriyet University

Cumhuriyet Science Journal (CSJ)

Journal Previous Name: Cumhuriyet Üniversitesi Fen-Edebiyat Fakültesi Fen Bilimleri Dergisi

Old ISSN: 1300-1949

Abstracted&Indexeding

ULAKBİM TR-Dizin

Index Copernicus (ICI Journals Master List)

Clarivate Analytics Zoological Record

Crossref

WorldCat

Akademik Dizin

Arastirmax Bilimsel Yayın İndeksi

Bielefeld Academic Search Engine (BASE)

Directory of Research Journal Indexing (DRJI)

Google Scholar

Research Gate

Idealonline

Publication Type: Peer Reviewed Journal

Cite Type: Cumhuriyet Sci. J.

Contact Information

Faculty of Science Cumhuriyet University
58140 Sivas- TURKEY
Phone: +90 (346) 487 13 72
Fax: +90 (346) 219 11 86
e-mail: csj@cumhuriyet.edu.tr
http://dergipark.gov.tr/csj

	CONTENTS		PAGES
1	Metabolic Infrastructure of Pregnant Women with Fetuses Having Nervous System Abnormalities; Metabolomic Analysis **Tuba REÇBER Emirhan NEMUTLU Emine AYDIN Murat CAGAN Hanife Güler DÖNMEZ Sedef KIR M.Sinan BEKSAC**	*Research Article*	236-243
2	Concomitant strain of Bacillus vallismortis BR2 and Escherichia coli Khodavandi-Alizadeh-2 for Biocatalytic Synthesis of Fatty Acid Methyl Ester from Waste Oil Feedstock **Michael OSHO Olayinka Mary OTOLORİN**	*Research Article*	244-253
3	T-type Calcium Channel Blocker, NNC 55-0396, Suppress Cell Proliferation and Promote Apoptosis in SNU-1 Gastric Cancer Cells **Mustafa ERGÜL**	*Research Article*	254-257
4	Synthesis, Anticancer Activity and Carbonic Anhydrase Inhibitory Activity of new Thiadiazole-hydrazone Derivatives **Hayrani Eren BOSTANCI Ulviye ACAR ÇEVİK**	*Research Article*	258-262
5	Investigation of The Antiproliferative Effect of Colchicine on SNU-1 Gastric Cancer Cells **Fatih YULAK**	*Research Article*	263-267
6	Trifloxystrobin Pretreatment Alleviates Excessive Copper Stress in Wheat (Triticum aestivum L.) **Oksal MACAR Tuğçe KALEFETOĞLU MACAR Tolga KARAKÖY**	*Research Article*	268-275
7	Some Population Parameters of Morocco dentex, Dentex maroccanus Valenciennes, 1830 in the Northeastern Mediterranean Sea **Seda KONTAŞ YALÇINKAYA**	*Research Article*	276-282
8	Investigation on the Flow Behaviour of Agar Solution and Rheological Modelling **Mukaddes KARATAŞ**	*Research Article*	283-288
9	Synthesis and Characterization of Tetradentate Schiff Base Ligand Containing 3,4-Diamino Benzophenone and Investigation of Complex Formation with Ni (II), Cu (II) and Co (II) metal ions **Mustafa BAL**	*Research Article*	289-295
10	Chemical Reactivities and Organic Light-emitting Diode Properties of some Polyaromatic Molecules **Mustafa ELİK**	*Research Article*	296-301
11	Design, Characterization and in vitro Simulations of nano-HAP/GO Composite Drug Delivery System Produced by Hydrothermal Methods Loaded with Paclitaxel **Fatih ÇİFTÇİ**	*Research Article*	302-314
12	Parametric Extension of a Certain Family of Summation-Integral Type Operators **Nadire Fulda ODABAŞI İsmet YÜKSEL**	*Research Article*	315-327
13	The Intersection of Two Ruled Surfaces Corresponding to Spherical Indicatrix Curves on the Unit Dual Sphere **Yunus ÖZTEMİR Mustafa ÇALIŞKAN**	*Research Article*	328-335
14	Obtaining The Finite Difference Approximation of The Lame System By Using Barycentric Coordinates **Vildan YAZICI**	*Research Article*	336-344
15	Chaos in a Three-Dimensional Cancer Model with Piecewise Constant Arguments **Senol KARTAL**	*Research Article*	345-355
16	Inverse Nodal Problem for a Conformable Fractional Diffusion Operator With Parameter-Dependent Nonlocal Boundary Condition **Yaşar ÇAKMAK**	*Research Article*	356-363

17	Comparative Estimation of Global Solar Radiation over Two Nigerian Cities, Using Artificial Neural Network and Empirical Models **Gbadebo İsmaila OLATONA Oluwapelumi AJİLORE Fakunle MUTİU ALANİ Paul OLANİYİ Makinde TOSİN**	*Research Article*	364-369
18	The Energy Spectra of Electric Induced Mathieu Quantum Dot with Hydrogenic Impurity Implanted in Quantum Plasma **Mustafa Kemal BAHAR**	*Research Article*	370-376
19	Numerical Investigation of Diffraction Patterns of Small Size Apertures Using Light Sources From Xuv to The Visible Region: Simulation for The Small Size Structures **Muhammed SAYRAÇ Emine KAYNAR Fatih UNGAN**	*Research Article*	377-383
20	Comparison of Single and Multiple Treatment Plans Made in CyberKnife® Radiosurgery System on Phantom **Kevser SÖZEN Hasan UYSAL Nihal BÜYÜKÇİZMECİ Kaan OYSUL**	*Research Article*	384-388
21	Investigation of Thermal Quenching Effect for Lithium Fluoride (LiF) Type Dosimeters **Engin AŞLAR**	*Research Article*	389-395
22	Influence of The Substrate-Target Angle and Sputter Temperature On The Properties of CIGS Thin Films Sputtered From Single Quaternary Target **Filiz KELEŞ Furkan GÜÇLÜER**	*Research Article*	396-402
23	Amazonite in Pakistan: A Comprehensive Study with XRD, XPS, SEM, and PL Analyses **Eren Cihan KARSU ASAL**	*Research Article*	403-410
24	Determination of Impact Size by Canonic Correlation Analysis of the Factors Affecting the Buying or Selling Agricultural Lands **İsmail GÖK Mustafa ŞAHİN Tolga TOLUN**	*Research Article*	411-417

Cumhuriyet Sci. J., 44(2) (2023) 236-243
DOI: https://doi.org/10.17776/csj.1246590

Cumhuriyet Science Journal

| csj.cumhuriyet.edu.tr | Founded: 2002 ISSN: 2587-2680 e-ISSN: 2587-246X Publisher: Sivas Cumhuriyet University

Metabolic Infrastructure of Pregnant Women with Fetuses Having Nervous System Abnormalities; Metabolomic Analysis

Tuba Reçber [1,a], Emirhan Nemutlu [1,b,*], Emine Aydın [2,c], Murat Cagan [2,d], Hanife Guler Donmez [3,e], Sedef Kır [1,f], Mehmet Sinan Beksac [2,g]

[1]*Department of Analytical Chemistry, Faculty of Pharmacy, Hacettepe University, Ankara, Türkiye,*
[2]*Division of Perinatology, Department of Obstetrics and Gynecology, Faculty of Medicine, Hacettepe University, Ankara, Türkiye,*
[3]*Department of Biology, Faculty of Science, Hacettepe University, Ankara, Türkiye*
**Corresponding author*

Research Article

History
Received: 02/02/2023
Accepted: 08/05/2023

ABSTRACT

Central nervous system diseases are neurological disorders that affect the structure or function of the brain and spinal cord that make up the central nervous system. In this study, it was aimed to examine the impaired/altered metabolomic profiles of pregnant women carrying fetuses with nervous system abnormalities (NSA). The study group consisted of 30 normal pregnancies with normal fetuses (control group) and 8 pregnancies with fetuses having NSA (study group), as determined by prenatal screening and diagnosis as part of an antenatal care program. Metabolomic analyses were carried out using gas chromatography-mass spectrometry (GC-MS). GC-MS-based metabolomics analysis was able to identify 95 metabolites and 27 of them were statistically significant between the two groups ($p<0.05$). Moreover, the pathway analysis, performed with significantly altered metabolites, showed alteration in the alanine, aspartate, and glutamate metabolism, citrate cycle, aminoacyl t-RNA biosynthesis, and glutathione metabolism. Alanine, aspartate and glutamate metabolism, citrate cycle, aminoacyl t-RNA biosynthesis, and glutathione metabolism seem to be critical in the prenatal screening of NSAs. However, abnormality-specific studies are necessary for further recommendations.

Keywords: Pregnancy, Congenital nervous system abnormalities, Metabolomics, Prenatal screening, Prenatal diagnosis.

[a] *tuba.recber@hacettepe.edu.tr* *https://orcid.org/0000-0001-8257-7628*
[b] *enemutlu@hacettepe.edu.tr* *https://orcid.org/0000-0002-7337-6215*
[c] *eminebaskurtaydin@gmail.com* *https://orcid.org/0000-0001-8877-2803*
[d] *drmuratcagan@gmail.com* *https://orcid.org/0000-0003-0629-4401*
[e] *hanifetanir@hacettepe.edu.tr* *https://orcid.org/0000-0002-7413-4939*
[f] *sekir@hacettepe.edu.tr* *https://orcid.org/0000-0003-1322-1665*
[g] *beksac@hacettepe.edu.tr* *https://orcid.org/0000-0001-6362-787X*

Introduction

Nervous system development involves 3 germinal layers and ectoderm is the key initiating player in the embryogenesis of the central nervous system (CNS) [1, 2]. Embryogenesis of CNS can be complicated and may result in mild, moderate or severe congenital defects [2, 3]. There is a wide spectrum of fetal nervous system abnormalities (NSA) such as anencephaly, craniorachischisis, iniencephaly, encephalocele, spina bifida, microcephaly, hydrocephaly etc., and these anomalies need to be prenatally diagnosed as early as possible [2-5]. Genetical, epigenetic and teratological factors are the main courses behind NSA and need to be investigated within the framework of antenatal care programs [6-12]. This necessitates the evaluation of maternal metabolism as well as other screening tests [6-15].

Developing better non-invasive tests is a necessity in perinatal medicine and the application of metabolomics could be extremely useful in the prenatal screening/diagnosis of congenital NSA [15-17]. Metabolomics is the identification and quantification of small-molecule metabolites (molecular weight <1000 Da) in tissues, cells and physiological fluids within a certain period of time [13-15]. Metabolites are intermediate products of various types of biochemical reactions that participate in bonding metabolic pathways [13, 15-17].

Metabolomics measures and analyses the products of cellular biochemistry and might be useful in the prenatal detection of NSA abnormalities. In this study, we aimed to configure impaired/altered metabolomic profiles of pregnant women carrying fetuses with NSA.

Materials and Methods

This study was consisted of 30 normal pregnancies with normal fetuses (control group) and 8 pregnancies with fetuses having NSAs with or without co-abnormalities (study group), as determined by second trimester ultrasonographic examination (14-22nd gestational weeks) as a part of antenatal care program. Antecubital venous bloods were withdrawn from the patients during the course of the examinations. All patients were delivered (or termination of pregnancy) at Hacettepe University. Hacettepe University Perinatology Registry was used for necessary clinical data collection. The study protocol was approved by the Ethical

Committee of Hacettepe University (GO 13/173), and informed consent was obtained from all patients.

Metabolomics Analysis

Metabolomic analyses were carried out using gas chromatography-mass spectrometry (GC-MS). A 100 µL of plasma was spiked with 900 µL methanol-water (8:1, v/v) mixture containing 5 µg/mL of internal standard (IS) myristic-d27 acid at ambient temperature. It was vortexed for 30 sec and centrifuged at 15000 rpm for 10 min. Afterward, 400 µL of supernatant was evaporated to dryness. The residues were methoxyaminated using methoxyamine hydrochloride (20 mg/mL in pyridine) and derivatized with MSTFA (N-Methyl-N-(trimethylsilyl) trifluoroacetamide with 1% TMCS (trimethylchlorosilane). After derivatization, the samples were transferred into GC–MS vials and analysed using GC–MS (Shimadzu GCMS-QP2010 Ultra) with a DB-5MS stationary phase column (30 m + 10 m DuraGuard × 0.25 mm i.d. and 0.25-µm film thickness). The mass range was set from 50 to 650 Daltons. The run time was 37.5 min.

Data Analysis

Data deconvolution, peak alignment, normalization, and data matrix creation were carried out using MS-DIAL (ver. 4.0) software. Metabolite identification for GC-MS was done using a commercially available retention index library (Fiehn Retention Index Library). For metabolite identification, retention time tolerance was determined as 0.05 minutes, m/z tolerance 0.5 Da, EI similarity cut off 70% and identification score cut off 70%. The data matrix obtained from MS-DIAL was normalized using the internal standard and then transferred to an Excel work file. Any metabolite traits having more than 50% of the values missing were excluded from the data matrix. Missing values in the data matrix were filled with the half value of the smallest concentration in the metabolite group. The final data matrix was imported into the SIMCA-P+ (v13.0, Umetrics, Sweden) and Metaboanalyst software for multivariate analyses. Within the scope of multivariate analyzes, partial least squares differentiation analysis (PLS-DA), variable importance in projection (VIP) analysis, coefficient plots, heatmap analysis, and pathway analysis were performed.

Results

Study groups showed no statistically significant difference in terms of demographic findings (p>0.05, for all). Table 1 shows Fetal NSAs and co-abnormalities (if any) of the study group cases.

A GC–MS-based metabolomic profiling study has been performed in pregnant women with NSA (n=8) and the control group (n=30). As a result of these analyses, 95 of 277 metabolites (182 unknown) were identified (Table 2). Twenty-seven of the identified metabolites were statistically significant between the two groups ($p<0.05$) (Table 2). Among these metabolites, 3-aminopropionitrile, linoleic acid, cysteine, tartaric acid, porphine, oxalic acid, ornithine, 5-hydroxy-L-tryptophan, pyruvic acid, glucose-6-phosphoric acid, phosphoric acid, 3-aminoisobutyric acid, citric acid, alpha-ketoglutaric acid, glycolic acid, tyrosine, pyrophosphate, glycine and lactic acid plasma levels were statistically significantly lower in second-trimester pregnancies having fetuses with NSAs compared to control group pregnancies. On the other hand, palatinose, tryptophan, sorbitol, epsilon-caprolactam, lauric acid, lactobionic acid, glucosaminic acid and creatinine plasma levels were found to be higher in study group pregnancies compared to controls.

The multivariate statistical analysis of GC–MS metabolomics results was performed using PLS-DA and heatmap and pathway analysis methods (Figure 1 and 2). The statistical goodness and robustness of the models were evaluated using R^2 and Q^2 values, respectively. The pathway analysis, performed with significantly altered metabolites, showed alteration in the alanine, aspartate and glutamate metabolism, citrate cycle, aminoacyl t-RNA biosynthesis and glutathione metabolism (Figure 3).

Table 1. Fetal nervous system abnormalities and co-abnormalities (if any) of the study group cases

Case no	Neurological defects	Co-abnormalities
NSA-1	Occipital encephalocele	None
NSA-2	Anencephaly	Fetal megacystis
NSA-3	Spina bifida	None
NSA-4	Cerebellar vermian hypoplasia Lateral ventricle dilatation	Increased renal echogenicity Single umbilical artery Bilateral cleft lip and cleft palate Aortic stenosis
NSA-5	Bilateral ventriculomegaly Spina bifida	Hyperechogenic fetal bowel Oligohydramnios
NSA-6	Lobar holoprosencephaly Microcephaly	Cleft lip and cleft palate
NSA-7	Mega cisterna magna	Cleft lip and cleft palate Bilateral clench hand Aortic coarctation
NSA-8	Cerebellar hypoplasia	Hydrops fetalis

Table 2. Metabolites and relative amounts identified by GC-MS analysis

Metabolite name	NSA			Control			p value
	Mean±SE			Mean±SE			
2-butyne-1,4-diol	0.945	±	0.124	0.951	±	0.152	0.983
2-hydroxybutyric acid	1.149	±	0.149	0.942	±	0.060	0.155
2-ketoisocaproic acid	1.006	±	0.097	1.028	±	0.068	0.879
2-keto-L-gulonic acid	0.706	±	0.125	1.199	±	0.193	0.214
3-aminoisobutyric acid	0.924	±	0.064	1.121	±	0.028	0.005
3-aminopropionitrile	0.678	±	0.074	1.237	±	0.042	<0.000
3-indoleacetic acid	0.882	±	0.209	1.156	±	0.174	0.456
3-methyl-2-oxobutanoic acid	0.920	±	0.082	1.093	±	0.060	0.182
3-Phosphoglyceric acid	1.230	±	0.197	0.971	±	0.116	0.315
5-hydroxy-L-tryptophan	0.564	±	0.092	1.230	±	0.084	0.001
Alanine	1.014	±	0.060	1.030	±	0.041	0.851
Alpha ketoglutaric acid	0.580	±	0.055	1.093	±	0.062	<0.000
Asparagine	0.937	±	0.070	1.014	±	0.074	0.615
Aspartic acid	1.072	±	0.131	0.935	±	0.085	0.460
Benzoic acid	1.000	±	0.039	1.043	±	0.036	0.562
Biuret	0.799	±	0.106	0.727	±	0.104	0.739
Capric acid	0.777	±	0.108	0.837	±	0.114	0.800
Cholesterol	0.899	±	0.075	1.084	±	0.045	0.069
Citric acid	0.822	±	0.063	1.117	±	0.058	0.018
Creatinine	1.569	±	0.163	0.798	±	0.067	<0.000
Cycloleucine	0.958	±	0.212	1.041	±	0.091	0.697
Cysteine	0.831	±	0.076	1.160	±	0.042	0.001
Epsilon-caprolactam	1.416	±	0.155	0.667	±	0.072	<0.000
Fructose	1.732	±	0.978	0.831	±	0.086	0.108
Fucose	0.879	±	0.111	1.118	±	0.076	0.149
Glucoheptonic acid	0.988	±	0.103	1.020	±	0.046	0.768
Gluconic acid	0.792	±	0.351	1.238	±	0.389	0.578
Gluconic acid lactone	0.990	±	0.177	1.065	±	0.085	0.699
Glucosaminic acid	1.264	±	0.144	0.981	±	0.058	0.047
Glucose	0.946	±	0.090	1.075	±	0.065	0.358
Glucose-6-phosphoric acid	0.720	±	0.068	1.152	±	0.059	0.001
Glucuronic acid	1.060	±	0.099	1.054	±	0.153	0.985
Glutamic acid	0.956	±	0.105	0.872	±	0.082	0.630
Glutamine	1.237	±	0.118	0.969	±	0.103	0.220
Glyceric acid	0.924	±	0.074	1.026	±	0.068	0.476
Glycerol	0.967	±	0.051	1.075	±	0.036	0.172
Glycine	0.862	±	0.100	1.144	±	0.061	0.040
Glycolic acid	0.900	±	0.068	1.082	±	0.031	0.016
Heptadecanoic acid	1.055	±	0.097	0.987	±	0.034	0.425
Iminodiacetic acid	1.020	±	0.162	0.985	±	0.089	0.859
Indole-3-acetamide	0.793	±	0.291	1.209	±	0.178	0.289
Isoleucine	0.915	±	0.077	1.040	±	0.069	0.383
Isopropyl beta-D-1-thiogalactopyranoside	1.101	±	0.181	1.067	±	0.129	0.900
Lactamide	0.875	±	0.266	0.886	±	0.098	0.965
Lactic acid	0.714	±	0.089	1.172	±	0.110	0.049
Lactobionic acid	1.213	±	0.152	0.962	±	0.036	0.026
Lauric acid	1.276	±	0.126	1.019	±	0.040	0.018
Linoleic acid	0.804	±	0.106	1.098	±	0.059	0.030
Lysine	1.094	±	0.123	1.026	±	0.058	0.613
Malic acid	0.980	±	0.051	1.052	±	0.048	0.470
Malonic acid	0.875	±	0.266	0.886	±	0.098	0.965
Methionine	0.943	±	0.065	1.053	±	0.071	0.449
Methyl linolenate	0.632	±	0.117	1.399	±	0.309	0.223
Methyl Palmitate	0.830	±	0.177	1.319	±	0.254	0.347
Methyl Stearate	0.865	±	0.232	1.264	±	0.249	0.439
Mucic acid	1.017	±	0.120	1.065	±	0.063	0.732
Myristic acid	0.866	±	0.134	0.985	±	0.061	0.406
N-(2-hydroxyethyl)iminodiacetic acid	0.852	±	0.092	1.131	±	0.145	0.348
N-acetyl-D-glucosamine	1.107	±	0.097	1.068	±	0.062	0.772
N-carbamyl-L-glutamic acid	0.810	±	0.179	1.086	±	0.097	0.209
N-ethylglycine	1.090	±	0.079	0.963	±	0.063	0.342
Norvaline	0.964	±	0.065	1.036	±	0.059	0.566
Oleic acid	0.758	±	0.153	1.063	±	0.088	0.122

O-phosphocolamine	0.960	±	0.123	1.095	±	0.083	0.450
Ornithine	0.762	±	0.051	1.165	±	0.092	0.036
Oxalic acid	0.479	±	0.076	1.322	±	0.074	<0.000
Palatinose	2.388	±	1.058	0.583	±	0.069	0.004
Palmitic acid	0.990	±	0.083	1.026	±	0.044	0.716
Palmitoleic acid	0.986	±	0.389	0.967	±	0.120	0.952
Phenylalanine	1.054	±	0.081	1.026	±	0.042	0.772
Phosphoric acid	0.834	±	0.047	1.094	±	0.043	0.006
Pipecolic acid	1.279	±	0.204	0.925	±	0.098	0.121
Porphine	0.482	±	0.089	1.314	±	0.105	<0.000
Proline	0.902	±	0.097	1.026	±	0.089	0.505
Pyroglutamic acid	1.050	±	0.053	1.051	±	0.032	0.997
Pyrophosphate	0.860	±	0.083	1.125	±	0.046	0.013
Pyruvic acid	0.391	±	0.100	1.401	±	0.165	0.004
Ribitol	0.975	±	0.072	1.089	±	0.063	0.393
Ribose	0.869	±	0.265	1.245	±	0.371	0.620
Sedoheptulose anhydride monohydrate	0.862	±	0.194	1.175	±	0.188	0.426
Serine	0.907	±	0.055	1.041	±	0.055	0.249
Sorbitol	1.260	±	0.100	0.954	±	0.036	0.002
Stearic acid	1.005	±	0.072	1.029	±	0.049	0.827
Tartaric acid	0.725	±	0.130	1.155	±	0.085	0.024
Tartronic acid	0.880	±	0.139	1.118	±	0.089	0.223
Threitol	1.021	±	0.204	1.076	±	0.055	0.724
Threonine	0.968	±	0.082	1.037	±	0.048	0.517
Trans-4-hydroxy-L-proline	0.850	±	0.037	1.076	±	0.093	0.229
Trans-dehydroandrosterone	1.079	±	0.116	1.043	±	0.053	0.768
Trehalose	0.866	±	0.123	1.199	±	0.113	0.164
Tryptophan	1.627	±	0.188	0.764	±	0.100	<0.000
Tyrosine	0.783	±	0.089	1.133	±	0.067	0.017
Urea	0.958	±	0.094	1.047	±	0.057	0.473
Uric acid	0.800	±	0.139	1.116	±	0.106	0.166
Valine	0.913	±	0.073	1.084	±	0.050	0.121

Metabolites that differ between groups are written in bold.
*: P <0.05 indicates that the difference is statistically significant.
**: Data value after normalization to Internal standard.

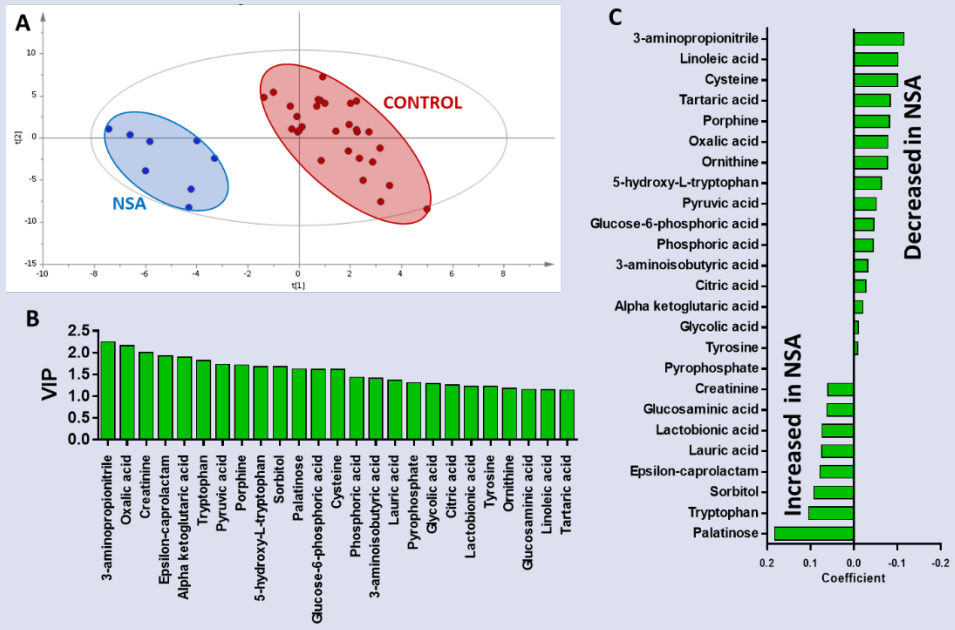

Figure 1. Comparison of plasma metabolic profiling of the control and nervous system abnormalities groups (A) Partial least squares differentiation analysis (PLS-DA) score plot showing a clear distinction between the groups (R^2: 0.614 and Q^2: 0.612); (B) Variable importance in projection (VIP) charts of metabolites that are effective in separating the groups; (C) Coefficient plots of the metabolic variables in the PLS-DA model.

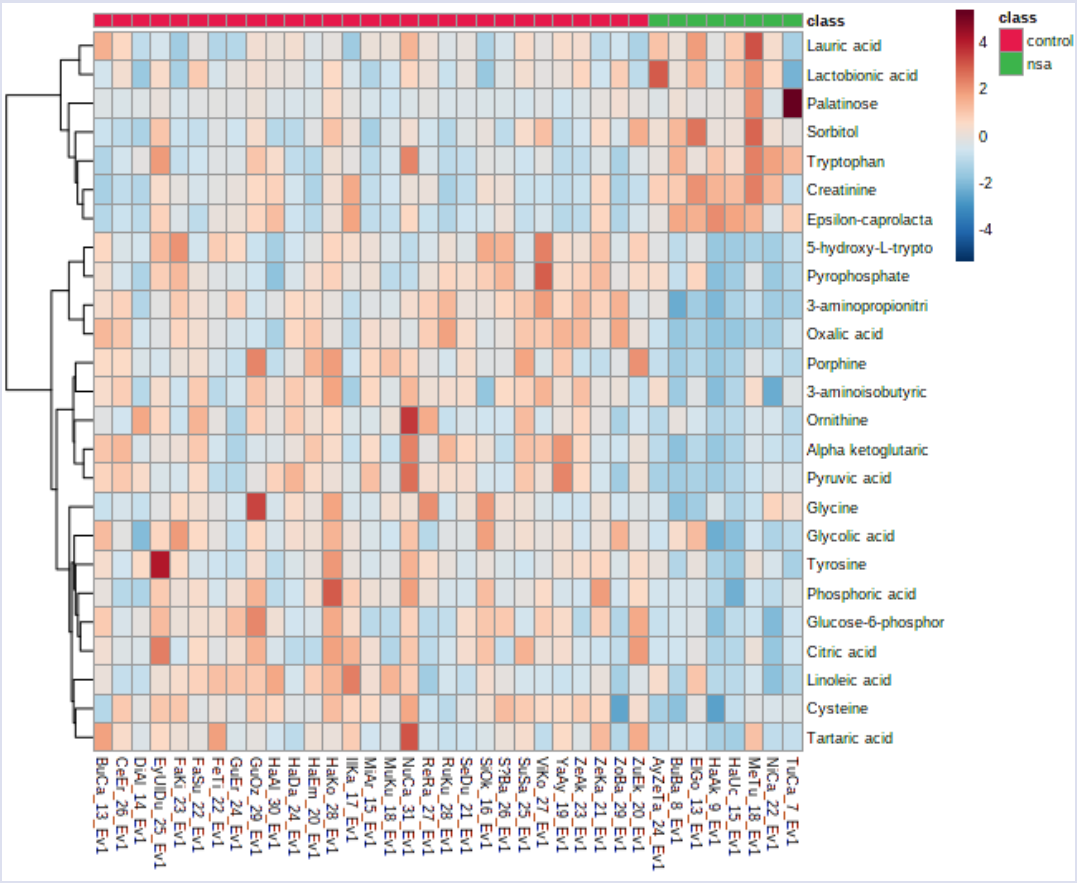

Figure 2. Heat color graphics of selected metabolites that are effective in the differentiation of metabolic profiles.

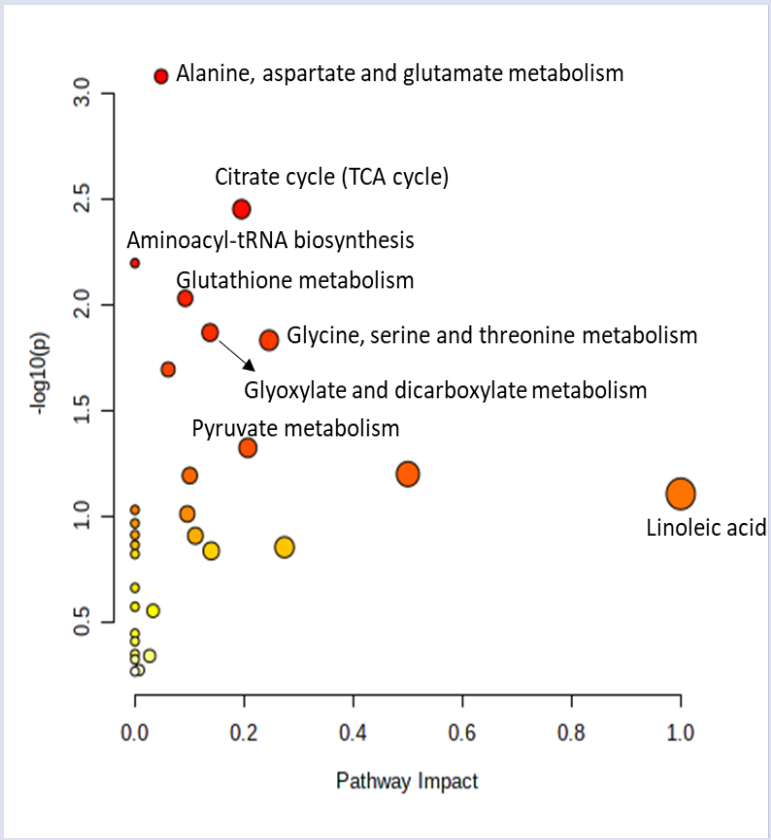

Figure 3. Pathway analysis.

Discussion

Numerous studies have revealed the involvement of the lysyl oxidase enzyme family in mouse models of tissue fibrosis in organs. Lsyl oxidase inhibitor 3 Aminopropionitrile inhibits LOX activity and inhibits the formation of collagen cross-links and fibrosis [18]. Linoleic acid is a long-chain polyunsaturated fatty acid. It is found in the brain's gray matter and makes up about 15% of the fatty acids in the human frontal cortex. Linoleic acid is of great importance for the development of the fetal brain and its deficiency may responsible for the development of neurological abnormalities [19-21]. Lauric acid, middle chain fatty acids, typically increased the mRNA expression of glial-derived neurotrophic factor (*GDNF*), interleukin-6 (*Il6*), and C–C motif chemokine 2 (*Ccl2*) in astrocytes and enhances the presynaptic maturation [22]. Cysteine, which plays a role in protein synthesis, also has critical importance in redox homeostasis due to its strong antioxidant properties. Redox-modulated events do not only occur in peripheral tissues, but it is better understood in the light of new information that these events also play critical roles in the brain. It is known that irregularities in cysteine metabolism are associated with various neurodegenerative disorders [23]. The dysregulation of lipid and redox homeostasis may be responsible for the development of neurological abnormalities.

The low level of intrinsic antioxidants such as tartaric acid and citric acid in the brain and the high level of polyunsaturated fatty acids pose a risk of oxidative stress-induced molecular damage [24]. Moreover high level of tartaric acid were found in autistic children [25]. The increase in the production of porphyrins and porphyrin precursors was found to result from partial enzyme blocks along the heme biosynthetic pathway, resulting in secondary depression of the enzyme Aminolevulinic acid synthase (ALA-synthase). Therefore, it is thought that neurological manifestations may be related to a decrease in essential heme proteins or other heme-containing compounds in the nervous system or to the toxic effect of overproduction of the porphyrin precursors ALA and porphobilinogen (PBG) [26]. The impact of the presence of oxalic acid was studied in the diseases of central nervous system, especially in schizophrenia [27, 28].

Ornithine carbamoyltransferase deficiency is the commonest of the inherited urea cycle disorders going together with disabling neurological complications [29]. L-5-hydroxytryptophan, which plays a role in various neurological and metabolic diseases, is a limiting step in the biosynthesis of serotonin and melatonin with its synthesis from tryptophan [30]. It has been reported that measurement of lactic acid and pyruvic acid in cerebrospinal fluid may be of help to detect various infectious diseases with central nervous system involvement [31, 32].

Glucose-6-phosphate (G6P) is a key metabolite in energy metabolism. The alteration of G6P may relate to either glucose-6-phosphate isomerase (GPI) or glucose-6-phosphate dehydrogenase (G6PD). Both deficiencies have an effect on neurological impairment and neuroprotection [33, 34]. In addition, muscle phosphate metabolism may be altered in various central nervous system disorders by different metabolic impairments [35]. β-hydroxybutyrate, a ketone body, is one of the main mediators of brain growth and myelin formation, as it is the main substrate of phospholipid and sphingolipid synthesis [36]. The alteration of the β-hydroxybutyrate in NSA may also evaluate inadequate nervous system development.

Alpha-ketoglutarate and citric acid are important molecules involved in the Krebs cycle. These molecules have critical roles in various metabolic pathways, especially in cellular energy metabolism. Moreover, alpha-ketoglutarate, which is a source of glutamate and glutamine, stimulates protein synthesis and prevents protein degradation in muscles, as it is a nitrogen scavenger [37].

The idea that the development of chronic metabolic diseases may be caused by excessive sugar consumption is increasing the use of sweeteners around the world. Palatinose is absorbed from the intestine and metabolized slowly by isomaltase, but the rate of insulin stimulation is very low. Different sweeteners are notable for human health because they affect the central nervous system, gut hormones, and gut microbiota [38]. Metabolism of tryptophan takes place along the kynurenine pathway, which has pronounced effects on neurons in the central nervous system. Changes in kynurenine levels are implicated in several central nervous system disorders such as AIDS-dementia complex and Huntington's disease [39]. It has been reported that sorbitol and myo-inositol metabolism are critical in the pathogenesis of peripheral neuropathy in patients with diabetes mellitus [40].

In this study, we have demonstrated that 3-aminopropionitrile, linoleic acid, cysteine, tartaric acid, porphine, oxalic acid, ornithine, 5-hydroxy-L-tryptophan, pyruvic acid, glucose-6-phosphoric acid, phosphoric acid, 3-aminoisobutyric acid, citric acid, alpha-ketoglutaric acid, glycolic acid, tyrosine, pyrophosphate, glycine and lactic acid plasma levels were statistically significantly lower in second-trimester pregnancies having fetuses with NSAs compared to control group pregnancies. On the other hand, palatinose, tryptophan, sorbitol, epsilon-caprolactam, lauric acid, lactobionic acid, glucosaminic acid and creatinine plasma levels were found to be higher in study group pregnancies compared to controls. Moreover, the pathway analysis, performed with significantly altered metabolites, showed alteration in the alanine, aspartate and glutamate metabolism, citrate cycle, aminoacyl t-RNA biosynthesis and glutathione metabolism. Thusly, this study identified altered pathways and suggested candidate biomarkers that could be used for the screening of NSA within the

framework of antenatal care programs. However, the finding must be validated with wider groups.

Our findings indicate a special type of altered metabolic status in pregnant women carrying fetuses with NSA(s) with or without co-abnormalities. It could be speculated that this altered metabolic status might influence both gametogenesis, embryogenesis and organogenesis at various levels. The main limitation of this study is the number of patients, heterogeneity of the NSAs and the presence co-abnormalities in 75% of the cases. On the other hand, this study will encourage prenatal screening/diagnosis programs to diversify their methodological approaches in this medical field.

In conclusion, "alanine, aspartate and glutamate metabolism", citrate cycle, aminoacyl t-RNA biosynthesis and glutathione metabolism seem to be critical in the prenatal screening of NSAs. However, abnormality specific studies are necessary for further recommendations.

Conflicts of interest

There are no conflicts of interest in this work.

References

[1] Joan S., Terry L., The basics of brain development, *Neuropsychol Rev,* 20 (2010) 327-348.

[2] Kaplan K.M,. Spivak J.M., Bendo J.A., Embryology of the spine and associated congenital abnormalities, *The Spine Journal,* 5 (5) (2005) 564-576.

[3] Spirt B., Oliphant M., Gordon L., Fetal central nervous system abnormalities, *Radiologic Clinics of North America,* 28 (1) (1990) 59-73.

[4] Aydın E., Tanacan A., Büyükeren M., Uçkan H., Yurdakök M., Beksaç M.S., Congenital central nervous system anomalies: Ten-year single center experience on a challenging issue in perinatal medicine, *Journal of the Turkish German Gynecological Association,* 20 (3) (2019) 170.

[5] Tanacan A., Ozgen B., Fadiloglu E,. Unal C., Oguz K.K., Beksac M.S., Prenatal diagnosis of central nervous system abnormalities: Neurosonography versus fetal magnetic resonance imaging, *European Journal of Obstetrics & Gynecology and Reproductive Biology,* 250 (2020) 195-202.

[6] Pulikkunnel S.T., Thomas S., Neural tube defects: pathogenesis and folate metabolism, *The Journal of the Association of Physicians of India,* 3 (2005) 127-135.

[7] Obeid R., Oexle K., Rißmann A., Pietrzik K., Koletzko B., Folate status and health: challenges and opportunities, *Journal of perinatal medicine,* 44 (3) (2016) 261-268.

[8] Greene N.D., Leung K.Y., Copp A.J., Inositol, neural tube closure and the prevention of neural tube defects, *Birth defects research,* 109 (2) (2017) 68-80.

[9] Beaudin A.E., Stover P.J., Folate-mediated one-carbon metabolism and neural tube defects: Balancing genome synthesis and gene expression, *Birth Defects Research Part C: Embryo Today: Reviews,* 81 (3) (2007) 183-203.

[10] Stokes B.A., Sabatino J.A., Zohn I.E., High levels of iron supplementation prevents neural tube defects in the Fpn1ffe mouse model, *Birth defects research,* 109 (2) (2017) 81-91.

[11] Berihu B.A., Welderufael A.L., Berhe Y., Magana T., Mulugeta A., Asfaw S., Gebreselassie K., Maternal risk factors associated with neural tube defects in Tigray regional state of Ethiopia, *Brain and Development,* 41 (1) (2019) 11-18.

[12] Welderufael A.L., Berihu B.A., Berhe Y., Magana T., Asfaw S., Gebreselassie K., Belay E., Kebede H., Mulugeta A., Nutritional status among women whose pregnancy outcome was afflicted with neural tube defects in Tigray region of Ethiopia, *Brain and Development,* 41 (5) (2019) 406-412.

[13] Recber T., Orgul G., Aydın E., Tanacan A., Nemutlu E., Kır S., Beksac M.S., Metabolic infrastructure of pregnant women with methylenetetrahydrofolate reductase polymorphisms: A metabolomic analysis, *Biomedical Chromatography,* 34 (8) (2020) e4842.

[14] Beksaç M.S., Durak B., Özkan Ö., Çakar A.N., Balci S., Karakaş Ü., Laleli Y., An artificial intelligent diagnostic system with neural networks to determine genetical disorders and fetal health by using maternal serum markers, *European Journal of Obstetrics & Gynecology and Reproductive Biology,* 59 (2) (1995) 131-136.

[15] Nemutlu E., Orgul G,. Recber T., Aydin E., Ozkan E., Turgal M., Alikasifoglu M., Kir S., Beksac M.S., Metabolic infrastructure of pregnant women with trisomy 21 fetuses; metabolomic analysis, *Zeitschrift für Geburtshilfe und Neonatologie,* 223 (05) (2019) 297-303.

[16] Monni G., Atzori L., Corda V., Dessolis F., Iuculano A., Hurt K.J., Murgia F. Metabolomics in prenatal medicine: A review, *Frontiers in Medicine,* 771 (2021).

[17] Özkan E., Nemutlu E., Beksac M.S., Kır S., GC–MS analysis of seven metabolites for the screening of pregnant women with Down Syndrome fetuses, *Journal of Pharmaceutical and Biomedical Analysis,* 188 (2020) 113427.

[18] González-Santamaría J., Villalba M., Busnadiego O., López-Olañeta M.M., Sandoval P., Snabel J., López-Cabrera M., Erler J.T., Hanemaaijer R., Lara-Pezzi E., Matrix cross-linking lysyl oxidases are induced in response to myocardial infarction and promote cardiac dysfunction, *Cardiovascular research,* 109 (1) (2016) 67-78.

[19] Holman R., Johnson S., Hatch T., A case of human linolenic acid deficiency involving neurological abnormalities, *The American journal of clinical nutrition,* 35 (3) (1982) 617-623.

[20] Meng H., A case of human linolenic acid deficiency involving neurological abnormalities, *The American journal of clinical nutrition,* 37 (1) (1983) 157-159.

[21] Basak S., Mallick R., Duttaroy A.K., Maternal docosahexaenoic acid status during pregnancy and its impact on infant neurodevelopment, *Nutrients,* 12 (12) (2020) 3615.

[22] Nakajima S., Kunugi H., Lauric acid promotes neuronal maturation mediated by astrocytes in primary cortical cultures, *Heliyon,* 6 (5) (2020) e03892.

[23] Paul B.D., Sbodio J.I., Snyder S.H., Cysteine metabolism in neuronal redox homeostasis, *Trends in pharmacological sciences,* 39 (5) (2018) 513-524.

[24] Gutteridge J., Oxidative stress in neurobiology: An important role for iron. In: *Oxidative Stress and Aging.* edn.: Springer, (1995) 287-302.

[25] Shaw W., Kassen E,. Chaves E., Increased urinary excretion of analogs of Krebs cycle metabolites and arabinose in two brothers with autistic features, *Clinical chemistry,* 41 (8) (1995) 1094-1104.

[26] Becker D.M., Kramer S., The neurological manifestations of porphyria: a review, *Medicine,* 56 (5) (1977) 411-423.

[27] Kuberski Z., Behavior of oxalic acid in diseases of the central nervous system with regard to investigation of cerebrospinal fluid, *Neurologia, neurochirurgia i psychiatria polska,* 6 (5) (1956) 521-526.

[28] Sciorta A., Blood and cerebrospinal fluid level of oxalic acid in schizophrenia, *Rivista sperimentale di freniatria e medicina legale delle alienazioni mentali,* 78 (2) (1954) 391-408.

[29] Nicolaides P., Liebsch D., Dale N., Leonard J., Surtees R., Neurological outcome of patients with ornithine carbamoyltransferase deficiency, *Archives of disease in childhood,* 86 (1) (2002) 54-56.

[30] Maffei M.E., 5-Hydroxytryptophan (5-HTP): Natural occurrence, analysis, biosynthesis, biotechnology, physiology and toxicology, *International journal of molecular sciences,* 22 (1) (2020) 181.

[31] Choremis K., Constantinides V., Nicolaides P., Pyruvic acid in the cerebrospinal fluid during various infectious diseases with central nervous system involvement. In: *Annales paediatrici International review of pediatrics,* (*1*953) 337-345.

[32] Duinkerke S., Gabreëls F., Boerbooms A.T., Kok J., Renier W., Can determination of lactic acid and pyruvic acid in cerebrospinal fluid help in diagnosing central nervous system involvement in systemic lupus erythematosus?, *Clinical neurology and neurosurgery,* 85(4) (1983) 225-230.

[33] Kugler W., Breme K., Laspe P., Muirhead H., Davies C., Winkler H., Schröter W., Lakomek M., Molecular basis of neurological dysfunction coupled with haemolytic anaemia in human glucose-6-phosphate isomerase (GPI) deficiency, *Human genetics,* 1998, 103 (4) (1998) 450-454.

[34] Tiwari M., Glucose 6 phosphatase dehydrogenase (G6PD) and neurodegenerative disorders: Mapping diagnostic and therapeutic opportunities, *Genes & diseases,* 4 (4) (2017) 196-203.

[35] Argov Z., De Stefano N., Arnold D., Muscle high-energy phosphates in central nervous system disorders. The phosphorus MRS experience, *The Italian Journal of Neurological Sciences,* 18 (6) (1997) 353-357.

[36] Tanianskii D.A., Jarzebska N., Birkenfeld A.L., O'Sullivan J.F., Rodionov R.N., Beta-aminoisobutyric acid as a novel regulator of carbohydrate and lipid metabolism, *Nutrients,* 11 (3) 2019) 524.

[37] Wu N., Yang M., Gaur U., Xu H., Yao Y., Li D., Alpha-ketoglutarate: physiological functions and applications, *Biomolecules & therapeutics,* 24 (1) (2016) 1.

[38] Moriconi E., Feraco A,. Marzolla V., Infante M., Lombardo M., Fabbri A., Caprio M., Neuroendocrine and metabolic effects of low-calorie and non-calorie sweeteners, *Frontiers in Endocrinology, (*2020) 444.

[39] Stone T.W., Mackay G.M., Forrest C.M., Clark C.J., Darlington L.G., Tryptophan metabolites and brain disorders, (2003).

[40] Mosiewicz J., Grzywa M., Disorders of sorbitol and myoinositol metabolism and the activity of sodium, potassium ATPase in the pathogenesis of peripheral neuropathy in patients with diabetes mellitus, *Polski Tygodnik Lekarski (Warsaw, Poland: 1960),* 47 (1-2) (1992) 56-58.

Cumhuriyet Sci. J., 44(2) (2023) 244-253
DOI: https://doi.org/10.17776/csj.1206615

Cumhuriyet Science Journal

| csj.cumhuriyet.edu.tr | Founded: 2002 ISSN: 2587-2680 e-ISSN: 2587-246X Publisher: Sivas Cumhuriyet University

Concomitant strain of *Bacillus vallismortis* BR2 and *Escherichia coli* Khodavandi-Alizadeh-2 for Biocatalytic Synthesis of Fatty Acid Methyl Ester from Waste Oil Feedstock

Michael Bamitale Osho [1,a,*], Olayinka Mary Otolorin [1,b]

[1] *Department of Biological Sciences (Microbiology Unit), College of Natural and Applied Sciences, McPherson University, Km 96, Lagos-Ibadan Expressway, Seriki Sotayo, P.M.B. 2094, Sapon, Abeokuta, Ogun State, Nigeria*

**Corresponding author*

Research Article

History
Received: 18/11/2022
Accepted: 20/06/2023

ABSTRACT

Bacillus vallismortis BR2 and Escherichia coli Khodavandi-Alizadeh-2 lipases (E.C.3.1.1.3) were used to produce fatty acid methyl ester (FAME), a sustainable source of fuel. The lipase activity was measured using the titrimetric method after it was extracted from a solid fermented substrate in phosphate buffer. The use of Central Composite Design to optimize condition parameters was examined, while qualitative and quantitative assessments of FAME samples were performed using GC-MS with MSD in scan mode and selective ion monitoring. Lipase activity peaked at 24 h and then declined as the incubation time went on. The independent variables, such as pH, temperature, agitation, incubation time and enzyme quantity, all had an effect on biodiesel yield since they were all significant in the rate of biodiesel yield. FAME yield increased significantly after adding 1 to 2 mL of enzyme and a pH range of 4.57143 to 7.42857, but thereafter declined. The chromatograms indicated a peak of cis-10-Heptadecanoic acid methyl ester with concentrations of 39.95 mg/L and 58.95 mg/L in the FAME molecules. The viscosity (3.67 m3/s), specific gravity (0.813 g/cm3), flash point (102.70 °C), cetane number (55.52), and pour point (-24 °C) of the fuel were also measured. The synthesized biodiesel from the spent oil through the synergic enzymes were found to be a simple, effective, and sustainable fuel production process, as well as a potential means of eliminating pollution caused by haphazard waste cooking oil disposal.

Keywords: Bacillus vallismortis BR2, Concomitant Lipase, Escherichia coli Khodavandi-Alizadeh-2, Fatty Acid Methyl Ester, Waste cooking Oil.

[a] oshomb@mcu.edu.ng https://orcid.org/0000-0003-1177-8363 [b] otolorinolayinka@gmail.com https://orcid.org/0009-0000-1306-1839

Introduction

The sources of non-renewable energy are natural gas and petroleum (about 90% of the global energy production that powers the economy). Due to the unavailability and exhaustibility of this fossil fuel as a result of increasing population and industrialization, another substitute like waste cooking oil (WCO) is hereby sourced [1,2]. Biodiesel is a fuel replacement because it is environmentally safe and benign, and it can be blended or used directly with conventional gasoline in uncontaminated diesel engines. It contains no sulfur, no aromatics and possesses a higher cetane number (> 47), with 10%–11% oxygen by weight, as in contrast with petrol [3], thereby minimizing the emission of hydrocarbons, carbon monoxide and particle pollution in the exhaust gas. Biodiesel is usually synthesized by transesterification of pure vegetable oils with short-chain alcohols using alkaline catalysts. A high-quality food-grade vegetable oil is needed with a low level of free fatty acids (FFA), leading to low biodiesel conversion and difficulties in glycerol separation, so saponification is avoided.

Several reports have been made in regard to the utilization of lipase from single strains of organisms such as Alternaria sp. MGGP 06, Aspergillus niger ATCC 1015; Candida rugosa PV 0514; Aspergillus niger F7-02; Aspergillus terreus [4-8] but a coexisting mixture of such enzymes is being reported to enhance the specificity of the enzyme.

Response surface methodology (RSM) has been widely applied in biodiesel production and as an assemblage of statistical and mathematical techniques useful for patterning and evaluating problems in which a desired response is controlled by some variables [8]. Variable factors include substrate molar ratio, pH, temperature, agitations optimized for biodiesel synthesis using immobilized lipase in biomimetic silica, or flow rate, substrate molar ratio, and temperature using a lipase-catalyzed packed-bed reactor for steady biodiesel production [2]. Several variables influence the transesterification reaction, including catalyst concentration, presence of water, substrate molar ratio of alcohol and free fatty acid content in oil feedstock, time, agitation speed, and temperature. In order to make environmentally friendly and economically viable biodiesel, an understanding of the factors is very important [9-10].

This present study is aimed at optimizing the synthesis of biodiesel from a cheaper waste oil using the

concomitant lipase of *Bacillus vallismortis* BR2 and *Escherichia coli* Khodavandi-Alizadeh-2 strains. The relative effects of some condition parameters and their concentrations were determined. GC-MS was used to analyze the chemical constituents of biodiesel, and the fuel characteristics were also checked for conformity to American Society for Testing Materials (ASTM) standards.

Materials and Methods

Materials

Potential microorganisms were isolated from soil samples collected from a mechanic workshop in Mowe, Ogun State (Longitude 6.811°N and Latitude 3.437°E) and McPherson University, Seriki Sotayo, Obafemi Owode Local Government Area, Ogun State, Nigeria.

Methods

Sample Collection

The soil sample was obtained from an oil-polluted site at Mowe, Obafemi Owode, and McPherson University, Seriki Sotayo, Ogun State. Soil samples and waste cooking oil were packed in sterile bottles and taken to the laboratory.

Isolation of lipase producing bacteria

Isolation of potential bacterial isolates that can degrade petroleum was carried out using the serial dilution and the pour plate methods on Nutrient Agar and was incubated at 37 °C for 24 h. Pure cultures of the isolates were maintained on slants at 27 °C and sub-cultured for fourteen consecutive days to conserve their efficaciousness.

Lipase Production on Solid-State Fermentation (SSF)

Solid-state fermentation was used to produce the lipase. The medium used to be made up of a specific wheat offal solid substrate (10 g). The petri dish media was wet with 15 mL distilled water, autoclaved for 15 min at 121 °C, and allowed to cool. It was inoculated with 0.5 mL of three-day-old broth cultures of *E. coli* Khodavandi-Alizadeh-2 and *B. vallismortis* BR2 and incubated for 24-96 h at 37 °C. One (1) gram of culture was placed in a test tube with 10 mL of phosphate buffer (mixed) and centrifuged for 10 minutes at 4000 rpm. The extracellular enzyme (supernatant) was collected in sterile test tubes and utilized to determine lipase activity. The enzyme activity was determined using the titrimetric method with olive oil as a substrate according to Pualsa *et al.,* [11]. The enzyme (0.1 mL) was added to an emulsified olive oil substrate (buffered with 0.1 M potassium phosphate pH 7) and incubated for 15 minutes at 37 °C. Fatty acid was extracted using a 1.0 mL acetone-ethanol (1:1) solution, and the amount liberated was determined using a titration against 0.1 N NaOH with phenolphthalein indicator until light pink coloring appeared. A blank reading (no enzyme) was taken.

The activity of lipase was measured using:

$$\mathrm{U/mL} = \frac{[(\text{mL NaOH for sample} - \text{mL NaOH for blank}] \text{ x N}}{\text{Amount of Lipase (mL) x Reaction time}} \qquad \text{Eq. 1}$$

Where N= Normality of NaOH

One unit of lipase is defined as the amount of lipase needed to hydrolyze 1 mol of fatty acids from triglycerides equivalent per minute under the assay conditions.

Fatty Acid Methyl Ester (Biodiesel) from WCO

Mixed lipases from *Escherichia coli* Khodavandi-Alizadeh-2 and *Bacillus vallismortis* BR2 were used to produce biodiesel. Muslin cloth was used to treat waste cooking oil (WCO) to remove dirt and other undesired particles that could interfere with the biodiesel synthesis process. Thus, the WCO is being refined for improved performance. In three sequential methanol additions for biodiesel manufacture using waste cooking oil, the substrate molar ratio of oil to methanol (3:1) was employed. The reaction was co-catalyzed by free lipase of the two distinct microorganisms (1 mL each) at 45 °C for 200 rpm in a shaking incubator during varied reaction time intervals of 24 h, 48 h, and 72 h, respectively. After 72 h of reaction time, the mixture was put into a 100 ml separating funnel to separate the fatty acid methyl ester and placed in a sterile vial for analysis.

Concurrent lipase from E. coli Khodavandi-Alizadeh 2 and B. vallismortis BR2 used to Optimize Biodiesel Production

Design of experiments

Response surface methodology (RSM) provided by Design-Expert software 13.0 was used to create and optimize the biodiesel synthesis (Stat-Ease Inc., Minneapolis, USA). The catalyzed transesterification reaction variable was investigated using the central composite design (CCD), a common RSM design technique. The six identified independent factors are pH (4–8), agitation (100–300 rpm), incubation period (24–96 h), substrate molar ratio (1:1–1:4 methanol: oil), enzyme amount (1–3 ml), and temperature (35–55 °C). A five-level central composite matrix was used, and 13 runs were performed in random order. To circumvent lipase inhibition, methanol was added in three steps for biodiesel production utilizing modifier's approach of Fan *et al*. [12]. The first batch was made at the start of the reaction, and the others were made at 16 h, 32 h, and 48 h into the reaction, which took 96 h in a 100 mL conical flask and was incubated in a shaker incubator for 96 h. The sample was poured into a 100 mL screwedcapped se parating funnel at the end of the reaction. The upper layer was used to calculate the % yield using Nazir *et al*. [13]. Following that, gas chromatograph-mass spectroscopy (GC-MS) analysis was performed as previously reported.

Analysis of Biodiesel

Yield of biodiesel estimation

The FAME yield (percent) was a dependent variable that was defined as the weight of methyl ester divided by the expressible weight of oil. Equation 2 below shows how the yield of FAME in the samples was estimated.

$$\text{Yield (Y)} = \frac{\text{methyl ester weight x } 100\%}{\text{Weight of oil}} \quad \text{Eq. 2}$$

Fatty Methyl Ester (Biodiesel) Gas Chromatography (GC) Analysis

Sigma Aldrich provided a SUPELCO 37-Component FAME MIX (Catalog Number: LRAC1814), which had 37 FAMES components. Before calibration, the MS was auto-tuned to perfluorotributylamine (PFTBA) by checking the abundance of m/z 69, 219, 502 and other instrument optimum and sensitivity settings. To ensure low-level detection of the target constituents, the levels of FAMES in the sample were determined using GC-MS in selective ion monitoring (SIM) and Scan mode.

Preparation of Samples

The samples were diluted by a factor of 5 (100 uL sample + 400 uL n-Hexane) in vials before GC analysis. An Agilent 6890N gas chromatograph coupled to a 5973C inert mass spectrometer (with triple-axis detector) with an electron-impact source (Agilent Technologies) was used. The stationary phase of separation of the compounds was the HP-5 capillary column coated with 5% Phenyl Methyl Siloxane (30m length x 0.32mm diameter x 0.25m film thickness) (Agilent Technologies). The carrier gas was hydrogen, used at a constant flow of 1.48 mL/min at an initial nominal pressure of 1.49 psi and an average velocity of 44.22 cm/sec. Each sample (1µL) was injected in splitless mode at 300 °C injection temperature. The purge flow rate to the spilled vent was 15.0 mL/min for 0.75 min, for a total flow of 16.67 mL/min, with gas saver mode turned off. The oven was set at 100 °C for 5 mins before ramping up to 250 °C at a rate of 7 °C per minute (2 min). With a three-minute solvent delay, the overall run time was 28 mins. The mass spectrometer was run in electron-impact ionization mode at 70eV with a 230 °C ion source, 150 °C quadrupole, and 300 °C transfer line. Following calibration, the samples were examined, and corresponding FAME concentrations were calculated using the calibration curve equation, if detected based on a retention time match of the FAME standard. The quantity (g/mL). The following formula is used to determine the amount of FAME in the sample (g/mL):

$$\text{g/mL of FAME} = \frac{(\text{Total Amount (Ug/mL) x DF x 1g})}{1000000\text{ug}} \quad \text{Eq. 3}$$

where DF = 5

g/mL was multiplied by 100 to get g/100mL = % (w/v) FAME

Characterizations of Biodiesel

The fatty acid methyl ester samples from the optimal experimental point were characterized for cloud point, pour point, flash point, viscosity, cetane number, and specific gravity to see if the standards set by the American Society for Testing Materials (ASTM) and the European Union (DIN EN-14214) were met.

Measurement of Viscosity

The viscosity of the samples was determined using a viscometer according to the ASTMD 445 protocol. A screw on the vertical pole was used to raise the viscometer to its greatest level. The viscometer was lowered until the spindle was submerged to the spindle's mark and reading taken within 60 s.

Pour-Point Determination

The level mark was filled with two grams of the sample. The test jar was immersed in a bath of crushed ice and the cork carrying the test thermometer was carefully closed. The test jar was inspected every three (3) min by placing it in a horizontal position for a few seconds before returning it to cool. When the oil surface remained upright for 5 s without sagging, it was considered to be at the pour point. The thermometer was inserted at this point and allowed to cool for 10 s before taking the oil's temperature.

Flash Point Determination

Using an ASTM D 93 flash tester, the sample's flashpoint was determined to be 120 °C as outlined in ASTM D 93. A closed-cup test that retains the fumes created and effectively simulates the situation where an ignite source is mistakenly introduced into a container. The oil was placed in a cup, which had a tight-fitting lid. Heat was applied to the cup and the oil. Apertures in the lid were then opened to allow air into the cup, and the ignition source was dipped into the vapors to see if a flash occurred. The flashpoint was determined by heating the oil in a cup and then inserting a tiny flame slightly above the liquid surface. The flash/ignition temperature is recorded as the flash point.

Determination of Specific Gravity

A 25 ml crystal clear specific gravity bottle was weighed, filled, and reweighed with the sample (W1). After washing and drying the density bottle, the sample was replaced with water, and the weight was recorded as W2. The specific gravity (S.G.) was calculated using the following formula:

$$\text{S.G.} = \frac{W1 - W0}{W2 - W0}$$

W0 = Initial weight of density bottle

Analytical Statistics

The response surface methodology of Design-Expert Software 13 was used to analyze the experimental data collected from the CCD. The ideal point between the

response variable (FAME yield) and the independent variables of transesterification is predicted using a second-order polynomial equation model. The coefficients of determination (R2) and the regression coefficient significant were used to assess the fit model's quality (analysis of variance [ANOVA]). By keeping two of the independent variables fixed while changing the other three, response surfaces and contour plots were created using the quadratic polynomial equation obtained through regression analysis of experimental data.

Results and Discussion

Lipase-producing Bacterial Isolation and Identification

From the soil samples, four microorganisms were recovered. The most promising microbe was chosen and identified by morphological, biochemical, and molecular characterization utilizing 16S r sequencing-based. Because of the abundance of lipids, oil-contaminated soil is thought to be a perfect habitat for lipase-producing bacteria. These lipids are used as a source of nutrition by the bacteria that live there [14]. Jenisha & Renuga [15] described the occurrence of lipase positive strains from comparable sources in isolate samples taken from various habitats. The lipase activity of the *Escherichia coli* strain detected in soil samples from the mechanic's workshop was greater. This adds to the evidence that the biological system's state and behavior are influenced by the environment [16]. The identification of *Escherichia coli* and *Bacillus vallismortis* in petroleum-contaminated locations is consistent with prior research by Giwa and Ibitoye [17]; Rong et al. [18], which discovered *E. coli* and *Bacillus* sp. in similar conditions among other microbes. The microbes were cultured on wheat offal and lipase was produced by solid state fermentation. The organisms' development on a wheat offal substrate matches previous study by D'hoe et al., [19]; Ji et al., [20], in which wheat offal was used to synthesis enzymes including amylase and lipase.

Polymerase Chain Reaction (PCR) and PCR-amplified DNA Identification

The DNA was amplified using standard PCR and illuminations (Not shown), and then seen on an agarose gel electrophoresis under UV light. The molecular weight was determined using a 1 kb DNA ladder, and the amplicon size was around 1500 bp. Table 1 shows the distribution of species detected in the DNA bacterium isolate library based on an investigation of a PCR product sequence in the non-redundant nucleotide database of the National Center for Biotechnology Information (NCBI). *Escherichia coli* Khodavandi-Alizadeh-2 and *Bacillus vallismortis* BR2 were identified as the isolates with accession numbers MN186856 and MK880631, respectively. The highest percentages of identity were 84 percent and 74%, respectively. On agarose gel electrophoresis of the template DNA amplified by PCR, the base pair of the isolated microorganisms was indicated in comparison to the PCR marker (Not shown). The gene template had the same molecular weight as the gene itself, at 1500 bp. Figures 1 and 2 show the phylogenic trees for the query organisms *Escherichia coli* Khodavandi-Alizadeh-2 and *Bacillus vallismortis* BR2 as well as nearby species. The organisms' nucleotide sequences matched those of *Escherichia coli* and *Bacillus vallismortis* in the NCBI database. Using the nucleotide sequence as a query, a gene bank and phylogenetic trees indicating comparable organisms were generated.

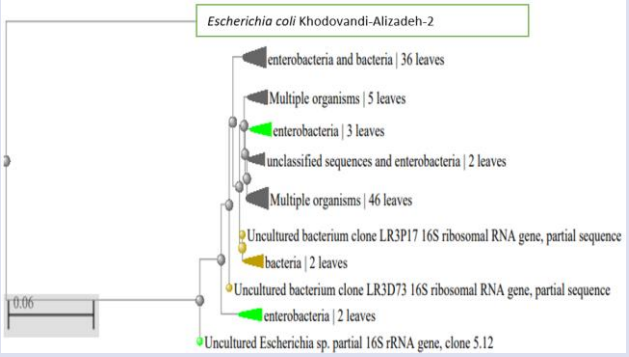

Figure 1: Phylogenic tree showing the query organism *Escherichia coli* Khodavandi-Alizadeh-2 and close species

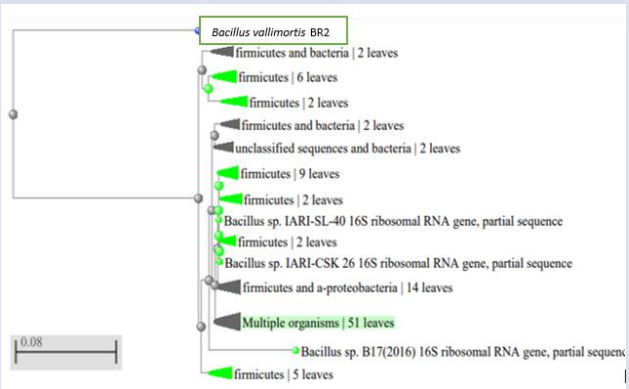

Figure 2: Phylogenic tree showing the query organism *Bacillus vallismortis* BR2 and close species

Lipase Activity Determination

Lipase activity was determined using the titrimetric method according to Pualsa et al. [11] approach, which was described in section 3.3.2, and the lipase activity was estimated using Equation 1. The lipase activity increases after 24 h and diminishes as the incubation duration increases (Fig 3). The lipase activity was measured using the titrimetric method with olive oil (10% v/v) as a substrate, emulsified with gum Arabic (5% w/v) in 0.1M potassium phosphate pH 7.0 and 0.1ml of enzyme, then incubated at 37 °C for 15 minutes. After 24 h, the lipase activity rose, which is consistent with Çağatay and Aksu [21] findings on lipase produced from waste cooking oil. The application of complicated composites design was offered by Stat-Ease Inc.'s Design Expert software 13.0 (Minnepolis, USA). Independent variables such as pH, temperature, agitatio

n, and others influenced the increase and reduction of bi odiesel output, as they all have a substantial impact on th e rate of biodiesel yield. Mohammed et al., [22] used a si milar methodology and came to the same conclusions as the study.

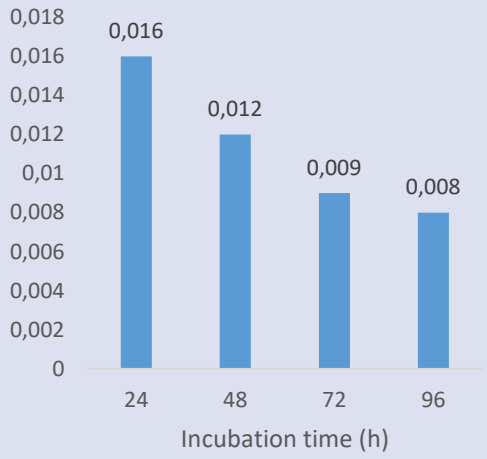

Figure 3: Activity of concomitant lipase of *Escherichia coli* Khodavandi-Alizadeh-2 and *Bacillus vallismortis* BR2 on Solid State Fermentation medium

Optimization of Biodiesel

Statistical model analysis

Figure 4 shows the results of the 13 experimental runs performed using the Design Expert 13.0 software. The outcome was studied and a second polynomial equation was fitted (Equation 1).

$$Y = \beta o + \Sigma 3i=1\ \beta iXi + \Sigma 3i=1\ \beta iiXi2 + \Sigma\Sigma 3i<i=1 \beta ijXiXj \quad \text{Eq. 1}$$

Where Y is response (Lipase production); β (0=intercept, i=linear, ii=quadratic and ij=interaction) and Xi, Xj (i=1, 4; j=1, 4; I ≠ j represent the coded independent variables) are the model coefficients.

Final Equation in Terms of Coded Factors

$$\begin{aligned}\text{FAME Yield} = {} & +23.00 + 0.0000x1 + 2.24x2 + 2.24x3 + \\ & 2.56x4 - 3.51x5 - 4.15x6 + 0.0000x1x2 + 0.0000x1x3 \\ & + 0.0000x1x4 + 0.0000x1x5 + 0.0000x1x6 + \\ & 0.0000x2x3 + 0.0000x2x4 + 0.0000x2x5 + \\ & 0.0000x2x6 + 0.0000x3x4 + 0.0000x3x5 + \\ & 0.0000x3x6 + 0.0000x4x5 + 0.0000x4x6 + \\ & 0.0000x5x6 - 4.90x12 + 3.47x22 + 1.84x32 + 3.27x42 \\ & + 0.2041x52 + 6.33x62\end{aligned} \quad \text{Eq. 2}$$

The best fit model, rather than the linear or cubic models, was suggested by the Statistical Model Fit Summary (which comprises of a sequential model sum of squares and a lack of fit tests). Although the cubic model has a smaller standard error than the quadratic model, the cubic model's presence of multiple aliased terms renders it unsuitable for representing the study. The data value in the quadratic model was aligned to the unit slope, indicating that it was the best model to capture the factor affecting biodiesel yield.

Table 1: Experimental design and response (biodiesel yield) of different experimental runs. Response of different experimental runs

		Factor 1	Factor 2	Factor 3	Factor 4	Factor 5	Factor 6	Response 1
Std	Run	A: pH	B: Temperature °C	C: Agitation rpm	D: Substrate Molar ratio mL	E: Enzyme Quantity mL	F: Incubation Time h	Biodiesel Yield %
3	1	6	35	200	2.5	2	60	28
11	2	6	45	200	2.5	2	24	45
10	3	6	45	200	2.5	3	60	18
12	4	6	45	200	2.5	2	96	32
13	5	6	45	200	2.5	2	60	23
4	6	6	55	200	2.5	2	60	35
7	7	6	45	200	1	2	60	27
5	8	6	45	100	2.5	2	60	24
2	9	8	45	200	2.5	2	60	11
6	10	6	45	300	2.5	2	60	31
1	11	4	45	200	2.5	2	60	11
8	12	6	45	200	4	2	60	35
9	13	6	45	200	2.5	1	60	29

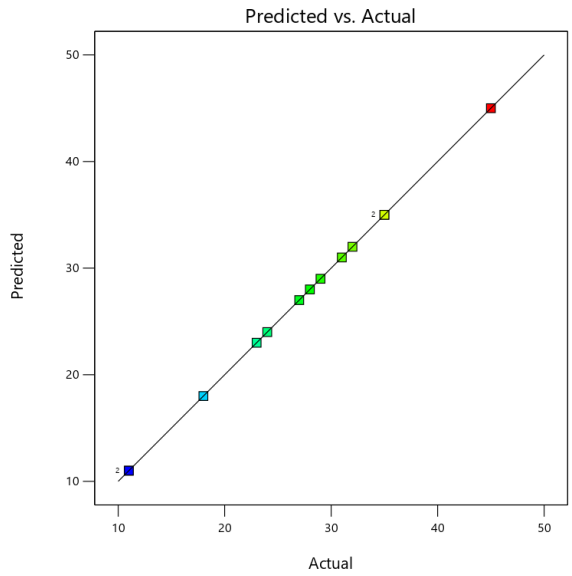

Figure 4: Model Fit Profile of Quadratic Model

FAME yield as a function of operational variables

FAME yield as a result of the main effect variables

The statistical analysis of the experiment range tested identified pH, temperature, agitation, and incubation time as significant determinants on the biodiesel yield response, as shown in Fig.5, although enzyme quantity and substrate molar ratio were the least significant factors. As the pH rises, so does the yield (fig.5a). Temperature had an effect on yield, with yield decreasing around 45 °C. Because the optimum yield was at 200 rpm and increasing agitation would have produced more yield, agitation has minimal effect on yield. Because the yield declined as the enzyme quantity was increased, the substrate molar ratio had no effect on yield.

The second-order models can be plotted as interactive contour and response surface graphs for each response, representing the biodiesel yield as a function of four of the six factors at the operating condition's center point value; thus, Fig 6 to 8 shows the interactive contour and response surface plot for the fitted model of the biodiesel molar yield.

The simultaneous dependency of FAME yield on enzyme quantity and reaction pH is shown in Figure 6. Temperature, agitation, substrate molar ratio, and incubation duration were all set to 45 °C, 200 rpm, 2.5 mL, and 48 h. FAME yield increased by 44 percent when the enzyme quantity was increased from 1 mL to 2 mL and the pH was elevated from 4.57143 to 7.42857, but subsequently declined as the enzyme quantity was increased from 2 mL to 3 mL. This means that the optimum yield can be obtained with 1 to 2 mL of enzyme and a pH range of 4.45143 to 7.42857.

The statistical analysis of the experiment range tested identified pH, temperature, agitation, and incubation time as significant determinants on the biodiesel yield response, as shown in Fig.5, although enzyme quantity and substrate molar ratio were the least significant factors. As the pH rises, so does the yield (fig.5a). Temperature had an effect on yield, with yield decreasing around 45 °C. Because the optimum yield was at 200 rpm and increasing agitation would have produced more yield, agitation has minimal effect on yield. Because the yield declined as the enzyme quantity was increased, the substrate molar ratio had no effect on yield.

The second-order models can be plotted as interactive contour and response surface graphs for each response, representing the biodiesel yield as a function of four of the six factors at the operating condition's center point value; thus, Fig 6 to 8 shows the interactive contour and response surface plot for the fitted model of the biodiesel molar yield.

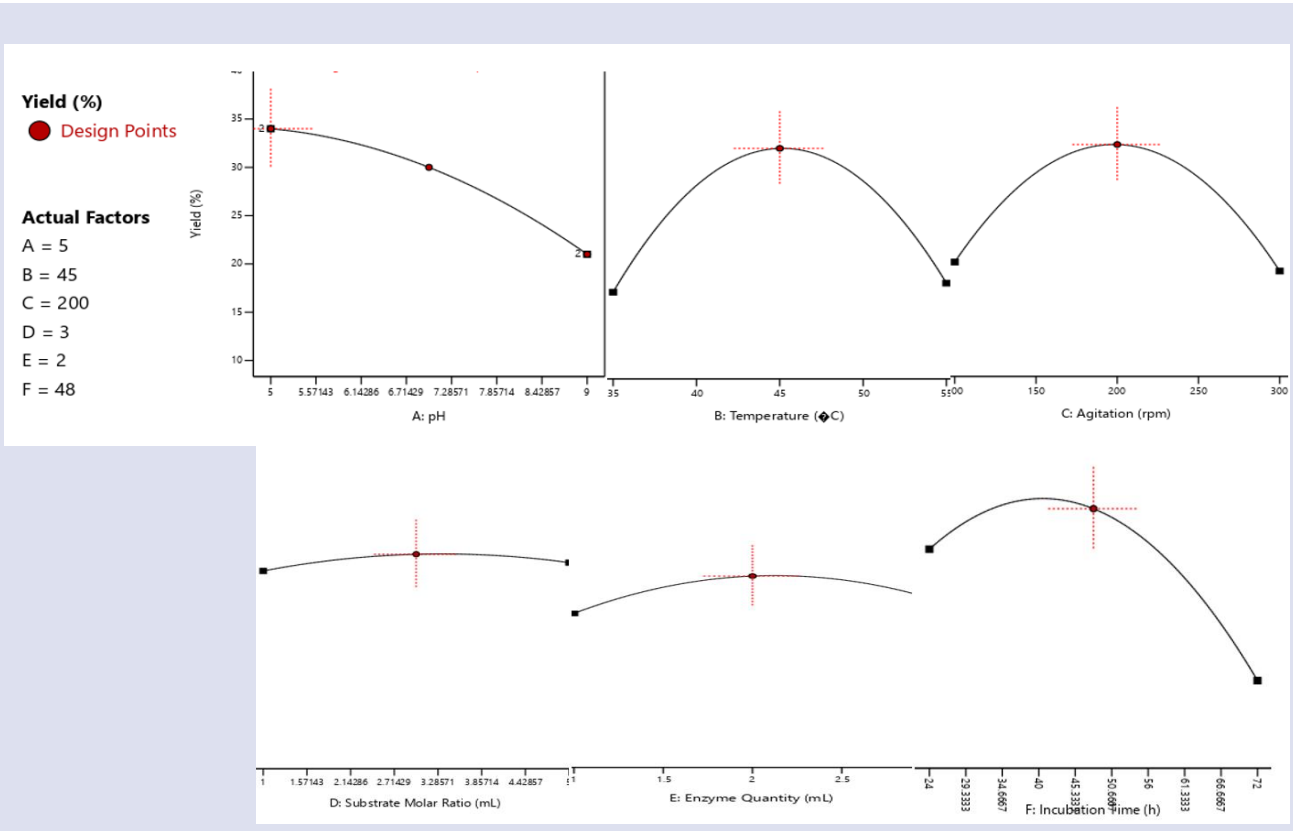

Figure 5(a- f): Plots of main variable effects of the FAME yield

The simultaneous dependency of FAME yield on enzyme quantity and reaction pH is shown in Figure 6. Temperature, agitation, substrate molar ratio, and incubation duration were all set to 45 °C, 200 rpm, 2.5 mL, and 48 h. FAME yield increased by 44 percent when the enzyme quantity was increased from 1 mL to 2 mL and the pH was elevated from 4.57143 to 7.42857, but subsequently declined as the enzyme quantity was increased from 2 mL to 3 mL. This means that the optimum yield can be obtained with 1 to 2 mL of enzyme and a pH range of 4.45143 to 7.42857

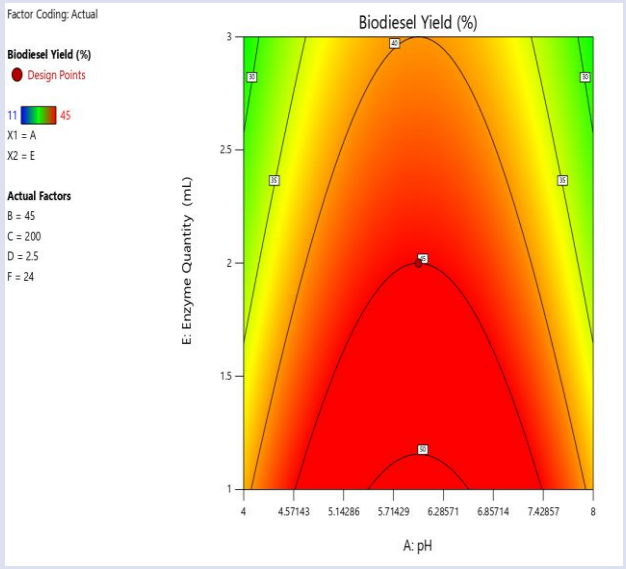

Figure 6: Interactive contour plot of biodiesel yield as function of Enzyme Quantity and pH: temperature (45° C); Agitation (200 rpm); Substrate molar ratio (2.5 ml); Incubation time (24 h)

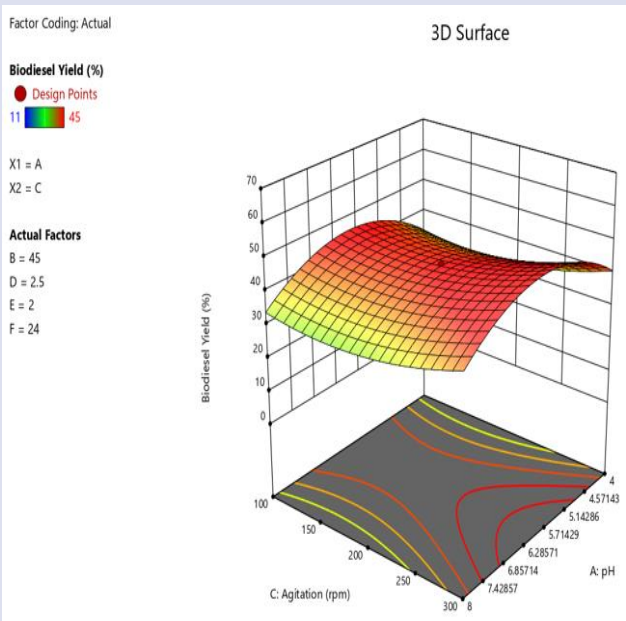

Figure 7: Response surface plot of biodiesel yield as function of Agitation and pH: temperature (45° C); Substrate molar ratio (2 ml); Enzyme Quantity (2 ml); Incubation time (24 h)

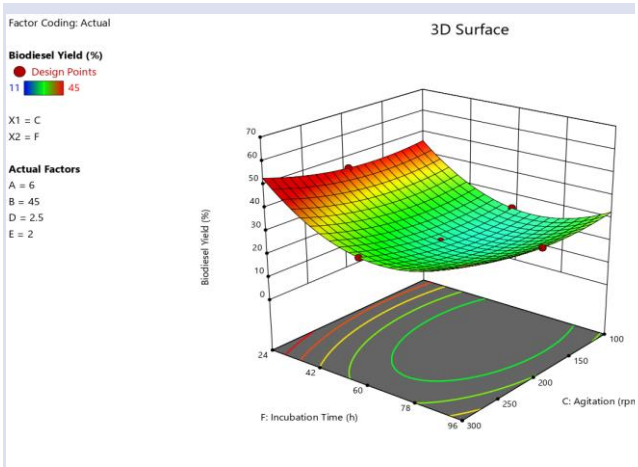

Figure 8: Response surface plot of biodiesel yield as function of Incubation time and Agitation: pH (6); temperature (45° C); substrate molar ratio (2.5 ml); Enzyme Quantity (2 ml)

Concurrent Lipases Catalyze the Transesterification of Waste Cooking Oil (WCO)

FAME produced by mixed lipase from *E. coli* Khodavandi-Alizadeh-2 and *B. vallismortis BR2* in the transesterification of WCO and methanol to a control experiment (without enzyme) (Not shown). Mixed lipase from *E. coli* Khodavandi-Alizadeh-2 and *B. vallismortis* BR2 were used in the flask's upper layer. The third layer of the flask contained fatty acid methyl ester, followed by glycerol, and the third layer was crude enzyme sediments. Two separate layers were visible in the control. The unreacted methanol is on top, and the oil is on the bottom.

Some FAME compounds, such as methyl stearate, cis-10-Heptadecanoic acid methyl ester, Oleoic acid methyl ester, Eladic acid methyl ester, Palmitic acid methyl ester, 9,12-Octadecanoic acid methyl ester, Arachidonic acid methyl ester, 13-Docosenoic acid methyl ester, and Lignoceric acid methyl ester, indicated that the free fatty acids were able to convert to methyl esters. This was observed in the study of Aboelazayem *et al*. [23], where several of these FAME compounds were discovered in the WCO after gas chromatography examination of free fatty acids. It also demonstrated that opportunistic bacteria with lipase-producing capacity, such as *E. coli* and *B. valllismortis*, can make biodiesel from waste cooking oil. The use of enzyme catalysts can eliminate the need for chemical catalysts, making the process more cost-effective and ecologically benign.

Fatty Acid Methyl Ester Analysis by Gas Chromatography (GC)

The fatty acid methyl ester profile yielded 64.3 mg/L and 74.85 mg/L concentration components of the FAMES from waste cooking oil, respectively. Tables 3 and 4 indicate the Fatty Acid Methyl Ester components of examined samples as determined by GCMS. As shown in Figures 9 and 10, the gas chromatograms of the two samples indicated 39.95 mg/L and 58.95 mg/L, respectively, when the peak area of the cis-heptadecanoic acid methyl ester was taken into account.

Table 2: Profile of WCO Fatty Acid Methyl Ester (FAME) of mixed lipase by *Eschericia coli* Khodavandi-Alizadeh-2 and *Bacillus vallismortis* BR2 from one of the Experimental Run 2

FAMES Compound	Retention Time	Response	Conc. (Unit)	Dev. (min)
Methyl myristoleate	12.441	1087	2.85 mg/L	48
Palmitic acid, methyl ester	16.030	22424	9.55 mg/L	91
Cis-10-Heptadecenoic acid Methyl ester	16.885	12899	39.95 mg/L	59
9,12-Octadecadienoic acid Methyl ester	18.307	1447	3.25 mg/L	72
Oleic acid Methyl ester	18.385	3925	2.70 mg/L	100
Elaidic acid, methyl ester	18.296	1860	0.65 mg/L	42
Methyl stearate	18.385	3925	3.95 mg/L	5
13-Docosenoic acid, methyl ester	23.051	535	0.75 mg/L	19
Lignoceric acid, methyl ester	25.106	201	0.65 mg/L	19
TOTAL			64.3 mg/L	

Table 3: Profile of WCO Fatty Acid Methyl Ester (FAME) of lipase by *Escherichia coli* Khodavandi-Alizadeh-2 and *Bacillus vallismortis* BR2 from one of the Experimental Run 11

FAMES Compound	Retention Time	Response	Conc. (Unit)	Dev. (min)
Methyl myristoleate	12.441	497	1.30 mg/L	24
Palmitic acid, Methyl ester	16.030	1357	4.85 mg/L	86
Cis-10-Heptadecenoic acid Methyl ester	16.941	9037	58.95 mg/L	58
9,12-Octadecadienoic acid Methyl ester	18.307	865	1.95 mg/L	40
Oleic acid Methyl ester	18.385	1835	1.25 mg/L	100
Elaidic acid, Methyl ester	18.085	209	0.05 mg/L	16
Methyl stearate	18.385	1835	1.85 mg/L	1
Arachidonic acid Methyl ester	19.663	211	0.85 mg/L	30
13-Docosenoic acid, Methyl ester	22.862	1293	1.85 mg/L	60
Lignoceric acid, methyl ester	25.128	611	1.95 mg/L	19
TOTAL			74.85mg/L	

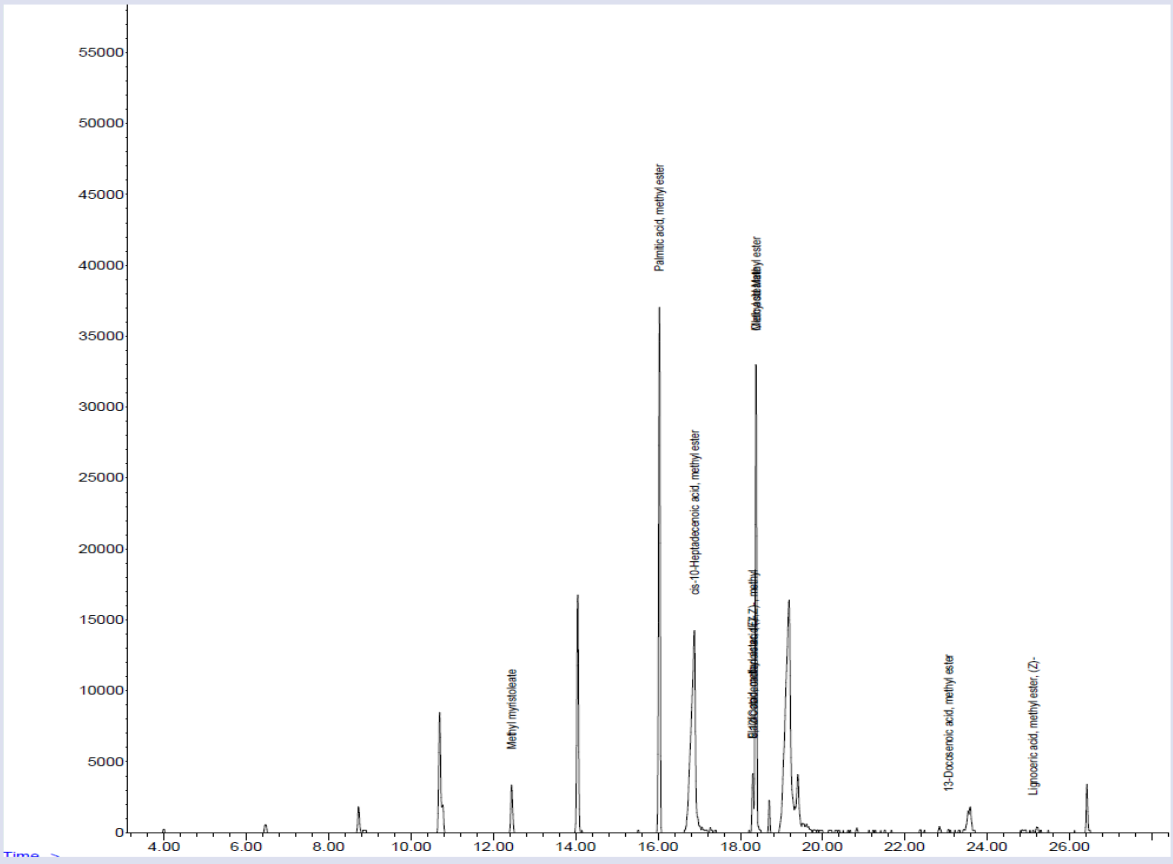

Figure 9: Gas Chromatography of WCO Fatty Acid Methyl Esters from mixed lipase of *Escherichia coli* Khodavandi-Alizadeh-2 and *Bacillus vallismortis* BR2 from Experimental (Run 2)

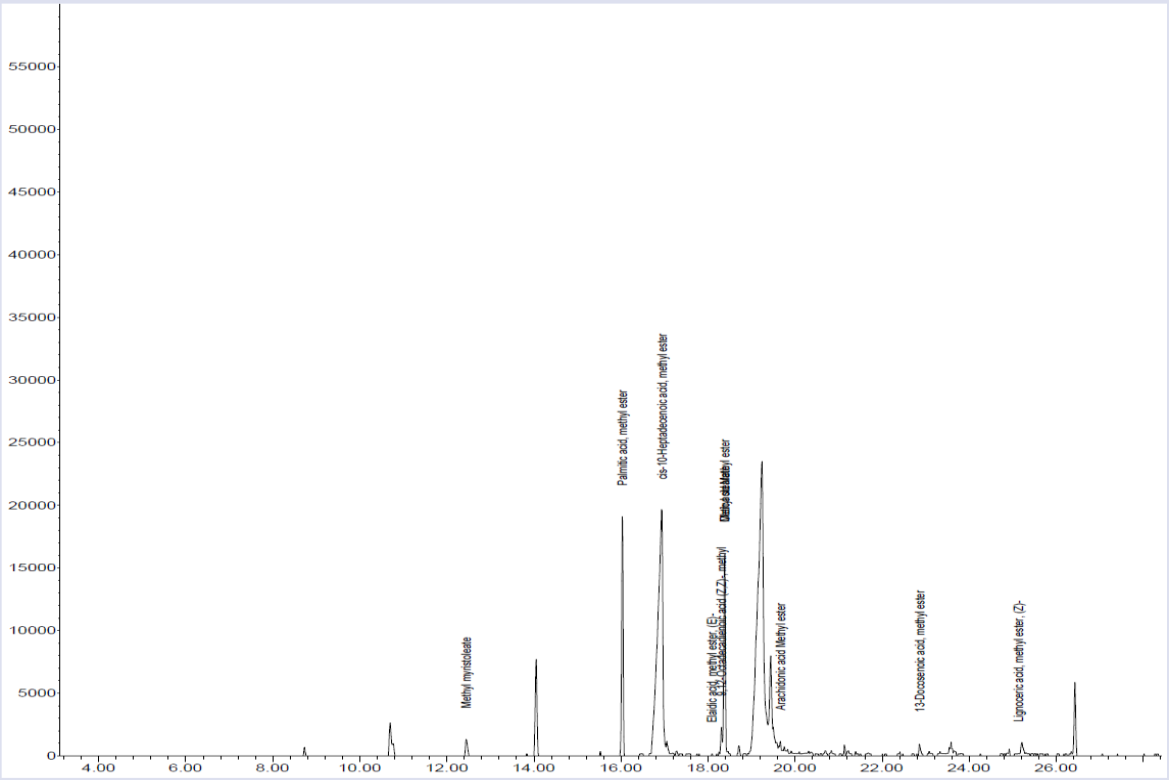

Fig. 10 Gas Chromatography of WCO Fatty Acid Methyl Esters from mixed lipase of *Escherichia coli* Khodavandi-Alizadeh-2 and *Bacillus vallismortis* BR2 from experimental (Run 11)

The Fuel Properties of Biodiesel (Fame)

The fuel parameters of fatty acid methyl ester (biodiesel) are compared to those of the biodiesel standard in Table 4. The current findings revealed that the transesterification method enhanced the viscosity, flash point, and pour point of the gasoline. When the flash point, pour point, cloud point, cetane number, and viscosity of the biodiesel were compared to those of the biodiesel standard, it was discovered that the transesterification procedure improved these attributes. The cetane number (CN) is one of the most important qualities of biodiesel fuels that indicates the ignition characteristics and quality of motor power, and it correlates to Huang *et al.* [24] study as well as the ASTM and EU regulations (DIN EN-14214). A property's flash point was substantially improved, as a higher flash point prevents any type of fire outbreak. The biodiesel yield can also be used in cold weather due to reduced pour point and cloud point features.

Table 4 Properties of Biodiesel (FAME) from Waste Cooking Oil

Property	Unit	Run A	Run B	ASTM standard D6751-02	EU Standard EN-14214
Specific gravity	g/cm3	0.946	0.818	0.880	0.886-0.90
Viscosity	m2/s	3.80	4.20	1.9 – 6.0	3.5 – 5.0
Flash point	°C	105.84	102.90	> 130	> 120
Cloud point	°C	0.00	0,.00	summer -4 winter -1	-
Pour point	°C	-25	-24	15-18	-
Cetane		51.40	52.65	>47	>

ss

Conclusion

The excessive use of fossil fuels depletes reserves, and continuing greenhouse gas emissions as a result of global climate change have an impact on the country's socioeconomic development. As a result, renewable energy sources are being used as a substitute. With the constant depletion of fossil fuels, the biotransformation of domestic spent cooking oil into a value-chain product such as biofuel is critical, particularly for Sub-Saharan African countries.

The goal of this study was to use a concurrent hydrolyzing enzyme to convert waste cooking oil into fatty acid methyl ester and to optimize the parameter circumstances to favor good output. As quantitative and qualitative assessments of the biofuel samples were subjected to instrumentation utilizing Gas Chromatography-Mass Spectrometry, a major statistical tool was used to collaborate on the efficient operations. The rate of biodiesel yield was affected by all variables, including pH, temperature, agitation, and enzyme concentration. The FAME properties found were within ASTM and EU guidelines.

Conflict of interest

The authors have no competing interests to declare that are relevant to the content of this article.

References

[1] Sarno M., Iuliano M., Biodiesel production from waste cooking oil, *Green Process Syn.,* 8 (2019) 828–836.

[2] Chen C., Chitose A., Kusadokoro M., Nje H., Xu W., Yang F., Yang S., Sustainability and challenges in biodiesel production from waste cooking oil: An advance bibliometric analysis, *Energy Rep.*, 7 (2021) 4022-4034

[3] Canakci M, Gerpen Van J., Biodiesel Production from oils and fats With High Free Fatty Acids*, Transactions of the ASAE*, 44(6) (2001) 1429–1436.

[4] Osho M.B., Popoola T.O.S., Kareem S.O., Arowolo T.A., Transesterification of Jatropha seeds oil by vegetative sponge immobilized lipase of *Alternaria sp.* MGGP 06 for fatty acid methyl ester production under optimized conditions, *Petroleum Technol. Develop. J. An International Journal*, 1(2014a) 56-70.

[5] Osho M.B., Omemu A.M., Popoola T.O.S., Adeleye T., Enzymatic production of fatty acid methyl ester by *Aspergillus niger* ATCC 1015 lipase from non-edible oil, *Petroleum Technol. Develop. J. An International Journal*, 2 (2014b) 51-59.

[6] Osho M.B., Popoola T.O.S, Arowolo T.A., Biosynthesis of fatty acid methyl esters from vegetable oils using Sponge-immobilized lipase of *Candida rugosa* PV 0514, *J. Biotechnol. Bioinfor, Bioengnr.*, 2(3) (2015)13-18.

[7] Kareem S.O., Adio O.Q., Osho M.B., Banjo T.T., Omeike S.O., Optimization of Biodiesel Production from Spent Cooking Oil by Fungal Lipase Using Response Surface Methodology*, Nigerian J. Biotechnol.,* 35 (2018) 25-33.

[8] Shafiq F., Mumtaz M.W., Mukhtar H., Touqeer T., Raza S.A., Rashid U., Nehdi I.A., Choong T.S.Y., Response Surface Methodology Approach for optimized biodiesel production from waste chicken fat oil, *Catalysis*, 10(6) (2020) 633.

[9] Kuan I.C., Lee C.C., Tsai B.H., Lee S.L., Lee W.T., Yu C.Y., Optimizing the Production of Biodiesel Using Lipase Entrapped in Biomimetic Silica, *Energies,* 6(4) (2013) 2052–2064.

[10] Touqeer T., Mumtaz M.W., Mukhtar H., Irfan A., Akram S., Shabbir A., Rashid U., Nehdi I.A., Choong T.S.Y., Fe_3O_4-PDA Lipase as surface functionalized nano biocatalyst for the production of biodiesel using waste cooking oil as feedstock: Characterization and process optimization, *Energies,* 13(1) (2020)177.

[11] Pualsa J., Verma D., Gavankar R., Bhagat R.D., Production of Microbial Lipases Isolated from Curd Using Waste Oil as Substrate, *Research J. Pharmaceut. Biology Chemical Source*, 4(3) (2013) 834-835.

[12] Fan J., Andre C., Xu C., A Chloroplast pathway for the de novo biosynthesis of triacylglycerol in *Chlamydomonas reinhardtti., J. Energy*, 585 (2016)1985-1991.

[13] Nazir N., Ramli N., Mangunwidjaja D., Hambali E., Setyaningsih D., Yuliani S., Salimon J., Extraction, transesterification and process control in biodiesel production from *Jatropha curcas*, *European J. Lipid Sc. Technol.,* 18 (2) (2009) 1185-1200.

[14] Polyak Y.M., Bakina L.G., Chugunova M.V., Mayachkina N.V, Gerasimov A.O., Bure V.M., Effect of Remediation Strategies on Biological Activity of Oil Contaminated soil – A field study, *International J. Biodeterior. Biodegrad.*, 126 (2018)57-68

[15] Jenisha M.J., Renuga F.B., Isolation of Oil Degrading Bacteria from Engine Oil Contaminated Soil, *Uttar Pradesh J. Zoology*, (2021) 71–81.

[16] Ilesanmi O.I., Adekunle A.E., Omolaiye J.A., Olorode E.M., Ogunkanmi A.L., Isolation, optimization and molecular characterization of lipase producing bacteria from contaminated soil, *Scientific African,* 8 (2020) e00279.

[17] Giwa O.E., Ibitoye F.O., Bioremediation of heavy metal in crude oil contaminated soil using isolated Indigenous microorganism cultured with *E coli* DE3 BL21, *Int. J. Engineering & Application Science*, 4(6) (2017).

[18] Rong L., Zheng X., Oba B.T., Shen C., Wang X., Wang H., Luo Q., Sun L., Activating soil microbial community using bacillus and rhamnolipid to remediate TPH contaminated soil, *Chemosphere*, 275 (2021) 130062.

[19] D'hoe K., Conterno L., Fava F., Falony G., Vieira-Silva S., Vermeiren J., Tuohy K., Raes J., Prebiotic Wheat Bran Fractions Induce Specific Microbiota Changes, *Frontier Microbiology,* 9 (2018).

[20] Ji M., Li S., Chen A., Liu Y., Xie Y., Duan H., Shi J., Sun J., A wheat bran inducible expression system for the efficient production of α Larabinofuranosidase in *Bacillus subtilis*, *Enzyme Microb. Technol.,* 144 (2021) 109726.

[21] Çağatay Ş., Aksu Z., Use of different kinds of wastes for lipase production: Inductive effect of waste cooking oil on activity, *Journal of Biosciences & Bioengineering,* (2021).

[22] Mohammed N.I., Kabbashi N.A., Alam M.Z., Mirghani M.E.S, Optimization of *Jatropha* Biodiesel Production by Response Surface Methodology, *Green Sustainable Chem.*, 11(01) (2021) 23–37.

[23] Aboelazayem O., Gadalla M., Saha B., Derivatisation-free characterisation and supercritical conversion of free fatty acids into biodiesel from high acid value waste cooking oil, *Renewable Energy,* 143 (2019) 77–90.

[24] Huang S.H., Liao M.H., Chen D.H., Direct Binding and Characterization of Lipase onto Magnetic Nanoparticles, *Biotechnol. Progress,* 19(3) (2003) 1095–1100.

Cumhuriyet Sci. J., 44(2) (2023) 254-257
DOI: https://doi.org/10.17776/csj.1238418

Cumhuriyet Science Journal

| csj.cumhuriyet.edu.tr | Founded: 2002 ISSN: 2587-2680 e-ISSN: 2587-246X Publisher: Sivas Cumhuriyet University

T-type Calcium Channel Blocker, NNC 55-0396, Suppress Cell Proliferation and Promote Apoptosis in SNU-1 Gastric Cancer Cells

Mustafa Ergül [1,a,*]

[1] *Department of Biochemistry, Faculty of Pharmacy, Sivas Cumhuriyet University, Sivas, Türkiye*
**Corresponding author*

Research Article

History
Received: 18/01/2023
Accepted: 07/06/2023

ABSTRACT

Accumulating evidence reports that T-type calcium channels play crucial roles in tumor formation and development. However, the roles of inhibiting calcium channels in tumor cells with various inhibitors in tumor progression remain unclear. This study aimed to investigate the cytotoxic and apoptotic effects of NNC 55-0396, a T-type calcium channel inhibitor, against SNU-1 gastric cancer cells. Cytotoxic and apoptotic effects of NNC 55-0396 were evaluated by the XTT assay and flow cytometry. The results showed that NNC 55-0396 had concentration-dependent cytotoxicity in SNU-1 cells and its the half-maximal inhibitory concentration (IC50) value was calculated as 4.17 µM. The results of the Annexin V experiments also showed that this inhibitor significantly increased apoptosis in SNU-1 cells. In conclusion, these results demonstrated that NNC 55-0396 induces cytotoxic effects by increasing apoptosis in gastric cancer cells. However, further research is required for its use as a possible therapeutic agent in the treatment of gastric cancer.

Keywords: Gastric cancer, NNC 55-0396, Cytotoxicity,Apoptosis.

[a] *m.ergul@yahoo.com.tr* *https://orcid.org/0000-0003-4303-2996*

Introduction

Gastric cancer, the fifth most diagnosed malignancy worldwide, is still considered a major health problem. Because of its often advanced stage at diagnosis, gastric cancer has a high mortality rate and is the third leading cause of cancer-related deaths, with 784,000 deaths worldwide in 2018 [1]. Many factors such as age, gender, genetic factors, smoking, race, unhealthy diet, and being infected with Helicobacter pylori bacteria are known as important risk factors for gastric cancer. Traditionally, chemotherapy, radiotherapy, surgery, and immunotherapy have been used success in its treatment [2, 3]. However, unfortunately, most of the patients cannot overcome the side effects associated with these treatments [4]. Therefore, new cellular targets urgently need to be discovered to increase the therapeutic efficacy and minimize the side effects of existing treatment modalities.

Collective reports have revealed that ion channels, the special membrane proteins that allow ion flow, play a role in the development of many diseases, including cancer [5]. The regulation of calcium signaling is used for various therapeutic purposes such as hypertension, coronary artery disease, and pain control [6]. Moreover, as a secondary messenger, calcium plays important roles in cell proliferation, cell cycle progression, differentiation, migration, and apoptosis. It is also known that abnormal activation of calcium channels is related to tumor formation and development [7, 8]. Therefore, calcium channel blockers (CCBs) appear to be a notable anticancer target, as both decreased and increased intracellular calcium levels induce apoptotic cell death [9]. A large number of reports have also shown that the expression of T-type calcium channels is significantly increased in many cancer types such as glioma, hepatoma, colon, breast, esophageal, and ovarian cancers. Besides, high calcium channel levels can be detected in tumor tissue samples collected from various cancer patients [10].

In light of CCB data obtained in the last decades, blocking T-type calcium channels is seen as a promising strategy in cancer treatment. However, the use of NNC 55-0396 in SNU-1 gastric cancer cells has not yet been disclosed. This study aimed to investigate the cytotoxic and apoptotic effects of NNC 55-0396, which is used as T-type CCB, on gastric cancer SNU-1 cells.

Materials and Methods

Cell Culture

Human stomach cancer cells SNU-1 were purchased from ATCC (CRL-5971) and incubated at 37°C under a 5% CO_2 humidified atmosphere. The cells were cultured in an RPMI-1640 (Sigma-Aldrich) mixture supplemented with 10% fetal bovine serum (FBS, Gibco, Thermo Fisher Scientific) and 50 U/mL penicillin/streptomycin (Gibco, Thermo Fisher Scientific). A 10 mM stock solution of NNC 55-0396 (Tocris) in DMSO was prepared and the concentrations to be applied to the cells were prepared from this stock by diluting with RPMI-1640 mixture.

Cell Viability Assay

After 24 h incubation, cell viability was evaluated by the XTT assay (Roche Diagnostic) as described previously [11]. In short, SNU-1 cells were exposed to NNC 55-0396 at increasing concentrations (1, 5, 10, 20, and 40 µM) for 24 h, and XTT test was carried out. The half-maximal inhibitory concentration (IC50) value of NNC 55-0396 in SNU-1 cells was calculated using Graph Prism 7 software.

Annexin V Binding Assay

Initially, SNU-1 cells were treated with NNC 55-0396 at the previously determined IC_{50} concentration and incubated for 24 h. After the incubation period, the cells were collected by centrifugation and incubated in 100 µL of Annexin V reagent (Millipore) for 20 min in the dark [11]. Then, the apoptotic effect of NNC 55-0396 was determined using the muse cell analyzer (Merck, Millipore).

Results

Cytotoxic Effect of NNC 55-0396 in SNU-1 Cells

Cell viability findings are shown in Figure 1 and it has been demonstrated that when compared to the untreated cells NNC 55-0396 has a dose-dependent inhibitory effect at 24 h ($P < 0.01$). The IC_{50} value of NNC 55-0396 was determined as 4.17 µM for 24 h in SNU-1 cells and this value was utilized for the subsequent apoptosis assessment experiments.

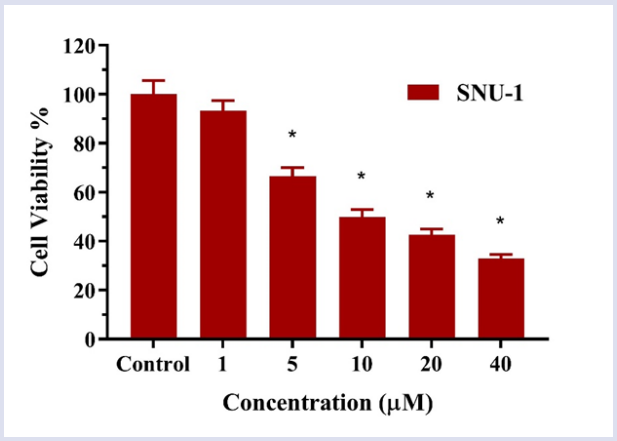

Figure 1. Antiproliferative effect of NNC 55-0396 treatment in SNU-1 cells. Results are exhibited as mean with a standard deviation of the independent three replicates. *Significantly different when compared to cell viability of untreated cells ($P < 0.01$).

Apoptotic Effect of NNC 55-0396 in SNU-1 Cells

According to the findings, when compared to the untreated cells, NNC 55-0396 treatment markedly promoted the early and late apoptotic cell population ($P < 0.01$). As presented in Figure 2, the early, late apoptotic cell population % and dead cell population % in untreated cells (4.27 ± 1.30%, 5.77 ± 1.10 %, and 0.76 ± 0.90%, respectively) significantly increased to 11.03 ± 1.79% and 49.42 ± 3.68%, and 7.38 ± 1.07%, respectively, in NNC 55-0396 administered group ($P < 0.01$).

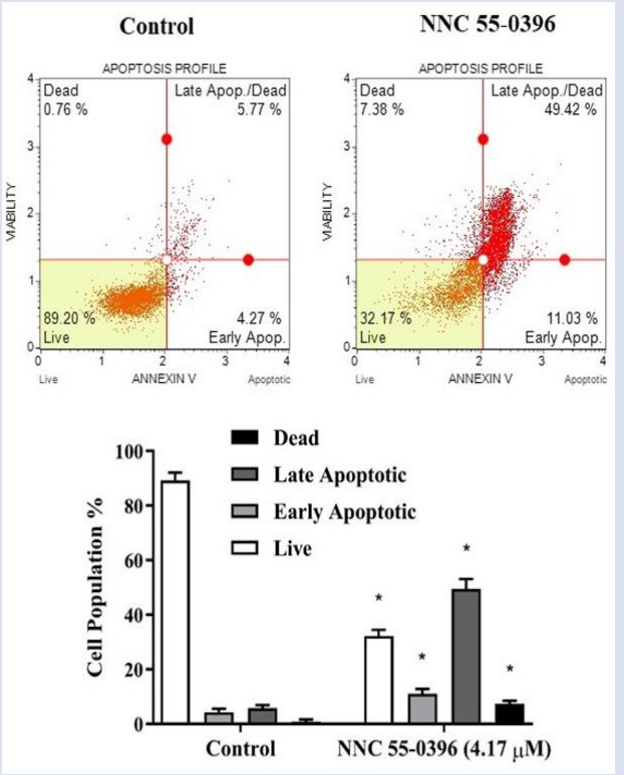

Figure 2. Apoptotic effect of NNC 55-0396 treatment in SNU-1 cells. All experiments were carried out in triplicate. *Significantly different when compared to the cell population rate of control cells ($P < 0.01$).

Discussion

Although several researchers reported the anticancer potential of NNC 55-0396 in various cancer cells, as far as we know, there is a gap in the literature evaluating the cytotoxic and apoptotic effects of NNC 55-0396 in SNU-1 cells. In this context, the current investigation demonstrated that gastric cancer cells showed reduced cell proliferation when treated with selective T-type CCB, NNC 55-0396, in a concentration-dependent manner. Mechanistically, this inhibitor was found to cause significant apoptotic cell death in SNU-1 gastric cancer cells. These data revealed that calcium channel inhibition by NNC 55-0396 may cause meaningful anticancer effects through the promotion of apoptosis in SNU-1 gastric cancer cells.

It has long been known that significant changes in intracellular calcium levels are closely associated with apoptotic cell death. In connection with this, in cells, calcium channels play several roles in physiological and pathological processes, including cancer. Especially, T-type calcium channels are also frequently abnormally expressed in various cancer cells and are involved in the proliferation, cell cycle progression, and survival [12]. Moreover, abnormal activation of T-type calcium channels is associated with various pathological conditions and has made these channels fascinating drug

targets [13]. In this context, many studies have shown that pharmacological or RNAi-mediated suppression of calcium channels diminishes cell proliferation and increases cell death in various cancer cells [14, 7]. In a previous study, Huang et al. reported that NNC 55-0396 application showed a concentration-dependent cytotoxic effect on different leukemia cells by increasing calcium transfer from the endoplasmic reticulum to the cytosol. In the same study, the NNC 55-0396 application showed a significant apoptotic effect, especially late apoptosis, in Jurkat and MOLT-4 cells [10]. In a similar fashion, Nam et al. showed that newly synthesized CCBs were significantly cytotoxic in two human cancer cells (colon cancer HCT-116 and lung cancer A549) [13]. In another study, it was shown that the treatment of specific T-type calcium channel blockers mibefradil or pimozide had significant cytotoxic effects on melanoma cells M16 and JG cells. Inhibitors have also been shown to induce apoptotic cell death in the cells in a caspase-dependent manner [15]. In different studies, the T-type calcium channel inhibitor mibefradil has also been shown to have significant apoptotic effects on breast and brain cancer cells [16, 17]. Many previous studies have also reported that calcium channel antagonists such as mibefradil or NNC 55-0396 have cytotoxic and apoptotic effects on various cancer cells such as colon, pancreas (MiaPaCa2), glioma (U87MG) and lung (A549), in line with our data [18].

All the studies mentioned in the previous paragraph exhibit that T-type calcium channel blockers play a crucial role in cancer development and progression, and inhibition of these channels with specific inhibitors suppresses the proliferation of cancer cells. Consistent with these studies, it has been shown in this study that NNC 55-0396, a specific calcium channel blocker, has significant cytotoxic and apoptotic effects on SNU-1 gastric cancer cells. At the same time, this study has some limitations. The use of different gastric cancer cell lines and the evaluation of the apoptotic effect of NNC 55-0396 with different methods may support the obtained data. Moreover, further in vitro and in vivo studies are needed to elucidate the potential use of NNC 55-0396 for gastric cancer therapy.

Conflicts of interest

The author declared no conflict of interest.

References

[1] Smyth E.C., Nilsson M., Grabsch H.I., van Grieken N.C., & Lordick F., Gastric cancer, Lancet (London, England), 396 (10251) (2020) 635–648.

[2] Karimi P., Islami F., Anandasabapathy S., Freedman N.D., & Kamangar F., Gastric cancer: descriptive epidemiology, risk factors, screening, and prevention, *Cancer Epidemiol Biomarkers Prev*., 23 (5) (2014) 700–713.

[3] Joshi S.S., Badgwell B.D., Current treatment and recent progress in gastric cancer, *CA Cancer J Clin.*, 71 (3) (2021) 264-279.

[4] Harada K., Sakamoto N., Ukai S., Yamamoto Y., Pham Q.T., Taniyama D., Honma R., Maruyama R., Takashima T., Ota H., Takemoto Y., Tanabe K., Ohdan H., & Yasui, W., Establishment of oxaliplatin-resistant gastric cancer organoids: importance of myoferlin in the acquisition of oxaliplatin resistance, *Gastric Cancer*, 24(6) (2021) 1264–1277.

[5] Gonçalves J.C.R., Coulidiati T.H., Monteiro A.L., Carvalho-Gonçalves L.C.T., Valença W.O., Oliveira R.N., Câmara C.A., Araújo D.A.M., Antitumoral activity of novel 1,4-naphthoquinonederivative involves L-type calcium channel activation in human colorectal cancer cell line, *Journal of Applied Biomedicine*, 14(3) (2016) 229-234.

[6] Monteith G.R., Davis F.M., Roberts-Thomson S.J., Calcium channels and pumps in cancer: changes and consequences, *J. Biol. Chem.*, 287(38) (2012) 31666-31673.

[7] Wu L., Lin W., Liao Q., Wang H., Lin C., Tang L., Lian W., Chen Z., Li K., Xu L., Zhou R., Ding Y., & Zhao, L., Calcium Channel Blocker Nifedipine Suppresses Colorectal Cancer Progression and Immune Escape by Preventing NFAT2 Nuclear Translocation, *Cell Reports*, 33(4) (2020) 108327.

[8] Phan N.N., Wang C.Y., Chen C.F., Sun Z., Lai M.D., & Lin Y.C., Voltage-gated calcium channels: Novel targets for cancer therapy, *Oncology Letters*, 14(2) (2017) 2059–2074.

[9] Mason R.P., Calcium channel blockers, apoptosis and cancer: is there a biologic relationship?, *Journal of the American College of Cardiology*, 34(7) (1999) 1857–1866.

[10] Huang W., Lu C., Wu Y., Ouyang S., & Chen Y., T-type calcium channel antagonists, mibefradil and NNC-55-0396 inhibit cell proliferation and induce cell apoptosis in leukemia cell lines, *J. Exp. Clin. Cancer Res*., 34(1) (2015) 54.

[11] Ergul M., Bakar-Ates F., A specific inhibitor of polo-like kinase 1, GSK461364A, suppresses proliferation of Raji Burkitt's lymphoma cells through mediating cell cycle arrest, DNA damage, and apoptosis, *Chem Biol Interact*., 332 (2020) 109288.

[12] Dziegielewska B., Gray L.S., Dziegielewski J., T-type calcium channels blockers as new tools in cancer therapies, *Pflugers Arch*., 466(4) (2014) 801-810.

[13] Nam Y., Ryu K.D., Jang C., Moon Y.H., Kim M., Ko D., Chung K.S., Gandini M.A., Lee K. T., Zamponi G.W., & Lee J.Y., Synthesis and cytotoxic effects of 2-thio-3,4-dihydroquinazoline derivatives as novel T-type calcium channel blockers, *Bioorganic & Medicinal Chemistry*, 28(11) (2020) 115491.

[14] Panner A., & Wurster R.D., T-type calcium channels and tumor proliferation, *Cell Calcium*, 40(2) (2006) 253–259.

[15] Das A., Pushparaj C., Herreros J., Nager M., Vilella R., Portero M., Pamplona R., Matias-Guiu X., Martí R.M., & Cantí C., T-type calcium channel blockers inhibit autophagy and promote apoptosis of malignant melanoma cells, *Pigment cell & Melanoma Research*, 26(6) (2013) 874–885.

[16] Valerie N.C., Dziegielewska B., Hosing A.S., Augustin E., Gray L.S., Brautigan D.L., Larner J.M., & Dziegielewski J., Inhibition of T-type calcium channels disrupts Akt signaling and promotes apoptosis in glioblastoma cells, *Biochemical Pharmacology*, 85(7) (2013) 888–897.

[17] Ohkubo T., & Yamazaki J., T-type voltage-activated calcium channel Cav3.1, but not Cav3.2, is involved in the inhibition of proliferation and apoptosis in MCF-7 human breast cancer cells, *International Journal of Oncology*, 41(1) (2012) 267–275.

[18] Granados K., Hüser L., Federico A., Sachindra S., Wolff G., Hielscher T., Novak D., Madrigal-Gambo, V., Sun Q., Vierthaler M., Larribère L., Umansky V., & Utikal J., T-type calcium channel inhibition restores sensitivity to MAPK inhibitors in de-differentiated and adaptive melanoma cells, *British Journal of Cancer*, 122(7) (2020) 1023–1036.

Cumhuriyet Sci. J., 44(2) (2023) 258-262
DOI: https://doi.org/10.17776/csj.1225497

Cumhuriyet Science Journal

| csj.cumhuriyet.edu.tr | Founded: 2002 ISSN: 2587-2680 e-ISSN: 2587-246X Publisher: Sivas Cumhuriyet University

Synthesis, Anticancer Activity and Carbonic Anhydrase Inhibitory Activity of new Thiadiazole-hydrazone Derivatives

Hayrani Eren Bostancı [1,a,*], Ulviye Acar Çevik [2,b]

[1] *Department of Biochemistry, Faculty of Pharmacy, Sivas Cumhuriyet University, Sivas, Türkiye*
[2] *Department of Pharmaceutical Chemistry, Faculty of Pharmacy, Anadolu University, Eskişehir 26470,Türkiye*
**Corresponding author*

Research Article

History
Received: 28/12/2022
Accepted: 08/06/2023

ABSTRACT

In five steps, new compounds 5a, 5b of thiadiazole-hydrazone derivatives were synthesized. Various spectral methods, such as ^{1}H NMR, ^{13}C NMR, and elemental analyses, were used to clarify the structures of the compounds. Three cancer cell lines (MCF7, MDA, and HT-29) and one healthy cell line (L929) were tested for the cytotoxicity activity of synthetic compounds, as well as their inhibitory action against carbonic anhydrase I and II isoenzymes (hCA I and hCA II). Among them, the compound 5b exhibited remarkable CA inhibitory activities compared to a standard inhibitor with IC_{50} values at of 27 µM for hCA I and 33,46 µM for hCA II. The compounds have been found to be ineffective against cancer cell lines. Furthermore, the compounds were found to be non-toxic to the healthy cell line.

Keywords: Thiadiazole, Hydrazone, Anticancer, Carbonic anhydrase.

[a] *erenbostanci@hotmail.com* *https://orcid.org/0000-0001-8511-2316* [b] *uacar@anadolu.edu.tr* *https://orcid.org/0000-0003-1879-1034*

Introduction

The carbonic anhydrase (CA) enzyme is a group of enzymes that convert carbon dioxide (CO_2) and water (H_2O) into proton (H^+) and bicarbonate anion (HCO_3^-) [1,2]. There are 15 different CA isoforms in humans [3]. These isoforms can be categorized based on where they are found in the body, including cytosolic isoforms (CA I, CA II, CA III, CAVII, CAXIII), mitochondrial isoforms (CA VA, CAVB), transmembrane-bound isoforms (CA IV, CA IX, CA XII, CA XIV), and CA VI, which is found in body fluids like saliva [4,5]. These enzymes are essential for a wide range of physiological and cellular functions, including the transfer of carbon dioxide, control of the acid-base balance, electrolyte secretion, and biosynthetic pathways [6]. Diuretic, anti-Alzheimer, anti-obesity, anti-epileptic, anti-cancer, and anti-infective effects are among the bioactivities of hCA activators and/or inhibitors (hCAIs) [7,8].

Cancer is one of the most dangerous diseases and is one of the leading causes of mortality, despite numerous improvements in drug discovery for its control and treatment. The cancer problem is confined to a specific area due to the disease's metastasis and extensive nature as well as the anticancer medications' high side effect rate due to their lack of selectivity. Additionally, the issue gets worse as a result of ongoing resistance-producing mutations in numerous anti-cancer treatment targets. The development of new anticancer drugs with great selectivity and the ability to overcome drug resistance has recently been the focus of medicinal chemists [9]. Human carbonic anhydrase (hCA) enzymes have recently become the focus of anticancer drugs [10]. CA II, one of the CA isoforms, is frequently linked to several malignancies. In esophageal, melanoma, renal, and lung cancers, CA II is expressed in the endothelium of neovessels, according to a recent study. In other studies, CA II has been connected to the essential target antigen that causes melanoma patients to produce autoantibodies. Furthermore, a number of cancer forms have been found to overexpress CAII, according to several recent investigations [11-13].

Five-membered heterocycle-containing molecules have drawn more and more attention in recent years when it comes to creating anticancer drugs. The 1,3,4-thiadiazole system is regarded as one of the promising structures [14]. The antitumor activity of 1,3,4-thiadiazole derivatives has been extensively investigated. Thiadiazole derivatives can be found in a variety of over-the-counter drugs (Figure 1).

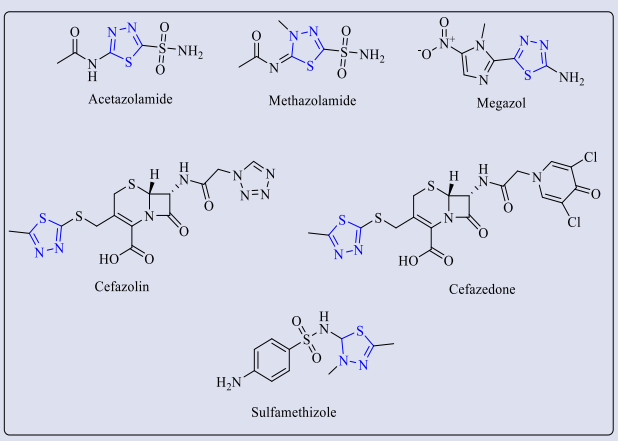

Figure 1. Representative thiadiazole-based drug molecules.

Methazolamide and acetazolamide, for instance, are potent inhibitors of carbonic anhydrase. Sulfamethizole has antibacterial properties, while megazol has antitrypanosomal properties. Members of the first generation of the cephalosporin family include cefazolin and cefazedone [15-17].

N-Acylhydrazones with the -CO-NH-N= unit have drawn attention due to their intriguing characteristics for a long time and have been used in medicine [18]. It is believed that the capacity of molecules with the hydrazone moiety to form hydrogen bonds with molecular targets is a factor in their bioactivity, which enables them to attach to a variety of enzymes and receptors [19]. Examples of drugs containing the hydrazone structure are shown in Figure 2.

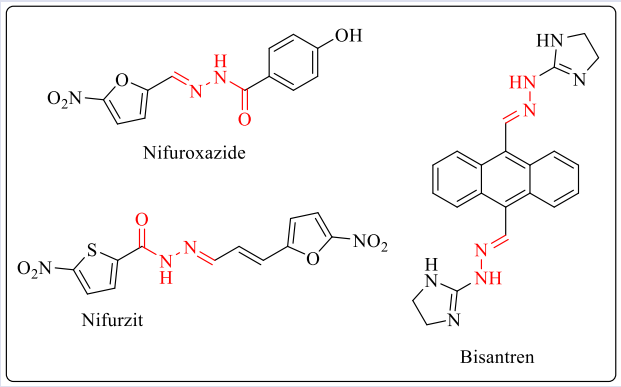

Figure 2. Chemical structure of nifuroxazide, nifurzide and bisanthrene drugs

The facts cited above inspired us to create hybrid molecules that combine the two crucial moieties, hydrazone and thiadiazole, into a single molecule. In order to create novel medication candidates with less cytotoxic effects, this was done. The synthetic substances were tested against three cell lines and a healthy cell line. In addition, the inhibitory activities of the compounds against hCAI and hCAII enzymes were evaluated.

Materials and Methods

Chemistry

Synthesis of *N*-(4-chlorophenyl) hydrazinecarbothioamide (1):

The isothiocyanate (0.02 mol) derivatives are dissolved in ethanol and placed in an ice bath. Hydrazine hydrate (0.024 mol) in ethanol is added dropwise to the reaction content. After the dripping process is finished, the precipitated product is filtered off.,

Synthesis of 5-(4-chlorophenylamino)-1,3,4-thiadiazole-thiol (2):

The compound N-(4-substitutedphenyl) hydrazinecarbothioamide (2) is dissolved in ethanol and carbon disulfide and NaOH are added. The reaction is stirred under reflux for 3-4 hours. Reaction end is controlled by TLC. At the end of the reaction, the product content is poured into ice water and the product is precipitated with HCl acid and filtered.

Synthesis of 2-((5-((4-chlorophenyl)amino)-1,3,4-thiadiazol-2-yl)thio)acetate (3): Acetone is used to dissolve compound 2, potassium carbonate and chloroethylacetate. The mixture is stirred for two hours at 40 °C while in reflux. Filtered off, cleaned with water, and crystallized from ethanol is the precipitated product.

Synthesis of 2-((5-((4-chlorophenyl)amino)-1,3,4-thiadiazol-2-yl)thio)acetohydrazide (4): Hydrazine hydrate was added after compound 3 had been dissolved in ethanol. The mixture was heated for two hours at reflux, and the precipitated portion was removed by filtering.

Synthesis of 2-((5-((4-chlorophenyl)amino)-1,3,4-thiadiazol-2-yl)thio)-N'-(substituted benzylidene) acetohydrazide (5a-5b): A few drops of acetic acid and an aldehyde derivative (0.001 mol) were added after compound 4 had been dissolved in ethanol. Two hours of reflux heating the mixture resulted in the precipitate, which was filtered out and crystallized from butanol.

2-((5-((4-chlorophenyl)amino)-1,3,4-thiadiazol-2-yl)thio)-*N*'-(2,4-dichlorobenzylidene) acetohydrazide (5a): Yield: 82 %, M.P.= 256 °C. ^{1}H-NMR (300 MHz, DMSO-d_6): δ: 4.43 (2H, s, -S-CH_2), 7.34-7.38 (2H, m, -Aromatic CH), 7.44-7.47 (1H, m, -Aromatic CH), 7.55-7.62 (3H, m, Aromatic CH), 7.92-7.94 (1H, m, Aromatic CH), 8.32 (1H, s, -CH), 10.45 (1H, s, NH), 11.86 (1H, s, NH). ^{13}C-NMR (75 MHz, DMSO-d_6): δ: 36.22, 119.34, 125.87, 128.48, 129.32, 129.75, 130.70, 134.11, 135.43, 139.25, 139.64, 142.57, 153.08, 165.28, 169.42. For $C_{17}H_{12}Cl_3N_5OS_2$, C, 43.19; H, 2.56; N, 14.81. Found: C, 43.25; H, 2.56; N, 14.83.

2-((5-((4-chlorophenyl)amino)-1,3,4-thiadiazol-2-yl)thio)-*N*'-(2,4-dimethoxybenzylidene) acetohydrazide (5b): Yield: 83 %, M.P.= 217.4 °C. ^{1}H-NMR (300 MHz, DMSO-d_6): δ: 3.78-3.82 (6H, m, -OCH_3),4.39 (2H, s, -S-CH_2), 6.56-6.62 (2H, m, -Aromatic CH), 7.35-7.39 (2H, m, -Aromatic CH), 7.57-7.62 (2H, m, Aromatic CH), 7.68-7.71 (1H, m, Aromatic CH), 8.25 (1H, s, -CH), 10.46 (1H, s, NH), 11.47 (1H, s, NH). ^{13}C-NMR (75 MHz, DMSO-d_6): δ: 36.41, 55.86, 56.23, 98.76, 106.91, 115.24, 119.35, 125.82, 127.03, 129.34, 139.71, 140.04, 143.29, 159.49, 162.79, 165.12, 168.75. For $C_{19}H_{18}ClN_5O_3S_2$, C, 49.19; H, 3.91; N, 15.09. Found: C, 49.27; H, 3.90; N, 15.11.

Anticancer Activity

The anticancer activities of compounds **5a** and **5b** were determined by the absorbance values obtained from MTT assays. The MTT method was performed as previously described [20]. The anticancer activities of the compounds were evaluated against 3 cancer cell lines (MCF-7, MDA and HT-29). L929 healthy mouse fibroblast cells were used to evaluate the selectivity of the compounds. In this section, cisplatin was used as a reference drug in cell lines.

Carbonic Anhyrase I/II Inhibition Assay

The esterase activity method is the method used for the determination of the carbonic anhydrase enzyme. With this method, esterase activity of carbonic anhydrase enzyme can be determined. Esterases responsible for the hydrolysis of carboxylic acids are capable of hydrolyzing many substrates. p-Nitrophenyl acetate is a substrate used in esterase and lipase activity assays. Hydrolysis of 1,4 p-nitrophenyl acetate yields p-nitrophenol or p-nitrophenolate, which gives maximum absorbance at 405 nm. The measurement is not affected because the two formed structures peak at the same absorbance value [21, 22].

Carbonic anhydrase inhibitors are currently used in the treatment of many diseases. Edema, epilepsy, ocular hypertension and glaucoma are examples of these disorders. Today, it is tried to create pharmaceutically effective drugs especially for epilepsy and Alzheimer's diseases. Inhibition of this isoenzyme also plays an important role in the treatment of these diseases [23].

Results and Discussion

The process used to create the compound 2-((5-((4-chlorophenyl)amino)-1,3,4-thiadiazol-2-yl)thio)-N'-(substituted benzylidene) acetohydrazide (5a-5b) is shown in Figure 3. NMR and elemental analyses were used to identify every chemical that was produced. 4-Chloroisothiocyanate on treatment with 99% hydrazine hydrate in the presence of ethanol yield N-(4-chlorophenyl)hydrazinecarbothioamide (1). The resulting product 1 is then subjected to cyclization in the following step through a reaction with carbon disulfide and NaOH in ethanol, yielding 5-(4-chlorophenylamino)-1,3,4-thiadiazole-thiol (2). Compound 2 and chloroethylacetate were combined with anhydrous potassium carbonate and refluxed for eight hours. To obtain 2-((5-((4-chlorophenyl)amino)-1,3,4-thiadiazol-2-yl)thio)acetohydrazide (4), compound 3 was refluxed with hydrazine hydrate in ethanol. Target compounds were produced by refluxing a combination of hydrazide derivative (4) and the corresponding benzaldehyde derivatives in EtOH (5a-5b).

By using ^{1}H NMR, ^{13}C NMR, and elemental analysis, the target compounds (5a-5b) had their chemical structures verified. The singlet signals observed in all the spectra at δ 8.25-8.32 ppm (N=CH) and δ 11.47 -11.86 ppm (O=C-NH) confirmed the N-acylhydrazone skeleton in the structures of compounds 5a-5b. The compounds 5a and 5b's ^{1}H NMR spectrum analysis revealed that the S-CH_2 (methylene) protons were detected as a singlet between 4.39 and 4.43 ppm. NH protons between thiadiazole and phenyl rings were observed as singlet in the range of 10.45-10.46 ppm.

The anticancer activity results of compounds 5a, 5b against MCF7, MDA, HT-29 and L929 are presented in Table 1. Cisplatin was used as a reference drug. When the effects of the compounds on cancer cell lines were examined, it was observed that the compounds were ineffective against both cancer cells and healthy cells.

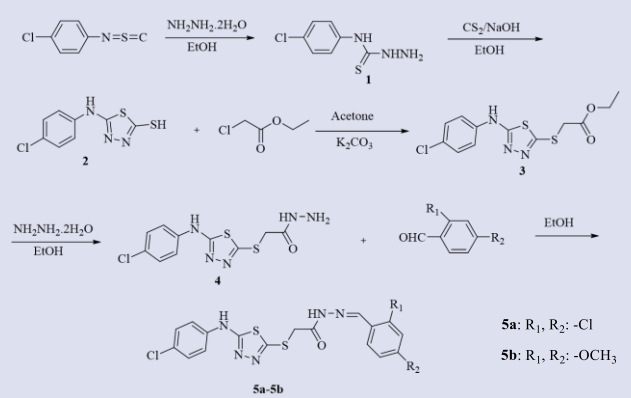

Figure 3. Synthesis pathway of compounds 5a and 5b

Table 1. IC_{50} values (μM) and percent vitality of compounds 5a, 5b and reference drug cisplatin for MCF-7, MDA, HT-29 and L929 cell lines

	IC_{50} values (μM)			
	L929	**MCF7**	**MDA**	**HT-29**
Control	>100	>100	>100	>100
Comp. 5a	>100	>100	>100	>100
Comp. 5b	>100	>100	>100	>100
Cisplatin	4,98	3,145	3,69	7,87

Our synthetic structures were investigated using the esterase assay method with two physiologically relevant isoenzymes carbonic anhydrase. Among these enzymes, carbonic anhydrase-I (hCAI) has a slower cytosolic isoform and carbonic anhydrase-II (hCA II) has a faster inhibition potential. Inhibition data of compounds against hCAI and hCAII isoforms are summarized in Table 2 and Figure 4. While the inhibition effect of the first synthesis was not found, it was determined that our second synthesis had an inhibitory effect on both isoenzymes. The obtained results were compared with the Acetazolamide used as the standard and it was determined that our second synthesis was better than the standard. With these results, it was determined that the compound 5b could be used as an alternative carbonic anhydrase inhibitor. Among them, the compound 5b exhibited remarkable CA inhibitory activities compared to a standard inhibitor with IC_{50} values in the range of 27 μM for hCA I and 33,46 μM for hCA II. Although the compound 5a carrying the chloro substituent on the phenyl ring was ineffective, the compound 5b carrying the methoxy substituent on the phenyl ring was found to be more effective on hCA I and II than the reference drug acetazolamide. It has been determined that the presence of chloro substituent, which is an electron withdrawing group, reduces the effect on hCA, while the methoxy group, which is an electron donating group, increases the activity.

While the compounds are expected to have an effect on both the carbonic anhydrase enzyme and cancer cells, as a result of the activity tests, only an effect on the carbonic anhydrase enzyme was obtained. In this study, we found that compound 5b has carbonic anhydrase activity independent of its anticancer effect. When the literature is examined, diseases that occur as a result of different interactions related to carbonic anhydrase I and II have been associated. These interactions include COX, LOX [24], antioxidant [25], α-glucosidase [26], β-glucuronidase [27], antiulcer [28], acetylcholinesterase [29] and antiglaucoma [30]. Furthermore, according to in vitro assay, it is noteworthy that compound 5b showed significant hCA I and hCA II inhibitory activity, although this compound do not carry a sulfonamide group, which is an important pharmacophore for hCA inhibitory activity.

Altintop et al. The hCA I and hCA II enzyme activities of the compounds carrying the thiadiazole-hydrazone structure were investigated and high activity was obtained in some compounds [31]. When the literature was examined, no studies were found in which both cancer and carbonic anhydrase enzyme activities of compounds with thiadiazole-hydrazone structure were studied. In this study, it is thought that examining both activities will contribute to the literature.

Table 2. IC_{50} (μM) values against hCA I and hCA II enzymes

Comp.	IC_{50} (μM)			
	hCA I	r^2	hCA II	r^2
5a	-	-	-	-
5b	27	0.9691	33.46	0.9546
AZA*	28.11	0.9387	35.65	0.9756

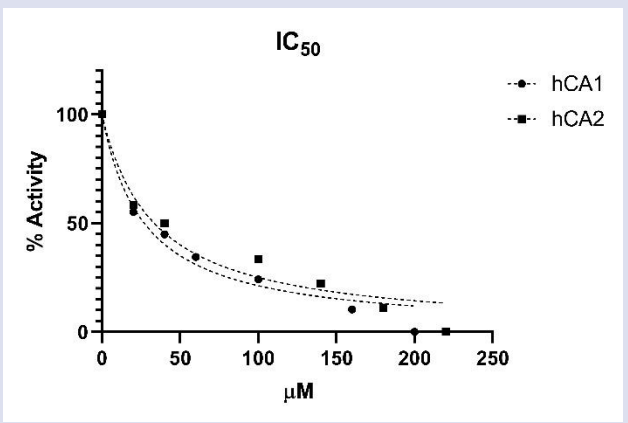

Figure 4. IC_{50} graphs for molecules with the most effective inhibition values against hCA I and II isoenzymes

Conclusion

In this study, two thiadiazole-hydrazone derivatives 5a, 5b were synthesized. The compounds are derivatized via the phenyl ring using the chloro and methoxy substituent. The structures of the compounds were elucidated using spectroscopic methods. The anticancer effects of the compounds were evaluated on the MCF7, MDA, HT-29. In addition, L929 healthy mouse fibroblast cells were used to determine the selectivities of the compounds. In addition, the inhibitory properties of the compounds on hCAI and hCAII enzyme were evaluated. When the anticancer properties of the compounds were examined, it was seen that the compounds were ineffective on cancer cells. When the inhibitory effects of the compounds on the carbonic anhydrase enzyme were evaluated, it was seen that compound 5b was effective on both hCAI and hCAII. The 2,4-dimethoxy groups in the structure of compound 5b seem to be important in both hCAI and hCA II enzyme activity. It was determined that the compounds were not effective on cancer cells, but it was found that the compounds were not toxic on the healthy cell line. In this finding, while the compound 5b is effective against hCA I and hCA II enzymes, it has no toxic effect, which makes this compound more valuable.

Conflicts of interest

The authors declare that there are no conflicts of interest.

References

[1] Tapera M., Kekeçmuhammed H., Tüzün B., Sarıpınar E., Koçyiğit Ü. M., Yıldırım E., Doğen M., Zorlu Y., Synthesis, carbonic anhydrase inhibitory activity, anticancer activity and molecular docking studies of new imidazolyl hydrazone derivatives, *J. Mol. Struct.,* 1269 (2022) 133816.

[2] Bilginer S., Bardaweel S. K., Demir Y., Gulcin I., & Kazaz C., Synthesis, cytotoxicities, and carbonic anhydrase inhibition activities of pyrazoline–benzenesulfonamide derivatives harboring phenol/polyphenol moieties, *Med. Chem. Res.,* (2022) 1-11.

[3] Bonardi A., Bua S., Combs J., Lomelino C., Andring J., Osman S. M., Toti A., Mannelli L.D.C., Gratteri P., Ghelardini C., McKennac R., Nocentini A., The three-tails approach as a new strategy to improve selectivity of action of sulphonamide inhibitors against tumour-associated carbonic anhydrase IX and XII, *J. Enzyme Inhib. Med. Chem.,* 37(2022) 930-939.

[4] Arrighi G., Puerta A., Petrini A., Hicke F. J., Nocentini A., Fernandes M. X., Padron J.M., Supuran C.T., Fernandes-Bolanos J.M., López Ó., Squaramide-Tethered Sulfonamides and Coumarins: Synthesis, Inhibition of Tumor-Associated CAs IX and XII and Docking Simulations, *Int. J. Mol. Sci.,* 23 (2022) 7685.

[5] Tawfik H. O., Petreni A., Supuran C. T., & El-Hamamsy M. H., Discovery of new carbonic anhydrase IX inhibitors as anticancer agents by toning the hydrophobic and hydrophilic rims of the active site to encounter the dual-tail approach, *Eur. J. Med. Chem.,* 232 (2022) 114190.

[6] Al-Warhi T., Elbadawi M. M., Bonardi A., Nocentini A., Al-Karmalawy A. A., Aljaeed N., Alotaibi O.J., Abdel-Aziz H.A., Supuran C.T., Eldehna W. M., Design and synthesis of benzothiazole-based SLC-0111 analogues as new inhibitors for the cancer-associated carbonic anhydrase isoforms IX and XII, *J. Enzyme inhib. Med. Chem.,* 37(2022) 2635-2643.

[7] Elimam D. M., Eldehna W. M., Salem R., Bonardi A., Nocentini A., Al-Rashood S. T., Elaasser M.M., Gratteri P., Supuran C.T., Allam H. A., Natural inspired ligustrazine-based

SLC-0111 analogues as novel carbonic anhydrase inhibitors, *Eur. J. Med. Chem.,* 228 (2022) 114008.

[8] Vanjare B. D., Choi N. G., Eom Y. S., Raza H., Hassan M., Lee K. H., & Kim S. J., Synthesis, carbonic anhydrase inhibition, anticancer activity, and molecular docking studies of 1, 3, 4-oxadiazole derivatives, *Mol. Diver.* (2022) 1-16.

[9] Hagras M., Saleh M. A., Ezz Eldin R. R., Abuelkhir A. A., Khidr E. G., El-Husseiny A. A., El-Mahdy H.A., Elkaeed E.B., Eissa I. H., 1,3,4-Oxadiazole-naphthalene hybrids as potential VEGFR-2 inhibitors: design, synthesis, antiproliferative activity, apoptotic effect, and in silico studies. *J. Enzyme inhib. Med. Chem.,* 37 (2022) 386-402.

[10] Abdelgawad M. A., Bukhari S. N., Musa A., Elmowafy M., Elkomy M. H., Nayl A. A., ... & Elshemy, H. A., New Sulfamethoxazole Derivatives as Selective Carbonic Anhydrase IX and XII Inhibitors: Design, Synthesis, Cytotoxic Activity and Molecular Modeling, *Pharmaceuticals.,* 15 (2022) 1134.

[11] Elkamhawy A., Woo J., Nada H., Angeli A., Bedair T. M., Supuran C. T., & Lee K., Identification of Novel and Potent Indole-Based Benzenesulfonamides as Selective Human Carbonic Anhydrase II Inhibitors: Design, Synthesis, In Vitro, and In Silico Studies, *Int. J. Mol. Sci.,* 23 (2022) 2540.

[12] Abdel-Mohsen H. T., Omar M. A., Petreni A., & Supuran C. T., Novel 2-substituted thioquinazoline-benzenesulfonamide derivatives as carbonic anhydrase inhibitors with potential anticancer activity, *Arch. Pharm.,* (2022) e2200180.

[13] Nada H., Elkamhawy A., Abdellattif M. H., Angeli A., Lee C. H., Supuran C. T., & Lee K., 4-Anilinoquinazoline-based benzenesulfonamides as nanomolar inhibitors of carbonic anhydrase isoforms I, II, IX, and XII: design, synthesis, in-vitro, and in-silico biological studies, *J. Enzyme Inhib. Med. Chem.,* 37 (2022) 994-1004.

[14] Janowska S., Khylyuk D., Gornowicz A., Bielawska A., Janowski M., Czarnomysy R., ... & Wujec M., Synthesis and Anticancer Activity of 1, 3, 4-Thiadiazoles with 3-Methoxyphenyl Substituent, *Molecules*., 27 (2022) 6977.

[15] Janowska S., Khylyuk D., Gornowicz A., Bielawska A., Janowski M., Czarnomysy R., ... & Wujec M., Synthesis and Anticancer Activity of 1, 3, 4-Thiadiazoles with 3-Methoxyphenyl Substituent. *Molecules.,* 27 (2022) 6977.

[16] Janowska S., Khylyuk D., Bielawska A., Szymanowska A., Gornowicz A., Bielawski K., ... & Wujec M., New 1,3,4-Thiadiazole Derivatives with Anticancer Activity, *Molecules.,* 27 (2022) 1814.

[17] Ibrahim S. A., Salem M. M., Abd Elsalam H. A., & Noser A. A., Design, synthesis, in-silico and biological evaluation of novel 2-Amino-1,3,4-thiadiazole based hydrides as B-cell lymphoma-2 inhibitors with potential anticancer effects, *J. Mol. Struct.,* 1268 (2022) 133673.

[18] Vilková M., Hudáčová M., Palušeková N., Jendželovský R., Almáši M., Béres T., ... & Kožurková M., Acridine Based N-Acylhydrazone Derivatives as Potential Anticancer Agents: Synthesis, Characterization and ctDNA/HSA Spectroscopic Binding Properties, *Molecules.,* 27 (2022) 2883.

[19] Tapera M., Kekeçmuhammed H., Tüzün B., Sarıpınar E., Koçyiğit Ü. M., Yıldırım E., ... & Zorlu Y., Synthesis, carbonic anhydrase inhibitory activity, anticancer activity and molecular docking studies of new imidazolyl hydrazone derivatives, *J. Mol. Struct.,* 1269 (2022)133816.

[20] Ayşen I., Çevik U. A., Çelik I., Bostancı H. E., Karayel A., Gündoğdu G., ... & Kaplancıklı Z. A., Benzimidazole-hydrazone derivatives: Synthesis, in vitro anticancer, antimicrobial, antioxidant activities, in silico DFT and ADMET studies, *J. Mol. Struct.,* 1270 (2022) 133946.

[21] Valkova N., Lépine F., Labrie L., Dupont M., & Beaudet R., Purification and Characterization of PrbA, a New Esterase fromEnterobacter cloacae Hydrolyzing the Esters of 4-Hydroxybenzoic Acid (Parabens), *J. Biol. Chem.,* 278 (2003) 12779-12785.

[22] Henke E., & Bornscheuer U., Esterases from Bacillus subtilis and B. stearothermophilus share high sequence homology but differ substantially in their properties. *Appl. Microbiol. Biotechnol,* 60 (2002) 320-326.

[23] Ciccone L., Cerri C., Nencetti S., & Orlandini E., Carbonic anhydrase inhibitors and epilepsy: State of the art and future perspectives, *Molecules,* 26 (2021) 6380.

[24] Ragab M. A., Eldehna W. M., Nocentini A., Bonardi A., Okda H. E., Elgendy B., Ibrahim T.S., Abd-Alhaseeb M.M., Gratteri P., Supuran, C.T., Al-Karmalawy A.A., Elagawany M., 4-(5-Amino-pyrazol-1-yl) benzenesulfonamide derivatives as novel multi-target anti-inflammatory agents endowed with inhibitory activity against COX-2, 5-LOX and carbonic anhydrase: Design, synthesis, and biological assessments, *Eur. J. Med. Chem.,* 250 (2023) 115180.

[25] Küçükoğlu K., Acar Çevik U., Nadaroglu H., Celik I., Işık A., Bostancı H. E., Ozkay Y., Kaplancıklı Z. A., Design, synthesis and molecular docking studies of novel benzimidazole-1, 3, 4-oxadiazole hybrids for their carbonic anhydrase inhibitory and antioxidant effects, *Med. Chem. Res.,* 31 (2022) 1771-1782.

[26] Ahmed A., Shafique I., Saeed A., Shabir G., Saleem A., Taslimi P., Tok T.T., Kirici M., Üç E.M., Hashmi M. Z., Nimesulide linked acyl thioureas potent carbonic anhydrase I, II and α-glucosidase inhibitors: Design, synthesis and molecular docking studies, *Eur. J. Med. Chem. Rep.,* 6 (2022) 100082.

[27] Arif N., Shafiq Z., Mahmood K., Rafiq M., Naz S., Shahzad S. A., Farooq U., Bahkali A.H., Elgorban A.M., Yaqup M., El-Gokha A., Synthesis, Biological Evaluation, and In Silico Studies of Novel Coumarin-Based 4H, 5H-pyrano [3,2-c] chromenes as Potent β-Glucuronidase and Carbonic Anhydrase Inhibitors, *ACS Omega.,* 7 (2022) 28605-28617.

[28] Güller U., Beydemir Ş., & Küfrevioğlu Ö. İ., In vitro and in silico interactions of antiulcer, glucocorticoids and urological drugs on human carbonic anhydrase I and II isozymes, *Biopharm. Drug Dispos.,* 43 (2022) 47-56.

[29] Bulut Z., Abul N., Poslu A. H., Gülçin İ., Ece A., Erçağ E., Koz Ö., Koz G., Structural characterization and biological evaluation of uracil-appended benzylic amines as acetylcholinesterase and carbonic anhydrase I and II inhibitors, *J. Mol. Struct.,* 1280 (2023) 135047.

[30] Chiaramonte N., Angeli A., Sgambellone S., Bonardi A., Nocentini A., Bartolucci G., Braconi L., Dei S., Lucarini L., Teodori E., Gratteri P., Wünsch B., Supuran C.T., Romanelli M. N., 2-(2-Hydroxyethyl) piperazine derivatives as potent human carbonic anhydrase inhibitors: Synthesis, enzyme inhibition, computational studies and antiglaucoma activity, *Eur. J. Med. Chem.,* 228 (2022) 114026.

[31] Altıntop M. D., Sever B., Özdemir A., Kucukoglu K., Onem H., Nadaroglu H., & Kaplancıklı Z. A., Potential inhibitors of human carbonic anhydrase isozymes I and II: Design, synthesis and docking studies of new 1, 3, 4-thiadiazole derivatives, *Bioorg. Med. Chem.,* 25 (2017) 3547-3554.

Cumhuriyet Sci. J., 44(2) (2023) 263-267
DOI: https://doi.org/10.17776/csj.1256954

Cumhuriyet Science Journal

| csj.cumhuriyet.edu.tr | Founded: 2002 ISSN: 2587-2680 e-ISSN: 2587-246X Publisher: Sivas Cumhuriyet University

Investigation of The Antiproliferative Effect of Colchicine on SNU-1 Gastric Cancer Cells

Fatih Yulak [1,a,*]

[1] *Department of Physiology, School of Medicine, Sivas Cumhuriyet University, Sivas, Türkiye*
**Corresponding author*

Research Article

History
Received: 27/02/2023
Accepted: 17/06/2023

ABSTRACT

In this study, colchicine's cytotoxic effects on SNU-1 cells were examined, and a probable mechanism behind its cytotoxicity was revealed. According to the results of the study, colchicine displayed considerable cytotoxicity with an IC_{50} value of 14.81ng/ml when it was administered to the cells for 24 hours at different doses ranging from 5 to 100ng/ml. Furthermore, according to mechanistic studies, usege of colchicine significantly increased both early and late apoptotic cells in flow cytometry experiments. The late apoptotic cell population percentage in the control group (5.14 ± 1.27%) dramatically increased to 22.83 ± 1.38% in 14.81ng/ml colchicine treated cells. The early apoptotic cell population percentage in the control group (2.00 ± 1.12%) increased to 6.57 ± 2.35% in 14.81ng/ml colchicine treated cells. ELISA method was used to evaluate how colchicine affects the expression of pro- and anti-apoptotic proteins in SNU-1 cells. Colchicine treatment increased pro-apoptotic Bax and cleaved caspase 3 activities, while anti-apoptotic BCL-2 levels decreased. It is concluded that colchicine increases apoptosis in SNU-1 cells, which leads to an overall increase in cell death. Colchicine's promise as an anticancer drug to treat stomach cancer, however, needs additional research to be determined.

Keywords: *Gastric cancer, Colchicine, Antiproliferative effect, Apoptozis.*

[a] *fatihyulak@gmail.com* *https://orcid.org/0000-0003-3708-6752*

Introduction

Gastric cancer(GC) is a multifactorial disease, where many factors can influence its development, both environmental and genetic[1]. Globally, GC, the most prevalent form of gastrointestinal cancer, is the leading cause of death[2]. Every year, around 990,000 people are diagnosed with GC worldwide, of whom approximately 738,000 die[3]. GC is the fourth most common incident cancer and the second most common cause of cancer death[4]. The survival rate for advanced GC is less than 12 months[5]. GC is still a global health problem as a very aggressive malignancy with a complex nature[6]. Therefore, alternative prevention, considered as proper nutrition, early detection and follow-up of appropriate treatments, leads to a reduction in recorded cases[7]. There are still treatment options available for those with GC, such as surgery, chemotherapy, and radiotherapy[8]. Nonetheless, the most effective treatment for patients with the incurable condition is chemotherapy, preventing tumor invasion and metastasis [9]. Luo et al. (2010) implies that its effects are stable with overall 5-year survival ratioes ranging from 5% to 15%[10]. Despite recent advancements in treatment of GC, overall survival statistics for patients with gastric cancer continue to be poor, which implies the urgency of discovering and developing new therapeutic approaches or agents for GC. According to Bhat and Singh (2008), a growing number of naturally occurring bioactive compounds have been investigated as potential anticancer medications due to their high effect power and low damaging effect, in view of their ability to affect key stages in the genesis of cancer[11]. Because the rise in mitosis, one of the most well-known characteristics of cancer cells, depends on the arrangement microtubules, agents that target microtubules are being investigated as potential targets for chemotherapy[12]. In addition, studies by Huang et al. (2015) states that that a variety of plant-derived anti-microtubule medications, including vincristine, vinblastine and paclitaxel, have begun to be involved in clinical practice as chemotherapeutics or under laboratory work to gain approval for chemotherapy[13]. One of plant-derived anti-microtubule medications, called colchicine, is an alkaloid found in meadow saffron (Colchicum autumnale L.) and has been used for thousands of years to treat acute gout attacks and other inflammatory disorders[14]. According to the study by Kaplan et al. (1986), colchicine has been shown to be effective against some types of cancer and some liver diseases [15]. Colchicine exerts reduces an antiproliferative impact by hindering microtubule formation, resulting in the mitotic arrest and cell death through apoptosis [16]. Due to their effectiveness in inhibiting mitosis, colchicine and its semi-synthetic derivatives have the potential to be employed as chemotherapeutic drugs for the treatment of cancer [17]. Additionally, cancer cells have a much higher

mitotic rate and are more sensitive to colchicine than normal cells[18].

Colchicine has been proven in numerous studies to have antiproliferative effects on a variety of cancer cell lines, but the underlying processes are still unknown. The aim of the current study was to investigate the antiproliferative effects of colchicine on gastric carcinoma cells and the mechanisms behind colchicine's antiproliferative effects on gastric cancer cells.

Material and Methods

Cell Line and Cell Culture

American Type Culture Collection provided the SNU-1(CRL-5971) cell line (ATCC, USA) for the study. For SNU-1 cultures, RPMI-1640 media (Sigma-Aldrich) was employed. 10% Fetal Bovine Serum (FBS) (Gibco, Thermo Fisher Scientific), antibiotic combinations of 50 U/mL penicillin/streptomycin (Gibco, Thermo Fisher Scientific) was added to this medium. Cells were cultured at 37°C in a humidified environment with 5% CO_2. Before treatment, DMSO-dissolved colchicine (Sigma-Aldrich) was diluted in culture media to have a final DMSO level of less than 0.1%.

Cell Viability Assay

XTT assay (Roche Diagnostic, Germany) was employed to assess the antiproliferative activity of colchicine against cancer. Briefly stated, the cells were incubated in 96-well cell culture plates with an adjusted density of 1×10^4 cells per well in triplicates for 24 hours with chosen colchicine concentrations (5, 10, 25, 50, 100ng/ml). A 50-µL XTT labelling cocktail was then added to each well to measure living cells, and the cells were then incubated for an additional 4 h. The absorbance was then measured at 450 nm using an ELISA microplate reader (Epoch, Biotec, USA). The cell viability was recorded as % related to control (% of control). Graph Prism 7 software (GraphPad, Software, Inc., USA) was used to determine the half maximal inhibitory concentration(IC_{50}) values of colchicine in examined cell line, and the IC_{50} value of colchicine in SNU-1 gastric carcinoma cells was used in the ELISA and flow cytometry experiments that are detailed below.

Annexin V Binding Assay

Prepared SNU-1 gastric carcinom cells were initially put in six-well plate. The measured IC_{50} concentration of colchicine was applied to the cells. Cells were harvested after 24 hours of incubation and then incubated with Muse™ Annexin V & Dead Cell kit reagent. The method employed during the procedure was the one advised by the manufacturer. Four distinct populations—live, early apoptotic, late apoptotic, and dead—were observed on the Cell Analyzer (Muse, Millipore) using Annexin V and/or 7-AAD positive.

Bax, Cleaved Caspase 3 and BCL-2 Expression Analyses

Bax ELISA Kit (Abcam, Catalog #ab199080), Caspase 3 (cleaved) ELISA Kit (Invitrogen, Catalog #KHO1091), BCL-2 ELISA Kit (Invitrogen, Catalog #BMS244-3) were used, respectively, to measure the levels of Bax, cleaved caspase 3, BCL-2 proteins in the colchicine-treated and untreated SNU-1 gastric carcinom cells. Briefly, the IC_{50} concentration of colchicine as determined by antiproliferative effect experiments was applied to SNU-1 cells planted in a 6-well plate for 24 hours. After that, Bax, BCL-2, cleaved caspase 3 levels in the cell lysates were assessed in accordance with the manufacturer's instructions after colchicine-treated and untreated SNU-1 gasric carcinom cells were lysed using the lysis buffer. Using the BCA assay, the total protein concentration in SNU-1 cells were also determined (Pierce Biotechnology, Rockford, IL, USA).

Statistical Analysis

Each experiment was performed in triplicate, and the findings were provided as mean standard deviation. The post hoc Dunn test, Mann-Whitney test, and Kruskal-Wallis ANOVA test were carried out when necessary to compare the variables measured as a result of the treatment with colchicine with the control. A statistical difference was considered significant when $P<0.05$.

Results

Colchicine Suppressed the Proliferation of Snu-1 Gastric Carcinoma Cells

Initially, colchicine's antiproliferative effect was determined in SNU-1 gastric carcinom cells. Colchicine significantly reduced the growth of the SNU-1 cells at concentrations of 10ng/mL and higher when compared to untreated cells, as seen in Fig. 1 ($P < 0.01$). Colchicine's IC_{50} value was calculated to be 14.81 ng/mL for 24 hours in SNU-1 cells.

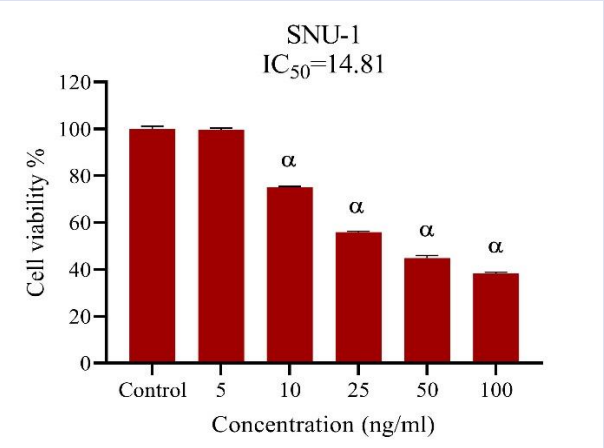

Fig. 1. Colchicine's effects on the viability of SNU-1 gastric carcinoma cells. Colchicine was applied to the cells for 24 hours at a concentration range between 5 and 100 ng/mL, and the number of viable cells was assessed using the XTT assay. The data are provided as a proportion of viable cells compared to the untreated control. The data are the mean and standard deviation from two separate experiments. The differences are $^{\alpha}P < 0.01$ compared with control.

Colchicine-induced Apoptosis of Snu-1 Gastric Carcinoma Cells

Initially, flow cytometric analysis and an Annexin V-FITC staining assay were conducted to evaluate the apoptotic effects of colchicine on SNU-1 cells.

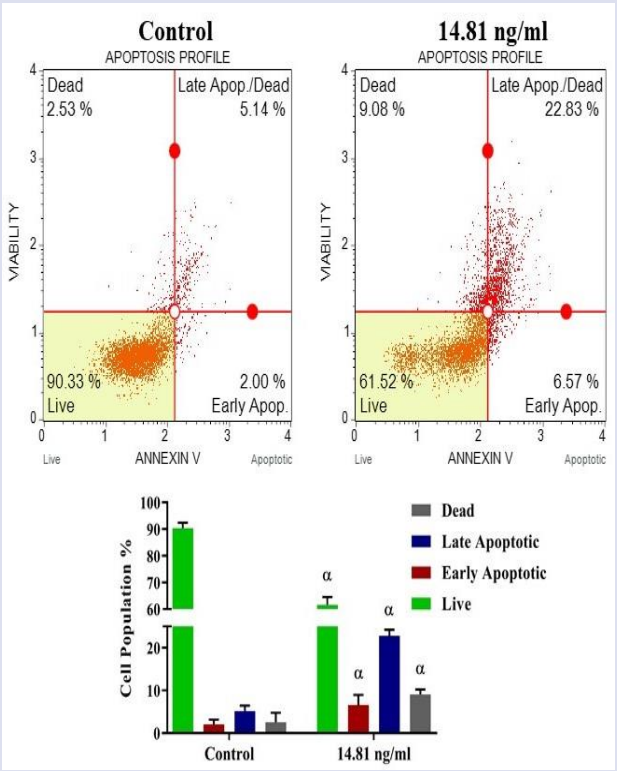

Fig. 2A. Annexin V-determined apoptosis in SNU-1 gastric carcinoma cells after 24 hours of colchicine administration. Cells were exposed to 14.81 ng/mL colchicine and the amount of apoptotic cells was determined by Muse cell analyzer (Merck Millipore) as described above. Early and late apoptotic cell percentages increased significantly in 14.81 ng/mL colchicine-treated cells. Experiments were repeated three times. $^{\alpha}P$ value <0.01 vs. Untreated SNU-1 gastric carcinoma cells and 14.81 ng/mL colchicine-treated groups.

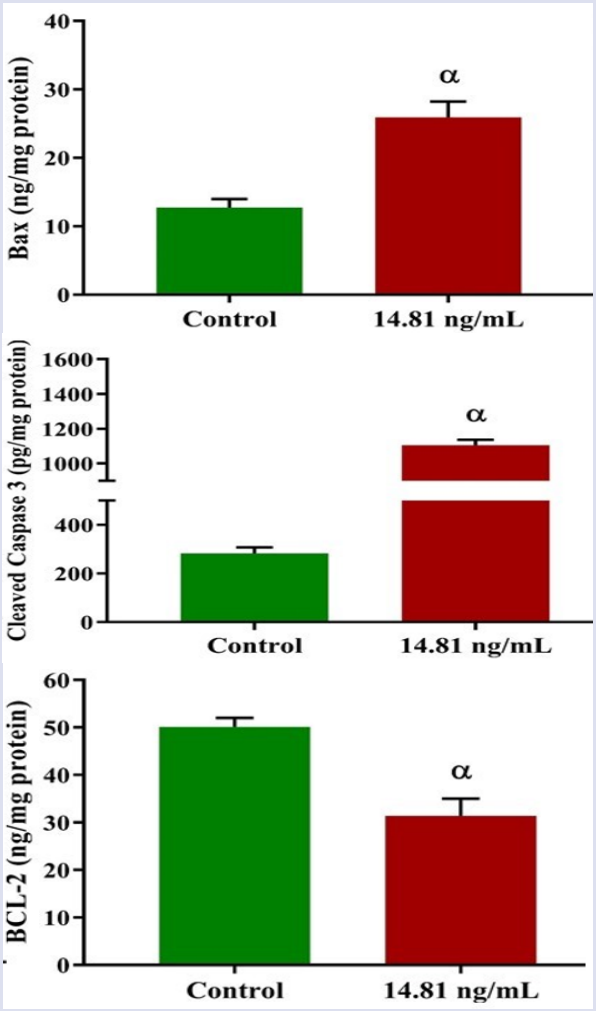

Fig. 2B. Colchicine was administered to SNU-1 cells 14.81 ng/mL for 24 hours, after which the levels of Bax, cleaved caspase 3, and BCL-2 were measured using ELISA kit. Bax and cleaved caspase 3 levels increased significantly in 14.81 ng/mL colchicine-treated cells. BCL-2 levels decreased significantly in 14.81 ng/mL colchicine-treated cells. $^{\alpha}$Significantly different when compared to untreated cells ($^{\alpha}P < 0.01$).

Colchicine treatment significantly enhanced the percentage of early and late apoptotic cells in 14.81 ng/ml doses as compared to the untreated cells, according to the Annexin V binding assay in Fig. 2A. The late apoptotic cell population percentage in the control group (5.14 ± 1.27%) dramatically increased to 22.83 ± 1.38% in 14.81ng/ml colchicine treated cells ($^{\alpha}P < 0.01$). The ELISA measurements were used to assess how colchicine treatment affected the expression of pro- and anti-apoptotic proteins in SNU-1 cells. As can be seen in Fig. 2B, the compound treatment markedly increased Bax ($^{\alpha}P < 0.01$) and cleaved caspase 3 $^{\alpha}P < 0.01$) activities, while anti-apoptotic BCL-2 levels decreased ($^{\alpha}P < 0.01$).

Discussion

Less than a century ago, gastric carcinoma was probably the most common type of cancer worldwide, according to Ferlay et al[19]. Because of its heterogeneous form and high aggressiveness, gastric cancer continues to be a threat for global health.[20]. For this reason, alternative preventative measures like a balanced diet, early detection, and suitable follow-up treatments lower the frequency of incidents that are recorded[21].

A crucial stage of mitosis that directly affects cancer cell growth is microtubule creation and structure. As a result, targeting microtubules is being considered as a study issue by scientists as they look for new chemicals to develop chemotherapeutics. Microtubule-targeting drugs may also be more effective at reducing the

proliferation of cancer cells due to the higher rate of mitosis in cancer cells.

A well-known and effective microtubule targeting drug is colchicine. It causes mitotic arrest (hyperploidy) by binding to different locations on -tubulin, disrupting microtubule functions[[22], [23], [24], [25]]. Colchicine dissociates microtubules into tubulin dimers upon attaching to them, preventing the polymerization of tubulin and disrupting microtubule dynamics [[26], [27]]. Colchicine has long been used to treat gout and FMF(familial Mediterranean fever), but new research has shown that it also significantly inhibits the growth of a number of cancer cell lines, including those from the colon, gastric, liver, and lung[28],[13]. In cancer cells, the rate of mitosis is enhanced, and the microtubules that are created during mitosis are thought to be a prime target for anticancer treatments[29]. We are currently unaware of its cytotoxic effects and cell death mechanisms in stomach cancer. In the current study, colchicine's inhibitory effects on SNU-1 gastric carcinom cells were examined to gain additional information regarding the potential molecular processes underlying these antiproliferative activities.

There are numerous studies in the literature describing the anticancer activity of different substances with pharmacological action in SNU-1 cells, including amlodipine, verapamile, and propranolol. Parallel to the above, we looked into the antiproliferative effects of colchicine, a drug not typically utilized in chemotherapeutics, on SNU-1 cells in this work. At the beginning, XTT tests were carried out to look into the concentration-dependent cytotoxicity of colchicine on SNU-1 cells. Colchicine strongly suppressed SNU-1 cell proliferation, according to experimental results, and its IC_{50} value was found to be 14.81 ng/mL for 24 hours.

According to Chen et al., induction of apoptosis with natural product-derived anticancer drugs is a very important strategy to get rid of cancer cells, and promoting apoptosis in cancer cells has an important place in anticancer therapies[[30], [31], [32]]. Hickman (1996) states that apoptosis is well acknowledged to have a significant role in the molecular pathogenesis of cancer and affect how well chemotherapy and radiation therapy work[33]. In the apoptotic process, the proapoptotic protein Bax enables the migration of cytochrome c from the mitochondria to the cytoplasm, and cytochrome c stimulates the apoptotic process[34]. Contrarily, the anti-apoptotic protein BCL-2 blocks the release of cytochrome c from mitochondria and inhibits apoptosis. Increased pro-apoptotic Bax level and decreased BCL-2 level strongly correlated with the mechanism of cell death. The fate of the cell is often determined by the ratio of pro- and anti-apoptotic (Bax and BCL-2) proteins[35]. Caspases are also essential for the apoptotic process, particularly when it comes to the proteolytic cleavage of proteins. According to Bakar-Ates et al. (2020), they are formed by cells as zymogens, and when cells are exposed to cytotoxic substances, they divide to form substrates that induce apoptosis[36]. The most noticeable caspase is caspase 3, which triggered the endonuclease CAD (Caspase-activated DNAse), which results in chromatin condensation and chromosomal DNA destruction[37].

This study used flow cytometry-based testing and ELISA research to determine whether colchicine treatment inhibits cell development as a result of apoptotic changes. Our results demonstrated that colchicine therapy induced apoptosis by enhancing pro-apoptotic Bax, cleaved caspase 3, Annexin V binding, and lowering anti-apoptotic BCL-2 protein in SNU-1 cells. These phenomena provided strong evidence that colchicine can cause SNU-1 cells to apoptose. A recent study by Wang et al. (2017) has shown that cancer cells treated with colchicine frequently induce apoptosis [38]. Colchicine, according to the study of Bhat and Singh (2008), greatly boosted apoptosis in human colon cancer HT-29 cells.[13]. Several studies also discovered colchicine's similar apoptosis-inducing actions in a range of cancer cells[[28], [39]].

Conclusion

This study shows that colchicine increses apoptosis in SNU-1 cells. Colchicine exhibits high cytotoxic efficacy against SNU-1 gastric cancer cells overall, but more research is needed before it can be used as a new gastric cancer chemotherapeutic drug.

Acknowledgments

The author is grateful to the CÜTFAM research center that provided the infrastructure for the experiments.

Conflicts of interest

There are no conflicts of interest in this work.

References

[1] A. R. Yusefi, K. Bagheri Lankarani, P. Bastani, M. Radinmanesh, and Z. Kavosi, Risk Factors for Gastric Cancer: A Systematic Review, *Asian Pac. J. Cancer Prev.*, 19(3) (2018) 591–603.

[2] J. Machlowska, J. Baj, M. Sitarz, R. Maciejewski, and R. Sitarz, Molecular Sciences Gastric Cancer: Epidemiology, Risk Factors, Classification, Genomic Characteristics and Treatment Strategies, International J. of Molecular Sciences, 21(11) (2020) 4012.

[3] J. Ferlay, H. R. Shin, F. Bray, D. Forman, C. Mathers, and D. M. Parkin, Estimates of worldwide burden of cancer in 2008, *Int. J. Cancer*, 127(12) (2010) 2893–2917.

[4] A. Jemal, M. M. Center, C. DeSantis, and E. M. Ward, Global patterns of cancer incidence and mortality rates and trends, *Cancer Epidemiol. biomarkers Prev. a Publ. Am. Assoc. Cancer Res. cosponsored by Am. Soc. Prev. Oncol.*, 19(8) (2010) 1893–1907.

[5] X.-Y. Zhang, P.-Y. Zhang, Gastric cancer: somatic genetics as a guide to therapy., *J. Med. Genet.*, 54(5) (2017) 305–312.

[6] J.-P. Gao, W. Xu, W.-T. Liu, M. Yan, and Z.-G. Zhu, Tumor heterogeneity of gastric cancer: From the perspective of tumor-initiating cell., *World J. Gastroenterol.*, 24(24) (2018) 2567–2581.

[7] J. Y. Park, L. von Karsa, and R. Herrero, Prevention strategies for gastric cancer: a global perspective., *Clin. Endosc.*, 47(6) (2014) 478–489.

[8] H. H. Hartgrink, E. P. M. Jansen, N. C. T. Van Grieken, and A. V. L. Hospital, *HHS Public Access*, 374(9688) (2015) 477–490.

[9] D. Roda, E. Rodrı, A. Cervantes, and S. Rosello, The treatment of advanced gastric cancer : current strategies and future perspectives, 19(Supplement 5) (2008) 103–107.

[10] H. Luo *et al.*, Cetuximab enhances the effect of oxaliplatin on hypoxic gastric cancer cell lines, Oncology Reports, 23(6) (2010) 1735–1745.

[11] T. A. Bhat and R. P. Singh, Tumor angiogenesis - A potential target in cancer chemoprevention, *Food Chem. Toxicol.*, 46(4) (2008) 1334–1345.

[12] S. Bhattacharya, A. Das, S. Datta, A. Ganguli, and G. Chakrabarti, Colchicine induces autophagy and senescence in lung cancer cells at clinically admissible concentration: potential use of colchicine in combination with autophagy inhibitor in cancer therapy, *Tumor Biol.*, 37(8) (2016) 10653–10664.

[13] Z. Huang, Y. Xu, and W. Peng, Colchicine induces apoptosis in HT-29 human colon cancer cells via the AKT and c-Jun N-terminal kinase signaling pathways, *Mol. Med. Rep.*, 12(4) (2015) 5939–5944.

[14] I. Dudkiewicz, T. Brosh, M. Perelman, and M. Salai, Colchicine inhibits fracture union and reduces bone strength - In vivo study, *J. Orthop. Res.*, 23(4) (2005) 877–881.

[15] Marshall M. Kaplan, Raoul Poupon, Treatment with immunosuppressives in patients with primary biliary cirrhosis who fail to respond to ursodiol, Hepatology, 50(2) (2009) 652.

[16] A. Kumar, B. Singh, P. R. Sharma, S. B. Bharate, A. K. Saxena, and D. M. Mondhe, A novel microtubule depolymerizing colchicine analogue triggers apoptosis and autophagy in HCT-116 colon cancer cells, *Cell Biochem. Funct.*, 34(2) (2016) 69–81.

[17] G. C. Sun, H. H. Chen, W. Z. Liang, and C. R. Jan, Exploration of the effect of the alkaloid colchicine on Ca 2+ handling and its related physiology in human oral cancer cells, *Arch. Oral Biol.*, 102(April) (2019) 179–185.

[18] A. Kumar, P. R. Sharma, and D. M. Mondhe, Potential anticancer role of colchicine-based derivatives: An overview, *Anticancer. Drugs*, 28(3) (2016) 250–262.

[19] J. Ferlay, H.-R. Shin, F. Bray, D. Forman, C. Mathers, and D. M. Parkin, Estimates of worldwide burden of cancer in 2008: GLOBOCAN 2008, *Int. J. Cancer*, 127(12) (2010) 2893–2917.

[20] J. P. Gao, W. Xu, W. T. Liu, M. Yan, and Z. G. Zhu, Tumor heterogeneity of gastric cancer: From the perspective of tumor-initiating cell, *World J. Gastroenterol.*, 24(24) (2018) 2567–2581.

[21] O. Handa and Y. Naito, Prevention strategy for gastric cancer, *Gastric Cancer With Spec. Focus Stud. from Japan*, 1st ed. Japan, (2018) 193–201.

[22] M. A. Jordan and L. Wilson, "Microtubules and actin filaments: Dynamic targets for cancer chemotherapy, *Curr. Opin. Cell Biol.*, 10(1) (1998) 123–130.

[23] M. A. Jordan and L. Wilson, Microtubules As a Target for Anticancer Drug, Nature Reviews Cancer, 4 (2004) 253-265.

[24] G. V Ronnett and C. Moon, G Proteins and Olfactory Signal Transduction, Annual Review of Physiology, 64(5) (2002) 189–222.

[25] E. K. Rowinsky and R. C. Donehower, The clinical pharmacology and use of antimicrotubule agents in cancer chemotherapeutics, *Pharmacol. Ther.*, 52(1) (1991) 35–84.

[26] E. W. Taylor, The Mechanism of Colchicine Inhibition of Mitosis. I. Kinetics of Inhibition and the Binding of H3-Colchicine., *J. Cell Biol.*, 25(1), (1965) 145–160.

[27] L. L. Fessler, Michael B.; Rudel, "基因的改变NIH Public Access, *Bone*, 23(1) (2011) 1–7.

[28] S. Bhattacharya, A. Das, S. Datta, A. Ganguli, and G. Chakrabarti, Colchicine induces autophagy and senescence in lung cancer cells at clinically admissible concentration: potential use of colchicine in combination with autophagy inhibitor in cancer therapy, Tumor Biology, 37 (2016) 10653–10664

[29] Z. Y. Lin, C. C. Wu, Y. H. Chuang, and W. L. Chuang, Anti-cancer mechanisms of clinically acceptable colchicine concentrations on hepatocellular carcinoma, *Life Sci.*, 93(8) (2013) 323–328.

[30] X. Zhu *et al.*, Osthole inhibits the PI3K/AKT signaling pathway via activation of PTEN and induces cell cycle arrest and apoptosis in esophageal squamous cell carcinoma, *Biomed. Pharmacother.*, 102(november) (2018) 502–509.

[31] A. Maryam, T. Mehmood, Q. Yan, Y. Li, M. Khan, and T. Ma, Proscillaridin A promotes oxidative stress and ER stress, inhibits STAT3 activation, and induces apoptosis in A549 lung adenocarcinoma cells, *Oxid. Med. Cell. Longev.*, 2018 (2018) 1-17.

[32] Z. Chen, B. Zhang, F. Gao, and R. Shi, Modulation of G2/M cell cycle arrest and apoptosis by luteolin in human colon cancer cells and xenografts, *Oncol. Lett.*, 15(2) (2018) 1559–1565.

[33] J. A. Hickman, Apoptosis and chemotherapy resistance, *Eur. J. Cancer*, 32(6) (1996) 921–926.

[34] B. A. Carneiro and W. S. El-Deiry, Targeting apoptosis in cancer therapy, *Nat. Rev. Clin. Oncol.*, 17(7) (2020) 395–417.

[35] G. C. Cavalcante *et al.*, A cell's fate: An overview of the molecular biology and genetics of apoptosis, *Int. J. Mol. Sci.*, 20(17) (2019) 1–20.

[36] F. Bakar-Ates, E. Ozkan, and C. T. Sengel-Turk, Encapsulation of cucurbitacin B into lipid polymer hybrid nanocarriers induced apoptosis of MDAMB231 cells through PARP cleavage, *Int. J. Pharm.*, 586(April) (2020) 119565.

[37] R. Jan and G.-S. Chaudhry, Understanding Apoptosis and Apoptotic Pathways Targeted Cancer Therapeutics, *Adv Pharm Bull*, 2019(2) (2019) 205–218.

[38] R. C. Wang *et al.*, Sensitivity of docetaxel-resistant MCF-7 breast cancer cells to microtubule-destabilizing agents including vinca alkaloids and colchicine-site binding agents, *PLoS One*, 12(8) (2017) 1–22.

[39] Q. Guo *et al.*, Ligand- and structural-based discovery of potential small molecules that target the colchicine site of tubulin for cancer treatment, *Eur. J. Med. Chem.*, 196 (2020) 112328.

Cumhuriyet Sci. J., 44(2) (2023) 268-275
DOI: https://doi.org/10.17776/csj.1166108

Cumhuriyet Science Journal

| csj.cumhuriyet.edu.tr | Founded: 2002 ISSN: 2587-2680 e-ISSN: 2587-246X Publisher: Sivas Cumhuriyet University

Trifloxystrobin Pretreatment Alleviates Excessive Copper Stress in Wheat (*Triticum aestivum* L.)

Oksal Macar [1,a,*], Tuğçe Kalefetoğlu Macar [1,b], Tolga Karaköy [2,c]

[1] *Department of Food Technology, Şebinkarahisar School of Applied Sciences, Giresun University, Giresun, Türkiye*
[2] *Faculty of Agricultural Sciences and Technology, Sivas University of Science and Technology, Sivas, Türkiye*
**Corresponding author*

Research Article

History
Received: 24/08/2022
Accepted: 21/05/2023

ABSTRACT

Protective role of Trifloxystrobin pretreatment against excessive copper-related abiotic stress in *Triticum aestivum* L. was determined in two Turkish wheat cultivars, Sönmez and Gerek 79. Ten-day-old seedlings were pretreated with 20 µM and 80 µM Trifloxystrobin. A group of seedlings was harvested without exposure to Trifloxystrobin as a control. Two days after, seedlings were treated with copper(II) chloride. Seedlings were harvested on the 20th day after sowing. The growth level of the groups was evaluated by measuring the length, fresh weight and shoot dry weight of shoots. Chlorophyll a + b, carotenoid and anthocyanin contents as well as proline levels were assessed. Lipid peroxidation and total activities of superoxide dismutase, peroxidase and glutathione reductase were analyzed to predict the oxidative stress levels. Both cultivars exhibited similar responses to the treatments. Trifloxystrobin doses did not cause damage on plants when applied alone. Seedlings subjected to excessive doses of copper showed significant reductions in growth parameters, as well as chlorophyll and carotenoid pigments. Conversely, copper caused a remarkable increase in anthocyanin, proline and malondialdehyde accumulation. Superoxide dismutase and peroxidase activities increased, while glutathione reductase activity decreased in copper-stressed plants. Trifloxystrobin pretreatment strengthens the antioxidant defense system. All parameters were positively affected by Trifloxystrobin pretreatment. As the dose of Trifloxystrobin increased, the severity of stress decreased in both genotypes. Trifloxystrobin pretreatment is a promising method for reducing copper-induced damage in *T. aestivum*.

Keywords: Antmicrobial, Crystallinity, FT-IR, Poly ε-caprolactone, *Rumex patientia.*

[a] *oksal.macar@giresun.edu.tr* *https://orcid.org/0000-0002-5067-8712*
[b] *tugce.macar@giresun.edu.tr* *https://orcid.org/0000-0002-9946-8054*
[c] *tkarakoy@sivas.edu.tr* *https://orcid.org/0000-0002-5428-1907*

Introduction

Wheat (*Triticum aestivum* L.) is the third most grown cereal in the world, following rice and corn. Due to its high adaptability and affordable price, it has become extremely popular for both agriculture and human consumption. Wheat grains are rich wellsprings of resistant starch, protein, inulin, tocopherol, phenolic acids, phytates, carotenoids, β-glucans, lignans and sterols. As a staple food, it provides approximately 55% of the starch, at least 20% of the total calories and 25% of the protein consumed in the world. Besides being a satisfying food grain, it is considered a rich source of dietary fiber. Türkiye, one of the gene centers of *T. aestivum*, is among the leading wheat producers in the world and has 201 officially registered bread wheat varieties [1]. One of the agricultural importance of wheat in Türkiye is its rotation with other field crops such as sugar beet and corn [2]. It is predicted that the demand for wheat, which will be required to feed the world population, which is expected to be 9.7 billion in 2050, will increase by 60%. Wheat exhibits a remarkable sensitivity to the stresses induced by various heavy metals [3]. Therefore, the protection of wheat from stress factors, including heavy metals, during the growing process should be the subject of research.

Copper (Cu) is a redox active transition metal which is needed for proper growth and development in plants. Due to being a vital micronutrient for plants, healthy physiological and biochemical functions can only be sustained in the presence of 5-30 mg kg^{-1} Cu [4]. Photosynthesis, aerobic respiration, electron transport chain, lignin biosynthesis, cell wall metabolism, hormone signaling, iron metabolism, transcription and oxidative stress response are among the processes in which Cu plays an active role [5]. It is also a crucial constituent of several regulatory proteins, including plastocyanin, cytochrome-c-oxidase, amino oxidase, polyphenol oxidase and laccase [6]. Cu, the second most employed non-ferrous metal in industrial fields, is a critical element in energy, agriculture, construction, electronics and transport industries [7]. It is mainly released to agricultural soils from fungicide applications, chemical fertilizers, liquid manures, traffic, mining and sewage sludge [7]. Despite all vital functions in plants, Cu amounts exceeding optimum concentrations cause growth retardation, chlorosis, oxidative stress, membrane defect, altered enzyme activities, cytotoxicity and genotoxicity [8].

The evolution of fungi began about a billion years ago. Since then, the number of known fungi species has reached 120,000, with 1500-2000 new species discovered each year [9]. Although fungicides are widely employed to protect crop plants against pathogenic fungi, it is ambiguous whether these chemicals also affect abiotic stress tolerance. Treatments based on synthetic phytoprotectants have become popular approaches to minimize metal-related damage to crops. Some of the fungicides, which show serious toxicity in the case of use or accumulation in high concentration, can reduce the damage of abiotic stress by strengthening the plant defense mechanisms at low concentration [10]. Trifloxystrobin is a promising fungicide from the Strobilurins, the most common fungicide family all over the world. Trifloxystrobin, similar to other Strobilurins, binds to cytochrome b from the Qo region, leading to a blockage in electron transfer from cytochrome b to cytochrome c1. Thus, as a result of inhibited mitochondrial respiration, the energy cycle is broken [11]. Since plants are eukaryotic organisms, the electron transport system of their mitocondrial respiration is partially suppressed following Trifloxystrobin application. However, there are various studies indicating the contribution of exogenous Trifloxystrobin to abiotic stress defense in plant cells [12]. Indeed, Strobilurins delay leaf senescence, enhance photosynthesis, improve chlorophyll synthesis, promote CO_2 uptake and plant growth. The aim of this study was to reveal whether Trifloxystrobin pretreatment has a protective role against excessive Cu-related abiotic stress in *T. aestivum* seedlings. To fulfill this purpose, fresh weight, dry weight, shoot length, chlorophyll-carotenoid-anthocyanin pigment levels, lipid peroxidation, proline content and the total antioxidant enzyme activities were assessed.

Materials and Methods

Preparation of Materials and Experimental Setup

The wheat grains used in the research were provided by Prof. Dr. Tolga Karaköy from Sivas University of Science and Technology. Sönmez and Gerek 79 cultivars, which are frequently cultivated in Turkey, were used as research materials. The grains were kept in a 2% sodium hypochlorite solution for 5 minutes to sterilize the surfaces. The residues were removed by rinsing the grains with distilled water for 15 minutes. A soil:perlite mixture of 200 g (1:1 ratio) per pot was prepared as the growing medium. Organic soil, which was taken from the fields in Giresun and found to be within the standard values in terms of required minerals, was used. In the study, no previous fertilizer or pesticide was used. In particular, the Cu content of the soil was 2.76 ppm. Six seeds per pot with a soil capacity of 0.2 kg were sown and the seedlings were grown under optimum climate chamber conditions (a cycle of 12 hours of dark and 12 hours of light at 23±1 °C) for 11 days. During this process, the pots were watered to match the field capacity. The pots were then divided into three groups (Figure 1). A commercial formula called “Trailer” consisting of 50% Trifloxystrobin content (Hektas Group, Kocaeli/Türkiye) was used to prepare Trifloxystrobin solutions. The first two groups were pretreated with 30 ml of 20 µM and 80 µM Trifloxystrobin solutions, respectively. The last group was irrigated with 30 ml of water (control). These treatments were continued for two days. Then, the group pretreated with 20 µM Trifloxystrobin was divided into two groups, one of which was irrigated with 30 ml of water (TFS02), while the other one was treated with 30 ml of CuCl2 solution with 8 g/L Cu content (TFS02Cu) for one day. The same procedure was applied to the group pretreated with 80 µM Trifloxystrobin to obtain the TFS08 and TFS08Cu groups. The control group was divided into two groups and one group was treated with 30 ml of CuCl2 solution with 8 g/L Cu content (Cu) for one day, while the other group continued to be irrigated with water (C). All groups continued to be irrigated with water until the end of the experiment. All seedlings were harvested on the 20th day after sowing the seeds. All pots were placed randomly throughout the experiments.

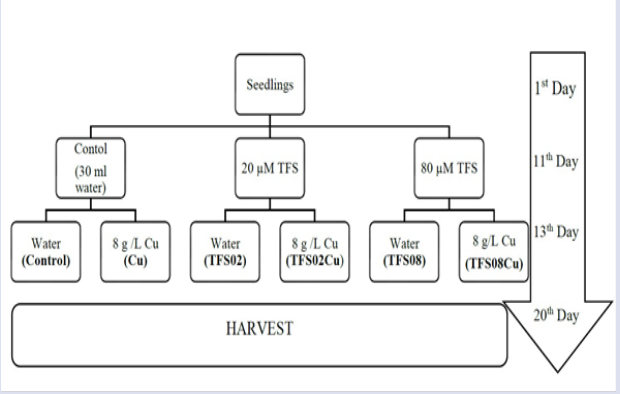

Figure 1. Diagram for experimental design.

Analysis of Growth Parameters

The part from the apex of the last emerged leaf to the surface of the soil-perlite mixture was measured with a ruler to obtain the shoot lengths (cm). A total of 3 seedlings were randomly selected for each group to evaluate the average shoot length. Following the harvest, the shoots of the seedlings were weighed using a precision scale and the fresh weight was determined (g). The shoots were then kept in a drying oven at 80 °C for 48 hours to determine the dry weight (g) (n = 3).

Analysis of Chlorophyll and Carotenoid Contents

Leaf segments (1 cm from the middle of each leaf) were weighed (g) and extracted in 2 ml of acetone (100%). Samples were kept in a refrigerator for 7 days in order to allow the pigments to pass into the solution. The absorbance of the samples was read at wavelengths of 470, 644.8, and 661.6 nm. The amounts of total chlorophyll (chl a + chl b) and total carotenoid (x + c) pigments were calculated using suggested extinction coefficients [13] (n = 3).

Analysis of Chlorophyll and Anthocyanin Contents

Leaf segments (1 cm from the middle of each leaf) were weighed (g) and extracted in 2 ml of acidified methanol. Samples were kept in a refrigerator for 7 days to allow the anthocyanin pigments to pass into the solution. The absorbance of the samples was read at wavelengths of 657 and 530 nm. The anthocyanin content of the samples was calculated according to the method suggested by Mancinelli et al. [14] (n = 3).

Analysis of Lipid Peroxidation

To estimate the peroxidation levels of membrane lipids, malondialdehyde (MDA) contents of the samples were assessed according to the modified method of Ohkawa et al. [15]. Fresh leaf samples (0.1 g) were homogenized in 1 ml of 5% trichloroacetic acid. After a centrifugation process (12,000 rpm), the supernatant was transferred into a mixture of 0.5% thiobarbituric acid and 20% trichloroacetic acid. Following a water bath treatment at 100 °C, all materials were ice-cooled to interrupt the reactions and centrifuged at 10,000 rpm. After recording the absorbance of the supernatants at 532 and 600 nm wavelengths, the MDA levels of the samples were calculated (n = 3).

Analysis of Proline Content

The method suggested by Bates et al. [16] was modified to determine the free proline levels of the seedlings. Fresh leaf samples (0.2 g) were extracted in 3% sulphosalicylic acid according to the method of Weimberg [17]. At the end of the extraction, the sample was mixed with the same volumes of ninhydrin reagent and glacial acetic acid. Following a water bath treatment at 100 °C, all materials were ice-cooled to interrupt the reactions. Four ml of toluene was added to the samples to separate the proline-containing fraction. The free proline content of the samples was calculated by measuring the absorbance spectrophotometrically at 520 nm and using a proline standard curve (n = 3).

Analysis of Antioxidant Enzyme Activities

Enzyme activities were assayed using fresh leaf segments (0.5 g) cut from seedlings for each treatment. The samples were ground in liquid nitrogen and transferred to potassium phosphate buffer containing tubes. The supernatant fractions were collected following centrifugation (14,000 rpm) for subsequent activity analyses. The Bradford [18] method was used to determine the protein amounts in the extracts.

The total catalytic activity of superoxide dismutase enzyme (SOD) (EC 1.15.1.1) was performed according to the method of Beyer and Fridovich [19] with slight modifications. The final volume of the reaction mixture, consisting of potassium phosphate buffer (50 mM; pH 7.8), methionine (9.9 mM), nitroblue tetrazolium (57µM) and determined volume of the extract, was 30.25 ml. The amount of SOD enzyme required to inhibit Nitroblue tetrazolium photoreduction by 50% was considered one unit of enzyme (n = 3).

The total catalytic activity of guaiacol peroxidase enzyme (POD) (EC 1.11.1.7) was evaluated by following the oxidation of guaiacol (E = 26.6 mM cm-1) by hydrogen peroxide spectrophotometrically at 470 nm [20]. The final volume of the reaction mixture, consisting of potassium phosphate buffer (100 mM; pH 7.0), guaiacol (20.1 mM), hydrogen peroxide (12.3 mM) and an appropriate amount of enzyme extract, was 3 ml. A unit of enzyme activity was considered as nm hydrogen peroxide decomposed per minute per mg of protein (n = 3).

The total catalytic activity of glutathione reductase enzyme (GR) (EC 1.6.4.2) was determined spectrophotometrically at 240 nm [21]. The medium prepared for extracting the GR enzyme consisted of potassium phosphate buffer (100 mM; pH 7.0), Na_2EDTA (1 mM) and PVP (2%). The reaction mixture for assaying GR activity contained potassium phosphate buffer (200 mM; pH 7.5), Na_2EDTA (0.2 mM), $MgCl_2$ (1.5 mM), GSSG (0.5 mM), NADPH (50 µM) and an appropriate amount of enzyme extract containing 100 µg protein (n = 3). Non-enzymatic oxidation of NADPH was recorded spectrophotometrically at a wavelength of 340 nm without adding GSSG to the reaction medium. Enzymatic catalysis was monitored at 340 nm by adding GSSG to the assay medium (n = 3).

Statistics

The data of the present study was analyzed through one-way ANOVA and Duncan's tests using IBM SPSS Statistics 26 Software. Differences between the results at $p < 0.05$ were accepted as statistically significant.

Results and Discussion

In order to evaluate the effects of Trifloxystrobin and Cu on growth, shoot length, shoot fresh weight and shoot dry weight were measured in all groups (Figure 2). The control group of Sönmez cultivar was taller than Gerek 79 cultivar in terms of natural genetic structure at the early seedling stage (Figure 2a). There was no significant difference between the shoot lengths of the Sönmez seedlings in the first three groups (C, TFS02 and TFS08). Similarly, Trifloxystrobin did not have any effect when applied alone on the fresh and dry weights of the seedlings of the Gerek 79 cultivar (Figure 2b and 2c). Therefore, the selected Trifloxystrobin doses were non-toxic for both wheat cultivars at an early seedling stage. On the other hand, Cu application caused a remarkable decrease in shoot elongation, fresh weight and dry weight in both wheat cultivars. Indeed, the shoot length of the seedlings treated with Cu decreased by 41% in the Sönmez cultivar and by 35% in the Gerek 79 cultivar compared to their own controls. In addition, the dry weight of the seedlings in the Cu group decreased by 36% in Sönmez and by 41% in Gerek 79 cultivars compared to their own controls. According to the results obtained from the TFS02Cu and TFS08Cu groups, Trifloxystrobin pretreatment provided a dose-dependent protection against subsequent Cu application in both cultivars. However, the results of the growth parameters of TFS02Cu and TFS08Cu groups never reached control levels in the cultivars. Our results were in

agreement with the study of Singh et al. [22] in which the growth retarding effect of Cu in wheat seedlings was noted. Furthermore, Atabayeva et al. [23] indicated that high doses of Cu treatment suppressed shoot length and dry weight in wheat varieties significantly. In addition, Lyoshyna et al. [24] proved a notable reduction in green mass and shoot length of wheat seedlings after Cu application. To our knowledge, this is the first study to show that Trifloxystrobin pretreatment reduces Cu stress-induced growth restriction in wheat. Strobilurins, including Trifloxystrobin, have the ability to alter plant physiology by causing changes in metabolism and growth. Mohsin et al. [12] showed that the application of Tebuconazole and Trifloxystrobin mixture improved dry weight and fresh weight in heavy metal (cadmium)-stressed wheat seedlings. According to Takahashi et al. [25], the physiological effects of "protective fungicides" such as Trifloxystrobin become more pronounced when the plants are under stress.

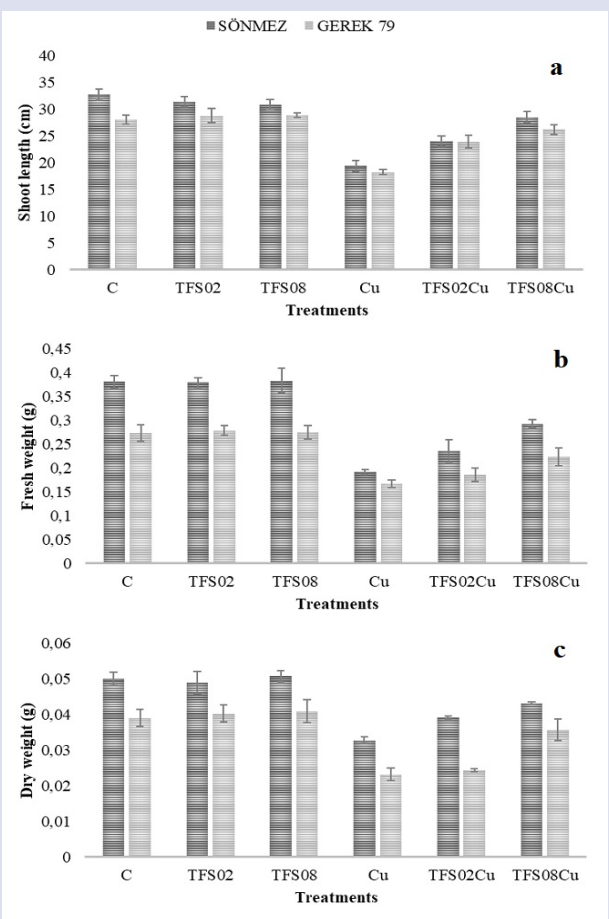

Figure 2. Effects of Trifloxystrobin pretreatment on growth of Cu-stressed wheat cultivars (a. Shoot lenght, b. Fresh weight, c. Dry weight) (C: control, TFS02: 20µM Trifloxystrobin, TFS08: 80 µM Trifloxystrobin, Cu: $CuCl_2$, TFS02Cu: 20µM Trifloxystrobin + $CuCl_2$, TFS08Cu: 80µM Trifloxystrobin + $CuCl_2$).

The total chlorophyll and carotenoid levels of Sönmez seedlings in the control group were higher than those of Gerek 79 (Figure 3). Trifloxystrobin applications in the TFS02 and TFS08 groups of both cultivars did not trigger a remarkable effect on pigment concentrations when compared to the control groups. However, Cu application resulted in a 60% and 53% chlorophyll reduction in Sönmez and Gerek 79, respectively, compared to their own controls (Figure 3a). Similarly, the carotenoid contents of Sönmez and Gerek 79 exposed to Cu decreased by 37% and 52%, respectively, compared to their controls. In both cultivars, the TFS02Cu and TFS08Cu groups pretreated with Trifloxystrobin solutions showed a dose-dependent protection against subsequent Cu application in terms of both chlorophyll and carotenoid. In these groups, the levels of the pigments increased with the increased Trifloxystrobin doses. Therefore, pretreatment with Trifloxystrobin largely prevented damage to both growth and photosynthetic pigments in wheat seedlings against Cu stress. The greater growth in the TFS02Cu and TFS08Cu groups than in the Cu group can be attributed to the preservation of pigments and thus to uninterrupted photosynthesis. Our results were in line with Atabayeva et al. [23], who reported that Cu reduces chlorophyll a, chlorophyll b and carotenoid pigments in wheat. Additionally, Zong et al. [26] suggested that Cu led to a devastating effect on the chlorophyll content of wheat seedlings when applied in high doses. Mohsin et al. [12] have already demonstrated the potential of Trifloxystrobin to prevent chlorophyll and carotenoid damage caused by heavy metals. Yet, this is the first study to demonstrate the protective role of pre-applied Trifloxystrobin in the amount of photosynthetic pigments in copper-stressed wheat seedlings. Under these circumstances, the results of our study confirmed the report of Banerjee and Roychoudhury [27], which mentioned the effect of Strobilurin-type fungicides on stress tolerance development against stresses such as drought, desiccation, heat, cold and light.

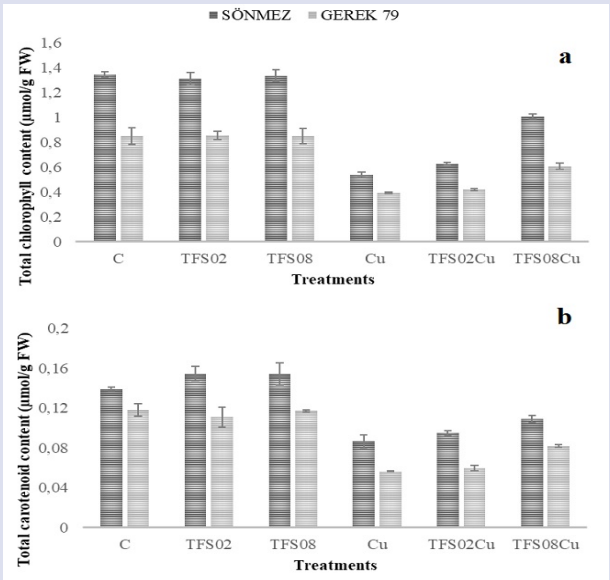

Figure 3. Effects of Trifloxystrobin pretreatment on chlorophyll and carotenoid contents of Cu-stressed wheat cultivars (a. Total chlorophyll content, b. Total carotenoid content) (C: control, TFS02: 20µM Trifloxystrobin, TFS08: 80 µM Trifloxystrobin, Cu: $CuCl_2$, TFS02Cu: 20µM Trifloxystrobin + $CuCl_2$, TFS08Cu: 80µM Trifloxystrobin + $CuCl_2$).

Anthocyanins, a group of flavonoids, are pigments found in flowers, fruits, roots, stems and leaves of plants and play vital roles in abiotic stress tolerance. Figure 4a presents the effects of Trifloxystrobin pretreatment on anthocyanin accumulation of Cu-stressed wheat seedlings. Considering the control groups, the initial anthocyanin content of the Sönmez cultivar was slightly higher than that of the Gerek 79 cultivar. In both cultivars, there was no significant difference between the anthocyanin levels of the TFS02, TFS08 and control groups. On the contrary, Cu application increased the anthocyanin levels in Sönmez and Gerek 79 to 2.17 and 1.34 times that of their own controls, respectively. While both doses of Trifloxystrobin were sufficient for the anthocyanin content of Gerek 79 to decrease to the control level, the decrease of the anthocyanin content to the control level in Sönmez was only possible with the pre-application of 80 µM Trifloxystrobin. Our results were in agreement with the older studies which showed that anthocyanin accumulates in *T. aestivum* shoots exposed to heavy metal stresses [28]. Tereshchenko et al. [29] reported that anthocyanin synthesis in wheat seedlings is closely correlated with responses to abiotic stresses, including heavy metals. One of the promptest influences of toxic doses of heavy metals in plant cells is the over-production of reactive oxygen species (ROS). Owing to their antioxidant properties, anthocyanins suppress oxidative stress by scavenging ROS and thus control growth inhibition and cell death. They also help ion homeostasis and osmotic balance be maintained under stressful conditions through their excellent ion chelating abilities.

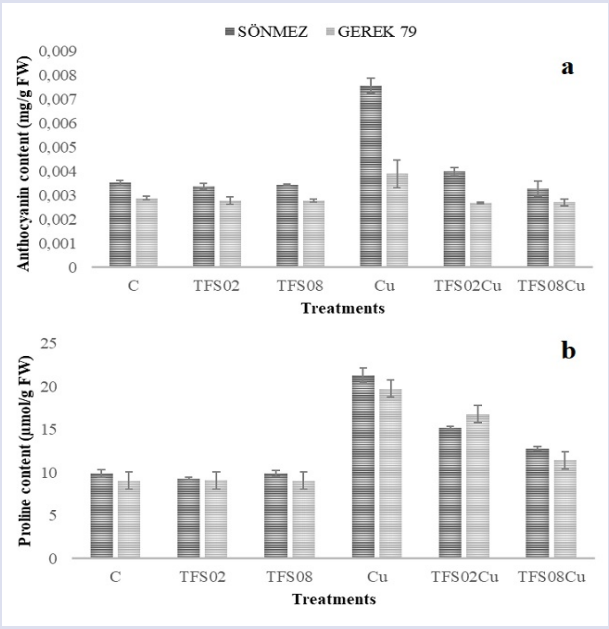

Figure 4. Effects of Trifloxystrobin pretreatment on anthocyanin and proline contents of Cu-stressed wheat cultivars (a. Anthocyanin content, b. Prolin content) (C: control, TFS02: 20µM Trifloxystrobin, TFS08: 80 µM Trifloxystrobin, Cu: $CuCl_2$, TFS02Cu: 20µM Trifloxystrobin + $CuCl_2$, TFS08Cu: 80µM Trifloxystrobin + $CuCl_2$)

Figure 4b shows the effects of Trifloxystrobin pretreatment on the proline content of Cu-stressed wheat seedlings. The proline contents of the first three groups (C, TFS02 and TFS=8) of Sönmez and Gerek 79 were statistically similar. Additionally, the control groups of both cultivars had similar proline levels. However, Cu application enhanced the proline levels in Sönmez and Gerek 79 to 2.16 and 2.18 times those of their own controls, respectively. TFS02Cu and TFS08Cu groups exposed to Trifloxystrobin pretreatment exhibited a gradual decrease in free proline levels depending on the Trifloxystrobin dose. However, even the higher Trifloxystrobin dose failed to reduce the proline content of the TFS08Cu group to control levels in both cultivars. Cu-induced free proline accumulation in the plant kingdom has been reported in many studies so far [30]. There are various investigations manifesting that toxic doses of heavy metals lead to growth retardation, chlorosis, necrosis, disrupted secondary structure of proteins and imbalances in the redox state of plant cells. It is known that the accumulation of proline lessens the destructive effects on plants and improves stress tolerance under abiotic stress conditions. In addition to eliminating ROS and increasing the activity of various cellular enzymes, proline acts as an osmoprotectant to overcome oxidative and osmotic stresses. We report that Trifloxystrobin pretreatment can greatly attenuate the proline accumulation by reducing the Cu-provoked stress in *T. aestivum* seedlings. Our results were in line with the study of Mohsin et al. [12], which showed that exogenous Trifloxystrobin alleviates the proline biosynthesis in wheat by suppressing cadmium-related stress.

MDA is a reactive organic compound and MDA accumulation has long been utilized as a marker of lipid peroxidation arising from oxidative stress in cellular membranes. The MDA content of wheat seedlings was determined to assess both the individual and combined effects of Trifloxystrobin and Cu on the membrane integrity (Figure 5). The MDA levels of the first three groups (C, TFS02 and TFS08) of the cultivars were close to each other. However, when Cu was applied alone, it caused a significant increase in the MDA content of Sönmez and Gerek 79. As a matter of fact, the MDA content of Cu groups of Sönmez and Gerek 79 cultivars was 3.29 and 2.22 times that of their own controls, respectively. The MDA levels of the TFS02Cu and TFS08Cu groups of both cultivars were significantly lower than their Cu-treated groups. Trifloxystrobin pretreatment prior to Cu application provided dose-dependent protection against Cu-induced membrane damage in both Sönmez and Gerek 79. Lipid peroxidation is a well-known chain reaction initiated by ROS on unsaturated fatty acids. In our experiment, Cu treatment caused severe membrane destabilization, and this phenomenon is often associated with enhanced ROS production. Our results confirmed Xu et al. [31], who suggested that toxic Cu concentrations lead to MDA accumulation in *T. aestivum* seedlings. Similar to our

results, Trifloxystrobin as an outstanding fungicide type was involved in protection against cadmium-induced membrane damage in wheat [12]. Hameed et al. [32] also stated that mercapto-triazole, another antifungal compound, reduced lipid peroxidation caused by heavy metal toxicity in wheat. In another study, it was reported that azoxystrobins delay lipid peroxidation with increased antioxidant defense activities [33].

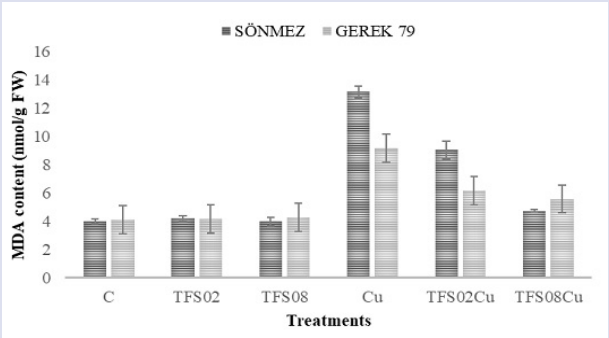

Figure 5. Effects of Trifloxystrobin pretreatment on MDA content of Cu-stressed wheat cultivars (C: control, TFS02: 20µM Trifloxystrobin, TFS08: 80 µM Trifloxystrobin, Cu: $CuCl_2$, TFS02Cu: 20µM Trifloxystrobin + $CuCl_2$, TFS08Cu: 80µM Trifloxystrobin + $CuCl_2$).

Cu is a redox active metal and although it is a very important part of many enzymes, an overdose of Cu triggers the formation of ROS. Indeed, even doses of Cu slightly greater than its optimum concentration induce ROS-mediated oxidative stress [34]. Since Cu is a transition metal, it has enormous oxidative power and the potential to participate in Fenton/Haber-Weiss reactions [3]. All kinds of stress adversely affect the normal functioning and final yield of plants. The ability of plants to withstand these stresses depends on their effective use of antioxidant systems. Antioxidant enzyme activities are considered sensitive biomarkers of stress in plants [23]. The SOD, POD and GR enzyme activities were monitored to evaluate the Cu-induced oxidative burst and the protective ability of Trifloxystrobin (Figure 6). The SOD activity of both cultivars exhibited a gradual increase with increasing Trifloxystrobin doses (Figure 6a). Therefore, the SOD activities of the TFS02 and TFS08 groups were higher than those of their own controls in Sönmez and Gerek 79. The electron transfer system interrupted by Strobilurins can lead to superoxide synthesis [35], resulting in a Trifloxystrobin-induced increase in the SOD activities in TFS02 and TFS08. The elevation pattern in the SOD activities of the cultivars peaked after Cu application. The SOD activities of Cu groups of Sönmez and Gerek 79 cultivars were approximately 6.32 and 5.79 times those of their own controls, respectively. Since the SOD enzyme catalyzes the decomposition of superoxide radicals into hydrogen peroxide and oxygen, the results of this study showed that Cu application induced superoxide formation in wheat and, accordingly, the SOD activity increased. The SOD activity of the TFS02Cu and TFS08Cu groups were lower than the Cu groups of both cultivars. Trifloxystrobin pretreatment reduced the SOD activities with increasing doses of the fungicide. In Gerek 79, this decrease only became statistically significant in the TFS08Cu application.

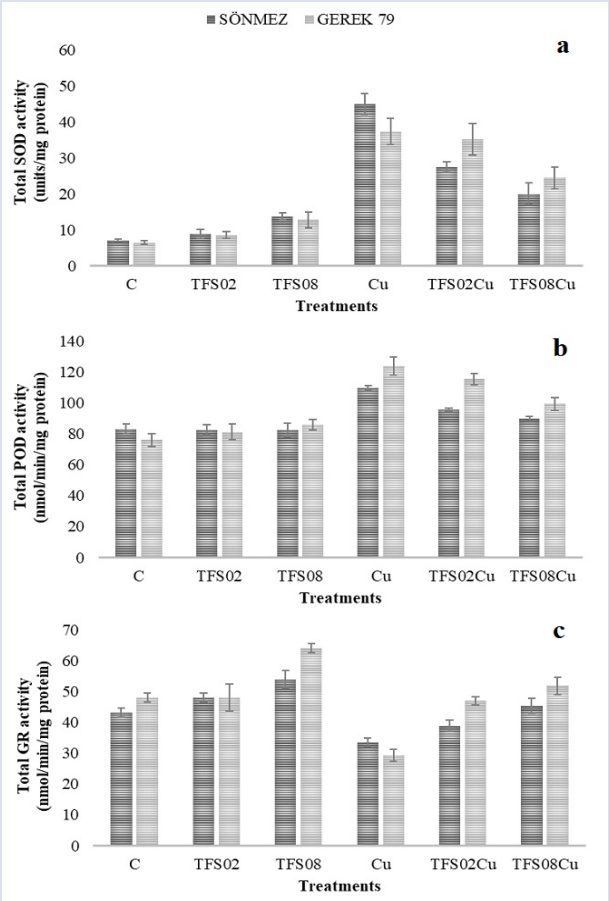

Figure 6. Effects of Trifloxystrobin pretreatment on antioxidant enzyme activities of Cu-stressed wheat cultivars (a. Total SOD activity, b. Total POD activity, c. Total GR activity) (C: control, TFS02: 20µM Trifloxystrobin, TFS08: 80 µM Trifloxystrobin, Cu: $CuCl_2$, TFS02Cu: 20µM Trifloxystrobin + $CuCl_2$, TFS08Cu: 80µM Trifloxystrobin + $CuCl_2$).

POD enzyme removes hydrogen peroxide from cells and helps to maintain biological membrane integrity by strengthening cell walls and preventing metal ions from entering cells [36]. In TFS02 and TFS08 groups of Sönmez and Gerek 79, the POD activities remained stable when compared to the control groups (Figure 6b). The Cu applied groups of the cultivars exhibited a significant increase in their POD activities. The POD activities of the Cu groups of Sönmez and Gerek 79 cultivars were 32% and 63% higher, respectively, than their controls. Trifloxystrobin pretreatment before Cu application induced a dose-dependent drop in the POD activities of cultivars compared to the control groups. However, the POD activities of the TFS02Cu and TFS08Cu groups in both cultivars were still higher than those of their respective

Our results confirmed the study of Gupta et al. [37], who stated that POD activity was associated with proline content to provide efficient membrane protection in wheat. In addition, the parallelism of changes in MDA accumulation and POD activity of the groups in the present study confirmed Díaz et al. [38], who suggested POD activity makes a major contribution to the cell wall stability of the plants under heavy metal stress.

The GR enzyme is localized in the chloroplast, cytosol, and mitochondria and converts oxidized glutathione to reduced glutathione as part of the ascorbate-glutathione cycle. In addition to being a stimulant for normal growth and development, it plays an important role in combating various stresses, including heavy metals. While a significant increase was observed in the GR activity of the Sönmez cultivar in the TFS02 and TFS08 groups compared to the control group, the GR activity of the Gerek 79 cultivar increased significantly only in the TFS08 group compared to the control group (Figure 6c). Surprisingly, Cu application caused a remarkable decrease in the GR activities of both cultivars compared to their respective controls. Our results were in agreement with previously published results by Mohsin et al. [18], who stated that heavy metal stress reduced GR activity in wheat. Similarly, Drążkiewicz et al. [39] showed that the application of Cu up to a certain dose in *Arabidopsis thaliana* L. dramatically reduced the GR activity. The GR activities of the TFS02Cu and TFS08 groups were significantly higher than those of their own Cu-treated groups. Indeed, the TFS02Cu and TFS08 groups of Sönmez and Gerek 79 did not exhibit a significant difference in GR activity compared to their own controls. Wu and von Tiedemann [40], confirming the results of our study, showed that previously applied Azoxystrobin, another kind of Strobilurin, reduced the ozone stress inducing the activity of the GR enzyme in wheat.

Conclusion

In conclusion, this study has clearly demonstrated that excessive Cu stress suppresses growth, reduces photosynthetic pigments, and causes membrane damage in wheat seedlings. On the other hand, proline and anthocyanin levels, which are among the defense mechanisms along with the antioxidant enzyme activities, increased in plants under Cu stress. Although Cu application increased anthocyanin accumulation and SOD activity in the Sönmez cultivar more than in Gerek 79, Sönmez had more membrane damage, shoot elongation deceleration and chlorophyll loss. In addition, the Cu-stressed Gerek 79 cultivar exhibited a higher rate of proline content and POD activity. However, the dry weight loss and carotenoid pigment decrease of Gerek 79 were at a higher rate when compared to the Sönmez cultivar. GR activities of Cu-stressed wheat seedlings decreased in both genotypes. The pretreatment with Trifloxystrobin, a frequently used fungicide, provided effective protection against all damage caused by Cu application in both cultivars. As the dose of Trifloxystrobin increased, the severity of stress decreased in both wheat genotypes. Trifloxystrobin pretreatment stimulated the antioxidant defense system, allowing the plant to be less affected by Cu stress. Considering the increase in Cu accumulation in the soil due to the pesticides used and the sensitivity of wheat to heavy metal stress, it should not be forgotten that every method to protect plants against this stress is valuable. It is no accident that research examining the exogenous and unconventional application of fungicides has multiplied. The findings of this study suggest that the potential of Trifloxystrobin pretreatment to protect valuable crops such as wheat against other metal toxicities should be investigated at different life stages and field conditions. To increase agricultural production and protect plants, the benefits of compounds such as Trifloxystrobin should be exploited to the fullest.

Conflicts of interest

There are no conflicts of interest in this work.

References

[1] Keser M., Gummadov N., Akin B., Belen S., Mert Z., Taner S., Topal A., Yazar S., Morgounov A., Sharma R.C., Ozdemir F., Genetic Gains in Wheat in Turkey: Winter Wheat for Dryland Conditions, *Crop J.*, 5(6) (2017) 533-540.

[2] Toklu F., Baloch F.S., Karaköy T., Özkan H., Effects of Different Priming Applications on Seed Germination and Some Agromorphological Characteristics of Bread Wheat (*Triticum aestivum* L.), *Turk. J. Agric. For.*, 39(6) (2015) 1005-1013.

[3] Gajewska E., Głowacki R., Mazur J., Skłodowska M. Differential Response of Wheat Roots to Cu, Ni and Cd Treatment: Oxidative Stress and Defense Reactions, *Plant Growth Regul.*, 71 (1) (2013) 13-20.

[4] Kumar V., Pandita S., Sidhu G.P.S., Sharma A., Khanna K., Kaur P., Bali A.S., Setia R., Copper Bioavailability, Uptake, Toxicity and Tolerance in Plants: A Comprehensive Review, *Chemosphere,* 262 (2021) 127810.

[5] Mir A.R., Pichtel J., Hayat S., Copper: Uptake, Toxicity and Tolerance in Plants and Management of Cu-Contaminated Soil, *BioMetals*, 34(4) (2021) 737-759.

[6] Zeng Q., Ling Q., Wu J., Yang Z., Liu R., Qi Y., Excess Copper-Induced Changes in Antioxidative Enzyme Activity, Mineral Nutrient Uptake and Translocation in Sugarcane Seedlings, *Bull. Environ. Contam. Toxicol.*, 103 (6) (2019) 834-840.

[7] Panagos P., Ballabio C., Lugato E., Jones A., Borrelli P., Scarpa S., Orgiazzi A., Montanarella L., Potential Sources of Anthropogenic Copper Inputs to European Agricultural Soils, *Sustainability*, 10(7) (2018) 2380.

[8] Kalefetoğlu Macar T., Macar O., Yalçın E., Çavuşoğlu K., Resveratrol Ameliorates the Physiological, Biochemical, Cytogenetic, and Anatomical Toxicities Induced by Copper (II) Chloride Exposure in *Allium cepa* L., *Environ. Sci. Pollut. Res.*, 27(1) (2020) 657-667.

[9] Tleuova A.B., Wielogorska E., Talluri V.P., Štěpánek F., Elliott C.T., Grigoriev D.O., Recent Advances and Remaining Barriers to Producing Novel Formulations of Fungicides for Safe and Sustainable Agriculture, *J. Control. Release*, 326 (2020) 468-481.

[10] Mohsin S.M., Hasanuzzaman M., Parvin K., Fujita M., Pretreatment of Wheat (*Triticum aestivum* L.) Seedlings With 2, 4-D Improves Tolerance to Salinity-Induced Oxidative Stress and Methylglyoxal Toxicity by Modulating Ion Homeostasis, Antioxidant Defenses, and Glyoxalase Systems, *Plant Physiol. Biochem*., 152 (2020) 221-231.

[11] Uçkun M., Özmen M., Evaluating Multiple Biochemical Markers in *Xenopus laevis* Tadpoles Exposed to The Pesticides Thiacloprid and Trifloxystrobin in Single and Mixed Forms, *Environ. Toxicol. Chem*., 40(10) (2021) 2846-2860.

[12] Mohsin S.M., Hasanuzzaman M., Parvin K., Hossain S., Fujita M., Protective Role of Tebuconazole and Trifloxystrobin in Wheat (*Triticum aestivum* L.) under Cadmium Stress Via Enhancement of Antioxidant Defense and Glyoxalase Systems, *Physiol. Mol. Biol. Plants*, 27(5) (2021) 1043-1057.

[13] Lichtenthaler H.K., Chlorophylls and Carotenoids: Pigments of Photosynthetic Membranes, *Methods Enzymol*., 148 (1987) 350-382.

[14] Mancinelli A.L., Yang C.P.H., Lindquist P., Anderson O.R., Rabino I., Photocontrol of Anthocyanin Synthesis: III. The Action of Streptomycin on The Synthesis of Chlorophyll and Anthocyanin, *Plant Physiol*., 55(2) (1975) 251-257.

[15] Ohkawa H., Ohishi N., Yagi K., Assay for Lipid Peroxides in Animal Tissues by Thiobarbituric Acid Reaction, *Anal. Biochem*., 95 (2) (1979) 351-358.

[16] Bates L.S., Waldren R.P., Teare I.D., Rapid Determination of Free Proline for Water-Stress Studies, *Plant Soil,* 39(1) (1973) 205-207.

[17] Weimberg R., Solute Adjustments in Leaves of Two Species of Wheat at Two Different Stages of Growth in Response to Salinity, *Physiol. Plant*., 70(3) (1987) 381-388.

[18] Bradford M.M., A Rapid and Sensitive Method for the Quantitation of Microgram Quantities of Protein Utilizing the Principle of Protein-Dye Binding, *Anal. Biochem*., 72(1-2) (1976) 248-254.

[19] Beyer W.F., Fridovich I., Assaying for Superoxide Dismutase Activity: Some Large Consequences of Minor Changes in Conditions. *Anal. Biochem*., 161(2) (1987) 559-566.

[20] Bergmeyer H.U., Section C: Methods for Determination of Enzyme Activity. In: Bergmeyer H.U., (Ed.). Methods of enzymatic analysis. 2nd ed. Vol II. New York: Academic Press, (1974) 685-690.

[21] Sgherri C.L.M, Loggini B., Puliga S., Navari-Izzo F., Antioxidant System in *Sporobolus stapfianus*: Changes in Response to Desiccation and Rehydration, *Phytochem*., 35(3) (1994) 561-565.

[22] Singh D., Nath K., Sharma Y.K., Response of Wheat Seed Germination and Seedling Growth under Copper Stress, *J. Environ. Biol*., 28(2) (2007) 409-414.

[23] Atabayeva S., Nurmahanova A., Asrandina S., Alybayeva R., Meldebekova A., Ablaikhanova N., Effect of Copper on Physiological and Biochemical Peculiarities of Wheat (*Triticum aestivum* L.) Varieties, *Pak. J. Bot*., 49(6) (2017) 2189-2196.

[24] Lyoshyna L., Tarasyuk O., Bulko O., Rogalsky S., Kamenieva T., Kuchuk M., Effect of Polymeric Biocide Polyhexamethylene Guanidine Hydrochloride on Morpho-Physiological and Biochemical Parameters of Wheat Seedlings under Copper Stress, *Agric. Sci. Pract*., 7 (1) (2020) 49-58.

[25] Takahashi N., Sunohara Y., Fujiwara M., Matsumoto H., Improved Tolerance to Transplanting Injury and Chilling Stress in Rice Seedlings Treated with Orysastrobin, *Plant Physiol. Biochem*., 113 (2017) 161-167.

[26] Zong X., Zhang J., Zhu J., Zhang L., Jiang L., Yin Y., Guo H., Effects of Polystyrene Microplastic on Uptake and Toxicity of Copper and Cadmium in Hydroponic Wheat Seedlings (*Triticum aestivum* L.), *Ecotoxicol. Environ. Saf*., 217 (2021) 112217.

[27] Banerjee A., Roychoudhury A., Oxylipins and Strobilurins as Protective Chemical Agents to Generate Abiotic Stress Tolerance in Plants. In: Roychoudhury A., Tripathi D.K., (Eds). Protective chemical agents in the amelioration of plant abiotic stress: biochemical and molecular perspectives. Croydon: Wiley Blackwell, (2020) 483-490.

[28] Shoeva O.Y., Khlestkina E.K., Anthocyanins Participate in the Protection of Wheat Seedlings against Cadmium Stress, *Cereal Res. Commun*., 46(2) (2018) 242-252.

[29] Tereshchenko O.Y., Gordeeva E.I., Arbuzova V.S., Khlestkina E.K., Anthocyanin Pigmentation in *Triticum aestivum* L.: Genetic Basis and Role under Abiotic Stress Conditions, *J. Stress Physiol. Biochem*., 8 (3) (2012) 16.

[30] Yetişsin F., Kurt F., Gallic Acid (GA) Alleviating Copper (Cu) Toxicity in Maize (*Zea mays* L.) Seedlings, *Int. J. Phytoremediation*, 22(4) (2020) 420-426.

[31] Xu Y., Yu W., Ma Q., Zhou H., Jiang C., Toxicity of Sulfadiazine and Copper and Their Interaction to Wheat (*Triticum aestivum* L.) Seedlings, *Ecotoxicol. Environ. Saf*., 142 (2017) 250-256.

[32] Hameed A., Hameed A., Ahmad M., Farooq T., Alleviation of Cadmium Toxicity by Mercapto-Triazole Priming in Wheat, *Arch. Agron. Soil Sci*., 66(11) (2020) 1467-1480.

[33] Zhang Y.J., Zhang X., Chen C.J., Zhou M.G., Wang H.C., Effects of Fungicides JS399-19, Azoxystrobin, Tebuconazloe, and Carbendazim on The Physiological and Biochemical Indices and Grain Yield of Winter Wheat, *Pestic. Biochem. Phys*., 98(2) (2010) 151-157.

[34] Thounaojam T.C., Panda P., Mazumdar P., Kumar D., Sharma G.D., Sahoo L., Sanjib P., Excess Copper Induced Oxidative Stress and Response of Antioxidants in Rice, *Plant Physiol. Biochem*., 53 (2012) 33-39.

[35] Mizutani A., Miki N., Yukioka H., Tamura H., Masuko M., A Possible Mechanism of Control of Rice Blast Disease by a Novel Alkoxyiminoacetamide Fungicide, SSF126, *Phytopathology*, 86(3) (1996) 295-300.

[36] Platonova N., Belous O., Relationship between the Activity of Guaiacol Peroxidase and the Content of Photosynthetic Pigments in Tea Leaves, *Slovak J. Food Sci*., 14 (2020), 1020-1026.

[37] Gupta N.K., Agarwal S., Agarwal V.P., Nathawat N.S., Gupta S., Singh G., Effect of Short-Term Heat Stress on Growth, Physiology and Antioxidative Defence System in Wheat Seedlings, *Acta Physiol. Plant*., 35(6) (2013) 1837-1842.

[38] Díaz J., Bernal A., Pomar F., Merino F., Induction of Shikimate Dehydrogenase and Peroxidase in Pepper (*Capsicum annuum* L.) Seedlings in Response to Copper Stress and Its Relation to Lignification, *Plant Sci*., 161(1) (2001) 179-188.

[39] Drążkiewicz M., Skórzyńska-Polit E., Krupa Z., Response of the Ascorbate–Glutathione Cycle to Excess Copper in *Arabidopsis thaliana* (L.), *Plant Sci*., 164(2) (2003) 195-202.

[40] Wu Y.X., von Tiedemann A., Physiological Effects of Azoxystrobin and Epoxiconazole on Senescence and the Oxidative Status of Wheat, *Pestic. Biochem. Phys*., 71(1) (2001) 1-10.

Cumhuriyet Sci. J., 44(2) (2023) 276-282
DOI: https://doi.org/10.17776/csj.1223962

Cumhuriyet Science Journal

| csj.cumhuriyet.edu.tr | Founded: 2002 ISSN: 2587-2680 e-ISSN: 2587-246X Publisher: Sivas Cumhuriyet University

Some Population Parameters of Morocco dentex, *Dentex maroccanus* Valenciennes, 1830 in the Northeastern Mediterranean Sea

Seda Kontaş Yalçınkaya [1,a,*]

[1] *Department of Fisheries Technology Engineering, Fatsa Faculty of Marine Sciences, Ordu University, Ordu, Türkiye*
**Corresponding author*

Research Article

History
Received: 30/12/2022
Accepted: 07/06/2023

ABSTRACT

In this study, a total of 95 *Dentex maroccanus* samples ($n_{♀}$=37, $n_{♂}$=58) were examined from the northeastern Mediterranean Sea. The sex ratio was calculated as 0.63:1. The mean total length (TL), fork length (FL), and standard length (SL) were 12.1 ± 0.082 cm, 11.1 ± 0.075 cm, and 10.0 ± 0.068 cm for all samples, respectively. The mean weight (W) was 32.81 ± 0.575 g. The length-length relationships were determined as TL=1.1367SL+0.7136, TL=1.0607FL+0.2804, and FL=1.0631SL+0.494 for all samples, respectively. The total length-weight relationships were determined as $W=0.08TL^{2.409}$, $W=0.1183TL^{2.246}$, and $W=0.0489TL^{2.613}$ and the growth was negative allometric for all individuals, females, and males, respectively. The mean condition factor was calculated as 1.84 for all individuals, 1.78 for females, and 1.88 for males. There are no previous studies about the population parameters of Morocco dentex and the present study gave the first information on the length-weight, length-length relationships, and condition factors of *D. maroccanus* population inhabiting the northeastern Mediterranean Sea.

Keywords: Condition factor, *Dentex maroccanus*, Length-weight relationship, Length-length relationship, Mediterranean Sea.

[a] *sedakontas@gmail.com* *https://orcid.org/0000-0002-6582-6722*

Introduction

Dentex maroccanus (Morocco dentex) is an Atlantic-Mediterranean fish [1] and a significant demersal commercial sparid species that is present throughout the Mediterranean [2]. Morocco dentex inhabits the muddy lower shelf [3] and lives independently of the bottom [4]. It is distributed from the Bay of Biscay to the Gulf of Guinea, the eastern Atlantic, and the southern Mediterranean [5,6]. It is reported from Algeria [6], and the Aegean Sea [3,7,8]. In addition, it was reported as one of the most abundant species from the shelf of Antalya Bay [1]. Dentex maroccanus feeds on both benthic macrofauna and pelagic species [4]. The morphological sexual dimorphism was determined for *D. maroccanus* inhabiting eastern Algeria [6,9].

The length-weight relationships used for fisheries biology and fisheries management, generally, aid to determine [10-12] and comparing [13,14] the regional-specific biological characteristics of the fish species. The length-weight relationship can be used for morphometric comparison and it allows the determination of the condition of fish species [15]. When only length measurements are provided, the length-weight relationship can be used to calculate the weight [16]. Little information is available for *D. maroccanus* which is a Mediterranean species, and the relationships between different length types (relationships of fork length-total length, standard length-total length, standard length-fork length) are very important for comparative growth studies. The knowledge of condition factors is particularly useful for studying fish biology. The condition factor (K) reflects data on the physiological condition of the fish concerning its welfare [17]. The sex ratio gives fundamental data to evaluate fish population stock sizes and evaluate their reproductive potential [18].

The Mediterranean Sea is regarded as one of the most complex marine habitats [19]. Despite the abundance of species in the eastern Mediterranean region, climate change and human activity are having an impact on coastal ecosystems [20,21]. Many fish stocks, particularly demersal ones, are regarded as being overfished or even depleted [22]. Regular fish stock monitoring and analysis is crucial for both fisheries management and fisheries biology to ensure the aquatic ecosystem's sustainability [23-26]. For this reason, it is necessary to examine the population characteristics of fish species.

There have been limited studies on the population parameter of *D. maroccanus*. The population parameters of *D. maroccanus* were mainly studied in the Aegean Sea on the coast of Turkey. It has been determined that there is no published study about the population parameters of this species inhabiting the Mediterranean Sea. There are several studies on age, growth, and reproduction in Algeria [6] and Saros Bay [2], on the length-weight relationship in Saros Bay [27] and the northeastern Aegean Sea [7], on ecological distribution on the shelf of Antalya Gulf [1], on diet composition in the central Turkish Aegean Sea [8]. In order to generate information

to assist future stock management and sustainable fishing, this study is the first to give some population parameters such as length-weight relationship (LWR), length-length relationship (LLR), and condition factor for *D. maroccanus* in the northeastern Mediterranean Sea.

Materials and Methods

Dentex maroccanus individuals were collected in March-April 2021 from the northeastern Mediterranean Sea (Mersin Bay). The total length (TL), fork length (FL), and standard length (SL) were measured to the nearest 1 mm, and the weight (W) was recorded to the nearest 0.1 g. The sex of *D. maroccanus* individuals was determined by macroscopic investigation of the gonads. The sex ratio (female:male) was calculated with the equation: the total number of females/total number of males [28]. Whether there was a statistical difference between the length and weight values of females and males was tested using the t-test. The exponential regression equation, $W = a \times TL^b$, was used to calculate length-weight relationships (LWRs) [29]. In this equation, W is weight in g, TL is the total length in cm, *a* and *b* are constants. The %95 confidence interval of *b* values of both sexes and all individuals were calculated [30]. The parameters of "*a*" and "*b*" were estimated from the linear regression equation "logW=log*a* + *b*logTL" applied to the log-transformed. The growth type is isometric when *b* is equal to 3, positive or negative allometric when the *b* value is greater or less than 3, respectively. Whether the *b* value obtained from the length-weight relationship is different from 3 was tested with the t-test and the growth type was determined. Length-length relationships (LLRs) such as FL-TL, SL-TL, and SL-FL were calculated from the equation: y = ax+ b, and the coefficient of determination (R^2) was determined. Fulton condition factor (K) was calculated from the equation: $K=100 \times (W/L^3)$ [31]. In this equation, K is the condition factor, W is the weight (g) and TL is the total length (cm). The statistical analyses were calculated by Minitab 16 software.

Results

A total of 37 females (38.9%) and 58 males (61.1%) of *Dentex maroccanus* individuals (n=95) were evaluated. The sex ratio (female:male) was calculated as 0.63:1. The descriptive statistics of weight, total length, fork length, standard length, and condition factor of both sexes and all individuals were given in Table 1. The mean total length and weight of all *D. maroccanus* samples, females and males were determined as 12.1±0.082 cm, 12.3±0.130 cm, 11.9±0.100 cm, and 32.81±0.575 g, 33.93±0.839 g, 32.10±0.766 g, respectively. The condition factor was 1.84 ± 0.017 for all samples, 1.78 ± 0.026 for females, and 1.88 ± 0.021 for males, respectively. The condition factor showed statistically significant variation between females and males of *D. maroccanus* (P<0.05).

Table 1. The descriptive statistics of the variables and condition factors of *D. maroccanus* in the northeastern Mediterranean Sea (S.E.: Standard error, Min: Minimum, Max: Maximum, F: females, M: males)

Mean±S.E. (Min. - Max.)	Weight (g)	Total Length (cm)	Fork Length (cm)	Standard Length (cm)	Condition Factor
F+M	32.81 ± 0.575 (17.80-52.00)	12.1 ± 0.082 (9.9-14.3)	11.1 ± 0.075 (9.1-12.9)	10.0 ± 0.068 (8.3-12.1)	1.84 ± 0.017 (1.49-2.25)
F	33.93 ± 0.839 (18.60-45.80)	12.3 ± 0130 (10.6-14.3)	11.3 ± 0.122 (9.5-12.9)	10.2 ± 0.115 (8.7-12.1)	1.78 ± 0.026 (1.49-2.07)
M	32.10 ± 0.766 (17.80-52.00)	11.9 ± 0.100 (9.9-13.5)	10.9 ± 0.090 (9.1-12.4)	9.8 ± 0.080 (8.3-11.2)	1.88 ± 0.021 (1.49-2.25)

The calculations were separately made for all individuals, females, and males because both the weight and total length were statistically different between males and females of Morocco dentex (t-test; P<0.05). The distributions of total length-frequency (%) and weight-frequency (%) (for ♀, ♂, ♀+♂) were shown in Figure 1.

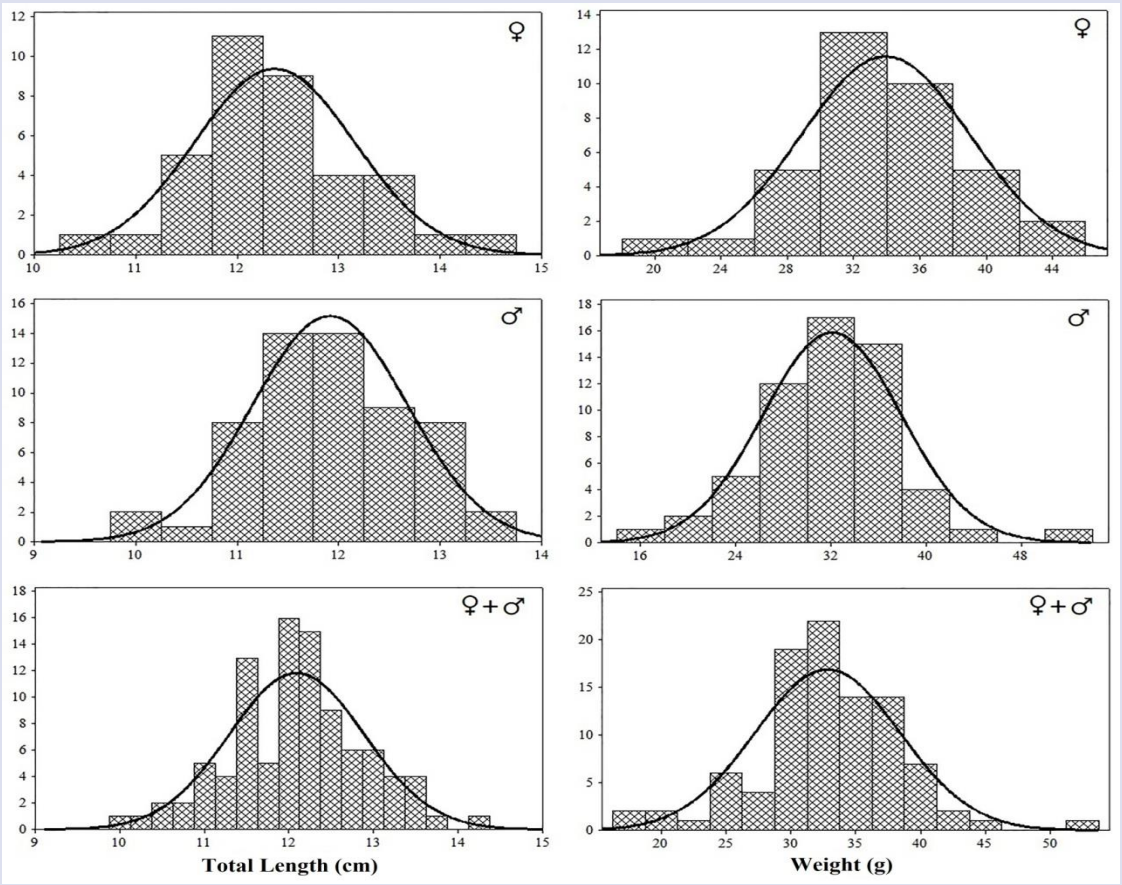

Figure 1. The distributions of length-frequency and weight-frequency for *D. maroccanus* individuals (♀, ♂, ♀+♂)

The length-weight and length-length relationships of *D. maroccanus* (♀, ♂, ♀+♂) were given in Figure 2-3. The LWR was $W=0.08TL^{2.409}$ ($R^2=0.79$) and the LLRs were $TL=1.0607FL+0.2804$ ($R^2=0.94$), $TL=1.1367SL+0.7136$ ($R^2=0.89$), $FL=1.0631SL+0.494$ ($R^2=0.93$) for all individuals, respectively (Figure 2).

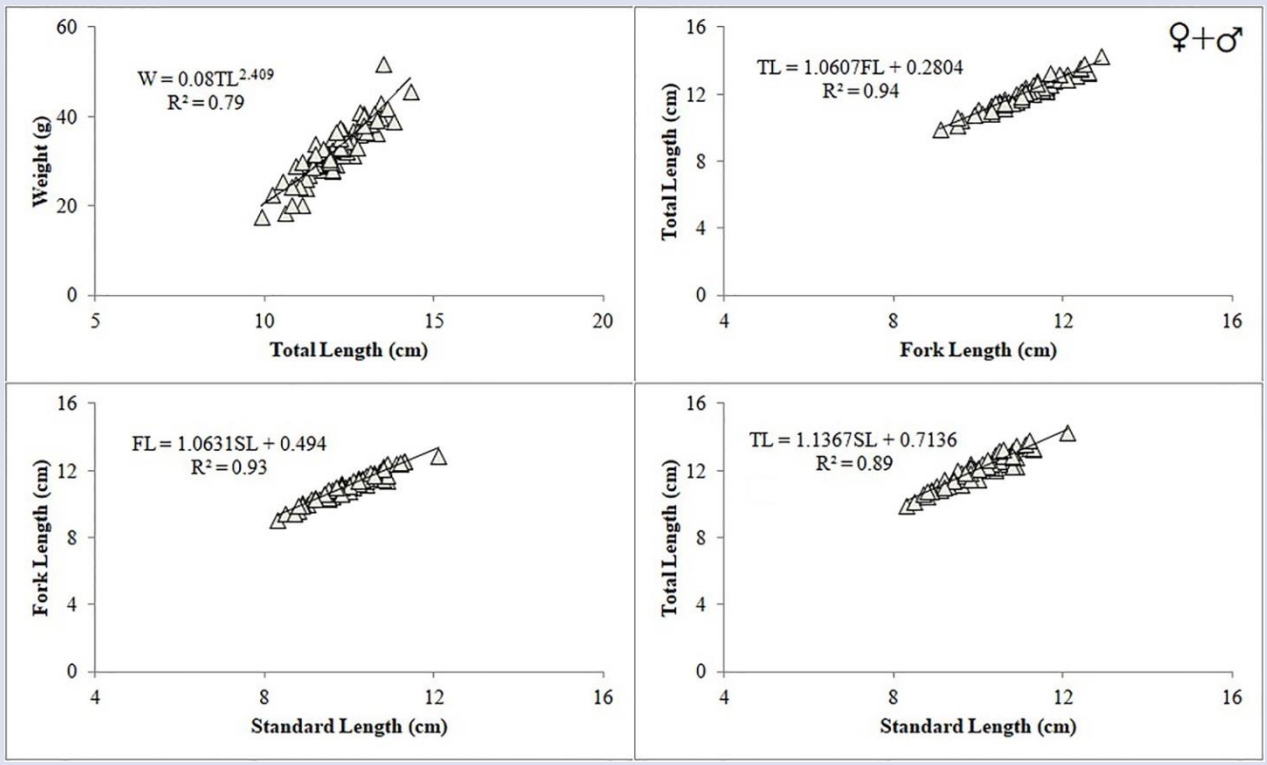

Figure 2. The LWR and LLRs of *D. maroccanus* for all individuals

The LWR was $W=0.1183TL^{2.247}$ ($R^2=0.77$) and the LLRs were determined as TL=1.0225FL+0.7418 ($R^2=0.92$), TL=1.0593SL+1.5395 ($R^2=0.88$), FL=1.0205SL+0.9387 ($R^2=0.92$) for females, respectively. The LWR was $W=0.0489TL^{2.613}$ ($R^2=0.81$) and the LLRs were determined as TL=1.075FL+0.1075 ($R^2=0.94$), TL=1.1795SL+0.2692 ($R^2=0.89$), FL=1.0921SL+0.2014 ($R^2=0.93$) for males, respectively (Figure 3).

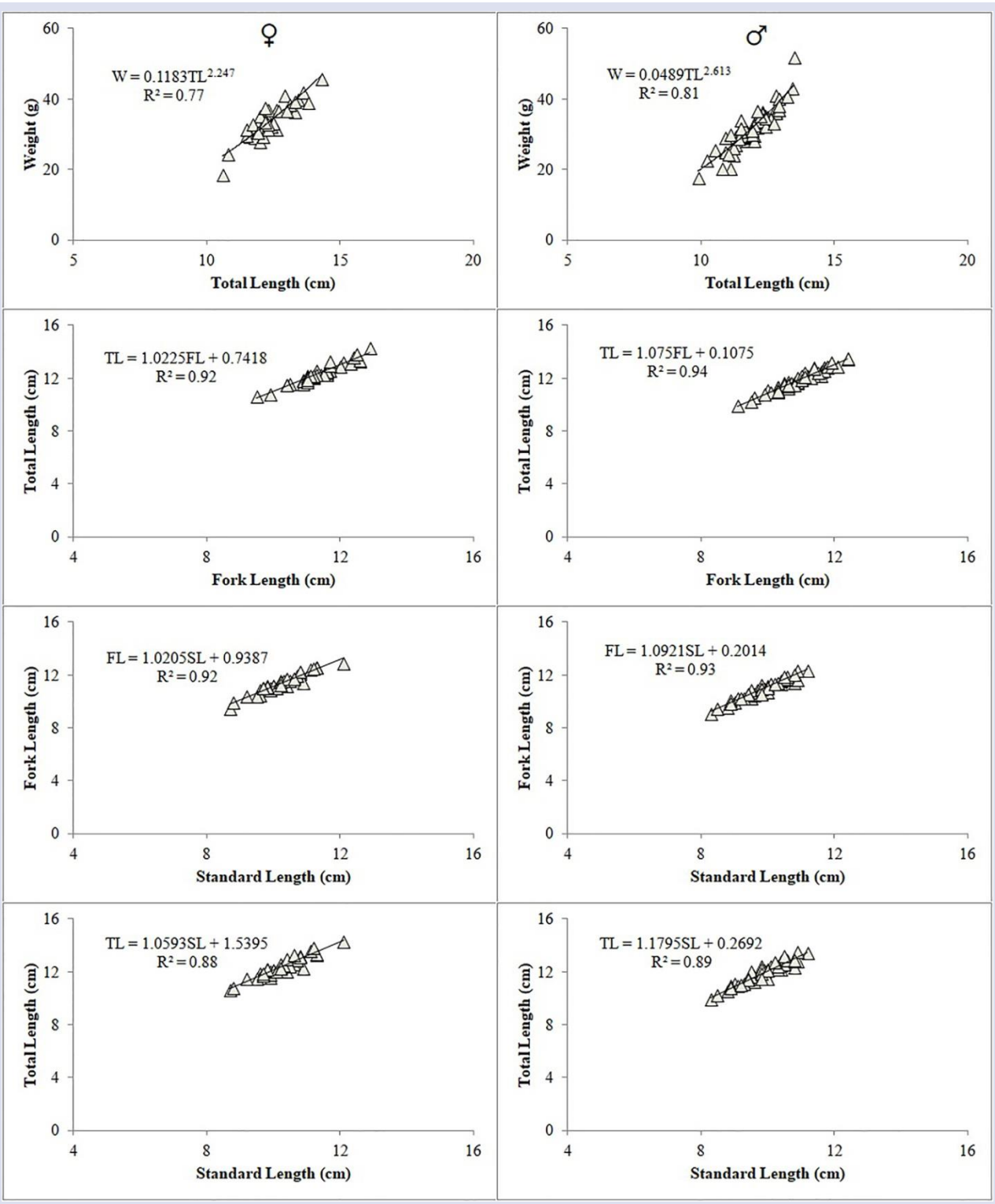

Figure 3. The LWR and LLRs of *D. maroccanus* for females and males

The *b* value was 2.409±0.003, and 95% C.I. of *b* ranged between 2.403-2.416 for all *D. maroccanus* individuals. The *b* value was 2.246±0.005 for females and 2.613±0.004 for males, respectively. 95% C.I. of *b* was 2.236-2.257 for females and 2.604-2.622 for males, respectively. The parameter *b* of length-weight relationships was significantly different from 3 (t-test, P<0.001), and it was determined that the growth was

negative allometric for both sexes and all of *D. maroccanus* inhabiting the northeastern Mediterranean Sea.

Discussion

Morocco dentex has economic importance as with the other members of Sparidae family. It has been determined that there were few studies on *Dentex maroccanus*, especially in the Mediterranean Sea, in the literature [1,6,32]. Therefore, this study represents the first information on sex ratio, length and weight frequency, condition factor, and relationships of length-weight and length-length of *D. maroccanus* in the Mediterranean Sea.

Understanding the relationship between individuals, their environment, and the state of the fish population requires knowledge of the sex ratio [33]. The females and males ratio of *D. maroccanus* (Algeria) was calculated as 49.74% and 46.49%, respectively, and the sex ratio (females:males) was reported as 1:0.9 [6]. [2] reported female:male ratio was 4.8:1 (%82 for females and %18 for males). The sex ratio of Morocco dentex in İzmir Bay was 67% for females and 33% for males [34]. In the present study, the sex ratio was 0.63:1 for *D. maroccanus* inhabiting the northeastern Mediterranean Sea. The males were more than females according to sex composition (58 males against 37 females). This may be explained by behavioral variations during sex change or by one sex being more susceptible to specific fishing equipment [35]. The sex ratio is expected to be 1:1, but several factors such as environmental conditions, food, and reproductive behavior can change this ratio [36].

D. maroccanus showed positive allometric, isometric, and negative allometric growth in previous studies. The *b* value and growth type of *D. maroccanus* from different locations were given in Table 2.

TL-W relationships were $W=0.012TL^{3.046}$ for females, W=0.011TL3.067 for males, W=0.016TL3.060 for both sexes, and growth type was positive allometric for both sexes and all individuals inhabiting the eastern coast of Algeria population [6].

Table 2. The *b* value and growth type of *D. maroccanus* from different locations (A(-): negative allometric growth, A(+): positive allometric growth, I isometric growth

b	*The growth*	*Location*	*References*
3.183	A(+)	The northern Aegean Sea	[7]
2.7236	-	Saros Bay	[27]
2.287	A(-)	Aegean Sea	[37]
2.96 (♀)	-	The coast of Kenya	
2.87 (♂)	-	The coast of Kenya	[38]
2.91 (♀+♂)	-	The coast of Kenya	
2.899 (♀)	A(-)	The north Aegean Sea	
3.067 (♂)	A(+)	The north Aegean Sea	[2]
3.012 (♀+♂)	-	The north Aegean Sea	
3.046 (♀)	A(+)	The eastern coast of Algeria	
3.067 (♂)	A(+)	The eastern coast of Algeria	[6]
3.060 (♀+♂)	A(+)	The eastern coast of Algeria	
3.017	I	The north Aegean Sea	[39]
2.924 (♀)	A(-)	The central Aegean Sea	
2.789 (♂)	A(-)	The central Aegean Sea	[34]
2.856 (♀+♂)	A(-)	The central Aegean Sea	
2.246 (♀)	A(-)	The northeastern Mediterranean Sea	
2.613 (♂)	A(-)	The northeastern Mediterranean Sea	This study
2.409 (♀+♂)	A(-)	The northeastern Mediterranean Sea	

In another study, the length-weight relationships were determined as $W=0.0194TL^{2.924}$, $W=0.0269TL^{2.789,}$ and $W=0.0228TL^{2.856}$ for females, males, and all individuals in the central Aegean Sea, respectively and the negative allometry was found for both sexes and all samples [34]. In this study, the total length-weight relationships were determined as $W=0.1183TL^{2.246}$, $W=0.0489TL^{2.613,}$ and $W=0.08TL^{2.409}$ for females, males, and all individuals, respectively. A different conclusion was obtained in this study. The *b* values were 2.409 for all individuals, 2.246 for females, and 2.613 for males, and negative allometry was determined for the northeastern Mediterranean Sea population. The females showed a strong negative allometric growth than the males. The males and females of the same population living in the same region may have different growth types. In this case, there has been excessive length growth relative to weight gain [40]. Similarly, [37] reported the *b* value as 2.287 for all individuals in the Aegean Sea. Generally, the *b* value ranged from 2.5 to 3.5 for all fish species [40]. According to [41], *b* value may vary from 2 to 4. Several biotic and abiotic factors affect

the length-weight relationship [40]. In addition, total length range, habitat, sex, the influence of fishing gear, and sample width can change the *b* value and growth type [27].

Many fisheries studies use length-length and length-weight relationships to provide information on the growth patterns and condition of fish species [29]. These relationships are useful for fisheries and they allow the calculation of fish conditions [42]. Condition factor is frequently used in fisheries studies. When contrasting two populations that exist under a particular climate, feeding density, and other circumstances, the condition factor provides information [17,41]. In this study, the condition factors of all individuals ranged between 1.49 and 2.25. The mean condition factor of males was higher than females ($P<0.05$) (Table 1). Similarly, Aura [38] reported that the mean condition factor of males was higher than females in Malindi-Ugwana Bay ($p = 0.04$). Condition factor can vary interspecies and intraspecies depending on diet, sex, age, and environmental conditions [43,44].

There is no investigation on the length-length relationship of *Dentex maroccanus* in Turkish seas. Therefore, the present study is the first research in the northeastern Mediterranean Sea. Length-length relationships help us to estimate the other length by using any of the total, fork, and standard lengths of morphologically damaged fish individuals [10]. It is also one of the very important parameters for comparative studies in fisheries management [15].

Conclusions

There is no study about the condition factor, LWRs, and LLRs of *Dentex moraccanus* from the northeastern Mediterranean Sea (Mersin Bay). Moreover, for the first time, the LLRs were determined for Morocco dentex population. The information from this study can provide the baseline data for fisheries. The obtained data will make an important contribution to the knowledge of the *D. moraccanus* population living in Mersin Bay. Thanks to data on the length-weight relationship of fish species inhabiting different geographical regions, researchers can compare the growth and condition differences of the same species. Length-weight parameters reported in this study will be used extensively in existing studies of Turkish commercial fisheries. This research may help with the management of *D. maroccanus* natural stocks, which are crucial for both economic and ecological reasons and may have been threatened by pollution and climate change. However, relatively little data is known about this species in Turkey. It is necessary to investigate the age determination and reproduction data of *Dentex maroccanus* in future studies.

Conflicts of interest

The author stated that did not have conflict of interests.

References

[1] de Meo I., Miglietta C., Mutlu E., Deval M.C., Balaban C., Olguner M.T., Ecological distribution of demersal fish species in space and time on the shelf of Antalya Gulf, Turkey, *Mar. Biodiv*., 48 (2018) 2105-2118.

[2] Gul G., Ismen A., Arslan M., Age, growth, and reproduction of *Dentex maroccanus* (Actinopterygii: Perciformes: Sparidae) in the Saros Bay (north Aegean Sea), *Acta Ichthyol. Piscat.*, 44(4) (2014) 295-300.

[3] Maravelias C.D., Tsitsika E.V., Papaconstantinou C., Evidence of Morocco dentex (*Dentex maroccanus*) distribution in the NE Mediterranean and relationships with environmental factors determined by Generalized Additive Modelling, *Fish. Oceanogr.*, 16 (2007) 294-302.

[4] Katsanevakis S., Maravelias C.D., Damalas D., Karageorgis A.P., Tsitsika E.V., Anagnostou C., Papaconstantinou C., Spatiotemporal distribution and habitat use of commercial demersal species in the eastern Mediterranean Sea, *Fish Oceanogr.*, 18 (2009) 439-457.

[5] Bauchot M.L., Hureau J.C., Sparidae. In: Whitehead P.J.P., Bauchot M.-L., Hureau J.-C., Nielsen J., Tortonese E., (Eds). Fishes of the North-eastern Atlantic and the Mediterranean. Volume 2. Paris: UNESCO, (1986) 883-907.

[6] Mohdeb R., Kara M.H., Age, growth and reproduction of the Morocco dentex *Dentex maroccanus* of the eastern coast of Algeria, *J.Mar. Biol. Assoc. UK*, 95(6) (2014) 1261-1270.

[7] Karakulak F.S., Erk H., Bilgin B., Length–weight relationships for 47 coastal fish species from the northern Aegean Sea, Turkey, *J. Appl. Ichthyol*., 22 (2006) 274-278.

[8] Bayhan B., Sever T.M., Heral O., Diet composition of the Morocco dentex: *Dentex maroccanus* Valenciennes, 1830 (Teleostei: Sparidae) in the central Turkish Aegean Sea, *Int. J.Oceanogr. and Hydrobiol.*, 46(2) (2017) 133-139.

[9] Mohdeb R., Kara M.H., Dimorphisme sexuel et croissance de denté de Maroc *Dentex maroccanus* (Valenciennes, 1830) des côtes d'El Kala en Est Algérien. *Rapport de la Commission Internationale pour l'Exploration Scientifique de la Méditerranée*, 40 (2013) 453.

[10] Bostancı D., Yedier S., Polat N., Condition factor, length-weight and length-length relationships of *Capoeta banarescui* living in Kurtuluş Stream (Perşembe-Ordu), *Bitlis Eren University Journal of Science*, 11(1) (2022) 79-87.

[11] Yedier S., Kontaş S., Bostancı D., Condition factor, length-length and length-weight relationships for *Pagellus acarne* (Risso, 1827) inhabiting the Sea of Marmara, *Journal of Anatolian Environmental and Animal Science,* 4 (2019) 82-88.

[12] Yedier S., Estimation of Some Population Parameters of *Squalius cephalus* (Linnaeus 1758) in Tabakane Stream (Ordu-Turkey), *Sakarya University Journal of Science*, 26(1) (2022) 14-23.

[13] Gonçalves J.M.S., Bentes L., Lino P.G., Ribeiro J., Canário A.V.M., Erzini K., Weight-length relationships for selected fish species of the small-scale demersal fisheries of the south and south-west coast of Portugal, *Fish. Res.*, 30(3) (1997) 253-256.

[14] Yalçın Özdilek Ş., Partal N., Length-weight relationships and condition factors of three fish species in the Karamenderes Stream (Çanakkale, Türkiye), *Turkish J.Biosci. Collect.*, 6(1) (2022) 21-25.

[15] Moutopoulos D.K., Stergiou K.I., Length–weight and length–length relationships of fish species from the Aegean Sea (Greece), *J.Appl. Ichthyol.*, 18(3) (2002) 200-203.

[16] Oliveira M.R., Costa E.F.S., Araújo A.S., Pessoa E.K.R., Carvalho M.M., Cavalcante L.F.M., Chellappa S., Sex ratio and length-weight relationship for five marine fish species from Brazil, *J.Mar. Biol. Oceanogr.*, 1(2) (2012) 1000103.

[17] Lambert Y., Dutil J.D., Can simple condition indices be used to monitor and quantify seasonal changes in the energy reserves of Atlantic cod (*Gadus morhua*)?, *Can. J. Fish. Aquat. Sci*., 54 (Suppl. 1) (1997) 104-112.

[18] Stratoudakis Y., Bernal M., Ganias K., Uriarte A., The daily egg production method: Recent advances, current applications and future challenges, *Fish Fish*, 7(1) (2006) 35-57.

[19] Santinelli C., DOC in the Mediterranean Sea. In: Hansell D., Carlson C., (Eds.). A biogeochemistry of marine dissolved organic matter. 2nd ed. Orlando (Florida): Academic Press, (2015) 579-608.

[20] Coll M., Piroddi C., Steenbeek J., Kaschner K., Lasram F.B.R., Aguzzi J., Ballesteros E., Bianchi C.N., Corbera J., Dailianis T., Danovaro R., Estrada M., Froglia C., Galil B.S., Gasol J.M., Gertwagen R., Gil J., Guilhaumon F., Kesner-Reyes K., Kitsos M.-S., Koukouras A., Lampadariou N., Laxamana E., Cuadra C.M.L.-F., Lotze H.K., Martin D., Mouillot D., Oro D., Raicevich S., Rius-Barile J., Saiz-Salinas J.I., Vicente C.S., Somot S., Templado J., Turon X., Vafidis D., Villanueva R., Voultsiadou E., The biodiversity of the Mediterranean Sea: estimates, patterns, and threats, *PLoS ONE*, 5(8) (2010) e11842.

[21] Rilov G., Multi-species collapses at the warm edge of a warming sea, *Sci. Rep*., 6 (2016) 36897.

[22] Tsikliras A.C., Dinouli A., Tsiros V.Z., Tsalkou E., The Mediterranean and Black Sea fisheries at risk from overexploitation, *PLoS One*, 10 (2015) e0121188.

[23] Froese R., Tsikliras A.C., Stergiou K.I., Editorial note on weight–length relations of fishes, *Acta Ichthyol. Piscat*., 41(4) (2011) 261-263.

[24] Bostanci D., Yedier S., Polat N., *Pseudorasbora parva* (Temminck & Schlegel, 1846): A New Threat to Fish Biodiversity in Ordu Province (Middle Black Sea Region), *Journal of Limnology and Freshwater Fisheries Research*, 6(1) (2020) 52-58.

[25] Yedier S., Bostanci D., Polat N., New distribution data for Prussian carp *Carassius gibelio* (Bloch 1782) in the middle Black Sea Region of Turkey, *Croatian Journal of Fisheries*, 79(2) (2021) 83-88.

[26] Bostanci D., Yedier S., Helli S., Polat N., First record of the *Carassius auratus* (Linnaeus, 1758) in inland waters of Ordu province and some data on the Ulugöl plateau pond population of the species, *Aquatic Research*, 4(3) (2021) 279-285.

[27] Ismen A., Ozen O., Altinagac U., Ozekinci U., Ayaz A., Weight–length relationships of 63 fish species in Saros Bay, Turkey, *J.Appl.Ichthyol.*, 23(6) (2007) 707-708.

[28] Vazzoler A.E.A.M., Reproduction Biology of Teleostean Fishes: Theory and Practice, Maringá, EDUEM, *Brazilian Society of Ichthyology*, (1996) 169.

[29] Bagenal T.E., Tesch W.F., Age and Growth. In: Bagenal T., (Eds). Methods for assessment of fish production in freswater. Oxford and Edinburgh: Blackwell Scientific Publications, (1978) 101-136.

[30] Zar J.H., Biostatistical Analysis. 4th ed. New Jersey: Prentice Hall, Upper Saddle River, (1999) 663.

[31] Pauly D., Some simple methods for the assessment of tropical fish stocks, *FAO Fisheries Technical Paper*, 234 (1983) 52.

[32] Michailidis N., Corrales X., Karachle P.K., Chartosia N., Katsanevakis S., Sfenthourakis S., Modelling the role of alien species and fisheries in an Eastern Mediterranean insular shelf ecosystem, *Ocean Coast Manag.*, 175 (2019) 152-171.

[33] Vicentini R.N., Araújo F.G., Sex ratio and size structure of *Micropogon asfurnieri* (Desmarest, 1823) (Perciformes, Sciaenidae) in Sepetiba Bay, Rio de Janeiro, *Braz. J.Biol.*, 63(4) (2003) 559-566.

[34] Heral O., Bayhan B., Age and growth of Morocco Dentex *Dentex maroccanus* Valenciennes, 1830 (Actinopterygii: Sparidae) in Izmir Bay, Central Aegean Sea, Turkey, *Acta Zool. Bulg.*, 72(1) (2020) 149-154.

[35] Anam R.O., Munga C.N., Gonda J.R., The biology of goldsilk sea bream (Family: Sparidae) from the inshore waters of north coast Kenya, *WIO J. Mar. Sci.*, 18(2) (2019) 77-86.

[36] Emlen S.T., Oring L.W., Ecology, sexual selection and the evolution of mating systems, *Science*, 197 (1977) 215-223.

[37] Ceyhan T., Akyol O., Erdem M., Length-weight relationships of fishes from Gökova Bay, Turkey (Aegean Sea), *Turk. J. Zool.*, 33 (2009) 69-72.

[38] Aura C.M., Anam R.O., Musa S., Kimani E., Length-weight relationship and condition factor (K constant) of *Dentex maroccanus*, Valenciennes 1830 (Family Sparidae) at Malindi, Kenya, *West. Indian Ocean J. Mar. Sci.,* 12(1) (2013) 79-83.

[39] Evagelopoulos A., Batjakas I., Koutsoubas D., Length–weight relationships of 9 commercial fish species from the north Aegean Sea, *Acta Adriat.*, 58 (1) (2017) 187-192.

[40] Froese R., Cube law, condition factor and weight-length relationships: History, meta-analysis and recommendations, *J. Appl.Ichthyol.*, 22(4) (2006) 241-253.

[41] Tesch F.W., Age and Growth. In: Ricker W.E., (Eds). Methods for assessment of fish production in fresh waters. Oxford, UK: Blackwell Scientific Publications, (1971) 98-130.

[42] Bostancı D., Yedier S., Kontaş S., Kurucu G., Polat N., Length-weight, length-length relationships and condition factors of some fish species in Yalıköy Stream (Ordu-Turkey), *Yunus Res. Bull.*, 17(4) (2017) 375-383.

[43] Petrakis G., Stergiou K., Weight-length relationships for 33 fish species in Greek waters, *Fish. Res.*, 21(3) (1995) 465-469.

[44] Yedier S., Kontaş S., Bostancı D., Length-length and length-weight relationships of lessepsian *Saurida undosquamis* from the İskenderun Bay (Eastern Mediterranean, Turkey), *Journal of the Institute of Science and Technology,* 10(1) (2020) 616-623.

Cumhuriyet Sci. J., 44(2) (2023) 283-288
DOI: https://doi.org/10.17776/csj.1068886

Cumhuriyet Science Journal

| csj.cumhuriyet.edu.tr | Founded: 2002 ISSN: 2587-2680 e-ISSN: 2587-246X Publisher: Sivas Cumhuriyet University

Investigation on the Flow Behaviour of Agar Solution and Rheological Modelling

Mukaddes Karataş [1,a,*]

[1] *Department of Chemical Engineering, Faculty of Engineering, Fırat University, Elazığ, Türkiye*
**Corresponding author*

Research Article

History
Received: 06/02/2022
Accepted: 07/06/2023

ABSTRACT

In this study, the effect of shear rate, agar concentration (15-35 kg/m^3) and temperature (30-60°C) on the apparent viscosity of the agar solution was investigated. Apparent viscosities at different shear rates were determined using a rotational viscometer. The findings show that the apparent viscosity decreasing with a rise of shear rate increased with increasing concentration. An increase in the tempearture, on the other hand, led to a decrease in the apparent viscosity. To illustrate both temperature and concentration changes together, the Bingham, power law, and Casson models were utilized in choosing the most suitable model. When the models were compared using statistical tests, the most compatible model was found to be the power-law model. The consistency coefficient and flow behaviour index calculated using the power law model showed that agar solutions exhibited shear-thinning flow behavior (pseudoplastic). This study suggests that power law, within the ranges of the temperature and concentration studied could be used to estimate the viscosity of the agar solutions in the applications requiring the knowledge of flow behavior.

Keywords: Flow behaviour, Rheological models, Agar-agar, Rotary viscometer.

[a] *mkozturk@firat.edu.tr* *https://orcid.org/0000-0001-5803-6821*

Introduction

Agar is linear polysaccharide consisting of β-D-galactopyranose and 3,6-anhydro-α-L-galactopyranose repeating units. Used in food, pharmaceutical and biotechnological applications due to its unique physico-chemical properties and gelling properties, agar is a valuable hydrocolloid found in red seaweed species. It is found as intercellular matrix material in many red seeweed species. Agar is an extract from some red algae (Gelidiacae, Sphaerococcaceae and Rhodophyceae) and contains agarose and agaropectin polysaccharides. Gelling of the agar is due to the agarose polysaccharide contained in it, however, it is the agaropectin fraction providing the viscosity [1-5].

Food, pharmaceuticals, cosmetics, microbiology and biotechnology, textiles and dentistry are some of the industries where agar-agar finds widespread use due to its unique properties and versatility. It is widely used as a vegetarian alternative to gelatin, especially in the food industry due to its gelling properties. It also acts as a thickening agent in soups and sauces, helping to give food a smooth and consistent texture without altering its flavor. Other common uses of agar-agar in food are as a stabilizer in food products to prevent component separation or precipitation, and as a nutrient culture medium for growing microorganisms for scientific research in laboratories or for the production of probiotics and other microbial products [2, 6, 7]. Agar is advantageous over other gelling means as it can form a stable gel at low concentrations and over a wide pH range [6-9]. In studies related to the gelation of agar, the transition temperature from the solution to gelation was reported to be 45 °C [10]. Also, the agar solution gelation is reversible as it is a physical gelation caused only by hydrogen bridges [11].

Determining the rheological properties of agar solutions is crucial for quality control, process optimization, formulation development, product stability, scaling production processes, and advancing scientific research in various industries. By characterizing the rheology, information is gained about the consistency, texture and flow behavior of agar solutions and manufacturers can ensure the quality and consistency of their agar products. Also, changes in viscosity, gel strength, or flow behavior over time may indicate degradation or aging of agar solutions, affecting their functionality and performance. Rheological data help establish storage conditions and determine appropriate expiration dates for agar-based products. Aqueous agar solution that do not comply rheologically with Newton's viscosity law is typical a Non-Newtonian fluid [9]. Many investigations have been done on the effects of shear rate, temperature, concentration, and molecular weight parameters on the apparent viscosity of agar aqueous solutions in the literature. [8, 12-15].

The apparent viscosity of agar-agar varies depending on factors such as its specific source and grade, the extraction method, and the experimental conditions used in the studies. This study aimed to provide critical information for product development, process optimization, quality control, stability, scale-up and basic research evaluation by investigating the effects of temperature, concentration and shear rate on the

rheological behavior of agar solutions as well as the combined effects of temperature and concentration on apparent viscosity.

Materials and Methods

Material

Agar was purchased from Smart Chemistry (Izmir, Turkey), a local producer. De-ionized water was used to prepare all solutions.

Preparation of Agar Solution at Different Concentrations

Firstly, 3, 4, 5, 6 and 7 g of agar were weighed and dissolved in 200 ml of distilled water to prepare agar solutions of different concentrations. In order for the agar to dissolve easily and the prepared solution to be homogeneous, the agar was slowly added to the distilled water heated to 90 °C. In order to remove air bubbles in the solution, which was stirred for 24 hours on a magnetic stirrer, the mixture was left at room temperature for 6 hours. The mass concentrations of the agar solutions prepared are 15, 20, 25, 30 and 35 kg / m^3, respectively.

Measuring the Apparent Viscosity of Agar Solution

Apparent viscosities were determined using a rotational viscometer. A Brookfield viscometer (model LVDV-E; Brookfield Engineering Laboratories. Inc., Stoughton, MA, USA) with spindle speeds of 10, 12, 20, 30, 50, 60 and 100 rpm was used.The water-jacketed stainless steel cylindrical vessel was utillized for all measurements. Approximately 150 ml of sample was filled into the cylindrical vessel with a volume of 200 ml for each measurement. The water-jacketed cylindrical vessel was connected to a temperature bath to maintain the temperature constant at the desired value. The shear rate was gradually increased from 1.32 to 22 s^{-1}. The torque measurements were performed and each measurement was repeated twice for reliability of the results.

Shear rates for agar solutions were calculated by utilizing the cylindrical spindle factors given by Brookfield (Brookfield Engineering Labs. Inc., Stoughton, MA, USA) for spindle LV-1.

$$-dV_\phi/dr=0.22N \quad (1)$$

where $-dV_\phi/dr$ (s^{-1}) is the shear rate, N is the spindle speed (rpm).

The viscometer was calibrated using the Brookfield silicone viscosity standard (nominal viscosity at 25 ° C: 1000 mPa s). The following equation was used to calculate spindle calibration factor for any spindle speed.

$$F=R/100 \quad (2)$$

where f is the spindle calibration factor, R is the full scale viscosity range.

The following equation was used to calibrate the apparent viscosity values (η_a).

$$\eta_a=f\ (\%Tork) \quad (3)$$

Equation 4 was used to calculate the shear stress.

$$\tau_{r\phi}= \eta_a\,(-dV_\phi/dr) \quad (4)$$

where $\tau_{r\phi}$ is the shear stress (mPa),η_a is the apparent viscosity (mPas), dV_ϕ/dr is the shear rate (s^{-1}), V_ϕ is the velocity in direction along the axis of rotation, r is the radial distance.

Determination of the Rheological Model

Flow curves for agar solutions were created by applying experimental data to power-law, bingham and casson models, which are the most commonly used models of Non-Newtonian models [12, 16-18]. The mathematical expression of these models is as follows:

$$\tau_{r\phi}= m\,(-dV_\phi/dr)^n \quad \text{(Power Law Model)} \quad (5)$$

$$\tau_{r\phi}=\tau_B + \eta_B\,(-dV_\phi/dr) \quad \text{(Bingham Model)} \quad (6)$$

$$\tau_{r\phi}{}^{0.5}=\tau_C + \eta_C\,(-dV_\varphi/dr)^{0.5} \quad \text{(Casson Model)} \quad (7)$$

where m is the consistency index (mPas) and n is the flow behaviour index (dimensionless), τ_B and η_B are the Bingham model parameters, τ_C and η_C are the Casson model parameters.

The model parameters were found by applying non-linear regression to these model equations at different temperatures and concentrations, and the highest correlation coefficient was used to determine the model that best fits the experimental data.

Statistical Analysis

The statistical software package (Statistica for Windows 5.0, 1995) was used to perform nonlinear regression analysis of experimental viscosity data of agar solutions. Variance analysis (ANOVA) was used to evaluate the effect of concentration on flow activation energy and consistency index statistically.

Results and Discussion

Determination of the Rheological Model

Model parameters of Power-law (Ostwald-de Waele), Bingham and Casson models, which are frequently used in engineering applications [18-20], were determined by nonlinear regression analysis for different temperatures and concentrations, and these values are given in Table 1.

Table 1. Model parameters and correlation coefficients of rheological models for agar solution at different temperatures and concentrations

T (°C)	C (kg/m³)	Power law model			Bingham model			Casson model		
		n	m (Pasⁿ)	r^2	η_B (Pas)	τ_B (Pa)	r^2	η_C $(Pas)^{0.5}$	τ_C $(Pa)^{0.5}$	r^2
30	15	0,4262	0,2491	0,9799	0,028	0,3275	0,8732	0,1166	0,4286	0,9344
	20	0,5199	0,4173	0,9882	0,0727	0,5402	0,9371	0,2049	0,5024	0,9655
	25	0,5401	0,6386	0,9992	0,1294	0,7623	0,9827	0,278	0,5833	0,995
	30	0,5201	0,8847	0,9906	0,1682	1,044	0,9797	0,3098	0,703	0,9857
	35	0,6468	1,1911	0,9979	0,028	0,3275	0,8732	0,498	0,6844	0,9927
40	15	0,2216	0,2277	0,9948	0,0101	0,258	0,9447	0,0509	0,4471	0,9845
	20	0,5046	0,3656	0,9921	0,064	0,4431	0,9704	0,1892	0,4633	0,9838
	25	0,5318	0,5883	0,9966	0,1123	0,7264	0,9676	0,2572	0,5748	0,9857
	30	0,5109	0,8101	0,9812	0,1479	0,9648	0,9642	0,288	0,6825	0,9718
	35	0,6863	0,9692	0,9974	0,3282	1,1135	0,9837	0,492	0,5773	0,9912
50	15	0,2908	0,1742	0,9962	0,0117	0,2021	0,9618	0,0626	0,3769	0,9923
	20	0,4086	0,3227	0,9779	0,0395	0,3771	0,9737	0,1356	0,4674	0,9868
	25	0,5547	0,4559	0,9939	0,0992	0,5329	0,9786	0,2474	0,4767	0,993
	30	0,5353	0,6579	0,9923	0,1299	0,7935	0,9745	0,2768	0,6001	0,9851
	35	0,6143	0,8465	0,994	0,2121	1,0863	0,9544	0,3782	0,6321	0,9775
60	15	0,1606	0,1597	0,9824	0,0044	0,1771	0,8868	0,0286	0,3854	0,9455
	20	0,4291	0,2433	0,9617	0,032	0,2895	0,9608	0,1252	0,4005	0,9761
	25	0,5265	0,3998	0,9867	0,0763	0,4855	0,9566	0,2131	0,4668	0,9842
	30	0,534	0,5772	0,9913	0,117	0,6727	0,98	0,2641	0,5487	0,9934
	35	0,575	0,7667	0,999	0,1734	0,9338	0,9767	0,3313	0,6188	0,9911

According to the data in Table 1, since the correlation coefficient (r^2) is higher than the other models, the power-law model is the model that best expresses the experimental data. The power law model estimating the apparent viscosities of polymer solutions is frequently encountered. Rahimi and Dehaghani (2021) developed a viscosity model based on the power law rheological model to estimate the viscosity of polymer solutions in their experimental study on a novel correlation predicting the apparent viscosity of sulfonated polyacrylamides. In another study, power law was used to generate flow curves from the rheological data of the water-carboxymethyl cellulose-salt system [22].

Flow behavior index (n) and consistency index (m) are important parameters that determine non-newtonian flow properties. In this model, it is seen that the flow behavior index is less than 1, so the flow behavior of agar solutions is pseudoplastic (shear thinning behavior). That is, the apparent viscosity decreases sharply at low shear rates, while this change is less at high shear rates. This indicates less resistance to flow due to the disorder of the long chain molecules [16].

The apparent viscosity of agar solutions in the concentration range of 15-35 kg/m^3 as a function of shear rate at constant temperature (40 °C) is shown graphically in Figure 1. An increase in the shear rate of the agar solutions resulted in a reduction in apparent viscosity.

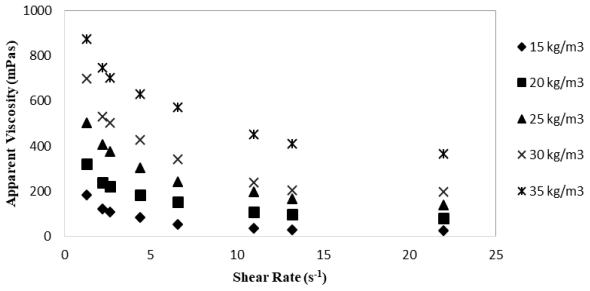

Figure 1. Typical flow curves for different concentrations of agar solutions at 40 °C.

Figure 1. shows that the apparent viscosity increases with increasing concentration. As the interaction between agar particles decreases at lower concentrations, apparent viscosity decreases compared to higher concentrations [12]. The non-Newtonian behavior of agar-agar solutions is attributed to the entanglement of the agarose chains and the formation of a three-dimensional network structure. Shear thickening behavior at low shear rates was associated with increased resistance to flow due to the entangled mesh. As the shear rate increased, the network began to deteriorate, causing shear thinning and a decrease in viscosity [23].

Effect of Temperature on the Rheological Behavior of Agar Solution

Since the agar solution is exposed to different shear rates in industrial applications, the equipment used can be better designed depending on the variation of viscosity with temperature at determined shear rates. It was determined that the apparent viscosity of the agar solutions decreased with increasing temperature. At lower temperatures, agar agar molecules are in a helical structure, which allows them to form a three-dimensional network, trapping water and creating a gel-like consistency. This gel network gives agar agar its high apparent viscosity. As the temperature increases, the heat energy disrupts the helical structure, causing the agar agar molecules to unwind and the gel network to weaken. At higher temperatures, the helical structure is completely disrupted, and the agar agar molecules exist in a random coil conformation. In this state, the agar agar molecules can move more freely, and the viscosity decreases. The breakdown of the gel structure leads to a decrease in the apparent viscosity of the agar agar solution [24]. The effect of temperature on the viscosity of polymer solutions is expressed by the Arrhenius equation and the equation is as follows:

$$\eta_a = Ae^{Ea/RT} \quad (8)$$

where η_a is the apparent viscosity (mPas), A is a constant (mPas), E_a is the activation energy of flow (kJ/mol), R is the universal gas constant (8.314×10^{-3} kJ/mol.K), T is the absolute temperature (K).

Flow activation energy is a measure of temperature sensitivity that is directly related to the size of the macromolecule and determines the degree of difficulty of the flow. The Arrhenius plot drawn for a given shear rate (11 s^{-1}) is shown in Figure 2.

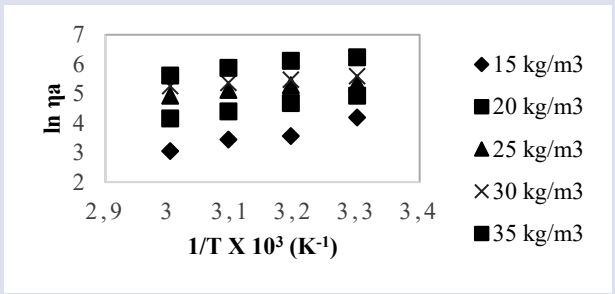

Figure 2. Arrhenius plot for different concentrations at shear rate 11 s^{-1}.

The maximum and minimum values for the different shear rates of the flow activation energies calculated from the slopes of the lines obtained by plotting ln η_a versus 1/T for different concentrations are shown in Table 1.

Considering the maximum values of flow activation energy, it has been found that the viscosity of agar solutions is relatively more sensitive to temperature change at high shear rates.

Table 2. The change of flow activation energy of agar solutions at different shear rates.

Shear rate (s^{-1})	Ea (kJ/mol)	r^2
1.32	9.906-14.36	0.9583-0.9862
2.20	12.44-19.25	0.9686-0.9933
2.64	12.06-20.68	0.9610-0.9989
4.40	13.49-23.56	0.9441-0.9960
6.60	14.70-27.14	0.9183-0.9707
11.0	9.509-29.95	0.9405-0.9995
13.2	7.558-28.76	0.9268-0.9973
22.0	12.08-30.12	0.9226-0.9891

Combined Effect of Temperature and Concentration on the Apparent Viscosity

The ability to derive a single equation that describes the combined effects of temperature and concentration on the apparent viscosity of agar solutions would be extremely useful in a variety of applications. The change of apparent viscosity with temperature can be written in two ways:

$$A = \delta(C)^{\varepsilon} \quad (9)$$

$$A = \delta_1 \exp(\varepsilon_1 C) \quad (10)$$

By substituting these equations in the Arrhenius equation, the following equations are obtained, which give the effect of temperature and concentration on the apparent viscosity of agar solutions.

$$\eta_a = \delta(C)^{\varepsilon} \exp(E_a/RT) \quad (11)$$

$$\eta_a = \delta_1 \exp(\varepsilon_1 C) \exp(E_a/RT) \quad (12)$$

Table 3. The change of agar solution to apparent viscosity with temperature and concentration (Eq. 11)

	$\eta_a = \delta(C)^{\varepsilon} \exp(E_a/RT)$			
Shear rate (s^{-1})	δ mPas(kg/m³)$^{-\varepsilon}$	ε [–]	E_a (kJ/mol)	Statistical tests
1.32	0.0129	1.854	11.84	MBE=0.4368; MPE= -1.086; EF=0.9940
2.20	0.0017	2.073	14.65	MBE=1.104; MPE= -1.513; EF=0.9956
2.64	0.0018	2.115	13.85	MBE=0.9339; MPE= -2.318; EF=0.9954
4.40	0.0004	2.368	15.07	MBE=0.5589; MPE= -1.506; EF=0.9880
6.60	0.0003	2.476	14.69	MBE=0.8706; MPE= -3.040; EF=0.9781
11.0	0.0002	2.613	14.43	MBE=1.322; MPE= -4.184; EF=0.9694
13.2	0.0001	2.790	15.68	MBE=0.3920; MPE= -0.7708; EF=0.9661
22.0	0.0001	2.819	16.67	MBE=0.2491; MPE= -4.438; EF=0.9739

The model parameters, flow activation energies and apparent viscosity values in these theoretical models were determined by using statistical package program (Statistica for Windows 5.0) with non-linear regression analysis. Using some statistical tests, the reliability of the model equations was investigated and the consistency of the experimental apparent viscosity values and the apparent viscosity values calculated from the model were determined (Table 3 and Table 4).

Table 4. The change of agar solution to apparent viscosity with temperature and concentration (Eq. 12)

Shear rate (s^{-1})	$\eta_a = \delta_1 \exp(\varepsilon_1 C)\exp(E_a/RT)$			
	δ_1 (mPas)	ε_1 ($kg/m^3)^{-1}$	E_a (kJ/mol)	Statistical tests
1.32	0.8205	0.0698	11.89	MBE=2.559; MPE= -4.623; EF=0.9797
2.20	0.1795	0.0773	14.69	MBE=2.713; MPE= -5.835; EF=0.9862
2.64	0.2165	0.0787	13.90	MBE=3.075; MPE= -7.237; EF=0.9844
4.40	0.0863	0.0873	15.15	MBE=1.934; MPE= -7.384; EF=0.9861
6.60	0.0739	0.0909	14.76	MBE=1.923; MPE= -9.776; EF=0.9784
11.0	0.0544	0.0957	14.58	MBE=0.9383; MPE= -11.62; EF=0.9720
13.2	0.0250	0.1013	15.87	MBE=0.2519; MPE= -9.201; EF=0.9715
22.0	0.0144	0.1020	16.81	MBE=0.9957; MPE= -15.55; EF=0.9738

As can be seen from the applied statistical tests, the best model for expressing the combined effect of temperature and concentration on the apparent viscosity of agar solutions is Eq. 11.

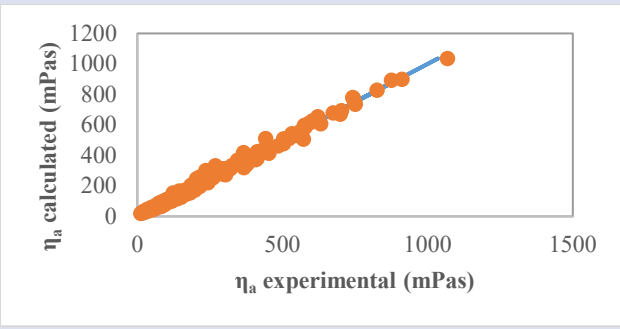

Figure 3. Comparison of the experimental apparent viscosity of agar solutions and the apparent viscosity values calculated from Eq. 11

The relationship between the experimental apparent viscosity values and the apparent viscosity values calculated from Eq. 11 is shown in Figure 3 for all shear rates, temperature and concentration.

The combined effect of temperature and concentration on viscosity is not simply additive or linear. The interaction between temperature and concentration can lead to complex and nonlinear changes in viscosity. The decrease in viscosity with increasing temperature was more pronounced at higher concentrations compared to lower concentrations [25].

Conclusions

As a result of the study, it was found that agar solutions exhibit a shear thinning (pseudo plastic) behavior due to the flow behavior index being less than 1. As a rheological model, it has been shown that it will be well represented by the power-law model. The viscosity of agar solutions increased with concentration. The increased viscosity of agar solutions with higher concentrations can be attributed to the larger number of agar molecules present in the solution. The viscosity of agar solutions decreased with an increase in temperature. Higher concentrations of agar, even with a decreasing viscosity trend with temperature, resulted in higher viscosities compared to lower concentrations at the same temperature. As a result of the study of the flow activation energy, it was found that the apparent viscosity of the agar solutions was relatively more sensitive to temperature change at high shear rates. The data obtained in the design of equipment necessary for processing agar solutions in the range of temperatures, concentrations and shear rates studied are valid.

Conflicts of interest

There are no conflicts of interest in this work.

References

[1] Stephen A.M., Philips G.O., Williams P.A., Food Polysaccharides and Their Applications.In: Stanley N.F., (Eds). Agars. 2nd ed. New York: CRC Press, (2016) 217-238.

[2] Rhein-Knudsen N., Ale M.T., Ajalloueian F., Yu L., Meyer A.S., Rheological properties of agar and carrageenan from Ghanaian red seaweeds, *Food Hydrocolloids*, 63 (2017) 50-58.

[3] Nishinari K., Fang Y., Relation between structure and rheological/thermal properties of agar. A mini-review on the effect of alkali treatment and the role of agaropectin, *Food Structure*, 13 (2017) 24-34.

[4] Laurienzo P., Marine Polysaccharides in Pharmaceutical Applications: An Overview. *Marine Drugs*, 8 (2010) 2435-2465.

[5] Araki C., Carbohydrates of Agar in Jikken Kagaku Koza, *Chemical Society of Japan*, 22 (1980) 468–87.

[6] Philips G.O., Williams P.A., Handbook of Hydrocolloids. In: Armisen R., Galatas F., (Eds). Agar. 2nd ed. Washington:Woodhead Publishing, (2009) 82-107.

[7] Nussinovitch A., Hydrocolloid Applications: Gum Technology in the Food and Other Industries. In: Nussinovitch A., (Eds). Agar. Boston :Springer, (1997) 1-18.

[8] Norziah M.H., Foo S.L., Karim A.A., Rheological Studies on Mixtures of Agar (Gracilaria changii) and κ-carrageenan, *Food Hydrocolloids*, 20 (2006) 204–217.

[9] Armisen R., World-wide Use and Importance of Gracilaria, *Journal of Applied Phycology*, 7 (1995) 231-243.

[10] Dai B., Matsukawa S., NMR Studies of the Gelation Mechanism and Molecular Dynamics in Agar Solutions, *Food Hydrocolloids*, 26 (2012) 181-186.

[11] Ghebremedhin M., Seiffert S., Vilgis T.A., Physics of agarose fluid gels: Rheological properties and microstructure, *Current Research in Food Science*, 4 (2021) 436-448.

[12] Zhang L., Che L., Zhou W., Chen X.D., Rheological Behavior of Agar Solution in Relation to the Making of Instant Edible Bird's Nest Products, *Int. J. Food Eng.,* 8(3) (2012) 1-20.

[13] Lahrech K., Safouane A., Peyrellasse J., Sol State Formation and Melting of Agar Gels Rheological Study, *Physica A: Statistical Mechanics and its Applications*, 355 (2005) 205-221.

[14] Zhang L., Xu J., Xue C., Gao X., Zhang D., Rheological properties and gel properties of agar, *Chinese Journal of Marine Drugs*, 28 (2009) 12-17.

[15] Tiwari S., Bhattacharya S., Aeration of Model Gels: Rheological Characteristics of Gellan and Agar Gels, *Journal of Food Engineering*, 107 (2011) 134-139.

[16] Karataş M., Arslan N., Flow behaviours of cellulose and carboxymethyl cellulose from grapefruit peel, *Food Hydrocolloids*, 58 (2016) 235-245.

[17] Hojjat M., Etemad S.Gh., Bagheri R., Thibault J., Rheological characteristics of non-Newtonian nanofluids: Experimental investigation, *International Communications in Heat and Mass Transfer,* 38 (2011) 144-148.

[18] Amaral T.N., Junqueira L.A., Prado M.E.T., Cirillo M.A., Abreu L.R., Costa F.F., Resende J.V., Blends of Pereskia aculeata Miller mucilage, guar gum, and gum Arabic added to fermented milk beverages, *Food Hydrocolloids*, 79 (2018) 331-342.

[19] Sarwar W., Ghafor K., Mohammed A., Modeling the rheological properties with shear stress limit and compressive strength of ordinary Portland cement modified with polymers, *Journal of Building Pathology and Rehabilitation*, 4 (2019) 25.

[20] Bhatti M.M., Ullah Khan S., Anwar Bég O., Kadir A., Differential transform solution for hall and ion-slip effects on radiative-convective Casson flow from a stretching sheet with convective heating, *Heat Transfer*, 49(2) (2020) 872-888.

[21] Rahimi R., Dehaghani A.S., An experimental study on the viscosity of SPAM solutions with a new correlation predicting the apparent viscosity of sulfonated polyacrylamides, *Petroleum*, 7(1) (2021) 64-69.

[22] Khaled B., Abdelbaki B., Rheological and electrokinetic properties of carboxymethylcellulose-water dispersions in the presence of salts, *Int. J. Phy. Sci*., 7 (2012) 1790-1798.

[23] Wei M., Lin K., Sun L., Shear thickening fluids and their applications, *Materials & Design*, 216 (2022) 110570.

[24] El-Hefian E.A., Yahaya A.H., Effects of temperature, shearing time and rate of shear on the viscosity of chitosan/agar-blend solutions, *Maejo Int. J. Sci. Technol*., 4(2) (2010) 261-267.

[25] Toğrul H., Arslan N., Mathematical model for prediction of apparent viscosity of molasses, *Journal of Food Engineering*, 62 (2004) 281-289.

Cumhuriyet Sci. J., 44(2) (2023) 289-295
DOI: https://doi.org/10.17776/csj.1210668

Cumhuriyet Science Journal

| csj.cumhuriyet.edu.tr | Founded: 2002 ISSN: 2587-2680 e-ISSN: 2587-246X Publisher: Sivas Cumhuriyet University

Synthesis and Characterization of Tetradentate Schiff Base Ligand Containing 3,4-Diamino Benzophenone and Investigation of Complex Formation with Ni (II), Cu (II) and Co (II) Metal Ions

Mustafa Bal [1,a,*]

[1] *Department of Materials Science and Engineering, Kahramanmaras Sutcu Imam University, Kahramanmaraş, 46100, Türkiye.*
**Corresponding author*

Research Article

History
Received: 27/11/2022
Accepted: 07/05/2023

ABSTRACT

Compound that is a novel tetradentate Schiff base ligand [(3,4-bis(((E)-4-(diethylamino)-2-hydroxybenzylidene)amino)phenyl)(phenyl) methanone] (1), 4-(diethylamino) It was synthesized by the reaction of (3,4-diaminophenyl)(phenyl)methanone with -2-hydroxybenzaldehyde. Complex reactions with Co(II) (1a), Cu(II) (1b) and Ni(II) (1c) metals were prepared based on the obtained Schiff base ligand. The synthesized Schiff base and its Ni(II), Cu(II) and Co(II) complexes were featured using FT-IR, UV-*vis*, photoluminescence, mass and ^{1}H and ^{13}C-NMR spectroscopy. The characterization processes show that the tetradentate Schiff base compound coordinates with metal ions, oxygen of the hydroxyl group and nitrogen of the azomethine group.

Keywords: Tetradentate Schiff base, Metal complex, Diaminobenzophenone.

[a] *mustafabal46@gmail.com* *https://orcid.org/0000-0003-2576-3947*

Introduction

The complex structures of Schiff base compounds with metals, obtained by the reaction of aromatic or aliphatic amines with substituted salicylaldehydes, represent a series of compounds that contain donor atoms such as nitrogen, sulfur and oxygen and have a wide study area [1–3]. Schiff base compounds, with intermolecular hydrogen bonding or proton transfer, are highly studied compounds in biochemistry [4]. Schiff bases and metal complexes have many applications in analytical, biological, pharmacology and industry [1,5]. Metal complexes synthesized from Schiff base compounds have an interesting side due to their antifungal, antibacterial and antitumor properties as well as their spectroscopic properties [6].

They coordinate with the transition metals O and N, which are involved in the biological activities required in living life. These structures play a very important role in life [7]. Schiff base compounds are accepted as the most important organic compound class because they have a wide range of studies in biological fields [7,8]. Extensive studies in this field of application have generated great interest in metal complexes derived from Schiff bases. Metal complexes obtained from Schiff bases are among the molecules with the most comprehensive study area due to their easy synthesis [9]. Some complexes of Schiff bases, which have applications in clinical and analytical fields, are molecules that model oxygen transport systems in biological activities [10]. It is known that complexes formed from tetradentate Schiff bases form stable complex structures with the N2O2 donor system [7,11]. Schiff base compounds induce substrate chirality, modulate metal-centered electronic events, and allow increased solubility and stability in homogeneous or heterogeneous catalysts [12].

The synthesis of aromatic Schiff bases has higher efficiency than aliphatic Schiff bases due to the partially stable strength of the imine bond given by the aryl groups attached to the N and C atoms. Metal complexes of imidazole-based aromatic Schiff bases have high performance in antimicrobial activity [11].

It is reported that metal complexes obtained from salen [bis(salicylidiene)ethylenediamine] compounds, which are a special type of Schiff bases, formed by the reaction of diamine-containing compound and aldehyde, are used as catalysts in most of the electrochemical reduction, molecular modification and reactions [13,14]. The best known of the salen compounds is bis(salicylaldehyde)ethylenediamine [15].

Salines have an acidic and tetradentate 2N, 2O) structure [16]. The application areas of metal complexes synthesized from salen compounds are quite wide. There are reactions in which they act as reactants and catalysts such as diels-Alder transformations, alkene epoxidation, electrochemical reduction, nucleic acid modification and hydroxyl addition [17,18].

Within the scope of this study, a new compound (1) of tetradentate Schiff bases, which is considered very valuable in terms of analytical and biological activity, was

synthesized. Complex compounds with Co(II) (1a), Cu(II) (1b) and Ni(II) (1c) metals were synthesized using the obtained tetradentate salen ligand. The structural characterization of ligand and complex compounds was carried out in accordance with the literature.

Materials and Methods

The chemicals used in the study were obtained from institutional companies (Aldrich or Merck) and were used directly without any processing. Schiff base ligand (1) and complex structures (1a,1b,1c) were prepared in accordance with the literature. No purification process was applied. The synthesized salen-type Schiff base ligand and the structure of the compounds obtained from the reaction of this ligand and metals were characterized using spectroscopic methods such as FT-IR, ^{1}H-NMR, and ^{13}C-NMR. Structural analysis of materials, FT-IR (ATR) measurements, Perkin Elmer Spectrum 400 Spectrophotometer, light absorption properties, Hitachi U3900h UV-*vis* spectrophotometer, emission properties HORIBA Jobin Yvon Triax 550 CCD, Photoluminescence Spectrophotometer, structure magnetic determination of molecule and ^{1}H-NMR, and ^{13}C-NMR (NMR) Bruker AVANCE III 400 Mhz NMR Spectrophotometer was used. Graded cups were used in sample preparation. 1 cm optical path quartz cuvette was used in the analysis.

Synthesis of Schiff Base Ligand

In the synthesis of the salen type Schiff base compound; 2.83 mmol of 4-(diethylamino)-2-hydroxybenzaldehyde was dissolved in methanol. It was stirred on a magnetic stirrer until the dissolution process was complete. 1.41 mmol (3,4-diaminophenyl) (phenyl)methanone was added to the prepared solution. The new mixture was refluxed for 48 hours. After the solvent was removed, the product was left to dry under room conditions (Fig. 1).

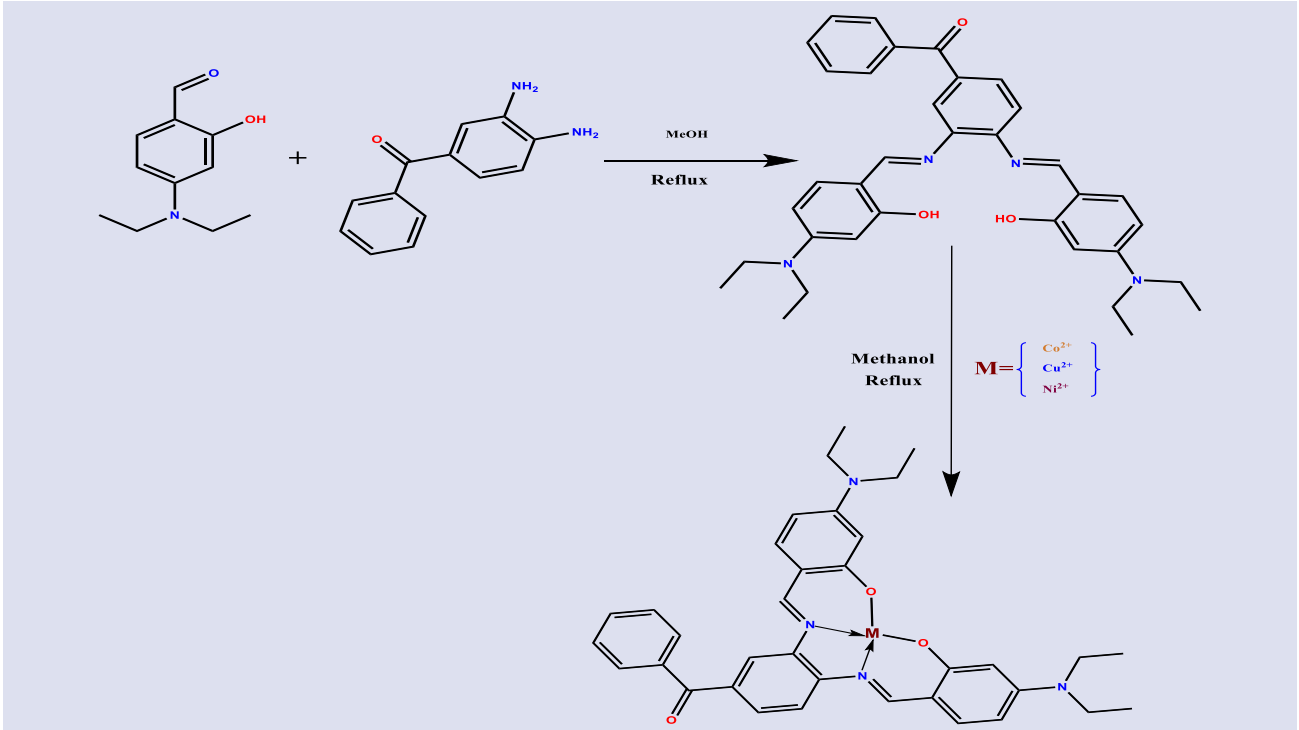

Figure 1 Synthesis of Schiff base ligand and metal complexes.

Synthesis of Metal Complexes

The complexation was performed by taking the salen type Schiff base ligand with the metal ion solution (1/1) ratio. The refluxing solutions of the ligand (0.53 mmol) in methanol (30 ml) were refluxed by adding $CoCl_2.6H_2O$ (0.53 mmol), $Cu(CH_3COO)_2$ (0.53 mmol) and $Ni(CH_3CO_2)_2{\cdot}4H_2O$ (0.53 mmol), respectively. The reaction solution was refluxed for 24 hours and then cooled to room temperature. The resulting product was filtered off and left to dry at room conditions (Fig. 1).

Data of the compounds synthesized within the scope of the work;

1: [(3,4-bis(((E)-4-(diethylamino)-2-hydroxybenzylidene)amino)phenyl)(phenyl)methanone], $C_{35}H_{38}N_4O_3$, Yield: 81%, Color: Dark red-viscous oil, Molecular Weight: 562.71, Mass spectrum (LC/MS, m/z): Calcd.: 562.29, found: 562.65 $[M]^+$. 562.29 (100.0%), Elemental Analysis (%):Calcd.: C, 74.71; N, 9.96; O, 8.53, found:C, 74.44; N, 9.67; O, 8.37

1a: $C_{35}H_{36}CoN_4O_3$, Yield: 88%, Melting point: 167 °C, Color: black powder, Molecular Weight: 619.63, Mass spectrum (LC/MS, m/z): Calcd.: 619.21, found: 619.27 $[M]^+$. 619.21 (100.0%), Elemental Analysis (%):Calcd.: C, 67.84; N, 9.04; O, 7.75, found:C, 67.57; N, 9.00; O, 7.44

1b: $C_{35}H_{36}CuN_4O_3$, Yield: 79%, Melting point: 205 °C, Color: brick color powder, Molecular Weight: 624.24, Mass spectrum (LC/MS, m/z): Calcd.: 623.21, found: 623.33 $[M]^+$. 623.21 (100.0%), Elemental Analysis (%):Calcd.: C, 67.34; N, 8.98; O, 7.69, found: C, 67.21; N, 8.38; O, 7.55

1c: Yield: $C_{35}H_{36}NiN_4O_3$, 84%, Melting point: 284 °C, Color: Bordeaux powder, Molecular Weight: 619.39, Mass spectrum (LC/MS, m/z): Calcd.: 618.21, found: 618.29 $[M]^+$. 618.21 (100.0%), Elemental Analysis (%):Calcd.: C, 67.87; N, 9.05; O, 7.75, found: C, 67.59; N, 9.01; O, 7.47

Results and Discussions

Within the scope of the study, firstly, the salen type Schiff base was synthesized. Complex structures were synthesized by reacting the obtained ligand with Co(II), Cu(II) and Ni(II) metals. Structural characterization of complexes synthesized from Salen-type Schiff base and its interaction with metals was performed by spectroscopic methods such as ^{1}H-NMR, ^{13}C-NMR, UV-*vis* and FT-IR analysis. In the results of the analyses performed, the spectroscopic data meet the expectations regarding the compounds and confirm the structures.

FT-IR Spectra of Schiff Base Ligand and Metal Complexes

When the FT-IR spectrum of the ligand is examined, the peak of the OH stretching vibration is around 3300 cm^{-1}, the peak of the azomethine (C=N) vibrations is at 1603 cm^{-1}, and the peak of the C=O stretching vibration is at 1645 cm^{-1}. As a result of the ligand binding with the metals, the peak of the OH stretching vibration disappeared. The peak belonging to the azomethine group is observed at 1611, 1610 and 1606 cm^{-1} for Co, Cu and Ni metals, respectively. The peak of C=O stretching vibrations is observed at 1637, 1649 and 1641 cm^{-1} for Co, Cu and Ni metals, respectively. In addition, weak peaks are observed in the range of 400-600 cm^{-1} because of the bonding of metal and O and N atoms. FT-IR data of ligand and complex structures are shown in Table 1.The disappearance of the absorbance peak of the OH group in the FT-IR spectrum of the ligand and the weak peaks in the range of 400-600 cm-1 after complexation with metals indicate that the targeted compounds were synthesized successfully.

Table 1 FT-IR data of ligand (1) and complex (1a, 1b, 1c) structures.

Compounds (cm^{-1})	*vC=O*	*vC=N*	*vC=C*	*vC-H Aliphatic*	*vO-H*	*vN-M*	*vO-M*
1	*1645*	*1603*	*1564*	*2971*	*3300-3500*	*-*	*-*
1a	*1637*	*1611*	*1557*	*2971*	*-*	*588*	*461*
1b	*1649*	*1610*	*1566*	*2968*	*-*	*586*	*457*
1c	*1641*	*1606*	*1557*	*2968*	*-*	*591*	*452*

The shifts in the spectrum of the azomethine group (-C=N) of the ligand at 1603 cm-1 show that the metal ions are bound through the (-C=N) group. FT-IR data of ligand and complex structures show that the metal is bound via phenolic oxygen and imino nitrogen. In addition, the FT-IR results of the study are consistent with the literature[19,20].

The FT-IR spectrum of the Schiff base ligand is given in Fig. 2 and the FT-IR spectra of the complex structures are given in (Fig. 3-5).

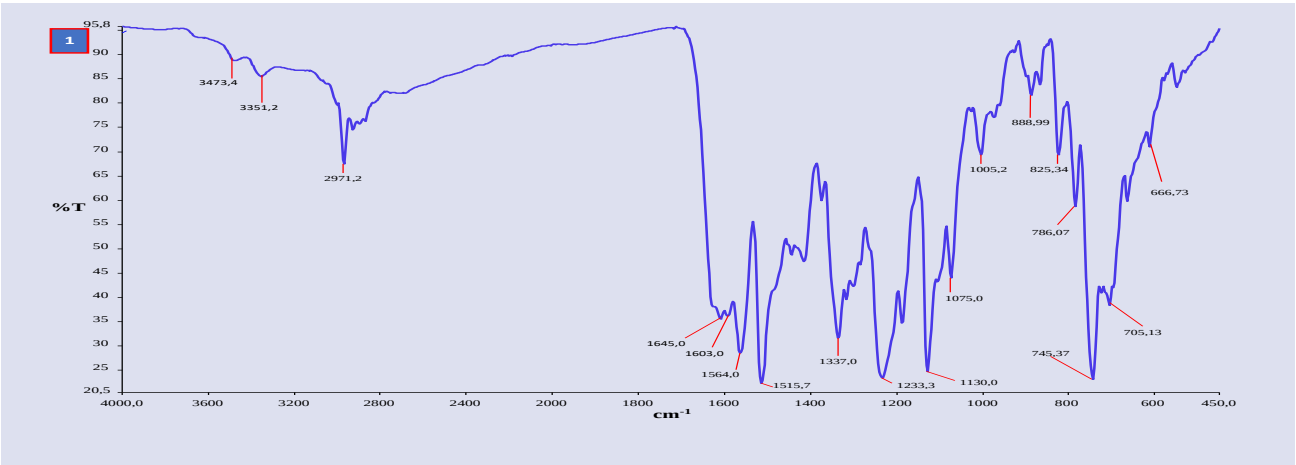

Figure 2 FT-IR spectrum of the Schiff base ligand.

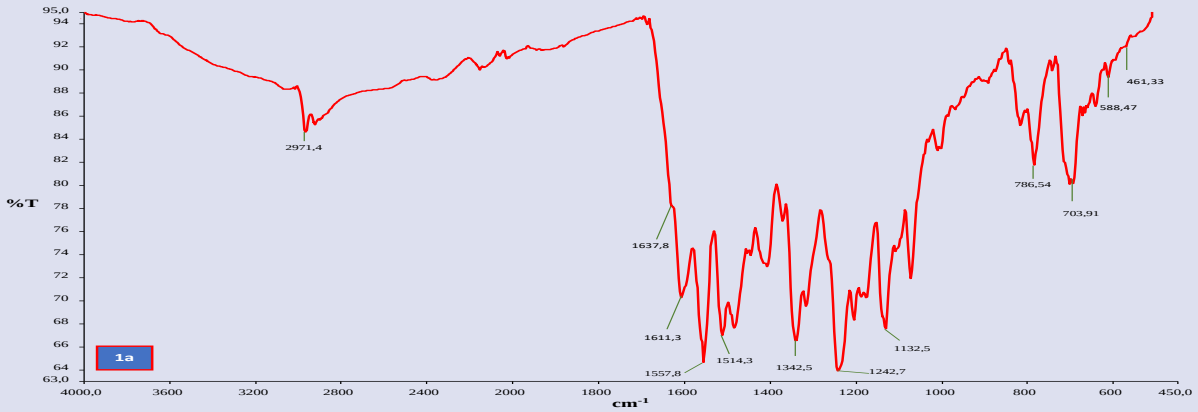

Figure 3 FTIR spectrum of the Co(II) - Ligand complex structure.

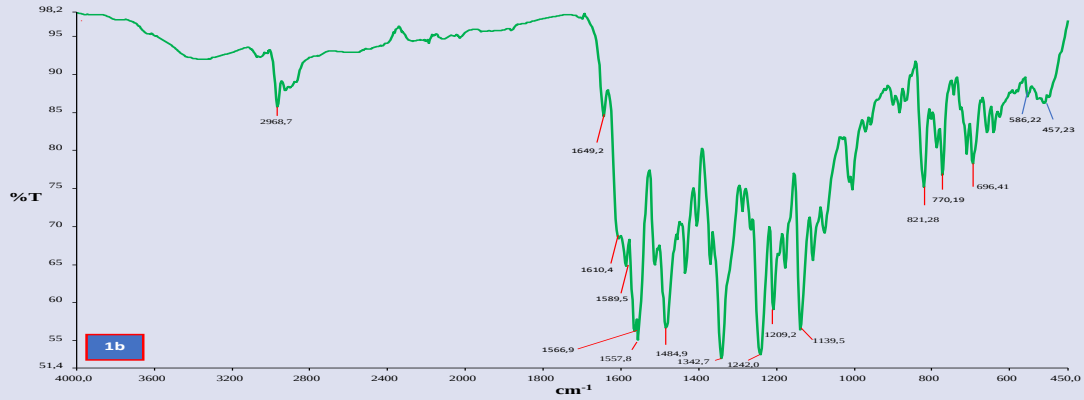

Figure 4 FTIR spectrum of the Cu(II) - Ligand complex structure.

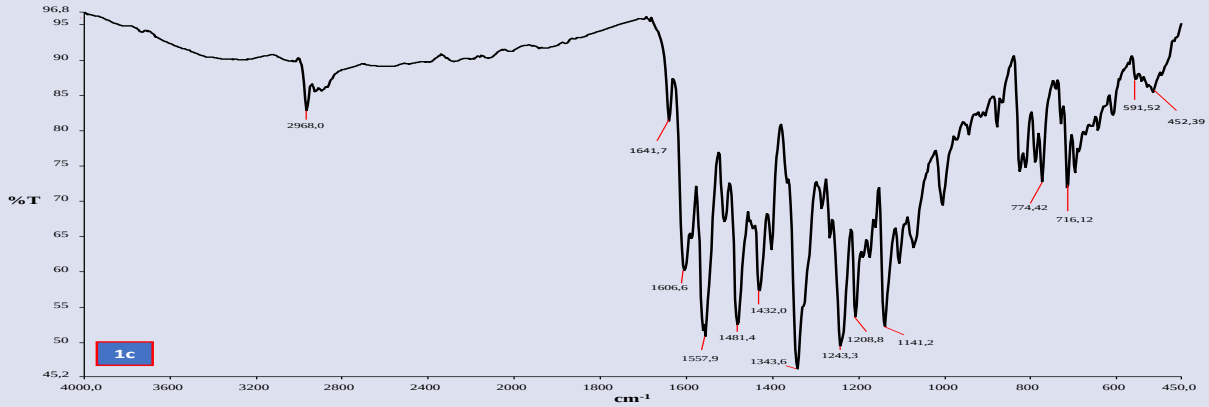

Figure 5 FTIR spectrum of the Ni(II) - Ligand complex structure.

^{1}H-NMR and ^{13}C-NMR Spectra of Compounds

When the ^{1}H-NMR [^{1}H NMR (400 MHz, $CDCl_3$) δ 11.70, 9.44, 8.40, 8.27, 7.80, 7.73, 7.59, 7.48, 7.28, 7.21, 7.01, 6.28, 6.22, 6.03, 5.94, 3.34, 3.24, 3.20, 1.13, 1.11, 1.05]; The signal observed in the range of δ1.05-1.13 ppm is the signal of protons belonging to the (-CH_3) group. The signal observed in the range of δ3.20-3.34 ppm is the signal of protons belonging to the (-CH_2-N-) group. The signal observed in the δ5.94-8.40 ppm range is the signal of the protons in the ring structures. The signal of the proton of the azomethine (-HC=N-) group is seen at δ9.44 ppm. Signals of protons belonging to the (-O-H) group attached to the aromatic ring are seen at δ11.70 ppm.

In the ^{13}C-NMR spectrum (^{13}C NMR (101 MHz, $CDCl_3$) δ 194.30, 162.00, 160.00, 153.30, 145.63, 139.91, 136.90, 134.77, 134.20, 131.50, 129.86, 127.72, 125.79, 112.73, 100.48, 47.76, 12.85); The signal for the "C" atoms of the end (-CH_3) group is seen at δ12.85 ppm. The signal of "C" atoms belonging to the (N-CH_2-) group is located at δ47.76 ppm. The signal seen in the range of δ100.48-153.30 ppm are the signal belonging to the "C" atoms in the ring structures. Signal at δ160.00 ppm is signal

belonging to the "C" atom of the azomethine (-HC=N-) group. Signal at δ162.00 ppm is signal belonging to the "C" atom of the (-C-OH) group. The signal at δ194.30 ppm is the signal for the "C" atom of the (-C=O) carbonyl group.

The signal of δ11.70 ppm protons of the OH group on the aromatic ring disappeared in the ^{1}H-NMR spectrum of the complex structure formed by the binding of the diamagnetic square plane structure Ni metal and the ligand. This indicates that the coupling (C-O-M) between the metal and the ligand has taken place. The data obtained within the scope of the study are similar to the data obtained from the " Tetradentate Schiff base ligands of 3,4-diaminobenzophenone: Synthesis, characterization and thermodynamics of complex formation with Ni(II), Cu(II) and Zn(II) metal ions" study of Asadi et al. in 2011[20].. In addition, the signal of the azomethine (-HC=N-) group proton at δ9.44 ppm is seen as a sharp singlet (δ9.05 ppm) after complexing with the metal. This indicates that in the presence of a planar ligand in the complex structure, binding occurs in a similar magnetic environment. Similarly, in the ^{13}C-NMR spectra, the signal of the "C" atom of the azomethine group at δ160.00 ppm was observed at δ163.67 ppm after complexation. The resulting shift indicates that the expected complexation has taken place.

UV-vis Spectra of Schiff Base Ligand and Metal Complexes

When the electron spectrum of the ligand is examined (Fig. 3), the intense band seen at λmax=345 nm can be attributed to molecular orbitals localized on the C=N group and π→π* transitions involving the benzene ring. The weak shoulder band seen around 400 nm can be attributed to the n→π* transition involving the C=N chromophore and the molecular orbitals of the benzene ring [20].

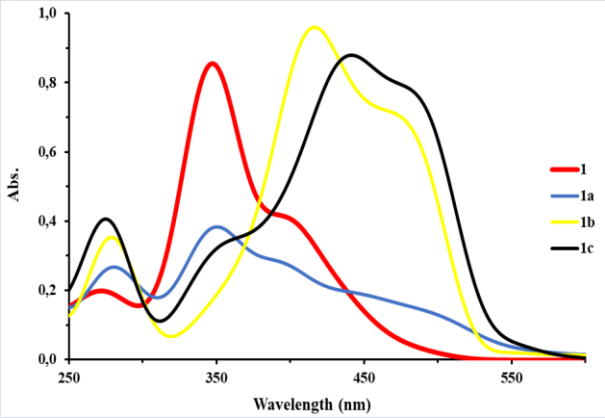

Figure 6 Uv-*vis* spectra of Schiff base ligand and metal complexes.

The absorbance bands of the ligand change when complexed with the metal (Fig. 3). As a result of the bonding of metal and nitrogen, the electron pair on the nitrogen stabilizes. In this case, the energy of the non-bonding orbital decreases and the transitions shifted to the longer wavelengths, or the absorbance band seen can be attributed to the π→π* transition, which includes the absorbance bands of the metal-ligand bond. Even at high concentration of complexes, d-d bands are hidden by a dense charge transfer band (Metal Ligand Charge Transfer) (Table 2).

Table 2 Ligand (1) ve kompleks (1a, 1b, 1c) yapıların elektronik spektral verileri.

Compounds	π→π* (C=N) (nm)	n→π* (nm)	π→π* (Metal-Ligand transition) (nm)
1	345	400	-
1a	350	-	465
1b	415	-	475
1c	440	-	480

Photoluminescence Spectra of Schiff Base Ligand and Metal Complexes

The ligand (1) showed a redshift with a 200 nm stokes shift value in response to the absorbance of π-π* transitions at 345 nm and gave emission at 545 nm. It showed a weak emission band at 740 nm with a stokes shift of 340 nm versus the absorbance at 400 nm of n-π* transitions. Photoluminescence spectra of Schiff base ligand and metal complexes are given in Fig. 4. Excitation and Emission spectra of Schiff base ligand and metal complexes are given in (Fig. 8-11).

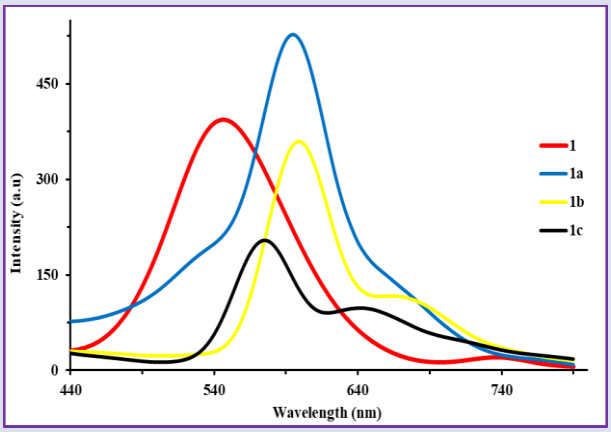

Figure 7 Photoluminescence spectra of Schiff base ligand and metal complexes.

The absorbance of the complex structures formed by the ligand with Co (1a), Cu (1b) and Ni (1c) metals at 350, 415, 440 nm of π-π* transitions, respectively, is 595, 600 with a stokes shift of 245, 185, 135 nm, respectively. showed a redshift tendency with the emission bands it showed at 675 nm. Similarly, the metal-ligand π-π* transitions exhibited a redshift by showing emission bands at 675, 685, 650 nm with a stokes shift of 210, 210, 170 nm versus absorbances at 465, 475, 480 nm. Absorption, photoluminescence and Stokes shift data of ligand and complex structures are given in Table 3.

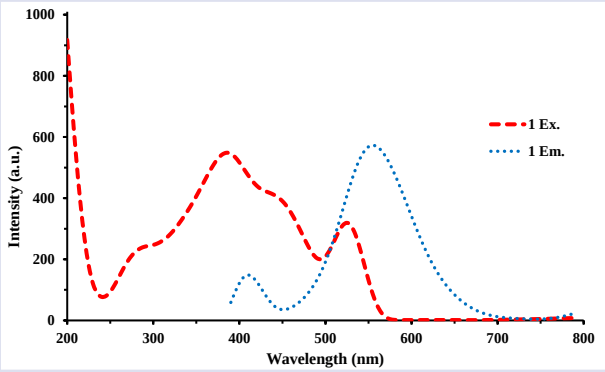

Figure 8 Excitation and Emission spectrum of Schiff base ligand

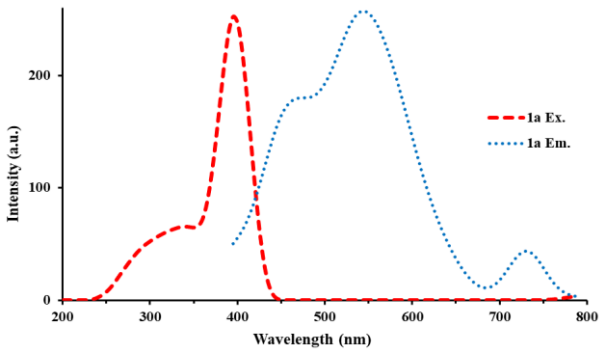

Figure 9 Excitation and Emission spectrum of the Co(II) - Ligand complex structure.

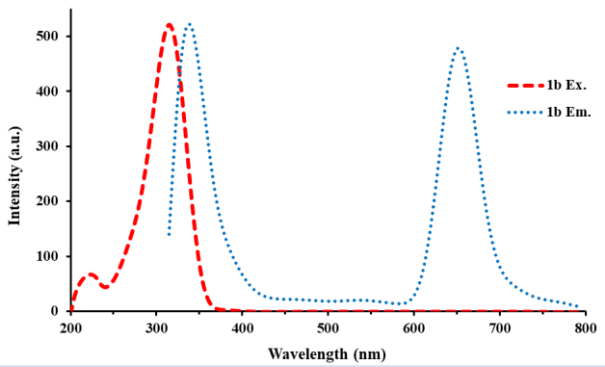

Figure 10 Excitation and Emission spectrum of the Cu(II) - Ligand complex structure.

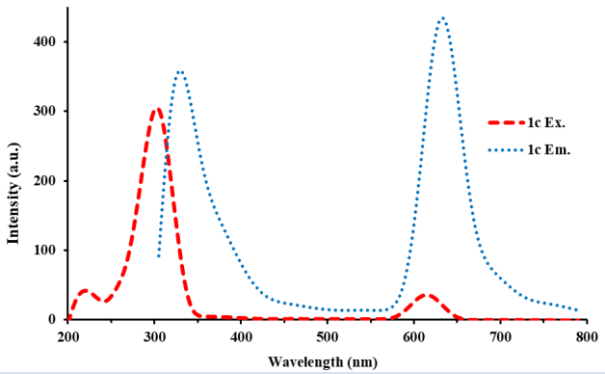

Figure 11 Excitation and Emission spectrum of the Ni(II) - Ligand complex structure.

Table 3 Absorption, photoluminescence, and Stokes shift data of ligand (1) and complex (1a, 1b, 1c) structures.

Compounds	λmax, nm		
	Absorption	Emission	Stokes shifts
1	345, 400	545, 740	200, 340
1a	350, 465	595, 675	245, 210
1b	415, 475	600, 685	185, 210
1c	440, 480	575, 650	135, 170

Conclusions

Elemental analyzes of the complexes obtained as a result of the reaction of Salen type Schiff base ligand and the reaction of this ligand with Co(II), Ni(II) and Cu(II) metals were made by FT-IR, ^{1}H, ^{13}C NMR, UV-*vis* methods. The OH Group peak at 3300-3500 cm^{-1} in the FT-IR spectrum of the Schiff base ligand was not seen in the FT-IR spectra of the complex structure consisting of metal-ligand interaction formation. This indicates that the associations between ligand and metal are lost due to chelation. From the FT-IR spectra, it was concluded that the ligand (**1**) coordinates to the metals via two azomethines N, and the Schiff base with the N2O2 region acts as a tetradentate ligand, with two phenolic OHs bonding to the metal leaving its proton. Absorption bands seen around 450 nm in the UV-*vis* spectrum of complex structures belong to the metal-ligand charge transition. This shows that the salen type Schiff base ligand and metal ions interact, and targeted complex structures are formed.

Conflicts of interest

There are no conflicts of interest in this work.

References

[1] Ejidike, I.P., Ajibade, P.A., Synthesis, characterization and biological studies of metal(II) complexes of (3E)-3-[(2-{(E)-[1-(2,4-Dihydroxyphenyl) ethylidene]amino}ethyl)imino]-1-phenylbutan-1-one schiff base, *Molecules*, 20 (6) (2015) 9788–9802.

[2] Ramesh, R., Suganthy, P.K., and Natarajan, K. Synthesis, spectra and electrochemistry of Ru(III) complexes with tetradentate schiff bases, *Synthesis and Reactivity in Inorganic and Metal-Organic Chemistry*, 26 (1) (1996) 47–60.

[3] Neelakantan M.A., Marriappan S.S., Dharmaraja J., Jeyakumar T., Muthukumaran K., Spectral, XRD, SEM and biological activities of transition metal complexes of polydentate ligands containing thiazole moiety, *Spectrochimica Acta - Part A: Molecular and Biomolecular Spectroscopy*, 71(2) (2008) 628–635.

[4] Joseyphus R.S., Nair M.S., Antibacterial and Antifungal Studies on Some Schiff Base Complexes of Zinc(II), *Mycobiology*, 36 (2) (2008) 93.

[5] Kumar, S., Dhar, D.N., and Saxena, P.N. Applications of metal complexes of Schiff bases-A review. *Journal of Scientific and Industrial Research*. 68 (3), (2009) 181–187.

[6] Tümer M., Köksal H., Serin S.,Digrak M., Antimicrobial activity studies of mononuclear and binuclear mixed-

ligand copper(II) complexes derived from Schiff base ligands and 1,10-phenanthroline, *Transition Metal Chemistry*, 24 (1), (1999) 13–17.

[7] Ammar, R.A.A. and Alaghaz, A.N.M.A. Synthesis, spectroscopic characterization and potentiometric studies of a tetradentate [N_2O_2] schiff base, N,N'-bis(2-hydroxybenzylidene)-1,1-diaminoethane and its Co(II),Ni(II),Cu(II) and Zn(II) complexes, *International Journal of Electrochemical Science*, 8(6) (2013) 8686–8699.

[8] de Fátima, Â., Pereira, C. de P., Olímpio, C.R.S.D.G., de Freitas Oliveira, B.G., Franco, L.L., and da Silva, P.H.C. Schiff bases and their metal complexes as urease inhibitors – A brief review, *Journal of Advanced Research,* 13, (2018) 113–126.

[9] More M.S., Joshi P.G., Mishra Y.K., , Khanna P.K., Metal complexes driven from Schiff bases and semicarbazones for biomedical and allied applications: a review, *Materials Today Chemistry*, 14 (2019) 100-195.

[10] I. Khan M., Gul S., Ali Khan, M. Schiff Bases, Their Metallic Derivatives: Highly Versatile Molecules with Biological and Abiological Perspective, *Stability and Applications of Coordination Compounds,* (2020) 1–15.

[11] Demir S., Güder A., Yazicilar T.K., Caglar S., Büyükgüngör O., Syntheses, crystallographic, mass-spectroscopic determination and antioxidant studies of Co(II), Ni(II) and Cu(II) complexes of a new imidazol based Schiff base, *Spectrochimica Acta - Part A: Molecular and Biomolecular Spectroscopy,* 150 (2015) 821–828.

[12] Romanowski G., Lis T., Chiral oxidovanadium(V) complexes with tridentate Schiff bases derived from S(+)-2-amino-1-propanol: Synthesis, structure, characterization and catalytic activity, *Inorganica Chimica Acta*., 394 (2013) 627–634.

[13] Khandar A.A., Shaabani B., Belaj F., Bakhtiari A., Synthesis, characterization and spectroscopic and electrochemical studies of new axially coordinated cobalt(III) salen (salen = N,N'-bis(salicylidene)-1,2-ethylenediamine) complexes. The crystal structure of [CoIII(salen)(aniline)2]ClO4, *Polyhedron,* 25(9) (2006) 1893–1900.

[14] Sunday Nworie, F. Bis(Salicylidene)Ethylenediamine(Salen) and Bis(Salicylidene)Ethylenediamine-Metal Complexes: from Structure to Biological Activity, *Journal of Analytical & Pharmaceutical Research,* 3(6) (2016) 1–9.

[15] Witt, K., Bożejewicz, D., and Kaczorowska, M.A. N,N'-bis(Salicylidene)ethylenediamine (salen) as an active compound for the recovery of Ni(II), Cu(II), and Zn(II) ions from aqueous solutions. *Membranes,* 10(4) (2020) 1–15.

[16] Tsantis, S.T., Tzimopoulos, D.I., Holyńska, M., and Perlepes, S.P. Oligonuclear actinoid complexes with schiff bases as ligands—older achievements and recent progress. (2020).

[17] DiMauro, E.F., Mamai, A., and Kozlowski, M.C. Synthesis, characterization, and metal complexes of a salen ligand containing a quinoline base. *Organometallics,* 22(4) (2003) 850–855.

[18] Tobal, I.E., Bautista, R., Diez, D., Garrido, N.M., and García-García, P. 1,3-cyclohexadien-1-als: Synthesis, reactivity and bioactivities, *Molecules*, 26 (6) (2021).

[19] Asadi, M. and Khah, M.S. Some new unsymmetrical diimino tetradentate schiff base derived from 3,4-diaminobenzophenone: Synthesis, characterization and the formation constant of Ni(II) and Cu(II) complexes, *Journal of the Iranian Chemical Society*, 7(4) (2010) 875–882.

Cumhuriyet Sci. J., 44(2) (2023) 296-301
DOI: https://doi.org/10.17776/csj.1252908

Cumhuriyet Science Journal

| csj.cumhuriyet.edu.tr | Founded: 2002 ISSN: 2587-2680 e-ISSN: 2587-246X Publisher: Sivas Cumhuriyet University

Chemical Reactivities and Organic Light-emitting Diode Properties of some Polyaromatic Molecules

Mustafa Elik [1,a,*]

[1] *Department of Mathematics and Science Education, Faculty of Education, Sivas Cumhuriyet University, Sivas, Türkiye*
**Corresponding author*

Research Article

History
Received: 18/02/2023
Accepted: 09/06/2023

ABSTRACT

High-performance organic-light emitting diode (OLED) display panels have been very popular lately due to their many advantages compared to liquid-crystal display (LCD) and light-emitting diode (LED) panels. It is also well known that the materials used in OLED panels are important in determining OLED performance. Starting with the selection of materials which have rich π-electrons will be a good start for the design of high-performance OLED materials. For this aim, the OLED properties of some cyclic aromatic structures with rich π-electrons such as 2,2'-bi-1,6-naphthyridine (BNP), 1,6-bis(4'-pyridine)-2,5-diazahexane (BPDH), 3,3'-bis[3-(2-pyridyl)pyrazol-1-yl]biphenyl (BPPB), 5,5'-dicyano-2,2'-bipyridine (DCBP), 2,2'-dimethyl-4,4'-bipyrimidine (DMBP), and 4'-phenyl-2,2':6'2"terpyridine (Ph-TERPY) were theoretically analyzed using computational chemistry tools. The calculations of monomeric and dimeric structures of mentioned molecules were carried out at B3LYP/6-31G(d) and B3LYP/TZP levels, respectively. The OLED properties of the investigated compound were explained by means of OLED parameters such as the reorganization energies, adiabatic-vertical ionization potentials and adiabatic-vertical electron affinities, the effective transfer integrals, and the charge transfer ratios. In the light of computational chemistry, it is indicated that these studied molecules will be utilized in which layers of OLED device. In addition to OLED analysis, in the light of the calculated reactivity descriptors, the chemical reactivities of the studied molecules were discussed.

Keywords: Compounds with rich π-electrons, Reorganization energies, Marcus theory, Charge transfer rate.

[a] *melik@cumhuriyet.edu.tr* *https://orcid.org/ 0000-0001-8245-4273*

Introduction

Computational chemistry has become very popular in molecular design in recent years[1-3]. With computational chemistry tools, theoretical chemists develop new and helpful rules and theories for explaining the properties of molecules[4, 5]. Nano-structures such as organic light-emitting diodes (OLEDs), organic field-effect transistors (OFET), organic-based photovoltaic (OPV) cells can be designed with these developed theories and theories[6, 7]. Among these nanostructures, scientists have concentrated on OLEDs, as they are superior in many respects to their successors, liquid-crystal display (LCD) and light-emitting diode (LED)[8-11]. In addition, in studies on OLED design, OLED design with high performance comes to the fore[12, 13]. In order to produce high performance OLED, the materials in the OLED layer, which consists of many layers, such as the electron injection layer (EIL), the electron transfer layer (ETL), the hole blocking layer (HBL), the emission layer (EL), the electron blocking layer (EBL), the hole transfer layer (HTL), the hole injection layer (HIL) sandwiched between anode and cathode electrodes, should be carefully selected[14-16]. Previous studies have shown that aromatic or π-electron-rich compounds are suitable for high-performance OLED devices[17-19]. For that reason, the organic compounds with aromatic rings or rich π- electrons in given their structures in Scheme 1 is preferred. The OLED performance of the studied molecules is predicted by means of OLED descriptors such as the reorganization energies, adiabatic-vertical ionization energies and adiabatic-vertical electron affinities, the effective transfer integrals, and the charge transfer rates using different computational chemistry tools[20-23].

The propose of this paper is to examine the OLED properties of the multiple aromatic compounds. In the light of the theoretically obtained results, the best OLED material among the structures examined will be determined. Via the popular Conceptual Density Functional Theoretical parameters like hardness, polarizability and electrophilicity, the chemical reactivities of the molecules will be discussed.

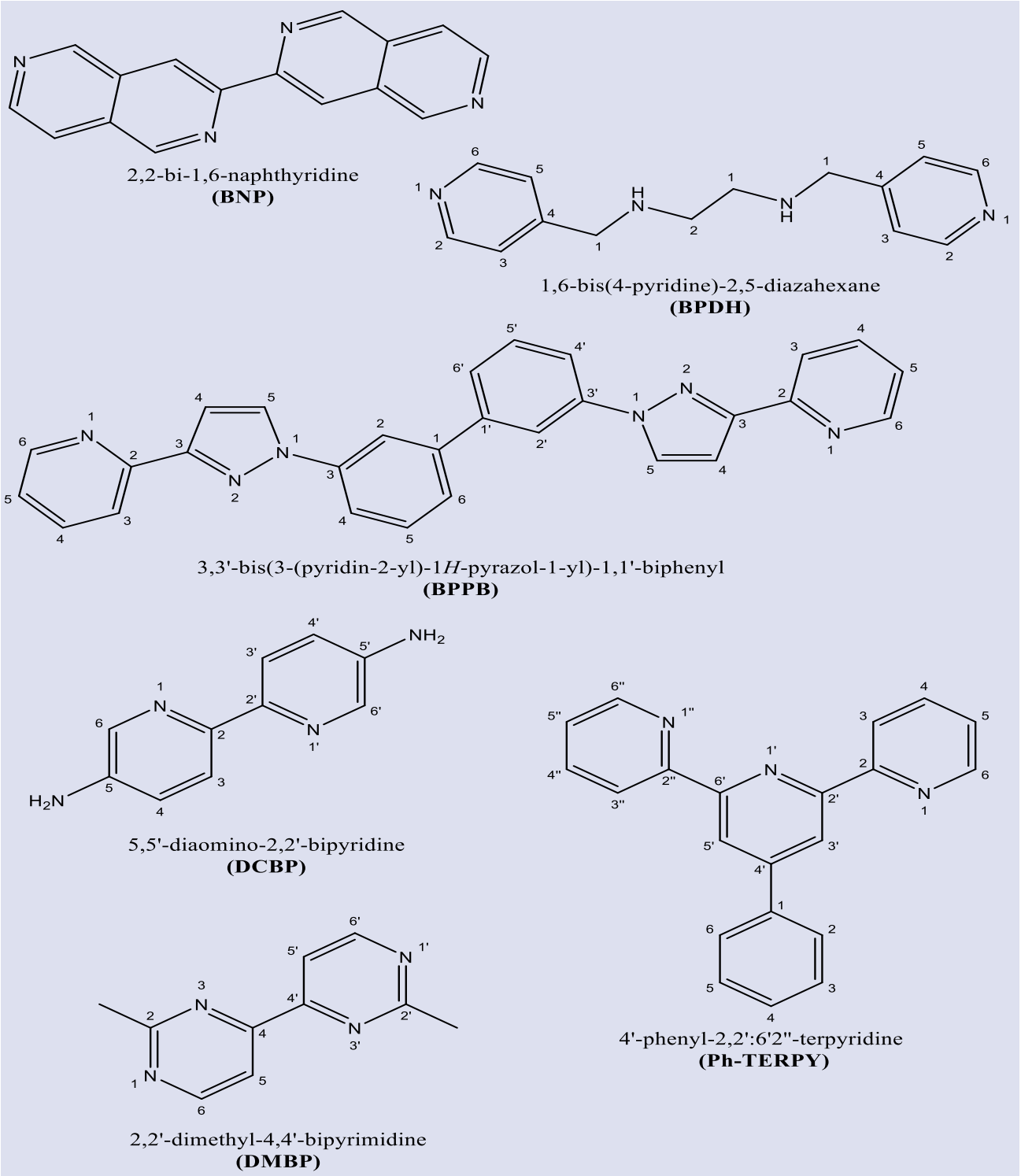

Scheme 1. The structures of the examined compounds.

Methods

In all calculations we used Gaussian 16 and GaussView 6 software[24, 25]. In the calculations regrading to the dimeric forms of the studied molecules, Amsterdam Density Functional (ADF) 2019 program was used[26]. It is seen from the published literature that hybrid B3LYP functional is widely considered to explain the charge transfer properties of the materials[27, 28]. Here, we also used same functional to get reliable results. In the computations about the monomeric and dimeric forms of the systems studied, B3LYP/631G(d) and B3LYP/TZP levels were taken into consideration, respectively. For the calculation of electronic hopping rate (K), the following formula derived by Marcus and Hush is used[29-31].

$$K = \frac{V^2}{\hbar}\left(\frac{\pi}{\lambda k_B T}\right)^{1/2} \exp\left(-\frac{\lambda}{4k_B T}\right) \quad (1)$$

In the given formula, V stands for the effective (generalized) transfer integral. λ means the reorganization energy, k_B is the Boltzmann constant. ħ and T determine reduced Planck's constant and the absolute temperature taken as 298.15 K in such computations. Additionally, the reorganization energies (λ) can be divided into two classes as external reorganization energy (λ_{ext}) and internal reorganization energy (λ_{int}). In this paper, in the analysis of OLED performances of studied compounds, it was focused on only λ_{int} because λ_{ext} values have been ignored in previous studies. The λ_{int} which are electron reorganization energy (λ_e) and hole reorganization energy (λ_h) were calculated by means of the following equations.

$$\lambda_e = (E_0^- - E_-^-) + (E_-^0 - E_0^0) \quad (2)$$

$$\lambda_h = (E_0^+ - E_+^+) + (E_+^0 - E_0^0) \quad (3)$$

To calculate the adiabatic-vertical ionization energies and adiabatic-vertical electron affinities of studied aromatic structures, the following equations can be used.

$$IPa = E_+^+ - E_0^0 \quad (4)$$

$$IPv = E_0^+ - E_0^0 \quad (5)$$

$$EAa = E_0^0 - E_-^- \quad (6)$$

$$EAv = E_0^0 - E_0^- \quad (7)$$

In the equations given above, where $E_0^-(E_0^+)$ stands for energy of the anion (cation) obtained from the neutral structures of the molecules examined. In the same way, $E_-^-(E_+^+)$ determines the energy of the anionic (cationic) structures obtained with the optimized anionic (cationic) forms, $E_-^0(E_+^0)$ refers to the energy of the neutral molecule computed at the anion (cationic) structures. Finally, E_0^0 shows the energy of the neutral form of structures at the ground state.

Conceptual Density Functional Theory (CDFT)[32] presents the following mathematical relations for the calculation of the chemical potential (μ), electronegativity (χ) and hardness (η). E and N appearing in the given relations are total electronic energy and total number of the electrons, respectively

$$\mu = -\chi = \left[\frac{\partial E}{\partial N}\right]_{v(r)} \quad (8)$$

$$\eta = \frac{1}{2}\left[\frac{\partial^2 E}{\partial N^2}\right]_{v(r)} \quad (9)$$

Based on the finite differences approach, Parr and Pearson derived the following formulae based on ground state ionization energy (I) and electron affinity (A) of chemical species.

$$\chi = \frac{I + A}{2} \quad (10)$$

$$\eta = \frac{I - A}{2} \quad (11)$$

Another important parameter of the chemical reactivity studies is electrophilicity index (ω) introduced by Parr, Szentpaly and Liu. This index is mathematically calculated as:

$$\omega = \chi^2 / 2\eta \quad (12)$$

For the calculation of electrodonating power (ω^-) and electroaccepting power (ω^+) of the molecular systems. Gazquez and coworkers derived the following equations.

$$\omega^+ = (I + 3A)^2 / (16(I - A)) \quad (13)$$

$$\omega^- = (3I + A)^2 / (16(I - A)) \quad (14)$$

Results and Discussion

To predict the chemical reactivity of any chemical systems, theoretical and computational chemists use widely well-known quantum chemical descriptors like hardness, electrophilicity and polarizability[33]. Electronic structure rules regarding these descriptors present the relation with chemical stability of the corresponding descriptor. The most popular parameter of the chemical reactivity analysis is the chemical hardness of Prof Pearson[34]. Hard molecules exhibit high resistance against electron cloud polarization. For that reason, the absolute hardness is reported as the resistance against the polarization of atoms, ions and molecules as given many papers penned by Kaya[35, 36]. The electronic structure rule emphasizing the powerful link between chemical stability and absolute hardness is Maximum Hardness Principle. According to this principle, a chemical system tends to reach maximum hardness and the hardness is a measure of stability". Looking to the inverse relation highlighted by Ghanty and Ghosh[37] between hardness and polarizability, Chattaraj and Sengupta[38] noted that "in stable states, polarizability should be minimized unlike the chemical hardness.

Another electronic structure rule introduced by Chattaraj and coworkers is Minimum Electrophilicity Principle. This principle also implies the minimization in stable states or forms of the electrophilicity index. The validity and limitations of Minimum Electrophilicity Principle[38] have been thoroughly examined by Szentpaly and Kaya[39]. In Fig. 1, The optimized structures of the monomeric forms of the investigated compounds at B3LYP/6-31G(d) level are given. Fig. 2 visually presents the optimized structures of the dimeric forms of the studied molecules at B3LYP/TZP level. Table 1 includes the calculated quantum chemical parameters reflecting the chemical reactivity ad stability of the studied molecules. According the calculated chemical hardness values, the hardest chemical system is BPDH. One can say that BPDH is the most stable molecule among the studied chemical systems. It is clear that polarizability of this molecule is also relatively low. It can be said that our results are in good agreement with Minimum Electrophilicity Principle because the hardest molecule has the lowest electrophilicity index value as can be seen in the related table. Electron transfer ability of BPDH compound is lower than that of others because its hard character.

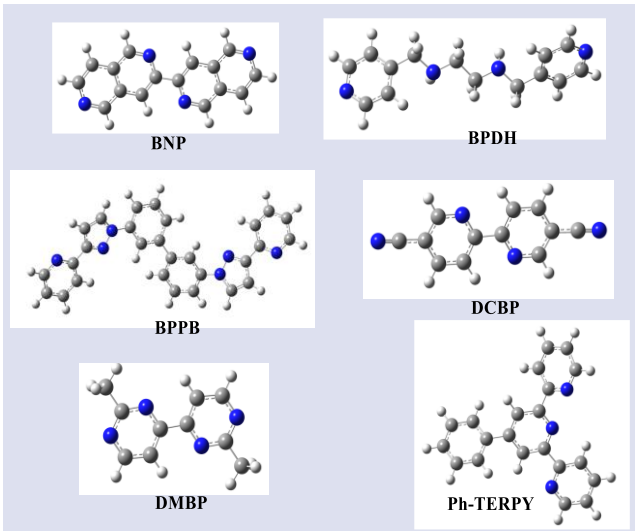

Figure 1. The optimized structures of the investigated monomer compounds at B3LYP/6-31G(d) level.

Marcus theory[40] is widely preferred to explain the charge transfer properties of molecules. As can be seen from the equation related to the mentioned theory that charge transfer ratio is closely related to the reorganization energy and the effective transfer integral. One can report that charge transfer ratio increases with increasing effective transfer integral while low reorganization energy values correspond to higher charge transfer ratios. The molecule having larger values of λe and λh act as electron blocking material and hole blocking material, respectively. It should be noted that DMBP is an electron blocking material while BPDH acts as a hole blocking material. In Table 2, the calculated reorganization energies, adiabatic-vertical ionization potentials, and adiabatic-vertical electron affinities are presented.

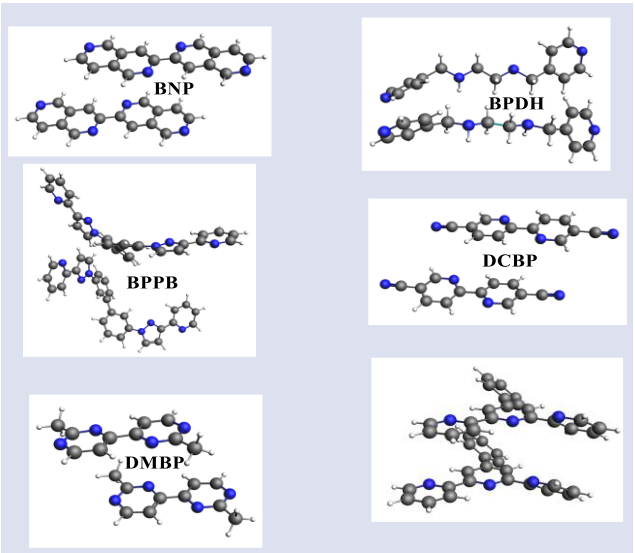

Figure 2. The optimized structures of the studied dimeric molecules at B3LYP/TZP level.

Table 1. The calculated quantum chemical descriptors (in eV) for studied molecules at B3LYP/6-31G(d) level

Compound	η	χ	ω	ω^+	ω^-	α (a.u)
BNP	2.06	4.04	3.95	2.19	6.22	214.74
BPDH	2.87	3.49	2.12	0.73	4.22	166.37
BPPB	2.33	3.52	2.66	1.19	4.71	364.69
DCBP	2.20	5.07	5.85	3.59	8.66	162.07
DMBP	2.38	4.48	4.22	2.28	6.76	128.04
Ph_TERPY	2.40	3.77	2.96	1.38	5.15	250.04

Table 2. The obtained reorganization energy, adiabatic-vertical ionization energy, and electron affinity values (all in eV) of molecules investigated at B3LYP/6-31G(d) level in vacuum.

Molecule	λe	λh	IPa	IPv	EAa	EAv
BNP	0.209	0.186	7.45	7.54	0.65	0.55
BPDH	0.357	1.386	7.24	7.92	-0.54	-0.73
BPPB	0.161	0.136	6.87	6.94	0.19	0.11
DCBP	0.355	0.204	8.74	8.84	1.47	1.29
DMBP	0.496	0.495	8.46	8.65	0.60	0.35
Ph_TERPY	0.351	0.245	7.45	7.58	0.20	0.02

It is seen previously published papers that for Alq3 complex used as reference electron transfer material λe is 0.276 eV. The compounds with lower λe value than that of Alq3 complex can be used as effective electron transfer material. If so, it can be seen from the Table 2 that BNP and BPPB molecules can act effective electron transfer material compared to others. The best one is BPPB molecule. TPD is one of the hole transfer materials used as reference in the literature. For this compound, determined λh is 0.290 eV. The molecule with lower λh values than 0.290 eV is effective hole transfer materials. Calculated hole reorganization energy values imply that BNP, BPPB, DCBP and Ph_TERPY molecules can act effective hole transfer material candidates for future

experimental studies. The best hole transfer material among them is BPPB. If so BPPB is both electron transfer material and hole transfer material. Such materials are called as ambipolar material. Ionization energy and electron affinity parameters provide important hints about electron-donating and electron-accepting capabilities of molecules. It is well-known that the materials with small ionization energy and high electron affinity values act as hole and electron transport materials, respectively. From this explanation, it is easy to predict that the best hole injection material and the best electron injection material are BPPB and DCBP compounds, respectively.

Table 3. The computed electron and hole transfer integrals[a] (in eV) and the charge transfer ratios (s^{-1}) of compounds studied in the gas phase.

Molecule	V_e	V_h	K_e	K_h
BNP	-0.03195	0.02448	$4.91x10^{12}$	$3.82x10^{12}$
BPDH	-0.00131	-0.00316	$1.50x10^{5}$	$1.98x10^{5}$
BPPB	0.00168	0.00015	$2.47x10^{10}$	$2.73x10^{8}$
DCBP	-0.01784	-0.02351	$2.84x10^{11}$	$2.82x10^{12}$
DMBP	0.00502	0.00007	$4.82x10^{9}$	$9.47x10^{5}$
Ph_TERPY	-0.04182	0.01404	$1.63x10^{12}$	$1.17x10^{11}$

[a]Transfer integrals were calculated at 298.15 K. For calculation of charge transfer rates, Boltzmann constant is $8.6173x10^{-5}$ eV

Table 3 shows the computed electron-hole transfer integrals and the charge transfer ratios of studied molecular systems. As the absolute value, the highest electron transfer integral value was obtained for Ph_TERPY although the highest hole transfer integral belongs to BNP molecule. Additionally, the optimized structures of the studied dimeric molecules are obtained at B3LYP/TZP level and they are presented in Fig. 2. Using optimized dimeric geometries, the electron and hole charge transfer integrals of the studied molecules are achieved at B3LYP/TZP level. Moreover, the charge transfer rates are calculated using the Marcus equation. From the obtained results, it can be said that the highest K_e and K_h values are obtained for BNP as presented in Table 2.

Conclusion

In this paper, firstly, we investigated the chemical reactivities of (BNP), (BPDH), (BPPB), (DCBP), (DMBP), and (Ph-TERPY) compounds using popular electronic structure rules. With the help of Maximum Hardness and Minimum Electrophilicity Principles, it was noted that the most stable compound between studied chemical systems is BPDH. From the calculations regarding to monomeric and dimeric forms, OLED performances of the studied molecules were predicted. The best candidates as electron transfer, electron injection, electron blocking, hole transfer, hole injection and hole blocking materials were determined. Based on the comparisons made with reference materials in the literature, this computational work will shed light on future experimental studies including the design of new OLED structures.

Acknowledgements

The numerical calculations reported in this paper were partially caried out at TUBITAK ULAKBIM, High Performance and Grid Computing Center (TRUBA resources).

Conflicts of interest

The authors declare that they have no conflict of interest.

References

[1] [Tendongmo H., et al., Theoretical Study of the Structural, Optoelectronic, and Reactivity Properties of N-[5 '-Methyl-3 '-Isoxasolyl]-N-[(E)-1-(-2-)]Methylidene] Amine and Some of Its Fe2+, Co2+, Ni2+, Cu2+, and Zn2+ Complexes for OLED and OFET Applications, *Journal of Chemistry*, (2022).

[2] Lougdali M., et al., Photoluminescence and nonlinear optical properties of Nickel bis-(8-hydroxyquinoline) thin film, *Materials Chemistry and Physics*, (2022) 284.

[3] Hebbali, R., Mekelleche S.M., Zaitri L.K., Computational study of optoelectronic properties of oxadiazole-based compounds for organic light emitting diodes, *Molecular Physics*, 120(14) (2022).

[4] Youssef A.A., et al., Designing Donor-Acceptor thienopyrazine derivatives for more efficient organic photovoltaic solar cell: A DFT study, *Physica B-Condensed Matter*, 560 (2019) 111-125.

[5] Omidyan R., Abbasi M. and Azimi G., Photophysical and optoelectronic properties of a platinum(II) complex and its derivatives, designed as a highly efficient OLED emitter: A theoretical study, International *Journal of Quantum Chemistry*, 119(3) (2019).

[6] Qin X., Dong H.L., and Hu W.P., Phthalocyanine-based organic semiconductors catalyzed C-H activation for heteroarenes functional materials in the sunlight, *Chinese Science Bulletin-Chinese.*, 65(5) (2020) 417-424.

[7] Ho P.Y., et al., Synthesis and characterization of a semiconducting and solution-processable ruthenium-based polymetallayne, *Polymer Chemistry*, 11(2) (2020) 472-479.

[8] Ochsenbein S.T., et al., Engineering Color-Stable Blue Light-Emitting Diodes with Lead Halide Perovskite Nanocrystals, *Acs Applied Materials & Interfaces.*, 11(24) (2019) 21655-21660.

[9] He Z.F., et al., High-Efficiency Red Light-Emitting Diodes Based on Multiple Quantum Wells of Phenylbutylammonium-Cesium Lead Iodide Perovskites, *Acs Photonics.*, 6(3) (2019) 587-594.

[10] Chauhan A.K., et al., Organic Devices: Fabrication, Applications and Challenge, *Journal of Electronic Materials*, 51(2) (2022) 447-485.

[11] Park J.W., Shin D.C., and Park S.H., Large-area OLED lightings and their applications, *Semiconductor Science and Technology*, 26(3) (2011).
[12] Liu N., et al., Effects of Charge Transport Materials on Blue Fluorescent Organic Light-Emitting Diodes with a Host-Dopant System, *Micromachines*, 10(5) (2019).
[13] Predeep P., et al., Organic Light Emitting Diodes: Effect of Annealing the Hole Injection Layer on the Electrical and Optical Properties, Latest Trends in Condensed Matter Physics: Experimental and Theoretical Aspects, 171 (2011) 39-50.
[14] Choudhary R.B., and Kandulna R., 2-D rGO impregnated circular-tetragonal-bipyramidal structure of PPY-TiO2-rGO nanocomposite as ETL for OLED and supercapacitor electrode materials, *Materials Science in Semiconductor Processing*, 94 (2019) 86-96.
[15] Liu Y.C., et al., All-organic thermally activated delayed fluorescence materials for organic light-emitting diodes, *Nature Reviews Materials*, 3(4) (2018).
[16] Kim J.H., Triambulo R.E., and Park J.W., Effects of the interfacial charge injection properties of silver nanowire transparent conductive electrodes on the performance of organic light-emitting diodes, *Journal of Applied Physics*, 121(10) (2017).
[17] Siddiqui Q.T., et al., Thermally Activated Delayed Fluorescence (Green) in Undoped Film and Exciplex Emission (Blue) in Acridone-Carbazole Derivatives for OLEDs, *Journal of Physical Chemistry C.*, 123(2) (2019) 1003-1014.
[18] Guo J.J., Zhao Z.J., and Tang B.Z., Purely Organic Materials with Aggregation-Induced Delayed Fluorescence for Efficient Nondoped OLEDs, *Advanced Optical Materials*, 6(15) (2018).
[19] Zajac D., et al., Conjugated silane-based arylenes as luminescent materials, *Electrochimica Acta*, 173 (2015) 105-116.
[20] Martin C., et al., Bipolar luminescent azaindole derivative exhibiting aggregation-induced emission for non-doped organic light-emitting diodes, *Journal of Materials Chemistry C*., 7(5) (2019) 1222-1227.
[21] Chakraborty A., et al., [8] Cyclo-1, 4-naphthylene: A possible new member in hole transport family, *Chemical Physics Letters*., 715 (2019) 153-159.
[22] Sutradhar T., and Misra A., Role of Electron-Donating and Electron-Withdrawing Groups in Tuning the Optoelectronic Properties of Difluoroboron-Napthyridine Analogues, *Journal of Physical Chemistry A.*, 122(16) (2018) 4111-4120.
[23] Surukonti N., and Kotamarthi B., Mono substituted pyrenes as multifunctional materials for OLED: Analysis of the substituent effects on the charge transport properties using DFT methods, *Computational and Theoretical Chemistry*, 1138 (2018) 48-56.
[24] Frisch M.J., et al., Gaussian 16 Rev. B.01., (2016) Wallingford, CT.
[25] Dennington R., Keith T.A., and Millam J.M., GaussView, Version 6., (2016) Semichem Inc.: Shawnee Mission, KS.
[26] te Velde G., et al., Chemistry with ADF., J*ournal of Computational Chemistry.*, 22(9) (2001) 931-967.
[27] Servan S.A., et al., Assessment of the Density-Fitted Second-Order Quasidegenerate Perturbation Theory for Transition Energies: Accurate Computations of Singlet-Triplet Gaps for Charge-Transfer Compounds, *J. Phys Chem A*., 124(34) (2020) 6889-6898.
[28] Samsonova L.G., et al., Experimental and theoretical study of photo- and electroluminescence of divinyldiphenyl and divinylphenanthrene derivatives, *Spectrochim Acta A Mol Biomol Spectrosc.*, 173 (2017) 59-64.
[29] Marcus R.A., Electron-Transfer Reactions in Chemistry - Theory and Experiment, *Reviews of Modern Physics*, 65(3) (1993) 599-610.
[30] Marcus R., Annu., Rev. Phys. Chem., (1964).
[31] Hush N.S., Adiabatic Rate Processes at Electrodes, I. Energy-Charge Relationships, *The Journal of Chemical Physics*, 28 (1958) 962-972.
[32] Chakraborty D., and Chattaraj P.K., Conceptual density functional theory based electronic structure principles, *Chemical Science*, 12(18) (2021) 6264-6279.
[33] Islam N. and Kaya S., Conceptual density functional theory and its application in the chemical domain, CRC Press., (2018).
[34] Ho T.L., Hard soft acids bases (HSAB) principle and organic chemistry, *Chemical Reviews*, 75(1) (1975) 1-20.
[35] Kaya S. and Kaya C., A new method for calculation of molecular hardness: a theoretical study, *Computational and Theoretical Chemistry*, 1060 (2015) 66-70.
[36] Kaya S. and Kaya C., A new equation for calculation of chemical hardness of groups and molecules, *Molecular Physics*, 113(11) (2015) 1311-1319.
[37] Ghanty, T.K. and Ghosh S.K., Correlation between hardness, polarizability, and size of atoms, molecules, and clusters, *The Journal of Physical Chemistry*, 97(19) (1993) 4951-4953.
[38] Chattaraj P. and Sengupta S., Popular electronic structure principles in a dynamical context, *The Journal of Physical Chemistry*, 100(40) (1996) 16126-16130.
[39] von Szentpály, L., Kaya S. and Karakuş N., Why and when is electrophilicity minimized, New theorems and guiding rules, *The Journal of Physical Chemistry A.*, 124(51) (2020) 10897-10908.
[40] Wang Y.G., et al., The reactivity of ambident nucleophiles: Marcus theory or hard and soft acids and bases principle, *Journal of Computational Chemistry*, 40(31) (2019) 2761-2777.

Cumhuriyet Sci. J., 44(2) (2023) 302-314
DOI: https://doi.org/10.17776/csj.1258573

Cumhuriyet Science Journal

| csj.cumhuriyet.edu.tr | Founded: 2002 ISSN: 2587-2680 e-ISSN: 2587-246X Publisher: Sivas Cumhuriyet University

Design, Characterization and in vitro Simulations of nano-HAP/GO Composite Drug Delivery System Produced by Hydrothermal Methods Loaded with Paclitaxel

Fatih Çiftçi [1,2,a,*]

[1] *Department of Biomedical Engineering, Fatih Sultan Mehmet Vakif University, İstanbul, Türkiye.*
[2] *Department of Technology Transfer Office, Fatih Sultan Mehmet Vakif University, İstanbul, Türkiye*
**Corresponding author*

Research Article

History
Received: 01/03/2023
Accepted: 19/06/2023

ABSTRACT

In this study, it was aimed to develop a nano drug system that can be used in passive targeting in pancreatic cancer treatment. Hydroxyapatite nanocrystals (n-HAP) produced by hydrothermal process and graphene oxide (GO) produced by hummers method were used to increase the carrier capacity of the nano drug system and to activate the drug release kinetics and drug loading capacity. Analyses performed for nanocomposite drug carrier systems; FT-IR, XRD, TGA, BET analysis, Zeta potential, TEM and SEM. Paclitaxel (PTX), a chemotherapeutic drug used in the treatment of pancreatic cancer, was loaded into HAP nanocrystals (PTX- loaded n-HAP) and its activity on pancreatic cancer cells was investigated. When PTX was 1 and 2 mg, Encapsulation Efficiency (EE) and Drug Loading Content (LC) were 79.17-72.24% and 80.01-80.27%, respectively, for H-n-HAP crystal structure only, while EE and LC were 88.57-81.57% and 90.84-110.57%, respectively, when H-n-HAP crystal structure was loaded with 1 and 2 mg PTX together with GO. Here, it was observed PTX release profiles are according to the Hixson model. According to Fick's law, release profile was observed with values of k=1.89, n=0.21, SSD=0.04, R^2=0.997, FIC=2.03, SD=0.004. In cell culture studies, as GO nanomaterials were loaded into H-n-HAP nanocrystal structure, the effect of PTX drug on pancreatic cancer increased and the viability of cancer cells decreased. It can be concluded that H-n-HAP/GO/PTX nanocomposite structure kills more pancreatic cancer cells with synergistic effect.

Keywords: Biodegradable material, Graphene, Nano-structures, Nanocomposite, Biopolymer.

[a] *faciftcii@gmail.com* *https://orcid.org/0000-0002-3062-2404*

Introduction

The main objectives in designing nanoparticles as drug delivery systems include controlling particle size, surface properties and release of pharmacologically active substances to ensure targeted site-specific delivery of the drug at therapeutically optimal rate and dose [1]. Nanoparticle-based drugs control and sustain the release of the drug during transport and at the site of localization, as well as enabling the distribution of the drug to organs and subsequent clearance of the drug to increase the therapeutic efficacy of the drug and reduce its side effects [2], [3]. The controlled release and particle degradation properties of nanoparticles can be easily modulated by the choice of matrix components. The drug loading of nanoparticles is relatively high and drugs can be incorporated into the systems without any chemical reaction, an important factor for maintaining drug activity. Site-specific targeting can be achieved by binding target ligands to the surface of the particles or by using magnetic guidance. Drug delivery systems created with nanoparticles can be used in various routes of administration, including oral, nasal, parenteral, intraocular [4], [5].

Many methods have been developed to produce nano-sized hydroxyapatite (n-HAP) crystals [6]. The most commonly used methods include sol-gel method, micro-emulsion method, hydrothermal method and wet chemical method. Among these, the hydrothermal method is the most widely used method because it is easy in terms of applicability. However, many studies have shown that the technique of nano-sized hydroxyapatite (H-n-HAP) synthesis by hydrothermal method can be improved with drug release enhancing surfactant additives [7]–[10].

Changing some parameters (temperature, time, pH value) during the hydroxyapatite (HAP) production process affects the solubility and crystallinity of the produced structure. HAP is used in many fields, especially in drug delivery systems and tissue engineering. Much of the 3D manufacturing of ceramics in biomedicine is for the creation of pure ceramic scaffolds that mimic the minerals, structures and mechanical properties naturally found in bone. In addition, powdered HAP is also widely used in 3D fabrication, thanks to its presence as a calcium phosphate phase in mineralized bone.

The other material to be used in this study is graphene oxide (GO), a surfactant and bioactive agent with drug release kinetics enhancing properties. GO, which will be used together with HAP in this study, is a highly oxidized

chemically modified graphene consisting of a one-atom thick layer of graphene sheets with carboxylic acid, epoxide and hydroxyl groups in the plane. GO, which is a carbon nanomaterial, acts as a bridge to cells and increases cell adhesion because it has more surface functional groups [11]. The basal plane also contains free surface π electrons from unmodified domains of graphene with π-π interaction capabilities for hydrophobic and non-covalent functionality. Thus, GO is an amphiphilic sheet-like molecule that can be used as a surfactant to stabilize hydrophobic molecules in a solution [12]. GO has low cytotoxicity and antibacterial properties. The large surface area volume and biocompatibility of GO, which has high mechanical properties and high corrosion resistance, increase its use in nanocomposite applications [12], [13]. GO's mechanical properties tolerate stress, thus improving interface bonding and chemical adhesion [14]. Furthermore, GO nanosheets have been used as a material with large surface area in drug delivery applications by increasing their loading capacity [15]. As an innovative application on this subject; in vitro cell viability tests were performed on GO and HAP and it was reported that antibacterial studies of these nanocomposites, which exhibited high cell viability, completely inhibited *E. coli* growth [16].

Localized or targeted delivery of chemotherapeutics has been used in recent trends to limit indiscriminate toxicities to normal tissues associated with chemotherapy. Paclitaxel (PTX), the first of a new class of microtubule-stabilizing agents, is recognized as an effective chemotherapeutic agent for a wide range of solid tumors. The clinical application of this highly effective drug in cancer therapy is limited due to its poor aqueous solubility and poor oral bioavailability. To date, only two commercial formulations have been developed. The first formulation developed uses a 1:1 mixture of CremophorEL and ethanol to improve the solubility of intravenously administered paclitaxel. CremophorEL has been shown to have serious side effects including severe hypersensitivity reactions, neurotoxicity and hypotensive vasodilation. The most recent development in PTX administration is that an injectable suspension of albumin bound PTX nanoparticles called Abraxane has shown effective results. However, not only is bone marrow suppression a dose-dependent and dose-limiting toxicity but neuropathy toxicity has also been shown to be remarkably increased compared to the conventional PTX formulation. Therefore, safe and effective drug delivery systems are needed to improve the safety and therapeutic efficacy of current clinical chemotherapeutic treatments.

This study aims to develop a model to enhance the release kinetics activity of paclitaxel (PTX) in pancreatic cancer by doping surface-activating graphene oxides (GOs) into nano-sized hydroxyapatites (n-HAP) produced using the hydrothermal method. The objective is to investigate and determine whether chemotherapeutic drugs used in cancer treatment, along with active agents, can exhibit increased shelf-life effects. The feasibility of a proposed approach using PTX as the model drug for controlled drug delivery devices is explored. The study focuses on searching for the optimal differences in Quantitative Structure-Property Relationship (QSPR) models for mutual diffusion, as well as predictive QSPR models for release kinetics based on the Hixson mathematical model.

Materials and Methods

Production of Hydroxyapatite Crystals by Hydrothermal Method

The chemicals used were calcium nitrate tetrahydrate ($Ca(NO_3)_2.4H_2O$; Merck KGaA, Darmstadt, Germany) and di-ammonium hydrogen phosphate ($(NH_4)2HPO_4$; Merck, KGaA, Darmstadt, Germany). The amount of starting materials for Hydroxyapatite (HAP) synthesis was determined as Ca/P ratio of 1.67. 23.66 g of $Ca(NO_3)_2.4H_2O$ was dissolved in 100 ml of water. The prepared $Ca(NO_3)_2.4H_2O$ and $(NH_4)2HPO_4$ were mixed in an ultrasonic bath for 15 minutes. A stock solution was prepared by dissolving 7.93 g of $(NH_4)2HPO_4$ in 100 ml of water. The pH of the prepared solutions was adjusted to pH≥10 with a drop of ammonia solution (NH_4OH, 28%, Merck Co. Darmstadt, Germany) to bring the pH ≥10. Prepared $Ca(NO_3)_2.4H_2O$ and $(NH_4)2HPO_4$ stock solutions were taken 20 ml each and mixed dropwise. The resulting nano-sized hydroxyapatite (n-HAP) crystals were kept at room temperature for 24 hours to precipitate. It was washed 6 times at 4100 rpm for 5 minutes to remove the residues formed as a result of the reaction. As in the wet chemical method, the n-HAPs produced were placed in the cell in the hydrothermal reactor after waiting for 24 hours for precipitation. n-HAPs were poured into the cell of the hydrothermal reactor, placed in the hydrothermal reactor and tightly closed. The n-HAPs placed in the hydrothermal reactor were allowed to react at 200 °C for 2 hours. After the reaction, the hydrothermal reactor was allowed to cool down and the hydroxyapatites formed were carefully removed from the reactor. The hydroxyapatites were washed 6 times at 4100 rpm for 5 minutes to remove the residues formed as a result of the reaction.

PTX Albumin-stabilized Nanoparticle Formulation Hydrothermal Treatment of Nano-Sized Hydroxyapatite Crystals

A 1mg/ml PTX solution was prepared by dissolving 50 mg lyophilized PTX in 50 ml water for injection. Stock $Ca(NO3)_2{\cdot}4H_2O$ solution and stock $(NH_4)H_2PO_4$ solution were taken 20 ml each. The pH of these solutions was adjusted to ≥10 with ammonia. The prepared 1mg/ml PTX solution was added dropwise to the $Ca(NO3)_2{\cdot}4H_2O$ solution. The pH was checked again and if it was lower than 10, it was adjusted again by adding ammonia to ≥10. The resulting $Ca(NO3)_2{\cdot}4H_2O$-PTX solution was mixed dropwise into $(NH_4)H_2PO_4$ solution. The resulting PTX-loaded nanostructured n-HAP crystals were kept at room temperature for 24 hours to precipitate. After 24 hours at

room temperature, half of the PTX-loaded n-HAP crystals were separated and with washed pure water 10 times at 4100 rpm for 5 min to remove by-products and residues. After precipitation of PTX-loaded n-HAP crystals formed by wet chemical method, the separated half was poured into the cell inside the hydrothermal reactor. After placing the cell in the hydrothermal reactor, the reactor was closed tightly. The PTX-loaded n-HAPs in the reactor were allowed to react at 200°C for 2 hours. After the reaction took place, the hydrothermal reactor was allowed to cool down. After the reactor cooled down, the PTX-loaded n-HAP crystals in the reactor were washed 10 times at 4100 rpm for 5 min to remove by-products and residues. All samples obtained were frozen at -20 °C to prepare for the lyophilizer. n-HAP crystals, hydrothermal n-HAP crystals, PTX-loaded n-HAP crystals and hydrothermal PTX-loaded n-HAP crystals were placed in the lyophilizer for 24 hours.

GO Loading and Preparation of Ptx/N-Hap Nanostructures

In this study, GO was synthesized by Hummers' method [17]. The chemicals used for synthesis such as Graphite flake (mesh size 300), Sulfuric acid (H_2SO_4) potassium permanganate ($KMnO_4$, 99.9%), phosphoric acid (H_3PO_4) and hydrogen peroxide (H_2O_2 30%) were purchased from Merck and Sigma Aldrich. These 1% GO ratio solutions were prepared as the each given amount (ml) in 10 ml distilled water and 10 min. ultra-sonication were applied. These amounts were calculated to produce 1 g nanocomposite product. 2.35 g $Ca(NO3)_2{\cdot}4H_2O$ was added to each GO solutions pH adjusted ≥10 with ammonium. In the continuation 2,37 g $(NH_4)H_2PO_4$ were dissolved in 10 ml distilled water and pH adjusted ≥10 with ammonium for each 3 beakers for 1% GO ratio.

The hydrothermal system was loaded after different experimental runs to n-HAP of the two materials. First n-HAP production, then hydrothermal production by loading PTX into n-HAP, and finally hydrothermal method was realised by loading GO nanomaterial separately PTX/n-HAP and n-HAP. In this study, the working groups were separated as PTX/n-HAP/GO and n-HAP and the hydrothermal method was carried out after the wet chemistry method.

Characterizations

Particle Size, Size Distribution and Zeta Potential

The average particle size, polydispersity index and zeta potential of hydrothermal n-HAP crystals, hydrothermal n-HAP/GO nanocomposites, PTX-loaded n-HA crystals, hydrothermal PTX-loaded n-HAP/GO nanostructures were measured by photon correlation spectroscopy using Zetasizer (Nano ZS, Malvern, UK) with DLS method. Measurements were performed three times for each sample at a 90° angle and the samples were kept at 25 °C. Each sample was diluted with deionized water before measurement. The zeta potentials of the prepared nanoparticles were determined with an electric field electrophoretic cell using the same equipment.

Fourier-Transform Infrared Spectroscopy Analysis

GO functional groups and PTX chemical bonds and functional groups of hydrothermal n-HAP crystals, hydrothermal n-HAP/GO nanocomposites, PTX-loaded n-HA crystals, hydrothermal PTX-loaded n-HAP/GO nanostructures, GO functional groups and PTX chemical bonds and functional groups were determined by Fourier Transform Infrared Spectrophotometer (Alpha FTIR Spectroscopy, Bruker, USA) at wavelength 4000-750 cm^{-1}.

Scanning Electron Microscopy and EDS Mapping & Spotting

The morphological analysis of the nanocomposite structures was observed by scanning electron microscopy (SEM) (EVO LS 10, ZEISS). The operating conditions were 5 kV and secondary backscattered electrons mode. The imageable parts were examined with a voltage of 10 kV. All samples were coated with gold-palladium to ensure conductivity as the nanostructures lack this property. Morphological features, elemental analysis and homogeneity of the samples were analyzed by EDX (Energy Dispersive X-Ray Spectrometry). EDAX Element 2016 was used for EDS mapping and staining analysis. Elemental differences and homogeneity between two spots were investigated. Spots that appear different from each other were compared. Pore sizes were also measured. Staining was achieved by SEM with a Cathodoluminescence Detector (CL) attached. In some cases, the BSD-Back Scatter Detector was used to look for differences between elements. EDS spots (1-2-3) were showed in Figure 5.A as red, green and blue respectively.

Brunauer-Emmett-Teller Analysis

Hydrothermal n-HAP crystals, hydrothermal n-HAP/GO nanocomposites, PTX-loaded n-HA crystals, hydrothermal PTX-loaded n-HAP/GO nanostructures, PTX powders and GO carbon nanostructures were used to obtain information about the surface areas. The suspensions were prepared using a 1% sample concentration. To measure the surface area, standard BET (Brunauer-Emmett-Teller; Micromeritics TriStar II) degassing conditions were applied. The powders were heated for 1 hour at 90°C followed by 2 hours at 250°C to eliminate any organic substances present in both the synthetic water and the synthesized powders. This process ensured that the surface area measurements were accurate by removing any potential interference from organic compounds.

X-ray Diffraction Analysis

X-ray Diffraction (XRD; Braket XPERT-PRO; measurement with Cu (Copper) internal wavelengths anode) was used to determine the phase structures of hydrothermal n-HAP crystals, hydrothermal n-HAP/GO nanocomposites, PTX-loaded n-HA crystals, hydrothermal PTX-loaded n-HAP/GO nanostructures, PTX powders and GO carbon nanostructures. It was investigated patterns between 10 to 70^o angle by using 40 mA and 45 kV generator.

Thermogravimetric Analysis (TG-DTA)

The thermal behaviour of hydrothermal n-HAP crystals, hydrothermal n-HAP/GO nanocomposites, PTX-loaded n-HA crystals, hydrothermal PTX-loaded n-HAP/GO nanostructures, PTX powders and GO carbon nanostructures were studied by differential thermal analysis (DTA) and thermal gravimetric analysis (TGA) using an SDT Q600 analyser at 25- 900℃. The analyses were performed in dry air.

HPLC method

Percent nanoparticle yield was calculated as the ratio of the total weight of lyophilized nanoparticle powder obtained to the total weight of all formulation components used multiplied by 100. Percent PTX loading was calculated by multiplying 100 by the ratio of the total amount of drug extracted from the polymeric matrix with a known nanoparticle weight to the total weight of nanoparticles used prior to extraction. The encapsulation efficiency was calculated by multiplying 100 by the ratio of the weight of the drug contained in a nanoparticle batch to the weight of the drug used in the formulation (the actual amount). Briefly, approximately 10 mg of correctly weighted lyophilized nanoparticles were dispersed in an organic solvent (acetonitrile and water; 15 ml, 60:40 v/v). They were sonicated (Fisher Scientific FS 20, Fairlawn, NJ, USA) for 4 h to remove PTX for HPLC analysis (Shimadzu SP-10A VP, Columbia, MD, USA). HPLC analysis for PTX was performed on a C18 Zorbax column (150 x 4.6 mm, 5 µm; Phenomenex, Torrance, CA, USA) with a mobile phase consisting of 0.1M methanol (v/v/v) at a flow rate of 0.75 ml/min. Effluents were monitored at 227 nm and measured using the area under the peak from standard solutions dissolved in mobile phase (0.4 to 2 µg/ml) [18].

In Vitro Studies

Mathematical model of drug loading efficiency and release kinetics of PTX

The loading content (LC) and encapsulation efficiency (EE) of PTX were analysed using high-performance liquid chromatography (HPLC, Shimadzu SP-10A VP, (250 × 4.6 mm) Columbia, MD, USA) consisting of a P-900 gradient pump system and an Ultra C18 5 µm column. 1 mg of PTX/GO/H-n-HAP was first dissolved in dichloromethane (DCM) for 30 min. The resulting solution was then passed through a 0.45 µm filter. HPLC analysis was performed at a flow rate of 1.0 mL/min at 37°C using acetonitrile/water (v/v = 4:1) as mobile phase and detected at a wavelength of 227 nm (UV detector, Shimadzu SP-10A VP). LC and EE were calculated according to the following equations:

$$LC\% = \frac{weight\ of\ loaded\ drug}{weight\ of\ drug\ loaded - NP_s} x\ 100\% \quad (1)$$

$$EE\% = \frac{weight\ of\ loaded\ drug}{weight\ of\ drug\ feed} x\ 100\% \quad (2)$$

Cytotoxicity and cell culture

In vitro cell culture studies were conducted using the AsPC-1 (ATCC® CRL-1682™) pancreatic cell line derived from a metastatic site, while normal pancreatic cells (CRL-4023 human pancreatic duct epithelium) were used as a control. The cells were cultured in IMDM culture medium supplemented with 10% FBS, maintained at 37°C under 5% CO2. Passaging was performed every 72 hours. After one week, the cells were digested with trypsin containing 2% EDTA and washed with PBS. The resulting supernatant was discarded, and the cells were counted. To create frozen stocks, the cells were frozen in liquid nitrogen and subsequently thawed at 37°C. This freeze-thaw process was repeated three times. For the cytotoxicity assay, AsPC-1 pancreatic cells were seeded in 96-well plates at a density of 10,000 cells per well. The plates were then incubated in a 37°C incubator with 5% CO2 for 24 hours. The synthesized nanostructure was tested at two different concentrations (0.01 mg/ml and 0.05 mg/ml) on the AsPC-1 pancreatic cell line. Three replicates of each concentration were used. The compounds of different concentrations were added to the wells and incubated for 48 hours in the same incubation conditions. To assess cell viability, the MTT (3-(4,5-dimethylthiazol-2-yl)-2,5-diphenyltetrazolium bromide) assay was performed. In this assay, 10 µl of MTT salt solution was added to each well and incubated for 3 hours at 37°C. After the formation of formazan crystals, 100 µl of dimethyl sulfoxide (DMSO) was added to each well and kept in the dark for 30 minutes. The absorbance was then measured at 570 nm using an ELISA reader. Tumor cell antigens were prepared by centrifuging the cells at 1000 rpm for 5 minutes, followed by filter sterilization [19], [20].

Result And Discussion

Particle Size, Size Distribution and Zeta Potential

Zeta potential is related to surface charge density and double layer thickness. The surface charge density depends on the concentration of potential-determining ions. Since H+ ion is the potential-determining ion in many systems, the zeta potential depends on pH. The zeta potential is positive for low pH values and negative for high pH values. As seen in the graph, the zeta potential values of all samples were negative. As a result, this showed that the prepared samples were successfully produced at the desired pH values. When hydrothermal method was applied to n-HAP and PTX was loaded to H-n-HAP and H-n-HAP/GO, zeta potential values were observed more. This showed that the stability of the hydrothermally treated samples increased, i.e. the degradation rates decreased. However, the stability of PTX-loaded H-n-HAP and PTX-loaded H-n-HAP/GO was found to be higher than that of H-n-HAP alone. This implies that when the designed drug system is administered intravenously to the patient, the residence time in the blood will be higher than PTX alone. In conclusion, in zeta potential analysis, the more charged a

sample is, the better it disperses. A low zeta potential of the sample indicates that the material tends to agglomerate. Agglomeration causes embolization and clogs the vessel. A high zeta potential indicates that the designed drug delivery system will not cause vascular occlusion.

Table 1. Physicochemical characterization (Particle size, zeta potential, conductivity, electrophoretic) of PTX loaded H-n-HAP and H-n-HAP

Samples	Particle size (nm)	Zeta potential (mV)	Conductivity [mS/cm]	Electrophoretic [cm²/Vs]
H-n-HAP	815.12±8.35	-10.2±0.2	0.109	-30.10^{-6}±4. 10^{-6}
H-n-HAP/PTX(1mg)	446.17±3.66	-12.5±0.24	0.107	-49.10^{-6} ±3. 10^{-6}
H-n-HAP/PTX(2mg)	349.17±5.66	-16.1±0.24	0.112	-55.10^{-6}±3. 10^{-6}
H-n-HAP/GO%1	668.34±4.75	-29.5±0.12	0.152	-69.10^{-6}±5. 10^{-6}
H-n-HAP/GO%0.5	537.06±1.99	-27.2±0.43	0.132	-67.10^{-6}±5. 10^{-6}
H-n-HAP/GO%1-PTX(1mg)	226.7±0.70	-36.8±1.4	0.144	-76.10^{-6}±5. 10^{-6}
H-n-HAP/GO%0.5-PTX(2mg)	194.74±1.04	-35.6±1.2	0.133	-71.10^{-6}±5. 10^{-6}

BET analysis

Measurement of porous surface area and pore size by BET adsorption and desorption of Nitrogen (N_2) gas emission was performed. N_2 utilization based on adsorption by surface area can then be evaluated by N_2 gas consumed pore dispersion.

Table 2. BET and BJH adsorption & desorption (H-nHAP, H-n-HAP/GO, H-n-HAP/PTX, H-n-HAP/GO-PTX samples)

Samples		H-n-HAP	H-n-HAP/GO	H-n-HAP/PTX	H-n-HAP/GO-PTX
Spesific Surface Area (m^2/g)	BET	81.47	42.19	71.11	58.19
	Largmuir	187.12	82.85	172.85	152.85
	BJH Adsoption	80.93	38.20	71.20	63.34
	BJH Desorption	82.05	41.892	73.89	68.08

Table 2 shows the data obtained as a result of BET analysis. According to the results obtained, the specific surface area of PTX-loaded H-n-HAP was 71.11 m^2/g and the surface area of PTX/GO-loaded H-n-HAP was 58.19 m^2/g. GO loaded H-n-HAP surface area was 42.19 m^2/g. To see the difference in the surface area of the additives here, the H-n-HAP surface area was measured and found to be 81.47 m^2/g. As a result, it was observed that the more the H-n-HAP crystal structure is realized, the larger the surface area of the dopants.

FTIR Analysis

FTIR spectra magnification analysed between 4000 and 750 cm^{-1} wavenumbers (Figure 1). As a result of FTIR analysis of H-n-HAP functional groups; O-H bonds show a peak at 3378.51 cm^{-1}. A peak was observed at 1657.52 cm^{-1} for C=O bonds, 1051.07 cm^{-1} for P-O bond and 976.44 cm^{-1} for C=O. As a result of FTIR analysis of H-n-HAP functional groups, O-H bonds show a peak at 3388.93 cm-1. C=O bonds show a peak at 1421.54 cm^{-1}, P-O bond at 1020.34 cm^{-1} and C=O at 962.48 cm^{-1}.

As a result of FTIR analysis of PTX-loaded H-n-HAP functional groups; O-H bonds show a peak at 3425.58 cm^{-1} and a peak of C-H bond at 1338.60 cm^{-1}. A new peak appeared at 1658.78 cm^{-1} and was not found in PTX and pure hydroxyapatite. The new peak 1 at 1658.78 cm-1 may be due to PTX at 1543.05 cm^{-1} and undegraded HAP at 1427.32 cm^{-1}. A P-O peak is observed at 1028 cm^{-1}. The band at 1338 cm^{-1} does not exhibit a distinct shift, suggesting the absence of chemical bonding between HAP surface calcium ions and PTX radicals. The mechanism of drug loading appears to be mainly by electrostatic interaction between the positive calcium ions on the HA surface and the negative carboxylate radical on PTX.

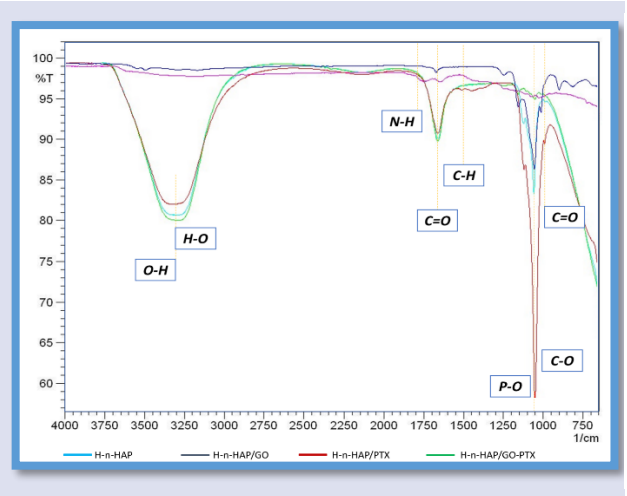

Figure 1. H-n-HAP, H-n-HAP/GO, H-n-HAP/PTX and H-n-HAP/GO-PTX of FTIR analysis

PTX-loaded H-n-HAP functional groups; a peak at 3394.72 cm^{-1} for O-H bonds and a peak at 1338.60 cm^{-1} for C-H bonds were observed. At 1651.07 cm^{-1}, new peaks without PTX and H-n-HAP appeared. The peak at 1651.07 cm^{-1} was observed to be due to the PTX at 1543.05 cm^{-1} and the undegraded H-n-HAP at 1421.54 cm^{-1}. At 1020.34 cm^{-1}, a peak belonging to P-O is observed. The band at

1338 cm^{-1} does not exhibit a distinct shift, suggesting the absence of chemical bonding between H-n-HAP surface calcium ions and PTX carboxylate radicals. The mechanism of drug loading was observed mainly by electrostatic interaction between the positive calcium ions on the HAP surface and the negative carboxylate radical on PTX. PTX functional groups O-H bonds by FTIR spectroscopy show a peak at 3388.93 cm^{-1}. A peak for N-H bond at 1543.05 cm^{-1}, a peak for C-H bond at 1338.60 cm^{-1} and a peak for C-O bond at 1031.92 cm^{-1} were observed.

XRD Analysis

When the XRD patterns of H-n-HAP, GO, PTX, H-n-HAP/GO, H-n-HAP/PTX and H-n-HAP/GO/PTX were compared, it was observed that the characteristic peaks of the crystal structures in H-n-HAP form and GO and PTX materials loaded into H-n-HAP crystal form were thinner and sharper (Figure 2).

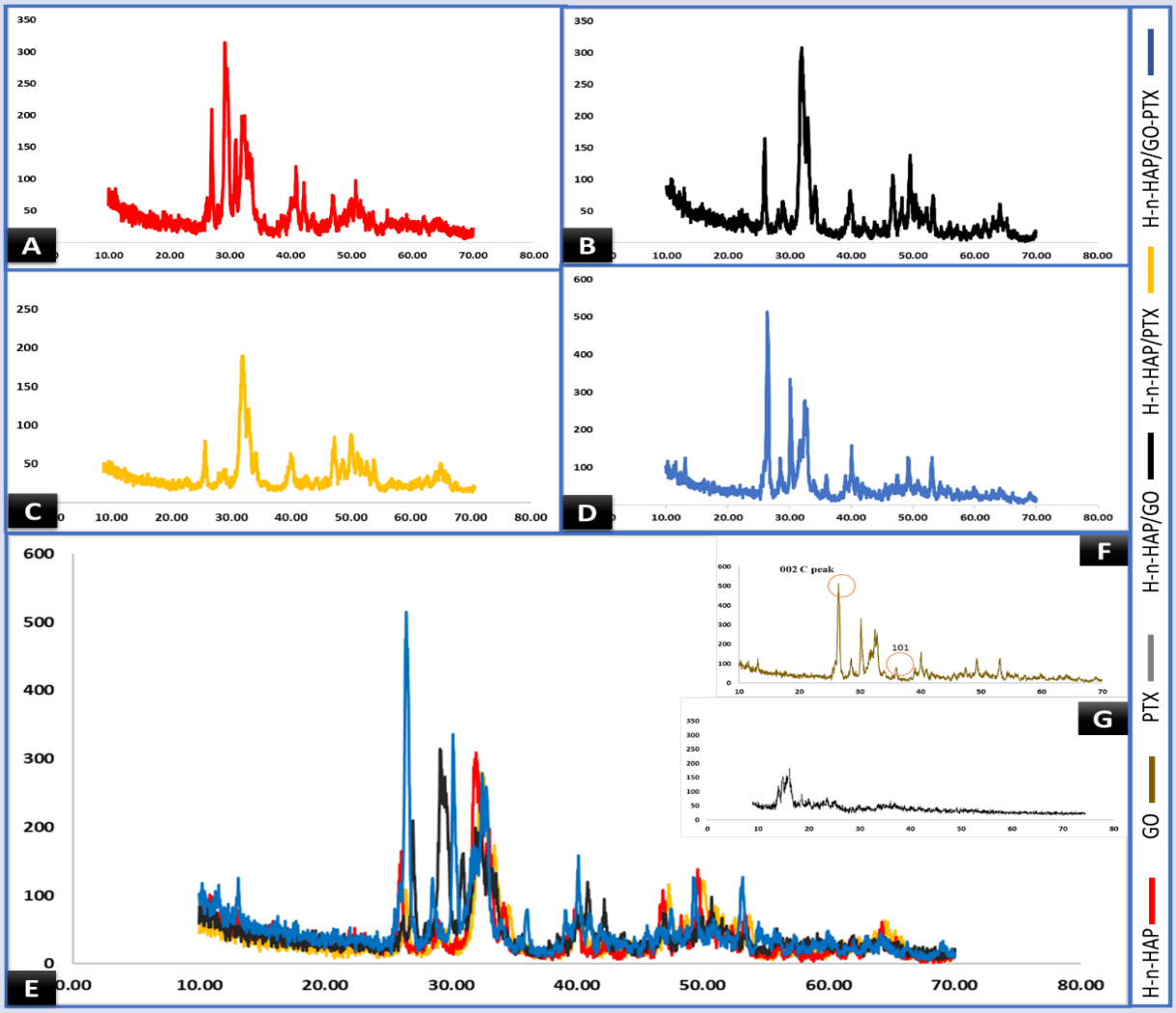

Figure 2. XRD of H-n-HAPs; A. H-n-HAP, B. H-n-HAP/GO, C. H-n-HAP/PTX, D. H-n-HAP/GO-PTX, E. All XRD pattern, F. GO, G. PTX

In a similar study, selective laser sintered H-n-HAP composite microspheres were designed for BTE applications. The XRD curves of nano-HA showed that the crystallization peaks of typical HAP, such as three strong peaks (211) (112) (300), correspond to angles of 31.93°, 32.65° and 33.82°, respectively [21]. These and similar studies support our XRD analysis as shown in Figure 2. For the XRD of amorphous materials, the position of the peak corresponded to the average distance between the chains [22]. The larger the average interchain distance, the smaller the angle. Thus, the value of the composites increased due to the introduction of H-n-HAP, while the non-crystalline peak of the composites shifted slightly to the left. Moreover, the presence of at least two peaks indicated that the materials have multiple average interchain distances [23].

TGA Analysis

The decomposition behaviour was studied by DTA and TGA curves for H-n-HAP/PTX and H-n-HAP/GO/PTX nanocomposite powders, Figure 3. The curves are divided into two endothermic zones ranging from 25 to 200 °C, the peak existing at about 250 °C corresponding to a 6% moisture loss due to thermal stability in H-n-HAPs. When

the temperature range was increased by 200-1000 °C, it corresponded to the de-hydroxylation precipitation complex due to OH loss and the loss of physically adsorbed water molecules of the H-n-HAP powder. This is shown in Region II.

In the TG-DTA plot of PTX-loaded H-n-HAP, a 14% loss of n-HAPs was observed. The loss in H-n-HAPs was observed to be about 6%. When H-n-HAP was compared with PTX-loaded H-n-HAP, it was observed that the loss of approximately 8% could be due to PTX in the drug system, lactose monohydrate and methylparaben.

For TG-DTA of PTX-loaded H-n-HAP/GO, a 4% loss in n-HAPs was observed. Compared to PTX-loaded H-n-HAP, the loss is less here. This may be because the drug PTX is incorporated into the n-HAP crystal, so it is not lost during the process or some molecules in the drug are disrupted during the hydrothermal process.

The thermal stability of H-n-HAP/PTX containing 1% GO at a temperature of about 200°C, where the thermal stability of GO decreased due to carboxylic decomposition and release of CO_2 gas and 1% of GO mass was lost [36].

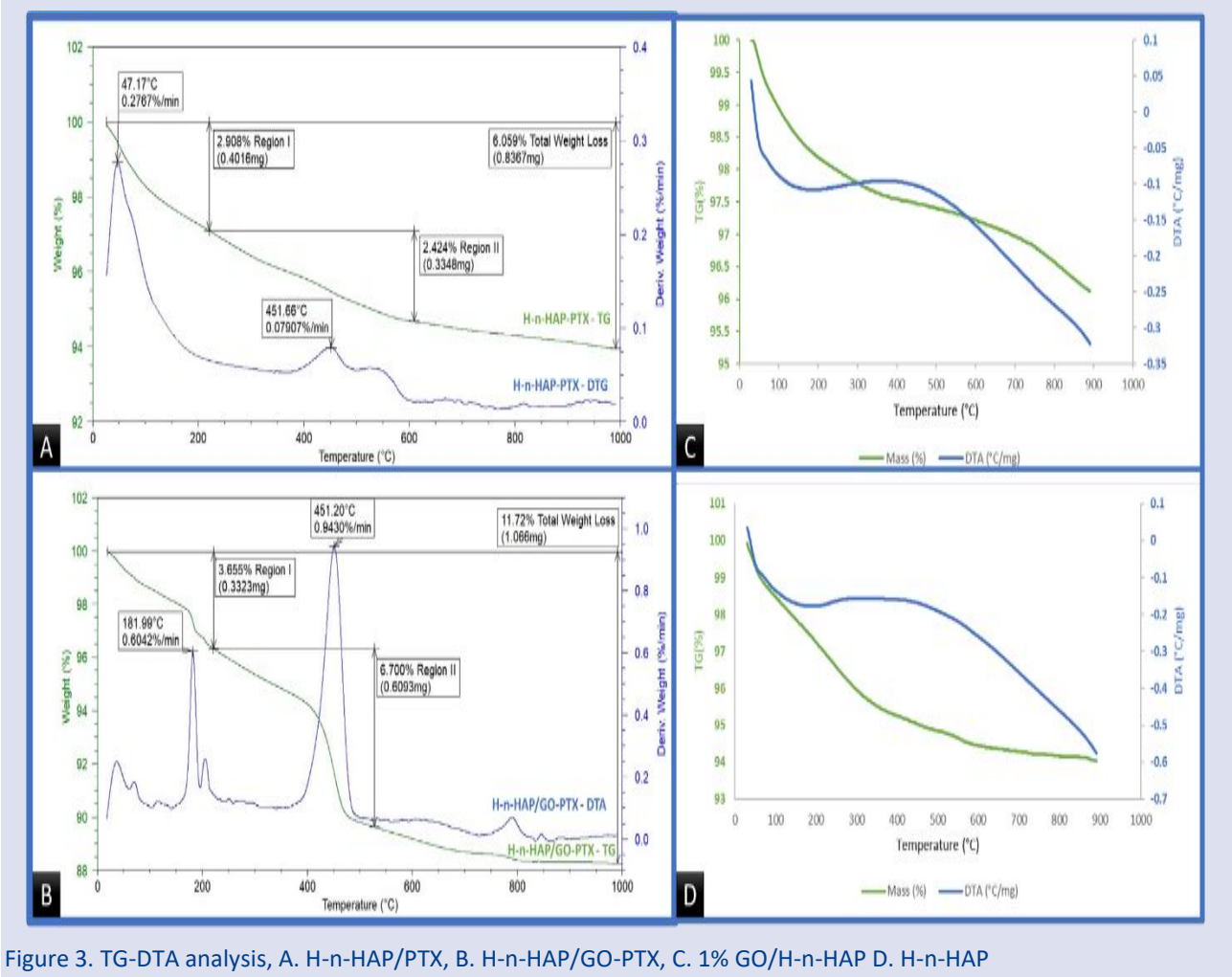

Figure 3. TG-DTA analysis, A. H-n-HAP/PTX, B. H-n-HAP/GO-PTX, C. 1% GO/H-n-HAP D. H-n-HAP

SEM and EDS Mapping / Spotting

In the SEM image for H-n-HAP/GO-PTX in Figure 4.D, a zoom of 2 µm was made, two different sizes were measured with ImageJ program in two different regions and seen as 153 nm and 438 nm, respectively. For H-n-HAP/GO, Figure 4.B shows the presence of GO nanostructures. It was observed that GO doped into H-n-HAP production enhanced the crystal surface growth of n-HAP. Even 1% doping of GO was observed to increase porosity with high surface area. The homogeneous distribution of n-HAPs synthesized by hydrothermal method showed the suitability of the studies carried out at the point of PTX doping [6], [24].

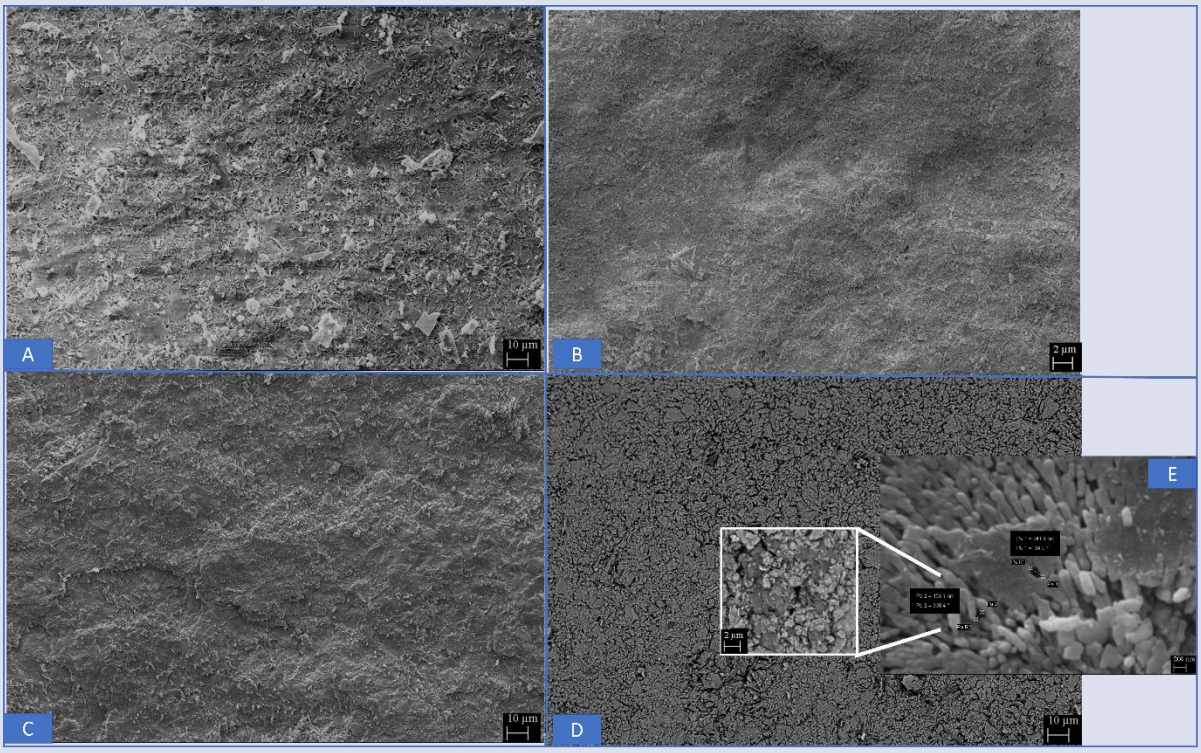

Figure 4. SEM of H-n-HAPs, size measurement at 200nm for A. H-n-HAP, B. H-n-HAP/GO, C. H-n-HAP/PTX, D. H-n-HAP/GO-PTX, E. H-n-HAP/GO-PTX; ImageJ

By EDS spotting, 3 different regions of the H-n-HAP/GO-PTX therapeutic nanoparticle structure were selected and the homogeneous distribution of the nanocomposite structure was confirmed (Figure 5).

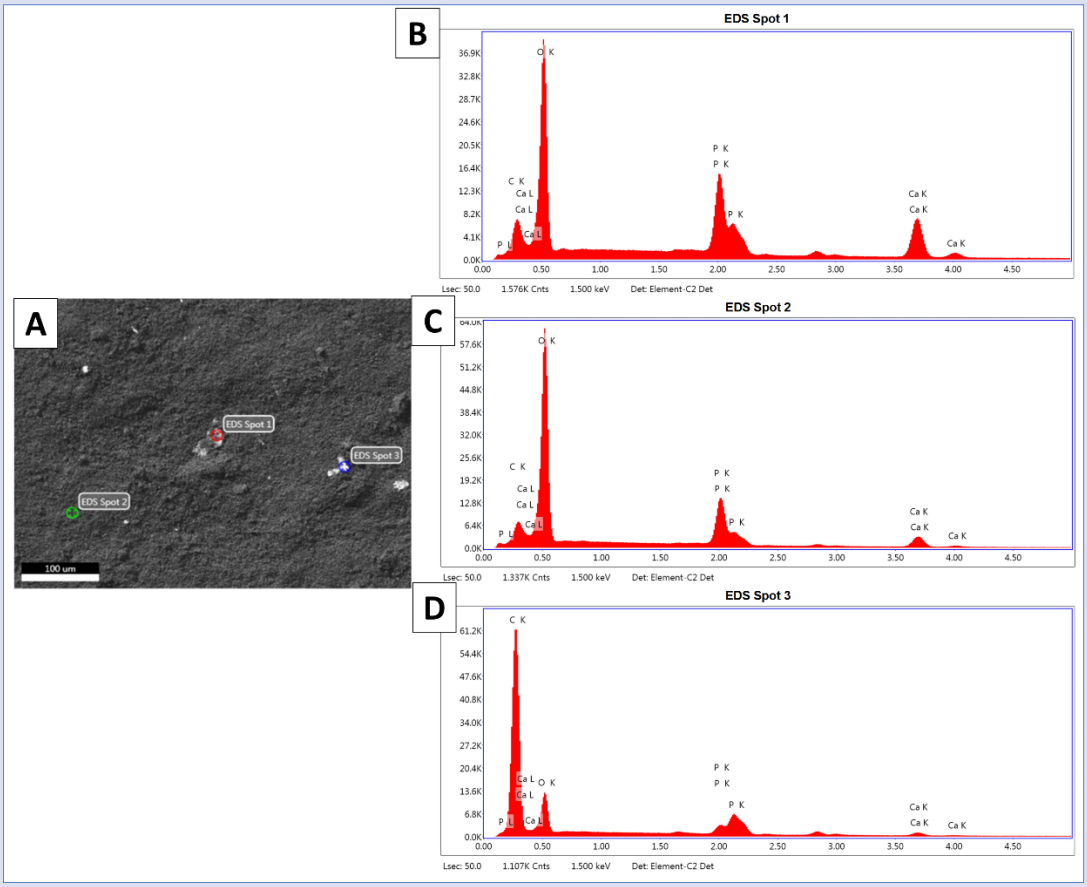

Figure 5. A. EDS mapping analysis and element analysis of nanoparticles samples. Three chosen spot to compare elementally in B. Spot 1, C. Spot 2, D. Spot 3

In EDS spot 1, EDS spot 2 and EDS spot 3 observations, the Ca/P ratio was approximately 1.66 and the elemental values were close to each other between the sintered and unsintered samples. The Ca/P ratio of the synthesized nanocomposite materials was found to be 1.69 ± 0.053. In the literature, n-HAP Ca/P ratio, which is considered thermodynamically stable, is known as 1.67. The difference in this study was estimated that the GO structure and PTX pharmodynamic effect may have increased the surface area. However, this will not change our conclusion that the result is close to the literature information, on the contrary, it will confirm it [25], [26].

Chromatographic Performance of PTX

The linearity of the method used for PTX was evaluated on the calibration curve of the assay. In Figure 6 the components of the drug PTX are shown in the peak areas. The specificity/selectivity of the analytical method was confirmed by analysing solutions containing 100% of the normal working concentration. The compositions of PTX, the pharmaceutical product tested qualitatively and quantitatively were determined by this analysis. The solubility between the peaks corresponding to the various substances of the pharmaceutical drug present in the GO and PTX formulations doped with H-n-HAPs, especially for the compounds with the closest elution concerning PTX, was analysed and shown in Figure 6.A with figures. According to these results; Figure 6.A1; 10-deacetyl-paclitaxel, Figure 6.A2; 10-deacetyl-7-epi-paclitaxel, Figure 6.A3; paclitaxel, Figure 6.A4; 7-epi-paclitaxel, Figure 6.A5; 10-deacetyl-bacatin III. A comparative analysis of the chromatograms (plate number, flow rate, and bar; Table 3) is shown in Figure 6.B. If the impurities eluted after PTX were > 1 with relative retention time (RRT), they were masked by the excipient matrix. Due to this interference, the method is not recommended for purity control in finished products. PTXs were preserved by doping into hydrothermally produced n-HAPs.

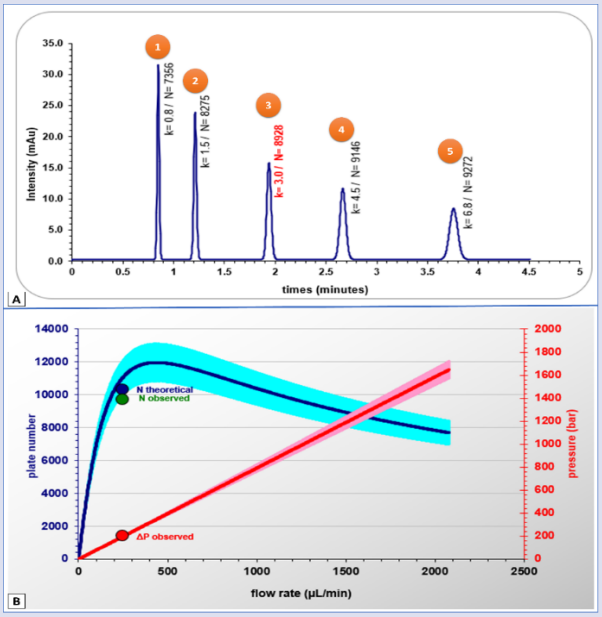

Figure 6. Chromatographic performance in isocratic mode, A. Chromatographic conditions, B. chromatographic performance

Table 3. HPLC method for PTX drug conditions and performance

Chromatographic conditions		Chromatographic performance	
Stationary support	Zorbax extend	Optimal flow rate	434 ul/min
Length	50 mm	Suggested working flow rate	887 ul/min
Diameter	2.1 mm	N theoretical	10319
Particle size	1.7 um	N observerd (for UPLC only)	9683
Organic solvent	(MeOH)	%N loss (due to UPLC instrumentation)	6%
Mobile phase temperature	65 °C	%N loss (due ton on-optimal flow rate)	%14
Mobile phase composition (%organic)	40%	%N loss (total)	%20
Flow-rate	250 ul/min	ΔP observed	198 bar
Solute molecular mass	200 g/mol		
Injection volüme	2.0 uL		
Detector time constant	100 ms		
Average retention factor –(k)	3		

PTX Loading Efficiency, Release Kinetics Mathematical Model

Polydispersity Index (PDI), Drug Loading Content (LC) and Encapsulation Efficiency (EE) values of PTX-loaded H-n-HAP and H-n-HAP/GO nanocrystalline composites at different mass ratios was showed in Table 4. When PTX was 1 and 2 mg, EE and LC were 79.17-72.24% and 80.01-80.27%, respectively, for H-n-HAP crystal structure only, while EE and LC were 88.57-81.57% and 90.84-110.57%, respectively, when H-n-HAP crystal structure was loaded with 1 and 2 mg PTX together with GO. As expected, increases in LC were observed with GO doping in the loading.

Table 4. PDI, LC and EE of PTX-doped H-n-HAP and H-n-HAP/GO at different mass ratios of drug and carriers

Samples	PDI	EE (%)	LC (%)
H-n-HAP/PTX(1mg)	0.289±0.034	79.17±3.04	80.01±0.21
H-n-HAP/PTX(2mg)	0.295±0.024	72.24±1.18	80.27±0.67
H-n-HAP/GO%1-PTX(1mg)	0.369±0.045	88.57±2.53	90.84±1.47
H-n-HAP/GO%0.5-PTX(2mg)	0.410±0.034	81.57±2.04	110.57±0.81

Table 5. Mathematical kinetic release model parameters for in vitro release of paclitaxel from formulation H-n-HAP/PTX and H-n-HAP/GO-PTX

PTX Loaded samples	Time (hours)	Cumulative PTX release %	% Remaining PTX bioactive ingredient	Square root of time	log % remaining PTX bioactive substance	Time log	log Cumulative PTX release %	(Wt)	Wo-Wt
H-n-HAP	1-2	28.7-42.7	71.3-57.3	1.000-1.414	1.853-1.758	0.000-0.301	0.000-1.630	4.147-3.855	0.000-0.787
	4-6	58.7-67.9	41.3-32.1	2.000-2.449	1.616-1.507	0.602-0.778	1.769-1.832	3.457-3.178	1.185-1.464
	8-24	88.8-92.7	11.2-7.3	2.828-4.899	1.049-0.863	0.903-1.380	1.948-1.967	2.237-1.940	2.405-2.702
H-n-HAP/GO	1-2	33.3-48.9	66.7-51.1	1.000-1.414	1.824-1.708	0.000-0.301	0.000-1.689	4.055-3.711	0.000-0.931
	4-6	64.2-71.3	35.8-28.7	2.000-2.449	1.554-1.458	0.602-0.778	1.808-1.853	3.296-3.062	1.346-1.580
	8-24	88.9-99.5	11.1-0.5	2.828-4.899	1.045-(-0.301)	0.903-1.380	1.949-1.998	2.231-0.794	2.411-3.848

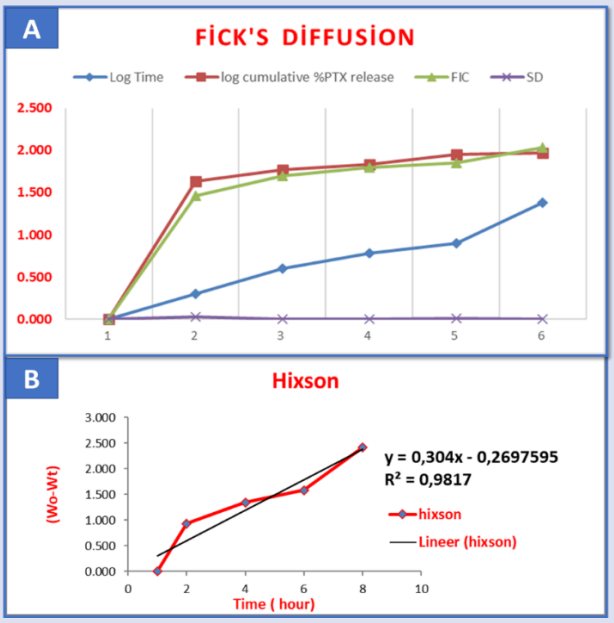

Figure 7. A. In vitro PTX release in Fick's diffusion law, B. Graphical representation of Hixson release model

During the preparation of PTX-loaded nanostructured composites from the co-delivery system PTX, GO carbon nanomaterials were chemically bound to the H-n-HAP structures and PTX molecules were physically loaded into the micelle core. The release profiles were pH-dependent, but the release mechanism needed to be studied. Here, the drug release mechanism was investigated using a comprehensive semi-empirical model. Based on the experimental data in Table 5, the drug release process was evaluated from 1-24 hours. The formulations used in this evaluation process were divided into two groups, H-n-HAP/PTX and H-n-HAP/GO/PTX. The results obtained according to the mathematical models of release kinetics in Table 5 are presented in a theoretical curve based on Fick's law (Figure 7.A). Here, it was observed that the release exponent (n) and rate constant (k) were by the Hixson model for the two stages of PTX release profiles (Figure 7.B). According to Fick's law, K=1.89, n=0.21, SSD=0.04, R^2=0.997, FIC=2.03, SD=0.004.

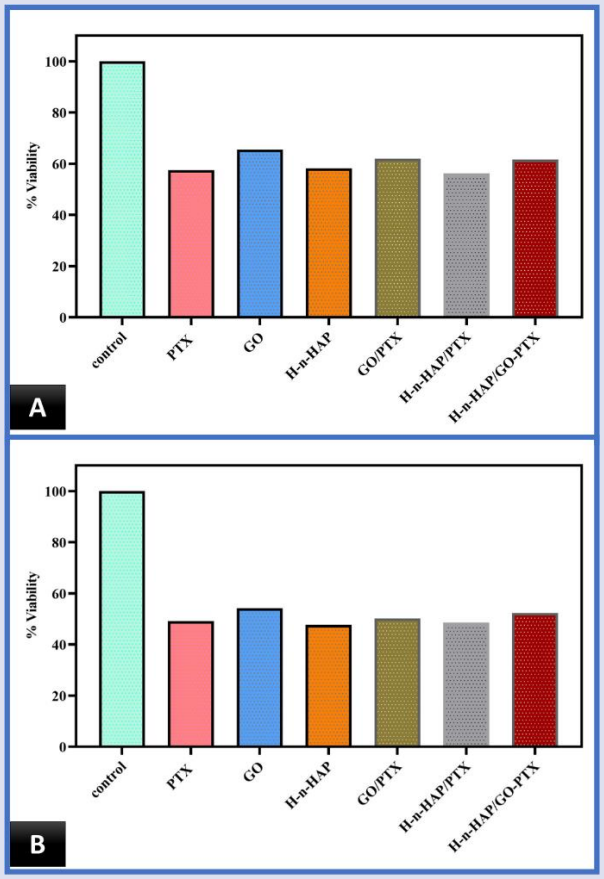

Figure 8. Graph for cell viability rate A. 10% concentration and B. 50% concentration

Cell Culture Study

In this graph, Figure 8.A shows the results of the MTT viability test for samples prepared at 10% concentration, while Figure 8.B shows the results of the MTT viability test for samples prepared at 50% concentration. At 10% concentration, the viability rate for H-n-HAP was 57.8%, for H-n-HAP/GO/PTX 59.8%, PTX 46.6%, H-n-HAP/GO 57.2% and PTX 48.8%. At 50% concentration, H-n-HAP viability was 40.5%, H-n-HAP/GO/PTX 49.5%, H-n-HAP/GO/PTX 38.8%, GO 43.4% and PTX 40.0%. As can be seen from the results, all samples were successful in

excluding cells in the pancreatic cancer cell line. As GO nanomaterials were loaded into the H-n-HAP nanocrystal structure, the effect of PTX drug on pancreatic cancer increased and the viability of cancer cells decreased. It can be concluded that H-n-HAP/GO/PTX nanocomposite structure kills more pancreatic cancer cells by synergetic effect [27], [28].

Simulation; In Silico Modelling

In the study, the absorption rate and duration of the 500 mg dose and its safety were modelled. This modelling for the bioavailability of PTX is a unique contribution to the literature. The low bioavailability of PTX is a factor that may reduce PTX efficacy. Although in vitro studies show the high efficacy of PTX in its biologically beneficial effects in cells, its distribution in tissues is known to be very low. Consequently, in vitro studies should be interpreted with caution when trying to predict their effect in vivo studies.

Due to its chemical and physical properties, PTX can passively cross cell membranes or interact with membrane receptors. It can therefore interact with extracellular and intracellular molecules. Its mechanism of action at the cellular level can therefore be triggered either by activating signalling pathways when binding to cell membrane receptors, by activating intracellular mechanisms, or even by developing its effects within the nucleus.

Controlled drug delivery devices have been envisioned in the reverse engineering framework for the controlled release of PTX, an anticancer drug widely used in the treatment of pancreatic cancer. A framework was established using quantitative structure-property relationship (QSPR) models for the mutual diffusion coefficients of PTX doped into the H-n-HAP/GO nanostructure we obtained as a biocompatible and biodegradable composite structure and the partition coefficients of the drug between polymers and blood. It was developed to predict optimal drug delivery devices for desired dosage regimens. In Franz diffusion modelling, release kinetics were based on Hixson. Based on the selected clinical application of pancreatic cancer, the optimal design parameters were estimated for the maximum bioavailability of the drug, along with the selection of the optimal polymeric composite H-n-HAP/GO suitable for different dosing regimens [29]–[31].

An *in-silico* fluid flow model with *in silico* assumptions (Figure 9.A and B) was used in Python program. In the reversible engineering problem, the objective was to maximize the bioavailability of the drug calculated in terms of AUC, while adjusting the drug concentration to ensure that the specified dosing regimens (24 h) remain within the therapeutic range. Genetic Algorithms (GA) implemented in Python were used to calculate Cmax, Tmax, and AUC. Python was used to simulate the drug release model (forward problem) while GA was used to solve the inverse problem. In GA, body weight was set to 70 and dose to 500 [32].

Table 6. *In vivo* Cp prediction from in vitro dissolution (AUC; area under the drug concentration and time curve)

Time	*1*	*2.00*	*4.00*	*6*	*8.00*	*24*	*Total amount after absorption*	*Con. (ng/ml) at a Time*	*[AUC $_{0-t}$]*
%PTX release	0	54	63	140	71.5	58.5			
	1	0					0	0.00	129.1454
	2.00	54					54	258.29	624.2379
	4.00	13.50735	63				76.51	365.95	1127.127
	6	3.378674	15.75857	140			159.14	761.18	1293.574
	8.00	0.845128	3.941787	35.01905	71.5		111.31	532.39	6497.742
	24.00	1.3E-05	6.04E-05	0.000537	0.001096	58.5	58.50	279.82	-3357.88

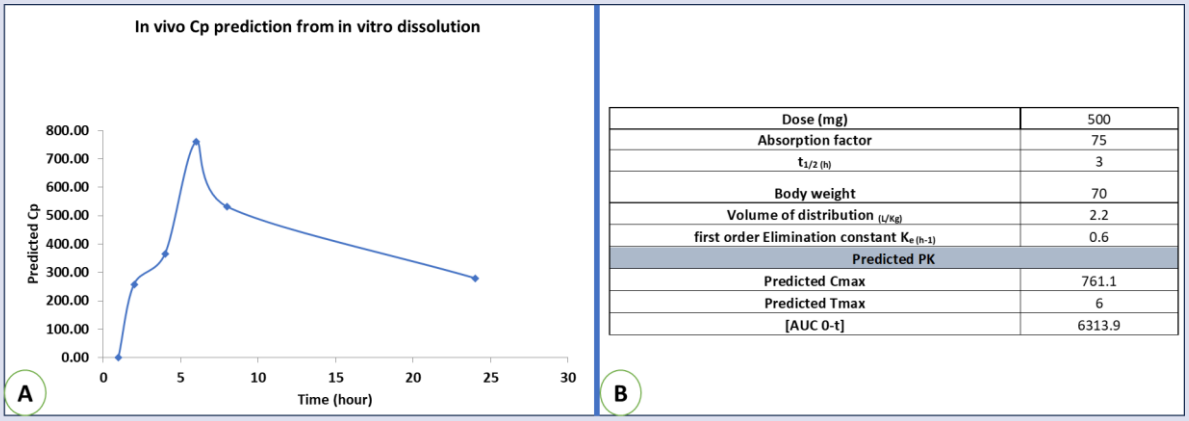

Figure 9. A. In vivo Cp prediction from in vitro dissolution, B. (Cmax; drug concentration in blood (mol/m3), Tmax; time at which the drug is desired to be released in the therapeutic range

Conclusion

The present study reverses engineered diffusion-controlled drug delivery devices of PTX, a drug used effectively in pancreatic cancer, by doping hydrothermally synthesized n-HAP crystals with GO, a surface activating carbon nanomaterial. The feasibility of the proposed approach was established using diffusion-controlled release of PTX, an established anti-cancer drug for the treatment of solid cancer. The synthesis of n-HAPs by hydrothermal method provides a large surface area, while GO-doped drug release kinetics are found to be enhanced. Mathematical models should be developed to design drug delivery systems in cancer types such as pancreatic cancer and should be actively used in in vivo and in vitro studies.

Conflicts of interest

The authors stated that did not have conflict of interests.

References

[1] V. Andretto, A. Rosso, S. Briançon, and G. Lollo, Nanocomposite systems for precise oral delivery of drugs and biologics, *Drug Deliv Transl Res.*, 11(2) 2021 445–470.

[2] F. Ciftci, Release kinetics modelling and in vivo-vitro, shelf-life study of resveratrol added composite transdermal scaffolds, *Int J Biol Macromol*., 235 (2023) 123769.

[3] S. Javanbakht and H. Namazi, Doxorubicin loaded carboxymethyl cellulose/graphene quantum dot nanocomposite hydrogel films as a potential anticancer drug delivery system, *Mater Sci Eng C.*, 87 (2018) 50–59.

[4] M. J. Mitchell, M. M. Billingsley, R. M. Haley, M. E. Wechsler, N. A. Peppas, and R. Langer, Engineering precision nanoparticles for drug delivery, *Nature Reviews Drug Discovery.*, 20(2) (2021) 101–124.

[5] Venkata V.V., Omathanu P.P., Nanosystems for Dermal and Transdermal Drug Delivery, in *Drug Delivery Nanoparticles Formulation and Characterization.*, 1st Edition. CRC Press, (2020) 146–175.

[6] A. C. Özarslan, C. Özel, M. D. Okumuş, D. Doğan, and S. Yücel, Development, structural and rheological characterization, and in vitro evaluation of the zinc-doped 45S5 bioactive glass-vaseline ointment for potential wound healing applications, *J Mater Res*, (2023).

[7] S. Hussain and K. Sabiruddin, Synthesis of eggshell based hydroxyapatite using hydrothermal method, *IOP Conf Ser Mater Sci Eng.*, 1189(1) (2021).

[8] H. S. Liu *et al.*, Hydroxyapatite synthesized by a simplified hydrothermal method, *Ceram Int.*, 23(1) (1997) 19–25.

[9] Y. P. Guo, Y. B. Yao, C. Q. Ning, Y. J. Guo, and L. F. Chu, Fabrication of mesoporous carbonated hydroxyapatite microspheres by hydrothermal method, *Mater Lett.*, 65(14) (2011) 2205–2208.

[10] G. Zhang, J. Chen, S. Yang, Q. Yu, Z. Wang, and Q. Zhang, Preparation of amino-acid-regulated hydroxyapatite particles by hydrothermal method, *Mater Lett.*, 65(3) (2011) 572–574.

[11] A. Razaq, F. Bibi, X. Zheng, R. Papadakis, S. H. M. Jafri, and H. Li, Review on Graphene-, Graphene Oxide-, Reduced Graphene Oxide-Based Flexible Composites: From Fabrication to Applications, *Materials*, (2022).

[12] A. Jiříčková, O. Jankovský, Z. Sofer, and D. Sedmidubský, Synthesis and Applications of Graphene Oxide, *Materials*., (2022).

[13] A. Raslan, L. Saenz del Burgo, J. Ciriza, and J. Luis Pedraz, Graphene oxide and reduced graphene oxide-based scaffolds in regenerative medicine, *Int J Pharm*, 580 (2020) 119226.

[14] C. Daulbayev *et al.*, Effect of graphene oxide/hydroxyapatite nanocomposite on osteogenic differentiation and antimicrobial activity, *Surfaces and Interfaces.*, (2022).

[15] F. Ciftci *et al.*, Selenium and clarithromycin loaded PLA-GO composite wound dressings by electrospinning method, *Int J Polym Mater Polym Biomater.*, (2022).

[16] M. S. Al Mogbel, M. T. Elabbasy, M. F. H. Abd El-Kader, R. S. Mohamed, M. E. Moustapha, and A. A. Menazea, Morphological, mechanical, and antibacterial investigation of a ternary nanocomposite contains hydroxyapatite, tellurium(IV) oxide (Te2O4), and graphene oxide in vitro, *Appl Phys A Mater Sci Process.*, (2022).

[17] Z. Benzait, P. Chen, and L. Trabzon, Enhanced synthesis method of graphene oxide, *Nanoscale Adv.*, (2021).

[18] F. Ciftci *et al.*, Antibacterial and cellular behavior of PLA-based bacitracin and zataria multiflora nanofibers produced by electrospinning method, *Int J Polym Mater Polym Biomater*, 72(4) (2023) 319–334.

[19] B. Wójcik *et al.*, Effects of metallic and carbon-based nanomaterials on human pancreatic cancer cell lines aspc-1 and bxpc-3, *Int J Mol Sci.*, 22(2) (2021).

[20] S. S. Kim *et al.*, Hyperthermal paclitaxel-bound albumin nanoparticles co-loaded with indocyanine green and hyaluronidase for treating pancreatic cancers, *Arch Pharm Res.*, 44(2) (2021) 182–193.

[21] K. Lin *et al.*, Selective laser sintered nano-HA/PDLLA composite microspheres for bone scaffolds applications, *Rapid Prototyp J.*, (2020).

[22] Y. Chen *et al.*, Dual Template, Three-Dimensional Hierarchical Porous Scaffolds Based on Graphene Oxide for Bone Tissue Engineering, *ECS Meet Abstr.*, (2020).

[23] J. Prakash, D. Prema, K. S. Venkataprasanna, K. Balagangadharan, N. Selvamurugan, and G. D. Venkatasubbu, Nanocomposite chitosan film containing graphene oxide/hydroxyapatite/gold for bone tissue engineering, *Int J Biol Macromol.*, (2020).

[24] A. C. Özarslan and S. Yücel, Comprehensive assessment of SrO and CuO co-incorporated 50S6P amorphous silicate bioactive glasses in vitro: Revealing bioactivity properties of bone graft biomaterial for bone tissue engineering applications, *Ceram Int.*, (2023).

[25] I. P. Khosalim, Y. Y. Zhang, C. K. Y. Yiu, and H. M. Wong, Synthesis of a graphene oxide/agarose/hydroxyapatite biomaterial with the evaluation of antibacterial activity and initial cell attachment, *Sci Rep.*, (2022).

[26] F. Miculescu *et al.*, Considerations and Influencing Parameters in EDS Microanalysis of Biogenic Hydroxyapatite, *J Funct Biomater.*, (2020).

[27] A. C. Özarslan, Y. B. Elalmis, and S. Yücel, Production of biosilica based bioactive glass-alginate composite putty as bone support material, and evaluation of in vitro properties; bioactivity and cytotoxicity behavior, *J Non Cryst Solids*, (2021).

[28] M. N. Ozder, F. Ciftci, O. Rencuzogullari, E. D. Arisan, and C. B. Ustündag, In situ synthesis and cell line studies of nano-hydroxyapatite/graphene oxide composite materials for bone support applications, *Ceram Int.*, (2023).

[29] M. Ikram *et al.*, Photocatalytic and antibacterial activity of graphene oxide/cellulose-doped TiO2 quantum dots: in silico molecular docking studies, *Nanoscale Adv.*, 4(18) (2022) 3764–3776.

[30] A. Alangari *et al.*, Antimicrobial, anticancer, and biofilm inhibition studies of highly reduced graphene oxide (HRG): In vitro and in silico analysis, *Front Bioeng Biotechnol.*, 11 (2023).

[31] E. Peng, N. Todorova, and I. Yarovsky, Effects of Size and Functionalization on the Structure and Properties of Graphene Oxide Nanoflakes: An in Silico Investigation, *ACS Omega.*, 3(9) (2018) 11497–11503.

[32] P. S. Gade, R. M. Sonkar, and P. Bhatt, Graphene oxide-mediated fluorescence turn-on GO-FAM-FRET aptasensor for detection of sterigmatocystin, *Anal Methods.*, 14(39) (2022) 3890–3897.

Cumhuriyet Sci. J., 44(2) (2023) 315-327
DOI: https://doi.org/10.17776/csj.1173496

Cumhuriyet Science Journal

| csj.cumhuriyet.edu.tr | Founded: 2002 ISSN: 2587-2680 e-ISSN: 2587-246X Publisher: Sivas Cumhuriyet University

Parametric Extension of a Certain Family of Summation-Integral Type Operators

Nadire Fulda Odabaşı [1,a,*], İsmet Yüksel [1,b]

[1] *Department of Mathematics, Faculty of Sciences, Gazi University, Ankara, Türkiye.*

**Corresponding author*

Research Article

History
Received: 10/09/2022
Accepted: 24/02/2023

ABSTRACT

In this paper, we introduce a parametric extension of a certain family of summation-integral type operators on the interval [0,∞). Firstly, we obtain test functions and central moments. Secondly, we investigate weighted approximation properties for these operators and estimate the rate of convergence. Then, we give a pointwise approximation for the Peetre K-functional and functions of the Lipschitz class. Moreover, we demonstrate Voronovskaja type theorem for the operators. Finally, the convergence properties of operators to some functions are illustrated by graphics.

Keywords: Rate of convergence, Weighted spaces, Weighted modulus of continuity.

[a] *nadirefulda.odabasi@gazi.edu.tr* *https://orcid.org/0000-0001-5825-1177* [b] *iyuksel@gazi.edu.tr* *https://orcid.org/0000-0002-2631-2382*

Introduction

Approximation to real-valued continuous functions with the help of positive linear operators is an important area in the approximation theory. All studies in this area originate from the Weierstrass theory [1]. A sequence of positive linear operators was introduced by Baskakov in 1957 [2], and in 1967, Durrmeyer defined a sequence of positive linear operators [3]. In 1977, Phillips defined an operator [4]. In 2003, Gupta introduced a general sequence of summation integral type operators $G_{n,c}$ [5], and then the approximation properties of the operators $G_{n,c}$ for continuous and unbounded functions specified on the interval [0,∞) were studied by Yüksel and İspir [6,7]. Chen, Tan and Liu studied on generalized Bernstein operators [8]. Later, Cai, Lian and Zhou introduced λ-Bernstein operators with parameter $\lambda\in[-1,1]$ [9]. Recently, Aral proposed Baskakov operators which have a non-negative real parametric generalization [10]. A lot of studies concerning generalizations of a sequence of linear positive operators have been done by many researchers [11-31].

In this paper, motivated by the α-Baskakov operators by Aral [10], we introduce a parametric extension of summation integral type operators named them $G_{n,c}^{\alpha}$ operators and study the approximation properties of these operators.

$G_{n,c}^{\alpha}$ operators

Let us define $G_{n,c}^{\alpha}$ operators on subset of all continuous functions on $[0,\infty)$ for which the following integral exists finitely.

$$G_{n,c}^{\alpha}(f;x)=n\sum_{k=1}^{\infty}P_{n,k}^{\alpha}(x;c)\int_{0}^{\infty}P_{n+c,k-1}(t;c)\,f(t)dt+P_{n,0}^{\alpha}(x;c)f(0)$$

$$P_{n,k}^{\alpha}(x;c)=\begin{cases}e^{-nx}\dfrac{(nx)^k}{k!}, & if\ c=0\\ \dfrac{(cx)^{k-1}}{(1+cx)^{\frac{n}{c}+k-1}}\left\{\dfrac{\alpha cx}{(1+cx)}\dfrac{\Gamma\left(\frac{n}{c}+k\right)}{k!\,\Gamma\left(\frac{n}{c}\right)}+(1-\alpha)(cx)\dfrac{\Gamma\left(\frac{n}{c}+k\right)}{k!\,\Gamma\left(\frac{n}{c}\right)}\right\}, & if\ c\in\mathbb{N}\backslash\{0\}\ and\ k\in\{0,1\}\\ \dfrac{(cx)^{k-1}}{(1+cx)^{\frac{n}{c}+k-1}}\left\{\dfrac{\alpha cx}{(1+cx)}\dfrac{\Gamma\left(\frac{n}{c}+k\right)}{k!\,\Gamma\left(\frac{n}{c}\right)}-(1-\alpha)(1+cx)\dfrac{\Gamma\left(\frac{n}{c}+k-2\right)}{(k-2)!\,\Gamma\left(\frac{n}{c}\right)}+(1-\alpha)(cx)\dfrac{\Gamma\left(\frac{n}{c}+k\right)}{k!\,\Gamma\left(\frac{n}{c}\right)}\right\}, & if\ c\in\mathbb{N}\backslash\{0\}\ and\ k\in\mathbb{N}\backslash\{0,1\}\end{cases} \quad (1)$$

with

$$P_{n+c,k-1}(t;c)=\frac{\Gamma\left(\frac{n}{c}+k\right)}{(k-1)!\Gamma\left(\frac{n}{c}+1\right)}\frac{(cx)^{k-1}}{(1+cx)^{\frac{n}{c}+k}}. \quad (2)$$

Theorem 2.1 The $G_{n,c}^{\alpha}$operators for $f(x)$ satisfy the following equation for $n > c$.

$$G_{n,c}^{\alpha}(f;x) = \alpha G_{n,c}(f;x) + (1-\alpha)\tilde{G}_{n,c}(f;x),$$

where

$$\tilde{G}_{n,c}(f;x) = n\sum_{k=1}^{\infty} P_{n-c,k}(x;c)\int_0^{\infty} g_{n,k}(t;c)\,f(t)dt + P_{n-c,0}(x;c)f(0)$$

and

$$g_{n,k}(t;c) = \left[\left(1+\frac{k}{\frac{n-c}{c}}\right)P_{n+c,k-1}(t;c) - \left(\frac{k}{\frac{n-c}{c}}\right)P_{n+c,k}(t;c)\right].$$

Proof.

The following identities hold.

$$\left(1+\frac{k}{\frac{n-c}{c}}\right)\frac{\Gamma\left(\frac{n-c}{c}+k\right)}{k!\,\Gamma\left(\frac{n-c}{c}\right)} = \frac{\Gamma\left(\frac{n-c}{c}+k+1\right)}{k!\,\Gamma\left(\frac{n-c}{c}+1\right)}, \tag{3}$$

$$\frac{\Gamma\left(\frac{n-c}{c}+k\right)}{(k-1)!\,\Gamma\left(\frac{n-c}{c}+1\right)} = \left(\frac{k}{\frac{n-c}{c}}\right)\frac{\Gamma\left(\frac{n-c}{c}+k\right)}{k!\,\Gamma\left(\frac{n-c}{c}\right)}. \tag{4}$$

$$G_{n,c}^{\alpha}(f;x) = \alpha n\sum_{k=1}^{\infty}\frac{\Gamma\left(\frac{n}{c}+k\right)}{k!\,\Gamma\left(\frac{n}{c}\right)}\frac{(cx)^k}{(1+cx)^{\frac{n}{c}+k}}\int_0^{\infty} P_{n+c,k-1}(t;c)\,f(t)dt + \frac{\alpha}{(1+cx)^{\frac{n}{c}}}f(0) + (1-\alpha)\left(k_{n,c}^1(f;x) - k_{n,c}^2(f;x)\right)$$

where

$$k_{n,c}^1(f;x) = n\sum_{k=1}^{\infty}\frac{\Gamma\left(\frac{n-c}{c}+k+1\right)}{k!\,\Gamma\left(\frac{n-c}{c}+1\right)}\frac{(cx)^k}{(1+cx)^{\frac{n-c}{c}+k}}\int_0^{\infty} P_{n+c,k-1}(t;c)\,f(t)dt + \frac{1}{(1+cx)^{\frac{n-c}{c}}}f(0).$$

If we use equation (3), we get

$$k_{n,c}^1(f;x) = n\sum_{k=1}^{\infty}\left(1+\frac{k}{\frac{n-c}{c}}\right)\frac{\Gamma\left(\frac{n-c}{c}+k\right)}{k!\,\Gamma\left(\frac{n-c}{c}\right)}\frac{(cx)^k}{(1+cx)^{\frac{n-c}{c}+k}}\int_0^{\infty} P_{n+c,k-1}(t;c)\,f(t)dt + \frac{1}{(1+cx)^{\frac{n-c}{c}}}f(0)$$

$$= n\sum_{k=1}^{\infty}\frac{\Gamma\left(\frac{n-c}{c}+k\right)}{k!\,\Gamma\left(\frac{n-c}{c}\right)}\frac{(cx)^k}{(1+cx)^{\frac{n-c}{c}+k}}\int_0^{\infty}\left(1+\frac{k}{\frac{n-c}{c}}\right)P_{n+c,k-1}(t;c)\,f(t)dt + \frac{1}{(1+cx)^{\frac{n-c}{c}}}f(0).$$

Similarly, we have

$$k_{n,c}^2(f;x) = n\sum_{k=2}^{\infty}\frac{\Gamma\left(\frac{n-c}{c}+k-1\right)}{(k-2)!\,\Gamma\left(\frac{n-c}{c}+1\right)}\frac{(cx)^{k-1}}{(1+cx)^{\frac{n-c}{c}+k-1}}\int_0^{\infty} P_{n+c,k-1}(t;c)\,f(t)dt.$$

When we write $k+1$ instead of k in $k_{n,c}^2(f;x)$, we obtain

$$k_{n,c}^2(f;x) = n\sum_{k=1}^{\infty}\frac{\Gamma\left(\frac{n-c}{c}+k\right)}{(k-1)!\,\Gamma\left(\frac{n-c}{c}+1\right)}\frac{(cx)^k}{(1+cx)^{\frac{n-c}{c}+k}}\int_0^{\infty} P_{n+c,k}(t;c)\,f(t)dt.$$

Again, if we use equation (4), we get

$$k_{n,c}^2(f;x) = n\sum_{k=1}^{\infty}\left(\frac{k}{\frac{n-c}{c}}\right)\frac{\Gamma\left(\frac{n-c}{c}+k\right)}{k!\,\Gamma\left(\frac{n-c}{c}\right)}\frac{(cx)^k}{(1+cx)^{\frac{n-c}{c}+k}}\int_0^{\infty}P_{n+c,k}(t;c)\,f(t)dt$$

$$= n\sum_{k=1}^{\infty}\frac{\Gamma\left(\frac{n-c}{c}+k\right)}{k!\,\Gamma\left(\frac{n-c}{c}\right)}\frac{(cx)^k}{(1+cx)^{\frac{n-c}{c}+k}}\int_0^{\infty}\left(\frac{k}{\frac{n-c}{c}}\right)P_{n+c,k}(t;c)\,f(t)dt\,.$$

Finally, substracting $k_{n,c}^2(f;x)$ from $k_{n,c}^1(f;x)$, we have

$$k_{n,c}^1(f;x) - k_{n,c}^2(f;x) = n\sum_{k=1}^{\infty}\frac{\Gamma\left(\frac{n-c}{c}+k\right)}{k!\Gamma\left(\frac{n-c}{c}\right)}\frac{(cx)^k}{(1+cx)^{\frac{n-c}{c}+k}}\int_0^{\infty}\left[\left(1+\frac{k}{\frac{n-c}{c}}\right)P_{n+c,k-1}(t;c) - \left(\frac{k}{\frac{n-c}{c}}\right)P_{n+c,k}(t;c)\right]f(t)dt + \frac{1}{(1+cx)^{\frac{n-c}{c}}}f(0)$$

$$= n\sum_{k=1}^{\infty}\frac{\Gamma\left(\frac{n-c}{c}+k\right)}{k!\Gamma\left(\frac{n-c}{c}\right)}\frac{(cx)^k}{(1+cx)^{\frac{n-c}{c}+k}}\int_0^{\infty}g_{n,k}(t;c)\,f(t)dt + \frac{1}{(1+cx)^{\frac{n-c}{c}}}f(0)$$
$$= n\sum_{k=1}^{\infty}P_{n-c,k}(x;c)\int_0^{\infty}g_{n,k}(t;c)\,f(t)dt + P_{n-c,0}(x;c)f(0)$$
$$= \tilde{G}_{n,c}(f;x)$$

and proof of the Theorem 2.1 is completed.

According to Theorem 2.1, $G_{n,c}^{\alpha}$ operators are positive provided that $\alpha \in [0,1]$. Here, the operators reduce to $G_{n,c}$ operators [7] for $\alpha = 1$.

Lemma 2.1 Let $\sum_{k=0}^{\infty}k^m P_{n,k}^{\alpha}(x;c)$ be series of $P_{n,k}^{\alpha}$ base functions defined in equation (1). Then, we have the following equalities for $m \in \{0,1,2,3,4\}$.

(i) $\sum_{k=0}^{\infty}k^0 P_{n,k}^{\alpha}(x;c) = 1,$

(ii) $\sum_{k=0}^{\infty}k^1 P_{n,k}^{\alpha}(x;c) = nx - 2(1-\alpha)cx,$

(iii) $\sum_{k=0}^{\infty}k^2 P_{n,k}^{\alpha}(x;c) = nx - 4(1-\alpha)cx - 4nc(1-\alpha)x^2 + n(n+c)x^2,$

(iv) $\sum_{k=0}^{\infty}k^3 P_{n,k}^{\alpha}(x;c) = nx - 8(1-\alpha)cx - 18nc(1-\alpha)x^2 + 3n(n+c)x^2$
$-6nc(n+c)(1-\alpha)x^3 + n(n+c)(n+2c)x^3,$

(v) $\sum_{k=0}^{\infty}k^4 P_{n,k}^{\alpha}(x;c) = nx - 16c(1-\alpha)x - 64nc(1-\alpha)x^2$
$+7n(n+c)x^2 - 48nc(n+c)(1-\alpha)x^3$
$+6n(n+c)(n+2c)x^3 - 8nc(n+c)(n+2c)(1-\alpha)x^4$
$+n(n+c)(n+2c)(n+3c)x^4.$

Proof.

(i) $\sum_{k=0}^{\infty}k^0 P_{n,k}^{\alpha}(x;c) = \alpha\sum_{k=0}^{\infty}\frac{(cx)^k}{(1+cx)^{\frac{n}{c}+k}}\frac{\Gamma\left(\frac{n}{c}+k\right)}{k!\Gamma\left(\frac{n}{c}\right)} - (1-\alpha)\sum_{k=2}^{\infty}\frac{(cx)^{k-1}}{(1+cx)^{\frac{n}{c}+k-2}}\frac{\Gamma\left(\frac{n}{c}+k-2\right)}{(k-2)!\Gamma\left(\frac{n}{c}\right)}$
$+(1-\alpha)(1+cx)\sum_{k=0}^{\infty}\frac{(cx)^k}{(1+cx)^{\frac{n}{c}+k}}\frac{\Gamma\left(\frac{n}{c}+k\right)}{k!\Gamma\left(\frac{n}{c}\right)}.$

When we write $k+2$ instead of k in the second term of the above equation, we get

$$\sum_{k=0}^{\infty}k^0 P_{n,k}^{\alpha}(x;c) = \alpha\sum_{k=0}^{\infty}\frac{(cx)^k}{(1+cx)^{\frac{n}{c}+k}}\frac{\Gamma\left(\frac{n}{c}+k\right)}{k!\Gamma\left(\frac{n}{c}\right)} - (1-\alpha)\sum_{k=0}^{\infty}\frac{(cx)^k cx}{(1+cx)^{\frac{n}{c}+k}}\frac{\Gamma\left(\frac{n}{c}+k\right)}{k!\Gamma\left(\frac{n}{c}\right)}$$
$$+(1-\alpha)(1+cx)\sum_{k=0}^{\infty}\frac{(cx)^k}{(1+cx)^{\frac{n}{c}+k}}\frac{\Gamma\left(\frac{n}{c}+k\right)}{k!\Gamma\left(\frac{n}{c}\right)}$$
$$= \alpha - (1-\alpha)cx + (1-\alpha)(1+cx)$$
$$= 1.$$

(ii) $\sum_{k=0}^{\infty}k^1 P_{n,k}^{\alpha}(x;c) = \sum_{k=1}^{\infty}\frac{\alpha(cx)^k}{(1+cx)^{\frac{n}{c}+k}}\frac{\Gamma\left(\frac{n}{c}+k\right)}{k!\Gamma\left(\frac{n}{c}\right)}k - (1-\alpha)\sum_{k=2}^{\infty}\frac{(cx)^{k-1}}{(1+cx)^{\frac{n}{c}+k-2}}\frac{\Gamma\left(\frac{n}{c}+k-2\right)}{(k-2)!\Gamma\left(\frac{n}{c}\right)}k$
$(1-\alpha)(1+cx)\sum_{k=1}^{\infty}\frac{(cx)^k}{(1+cx)^{\frac{n}{c}+k}}\frac{\Gamma\left(\frac{n}{c}+k\right)}{k!\Gamma\left(\frac{n}{c}\right)}k\,.$

When we write $k+1$ instead of k in first and third terms of the above equation, we get

$$\sum_{k=0}^{\infty}k^1 P_{n,k}^{\alpha}(x;c) = \alpha\sum_{k=0}^{\infty}\frac{(cx)^{k+1}}{(1+cx)^{\frac{n}{c}+k+1}}\frac{\Gamma\left(\frac{n}{c}+k+1\right)}{(k+1)k!\Gamma\left(\frac{n}{c}\right)}(k+1) - (1-\alpha)\sum_{k=2}^{\infty}\frac{(cx)^{k-1}}{(1+cx)^{\frac{n}{c}+k-2}}\frac{\Gamma\left(\frac{n}{c}+k-2\right)}{(k-2)!\left(\frac{n}{c}\right)}k$$
$$+(1-\alpha)(1+cx)\sum_{k=0}^{\infty}\frac{(cx)^{k+1}}{(1+cx)^{\frac{n}{c}+k+1}}\frac{\Gamma\left(\frac{n}{c}+k+1\right)}{(k+1)k!\Gamma\left(\frac{n}{c}\right)}(k+1).$$

When we write $k+2$ instead of k in the second term of the above equation, we get

$$\begin{aligned}\sum_{k=0}^{\infty} k^1 P_{n,k}^{\alpha}(x;c) &= \alpha \sum_{k=0}^{\infty} \frac{(cx)^k cx}{(1+cx)^{\frac{n}{c}+k+1}} \frac{\Gamma\left(\frac{n}{c}+k+1\right)}{k!\Gamma\left(\frac{n}{c}\right)} - (1-\alpha)\sum_{k=0}^{\infty} \frac{(cx)^{k+1}}{(1+cx)^{\frac{n}{c}+k}} \frac{\Gamma\left(\frac{n}{c}+k\right)}{k!\Gamma\left(\frac{n}{c}\right)} \ (k+2) \\ &\quad +(1-\alpha)(1+cx)\sum_{k=0}^{\infty} \frac{(cx)^k cx}{(1+cx)^{\frac{n}{c}+k+1}} \frac{\Gamma\left(\frac{n}{c}+k+1\right)}{k!\Gamma\left(\frac{n}{c}\right)} \\ &= \alpha \sum_{k=0}^{\infty} \frac{(cx)^k cx}{(1+cx)^{\frac{n}{c}+k+1}} \frac{\Gamma\left(\frac{n}{c}+k+1\right)}{k!\Gamma\left(\frac{n}{c}\right)} - 2(1-\alpha)\sum_{k=0}^{\infty} \frac{(cx)^k cx}{(1+cx)^{\frac{n}{c}+k}} \frac{\Gamma\left(\frac{n}{c}+k\right)}{k!\Gamma\left(\frac{n}{c}\right)} \\ &\quad -(1-\alpha)\sum_{k=1}^{\infty} \frac{(cx)^k cx}{(1+cx)^{\frac{n}{c}+k}} \frac{\Gamma\left(\frac{n}{c}+k\right)}{k!\Gamma\left(\frac{n}{c}\right)} \ k + (1-\alpha)(1+cx)\sum_{k=0}^{\infty} \frac{(cx)^k cx}{(1+cx)^{\frac{n}{c}+k+1}} \frac{\Gamma\left(\frac{n}{c}+k+1\right)}{k!\Gamma\left(\frac{n}{c}\right)}.\end{aligned}$$

When we write $k+1$ instead of k in the third term of the above equation, we yield

$$\begin{aligned}\sum_{k=0}^{\infty} k^1 P_{n,k}^{\alpha}(x;c) &= \alpha \sum_{k=0}^{\infty} \frac{(cx)^k cx}{(1+cx)^{\frac{n}{c}+k+1}} \frac{\Gamma\left(\frac{n}{c}+k+1\right)}{k!\Gamma\left(\frac{n}{c}\right)} - 2(1-\alpha)\sum_{k=0}^{\infty} \frac{(cx)^k cx}{(1+cx)^{\frac{n}{c}+k}} \frac{\Gamma\left(\frac{n}{c}+k\right)}{k!\Gamma\left(\frac{n}{c}\right)} \\ &\quad -(1-\alpha)\sum_{k=0}^{\infty} \frac{(cx)^{k+1} cx}{(1+cx)^{\frac{n}{c}+k+1}} \frac{\Gamma\left(\frac{n}{c}+k+1\right)}{(k+1)k!\Gamma\left(\frac{n}{c}\right)} \ (k+1) \\ &\quad +(1-\alpha)(1+cx)\sum_{k=0}^{\infty} \frac{(cx)^k cx}{(1+cx)^{\frac{n}{c}+k+1}} \frac{\Gamma\left(\frac{n}{c}+k+1\right)}{k!\Gamma\left(\frac{n}{c}\right)}.\end{aligned}$$

When we multiply and divide first, third and fourth terms of the above equation with n/c, we get

$$\begin{aligned}\sum_{k=0}^{\infty} k^1 P_{n,k}^{\alpha}(x;c) &= \alpha \sum_{k=0}^{\infty} \frac{(cx)^k cx}{(1+cx)^{\frac{n}{c}+k+1}} \frac{\Gamma\left(\frac{n}{c}+k+1\right)}{k!\Gamma\left(\frac{n}{c}+1\right)} \frac{n}{c} - 2(1-\alpha)\sum_{k=0}^{\infty} \frac{(cx)^k cx}{(1+cx)^{\frac{n}{c}+k}} \frac{\Gamma\left(\frac{n}{c}+k\right)}{k!\Gamma\left(\frac{n}{c}\right)} \\ &\quad -(1-\alpha)\sum_{k=0}^{\infty} \frac{(cx)^k (cx)^2}{(1+cx)^{\frac{n}{c}+k+1}} \frac{\Gamma\left(\frac{n}{c}+k+1\right)}{k!\Gamma\left(\frac{n}{c}+1\right)} \frac{n}{c} + (1-\alpha)(1+cx)\sum_{k=0}^{\infty} \frac{(cx)^k cx}{(1+cx)^{\frac{n}{c}+k+1}} \frac{\Gamma\left(\frac{n}{c}+k+1\right)}{k!\Gamma\left(\frac{n}{c}+1\right)} \frac{n}{c} \\ &= \alpha nx - 2(1-\alpha)cx - (1-\alpha)ncx^2 + (1-\alpha)(1+cx)nx \\ &= nx - 2(1-\alpha)cx.\end{aligned}$$

We have proof (i) and (ii). Finally, making same process in (i) and (ii), we can obtain (iii), (iv) and (v) easily.

Lemma 2.2 Let $e_i(t) = t^i$, $n \neq jc$ and $j \leq i$ for every $i, j \in \{0,1,2,3,4\}$. We have

(i) $G_{n,c}^{\alpha}(e_0;x) = 1$,

(ii) $G_{n,c}^{\alpha}(e_1;x) = \frac{n+2(\alpha-1)c}{n-c}x$,

(iii) $G_{n,c}^{\alpha}(e_2;x) = \frac{n(n+c)+4(\alpha-1)nc}{(n-c)(n-2c)}x^2 + \frac{2n+6(\alpha-1)c}{(n-c)(n-2c)}x$,

(iv) $G_{n,c}^{\alpha}(e_3;x) = \frac{n(n+c)(n+2c)+6(\alpha-1)n(n+c)c}{(n-c)(n-2c)(n-3c)}x^3 + \frac{6n(n+c)+30(\alpha-1)nc}{(n-c)(n-2c)(n-3c)}x^2 + \frac{6n+24(\alpha-1)c}{(n-c)(n-2c)(n-3c)}x$,

(v) $G_{n,c}^{\alpha}(e_4;x) = \frac{n(n+c)(n+2c)(n+3c)+8(\alpha-1)n(n+c)(n+2c)c}{(n-c)(n-2c)(n-3c)(n-4c)}x^4 + \frac{12n(n+c)(n+2c)+84(\alpha-1)n(n+c)c}{(n-c)(n-2c)(n-3c)(n-4c)}x^3$

$+\frac{36n(n+c)+216(\alpha-1)nc}{(n-c)(n-2c)(n-3c)(n-4c)}x^2 + \frac{24n+120(\alpha-1)c}{(n-c)(n-2c)(n-3c)(n-4c)}x$.

Proof.

The following identities are derived from Beta functions and equation (2).

$$\int_0^{\infty} P_{n+c,k-1}(t;c)\, t^i dt = \frac{\Gamma\left(\frac{n}{c}+k\right)}{(k-1)!\,\Gamma\left(\frac{n}{c}+1\right)} \frac{B\left(k+i, \frac{n}{c}-i\right)}{c^{i+1}}. \tag{5}$$

From equation (5) and Lemma 2.1, we have

$$\begin{aligned}\text{(i) } G_{n,c}^{\alpha}(e_0;x) &= n\sum_{k=1}^{\infty} P_{n,k}^{\alpha}(x;c)\frac{1}{n} + P_{n,0}^{\alpha}(x;c) \\ &= \sum_{k=0}^{\infty} P_{n,k}^{\alpha}(x;c) \\ &= 1, \\ \text{(ii) } G_{n,c}^{\alpha}(e_1;x) &= n\sum_{k=1}^{\infty} P_{n,k}^{\alpha}(x;c)\frac{k}{n(n-c)}\end{aligned}$$

$$= \frac{1}{n-c}\sum_{k=0}^{\infty} P_{n,k}^{\alpha}(x;c)k$$
$$= \frac{n+2(\alpha-1)c}{n-c}x,$$

(iii) $G_{n,c}^{\alpha}(e_2;x) = n\sum_{k=1}^{\infty} P_{n,k}^{\alpha}(x;c)\frac{k(k+1)}{n(n-c)(n-2c)}$

$$= \sum_{k=0}^{\infty} P_{n,k}^{\alpha}(x;c)\frac{k^2}{(n-c)(n-2c)} + \sum_{k=0}^{\infty} P_{n,k}^{\alpha}(x;c)\frac{k}{(n-c)(n-2c)}$$
$$= \frac{1}{(n-c)(n-2c)}\sum_{k=0}^{\infty} P_{n,k}^{\alpha}(x;c)k^2 + \frac{1}{(n-c)(n-2c)}\sum_{k=0}^{\infty} P_{n,k}^{\alpha}(x;c)k$$
$$= \frac{n(n+c)+4(\alpha-1)nc}{(n-c)(n-2c)}x^2 + \frac{2n+6(\alpha-1)c}{(n-c)(n-2c)}x.$$

We have proof (i), (ii) and (iii). Finally, if we make same process in (i), (ii) and (iii), we obtain (iv) and (v) easily.

Lemma 2.3 Let $\eta_i(t) = (t-x)^i$, $i \in \{1,2,4\}$ and $n \neq jc,\ j \leq i$ for every $j \in \{0,1,2,3,4\}$. We have

(i)$G_{n,c}^{\alpha}(\eta_1;x) = \frac{c+2(\alpha-1)c}{(n-c)}x,$

(ii) $G_{n,c}^{\alpha}(\eta_2;x) = \frac{2(n+c)c+8(\alpha-1)c^2}{(n-c)(n-2c)}x^2 + \frac{2n+6(\alpha-1)c}{(n-c)(n-2c)}x,$

(iii) $G_{n,c}^{\alpha}(\eta_4;x) = \frac{12n^2c^2+156nc^3+24c^4+8(\alpha-1)c(24nc^2+24c^3)}{(n-c)(n-2c)(n-3c)(n-4c)}x^4$
$$+ \frac{24n^2c+264nc^2+12(\alpha-1)c(26nc+36c^2)}{(n-c)(n-2c)(n-3c)(n-4c)}x^3$$
$$+ \frac{12n^2+132nc+24(\alpha-1)c(5n+16c)}{(n-c)(n-2c)(n-3c)(n-4c)}x^2$$
$$+ \frac{24n+120(\alpha-1)c}{(n-c)(n-2c)(n-3c)(n-4c)}x$$

Weighted Approximation

$B_\rho[0,\infty)$ is the space of all functions that are defined on the unbounded interval $[0,\infty)$ satisfying the inequality

$$|f(x)| \leq M_f\rho(x),$$

where M_f is a positive constant only depending on function f and $\rho(x) = 1+\varphi(x)^2$. Here, $\varphi(x)$ is monotone increasing continuous function on the real axis. Also, let us define the spaces

$$C_\rho[0,\infty) = B_\rho[0,\infty) \cap C[0,\infty)$$

and

$$C_\rho^*[0,\infty) = \left\{f \in C_\rho[0,\infty): \lim_{x\to\infty}\frac{|f(x)|}{\rho(x)} < \infty\right\}$$

and endow them with the norm

$$\|f\|_\rho = \sup\left\{\frac{|f(x)|}{\rho(x)}: x \in [0,\infty)\right\}.$$

Theorem 3.1[32,33]
a) There exists a sequence of linear positive operators $A_n: C_\rho[0,\infty) \to B_\rho[0,\infty)$ such that

$$\lim_{n\to\infty}\|A_n(\varphi^\nu) - \varphi^\nu\|_\rho = 0, \quad \nu = 0,1,2, \tag{6}$$

and there exists a function $f^* \in C_\rho[0,\infty)\backslash C_\rho^*[0,\infty)$ with
$\lim_{n\to\infty}\|A_n(f^*) - f^*\|_\rho \geq 1.$

b) If conditions (6) are satisfied by a sequence of linear positive operators $A_n: C_\rho[0,\infty) \to B_\rho[0,\infty)$, then for every $f \in C_\rho^*[0,\infty)$, we have

$$\lim_{n\to\infty} \|A_n(f) - f\|_\rho = 0 .$$

Choosing $\rho(x) = 1 + x^2$, we obtain the following theorems.

Theorem 3.2 For every $f \in C_\rho^*[0,\infty)$, we have

$$\lim_{n\to\infty} \left\|G_{n,c}^{\alpha}(f) - f\right\|_\rho = 0.$$

Proof.

From Theorem 3.1, verifying the following three conditions is sufficient.

$$\lim_{n\to\infty} \left\|G_{n,c}^{\alpha}(e_i) - e_i\right\|_\rho = 0, \qquad i = 0,1,2. \tag{7}$$

Since $G_{n,c}^{\alpha}(e_0; x) = 1$, condition (7) holds for $i = 0$. From Lemma 2.2, we have the following inequality,

$$\begin{aligned}\left\|G_{n,c}^{\alpha}(e_1) - e_1\right\|_\rho &\le \sup_{x\ge 0} \frac{\left|\frac{n+2(\alpha-1)c}{n-c}x - x\right|}{1+x^2} \\ &\le \sup_{x\ge 0} \frac{\left|\frac{(2\alpha-1)c}{n-c}x\right|}{1+x^2} \\ &\le \left|\frac{(2\alpha-1)c}{n-c}\right|.\end{aligned}$$

Hence, for $\lim_{n\to\infty} \left\|G_{n,c}^{\alpha}(e_1) - e_1\right\|_\rho = 0$ which implies that the condition in (7) holds for $i = 1$.

Similarly, we can write the following inequality.

$$\begin{aligned}\left\|G_{n,c}^{\alpha}(e_2) - e_2\right\|_\rho &\le \sup_{x\ge 0} \frac{\left|\frac{n(n+c)+4(\alpha-1)nc}{(n-c)(n-2c)}x^2 + \frac{2n+6(\alpha-1)c}{(n-c)(n-2c)}x - x^2\right|}{1+x^2} \\ &\le \sup_{x\ge 0} \frac{\left|\left(\frac{4n\alpha c-2c^2}{(n-c)(n-2c)}\right)x^2 + \frac{2n+6(\alpha-1)c}{(n-c)(n-2c)}x\right|}{1+x^2} \\ &\le \left|\frac{4n\alpha c-2c^2+2n+6|\alpha-1|c}{(n-c)(n-2c)}\right|.\end{aligned}$$

Then, $\lim_{n\to\infty} \left\|G_{n,c}^{\alpha}(e_2) - e_2\right\|_\rho = 0$ which implies that the condition in (7) holds for $i = 2$.

Therefore, the proof is completed.

Rate of Convergence

We want to find the rate of convergence for the $G_{n,c}^{\alpha}$ operators in this section. As we know, if f isn't continuous uniformly on $[0,\infty)$, then $\omega(f,\delta)$ which is the usual first modulus of continuity doesn't tend to zero as $\delta \to 0$. For every $f \in C_\rho^*[0,\infty)$, a weighted modulus of continuity would be liked to define $\Omega(f,\delta)$ that tends to zero as $\delta \to 0$.

Let

$$\Omega(f,\delta) = \sup_{x\ge 0,|h|\le\delta} \frac{|f(x+h) - f(x)|}{(1+x^2)(1+h^2)}, \qquad \text{for } f \in C_\rho^*[0,\infty). \tag{8}$$

$\Omega(f,\delta)$ is called the weighted modulus of continuity of the function $f \in C_\rho^*[0,\infty)$ [34].

We will show that the weighted modulus of continuity defined in equation (8) has similar properties to the first modulus of continuity.

Lemma 4.1 [34] Let $f \in C_\rho^*[0,\infty)$. Then, we have

(i) $\Omega(f,\delta)$ is a monotonically increasing function of δ,

(ii) for every $f \in C_\rho^*[0,\infty)$, $\lim_{\delta\to 0^+} \Omega(f,\delta) = 0$,

(iii) for every $m \in \mathbb{N}$, $\Omega(f,m\delta) \le m\Omega(f,\delta)$,

(iv) for $\lambda \in \mathbb{R}^+$, $\Omega(f,\lambda\delta) \le (\lambda+1)\Omega(f,\delta)$.

Theorem 4.1 For $f \in C_{\rho}^{*}[0,\infty)$, $M > 0$ and $\bar{\rho}(x) = 1 + x^5$, we get

$$\left\|G_{n,c}^{\alpha}(f) - f\right\|_{\bar{\rho}} \leq M\Omega\left(f, \frac{1}{\sqrt{n}}\right).$$

.

Proof.

From the definition $\Omega(f,\delta)$ and Lemma 4.1(iv), we can write

$$|f(t) - f(x)| \leq (1 + (t-x)^2)(1+x^2)\left(1 + \frac{|t-x|}{\delta}\right)\Omega(f,\delta).$$

Then, we obtain

$$\begin{aligned}\left|G_{n,c}^{\alpha}(f(t) - f(x); x)\right| &\leq G_{n,c}^{\alpha}(|f(t) - f(x)|; x) \\ &\leq \Omega(f,\delta)(1+x^2)G_{n,c}^{\alpha}\left((1+(t-x)^2)\left(1+\frac{|t-x|}{\delta}\right); x\right) \\ &= \Omega(f,\delta)(1+x^2)\left[G_{n,c}^{\alpha}(1+(t-x)^2; x) + G_{n,c}^{\alpha}\left(\frac{|t-x|}{\delta}; x\right) + G_{n,c}^{\alpha}\left(\frac{|t-x|^3}{\delta}; x\right)\right]. \quad (9)\end{aligned}$$

Applying the Cauchy-Schwarz inequality to the second and third term of (9), we obtain

$$G_{n,c}^{\alpha}\left(\frac{|t-x|}{\delta}; x\right) \leq \sqrt{G_{n,c}^{\alpha}\left(\frac{|t-x|^2}{\delta^2}; x\right)}\sqrt{G_{n,c}^{\alpha}(1; x)}$$

and

$$G_{n,c}^{\alpha}\left(\frac{|t-x|^3}{\delta}; x\right) \leq \sqrt{G_{n,c}^{\alpha}((t-x)^4; x)}\sqrt{G_{n,c}^{\alpha}\left(\frac{|t-x|^2}{\delta^2}; x\right)}. \quad (10)$$

Due to (9) and (10) we get

$$G_{n,c}^{\alpha}(|f(t) - f(x)|; x) \leq \Omega(f,\delta)(1+x^2)\left[G_{n,c}^{\alpha}(1+(t-x)^2; x) + \frac{1}{\delta}\sqrt{G_{n,c}^{\alpha}((t-x)^2; x)} + \frac{1}{\delta}\sqrt{G_{n,c}^{\alpha}((t-x)^4; x)}\sqrt{G_{n,c}^{\alpha}((t-x)^2; x)}\right].$$

There exist positive constants M_1 and M_2 such that

$$G_{n,c}^{\alpha}(1+(t-x)^2; x) \leq M_1(1+x^2), \quad (11)$$

$$\sqrt{G_{n,c}^{\alpha}((t-x)^4; x)} \leq M_2(1+x^2). \quad (12)$$

Notice that from Lemma 2.3, we have

$$G_{n,c}^{\alpha}((t-x)^2; x) = \frac{2(n+c)c + 8(\alpha-1)c^2}{(n-c)(n-2c)}x^2 + \frac{2n + 6(\alpha-1)c}{(n-c)(n-2c)}x.$$

Hence, we get

$$\begin{aligned}\sqrt{G_{n,c}^{\alpha}\left(\frac{|t-x|^2}{\delta^2}; x\right)} &\leq \frac{1}{\delta}O\left(\frac{1}{\sqrt{n}}\right)\sqrt{(x+x^2)} \\ &\leq M_3\frac{(1+x)}{\delta\sqrt{n}}. \quad (13)\end{aligned}$$

Then, from (12) and (13) we yield

$$\sqrt{G_{n,c}^{\alpha}((t-x)^4; x)}\sqrt{G_{n,c}^{\alpha}\left(\frac{|t-x|^2}{\delta^2}; x\right)} \leq M_5\frac{1+x^3}{\delta\sqrt{n}}, \quad (14)$$

where $M_5 = M_2M_3M_4$ and $M_4 = \sup_{x\geq 0} \frac{(1+x^2)(1+x)}{1+x^3}$.

Lastly, from (11)−(14) and choosing $M_8 = M_1M_6 + M_3M_7 + M_5$ where $M_6 = \sup_{x\geq 0} \frac{1+x^2}{1+x^3}$, $M_7 = \sup_{x\geq 0} \frac{1+x}{1+x^3}$; choosing $M = M_8M_9$ where $M_9 = \sup_{x\geq 0} \frac{(1+x^2)(1+x^3)}{1+x^5}$ and choosing $\delta = \frac{1}{\sqrt{n}}$ then combining the estimate between (9) and (14), we end up with the result of

$$\left|G_{n,c}^{\alpha}(f(t) - f(x); x)\right| \leq M(1 + x^5)\Omega\left(f, \frac{1}{\sqrt{n}}\right).$$

Therefore, we reach the result of the theorem.

Pointwise approximation properties by $G_{n,c}^{\alpha}$

The usual modulus of continuity of $f \in \hat{C}_B[0,\infty)$ is given by

$$\omega(f,\delta) = \sup_{|x-y|\leq\delta} |f(x) - f(y)|, \tag{15}$$

where $\hat{C}_B[0,\infty)$ space of uniformly continuous and bounded functions on $[0,\infty)$.

Theorem 5.1 Let $f \in \hat{C}_B[0,\infty)$, then the following inequality holds

$$\left|G_{n,c}^{\alpha}(f;x) - f(x)\right| \leq 2\omega\left(f, \sqrt{\Theta_n(x)}\right),$$

where $\Theta_n(x) = G_{n,c}^{\alpha}(\eta_2; x)$.

Proof.

From Lemma 2.3 and Shisha Mond Theorem [35] which states that if $G_{n,c}^{\alpha}$ is a linear positive operator, then for any bounded function f we obtain

$$\begin{aligned}\left|G_{n,c}^{\alpha}(f;x) - f(x)\right| &\leq \omega(f,\delta)\left(1 + \frac{1}{\delta}\sqrt{G_{n,c}^{\alpha}(\eta_2; x)}\right)\\ &= \omega(f,\delta)\left(1 + \frac{1}{\delta}\sqrt{\Theta_n(x)}\right)\\ &\leq 2\omega\left(f, \sqrt{\Theta_n(x)}\right),\end{aligned}$$

where $\delta = \sqrt{\Theta_n(x)}$.

Now, we mention the rate of convergence of $G_{n,c}^{\alpha}$ whereby Peetre $\mathcal{K}$-functional [36].

Let us define the space $\hat{C}_B^2[0,\infty) = \{f \in \hat{C}_B[0,\infty): f', f'' \in \hat{C}_B[0,\infty)\}$ and endow it with the norm $\|f\|_{\hat{C}_B[0,\infty)} = \|f\|_{\hat{C}_B[0,\infty)} + \|f'\|_{\hat{C}_B[0,\infty)} + \|f''\|_{\hat{C}_B[0,\infty)}$ and $\hat{C}_B[0,\infty)$ with the norm $\|f\|_{\hat{C}_B[0,\infty)} = \sup\{|f(x)|: x \in [0,\infty)\}$.

For $g \in \hat{C}_B^2[0,\infty)$, $f \in \hat{C}_B[0,\infty)$ and $\delta > 0$, the Peetre $\mathcal{K}$-functional is defined by

$$\mathcal{K}(f,\delta) = \inf_{g\in\hat{C}_B^2[0,\infty)} \{\|f - g\|_{\hat{C}_B[0,\infty)} + \delta\|g''\|_{\hat{C}_B[0,\infty)}\}.$$

There exists an absolute constant $M \in \mathbb{R}^+$, such that

$$\mathcal{K}(f,\delta) \leq M\omega_2\left(f, \sqrt{\delta}\right),$$

where $\omega_2\left(f, \sqrt{\delta}\right)$ is the second order modulus of continuity of $f \in \hat{C}_B[0,\infty)$. $\omega_2\left(f, \sqrt{\delta}\right)$ defined as

$$\omega_2\left(f, \sqrt{\delta}\right) \leq \sup_{0<h\leq\sqrt{\delta}} \sup_{x,x+h\in[0,\infty)} |f(x + 2h) - 2f(x + h) + f(x)|.$$

Theorem 5.2 Let $f \in \hat{C}_B[0,\infty)$ and $x \in [0,\infty)$.Then, there exists a constant $M \in \mathbb{R}^+$ such that

$$\left|G_{n,c}^{\alpha}(f;x) - f(x)\right| \le 4M\omega_2\left(f,\sqrt{\delta_n(x)}\right) + \omega\left(f,\frac{2(\alpha-1)c+c}{n-c}x\right),$$

where $\delta_n(x) = \frac{2(n+c)c+8(\alpha-1)c^2}{(n-c)(n-2c)}x^2 + \frac{(2\alpha-1)^2c^2}{(n-c)(n-c)}x^2 + \frac{2n+6(\alpha-1)c}{(n-c)(n-2c)}x$, $n \neq c$ and $n \neq 2c$.

Proof.

Let $f \in \hat{C}_B[0,\infty)$ and $t \in [0,\infty)$. Then by Taylor's expansion we have

$$g(t) - g(x) = (t-x)g'(x) + \int_x^t (t-u)g''(u)du. \tag{16}$$

When we apply $G_{n,c}^{\alpha}$ to both sides of the above equation (16), we get $G_{n,c}^{\alpha}(t-x;x) \neq 0$. So, we must define an operator as follows

$$\breve{G}_{n,c}^{\alpha}(f;x) = G_{n,c}^{\alpha}(f;x) - f\left(\frac{n+2(\alpha-1)c}{n-c}x\right) + f(x). \tag{17}$$

Now, applying $\breve{G}_{n,c}^{\alpha}$ to both side of the equation (16), we get

$$\breve{G}_{n,c}^{\alpha}(g;x) - g(x) = \breve{G}_{n,c}^{\alpha}\left(\int_x^t (t-u)g''(u)du\,;x\right).$$

From the definition of equation (17), we yield

$$\breve{G}_{n,c}^{\alpha}(g;x) - g(x) = G_{n,c}^{\alpha}\left(\int_x^t (t-u)g''(u)du\,;x\right) - \int_x^{\frac{n+2(\alpha-1)c}{n-c}x}\left(\frac{n+2(\alpha-1)c}{n-c}x - u\right)g''(u)du + \int_x^x (x-u)g''(u)du.$$

Using linearity and positivity properties of $G_{n,c}^{\alpha}$, we write the inequality

$$\begin{aligned}\left|\breve{G}_{n,c}^{\alpha}(g;x) - g(x)\right| &\le \left|G_{n,c}^{\alpha}\left(\int_x^t (t-u)g''(u)du\,;x\right)\right| + \left|\int_x^{\frac{n+2(\alpha-1)c}{n-c}x}\left(\frac{n+2(\alpha-1)c}{n-c}x - u\right)g''(u)du\right| \\ &\le G_{n,c}^{\alpha}\left(\int_x^t |t-u||g''(u)|du\,;x\right) + \int_x^{\frac{n+2(\alpha-1)c}{n-c}x}\left|\frac{n+2(\alpha-1)c}{n-c}x - u\right||g''(u)|du.\end{aligned}$$

Then, we get

$$\left|\breve{G}_{n,c}^{\alpha}(g;x) - g(x)\right| \le \|g''\|_{\hat{C}_B[0,\infty)}\, G_{n,c}^{\alpha}((t-x)^2;x) + \|g''\|_{\hat{C}_B[0,\infty)}\left(\frac{n+2(\alpha-1)c}{n-c}x - x\right)^2.$$

From Lemma 2.3, we write

$$\begin{aligned}\left|\breve{G}_{n,c}^{\alpha}(g;x) - g(x)\right| &\le \|g''\|_{\hat{C}_B[0,\infty)}\left(\frac{2(n+c)c+8(\alpha-1)c^2}{(n-c)(n-2c)}x^2 + \frac{2n+6(\alpha-1)c}{(n-c)(n-2c)}x\right) \\ &\quad + \|g''\|_{\hat{C}_B[0,\infty)}\left(\frac{(2\alpha-1)^2c^2}{(n-c)(n-c)}x^2\right) \\ &= \|g''\|_{\hat{C}_B[0,\infty)}\left(\frac{2(n+c)c+8(\alpha-1)c^2}{(n-c)(n-2c)}x^2 + \frac{(2\alpha-1)^2c^2}{(n-c)(n-c)}x^2 + \frac{2n+6(\alpha-1)c}{(n-c)(n-2c)}x\right) \\ &= \|g''\|_{\hat{C}_B[0,\infty)}\,\delta_n(x),\end{aligned} \tag{18}$$

where $\delta_n(x) = \frac{2(n+c)c+8(\alpha-1)c^2}{(n-c)(n-2c)}x^2 + \frac{(2\alpha-1)^2c^2}{(n-c)(n-c)}x^2 + \frac{2n+6(\alpha-1)c}{(n-c)(n-2c)}x$.

From equation (17) for $f \in \hat{C}_B[0,\infty)$, we get

$$\begin{aligned}\left|\breve{G}_{n,c}^{\alpha}(f;x)\right| &\le \left|G_{n,c}^{\alpha}(f;x)\right| + \left|f\left(\frac{n+2(\alpha-1)c}{n-c}x\right)\right| + |f(x)| \\ &\le G_{n,c}^{\alpha}(|f|;x) + \|f\|_{\hat{C}_B[0,\infty)} + \|f\|_{\hat{C}_B[0,\infty)} \\ &\le 3\|f\|_{\hat{C}_B[0,\infty)}.\end{aligned} \tag{19}$$

From equation (17), we obtain

$$\left|G_{n,c}^{\alpha}(f;x)-f(x)\right| \leq \left|\widetilde{G}_{n,c}^{\alpha}((f-g);x)-(f-g)(x)\right| + \left|\widetilde{G}_{n,c}^{\alpha}(g;x)-g(x)\right| + \left|f\left(\frac{n+2(\alpha-1)c}{n-c}x\right)-f(x)\right|. \tag{20}$$

From (15) and (17)−(20), we yield

$$\left|G_{n,c}^{\alpha}(f;x)-f(x)\right| \leq 4\|f-g\|_{\hat{C}_B[0,\infty)} + \|g''\|_{\hat{C}_B[0,\infty)}\ \delta_n(x) + \omega\left(f,\frac{2(\alpha-1)c+c}{n-c}x\right).$$

Taking infimum on the right side of the above inequality overall $g \in \hat{C}_B^2[0,\infty)$, we get

$$\left|G_{n,c}^{\alpha}(f;x)-f(x)\right| \leq 4\mathcal{K}\left(f,\delta_n(x)\right) + \omega\left(f,\frac{2(\alpha-1)c+c}{n-c}x\right).$$

Consequently, we get

$$\left|G_{n,c}^{\alpha}(f;x)-f(x)\right| \leq 4M\omega_2\left(f,\sqrt{\delta_n(x)}\right) + \omega\left(f,\frac{2(\alpha-1)c+c}{n-c}x\right).$$

Theorem 5.3 Let $f \in \mathrm{Lip}_M(\sigma)$ with $M > 0$ and $0 < \sigma \leq 1$. Then the operators $G_{n,c}^{\alpha}$ satisfy

$$\left|G_{n,c}^{\alpha}(f;x)-f(x)\right| \leq M\left(\Theta_n(x)\right)^{\sigma/2},$$

where $\mathrm{Lip}_M(\sigma) := \left\{f \in \hat{C}_B[0,\infty) : |f(t)-f(x)| \leq M|t-x|^{\sigma},\ \ t,x \in [0,\infty)\right\}$.

Proof.

If f satisfies the Lipschitz conditions, we have

$$|f(t)-f(x)| \leq M|t-x|^{\sigma}. \tag{21}$$

By the linearity and positivity properties of $G_{n,c}^{\alpha}$ and inequality (21), we get

Thanks to Lemma 2.3 and using Hölder inequality with $p = \frac{2}{\sigma}$, $q = \frac{2}{2-\sigma}$,we have

$$\begin{aligned}\left|G_{n,c}^{\alpha}(f;x)-f(x)\right| &\leq MG_{n,c}^{\alpha}((t-x)^2;x)^{\sigma/2}\\ &= M\left(\frac{2(n+c)c+8(\alpha-1)c^2}{(n-c)(n-2c)}x^2 + \frac{2n+6(\alpha-1)c}{(n-c)(n-2c)}x\right)^{\sigma/2}\\ &= M\left(\Theta_n(x)\right)^{\sigma/2} \text{for } n \neq c \text{ and } n \neq 2c.\end{aligned}$$

Voronovskaja Type Theorem

Theorem 6.1 Let $f \in \hat{C}_B^2[0,\infty)$. Then the following equality holds

$$\lim_{n\to\infty} n\left(G_{n,c}^{\alpha}(f;x)-f(x)\right) = (2\alpha-1)(cx)f'(x) + (cx^2+x)f''(x).$$

.

Proof.

For any $x \geq 0$, using Lemma 2.3 we have

$$\lim_{n\to\infty} nG_{n,c}^{\alpha}(n_1;x) = (2\alpha-1)(cx), \tag{22}$$

$$\lim_{n\to\infty} nG_{n,c}^{\alpha}(n_2;x) = 2cx^2+2x, \tag{23}$$

$$\lim_{n\to\infty} n^2 G^{\alpha}_{n,c}(n_4; x) = 12c^2x^4 + 24cx^3 + 12x^2. \tag{24}$$

By using Taylor's formula, we write

$$f(t) = f(x) + f'(x)(t-x) + \frac{1}{2}f''(x)(t-x)^2 + \mu(t,x)(t-x)^2, \tag{25}$$

where $\mu(t;x)$ is Peano form of the remainder term and $\lim_{t\to x} \mu(t,x) = 0$.
When we apply $G^{\alpha}_{n,c}$ to (25) and use linearity of $G^{\alpha}_{n,c}$, we have

$$G^{\alpha}_{n,c}(f;x) - f(x) = f'(x)G^{\alpha}_{n,c}((t-x);x) + \frac{1}{2}f''(x)G^{\alpha}_{n,c}((t-x)^2;x) + G^{\alpha}_{n,c}(\mu(t,x)(t-x)^2;x). \tag{26}$$

When we multiply (26) by n, take the limit n goes to infinity and use (22) and (23), we achieve

$$\lim_{n\to\infty} n\left(G^{\alpha}_{n,c}(f;x) - f(x)\right) = (2\alpha-1)(cx)f'(x) + (cx^2+x)f''(x) + \lim_{n\to\infty} nG^{\alpha}_{n,c}(\mu(t,x)(t-x)^2;x). \tag{27}$$

If we use Cauchy-Schwarz inequality for the remainder term in equation (27), we obtain

$$nG^{\alpha}_{n,c}(\mu(t,x)(t-x)^2;x) \le \sqrt{G^{\alpha}_{n,c}(\mu^2(t,x);x)}\sqrt{n^2G^{\alpha}_{n,c}((t-x)^4;x)}.$$

.
Let $\psi(t,x) = \mu^2(t,x)$. Since $\psi(.,x)$ is continuous at $t \in [0,\infty)$ and $\lim_{t\to x} \mu(t,x) = 0$, we observe that

$$\lim_{t\to x} \mu^2(t,x) = \lim_{t\to x} \psi(t,x) = \psi(x,x) = 0. \tag{28}$$

When we use (24) and (28), we have

$$\lim_{n\to\infty} nG^{\alpha}_{n,c}(\mu(t,x)(t-x)^2;x) = 0. \tag{29}$$

Finally, from (27) and (29) we yield

$$\lim_{n\to\infty} n\left(G^{\alpha}_{n,c}(f;x) - f(x)\right) = (2\alpha-1)(cx)f'(x) + (cx^2+x)f''(x).$$

Therefore, we complete the proof.

Graphical Analysis

In this section, the convergence of the operators $G^{\alpha}_{5,c}$ with function $f(x) = x^2$ is illustrated in Figure 1 for different values of $\alpha = 1, \alpha = 1/10$ and $c = 1$ on the interval $[0,\infty)$. Also, the convergence of the operators $G^{\alpha}_{5,c}$ with the function $f(x) = x^3$ is illustrated in Figure 2 for different values of $\alpha = 1$, $\alpha = 1/10, \alpha = 1/1000$ and $c = 1$ on the interval $[0,\infty)$.

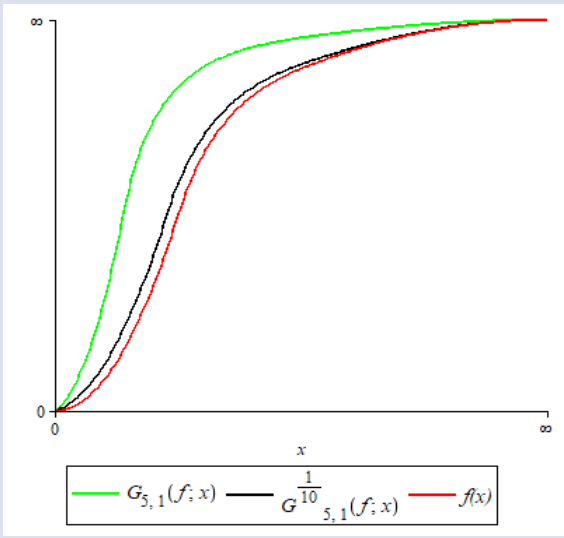

Figure 1. $n = 5$, $c = 1$ and $f(x) = x^2$

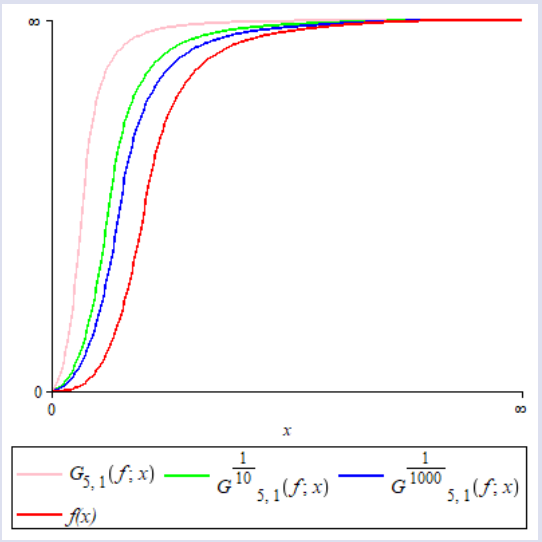

Figure 2. $n = 5$, $c = 1$ and $f(x) = x^3$

Acknowledgment

The authors would like to sincerely thank the editor and the reviewers for the helpful comments and suggestions.

Conflict of interests

The authors report no conflict of interest.

References

[1] Weierstrass K., Uber die analytische Darstellbarkeit sogenannter willkurlicher Functionen einer reellen Veranderlichen Sitzungsberichteder, *Koniglich Preussischen Akedemie der Wissenschcaften zu Berlin*, (1885) 633-639, 789-805.

[2] Baskakov V.A., An instance of sequance of linear positive operators in the space of continuous functions, *Dokl. Akad. Nauk. SSSR (N.S.)*, 113 (1957) 249-251.

[3] Durrmeyer J.L., Une Formule de d'inversion de la transform'ee de Laplace: applications`a la th'eorie des moments, *These de 3e cycle, Facult'e des Sciences de l'Universit'e de Paris*, (1967).

[4] May C.P., On Phillips operator, *J. Approximation Theory*, 20(4) (1977) 315–332.

[5] Srivastava H.M., Gupta V., A certain family of summation-integral type operators, *Math. Comput. Modelling*, 37(12-13) (2003) 1307-1315.

[6] İspir N., Yüksel İ., On the Bezier variant of Srivastava-Gupta operators, *Appl. Math. E-Notes,* 5 (2005) 129-137.

[7] Yüksel İ., İspir N., Weighted approximation by a certain family of summation integral-type operators, *Comput. Math. Appl.,* 52(10-11) (2006) 1463-1470.

[8] Chen X., Tan J., Liu Z., J.Xie J., Approximation of functions by a new family of generalized Bernstein operators. *J.Math. Anal. Appl.* 450 (2017), 244-261.

[9] Cai Q.-B., Lian B.-Y., Zhou G., Approximation properties of λ-Bernstein operators, *J. Inequal. Appl.,* 61 (2018) 1-11.

[10] Aral A., Erbay H., Parametric generalization of Baskakov operators, *Math. Commun*., 24(1) (2019) 119–131.

[11] Yüksel İ., Dinlemez Kantar Ü., Altın B., On approximation of Baskakov-Durrmeyer type operators of two variables, *Politehn. Univ. Bucharest Sci. Bull. Ser. A Appl. Math. Phys.,* 78(1) (2016) 123-134.

[12] İnce İlarslan H.G., Erbay H., Aral A., Kantorovich-type generalization of parametric Baskakov operators,*Math. Methods Appl. Sci.*, 42(18) (2019) 6580-6587.

[13] Nasiruzzaman Md., Rao N., Wazir S., Kumar R., Approximation on parametric extension of Baskakov-Durrmeyer operators on weighted spaces, *J. Inequal. Appl.,* 103 (2019).

[14] Cai Q.-B., Dinlemez Kantar Ü., Çekim B., Approximation properties for the genuine modified Bernstein-Durrmeyer-Stancu operators, *Appl. Math. J. Chinese Univ. Ser. B*, 35(4) (2020) 468-478.

[15] Mohiuddine S.A., Özger F., Approximation of functions by Stancu variant of Bernstein-Kantorovich operators based on shape parameter α, *Rev. R. Acad. Clenc. Exactas Fis. Nat. Ser. A Mat. RACSAM*, 114(70) (2020).

[16] Çetin N., Approximation by α-Bernstein-Schurer operator, *Hacet. J. Math. Stat*., 50(3) (2021) 732-743.

[17] Cai Q.-B., Torun G., Dinlemez Kantar Ü., Approximation properties of generalized λ-Bernstein-Stancu-Type operators, *J. Math*., (2021) 1-17.

[18] Sofyalıoğlu M., Kanat K., Çekim B., Parametric generalizaiton of the Meyer-König-Zeller operators, *Chaos Solitions Fractals*, 152 (2021).

[19] Cai Q.-B., Sofyalıoğlu M., Kanat K., Çekim B., Some approximation results for the new modification of Bernstein-Beta operators, *AIMS Math.*, 7(2) (2022) 1831-1844.

[20] Torun G., Mercan Boyraz M., Dinlemez Kantar Ü., Investigation of the asymptotic behavior of generalized Baskakov-Durrmeyer-Stancu type operators, *Cumhuriyet Sci. J.,* 43(1) (2022) 98-104.

[21] Mishra V.N., Patel P., Approximation properties of q-Baskakov-Durrmeyer-Stancu Operators, *Math. Sci*., 7 (2013) 38.

[22] Gupta V., Aral A., Some approximation properties of q-Baskakov-Durrmeyer operators, *Appl. Math. Comput*., 218(3) (2011) 783-788.

[23] Erdoğan S., Olgun A., Approximation properties of modified Jain-Gamma operators, *Carpathian Math. Publ*., 13(3) (2021) 651-665.

[24] Mishra V.N., Khatri K., Mishra L.N., Deepmala, Inverse result in simultaneous approximation by Baskakov-Durrmeyer-Stancu operators, *J. Inequal. Appl,* (2013) 586.

[25] Mishra V.N., Khatri K., Mishra L.N., Statistical approximation by Kantorovich type discrete q-beta operators, *Adv. Difference Equ.*, (2013) 345.

[26] Gandhi R.B., Deepmala, Mishra V.N., Local and global results for modified Szász-Mirakjan operators, *Math. Methods Appl. Sci.*, 40(7) (2017) 2491–2504.

[27] Mishra L.N., Pandey S., Mishra V.N., King type generalization of Baskakov operators based on (p,q) calculus with better approximation properties, *Analysis* 40(4) (2020) 163–173.

[28] Mishra L.N., Mishra V.N., Approximation by Jakimovski-Leviatan-Paltanea operators involving Boas-Buck-type polynomials, *Mathematics in Engineering, Science and Aerospace(MESA),* 12(4) (2021) 1153-1165.

[29] Sofyalıoğlu M., Kanat K., Approximation by the new modification of Bernstein-Stancu operators, *Cumhuriyet Sci. J.*, 42(4) (2021) 862-872.

[30] Raiz M., Kumar A., Mishra V.N., Rao N., Dunkl analogue of Szász-Schurer-Beta operators and their approximation behaviour, *Math. Found. Comput.*, 5 (2022) 315-330.

[31] Khatri K., Mishra V.N., Generalized Szász-Mirakyan operators involving Brenke type polynomials, *Appl. Math. Comput.*, 324 (2018) 228–238.

[32] Gadzhiev A.D., The convergence problem for a sequence of positive linear operators on unbounded sets, and theorems analogous to that of P.P. Korovkin, (in Russian)*, Dokl. Akad. Nauk. SSSR*, 218(5) (1974) 1001-1004; (in English)*, Sov. Math. Dokl.,* 15(5) (1974) 1433-1436.

[33] Gadzhiev A., Theorems of the type P.P. Korovkin type theorems, *Math. Zametki*, 20(5) (1976) 781-786; English Translation, *Math. Notes*, 20(5/6) (1976) 996-998.

[34] İspir N., On modified Baskakov operators on weighted spaces*, Turkish J. Math.*, 25(3) (2001) 355-365.

[35] Shisha O., Mond B., The degree of convergence of sequences of linear positive operators, *Proc. Nat. Acad. Sci. U.S.A.*, 60 (1968) 1196-1200.

[36] Peetre J., A theory of interpolation of normed spaces, notas de matematica 39, *Instituto de Matematica Pura e Aplicada, Conselho Nacional de Pesquisas, Rio de Janeiro*, (1968).

Cumhuriyet Sci. J., 44(2) (2023) 328-335
DOI: https://doi.org/10.17776/csj.1197746

Cumhuriyet Science Journal

| csj.cumhuriyet.edu.tr | Founded: 2002 ISSN: 2587-2680 e-ISSN: 2587-246X Publisher: Sivas Cumhuriyet University

The Intersection of Two Ruled Surfaces Corresponding to Spherical Indicatrix Curves on the Unit Dual Sphere

Yunus Öztemir [1,a,*], Mustafa Çalışkan [1,b]

[1] *Department of Mathematics, Faculty of Sciences, Gazi University, Ankara, Türkiye.*
**Corresponding author*

Research Article

History
Received: 01/11/2022
Accepted: 07/04/2023

ABSTRACT

In this study, we first investigate the intersection of two different ruled surfaces in $\mathbb{R}^3$ for two different tangential spherical indicatrix curves on DS^2 using the E. Study mapping. The conditions for the intersection of these ruled surfaces in $\mathbb{R}^3$ are expressed by theorems with bivariate functions. Secondly, considering two different principal normal spherical indicatrix curves on DS^2, we examine the intersection of two different ruled surfaces in $\mathbb{R}^3$ by using E. Study mapping. Similarly, the conditions for the intersection of these ruled surfaces in $\mathbb{R}^3$ are indicated by theorems with bivariate functions. Thirdly, using E. Study mapping, we explore the intersection of two different ruled surfaces in $\mathbb{R}^3$ by considering two different binormal spherical indicatrix curves on DS^2. Likewise, the conditions for the intersection of these ruled surfaces in $\mathbb{R}^3$ are denoted by theorems with bivariate functions. Fourthly, considering two different pole spherical indicatrix curves on DS^2, we study the intersection of two different ruled surfaces in $\mathbb{R}^3$ by using E. Study mapping. In the same way, the conditions for the intersection of these ruled surfaces in $\mathbb{R}^3$ are specified by theorems with bivariate functions. Finally, we provide some examples that support the main results.

Keywords: *Dual space, Dual sphere, Spherical indicatrix curve, Ruled surface, Surface intersection.*

[a] *yunusoztemir@gmail.com* *https://orcid.org/0000-0001-8292-1986* [b] *mustafacaliskan@gazi.edu.tr* *https://orcid.org/0000-0003-0342-571X*

Introduction

In geometry, surface theory has significant concepts in many disciplines such as surface modeling, kinematics, computer science, etc. One of the most important of these surfaces is the ruled surface. A ruled surface is represented by a straight line that moves along a curve [1]. Many authors have explored the application and geometric interpretation of ruled surfaces, see [2-4]. The surface-surface intersection problem (SSI) is also one of the significant research topics in geometry. B. U. Düldül and M. Çalışkan examined the unit tangent vector of the tangential intersection curve of two surfaces in all three types of SSI problems, see [5]. The intersections of parametric-parametric, implicit-implicit and parametric-implicit combinations of two surfaces are studied in detail, see [6]. For ruled surfaces, which are special cases of surfaces, the intersection of two ruled surfaces has been investigated. Furthermore, each connected component of the surface intersection curve corresponds to a connected component in the zero-set except for some singular points, redundant solutions and degenerate cases, see [7].

Dual numbers were first introduced by W. K. Clifford in 1873. Later, E. Study constructed the correspondence between the geometry of lines and the points of the unit dual sphere. E. Study says that there exists one-to-one correspondence between the oriented lines in Euclidean space and the points on the unit dual sphere. For more details on dual numbers, see [8]. Using the E. Study mapping, the curve on DS^2 corresponds to the ruled surfaces in $\mathbb{R}^3$, see [9-10]. Similarly, the spherical curves on DS^2 correspond to the ruled surfaces in $\mathbb{R}^3$, see [11].

In this article, we examine the intersections of two ruled surfaces corresponding to two different tangential spherical indicatrix curves, two different principal normal spherical indicatrix curves, two different binormal spherical indicatrix curves and two different pole spherical indicatrix curves on DS^2, respectively. Firstly, we consider the intersections of ruled surfaces corresponding to two different tangential spherical indicatrix curves on DS^2. Here, the intersection of the parameter curves of two ruled surfaces is shown by some theorems with the help of bivariate functions. Secondly, we investigate the intersections of ruled surfaces corresponding to two different principal normal spherical indicatrix curves on DS^2. In the same way, the intersection of the parameter curves of two ruled surfaces is given by some theorems with the help of bivariate functions. Thirdly, we discover the intersections of ruled surfaces corresponding to two different binormal spherical indicatrix curves on DS^2. Likewise, the intersection of the parameter curves of two ruled surfaces is expressed by some theorems with the help of bivariate functions. Fourthly, we explore the intersections of ruled surfaces corresponding to two different pole spherical indicatrix curves on DS^2. Similarly, the intersection of the parameter curves of two ruled surfaces is denoted by some theorems with the help of bivariate functions.

This study is organized as follows: In Section 2, we present the properties of dual vectors, dual spherical indicatrix curves, ruled surfaces and the intersection of two ruled surfaces. In Section 3, we examine the intersections of two ruled surfaces corresponding to two different tangential spherical indicatrix curves, two different principal normal spherical indicatrix curves, two different binormal spherical indicatrix curves, two different pole spherical indicatrix curves on the unit dual sphere DS^2, respectively. Additionally, we give some examples to illustrate the main theorems. In Section 4, we discussed the results obtained.

Preliminaries

In this section, we recall some basic definitions and theorems about dual vectors, dual spherical indicatrix curves, ruled surfaces and the intersection of two ruled surfaces.

The set of dual numbers is defined as

$$D = \{X = x + \varepsilon x^* : (x, x^*) \in \mathbb{R} \times \mathbb{R}, \varepsilon^2 = 0\}.$$

The combination of $\vec{x}$ and $\vec{x}^*$is called dual vectors in $\mathbb{R}^3$. These vectors are real part and dual part of $\vec{X}$, respectively. If $\vec{x}$ and $\vec{x}^*$are vectors in $\mathbb{R}^3$, then $\vec{X} = \vec{x} + \varepsilon\vec{x}^*$is defined as dual vector. Assume that $\vec{X} = \vec{x} + \varepsilon\vec{x}^*$and $\vec{Y} = \vec{y} + \varepsilon\vec{y}^*$ are dual vectors. The addition, inner product and vector product are presented as follows:
The addition is

$$\vec{X} + \vec{Y} = (\vec{x} + \vec{y}) + \varepsilon(\vec{x}^* + \vec{y}^*)$$

and their inner product is

$$\langle \vec{X}, \vec{Y} \rangle = \langle \vec{x}, \vec{y} \rangle + \varepsilon(\langle \vec{x}^*, \vec{y} \rangle + \langle \vec{x}, \vec{y}^* \rangle).$$

Also, the vector product is given as

$$\vec{X} \times \vec{Y} = \vec{x} \times \vec{y} + \varepsilon(\vec{x} \times \vec{y}^* + \vec{x}^* \times \vec{y}).$$

The norm of $\vec{X} = \vec{x} + \varepsilon\vec{x}^*$is defined as

$$|\vec{X}| = \sqrt{\langle \vec{x}, \vec{x} \rangle} + \varepsilon \frac{\langle \vec{x}, \vec{x}^* \rangle}{\sqrt{\langle \vec{x}, \vec{x} \rangle}}.$$

The norm of $\vec{X}$ exists only for $\vec{x} \neq 0$. If the norm of $\vec{X}$ is equal to 1, the dual vector is called unit dual vector. The unit dual sphere which consists of the all unit dual vectors is defined as

$$DS^2 = \{\vec{X} = \vec{x} + \varepsilon\vec{x}^* \in D^3 : |\vec{X}| = 1\}, \quad (1)$$

for detailed information on dual vectors, see [8].

Theorem 1 (E. Study mapping) There exists one-to-one correspondence between the oriented lines in $\mathbb{R}^3$ and the points of DS^2, see [8].

Theorem 2 Let $\bar{\alpha}(u) = \alpha(u) + \varepsilon\alpha^*(u)$ be a curve on DS^2. In $\mathbb{R}^3$, the ruled surface obtained by the curve $\bar{\alpha}(u)$ can be represented as

$$\phi(u, s) = \alpha(u) \times \alpha^*(u) + s\alpha(u), \quad (2)$$

where $C(u) = \alpha(u) \times \alpha^*(u)$ is the base curve of ϕ, see [9-10].

Definition 1 Let $\bar{\alpha} = \alpha + \varepsilon\alpha^*$ be a curve on DS^2. The dual Frenet vectors, dual curvature, dual torsion, dual Darboux vectors and dual pole vectors of this curve, respectively, can be presented as follows [11]:

$$\bar{T} = \bar{\alpha}', \quad \bar{N} = \frac{\bar{\alpha}''}{\|\bar{\alpha}''\|}, \quad \bar{B} = \bar{T} \times \bar{N}, \quad \bar{\kappa} = \langle \bar{T}', \bar{N} \rangle,$$
$$\bar{\tau} = \langle \bar{N}', \bar{B} \rangle, \quad \bar{W} = \bar{\tau}.\bar{T} + \bar{\kappa}.\bar{B}, \quad \bar{C} = \frac{\bar{W}}{\|\bar{W}\|}.$$

Theorem 3 Let $\bar{T}(u) = T(u) + \varepsilon T^*(u)$ be a tangential spherical indicatrix curve on DS^2. In $\mathbb{R}^3$, the ruled surface obtained by the curve $\bar{T}(u)$ can be shown as

$$\phi_{\bar{T}}(u, s) = T(u) \times T^*(u) + sT(u), \quad (3)$$

where $C_{\bar{T}}(u) = T(u) \times T^*(u)$ is the base curve of $\phi_{\bar{T}}$, see [9-11].

Theorem 4 Let $\bar{N}(u) = N(u) + \varepsilon N^*(u)$ be a principal normal spherical indicatrix curve on DS^2. In $\mathbb{R}^3$, the ruled surface obtained by the curve $\bar{N}(u)$ can be given as

$$\phi_{\bar{N}}(u, s) = N(u) \times N^*(u) + sN(u), \quad (4)$$

where $C_{\bar{N}}(u) = N(u) \times N^*(u)$ is the base curve of $\phi_{\bar{N}}$, see [9-11].

Theorem 5 Let $\bar{B}(u) = B(u) + \varepsilon B^*(u)$ be a binormal spherical indicatrix curve on DS^2. In $\mathbb{R}^3$, the ruled surface obtained by the curve $\bar{B}(u)$ can be expressed as

$$\phi_{\bar{B}}(u, s) = B(u) \times B^*(u) + sB(u), \quad (5)$$

where $C_{\bar{B}}(u) = B(u) \times B^*(u)$ is the base curve of $\phi_{\bar{B}}$, see [9-11].

Theorem 6 Let $\bar{C}(u) = C(u) + \varepsilon C^*(u)$ be a pole spherical indicatrix curve on DS^2. In $\mathbb{R}^3$, the ruled surface obtained by the curve $\bar{C}(u)$ can be denoted as

$$\phi_{\bar{C}}(u, s) = C(u) \times C^*(u) + sC(u), \quad (6)$$

where $C_{\bar{C}}(u) = C(u) \times C^*(u)$ is the base curve of $\phi_{\bar{C}}$, see [9-11].

Now, we give some proporties for the intersection curve of two ruled surfaces in $\mathbb{R}^3$.

Let $\phi^1(u, s)$ and $\phi^2(v, t)$ be two ruled surfaces defined by

$$\phi^1(u, s) = \eta_1(u) + se_1(u), \quad (7)$$

$$\phi^2(v, t) = \eta_2(v) + se_2(v). \quad (8)$$

Here, $\eta_1(u)$ and $\eta_2(v)$ are the base curves of surfaces $\phi^1(u,s)$ and $\phi^2(v,t)$, respectively.

The u-parameter curve of $\phi^1(u,s)$ with a constant s_0-parameter and the v-parameter curve of $\phi^2(v,t)$ with a constant t_0-parameter are denoted by $L_1(u)=\phi^1(u,s_0)$ and $L_2(v)=\phi^2(v,t_0)$, respectively, see [7].
If the ruled surfaces $\phi^1(u,s)$ and $\phi^2(v,t)$ intersect,

$$\phi^1(u,s)=\phi^2(v,t),$$

and we get

$$\eta_1(u)-\eta_2(v)=-se_1(u)+te_2(v).$$

Since these three vectors are linearly dependent, the following equation can be represented by [7]:

$$\lambda(u,v)=det\{e_1(u),e_2(v),[\eta_1(u)-\eta_2(v)]\}=0.$$

Theorem 7 Let $\phi^1(u,s)$ and $\phi^2(v,t)$ be two ruled surfaces in $\mathbb{R}^3$. If $\lambda(u,v)=0$, then the parameter curves $L_1(u)$ and $L_2(v)$ intersect, see [7].

In order to $\mu(u,v)=0$, $L_1(u)$ and $L_2(v)$ intersect. But, there are some points in the solution set of the equation $\mu(u,v)=0$ that is not at the intersection of these two ruled surfaces. The intersection contains these points when the directors of the ruled surfaces are $\phi^1(u,s)$ and $\phi^2(v,t)$ parallel. In this way, in the condition of parallelism of the direction vectors of two ruled surfaces, there may be some points that are not at the intersection of two ruled surfaces, see [7].

The parallelism of the direction vectors of the ruled surfaces $\phi^1(u,s)$ and $\phi^2(v,t)$ is expressed with bivariate functions as follows [7] :

$$\Delta(u,v)=\|e_1(u)\times e_2(v)\|^2.$$

The parallelism of $\eta_1(u)-\eta_2(v)$ and the direction vector of $\phi^1(u,s)$ are given by bivariate functions as follows [7] :

$$\delta_1(u,v)=\|e_1(u)\times[\eta_1(u)-\eta_2(v)]\|^2.$$

Similarly, the parallelism of $\eta_1(u)-\eta_2(v)$ and the direction vector of the $\phi^2(v,t)$ are presented with bivariate functions as follows [7] :

$$\delta_2(u,v)=\|e_2(v)\times[\eta_1(u)-\eta_2(v)]\|^2.$$

Theorem 8 The parameter curves $L_1(u)$ and $L_2(v)$ intersect if and only if

$$\Delta(u,v)=\delta_1(u,v)=\delta_2(u,v)=0,$$

see [7].

Intersection of Two Ruled Surfaces Corresponding to Spherical Indicatrix Curves on the Unit Dual Sphere

In this section, we examine the intersections of two ruled surfaces corresponding to two different tangential spherical indicatrix curves, two different principal normal spherical indicatrix curves, two different binormal spherical indicatrix curves, and two different pole spherical indicatrix curves on DS^2, respectively. Furthermore, we give some examples to support the main results.

Let $\bar{\alpha}_1=\alpha_1+\varepsilon\alpha_1^*$ and $\bar{\alpha}_2=\alpha_2+\varepsilon\alpha_2^*$ be two curves on DS^2. The tangential spherical indicatrix curves of these curves are $\bar{T}_1=T_1+\varepsilon T_1^*$ and $\bar{T}_2=T_2+\varepsilon T_2^*$, respectively. According to the E. Study mapping, $\phi_{\bar{T}_1}(u,s)$ and $\phi_{\bar{T}_2}(v,t)$ are the ruled surfaces corresponding to these tangential spherical indicatrix curves shown above in $\mathbb{R}^3$. These ruled surfaces are expressed as follows:

$$\phi_{\bar{T}_1}(u,s)=T_1(u)\times T_1^*(u)+sT_1(u), \tag{9}$$

$$\phi_{\bar{T}_2}(v,t)=T_2(v)\times T_2^*(v)+tT_2(v). \tag{10}$$

Here, the base curves of the ruled surfaces $\phi_{\bar{T}_1}(u,s)$ and $\phi_{\bar{T}_2}(v,t)$ are $C_{\bar{T}_1}(u)=T_1(u)\times T_1^*(u)$ and $C_{\bar{T}_2}(v)=T_2(v)\times T_2^*(v)$, respectively.

The u-parameter curve of $\phi_{\bar{T}_1}(u,s)$ with a constant s_0-parameter is represented by $L_{\bar{T}_1}(u)=\phi_{\bar{T}_1}(u,s_0)$. Similarly, the v-parameter curve of $\phi_{\bar{T}_2}(v,t)$ with a constant t_0-parameter is represented by $L_{\bar{T}_2}(v)=\phi_{\bar{T}_2}(v,t_0)$.

If $\phi_{\bar{T}_1}(u,s)$ and $\phi_{\bar{T}_2}(v,t)$ intersect, we can write

$$\phi_{\bar{T}_1}(u,s)=\phi_{\bar{T}_2}(v,t),$$

and

$$C_{\bar{T}_1}(u)-C_{\bar{T}_2}(v)=-sT_1(u)+tT_2(v).$$

Since these three vectors are linearly dependent, the following equation can be given

$$\lambda_{\bar{T}}(u,v)=det\{T_1(u),T_2(v),C_{\bar{T}_1}(u)-C_{\bar{T}_2}(v)\}=0.$$

Theorem 9 Let $\phi_{\bar{T}_1}(u,s)$ and $\phi_{\bar{T}_2}(v,t)$ be the two ruled surfaces corresponding to two different tangential spherical indicatrix curves on the unit dual sphere in $\mathbb{R}^3$. If $\lambda_{\bar{T}}(u,v)=0$, then the parameter curves $L_{\bar{T}_1}(u)$ and $L_{\bar{T}_2}(v)$ intersect.

According to the parallelism of these three vectors with each other, the bivariate functions are denoted as follows, respectively:

$$\Delta_{\bar{T}}(u,v)=\|T_1(u)\times T_2(v)\|^2,$$

$$\delta_{\bar{T}}^{1}(u,v) = \left\|T_1(u) \times \left[C_{\bar{T}_1}(u) - C_{\bar{T}_2}(v)\right]\right\|^2,$$

$$\delta_{\bar{T}}^{2}(u,v) = \left\|T_2(v) \times \left[C_{\bar{T}_1}(u) - C_{\bar{T}_2}(v)\right]\right\|^2.$$

Theorem 10 Let $L_{\bar{T}_1}(u)$ and $L_{\bar{T}_2}(v)$ be the parameter curves of the ruled surfaces $\phi_{\bar{T}_1}(u,s)$ and $\phi_{\bar{T}_2}(v,t)$, which correspond to two different tangential spherical indicatrix curves on DS^2. In this case, the parameter curves $L_{\bar{T}_1}(u)$ and $L_{\bar{T}_2}(v)$ intersect if and only if

$$\Delta_{\bar{T}}(u,v) = \delta_{\bar{T}}^{1}(u,v) = \delta_{\bar{T}}^{2}(u,v) = 0.$$

Let $\bar{\alpha}_1 = \alpha_1 + \varepsilon\alpha_1^*$ and $\bar{\alpha}_2 = \alpha_2 + \varepsilon\alpha_2^*$ be two curves on DS^2. The principal spherical indicatrix curves of these curves are $\bar{N}_1 = N_1 + \varepsilon N_1^*$ and $\bar{N}_2 = N_2 + \varepsilon N_2^*$, respectively. By the E. Study mapping, $\phi_{\bar{N}_1}(u,s)$ and $\phi_{\bar{N}_2}(v,t)$ are the ruled surfaces corresponding to these principal spherical indicatrix curves given above in $\mathbb{R}^3$. These ruled surfaces are denoted as follows:

$$\phi_{\bar{N}_1}(u,s) = N_1(u) \times N_1^*(u) + sN_1(u), \tag{11}$$

$$\phi_{\bar{N}_2}(v,t) = N_2(v) \times N_2^*(v) + tN_2(v). \tag{12}$$

Here, the base curves of the ruled surfaces $\phi_{\bar{N}_1}(u,s)$ and $\phi_{\bar{N}_2}(v,t)$ are $C_{\bar{N}_1}(u) = N_1(u) \times N_1^*(u)$ and $C_{\bar{N}_2}(v) = N_2(v) \times N_2^*(v)$.

The u-parameter curve of $\phi_{\bar{N}_1}(u,s)$ with a constant s_0-parameter is presented by $L_{\bar{N}_1}(u) = \phi_{\bar{N}_1}(u,s_0)$. Similarly, the v-parameter curve of $\phi_{\bar{N}_2}(v,t)$ with a constant t_0-parameter is given by $L_{\bar{N}_2}(v) = \phi_{\bar{N}_2}(v,t_0)$.

If $\phi_{\bar{N}_1}(u,s)$ and $\phi_{\bar{N}_2}(v,t)$ intersect, we can write
$\phi_{\bar{N}_1}(u,s) = \phi_{\bar{N}_2}(v,t)$,
and

$$C_{\bar{N}_1}(u) - C_{\bar{N}_2}(v) = -sN_1(u) + tN_2(v)$$

Since these three vectors are linearly dependent, the following equation can be expressed

$$\lambda_{\bar{N}}(u,v) = det\{N_1(u), N_2(v), C_{\bar{N}_1}(u) - C_{\bar{N}_2}(v)\} = 0.$$

Theorem 11 Let $\phi_{\bar{N}_1}(u,s)$ and $\phi_{\bar{N}_2}(v,t)$ be the two ruled surfaces corresponding to two different principal spherical indicatrix curves on the unit dual sphere in $\mathbb{R}^3$. If $\lambda_{\bar{N}}(u,v) = 0$, then the parameter curves $L_{\bar{N}_1}(u)$ and $L_{\bar{N}_2}(v)$ intersect.

According to the parallelism of these three vectors with each other, the bivariate functions are indicated as follows, respectively:

$$\Delta_{\bar{N}}(u,v) = \|N_1(u) \times N_2(v)\|^2,$$

$$\delta_{\bar{N}}^{1}(u,v) = \left\|N_1(u) \times \left[C_{\bar{N}_1}(u) - C_{\bar{N}_2}(v)\right]\right\|^2,$$

$$\delta_{\bar{N}}^{2}(u,v) = \left\|N_2(v) \times \left[C_{\bar{N}_1}(u) - C_{\bar{N}_2}(v)\right]\right\|^2.$$

Theorem 12 Let $L_{\bar{N}_1}(u)$ and $L_{\bar{N}_2}(v)$ be the parameter curves of the ruled surfaces $\phi_{\bar{N}_1}(u,s)$ and $\phi_{\bar{N}_2}(v,t)$, which correspond to two different principal spherical indicatrix curves on DS^2. In this case, the parameter curves $L_{\bar{N}_1}(u)$ and $L_{\bar{N}_2}(v)$ intersect if and only if

$$\Delta_{\bar{N}}(u,v) = \delta_{\bar{N}}^{1}(u,v) = \delta_{\bar{N}}^{2}(u,v) = 0.$$

Let $\bar{\alpha}_1 = \alpha_1 + \varepsilon\alpha_1^*$ and $\bar{\alpha}_2 = \alpha_2 + \varepsilon\alpha_2^*$ be two curves on DS^2. The binormal spherical indicatrix curves of these curves are $\bar{B}_1 = B_1 + \varepsilon B_1^*$ and $\bar{B}_2 = B_2 + \varepsilon B_2^*$, respectively. According to the E. Study mapping, $\phi_{\bar{B}_1}(u,s)$ and $\phi_{\bar{B}_2}(v,t)$ are the ruled surfaces corresponding to these binormal spherical indicatrix curves shown above in $\mathbb{R}^3$. These ruled surfaces are indicated as follows:

$$\phi_{\bar{B}_1}(u,s) = B_1(u) \times B_1^*(u) + sB_1(u), \tag{13}$$

$$\phi_{\bar{B}_2}(v,t) = B_2(v) \times B_2^*(v) + tB_2(v). \tag{14}$$

Here, the base curves of the ruled surfaces $\phi_{\bar{B}_1}(u,s)$ and $\phi_{\bar{B}_2}(v,t)$ are $C_{\bar{B}_1}(u) = B_1(u) \times B_1^*(u)$ and $C_{\bar{B}_2}(v) = B_2(v) \times B_2^*(v)$.

The u-parameter curve of $\phi_{\bar{B}_1}(u,s)$ with a constant s_0-parameter is given $L_{\bar{B}_1}(u) = \phi_{\bar{B}_1}(u,s_0)$. Similarly, The v-parameter curve of $\phi_{\bar{B}_2}(v,t)$ with a constant t_0-parameter is represented $L_{\bar{B}_2}(v) = \phi_{\bar{B}_2}(v,t_0)$.

If $\phi_{\bar{B}_1}(u,s)$ and $\phi_{\bar{B}_2}(v,t)$ intersect, we can write

$$\phi_{\bar{B}_1}(u,s) = \phi_{\bar{B}_2}(v,t),$$

and

$$C_{\bar{B}_1}(u) - C_{\bar{B}_2}(v) = -sB_1(u) + tB_2(v)$$

Since these three vectors are linearly dependent, the following equation can be denoted

$$\lambda_{\bar{B}}(u,v) = det\{B_1(u), B_2(v), C_{\bar{B}_1}(u) - C_{\bar{B}_2}(v)\} = 0.$$

Theorem 13 Let $\phi_{\bar{B}_1}(u,s)$ and $\phi_{\bar{B}_2}(v,t)$ be the two ruled surfaces corresponding to two different binormal spherical indicatrix curves on the unit dual sphere in $\mathbb{R}^3$. If $\lambda_{\bar{B}}(u,v) = 0$, then the parameter curves $L_{\bar{B}_1}(u)$ and $L_{\bar{B}_2}(v)$ intersect.

According to the parallelism of these three vectors with each other, the bivariate functions are expressed as follows, respectively:

$$\Delta_{\bar{B}}(u,v) = \|B_1(u) \times B_2(v)\|^2,$$

$$\delta_{\bar{B}}^{1}(u,v) = \left\|N_1(u) \times \left[C_{\bar{B}_1}(u) - C_{\bar{B}_2}(v)\right]\right\|^2,$$

$$\delta_{\bar{B}}^{2}(u,v) = \left\|B_2(v) \times \left[C_{\bar{B}_1}(u) - C_{\bar{B}_2}(v)\right]\right\|^2.$$

Theorem 14 Let $L_{\bar{B}_1}(u)$ and $L_{\bar{B}_2}(v)$ be the parameter curves of the ruled surfaces $\phi_{\bar{B}_1}(u,s)$ and $\phi_{\bar{B}_2}(v,t)$, which correspond to two different binormal spherical indicatrix curves on DS^2. In this case, the parameter curves $L_{\bar{B}_1}(u)$ and $L_{\bar{B}_2}(v)$ intersect if and only if

$$\Delta_{\bar{B}}(u,v) = \delta^1_{\bar{B}}(u,v) = \delta^2_{\bar{B}}(u,v) = 0.$$

Let $\bar{\alpha}_1 = \alpha_1 + \varepsilon\alpha_1^*$ and $\bar{\alpha}_2 = \alpha_2 + \varepsilon\alpha_2^*$ be two curves on the unit dual sphere DS^2. The pole spherical indicatrix curves of these curves are $\bar{C}_1 = C_1 + \varepsilon C_1^*$ and $\bar{C}_2 = C_2 + \varepsilon C_2^*$, respectively. By the E. Study mapping, $\phi_{\bar{C}_1}(u,s)$ and $\phi_{\bar{C}_2}(v,t)$ are the ruled surfaces corresponding to these pole spherical indicatrix curves taken above in $\mathbb{R}^3$. These ruled surfaces are given as follows:

$$\phi_{\bar{C}_1}(u,s) = C_1(u) \times C_1^*(u) + sC_1(u), \tag{15}$$

$$\phi_{\bar{C}_2}(v,t) = C_2(v) \times C_2^*(v) + tC_2(v). \tag{16}$$

Here, the base curves of the ruled surfaces $\phi_{\bar{C}_1}(u,s)$ and $\phi_{\bar{C}_2}(v,t)$ are $C_{\bar{C}_1}(u) = C_1(u) \times C_1^*(u)$ and $C_{\bar{C}_2}(v) = C_2(v) \times C_2^*(v)$.

The u-parameter curve of $\phi_{\bar{C}_1}(u,s)$ with a constant s_0-parameter is shown $L_{\bar{C}_1}(u) = \phi_{\bar{C}_1}(u,s_0)$. Similarly, the v-parameter curve of $\phi_{\bar{C}_2}(v,t)$ with a constant t_0-parameter is indicated $L_{\bar{C}_2}(v) = \phi_{\bar{C}_2}(v,t_0)$.
If $\phi_{\bar{C}_1}(u,s)$ and $\phi_{\bar{C}_2}(v,t)$ intersect, we can write

$$\phi_{\bar{C}_1}(u,s) = \phi_{\bar{C}_2}(v,t),$$

and

$$C_{\bar{C}_1}(u) - C_{\bar{C}_2}(v) = -sC_1(u) + tC_2(v)$$

Since these three vectors are linearly dependent, the following equation can be represented

$$\lambda_{\bar{C}}(u,v) = det\{C_1(u), C_2(v), C_{\bar{C}_1}(u) - C_{\bar{C}_1}(v)\} = 0.$$

Theorem 15 Let $\phi_{\bar{C}_1}(u,s)$ and $\phi_{\bar{C}_2}(v,t)$ be the two ruled surfaces corresponding to two different pole spherical indicatrix curves on the unit dual sphere in $\mathbb{R}^3$. If $\lambda_{\bar{C}}(u,v) = 0$, then the parameter curves $L_{\bar{C}_1}(u)$ and $L_{\bar{C}_2}(v)$ intersect.

According to the parallelism of these three vectors with each other, the bivariate functions are given as follows, respectively:

$$\Delta_{\bar{C}}(u,v) = \|C_1(u) \times C_2(v)\|^2,$$

$$\delta^1_{\bar{C}}(u,v) = \left\|C_1(u) \times \left[C_{\bar{C}_1}(u) - C_{\bar{C}_2}(v)\right]\right\|^2,$$

$$\delta^2_{\bar{C}}(u,v) = \left\|C_2(v) \times \left[C_{\bar{C}_1}(u) - C_{\bar{C}_2}(v)\right]\right\|^2.$$

Theorem 16 Let $L_{\bar{C}_1}(u)$ and $L_{\bar{C}_2}(v)$ be the parameter curves of the ruled surfaces $\phi_{\bar{C}_1}(u,s)$ and $\phi_{\bar{C}_2}(v,t)$, which correspond to two different pole spherical indicatrix curves on DS^2. In this case, the parameter curves $L_{\bar{C}_1}(u)$ and $L_{\bar{C}_2}(v)$ intersect if and only if

$$\Delta_{\bar{C}}(u,v) = \delta^1_{\bar{C}}(u,v) = \delta^2_{\bar{C}}(u,v) = 0.$$

Example 17. Let us consider $\bar{\alpha_1}(u) = (cos(u), sin(u), 0) + \varepsilon(-sin(u), cos(u), u^4)$ and $\bar{\alpha_2}(v) = (sin(v), cos(v), 0) + \varepsilon(-cos(v), sin(v), v^4)$. Since $\langle \alpha_1(u), \alpha_1^*(u)\rangle = 0$, $\langle \alpha_2(v), \alpha_2^*(v)\rangle = 0$ and $|\alpha_1(u)| = |\alpha_2(v)| = 1$, the $\bar{\alpha_1}(u)$ and $\bar{\alpha_2}(v)$ are on DS^2.

The dual tangential spherical indicatrix curves of the $\bar{\alpha_1}(u)$ and $\bar{\alpha_2}(v)$ are

$$\bar{T_1}(u) = (-sin(u), cos(u), 0) + \varepsilon(-cos(u), -sin(u), 4u^3),$$

$$\bar{T_2}(v) = (cos(v), -sin(v), 0) + \varepsilon(sin(v), cos(v), 4v^3).$$

The ruled surface corresponding to the $\bar{T_1}(u)$ is

$$\bar{\phi}_{\bar{T_1}}(u,s) = (4u^3\cos(u), 4u^3\sin(u), 1) + s(-\sin(u), \cos(u), 0)$$

where the base curve is $C_{\bar{T_1}}(u) = (4u^3\cos(u), 4u^3\sin(u), 1)$.

The ruled surface corresponding to the $\bar{T_2}(v)$ is

$$\bar{\phi}_{\bar{T_2}}(v,t) = (-4v^3\sin(v), -4v^3\cos(v), 1) + t(\cos(v), -\sin(v), 0)$$

where the base curve is $C_{\bar{T_2}}(v) = (-4v^3\sin(v), -4v^3\cos(v), 1)$.

Let's examine the intersection of two ruled surfaces corresponding to two different tangential spherical indicatrix curves on DS^2. Let $\bar{\phi}_{\bar{T_1}}(u,s) = \bar{\phi}_{\bar{T_2}}(v,t)$, the following equations can be written by

$$(4u^3\cos(u) + 4v^3\sin(v), 4u^3\sin(u) + 4v^3\cos(v), 0) = -s(-\sin(u), \cos(u), 0) + t(\cos(v), -\sin(v), 0).$$

Since $C_{\bar{T_1}}(u) - C_{\bar{T_2}}(v)$, $T_1(u)$ and $T_2(v)$ are linearly dependent, $\lambda_{\bar{T}}(u,v) = 0$. Hence, the parameter curves $L_{\bar{T_1}}(u)$ and $L_{\bar{T_2}}(v)$ intersect.
If $\Delta_{\bar{T}}(u,v), \delta^1_{\bar{T}}(u,v), \delta^2_{\bar{T}}(u,v)$ are calculated, we obtain

$$\Delta_{\bar{T}}(u,v) = (\cos(u+v))^2,$$

$$\delta^1_{\bar{T}}(u,v) = 16(u^3 + v^3\sin(u+v))^2,$$

$$\delta^2_{\bar{T}}(u,v) = 16(v^3 + u^3\sin(u+v))^2.$$

For the $\lambda_{\bar{T}}(u,v) = 0$, the solution of the $(u,v) = \left(\frac{3\pi}{4}, \frac{3\pi}{4}\right)$, $\Delta_{\bar{T}}(u,v) = \delta^1_{\bar{T}}(u,v) = \delta^2_{\bar{T}}(u,v) = 0$. Hence, the parameter curves $L_{\bar{T_1}}(u)$ and $L_{\bar{T_2}}(v)$ intersect. Then, $\bar{\phi}_{\bar{T_1}}(u,s)$ and $\bar{\phi}_{\bar{T_2}}(v,t)$ ruled surfaces intersect.

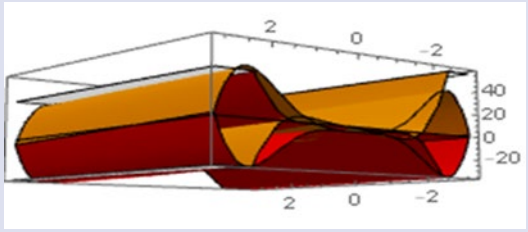

Figure 1. The intersection of $\bar{\phi}_{\bar{T}_1}$ and $\bar{\phi}_{\bar{T}_2}$ ruled surfaces.

The dual principal spherical indicatrix curves of the $\bar{\alpha}_1(u)$ and $\bar{\alpha}_2(v)$ are

$$\bar{N}_1(u) = (-\cos(u), -sin(u), 0) + \varepsilon(\sin(u), -\cos(u), 12u^2),$$

$$\bar{N}_2(v) = (-\sin(v), -\cos(v), 0) + \varepsilon(\cos(v), -\sin(v), 12v^2).$$

The ruled surface corresponding to the $\bar{N}_1(u)$ is

$$\bar{\phi}_{\bar{N}_1}(u,s) = (-12u^2\sin(u), 12u^2\cos(u), 1) + s(-\cos(u), -\sin(u), 0)$$

where the base curve is

$$C_{\bar{N}_1}(u) = (-12u^2\sin(u), 12u^2\cos(u), 1).$$

The ruled surface corresponding to the $\bar{N}_2(v)$ is

$$\bar{\phi}_{\bar{N}_2}(v,t) = (-12v^2\cos(v), 12v^2\sin(v), 1) + t(-\sin(v), -\cos(v), 0)$$

where the base curve is

$$C_{\bar{N}_2}(v) = (-12v^2\cos(v), 12v^2\sin(v), 1).$$

Let's examine the intersection of two ruled surfaces correspondig to two different principal normal spherical indicatrix curves DS^2. Let $\bar{\phi}_{\bar{N}_1}(u,s) = \bar{\phi}_{\bar{N}_2}(v,t)$, the following equation can be written by

$$(-12u^2\sin(u) + 12v^2\cos(v), 12u^2\cos(u) - 12v^2\sin(v), 0) = -s(-\cos(u), -\sin(u), 0) + t(-\sin(v), -\cos(v), 0).$$

Since $C_{\bar{N}_1}(u) - C_{\bar{N}_2}(v)$, $\bar{N}_1(u)$ and $\bar{N}_2(v)$ are linearly dependent, $\lambda_{\bar{N}}(u,v) = 0$. Therefore, the parameter curves $L_{\bar{N}_1}(u)$ and $L_{\bar{N}_2}(v)$ intersect.

If $\Delta_{\bar{N}}(u,v)$, $\delta^1_{\bar{N}}(u,v)$, $\delta^2_{\bar{N}}(u,v)$ are calculated, we obtain

$$\Delta_{\bar{N}}(u,v) = (\cos(u+v))^2,$$

$$\delta^1_{\bar{N}}(u,v) = 144(v^2\sin(u+v) - u^2)^2,$$

$$\delta^2_{\bar{N}}(u,v) = 144(v^2 - u^2\sin(u+v))^2.$$

For the $\lambda_{\bar{N}}(u,v) = 0$, the solution of the $(u,v) = \left(\frac{\pi}{4}, \frac{\pi}{4}\right)$, $\Delta_{\bar{N}}(u,v) = \delta^1_{\bar{N}}(u,v) = \delta^2_{\bar{N}}(u,v) = 0$. Therefore, the parameter curves $L_{\bar{N}_1}(u)$ and $L_{\bar{N}_2}(v)$ intersect. As a result, $\bar{\phi}_{\bar{N}_1}(u,s)$ and $\bar{\phi}_{\bar{N}_2}(v,t)$ ruled surfaces intersect.

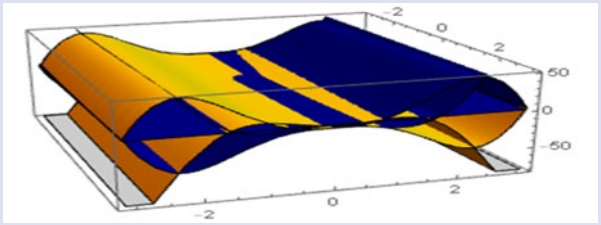

Figure 2. The intersection of $\bar{\phi}_{\bar{N}_1}$ and $\bar{\phi}_{\bar{N}_2}$ ruled surfaces.

The dual binormal spherical indicatrix curves of the $\bar{\alpha}_1(u)$ and $\bar{\alpha}_2(v)$ are

$$\bar{B}_1(u) = (0,0,1) + \varepsilon(4u^3\sin(u) + 12u^2\cos(u), -4u^3\cos(u) + 12u^2\sin(u), 0),$$

$$\bar{B}_2(v) = (0,0,-1) + \varepsilon(4v^3\cos(v) - 12v^2\sin(v), -4v^3\sin(v) - 12v^2\cos(v), 0).$$

The ruled surface corresponding to the $\bar{B}_1(u)$ is

$$\bar{\phi}_{\bar{B}_1}(u,s) = (4u^3\cos(u) - 12u^2\sin(u), 4u^3\sin(u) + 12u^2\cos(u), 0) + s(0,0,1)$$

where the base curve is $C_{\bar{B}_1}(u) = (4u^3\cos(u) - 12u^2\sin(u), 4u^3\sin(u) + 12u^2\cos(u), 0)$.

The ruled surface corresponding to the $\bar{B}_2(v)$ is

$$\bar{\phi}_{\bar{B}_2}(v,t) = (-4v^3\sin(v) - 12v^2\cos(v), -4v^3\cos(v) + 12v^2\sin(v), 0) + t(0,0,-1)$$

where the base curve is $C_{\bar{B}_2}(v) = (-4v^3\sin(v) - 12v^2\cos(v), -4v^3\cos(v) + 12v^2\sin(v), 0)$.

Let's examine the intersection of two ruled surfaces correspondig to two different binormal spherical indicatrix curves on DS^2. Let $\bar{\phi}_{\bar{B}_1}(u,s) = \bar{\phi}_{\bar{B}_2}(v,t)$, the following equation can be written by

$$(4u^3\cos(u) - 12u^2\sin(u) + 4v^3\sin(v) + 12v^2\cos(v), 4u^3\sin(u) + 12u^2\cos(u) + 4v^3\cos(v) - 12v^2\sin(v), 0) = -s(0,0,1) + t(0,0,-1).$$

Since $C_{\bar{B}_1}(u) - C_{\bar{B}_2}(v)$, $\bar{B}_1(u)$ and $\bar{B}_2(v)$ are linearly dependent, $\lambda_{\bar{B}}(u,v) = 0$. Hence, the parameter curves $L_{\bar{B}_1}(u)$ and $L_{\bar{B}_2}(v)$ intersect.

If $\Delta_{\bar{B}}(u,v), \delta_{\bar{B}}^1(u,v), \delta_{\bar{B}}^2(u,v)$ are calculated, we obtain

$$\Delta_{\bar{B}}(u,v) = 0,$$

$$\begin{aligned}\delta_{\bar{B}}^1(u,v) = 16\{&[3(v^2\sin(v) - u^2\cos(u)) \\ &- (v^3\cos(v) + u^3\sin(u))]^2 \\ &+ [3(v^2\cos(v) - u^2\sin(u)) \\ &+ (v^3\sin(v) + u^3\cos(u))]^2\},\end{aligned}$$

$$\begin{aligned}\delta_{\bar{B}}^2(u,v) = 16\{&[3(u^2\cos(u) - v^2\sin(v)) \\ &+ (u^3\sin(u) + v^3\cos(v))]^2 \\ &+ [3(u^2\sin(u) - v^2\cos(v)) \\ &- (u^3\cos(u) + v^3\sin(v))]^2\}.\end{aligned}$$

For the $\lambda_{\bar{B}}(u,v) = 0$, the solution of the $(u,v) = (0,0)$, $\Delta_{\bar{B}}(u,v) = \delta_{\bar{B}}^1(u,v) = \delta_{\bar{B}}^2(u,v) = 0$. Therefore, the parameter curves $L_{\bar{B}_1}(u)$ and $L_{\bar{B}_2}(v)$ intersect. Then, $\bar{\phi}_{\bar{B}_1}(u,s)$ and $\bar{\phi}_{\bar{B}_2}(v,t)$ ruled surfaces intersect.

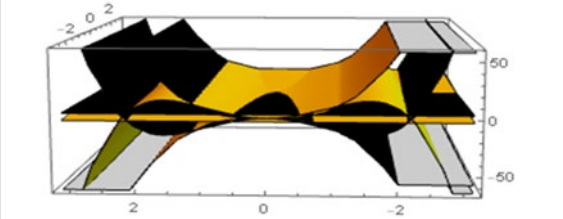

Figure 3. The intersection of $\bar{\phi}_{\bar{B}_1}$ and $\bar{\phi}_{\bar{B}_2}$ ruled surfaces.

The dual pole spherical indicatrix curves of the $\bar{\alpha}_1(u)$ and $\bar{\alpha}_2(v)$ are

$$\begin{aligned}\bar{C}_1(u) = (0,0,1) + \varepsilon(&12u^2\cos(u) \\ &- 24u\sin(u), 12u^2\sin(u) \\ &+ 24u\cos(u), 0),\end{aligned}$$

$$\bar{C}_2(v) = (0,0,-1) + \varepsilon(-12v^2\sin(v) - 24v\cos(v), -12v^2\cos(v) + 24v\sin(v), 0).$$

The ruled surface corresponding to the $\bar{C}_1(u)$ is

$$\begin{aligned}\bar{\phi}_{\bar{C}_1}(u,s) = (&-12u^2\sin(u) - 24u\cos(u), 12u^2\cos(u) \\ &- 24u\sin(u), 0) + s(0,0,1)\end{aligned}$$

where the base curve is $C_{\bar{C}_1}(u) = (-12u^2\sin(u) - 24u\cos(u), 12u^2\cos(u) - 24u\sin(u), 0)$.

The ruled surface corresponding to the $\bar{C}_2(v)$ is

$$\begin{aligned}\bar{\phi}_{\bar{C}_2}(v,t) = (&-12v^2\cos(v) + 24v\sin(v), 12v^2\sin(v) \\ &+ 24v\cos(v), 0) + t(0,0,-1)\end{aligned}$$

where the base curve is $C_{\bar{C}_2}(v) = (-12v^2\cos(v) + 24v\sin(v), 12v^2\sin(v) + 24v\cos(v), 0)$.

Let's examine the intersection of two ruled surfaces correspondig to two different pole spherical indicatrix curves on DS^2. Let $\bar{\phi}_{\bar{C}_1}(u,s) = \bar{\phi}_{\bar{C}_2}(v,t)$, the following equation can be written by

$$\begin{aligned}(&-12u^2\sin(u) - 24u\cos(u) \\ &+ 12v^2\cos(v) \\ &- 24v\sin(v), 12u^2\cos(u) \\ &- 24u\sin(u) - 12v^2\sin(v) \\ &- 24v\cos(v), 0) \\ &= -s(0,0,1) + t(0,0,-1).\end{aligned}$$

Since $C_{\bar{C}_1}(u) - C_{\bar{C}_2}(v)$, $\bar{C}_1(u)$ and $\bar{C}_2(v)$ are linearly dependent, $\lambda_{\bar{C}}(u,v) = 0$. Hence, the parameter curves $L_{\bar{C}_1}(u)$ and $L_{\bar{C}_2}(v)$ intersect.

If $\Delta_{\bar{C}}(u,v), \delta_{\bar{C}}^1(u,v), \delta_{\bar{C}}^2(u,v)$ are calculated, we obtain

$$\Delta_{\bar{C}}(u,v) = 0,$$

$$\begin{aligned}\delta_{\bar{C}}^1(u,v) = 144\{&[(v^2\sin(v) - u^2\cos(u)) \\ &+ 2(u\sin(u) + v\cos(v))]^2 \\ &+ [(v^2\cos(v) - u^2\sin(u)) \\ &- (u\cos(u) + v\sin(v))]^2\},\end{aligned}$$

$$\begin{aligned}\delta_{\bar{C}}^2(u,v) = 144\{&[(u^2\cos(u) - v^2\sin(v)) \\ &- 2(u\sin(u) + v\cos(v))]^2 \\ &+ [(u^2\sin(u) - v^2\cos(v)) \\ &+ 2(u\cos(u) + v\sin(v))]^2\}.\end{aligned}$$

For the $\lambda_{\bar{C}}(u,v) = 0$, the solution of the $(u,v) = (0,0)$, $\Delta_{\bar{C}}(u,v) = \delta_{\bar{C}}^1(u,v) = \delta_{\bar{C}}^2(u,v) = 0$. Therefore, the parameter curves $L_{\bar{C}_1}(u)$ and $L_{\bar{C}_2}(v)$ intersect. Then, $\bar{\phi}_{\bar{C}_1}(u,s)$ and $\bar{\phi}_{\bar{C}_2}(v,t)$ ruled surfaces intersect.

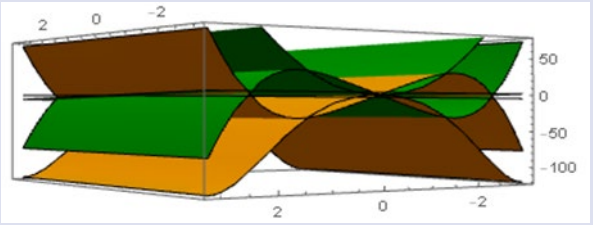

Figure 4. The intersection of $\bar{\phi}_{\bar{C}_1}$ and $\bar{\phi}_{\bar{C}_2}$ ruled surfaces.

Conclusion

E. Study mapping plays an important role to establish correspondence between dual space and Euclidean space. Considering the E. Study mapping, the curve on DS^2 corresponds to the ruled surfaces in $\mathbb{R}^3$. Also, the intersection curve of two ruled surfaces in $\mathbb{R}^3$ is represented by bivariate functions. In this study, two different ruled surfaces in $\mathbb{R}^3$ are examined with E. Study mapping to two different dual spherical indicatrix curves taken on DS^2. Later, the intersection curve for the corresponding ruled surfaces is presented by some main theorems. Additionally, these theorems are verified by giving examples. These results could have important applications in geometry, computer modeling systems, and solid modeling

Acknowledgment

The authors would like to present their sincere appreciation to the editor and referees for their time and efforts.

Conflict of interests

There are no conflicts of interest in this work.

References

[1] Carmo M. Do., Differential Geometry of Curves and Surfaces, Prentice Hall, Englewood Cliffs, New Jersey, (1976) 1-114.

[2] Karaca E., Çalışkan M., Ruled Surfaces and Tangent Bundle of Unit 2-Sphere of Natural Lift Curves, *Gazi Univ. J. Sci.,* 33(5) (2020) 751-759.

[3] Altınkaya A., Çalışkan M., On the Curvatures of the Ruled Surfaces of b-Lift Curves, *Cumhuriyet Sci. J.,* 42(4) (2021) 873-877.

[4] Izumiya S., Takeuchi N., New Special Curves and Developable Surfaces, *Turk. J. Math.*, 28(2) (2004) 153-163.

[5] Uyar Düldül B., Çalışkan M., On the Geodesic Torsion of a Tangential Intersection Curve of Two Surfaces in $\mathbb{R}^3$, *Acta Math. Univ. Comen.,* 82(2) (2013) 177-189.

[6] Ye X., Maekawa T., Differential Geometry of Intersection Curves of Two Surfaces, *Comput. Aided Geom. Des.,* 16(8) (1999) 767-788.

[7] Heo H-S., Kim M-S., Elber G., The Intersection of Two Ruled Surfaces, *Comput. Aided Des.*, 31(1) (1999) 33-50.

[8] Fischer I.S., Dual-Number Methods in Kinematics, Statics and Dynamics. Boca Raton, London, New York, Washington DC: CRC Press, (1999).

[9] Yaylı Y., Saraçoğlu S., Different Approaches to Ruled Surfaces, *SDU J. Sci.*, 7(1) (2012) 56-68.

[10] Karaca E., Çalışkan M., Dual Spherical Curves of Natural Lift Curve and Tangent Bundles of Unit 2-Sphere, *J. Sci.and Arts,* 3(48) (2019) 561-574.

[11] Arslan Güven İ., Kaya Nurhan S., Karacan M-K., Ruled Weingarten Surfaces Related to Dual Spherical Curves, *Gen. Math. Not.,* 24(2) (2014) 10-17.

Cumhuriyet Sci. J., 44(2) (2023) 336-344
DOI: https://doi.org/10.17776/csj.1058866

Cumhuriyet Science Journal

| csj.cumhuriyet.edu.tr | Founded: 2002 ISSN: 2587-2680 e-ISSN: 2587-246X Publisher: Sivas Cumhuriyet University

Obtaining The Finite Difference Approximation of The Lame System By Using Barycentric Coordinates

Vildan Yazıcı [1,a,*]

[1] *Department of Computer Engineering, Faculty of Engineering and Natural Sciences, Kocaeli Health & Technology University, Kocaeli, Türkiye.*

**Corresponding author*

Research Article

History
Received: 17/01/2022
Accepted: 30/04/2023

ABSTRACT

The elasto-plastic contact problem with an unknown contact domain (UCD) has attracted mathematicians, mechanics and engineers for decades. So, the problem of determining the stresses in the UCD is very important nowadays in terms of engineering and applied mathematics. To improve the finite element model, the remeshing algorithm is used for the considered indentation problem. The algorithm allows the determination of the UCD at each step of the indentation with high accuracy. This paper presents the analysis and numerical solution of the boundary value problem for the Lame system, and the modeling of the contact problem for rigid materials. By using barycentric coordinates, the finite difference approximation of the mathematical model of the deformation problem with undetermined bounded is obtained and the relations between the finite elements and finite differences are investigated.

Keywords: Barycentric coordinates, Finite Difference, Finite Element Method, Lame Equations.

[a] *vildan.yazici@kocaelisaglik.edu.tr* *https://orcid.org/0000-0001-5974-0167*

Introduction

The mathematical model of many engineering problems is expressed by undetermined bounded elliptic equations [1-3]. The most important feature of such problems is that some of the boundary conditions are given in the form of inequalities. Therefore, the general solution of the boundary problem satisfies not the integral identity but the integral inequality called the variational inequality [3]. Since the boundary conditions are in the form of inequalities, the generalized solution of the problem is sought in a closed convex subset of this space, not in any subspace of the Sobolev space. The solution of the equilibrium problem of an elastic body in any closed convex set (displacement set) was studied by the Italian mathematician Antonio Signorini in 1933 by bringing the functional to the minimization problem [4]. His study contributed greatly to the analysis of the boundary value problems of the elasticity theory in terms of variational inequalities. The variational inequalities of the elasticity theory were examined mathematically in G. Fichera's monograph [5], and then, the theory of variational inequalities was investigated by G. Duvaut, J.L. Lions [2], D. Kinderlehrerand, G. Stampacchia [3], J.L. Lions [6] and other authors. The extensive analysis of the numerical solutions of variational inequalities with undetermined bounded was given in various studies in the literature [1,7-9]. However, in all studies, when a numerical solution was found, a static mesh was used. That is, the indeterminate part of the boundary (contact domain) would be considered between the points of the static mesh. One of the most important difficulties of the problem is to determine the boundaries of the contact domain. The behavior of the solution at the boundary nodes for undetermined bounded elliptic equations was investigated previously [10]. The obtained results revealed the need to use adaptive (quasi/local-static) meshes in the solution of indeterminate bounded problems [11]. Weng P. et al. considered the elastic deformation of the indenter [12] in the contact process to establish a more accurate elastic-plastic transition model.

This study presents the processes of obtaining the numerical approximation of the variational inequality related to an elasto-plastic plane contact problem and its numerical solution. The main aims of the study were to obtain the finite difference approximation of the mathematical model of the deformation problem with undetermined bounded by using barycentric coordinates and investigate the relation between the finite elements and finite differences. The boundary value problem for the Lame system is detailed, and its variational formulation is given in Section 2. The local stiffness matrix (LSM) obtained by using barycentric coordinates and the finite difference equation (FDE) at any point obtained using the LSM are presented in Sections 3 and 4, respectively. Finally, the numerical solutions are presented, and the relations between the finite elements and finite differences are given in Section 5.

Materials and Methods

Formulation

In the case of plane deformation, the equilibrium problem of the object deformed by the effect of a rigid

punch is modeled mathematically with the boundary value problem for the Lame equation:

$$-(\lambda+\mu)graddivu-\mu\Delta u=F,\ (x,y)\in\Omega\subset\mathbb{R}^2 \qquad (1)$$

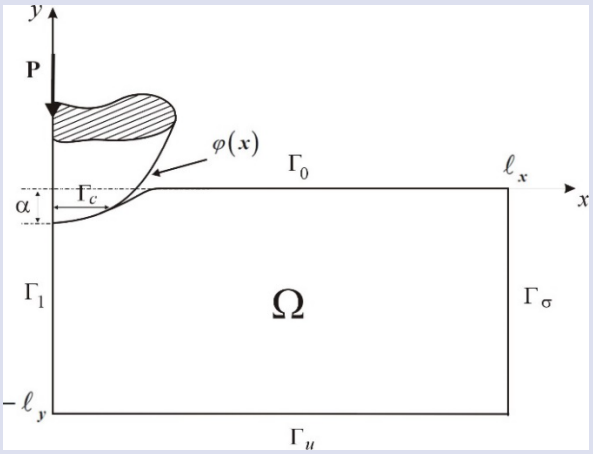

Figure 1. Geometry of the spherical indentation.

$$\begin{cases} u_2(s)\le\varphi(s),\quad \sigma_{22}(u)\le 0,\quad \sigma_{12}(u)=0,\\ \left[u_2(s)-\varphi(s)\right]\sigma_{22}(u)=0\quad ,\quad s\in\Gamma_0; \end{cases} \qquad (2)$$

$$\begin{cases} \sigma_{ij}(u)n_j=f_i,\quad i,j=1,2,\\ u(s)\equiv\left(u_1(s),u_2(s)\right)=0,\quad s\in\Gamma_u; \end{cases} \qquad (3)$$

$$\sigma_{12}(u)=0,\quad u_1(s)=0,\quad s\in\Gamma_1. \qquad (4)$$

Here, let $\Gamma_0=\{(x,y)\,|\,0\le x<\ell_x,\ y=0\}$,

$\Gamma_u=\{(x,y)\,|\,0\le x<\ell_x,\ y=-\ell_y\}$,

$\Gamma_\sigma=\{(x,y)\,|\,x=\ell_x,\ -\ell_y<y<0\}$ and

$\Gamma_1=\{(x,y)\,|\,x=0,\ -\ell_y<y<0\}$ be the boundaries of the rectangular region

$\Omega=\{(x,y)\,|\,0<x<\ell_x,\ -\ell_y<y<0,\quad \ell_x,\ell_y>0\}$

filled by the rigid body in the Oxy plane (Figure 1). The contact domain of the rigid body with the punch is at the unknown boundary $\Gamma_c=\{(x,y)\,|\,0\le x\le a,\quad y=0\}$, where a is an uncertain constant, and the boundary of the contact domain is denoted by Γ_c.

Supposing that the material deforms as much as $\alpha>0$ through the Oy axis when it is compressed by the punch under the effect of any force P, that is, the maximal displacement of the apex of the punch is α, in case the cross-section of the punch is $y=\varphi(x)$, the contact domain of the material with the punch will be $\tilde{\Gamma}_c=\{(x,y)\,|\,0\le x\le a,\quad y=-\alpha+\varphi(x)\}$.

The components of the stress tensors are

$$\sigma_{ii}=\lambda div(u)+2\mu\frac{\partial u_i}{\partial x_i},\qquad \sigma_{ij}=\mu\left(\frac{\partial u_i}{\partial x_j}+\frac{\partial u_j}{\partial x_i}\right),$$

$i,j=1,2$.

while the components of the deformation tensors are

$$\varepsilon_{ij}=\frac{1}{2}\left(\frac{\partial u_i}{\partial x_j}+\frac{\partial u_j}{\partial x_i}\right).$$

The Lame constants λ and μ are defined as follows:

$$\lambda=\frac{E\nu}{(1+\nu)(1-2\nu)},\ \mu=\frac{E}{2(1+\nu)}.$$

Here, E is the modulus of elasticity, and ν is the Poisson's constant. The Lame constants λ and μ are non-linear in the case of plastic deformation, and they are defined depending on displacements as follows:

$$\tilde{\lambda}=\lambda+\frac{2}{3}\mu\omega(e_u(u)),\ \tilde{\mu}=\mu\left[1-\omega(e_u(u))\right]$$

where $\omega(e_u)$ is the function that characterizes the plasticity case [13]:

$$\begin{cases} 0<\omega(e_u)<\dfrac{d\left[e_u\omega(e_u)\right]}{de_u}<1, & e_u>e_0\\ \omega(e_u)=0, & e_u\le e_0. \end{cases}$$

Here, e_0 is the elastic limit, and the intensity of deformation is

$$e_u(u)=\frac{\sqrt{2}}{3}\left\{(\varepsilon_{11}(u)-\varepsilon_{22}(u))^2+(\varepsilon_{22}(u)-\varepsilon_{33}(u))^2+(\varepsilon_{33}(u)-\varepsilon_{11}(u))^2+6\left[\varepsilon_{12}^2(u)+\varepsilon_{13}^2(u)+\varepsilon_{23}^2(u)\right]\right\}^{1/2}.$$

When $\omega(e_u)=0$ corresponding to the elastic case, even though Equation (1) is linear, the fact that the contact domain is not certain causes the problem to be non-linear.

Variational Formulation

It is known from the variational principle that the solution of problem (1) is minimized by the following functional:

$$J(u)=\frac{1}{2}a(u,u)-b(u) \qquad (5)$$

where the bilinear and the linear parts of functional (5) are as follows, respectively:

$$a(u,v)=\iint_{\Omega}\left\{\lambda divu.divv+2\mu\left(\frac{\partial u_1}{\partial x}\frac{\partial v_1}{\partial x}+\frac{\partial u_2}{\partial y}\frac{\partial v_2}{\partial y}\right)+\mu\left(\frac{\partial u_2}{\partial x}+\frac{\partial u_1}{\partial y}\right)\left(\frac{\partial v_2}{\partial x}+\frac{\partial v_1}{\partial y}\right)\right\}dxdy,$$

$$b(v)=\iint_{\Omega}F_i v_i ds+\int_{\Gamma_\sigma}f_i v_i ds,\quad i=1,2. \tag{6}$$

So, the problem turns into a minimization problem $\exists u\in V\quad J(u)=\min_{v\in V}J(u)$ in the set $V=\left\{v\in H^1(\Omega)\middle| v(s)=0, s\in\Gamma_u; v_N(s)\le\varphi(s), s\in\Gamma_0\right\}$. When the problem is being solved, the contact domain Γ_c is determined as in the study by A.A. Ilyushin [13]. Since the contact region is assumed to be certain at each step, the inequalities in the boundary conditions turn into equalities, and the problem becomes linear.

Obtaining Local Stiffness Matrix by Using Barycentric Coordinates

Suppose that the region Ω in which the problem is defined is divided into quadrilateral finite elements. In this case, we define the equal-step mesh as follows:

$$\omega_{h\tau}=\left\{\left\{(x_i,y_j)\middle| x_{i+1}=x_i+h, y_{j+1}=y_j+\tau, (x_1,y_1)=(0,-\ell_y),(x_N,y_M)=(\ell_x,0), i=\overline{1,N-1}, j=\overline{1,M-1}\right\}\right.$$

In the quadrilateral finite elements, the barycentric coordinates are equal to the form function, which is the projection of the Lagrange basis function $\xi_{ij}(x,y)$ on the finite element $e_{mn}=\left\{(x,y)\middle| x_m\le x\le x_{m+1}, y_n\le y\le y_{n+1}\right\}$, and it can be defined as

$$L_q(x,y)=\xi_{ij}(x,y)\Big|_{e_{mn}},\quad q=1,2,3,4. \tag{7}$$

Since this form function is the same as the barycentric coordinates in the quadrilateral finite element, it can be written in general with single indices as follows [14-15]:

$$L_q(x,y)=\frac{a_q+b_q x+c_q y+d_q xy}{S},\quad q=1,2,3,4. \tag{8}$$

Here, q is the local number of the vertices of the finite quadrilateral element e_{mn} (from down to up and from left to right), and S is the area of this finite element. It is ascertained that

$$\begin{aligned}
&a_1=x_{i+1}y_{j+1},\quad b_1=-y_{j+1},\quad c_1=-x_{i+1},\quad d_1=1;\\
&a_2=-x_{i+1}y_j,\quad b_2=-y_j,\quad c_2=x_{i+1},\quad d_2=-1;\\
&a_3=x_i y_{j+1},\quad b_3=y_{j+1},\quad c_3=x_i,\quad d_3=-1;\\
&a_4=x_i y_j,\quad b_4=-y_j,\quad c_4=-x_i,\quad d_4=1;
\end{aligned} \tag{9}$$

for the finite quadrilateral elements e_{ij}, since the components of the local stiffness matrix corresponding to the finite element e_{mn} are calculated with the help of the bilinear form $a(u,v)$,

$$a_{mn}^{1}\left(L_p,L_q\right)=\iint_{e_{mn}}\left\{\left(\lambda+2\mu\right)\frac{\partial L_p}{\partial x}\frac{\partial L_q}{\partial x}+\mu\frac{\partial L_p}{\partial y}\frac{\partial L_q}{\partial y}\right\}dxdy\,;$$

$$a_{mn}^{2}\left(L_p,L_q\right)=\iint_{e_{mn}}\left\{\lambda\frac{\partial L_p}{\partial x}\frac{\partial L_q}{\partial y}+\mu\frac{\partial L_p}{\partial y}\frac{\partial L_q}{\partial x}\right\}dxdy\,;$$

$$a_{mn}^{3}\left(L_p,L_q\right)=\iint_{e_{mn}}\left\{\lambda\frac{\partial L_p}{\partial y}\frac{\partial L_q}{\partial x}+\mu\frac{\partial L_p}{\partial x}\frac{\partial L_q}{\partial y}\right\}dxdy\,; \tag{10}$$

$$a_{mn}^{4}\left(L_p,L_q\right)=\iint_{e_{mn}}\left\{\left(\lambda+2\mu\right)\frac{\partial L_p}{\partial y}\frac{\partial L_q}{\partial y}+\mu\frac{\partial L_p}{\partial x}\frac{\partial L_q}{\partial x}\right\}dxdy\,.$$

Given that

$$\frac{\partial}{\partial x}L_i\left(x,y\right)=\frac{b_i+d_iy}{S},\quad \frac{\partial}{\partial y}L_i\left(x,y\right)=\frac{c_i+d_ix}{S},\quad i=1,2,3,4\,.$$

The expressions for the components of the local stiffness matrix are obtained as follows:

$$a_{m}^{1}\left(L_p,L_q\right)=\frac{h\tau}{6}\frac{1}{S^2}\left\{\left(\lambda+2\mu\right)\left[6b_pb_q+3\left(b_pd_q+b_qd_p\right)\left(y_{j+1}+y_j\right)+2d_pd_q\left(y_{j+1}^2+y_{j+1}y_j+y_j^2\right)\right]\right.$$
$$\left.\mu\left[6c_pc_q+3\left(c_pd_q+c_qd_p\right)\left(x_{i+1}+x_i\right)+2d_pd_q\left(x_{i+1}^2+x_{i+1}x_i+x_i^2\right)\right]\right\},$$

$$a_{m}^{2}\left(L_p,L_q\right)=\frac{h\tau}{4}\frac{1}{S^2}\left\{\lambda\left[4b_pc_q+2b_pd_q\left(x_{i+1}+x_i\right)+2c_qd_p\left(y_{j+1}+y_j\right)+d_pd_q\left(x_{i+1}+x_i\right)\left(y_{j+1}+y_j\right)\right]\right.$$
$$\left.\mu\left[4b_qc_p+2c_pd_q\left(y_{j+1}+y_j\right)+2b_qd_p\left(x_{i+1}+x_i\right)+d_pd_q\left(x_{i+1}+x_i\right)\left(y_{j+1}+y_j\right)\right]\right\},$$

$$a_{m}^{3}\left(L_p,L_q\right)=\frac{h\tau}{4}\frac{1}{S^2}\left\{\lambda\left[4b_qc_p+2c_pd_q\left(y_{j+1}+y_j\right)+2b_qd_p\left(x_{i+1}+x_i\right)+d_pd_q\left(x_{i+1}+x_i\right)\left(y_{j+1}+y_j\right)\right]\right.$$
$$\left.\mu\left[4b_pc_q+2b_pd_q\left(x_{i+1}+x_i\right)+2c_qd_p\left(y_{j+1}+y_j\right)+d_pd_q\left(x_{i+1}+x_i\right)\left(y_{j+1}+y_j\right)\right]\right\},$$

$$a_{m}^{4}\left(L_p,L_q\right)=\frac{h\tau}{6}\frac{1}{S^2}\left\{\left(\lambda+2\mu\right)\left[6c_pc_q+3\left(c_pd_q+c_qd_p\right)\left(x_{i+1}+x_i\right)+2d_pd_q\left(x_{i+1}^2+x_{i+1}x_i+x_i^2\right)\right]\right.$$
$$\left.\mu\left[6b_pb_q+3\left(b_pd_q+b_qd_p\right)\left(y_{j+1}+y_j\right)+2d_pd_q\left(y_{j+1}^2+y_{j+1}y_j+y_j^2\right)\right]\right\},$$

where *p,q=1,2,3,4.*

Finally, considering (9) for any finite element e_{mn}, the components of the local stiffness matrix A defined as

$$A=\left[A_{ij}\right]_{8\times8}=\begin{bmatrix}\mathcal{A}_{11} & \mathcal{A}_{12}\\ \mathcal{A}_{21} & \mathcal{A}_{22}\end{bmatrix}$$

are obtained as follows:

$$\mathcal{A}_{11}=\begin{bmatrix} \mu\frac{h}{3\tau}+(\lambda+2\mu)\frac{\tau}{3h} & -\mu\frac{h}{3\tau}+(\lambda+2\mu)\frac{\tau}{6h} & \mu\frac{h}{6\tau}-(\lambda+2\mu)\frac{\tau}{3h} & -\mu\frac{h}{6\tau}-(\lambda+2\mu)\frac{\tau}{6h} \\ -\mu\frac{h}{3\tau}+(\lambda+2\mu)\frac{\tau}{6h} & \mu\frac{h}{3\tau}+(\lambda+2\mu)\frac{\tau}{3h} & -\mu\frac{h}{6\tau}-(\lambda+2\mu)\frac{\tau}{6h} & \mu\frac{h}{6\tau}-(\lambda+2\mu)\frac{\tau}{3h} \\ \mu\frac{h}{6\tau}-(\lambda+2\mu)\frac{\tau}{3h} & -\mu\frac{h}{6\tau}-(\lambda+2\mu)\frac{\tau}{6h} & \mu\frac{h}{3\tau}+(\lambda+2\mu)\frac{\tau}{3h} & -\mu\frac{h}{3\tau}+(\lambda+2\mu)\frac{\tau}{6h} \\ -\mu\frac{h}{6\tau}-(\lambda+2\mu)\frac{\tau}{6h} & \mu\frac{h}{6\tau}-(\lambda+2\mu)\frac{\tau}{3h} & -\mu\frac{h}{3\tau}+(\lambda+2\mu)\frac{\tau}{6h} & \mu\frac{h}{3\tau}+(\lambda+2\mu)\frac{\tau}{3h} \end{bmatrix}$$

$$\mathcal{A}_{12}=\left(\mathcal{A}_{21}\right)^{T}=\begin{bmatrix} \frac{\lambda+\mu}{4} & \frac{-\lambda+\mu}{4} & \frac{\lambda-\mu}{4} & -\frac{\lambda+\mu}{4} \\ \frac{\lambda-\mu}{4} & -\frac{\lambda+\mu}{4} & \frac{\lambda+\mu}{4} & \frac{-\lambda+\mu}{4} \\ \frac{-\lambda+\mu}{4} & \frac{\lambda+\mu}{4} & -\frac{\lambda+\mu}{4} & \frac{\lambda-\mu}{4} \\ -\frac{\lambda+\mu}{4} & \frac{\lambda-\mu}{4} & \frac{-\lambda+\mu}{4} & \frac{\lambda+\mu}{4} \end{bmatrix}$$

$$\mathcal{A}_{22}=\begin{bmatrix} \mu\frac{\tau}{3h}+(\lambda+2\mu)\frac{h}{3\tau} & \mu\frac{\tau}{6h}-(\lambda+2\mu)\frac{h}{3\tau} & -\mu\frac{\tau}{3h}+(\lambda+2\mu)\frac{h}{6\tau} & -\mu\frac{\tau}{6h}-(\lambda+2\mu)\frac{h}{6\tau} \\ \mu\frac{\tau}{6h}-(\lambda+2\mu)\frac{h}{3\tau} & \mu\frac{\tau}{3h}+(\lambda+2\mu)\frac{h}{3\tau} & -\mu\frac{\tau}{6h}-(\lambda+2\mu)\frac{h}{6\tau} & -\mu\frac{\tau}{3h}+(\lambda+2\mu)\frac{h}{6\tau} \\ -\mu\frac{\tau}{3h}+(\lambda+2\mu)\frac{h}{6\tau} & -\mu\frac{\tau}{6h}-(\lambda+2\mu)\frac{h}{6\tau} & \mu\frac{\tau}{3h}+(\lambda+2\mu)\frac{h}{3\tau} & \mu\frac{\tau}{6h}-(\lambda+2\mu)\frac{h}{3\tau} \\ -\mu\frac{\tau}{6h}-(\lambda+2\mu)\frac{h}{6\tau} & -\mu\frac{\tau}{3h}+(\lambda+2\mu)\frac{h}{6\tau} & \mu\frac{\tau}{6h}-(\lambda+2\mu)\frac{h}{3\tau} & \mu\frac{\tau}{3h}+(\lambda+2\mu)\frac{h}{3\tau} \end{bmatrix}$$

Obtaining the Finite Difference Equation (FDE) at Any Point Using the Local Stiffness Matrix

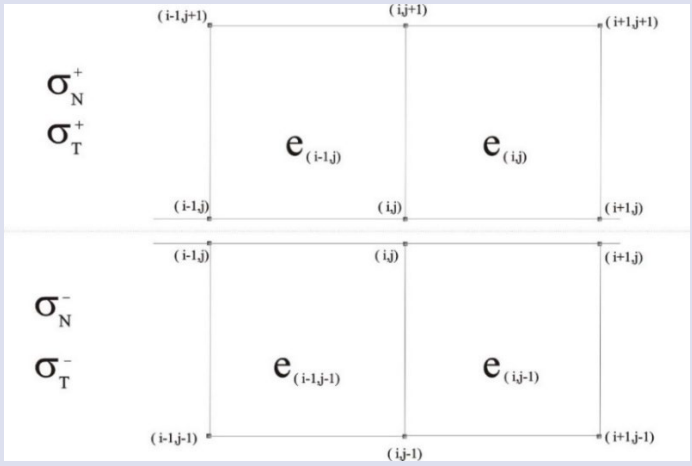

Figure 2. The interlayer finite elements.

In order to obtain the approximating expression of both normal σ_N and tangential σ_T components of the stresses, A_{ij} needs to be multiplied by u_{ij} and v_{ij}, where u_{ij} and v_{ij} are the displacement vectors on the x-axis and y-axis directions, respectively. Then, the results of these multiplications need to be summed up.

Firstly, the normal component of the stresses $\sigma_N=\sigma_{22}=(\lambda+2\mu)\frac{\partial v}{\partial y}+\lambda\frac{\partial u}{\partial x}$ has to be obtained. For the sake of simplicity, the top and bottom parts are considered separately in Figure 2. For this purpose, the FDE for the stress

tensors $\sigma_N = \sigma_N^- + \sigma_N^+$ is obtained in the normal direction by processing the relevant lines of the local stiffness matrix A and grouping them according to the displacement vectors u and v. So, to obtain the FDE of σ_N^-, the 6th and 8th lines of the local stiffness matrix A have to be multiplied by unknown vectors belonging to each finite element $e_{i,j-1}$ and $e_{i-1,j-1}$, respectively (Figure 3).

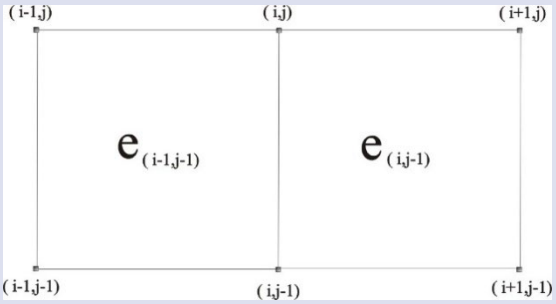

Figure 3. The bottom parts of interlayer finite elements.

Here, the unknown vectors u_{ij}, v_{ij} belonging to the finite elements $e_{i,j-1}$ and $e_{i-1,j-1}$ on the nodal points (x_i, y_j) are as follows:

$$e_{i-1,j-1} \Rightarrow (u_{i-1,j-1}, u_{i-1,j}, u_{i,j-1}, u_{i,j}, v_{i-1,j-1}, v_{i-1,j}, v_{i,j-1}, v_{i,j}),$$

$$e_{i,j-1} \Rightarrow (u_{i,j-1}, u_{i,j}, u_{i+1,j-1}, u_{i+1,j}, v_{i,j-1}, v_{i,j}, v_{i+1,j-1}, v_{i+1,j}).$$

Then, the results of these multiplications have to be summed up, and σ_N^- is obtained as follows:

$$\begin{aligned}\sigma_N^- &= A_{61}u_{i,j-1} + A_{62}u_{i,j} + A_{63}u_{i+1,j-1} + A_{64}u_{i+1,j} + A_{65}v_{i,j-1} + A_{66}v_{i,j} + A_{67}v_{i+1,j-1} + A_{68}v_{i+1,j} \\ &+ A_{81}u_{i-1,j-1} + A_{82}u_{i-1,j} + A_{83}u_{i,j-1} + A_{84}u_{i,j} + A_{85}v_{i-1,j-1} + A_{86}v_{i-1,j} + A_{87}v_{i,j-1} + A_{88}v_{i,j} \\ &= h\left[(\lambda+2\mu)v_{\bar{y}}^{(i,j)} + \lambda u_{\dot{x}}^{(i,j)} - \tau\frac{1}{2}(\lambda+\mu)u_{\dot{x}\bar{y}}^{(i,j)} - \tau\frac{\mu}{6}\left(v_{\bar{x}x}^{(i,j-1)} + 2v_{\bar{x}x}^{(i,j)}\right) + h^2\frac{(\lambda+2\mu)}{6}v_{\bar{y}x\bar{x}}^{(i,j)}\right].\end{aligned}$$

Similarly, in order to obtain the FDE of σ_N^+, the relevant lines (5th and 7th) of the local stiffness matrix A have to be multiplied by unknown vectors for the finite elements $e_{i,j}$ and $e_{i-1,j}$, respectively (Figure 4).

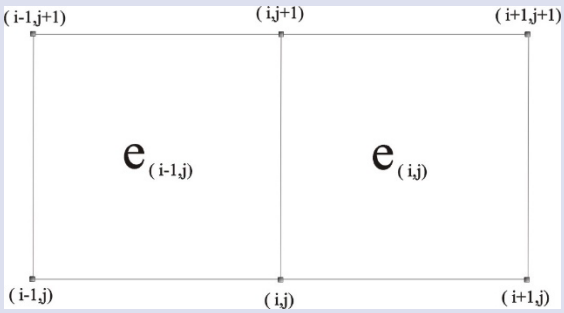

Figure 4. The top parts of interlayer finite elements.

$$e_{i-1,j} \Rightarrow (u_{i-1,j}, u_{i-1,j+1}, u_{i,j}, u_{i,j+1}, v_{i-1,j}, v_{i-1,j+1}, v_{i,j}, v_{i,j+1})$$

$$e_{i,j} \Rightarrow (u_{i,j}, u_{i,j+1}, u_{i+1,j}, u_{i+1,j+1}, v_{i,j}, v_{i,j+1}, v_{i+1,j}, v_{i+1,j+1})$$

Then, the results of these multiplications have to be summed up as above, and σ_N^+ is obtained as follows:

$$\sigma_N^+ = A_{51}u_{i,j} + A_{52}u_{i,j+1} + A_{53}u_{i+1,j} + A_{54}u_{i+1,j+1} + A_{55}v_{i,j} + A_{56}v_{i,j+1} + A_{57}v_{i+1,j} + A_{58}v_{i+1,j+1}$$
$$+ A_{71}u_{i-1,j} + A_{72}u_{i-1,j+1} + A_{73}u_{i,j} + A_{74}u_{i,j+1} + A_{75}v_{i-1,j} + A_{76}v_{i-1,j+1} + A_{77}v_{i,j} + A_{78}v_{i,j+1}$$
$$= -h\left[\left((\lambda+2\mu)v_y^{(i,j)} + \lambda u_{\dot{x}}^{(i,j)}\right) + \frac{1}{2}\tau(\lambda+\mu)u_{\dot{x}\dot{y}}^{(i,j)} + \tau\frac{\mu}{6}\left(v_{x\bar{x}}^{(i,j+1)} + 2v_{x\bar{x}}^{(i,j)}\right) + h^2\frac{(\lambda+2\mu)}{6}v_{y\dot{x}\bar{x}}^{(i,j)}\right].$$

Hence, $\sigma_N = \sigma_N^- + \sigma_N^+ = 0$ is satisfied for the normal component of the stresses, and

$$\sigma_N^- + \sigma_N^+ = h\left[(\lambda+2\mu)v_{\bar{y}}^{(i,j)} + \lambda u_{\dot{x}}^{(i,j)} - \tau\frac{1}{2}(\lambda+\mu)u_{\dot{x}\bar{y}}^{(i,j)} - \tau\frac{\mu}{6}\left(v_{\bar{x}x}^{(i,j-1)} + 2v_{\bar{x}x}^{(i,j)}\right) + h^2\frac{(\lambda+2\mu)}{6}v_{\bar{y}x\bar{x}}^{(i,j)}\right]$$
$$-h\left[\left((\lambda+2\mu)v_y^{(i,j)} + \lambda u_{\dot{x}}^{(i,j)}\right) + \frac{1}{2}\tau(\lambda+\mu)u_{\dot{x}\dot{y}}^{(i,j)} + \tau\frac{\mu}{6}\left(v_{x\bar{x}}^{(i,j+1)} + 2v_{x\bar{x}}^{(i,j)}\right) + h^2\frac{(\lambda+2\mu)}{6}v_{y\dot{x}\bar{x}}^{(i,j)}\right] = 0.$$

Secondly, the FDE of the tangential component of the stresses $\sigma_T = \sigma_{12} = \mu\left(\frac{\partial u}{\partial y} + \frac{\partial v}{\partial x}\right)$ is obtained. σ_T is calculated so that $\sigma_T = \sigma_T^- + \sigma_T^+$, by the same way as σ_N. In order to obtain the FDE of σ_T^-, the 2nd and 4th lines of the local stiffness matrix A have to be multiplied by unknown vectors belonging to each finite element $\mathrm{e}_{\mathrm{i,j-1}}$ and $\mathrm{e}_{\mathrm{i-1,j-1}}$, respectively. Then, the results of these multiplications have to be summed up, and σ_T^- is obtained as follows:

$$\sigma_T^- = A_{21}u_{i,j-1} + A_{22}u_{i,j} + A_{23}u_{i+1,j-1} + A_{24}u_{i+1,j} + A_{25}v_{i,j-1} + A_{26}v_{i,j} + A_{27}v_{i+1,j-1} + A_{28}v_{i+1,j}$$
$$+ A_{41}u_{i-1,j-1} + A_{42}u_{i-1,j} + A_{43}u_{i,j-1} + A_{44}u_{i,j} + A_{45}v_{i-1,j-1} + A_{46}v_{i-1,j} + A_{47}v_{i,j-1} + A_{48}v_{i,j}$$
$$= h\left\{\mu\left(u_{\bar{y}}^{(i,j)} + v_{\dot{x}}^{(i,j)}\right) + \frac{1}{6}\left[h^2\mu u_{\bar{y}x\bar{x}}^{(i,j)} - \tau(\lambda+2\mu)\left(u_{\bar{x}x}^{(i,j-1)} + 2u_{\bar{x}x}^{(i,j)}\right)\right] - \frac{1}{2}\tau(\lambda+\mu)v_{\bar{y}\dot{x}}^{(i,j)}\right\}.$$

Likewise, to obtain the FDE of σ_T^+, the relevant lines (1st and 3rd) of the local stiffness matrix A have to be multiplied by unknown vectors for $\mathrm{e}_{\mathrm{i,j}}$ and $\mathrm{e}_{\mathrm{i-1,j}}$, respectively, followed by summing up the results of these multiplications. Accordingly, σ_T^+ is obtained as follows:

$$\sigma_T^+ = A_{11}u_{i,j} + A_{12}u_{i,j+1} + A_{13}u_{i+1,j} + A_{14}u_{i+1,j+1} + A_{15}v_{i,j} + A_{16}v_{i,j+1} + A_{17}v_{i+1,j} + A_{18}v_{i+1,j+1}$$
$$+ A_{31}u_{i-1,j} + A_{32}u_{i-1,j+1} + A_{33}u_{i,j} + A_{34}u_{i,j+1} + A_{35}v_{i-1,j} + A_{36}v_{i-1,j+1} + A_{37}v_{i,j} + A_{38}v_{i,j+1}$$
$$= -h\left\{\mu\left(u_y^{(i,j)} + v_{\dot{x}}^{(i,j)}\right) + \frac{1}{6}\left[h^2\mu u_{y\dot{x}\bar{x}}^{(i,j)} + \tau(\lambda+2\mu)\left(2u_{x\bar{x}}^{(i,j)} + u_{x\bar{x}}^{(i,j+1)}\right)\right] + \frac{1}{2}\tau(\lambda+\mu)v_{y\dot{x}}^{(i,j)}\right\}.$$

Hence, the tangential component of the stresses $\sigma_T = \sigma_T^- + \sigma_T^+ = 0$ is satisfied, and

$$\sigma_T^- + \sigma_T^+ = h\left\{\mu\left(u_{\bar{y}}^{(i,j)} + v_{\dot{x}}^{(i,j)}\right) + \frac{1}{6}\left[h^2\mu u_{\bar{y}x\bar{x}}^{(i,j)} - \tau(\lambda+2\mu)\left(u_{\bar{x}x}^{(i,j-1)} + 2u_{\bar{x}x}^{(i,j)}\right)\right] - \frac{1}{2}\tau(\lambda+\mu)v_{\bar{y}\dot{x}}^{(i,j)}\right\} +$$
$$-h\left\{\mu\left(u_y^{(i,j)} + v_{\dot{x}}^{(i,j)}\right) + \frac{1}{6}\left[h^2\mu u_{y\dot{x}\bar{x}}^{(i,j)} + \tau(\lambda+2\mu)\left(2u_{x\bar{x}}^{(i,j)} + u_{x\bar{x}}^{(i,j+1)}\right)\right] + \frac{1}{2}\tau(\lambda+\mu)v_{y\dot{x}}^{(i,j)}\right\} = 0.$$

Numerical Results

The numerical solution of the problem is obtained using barycentric coordinates for the quadrilateral finite elements. The size mesh $N_x \times N_y$ as $N_x = 50$ and $N_y = 21$ is considered in the rectangular region Ω to obtain the numerical solution. A local adaptive mesh is used to find the contact area Γ_c with less error, and therefore, the mesh steps are considered smaller in the area close to the contact area (number of points in the contact area is $N_{a_c} = 19$).

For the numerical experiments, the modules of elasticity, Poisson's constant and elasticity limit of these materials are $E = 210\,GPa$, $\nu = 0.3$ and $e_0 = 0.027$, respectively. The geometric parameters of the region and the punch are then defined as $R = 0.2\times10^{-2}\,m$, $l_x = 1.5\times10^{-2}\,m$, $l_y = 1\times10^{-2}\,m$ such that $\varphi(x) = \sqrt{R^2 - x^2}$. In the case where the punch deforms the rigid body by $\alpha = 0.5\times10^{-4}\,m$, the initial value of the contact zone is taken as $\tilde{a}_c = 0.2\times10^{-3}\,m$, and the contact zone is found as $\tilde{a}_c = 3.1935\times10^{-3}\,m$ in seven iterations. Since the force acting on the punch to deform the rigid

body by as much as $\alpha = 0.5\times10^{-4}m$ is defined as $P[\alpha] = \int_{\Gamma_c(\alpha)} \sigma_N(u)dx$, it is found to be $P(\alpha) = 4.953\times10^{-2}GPa$. The values of the stress tensors σ_N and σ_T are calculated in each layer of the mesh defined in the region, and it is determined that the equilibrium conditions are satisfied ($P^{+}(\alpha) = 4.9532\times10^{-2}GPa$ and $P^{-}(\alpha) = 4.9584\times10^{-2}GPa$).

The plots of the functions σ_N and σ_T at the top of the deforming body and the thickness $y = 0.65$ are given in Figure 5. (a) and (b), respectively ($N_y^{0.65} = 23$).

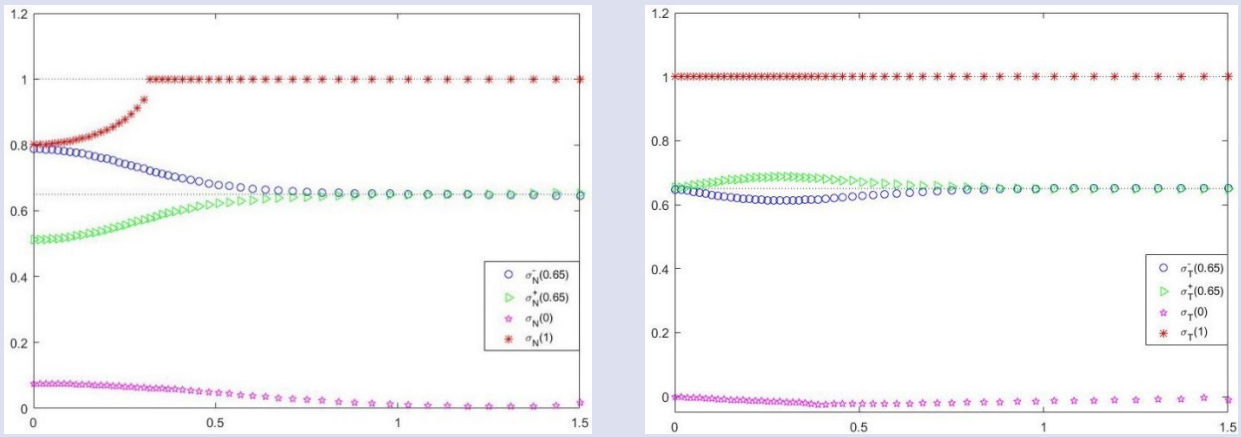

(a) (b)

Figure 5. The plots of the functions (a) σ_N and (b) σ_T at the top of the deforming body and $y=0.65$.

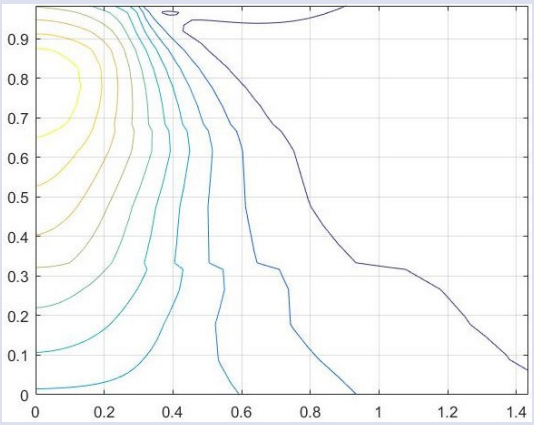

Figure 6. The distribution of plasticity in the rigid body.

Conclusion

Finite difference equations of the mathematical model of the elasto-plastic plane contact problem with undetermined bounded corresponding to the Lame equation system were obtained by using barycentric coordinates. Then, the geometric interpretations of the numerical solution obtained with the help of the prepared computer program were presented.

Conflict of interests

The authors state that did not have conflict of interests.

References

[1] Hlavacek I., Haslinger J., Necas J., Lovisek J., Solution of Variational Inequalities in Mechanics. Berlin: Springer, (1988) 109-262.

[2] Duvaut G., Lions J.L., Inequalities in Mechanics and Physics. Berlin: Springer-Verlag, (1989) 102-227.

[3] Kinderlehrer D., Stampacchia G., An Introduction to Variational Inequalities and Their Applications. New York: Academic Press, (1980) 1-274.

[4] Signorini A., Sopra Alcune Questioni di Elastostatica, Atti della Societa Italiana per il Progresso delle Scienze, 2 (2) (1933) 231-251.

[5] Fichera G., Existence Theorems in Elasticity. In: Truesdell C., (Eds). Linear Theories of Elasticity and Thermoelasticity. Springer-Verlag Berlin Heidelberg, (1973) 347-389.

[6] Lions J.L., Some Methods of Solving Non-Linear Boundary Value Problems. Paris: Dunod-Gauthier-Villars, (1969) 280-309.

[7] Glovinski R., Lions J.L., Trémolierès R., Analyse Numérique des Inéquations Variationnelles. Paris: Dunod, (1976) 1-268.

[8] Lee A., Komvopoulos K., Dynamic Spherical Indentation of Elastic-Plastic Solids, *International Journal of Solids and Structures*, 146 (2018) 180-191.

[9] Wagih A., Maim P., Blanco N., Trias D., Predictive Model for the Spherical Indentation of Composite Laminates with Finite Thickness, *Composite Structures*, 153 (2016) 468-477.

[10] Gasanov A.I., Numerical Method for Solving a Contact Problem of Elasticity Theory in the Absence of Friction Forces, Differ. Uravn., 18 (7) (1982) 1156–1161.

[11] Hasanov A., Seyidmamedov Z, Qualitative Behaviour of Solutions of Signorini Problem with Perturbing the Unknown Boundary II. The Multigrid Method, *Applied Mathematics and Computation*, 109 (2000) 261-271.

[12] Weng P., Yin X., Hu W., Yuan H., Chen C., Ding H., Yu B., Xie W., Jiang L., Wang H., Piecewise linear deformation characteristics and a contact model for elastic-plastic indentation considering indenter elasticity, *Tribology International*, 162 (2021) 107-114.

[13] Ilyushin A.A., Plasticity. Moscow: Gostekhizdat, (1948) 144-268, in Russian.

[14] Norrie D.H., De Vries G., An Introduction to Finite Element Analysis. New York: Academic Press, (1978) 1-301.

[15] Ciarlet P.G., The Finite Element Method for Elliptic Problems. 2nd ed. SIAM, (2002) 287-380.

Cumhuriyet Sci. J., 44(2) (2023) 345-355
DOI: https://doi.org/10.17776/csj.1239101

Cumhuriyet Science Journal

| csj.cumhuriyet.edu.tr | Founded: 2002 ISSN: 2587-2680 e-ISSN: 2587-246X Publisher: Sivas Cumhuriyet University

Chaos in a Three-Dimensional Cancer Model with Piecewise Constant Arguments

Şenol Kartal [1,a,*]

[1] *Department of Science and Mathematics Education, Faculty of Education, Nevsehir Hacı Bektas Veli University, Nevsehir, Türkiye.*
**Corresponding author*

Research Article

History
Received: 19/01/2023
Accepted: 01/05/2023

ABSTRACT

In this study, we analyze a cancer model which includes the interactions among tumor cells, healthy host cells and effector immune cells. The model with continuous case has been studied in the literature and it has been shown that it exhibits chaotic behavior. In this paper, we aim to build a better understanding of how both discrete and continuous times affect the dynamic behavior of the tumor growth model. So, we reconsider the model as a system of differential equations with piecewise constant argument. To analyze dynamical behavior of the model, we consider the solution of the system in a certain subinterval which leads to the system of difference equations. Some theoretical results are obtained for local behavior of the system. In addition, we study chaotic dynamic of the system through Neimark-Sacker bifurcation by using Lyapunov exponents

Keywords: *Tumor model, Difference equation, Stability, Neimark-Sacker bifurcation, Lyapunov exponents*

[a] *senol.kartal@nevsehir.edu.tr* *https://orcid.org/0000-0003-1205-069X*

Introduction

Interaction of tumor cells with other cells of the body, i.e. healthy host cells and immune system cells is very complex phenomenon because tumor cells have different dynamics such as unbounded growth, tumor dormancy, tumor recurrence and tumor remission. In order to understand the dynamic behavior of the disease, a variety of mathematical models have been developed in the literature [1-19]. Using the Lotka-Volterra equations in these models is one of the most common ideas. A very simple model based on the Lotka-Volterra predator-prey model has been presented by Costa and et al. [1]. Their model explains tumor aggressiveness, the diffusion of lymphocytes and the effect caused by cytokines on the tumor. Based on the Costa model, a family of Lotka-Volterra models has been investigated by D'Onofrio [2]. Another familiar tumor growth model has been proposed by Kuznetsov and et al. [3] and they have explained two different stages of the tumor: the dormant tumor and the sneaking-through mechanism. In 1998, Kirschner and Panetta [4] described the dynamics among tumor cells, immune effector cells and Interleukin-2 by using the generalized Kuznetsov model.

Recent studies have shown that some tumor growth models which are based on Lotka-Volterra type systems exhibit chaotic dynamics. Itik and Banks [5] have analyzed the chaotic dynamics of a very simple tumor growth model

$$\begin{cases} \dfrac{dx}{dt} = x(t)\big(1 - x(t)\big) - ax(t)y(t) - bx(t)z(t), \\ \dfrac{dy}{dt} = cy(t)\big(1 - y(t)\big) - dx(t)y(t), \\ \dfrac{dz}{dt} = \dfrac{ex(t)z(t)}{x(t) + f} - gx(t)z(t) - hz(t). \end{cases} \quad (1)$$

Calculating Lyapunov exponents and Lyapunov dimension show that a chaotic attractor occurs around the positive equilibrium point. Model (1.1) has also been studied by Galindo et al. [6]. They have observed that tumor cells, immune cells and healthy cells coexist through the Hopf bifurcation which causes a stable limit cycle. A more general form of this model with chemotherapy treatment has been studied in study [7].

In the early 1980s, Busenberg and Cooke [20], Cooke and Györi [21], Shah and Wiener [22] developed a new type of differential equation that is called differential equation with piecewise constant arguments [23]. Using the method of reduction to discrete equations, many authors have analyzed the existence and uniqueness of solutions; oscillations, stability and periodic solutions of these equations [23-27]. Besides the theoretical analysis, various types of biological models have been constructed using differential equations with piecewise constant arguments [20, 28-31]. The first biological model has been presented by Buseenberg and Cooke [20] to investigate vertically transmitted diseases. Following this work, Ozturk et al. [28], Bozkurt et al. [29], Gurcan et al. [30], Kartal and Gurcan [31], have constructed a mathematical model with piecewise constant arguments for some biological phenomena such as bacteria population and tumor growth.

In the present paper, our aim is a better understanding of how both discrete and continuous times affect the dynamic behavior of the tumor growth model (1). So we will reconsider the model as a system of differential equations with piecewise constant arguments such as;

$$\begin{cases} \dfrac{dx}{dt} = x(t)\big(1 - x(t)\big) - ax(t)y([\![t]\!]) - bx(t)z([\![t]\!]), \\ \dfrac{dy}{dt} = cy(t)\big(1 - y(t)\big) - dx([\![t]\!])y(t), \\ \dfrac{dz}{dt} = \dfrac{ex([\![t]\!])z(t)}{x([\![t]\!]) + f} - gx([\![t]\!])z(t) - hz(t). \end{cases} \quad (2)$$

In this model, $x(t)$, $y(t)$ and $z(t)$ represent the tumor cell, healthy host cell and effector immune cell population respectively. $[\![t]\!]$ denotes the integer part of $t \in [0, \infty)$ and all these parameters are positive. In the first equation, the first term is logistic growth of tumor cells, the second and last terms represent the negative effect due to the interaction tumor-host cells and tumor-immune cells respectively. In the second equation, the healthy cells also grow logistically, with growth rate c and have loss of their population due to interaction with tumor cells that are represented in the second term. In the last equation, the first term is the stimulation of the immune system by tumor cells, the second term describes the loss of immune cells due to interaction with tumor cells and last term represents the natural death rate of the effector immune cells [5-6].

Local Stability Analysis

System (2) can be written in the interval $t \in [n, n+1)$ as follows:

$$\begin{cases} \dfrac{dx}{dt} - x(t)\big(1 - ay(n) - bz(n)\big) = -x^2(t), \\ \dfrac{dy}{dt} - y(t)(c - dx(n)) = -cy^2(t), \\ \dfrac{dz}{dt} = z(t)\left[\dfrac{ex(n)}{x(n) + f} - gx(n) - h\right]. \end{cases} \quad (3)$$

Solving system (3) in the interval $t \in [n, n+1)$ and letting $t \to n+1$ gives system of difference equation

$$\begin{cases} x(n+1) = \dfrac{x(n)[1 - ay(n) - bz(n)]}{[1 - ay(n) - bz(n) - x(n)]e^{-[1-ay(n)-bz(n)]} + x(n)}, \\ y(n+1) = \dfrac{y(n)[c - dx(n)]}{[c - dx(n) - cy(n)]e^{-[c-dx(n)]} + cy(n)}, \\ z(n+1) = z(n)e^{\frac{ex(n)}{x(n)+f} - gx(n) - h}. \end{cases} \quad (4)$$

System (4) reflects the rich dynamical characteristics and the asymptotic behavior of the system of differential equations with piecewise constant argument. Now, we need to obtain the equilibrium points to study the local behavior of the system. The positive equilibrium point of system (4) can be obtained as $E = (\bar{x}, \bar{y}, \bar{z})$ where

$$\bar{x} = \frac{e - fg - h - q}{2g}, \quad \bar{y} = \frac{-de + 2cg + dfg + dh + dq}{2cg}, \bar{z} = \frac{-ad(-e + fg + h + q) + c(-e + 2g - 2ag + fg + h + q)}{2bcg}$$

and

$$q = \sqrt{e^2 + (-fg + h)^2 - 2e(fg + h)}.$$

Let

$$f\big(x(n), y(n), z(n)\big) = \frac{x(n)[1 - ay(n) - bz(n)]}{[1 - ay(n) - bz(n) - x(n)]e^{-[1-ay(n)-bz(n)]} + x(n)},$$

$$g\big(x(n), y(n), z(n)\big) = \frac{y(n)[c - dx(n)]}{[c - dx(n) - cy(n)]e^{-[c-dx(n)]} + cy(n)}$$

and

$$h\big(x(n), y(n), z(n)\big) = z(n)e^{\frac{ex(n)}{x(n)+f} - gx(n) - h}.$$

Then, the linearized system of (4) about $(\bar{x},\bar{y},\bar{z})$ is $w(n+1)=Aw(n)$ where the Jacobian matrix A can be calculated;

$$A=\begin{pmatrix} a_{11}=\dfrac{\partial f}{\partial x(n)}(\bar{x},\bar{y},\bar{z}) & a_{12}=\dfrac{\partial f}{\partial y(n)}(\bar{x},\bar{y},\bar{z}) & a_{13}=\dfrac{\partial f}{\partial z(n)}(\bar{x},\bar{y},\bar{z}) \\ a_{21}=\dfrac{\partial g}{\partial x(n)}(\bar{x},\bar{y},\bar{z}) & a_{22}=\dfrac{\partial g}{\partial y(n)}(\bar{x},\bar{y},\bar{z}) & a_{23}=\dfrac{\partial g}{\partial z(n)}(\bar{x},\bar{y},\bar{z}) \\ a_{31}=\dfrac{\partial h}{\partial x(n)}(\bar{x},\bar{y},\bar{z}) & a_{32}=\dfrac{\partial h}{\partial y(n)}(\bar{x},\bar{y},\bar{z}) & a_{33}=\dfrac{\partial h}{\partial z(n)}(\bar{x},\bar{y},\bar{z}) \end{pmatrix}. \tag{5}$$

The elements of the A matrix are

$$a_{11}=e^{\frac{-e+fg+h+q}{2g}}=e^{-\bar{x}},\ a_{12}=a\left(-1+e^{\frac{-e+fg+h+q}{2g}}\right)=a(-1+e^{-\bar{x}}),\ a_{13}=b\left(-1+e^{\frac{-e+fg+h+q}{2g}}\right)=b(-1+e^{-\bar{x}}),$$

$$a_{21}=\frac{d\left(-1+e^{-c-\frac{dq}{2g}}\right)}{c}=\frac{d}{c}(-1+e^{-c\bar{y}}),\ a_{22}=e^{-c-\frac{d(-e+fg+h+q)}{2g}}=e^{-c\bar{y}},\ a_{23}=0,$$

$$a_{31}=\bar{z}\frac{2g(-e^2+(fg-h)(-fg+h+q)+e(2fg+2h+q))}{(-e-fg+h+q)^2},\qquad a_{32}=0,\qquad a_{33}=1$$

Now, the characteristic equation of the matrix A can be obtained as

$$\begin{aligned} p(\lambda)=\lambda^3&+\lambda^2(-e^{-\bar{x}}-e^{-c\bar{y}}-1)\\ &+\lambda\left(-\frac{ad}{c}(1-e^{-\bar{x}})(1-e^{-c\bar{y}})+b(1-e^{-\bar{x}})a_{31}+e^{-\bar{x}}+e^{-c\bar{y}}+e^{-\bar{x}}e^{-c\bar{y}}\right)\\ &+\frac{ad}{c}(1-e^{-\bar{x}})(1-e^{-c\bar{y}})-b(1-e^{-\bar{x}})a_{31}e^{-c\bar{y}}-e^{-\bar{x}}e^{-c\bar{y}}=0 \end{aligned} \tag{6}$$

where

$$p_2=-e^{-\bar{x}}-e^{-c\bar{y}}-1,$$

$$p_1=-\frac{ad}{c}(1-e^{-\bar{x}})(1-e^{-c\bar{y}})+b(1-e^{-\bar{x}})a_{31}+e^{-\bar{x}}+e^{-c\bar{y}}+e^{-\bar{x}}e^{-c\bar{y}},$$

and

$$p_0=\frac{ad}{c}(1-e^{-\bar{x}})(1-e^{-c\bar{y}})-a_{31}b(1-e^{-\bar{x}})e^{-c\bar{y}}-e^{-\bar{x}}e^{-c\bar{y}}.$$

Theorem 1. Suppose that $E=(\bar{x},\bar{y},\bar{z})$ is the equilibrium point of the system (4) and the characteristic polynomial of the Jacobian matrix of the linearized system for the model (4) is

$$p(\lambda)=\lambda^3+p_2\lambda^2+p_1\lambda+p_0\,. \tag{7}$$

The equilibrium point of the system (4) is local asymptotically stable if and only if

a) $p(1)=1+p_2+p_1+p_0>0,$

b) $(-1)p(-1)=1-p_2+p_1-p_0>0,$

c) $D_2^+=1+p_1-{p_0}^2-p_0p_2>0,$

d) $D_2^-=1-p_1+p_0p_2-{p_0}^2>0.$

The conditions of Theorem 1 can be easily obtained from the Schur-Cohn criteria [32]. Because analyzing the conditions of Theorem 1 is quite difficult, we will analyze these conditions numerically. For the parameter values $c = 0.6,\ d = 1,\ e = 3.5,\ f = 1.8,\ g = 0.2, h = 0.5,\ b = 2, a = 0.5$ and initial conditions $x(1) = y(1) = z(1) = 0.5$ which satisfy the conditions of Theorem 1, the positive equilibrium point $(\bar{x}, \bar{y}, \bar{z}) = (0.3502, 0.416333, 0.220817)$ is local asymptotically stable where blue, red and black graphs represent population density of tumor, healthy and immune cells respectively. (Figure 1).

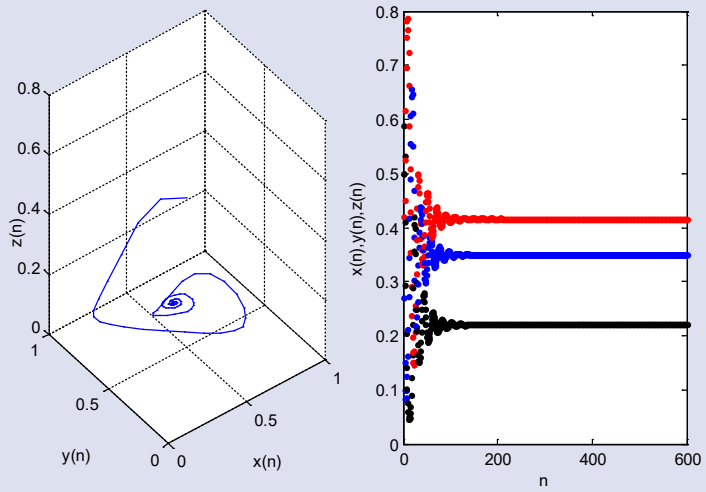

Figure 1. Graph of the iteration solution of x(n),y(n) and z(n) for the parameter values c=0.6,a=0.5,d=1,e=3.5,f=1.8, g=0.2,h=0.5,b=2 and initial conditions x(1)=y(1)=z(1)=0.5.

Neimark Sacker bifurcation and Chaotic Dynamics

In this section, we will prove that the system exhibits chaotic dynamics through Neimark-Sacker bifurcation which is a discrete version of Hopf bifurcation in continuous case. For this reason, we will calculate the Lyapunov exponent for the selected parameter sets.

Neimark Sacker bifurcation analysis

The following theorem gives necessary and sufficient algebraic conditions of Neimark-Sacker bifurcation.

Lemma [33]: Consider the following n-dimensional system:

$$X_{n+1} = f_q(X_n) \tag{8}$$

where $q \in R$ is considered as a bifurcation parameter. Suppose that characteristic polynomial of $J|_X$ about X of n-dimensional discrete dynamical system, which is depicted in system (8), is

$$P(\lambda) = \lambda^n + p_1\lambda^{n-1} + p_2\lambda^{n-2} + \cdots + p_n \tag{9}$$

Now considering the determinants: $\Delta_0^{\pm}(q) = 1, \Delta_1^{\pm}(q), \ldots, \Delta_n^{\pm}(q)$, which can be expressed as

$$\Delta_j^{\pm}(q) = \left| \begin{pmatrix} 1 & p_1 & p_2 & \ldots & p_{j-1} \\ 0 & 1 & p_1 & \ldots & p_{j-2} \\ 0 & 0 & 1 & \ldots & p_{j-3} \\ \ldots & \ldots & \ldots & \ldots & \ldots \\ 0 & 0 & 0 & \ldots & 1 \end{pmatrix} \mp \begin{pmatrix} p_{n-j+1} & p_{n-j+2} & \ldots & p_{n-1} & p_n \\ p_{n-j+2} & p_{n-j+3} & \ldots & p_n & 0 \\ \ldots & \ldots & \ldots & \ldots & \ldots \\ p_{n-1} & p_n & \ldots & 0 & 0 \\ p_n & 0 & \ldots & 0 & 0 \end{pmatrix} \right| \tag{10}$$

where j=1,…n. Furthermore, Neimark-sacker bifurcation occurs at critical value $q = q_0$ if following parametric condition hold:

NS1) Eigenvalue assignment: $P_{q_0}(1) > 0,\ (-1)^n P_{q_0}(-1) > 0,\ \Delta_{n-1}^{-}(q_0) = 0,\ \Delta_{n-1}^{+}(q_0) > 0, \Delta_j^{\pm}(q_0) > 0$ where $j = n-3, n-5, \ldots, 1$ (or 2), when n is even (or odd, respectively).

NS2) Transversality condition: $\frac{d}{dq}\Delta_{n-1}^{-}(q_0) \neq 0$

NS3) Nonresonance condition: $\frac{\cos(2\pi)}{l} \neq 1 - 0.5P_q(1)\frac{\Delta_{n-3}^{-}(q_0)}{\Delta_{n-2}^{-}(q_0)}$ or resonance condition $\frac{\cos(2\pi)}{l} = 1 - 0.5P_{q_0}(1)\frac{\Delta_{n-3}^{-}(q_0)}{\Delta_{n-2}^{-}(q_0)}$ where $l = 3,4, \ldots$

Theorem 2: Suppose that $E = (\bar{x}, \bar{y}, \bar{z})$ is the equilibrium point of the system (4). If

$$1 + p_2 + p_1 + p_0 > 0, \tag{11}$$

$$1 - p_2 + p_1 - p_0 > 0, \tag{12}$$

$$1 - p_1 + p_0 p_2 - {p_0}^2 = 0, \tag{13}$$

$$1 + p_1 - {p_0}^2 - p_0 p_2 > 0, \tag{14}$$

$$\frac{d}{dq}\left(\Delta_1^{-}(q)\right)|_{q=q_0} = \frac{d}{dq}(1 - p_1 + p_0 p_2 - {p_0}^2)|_{q=q_0} \neq 0 \tag{15}$$

and

$$\frac{\cos(2\pi)}{l} \neq 1 - 0.5P_q(1) = 1 - \frac{1 + p_2 + p_1 + p_0}{2} = \frac{1 - p_2 - p_1 - p_0}{2}. \tag{16}$$

Then the discrete dynamical system undergoes a Neimark-Sacker bifurcation about $E = (\bar{x}, \bar{y}, \bar{z})$

Proof:

The proof of the theorem can be easily seen from the conditions of Lemma for n=3.

Since it is very difficult to prove the conditions of Theorem 2 analytically, we will consider these conditions numerically. For this purpose we choose the parameter a as a bifurcation parameter and fixed all other parameter values such as $c = 0.6,\ d = 1.5,\ e = 3.5,\ f = 1.8,\ g = 0.2, h = 0.5,\ b = 0.2$. For these values we hold

$$p_2 = -2.58749,$$

$$p_1 = 2.20956 + 1.43128\,(0.6\,(0.25992 - 0.4\,a) + 0.21012\,a) - 0.0864656\,a$$

and

$$p_0 = -0.622072 - 1.26373(0.6(0.25992 - 0.4a) + 0.21012a) + 0.086456a.$$

From the solutions of equation (13), the critical Neimark-Sacker bifurcation is obtained as $\bar{a} = 0.877595$. In addition from the equations (11), (12) and (14) we have $1 + p_2 + p_1 + p_0 = 0.0217342 > 0,\ 1 - p_2 + p_1 - p_0 = 6.61698 > 0$ and $1 + p_1 - {p_0}^2 - p_0 p_2 = 0.977606 > 0$. In addition from the equations (15) and (16), one can obtain $\frac{d}{dq}\left(\Delta_1^{-}(q)\right)|_{q=q_0} = -0.0157666 \neq 0$ and $\frac{\cos(2\pi)}{l} \neq 0.989132$. Now all of the Neimark-Sacker bifurcation conditions are satisfied. For the critical value of $\bar{a}$, the eigenvalues are $\lambda_1 = 0.529395,\ \lambda_{2,3} = 0.977054 \pm 0.21299i$. Now, the conditions of Theorem 2 are satisfied and system (4) undergoes Neimark-Sacker bifurcation for the critical value $\bar{a} = 0.877595$ (Figure 2 and Figure 3).

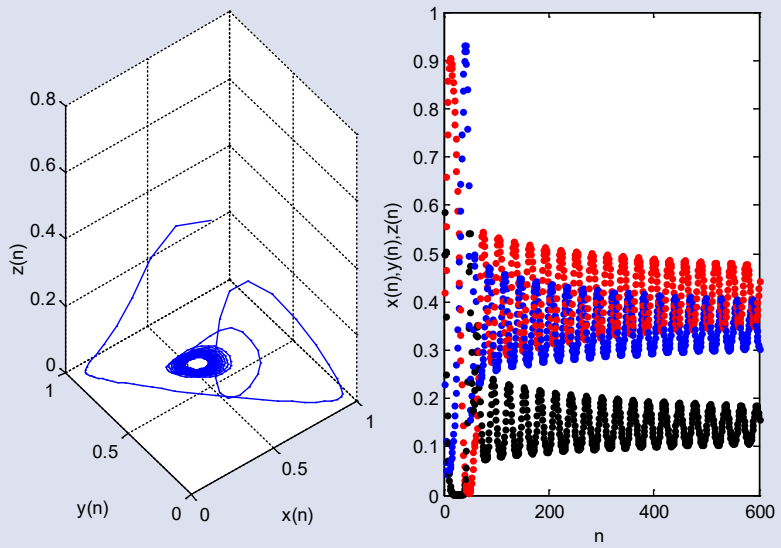

Figure 2. Time series plot and phase diagram of the discrete system (4) for $\bar{a} = 0.877595$. Initial conditions and other parameters are taken from Figure 1.

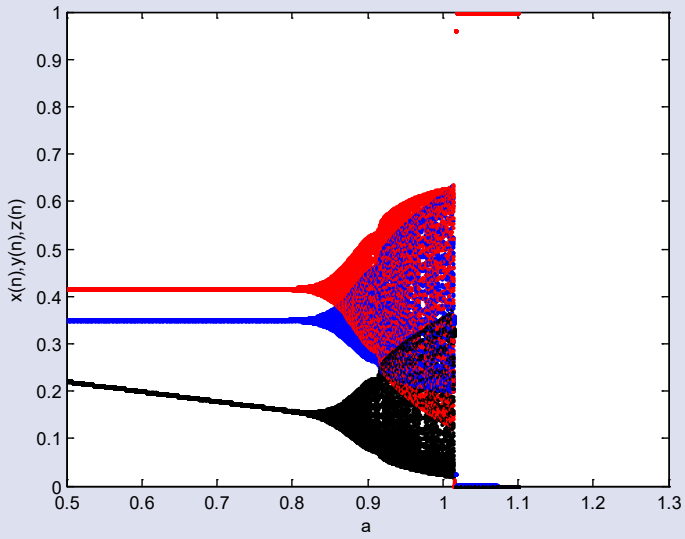

Figure 3. Bifurcation diagram of the discrete system (4) with respect to parameter a. Initial conditions and other parameters are the same as in Figure 1.

In addition, if we determine the bifurcation parameter as e then the critical bifurcation point is $\bar{e} = 4.47863$. In this situation, we have $p(1) = 0.0514048 > 0$, $(-1)p(-1) = 6.25374 > 0$ and $D_2^+ = 1.23655 > 0$ for the parameter value $\bar{e} = 4.47863$ where the eigenvalues of the Jacobian matrix are $\lambda_1 = 0.617838$, $\lambda_{2,3} = 0.932745 \pm 0.360538i$ (Figure 4 and Figure 5).

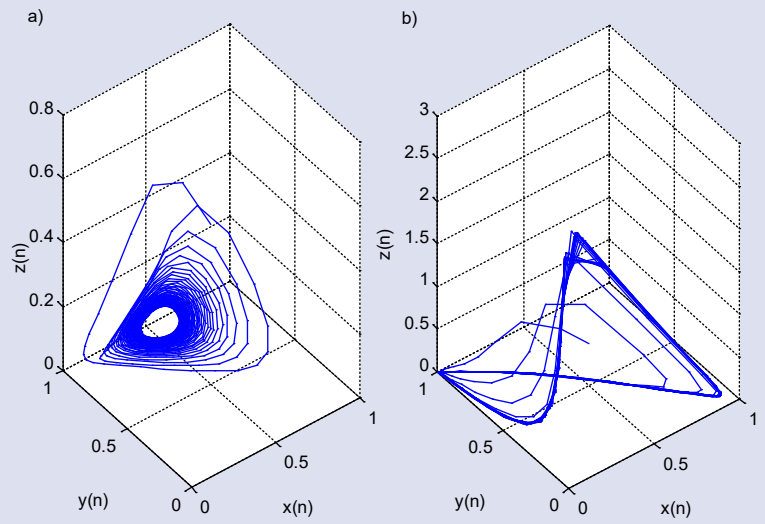

Figure 4. Time series plot and phase diagram of the discrete system (4) $\bar{e} = 4.47863$ (a) and e=6 (b) Initial conditions and other parameters are taken from Figure 1.

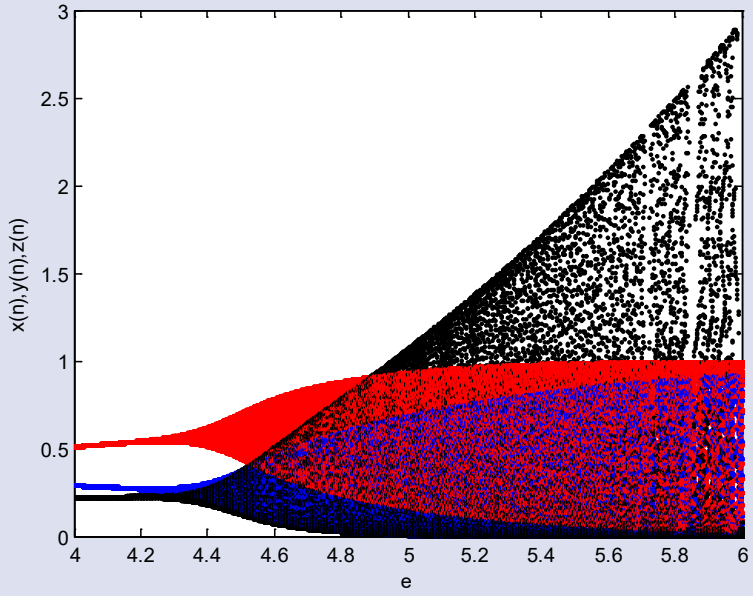

Figure 5. Bifurcation diagram of the system (4) with respect to parameter e. Initial conditions and other parameters are the same as in Figure 1.

The bifurcation point with respect to parameter f can be determined as $\bar{f} = 1.32821$, where $p(1) = 0.0499731 > 0$, $(-1)p(-1) = 6.24281 > 0$ and $D_2^+ = 1.24912 > 0$ and eigenvalues of the Jacobian matrix are $\lambda_1 = 0.61273$, $\lambda_{2,3} = 0.93548 \pm 0.353379i$ (Figure 6 and Figure 7).

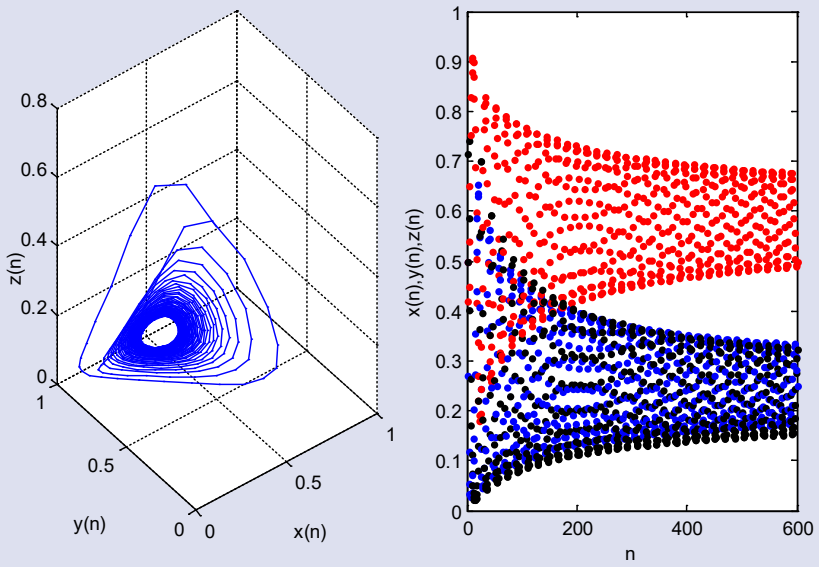

Figure 6. Time series plot and phase diagram of the discrete system (4) $\bar{f} = 1.32821$. Initial conditions and other parameters are taken from Figure 1.

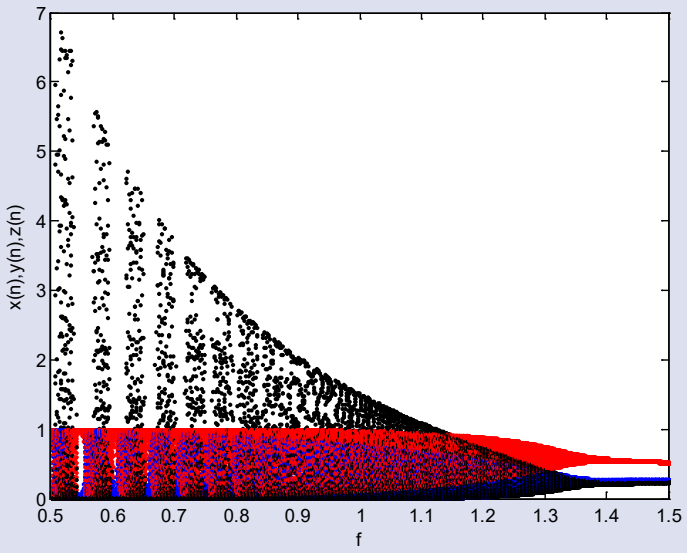

Figure 7. Bifurcation diagram of the discrete system (4) with respect to parameter f. Initial conditions and other parameters are the same as in Figure 1.

Chaotic Dynamics

In continuous and discrete dynamical systems, Lyapunov exponents or Lyapunov characteristic exponents (LCEs) are a useful tools to determine whether or not the system exhibits chaotic motion. If a Lyapunov exponent is positive, one can say that the system is chaotic. For discrete dynamical system $x_{k+1} = F(x_k), k = 0,1, \ldots$, one can use a method presented in [34-35] to determine Lyapunov exponents. The method is based on computing the QR decomposition of the Jacobian matrix A and can be summarized as follows:

Let Q_0 be an orthogonal matrix such that $Q_0{}^{T}.Q_0 = I$. Now, it can be obtained the decomposition $Z_{k+1} = Q_{k+1}.R_{k+1}$ by solving $Z_{k+1} = A_k.Q_k, k = 0,1, \ldots$, where Q_{k+1} is an orthogonal matrix and R_{k+1} is upper triangular matrix with positive diagonal elements [34]. Thus, the LCEs can be calculated as

$$\lambda_i = \lim_{k\to\infty} \frac{1}{k} \ln\left((R_i)_{jj}\right), \qquad j = 1, \ldots, m\,. \tag{17}$$

Now, we can obtain the Lyapunov exponents of the system by using the formula (17). The calculated LCEs of the system according to Figure 3, Figure 5 and Figure 7 are plotted in Figure 8, Figure 9 and Figure 10 respectively. It is understood from these figures that the system exhibits chaotic behavior for $a > \bar{a}$, $e > \bar{e}$ and $f > \bar{f}$.

Result and Discussion

In this paper we analyze a discrete-continuous time model describing the interactions among healthy cells, tumor cells and immune system cells. The idea of the model comes from the paper M. Itik and Banks [5]. Some numerical results are obtained for the local behavior of the model. To test these numerical results, most of the parameters values are taken from the study [5-6] in terms of consistency with the biological facts. Figure 1 shows the stable dynamics at the positive equilibrium point under the condition $a < 0.877595$ where all of the populations are exist.

For the bifurcation analysis, we select the parameters a, e, and f as bifurcation parameters. Neimark-Sacker bifurcation point is obtained as $\bar{a}$ =0.877595 (Figure 2). Increasing values of the parameter a shows that both tumor cells and immune system cells populations are extinct and healthy cells tend to their carrying capacity after the chaotic dynamics (Figure 3). This result is also valid for the study [6]. Another bifurcation points are obtained as $\bar{e}$ =4.47863 and $\bar{f} = 1.32821$ (Figure 4, Figure 5, Figure 6, Figure 7). Moreover, calculating Lyapunov exponents show that chaotic dynamics occur, if the parameter values a, e, f exceed bifurcation points (Figure 8, Figure 9 and Figure 10).

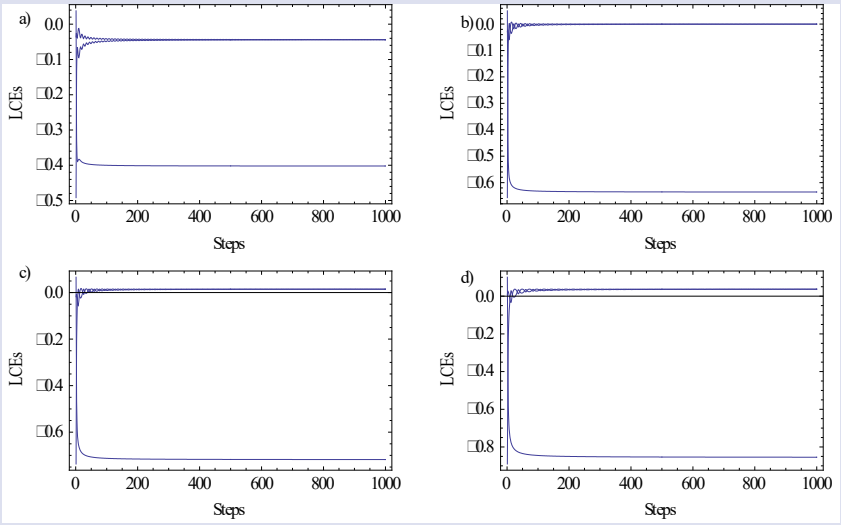

Figure 8. Converge plot of the Lyapunov spectrum for the system with respect to parameter a=1.5 (a), $\bar{a}$=0.87759 (b), a=1 (c) and r_1=1.2 (d).

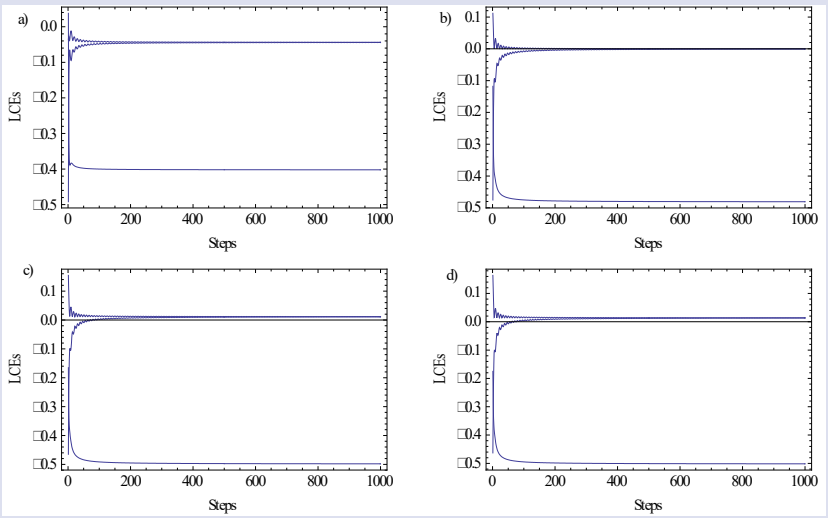

Figure 9. Converge plot of the Lyapunov spectrum for the system with respect to parameter e=3.5 (a), $\bar{e}$=4.47863 (b), e=4.9 (c) and e=5 (d).

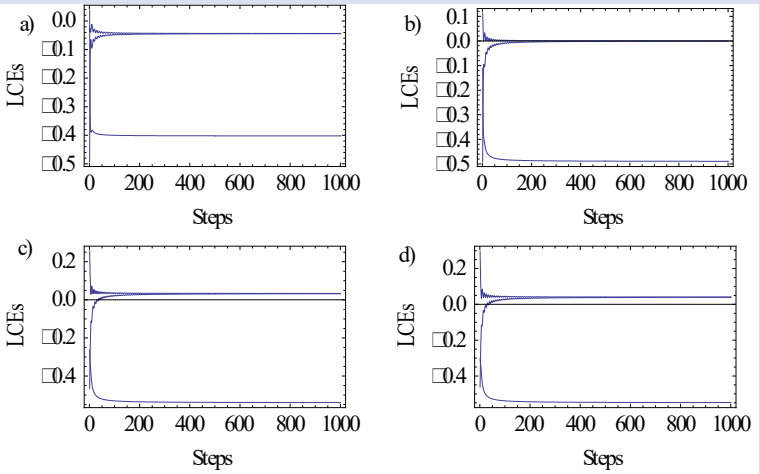

Figure 10. Converge plot of the Lyapunov spectrum for the system with respect to parameter f=1.8 (a), f=1.32821 (b), f=0.9 (c) and f=0.8 (d).

Conflicts of interest

There are no conflicts of interest in this work.

References

[1] Costa O.S., Molina L.M., Perez D.R., Antoranz J.C., Reyes M.C., Behavior of tumors under nonstationary therapy, *Physica D.,* 178 (2003) 242-253.

[2] Onofrio A.D., A general framework for modeling tumor-immune system competition and immunotherapy: mathematical analysis and biomedical inferences, *Physica D.,* 208 (2005) 220-235.

[3] Kuznetsov V.A., Makalkin I.A., Taylor M.A., Perelson A.S., Nonlinear dynamics of immunogenic tumors: parameter estimation and global bifurcation analysis, *Bull. Math. Biol.,* 56 (1994) 295-321.

[4] Kirschner D., Panetta J.C., Modeling immunotherapy of the tumor-immune interaction, *J. Math. Biol.*, 37 (1998) 235-252.

[5] Itık M., Banks S.P., Chaos in a three-dimensional cancer model, *Int. J. Bifurcat. Chaos.,* 20 (2010) 71-79.

[6] Galindo M.C., Nespoli C., Messias M., Hopf bifurcation, cascade of period-doubling, chaos, and the possibility of cure in a 3D cancer model, *Abstr. Appl. Anal.,* (2015) Article ID:354918.

[7] De Pillis L.G., Radunskaya A., The dynamics of an optimally controlled tumor model: A case study, *Math. Comput. Model.,* 37 (2003) 1221-1244.

[8] Sarkar R.R., Banerjee S., Cancer self remission and tumor stability- a stochastic approach, *Math. Biosci.,* 196 (2005) 65-81.

[9] Cho H., Lewis A.L, Storey K.M., Byrne H.M., Designing experimental conditions to use the Lotka–Volterra model to infer tumor cell line interaction types, *J. Theor. Biol.,* 559 (2023) 111377.

[10] Pham H., Mathematical Modeling the Time-Delay Interactions between Tumor Viruses and the Immune System with the Effects of Chemotherapy and Autoimmune Diseases, *Mathematics,* 10(5) (2022) 756.

[11] Das A., Dehingia K., Sarmah H.K., Hosseini K., Sadri K., Salahshour S., Analysis of a delay-induced mathematical model of cancer, *Adv. Cont. Discr. Mod.,* 15 (2022).

[12] Abernathy Z., Abernathy K., Stevens J., A mathematical model for tumor growth and treatment using virotherapy, *AIMS Math.,* 5(5) (2020) 4136-4150.

[13] Rihan F.A., Alsakaji H.J., Kundu S., Mohamed O., Dynamics of a time-delay differential model for tumour-immune interactions with random noise, *Alex. Eng. J.,* 61(12) (2022) 11913-11923.

[14] Bekker R.A., Kim S., Thomas S.P., Enderling H., Mathematical modeling of radiotherapy and its impact on tumor interactions with the immune system, *Neoplasia*, 28 (2022) 100796.

[15] Hussain J., Bano Z., Ahmed W., Shahid S., Analysis of stochastic dynamics of tumor with drug interventions, *Chaos Soliton Fract.,* 157 (2022) 111932.

[16] Hu X., Jang S.R.J., Dynamics of tumor–CD4–cytokine–host cells interactions with treatments, *Appl. Math. Comput.,* 321, (2018) 700-720.

[17] Rivaz A., Azizian M., Soltani M., Various Mathematical Models of Tumor Growth with Reference to Cancer Stem Cells: A Review, *Iran J. Sci. Technol. Trans. Sci.,* 4 (2019) 687–700.

[18] Kemwoue F.F., Deli V., Mendimi J.M., Gninzanlong C.L., Tagne J.F., Atangana J., Dynamics of cancerous tumors under the effect of delayed information: mathematical and electronic study, *Int. J. Dynam. Control.,* (2022).

[19] Banerjee S., Sarkar R.R., Delay-induced model for tumor-immune interaction and control of malignant tumor growth, *Biosystems.,* 91 (2008) 268-288.

[20] Busenberg, S., Cooke, K.L., Models of vertically transmitted diseases with sequential continuous dynamics, Nonlinear Phenomena in Mathematical Sciences, Academic Press, New York (1982).

[21] Cooke K.L., Györi I., Numerical approximation of the solutions of delay-differential equations on an infinite interval using piecewise constant argument, *Comput. Math. Appl.,* 28 (1994) 81-92.

[22] Shah S.M., Wiener J., Advanced differential equations with piecewise constant argument deviations*, Int. J. Math. Math. Sci.,* 6 (1983) 671–703.

[23] Akhmet M., Nonlinear hybrid continuous/discrete-time models, Atlantis Press (2011).

[24] Karakoç F., Oscillation of a first order linear impulsive delay differential equation with continuous and piecewise constant arguments, *Hacet. J. Math. Stat.,* 47(3) (2018) 601- 613.

[25] Chiu, K.S. Jeng, J.C. Stability of oscillatory solutions of differential equations with general piecewise constant arguments of mixed type, Math. *Nachrichten.,* 288(10) (2015) 1085-1097.

[26] Oztepe G.S., Existence and qualitative properties of solutions of a second order mixed type impulsive

[28] Ozturk, I., Bozkurt, F., Gurcan, F.: Stability analysis of a mathematical model in a microcosm with piecewise constant arguments, *Math. Biosci.*, 240 (2012) 85-91.

[29] Bozkurt F., Yousef A., Bilgil H., Baleanu D., A mathematical model with piecewise constant arguments of colorectal cancer with chemo-immunotherapy, *Chaos Soliton Fract.,* 168 (2023) 113207.

[30] Gurcan, F., Kartal, S., Ozturk, I., Bozkurt, F.: Stability and bifurcation analysis of a mathematical model for tumor-immune interaction with piecewise constant arguments of delay, *Chaos Soliton. Fract.* 68 (2014) 169-179.

[31] Kartal, S., Gurcan, F.: Stability and bifurcations analysis of a competition model with piecewise constant arguments, *Math. Methods. Appl. Sci.* 38 (2015) 1855-1866.

differential equation with piecewise constant arguments, *Hacet. J. Math. Stat.,* 46(6) (2017) 1077 – 1091.

[27] Oztepe G.S., Karakoç F., Bereketoglu H., Oscillation and Periodicity of a Second Order Impulsive Delay Differential Equation with a Piecewise Constant Argument, *Commun. Math.,* 25 (2017) 89–98.

[32] Li, X., Mou, C., Niu, W., Wang, D.: Stability analysis for discrete biological models using algebraic methods, *Math. Comput. Sci.* 5 (2011) 247-262.

[33] Khan, A.Q., Qureshi, S.M., Alotaibi, A.M.: Bifurcation analysis of a three species discrete-time predator-prey model, *Alex. Eng. J.* 61 (2022) 2853-7875.

[34] Sandri, M.: Numerical Calculation of Lyapunov Exponents, *The Mathematica Journal.*, 6 (1996) 78-84.

[35] Benettin, G., Galgani, L., Giorgilli, A., Strelcyn, J.M.: Lyapunov characteristic exponents for smooth dynamical systems and for Hamiltonian systems: A method for computing all of them. Part 2: Numerical application, 15 (1980) 21-30.

Cumhuriyet Sci. J., 44(2) (2023) 356-363
DOI: https://doi.org/10.17776/csj.1243136

Cumhuriyet Science Journal

| csj.cumhuriyet.edu.tr | Founded: 2002 ISSN: 2587-2680 e-ISSN: 2587-246X Publisher: Sivas Cumhuriyet University

Inverse Nodal Problem for a Conformable Fractional Diffusion Operator With Parameter-Dependent Nonlocal Boundary Condition

Yaşar Çakmak [1,a,*]

[1] *Department of Mathematics, Faculty of Sciences, Sivas Cumhuriyet University, Sivas, Türkiye.*
**Corresponding author*

Research Article

History
Received: 27/01/2022
Accepted: 06/06/2023

ABSTRACT

In this paper, we consider the inverse nodal problem for the conformable fractional diffusion operator with parameter-dependent Bitsadze–Samarskii type nonlocal boundary condition. We obtain the asymptotics for the eigenvalues, the eigenfunctions, and the zeros of the eigenfunctions (called nodal points or nodes) of the considered operator, and provide a constructive procedure for solving the inverse nodal problem, i.e., we reconstruct the potential functions $p(x)$ and $q(x)$ by using a dense subset of the nodal points.

Keywords: *Diffusion operator, Inverse nodal problem, Conformable fractional derivative, Nonlocal boundary condition.*

[a] *ycakmak@cumhuriyet.edu.tr* *https://orcid.org/0000-0002-6820-1322*

Introduction

Inverse nodal problem consists in reconstructing operators from given a dense set of zeros of eigenfunctions called nodal points or nodes. Inverse nodal problems for different differential operators have been studied for years. In 1988, McLaughlin gave a solution to inverse nodal problem for the Sturm–Liouville operator and sought to recover the potential function $\boldsymbol{q(x)}$ by using the zeros of the eigenfunctions (see [1]). In 1989, Hald and McLaughlin showed that it is sufficient to know the nodal points to uniquely determine the potential function of the Sturm–Liouville problem (see [2]). In 1997, Yang gave an algorithm to recover the potential function and boundary condition from any dense subset of the nodal points (see [3]). Inverse nodal problems have been investigated by several researchers for the Sturm—Liouville operators and the diffusion operators with the usual derivative (see [4]-[17] and references therein).

As known, there are two types of nonlocal boundary conditions, Bitsadze–Samarskii type conditions and integral type conditions. These conditions appear when data cannot be measured directly at the boundary and have many applications (see [18]-[19] and references therein). In 1969, firstly Bitsadze and Samarskii applied nonlocal boundary conditions to elliptic equations (see [20]). Some studies on inverse nodal problems for various types of operators with nonlocal boundary conditions can be seen in [21]-[27].

In 2014, Khalil et al. introduced new definition of fractional derivative called conformable fractional derivative of order α∈(0,1] (see [28]). In 2015, the basic properties and main results of this derivative were given by Abdeljawad and Atangana et al. ([29]-[30]). In recent years, the direct and inverse problems for the various operators which include conformable fractional derivatives have been studied (see [31]-[36] and references therein).

In current literature, there are any results on the inverse nodal problems for a diffusion operator with parameter-dependent Bitsadze–Samarskii-type nonlocal boundary condition, which include conformable fractional derivative.

Preliminaries

We give known some concepts of the conformable fractional calculus that more detail knowledge can be seen in [28]-[30] and [37].

Definition 2.1 Let $f:[0,\infty)\to\mathbb{R}$ be a given function. Then, the conformable fractional derivative of f of order α with respect to x is defined by

$$T_\alpha f(x)=\lim_{h\to 0}\frac{f(x+hx^{1-\alpha})-f(x)}{h},$$

$T_\alpha f(0)=\lim_{x\to 0^+}T_\alpha f(x)$, for all $x>0, \alpha\in(0,1]$.

If f is differentiable that is $f'(x)=\lim_{h\to 0}\frac{f(x+h)-f(x)}{h}$, then, $T_\alpha f(x)=x^{1-\alpha}f'(x)$.

Theorem 2.2 Let f, g be α −differentiable at $x, x>0$.

i) $T_\alpha(c_1f+c_2g)=c_1T_\alpha f+c_2T_\alpha g,\ \forall\, c_1,c_2\in\mathbb{R}$,
ii) $T_\alpha(x^r)=rx^{r-\alpha},\ \forall\, r\in\mathbb{R}$,
iii) $T_\alpha(c)=0,\ (c-const.)$
iv) $T_\alpha(fg)=T_\alpha(f)g+fT_\alpha(g)$,
v) $T_\alpha\left(\frac{f}{g}\right)=\frac{T_\alpha(f)g-fT_\alpha(g)}{g^2},\ (g\neq 0)$.

Definition 2.3 The conformable fractional integral is defined by

$$I_\alpha f(x) = \int_0^x f(t) d_\alpha t = \int_0^x t^{\alpha-1} f(t) dt, \text{for all } x > 0.$$

Theorem 2.4 (α −chain rule) Let $f, g: [0,\infty) \to \mathbb{R}$ be α −differentiable functions. Then, $f\big(g(x)\big)$ is α −differentiable function and for all x, $x \neq 0$, $g(x) \neq 0$

$$\Big(T_\alpha\big(f(g)\big)\Big)(x) = (T_\alpha f)\big(g(x)\big)(T_\alpha g)(x) g^{\alpha-1}(x).$$

Definition 2.5 (α −integration by parts) Let $f, g: [a,b] \to \mathbb{R}$ be α −differentiable functions. Then,

$$\int_a^b f(x) T_\alpha g(x) d_\alpha x = f(x) g(x)|_a^b - \int_a^b g(x) T_\alpha f(x) d_\alpha x.$$

Lemma 2.6 (α −Leibniz rule) Let $f(x,t)$ be a function such that $t^{\alpha-1} f(x,t)$ and $t^{\alpha-1} f_x(x,t)$ are continuous in t and x in some regions of the (x,t)-plane, including $a(x) \le t \le b(x)$, $x_0 \le x \le x_1$. If $a(x)$ and $b(x)$ are α −differentiable functions for $x_0 \le x \le x_1$, then,

$$T_\alpha\left(\int_{a(x)}^{b(x)} f(x,t) d_\alpha t\right) = T_\alpha b(x) f\big(x, b(x)\big) b^{\alpha-1}(x) - T_\alpha a(x) f\big(x, a(x)\big) a^{\alpha-1}(x) + \int_{a(x)}^{b(x)} T_\alpha f(x,t) d_\alpha t.$$

Definition 2.7 Let $1 \le p < \infty$, $a > 0$. The space $L_{p,\alpha}(0,a)$ consists of all functions $f: [0,a] \to \mathbb{R}$ satisfying the condition

$$\left(\int_0^a |f(x)|^p d_\alpha x\right)^{1/p} < \infty.$$

Lemma 2.8 The space $L_{p,\alpha}(0,a)$ associated with the norm function

$$\|f\|_{p,\alpha} := \left(\int_0^a |f(x)|^p d_\alpha x\right)^{1/p}$$

is a Banach space. Moreover if $p = 2$ then $L_{2,\alpha}(0,a)$ associated with the inner product for $f, g \in L_{2,\alpha}(0,a)$

$$\langle f, g\rangle := \int_0^a f(x)\overline{g(x)} d_\alpha x$$

is a Hilbert space.

Definition 2.9 Let $1 \le p < \infty$. The Sobolev space $W_{p,\alpha}^1[0,a]$ consists of all functions on $[0,a]$ such that $f(x)$ is absolutely continuous and $T_\alpha f(x) \in L_{p,\alpha}(0,a)$.

Asymptotics of the Eigenvalues and Eigenfunctions

In this section, we consider a diffusion operator with parameter-dependent Bitsadze–Samarskii-type nonlocal boundary condition which includes conformable fractional derivatives of order α instead of the ordinary derivatives in a traditional diffusion operator. The operator $L_\alpha = L_\alpha(p(x), q(x), \beta)$ is called a conformable fractional diffusion operator (CFDO) and is the form

$$\ell_\alpha y := -T_\alpha T_\alpha y + [2\lambda p(x) + q(x)] y = \lambda^2 y, \quad 0 < x < 1 \tag{1}$$

$$U_\alpha(y) := y(0) = 0 \tag{2}$$

$$V_\alpha(y) := \lambda y(1) - y(\beta) = 0 \tag{3}$$

where λ is the spectral parameter, $\alpha \in (0,1]$, $q(x) \in W_{2,\alpha}^1[0,1]$, $p(x) \in W_{2,\alpha}^2[0,1]$ are real-valued functions, $p(x) \neq const.$, $\beta \in (0,1)$, and for $\gamma = \beta, 1$

$$\int_0^\gamma p(x) d_\alpha x = 0. \tag{4}$$

From [35], the general solution of equation (1)

$$y(x,\lambda;\alpha)=c_1\cos\left(\frac{\lambda}{\alpha}x^\alpha-Q(x)\right)+c_2\sin\left(\frac{\lambda}{\alpha}x^\alpha-Q(x)\right)$$
$$+\int_0^x\frac{\sin\left(\frac{\lambda}{\alpha}(x^\alpha-t^\alpha)-Q(x)+Q(t)\right)}{\lambda-p(t)}\left((q(t)+p^2(t))y(t,\lambda;\alpha)+\frac{T_\alpha p(t)}{\lambda-p(t)}T_\alpha y(t,\lambda;\alpha)\right)d_\alpha t, \tag{5}$$

where,

$$Q(x):=\int_0^x p(t)d_\alpha t. \tag{6}$$

Let the functions $C=C(x,\lambda;\alpha)$ and $S=S(x,\lambda;\alpha)$ be solutions of equation (1) under the initial conditions

$$C(0,\lambda;\alpha)=1,\ T_\alpha C(0,\lambda;\alpha)=0 \text{ and } S(0,\lambda;\alpha)=0,\ T_\alpha S(0,\lambda;\alpha)=1 \tag{7}$$

respectively.

Thus, from (5), following solutions

$$C(x,\lambda;\alpha)=\cos\left(\frac{\lambda}{\alpha}x^\alpha-Q(x)\right)$$
$$+\int_0^x\frac{\sin\left(\frac{\lambda}{\alpha}(x^\alpha-t^\alpha)-Q(x)+Q(t)\right)}{\lambda-p(t)}\left((q(t)+p^2(t))C(t,\lambda;\alpha)+\frac{T_\alpha p(t)}{\lambda-p(t)}T_\alpha C(t,\lambda;\alpha)\right)d_\alpha t \tag{8}$$

and

$$S(x,\lambda;\alpha)=\frac{\sin\left(\frac{\lambda}{\alpha}x^\alpha-Q(x)\right)}{\lambda-p(0)}$$
$$+\int_0^x\frac{\sin\left(\frac{\lambda}{\alpha}(x^\alpha-t^\alpha)-Q(x)+Q(t)\right)}{\lambda-p(t)}\left((q(t)+p^2(t))S(t,\lambda;\alpha)+\frac{T_\alpha p(t)}{\lambda-p(t)}T_\alpha S(t,\lambda;\alpha)\right)d_\alpha t, \tag{9}$$

are obtained.

From [14], [35] and [38], for the asymptotic representations of the functions $C(x,\lambda;\alpha)$ and $S(x,\lambda;\alpha)$, the following lemma can be given.

Lemma 3.1 For $|\lambda|\to\infty$ and each fixed α, the following asymptotic formulae is valid:

$$C(x,\lambda;\alpha)=\cos\left(\frac{\lambda}{\alpha}x^\alpha-Q(x)\right)+O\left(\frac{1}{\lambda}\exp\left(|\mathrm{Im}\lambda|\frac{x^\alpha}{\alpha}\right)\right) \tag{10}$$

and

$$\begin{aligned}S(x,\lambda;\alpha)=&\frac{1}{\lambda}\sin\left(\frac{\lambda}{\alpha}x^\alpha-Q(x)\right)\\&+\frac{1}{2\lambda^2}\Big\{(p(x)+p(0))\sin\left(\frac{\lambda}{\alpha}x^\alpha-Q(x)\right)-c_1(x)\cos\left(\frac{\lambda}{\alpha}x^\alpha-Q(x)\right)\\&+\int_0^x(q(t)+p^2(t))\cos\left(\frac{\lambda}{\alpha}(x^\alpha-2t^\alpha)-Q(x)+2Q(t)\right)d_\alpha t\\&+\int_0^x(T_\alpha p(t))\sin\left(\frac{\lambda}{\alpha}(x^\alpha-2t^\alpha)-Q(x)+2Q(t)\right)d_\alpha t\Big\}\\&+\frac{1}{4\lambda^3}\Big\{c_3(x)\sin\left(\frac{\lambda}{\alpha}x^\alpha-Q(x)\right)-c_4(x)\cos\left(\frac{\lambda}{\alpha}x^\alpha-Q(x)\right)\Big\}\\&+O\left(\frac{1}{\lambda^4}\exp\left(|\mathrm{Im}\lambda|\frac{x^\alpha}{\alpha}\right)\right),\end{aligned} \tag{11}$$

where,

$$c_1(x)=\int_0^x (q(t)+p^2(t))d_\alpha t,\ c_2(x)=\int_0^x (q(t)+p^2(t))p(t)d_\alpha t,$$
$$c_3(x)=4p^2(0)+\frac{2(p(x)+p(0))^{1+\alpha}-2^{2+\alpha}p^{1+\alpha}(0)+(p(x)-p(0))^{1+\alpha}}{1+\alpha}-\frac{1}{2}\left(\int_0^x (q(t)+p^2(t))d_\alpha t\right)^2,$$
$$c_4(x)=\int_0^x (q(t)+p^2(t))(p(x)+p(0)+2p(t))d_\alpha t=(p(x)+p(0))c_1(x)+2c_2(x).$$

The eigenvalues of the problem L_α coincide with the zeros of its characteristic function given by

$$\Delta_\alpha(\lambda)=\begin{vmatrix} U_\alpha(C) & U_\alpha(S) \\ V_\alpha(C) & V_\alpha(S)\end{vmatrix}=\lambda S(1,\lambda;\alpha)-S(\beta,\lambda;\alpha). \tag{12}$$

Thus, using the formulae (4), (11), and (12), we obtain the following asymptotic formula for $\Delta_\alpha(\lambda)$

$$\begin{aligned}\Delta_\alpha(\lambda)=&\sin\frac{\lambda}{\alpha}+\frac{1}{2\lambda}\Big\{(p(1)+p(0))\sin\frac{\lambda}{\alpha}-c_1(1)\cos\frac{\lambda}{\alpha}-2\sin\frac{\lambda}{\alpha}\beta^\alpha\\&+\int_0^1 (q(t)+p^2(t))\cos\left(\frac{\lambda}{\alpha}(1-2t^\alpha)+2Q(t)\right)d_\alpha t\\&+\int_0^1 (T_\alpha p(t))\sin\left(\frac{\lambda}{\alpha}(1-2t^\alpha)+2Q(t)\right)d_\alpha t\Big\}\\&+\frac{1}{4\lambda^2}\Big\{c_3(1)\sin\frac{\lambda}{\alpha}-c_4(1)\cos\frac{\lambda}{\alpha}-2(p(\beta)+p(0))\sin\frac{\lambda}{\alpha}\beta^\alpha+2c_1(\beta)\cos\frac{\lambda}{\alpha}\beta^\alpha\Big\}\\&+O\left(\frac{1}{\lambda^3}\exp\frac{|\operatorname{Im}\lambda|}{\alpha}\right),|\lambda|\to\infty.\end{aligned} \tag{13}$$

By the method in [10], using (13) and Rouchè theorem and taking $\Delta_\alpha(\lambda_n)=0$ we can prove that the eigenvalues λ_n have the form

$$\begin{aligned}\lambda_n=&n\alpha\pi+\frac{c_1(1)-A_n^n+2(-1)^n\sin n\beta^\alpha\pi}{2n\pi}\\&+\frac{(p(1)+p(0))c_1(1)+2c_2(1)+2(-1)^n(p(\beta)+p(0))\sin n\beta^\alpha\pi-2(-1)^n c_1(\beta)\cos n\beta^\alpha\pi}{4n^2\alpha\pi^2}\\&+o\left(\frac{1}{n^2}\right),|n|\to\infty,\end{aligned} \tag{14}$$

where, for $n\in\mathbb{Z}\backslash\{0\}$, $x_n^0=0, x_n^n=1,\ \ j\in\mathbb{Z}$,

$$A_n^j=\int_0^{x_n^j}(q(t)+p^2(t))\cos(2n\pi t^\alpha-2Q(t))d_\alpha t-\int_0^{x_n^j}(T_\alpha p(t))\sin(2n\pi t^\alpha-2Q(t))d_\alpha t.$$

Inverse Nodal Problem

In this section, under condition (7) we obtain the asymptotics for the zeros of the function $\varphi(x,\lambda_n;\alpha)$ called the nodal points of the operator L_α and develop a constructive procedure for solving the inverse nodal problem.

It is clear from (14) that for sufficiently large $|n|$, there is exactly one eigenvalue λ_n in the domain $\Gamma_n=\{\lambda:|\lambda-n\alpha\pi|\le\delta\}$, $\delta>0$ and since the functions $p(x)$ and $q(x)$ are real-valued, λ_n are real. Thus, the functions $\varphi(x,\lambda_n;\alpha)$ are real-valued and

$$\varphi(x,\lambda_n;\alpha)=U_\alpha(C(x,\lambda_n;\alpha))S(x,\lambda_n;\alpha)-U_\alpha(S(x,\lambda_n;\alpha))C(x,\lambda_n;\alpha)=S(x,\lambda_n;\alpha) \tag{15}$$

are the eigenfunctions corresponding to the eigenvalues λ_n for sufficiently large $|n|$.

Thus, substituting (14) in (11), we get

$$\begin{aligned}\lambda_n\varphi(x,\lambda_n;\alpha)=&\sin(n\pi x^\alpha-Q(x))\\&+\frac{1}{2n\alpha\pi}\{[(c_1(1)-A_n^n+2(-1)^n\sin n\beta^\alpha\pi)x^\alpha-c_1(x)]\cos(n\pi x^\alpha-Q(x))\\&+(p(x)+p(0))\sin(n\pi x^\alpha-Q(x))\end{aligned}$$

$$
\begin{aligned}
&+\int_0^x (q(t)+p^2(t))\cos(n\pi(x^\alpha-2t^\alpha)-Q(x)+2Q(t))d_\alpha t\\
&+\int_0^x (T_\alpha p(t))\sin(n\pi(x^\alpha-2t^\alpha)-Q(x)+2Q(t))d_\alpha t\}\\
&+\frac{1}{4n^2\alpha^2\pi^2}\{[(p(1)+p(0))c_1(1)x^\alpha+2c_2(1)x^\alpha\\
&+2(-1)^n(p(\beta)+p(0))x^\alpha\sin n\beta^\alpha\pi-2(-1)^n c_1(\beta)x^\alpha\cos n\beta^\alpha\pi\\
&+(p(x)+p(0))(c_1(1)+2(-1)^n\sin n\beta^\alpha\pi)x^\alpha-c_4(x)]\cos(n\pi x^\alpha-Q(x))\\
&+[c_1(x)(c_1(1)+2(-1)^n\sin n\beta^\alpha\pi)x^\alpha\\
&-(c_1(1)+2(-1)^n\sin n\beta^\alpha\pi)^2x^{2\alpha}+c_3(x)]\sin(n\pi x^\alpha-Q(x))\\
&+o\left(\frac{1}{n^2}\right),|n|\to\infty,
\end{aligned}
\tag{16}
$$

uniformly in $x\in[0,1]$.

We can see from (16) that for sufficiently large $|n|$ and each fixed α, the eigenfunctions $\varphi(x,\lambda_n;\alpha)$ has exactly $|n|-1$ nodal points x_n^j, $j\in\mathbb{Z}$ in $(0,1)$ as

$$0<x_n^1<x_n^2<\ldots<x_n^{n-1}<1 \text{ for } n>0$$

and

$$0<x_n^{-1}<x_n^{-2}<\ldots<x_n^{n+1}<1 \text{ for } n<0.$$

Lemma 4.1 The numbers x_n^j satisfy the following asymptotic formula for sufficiently large $|n|$ and each fixed α:

$$
\begin{aligned}
\left(x_n^j\right)^\alpha&=\frac{j}{n}+\frac{Q(x_n^j)}{n\pi}\\
&+\frac{1}{2n^2\alpha\pi^2}\left[c_1\left(x_n^j\right)-c_1(1)(x_n^j)^\alpha-\left(A_n^j-A_n^n(x_n^j)^\alpha\right)-2(-1)^n(x_n^j)^\alpha\sin n\beta^\alpha\pi\right]\\
&+\frac{1}{2n^3\alpha^2\pi^3}\left[c_2\left(x_n^j\right)-\left(c_2(1)+\frac{(p(1)+p(0))c_1(1)}{2}\right)(x_n^j)^\alpha\right.\\
&\left.+(-1)^n(p(\beta)+p(0))(x_n^j)^\alpha\sin n\beta^\alpha\pi-(-1)^n c_1(\beta)(x_n^j)^\alpha\cos n\beta^\alpha\pi\right]\\
&+o\left(\frac{1}{n^3}\right),
\end{aligned}
\tag{17}
$$

uniformly with respect to *j*.

Proof. From (15) and taking $\varphi\left(x_n^j,\lambda_n;\alpha\right)=0$, we get

$$
\begin{aligned}
&\sin\left(n\pi\left(x_n^j\right)^\alpha-Q\left(x_n^j\right)\right)+\frac{1}{2n\alpha\pi}\left\{\left[(c_1(1)-A_n^n+2(-1)^n\sin n\beta^\alpha\pi)(x_n^j)^\alpha-c_1\left(x_n^j\right)\right]\cos\left(n\pi\left(x_n^j\right)^\alpha-Q\left(x_n^j\right)\right)\right.\\
&+\left(p(x_n^j)+p(0)\right)\sin\left(n\pi\left(x_n^j\right)^\alpha-Q\left(x_n^j\right)\right)+\int_0^{x_n^j}(q(t)+p^2(t))\cos\left(n\pi\left(\left(x_n^j\right)^\alpha-2t^\alpha\right)-Q(x_n^j)+2Q(t)\right)d_\alpha t\\
&\left.+\int_0^{x_n^j}(T_\alpha p(t))\sin\left(n\pi\left(\left(x_n^j\right)^\alpha-2t^\alpha\right)-Q(x_n^j)+2Q(t)\right)d_\alpha t\right\}+\frac{1}{4n^2\alpha^2\pi^2}\left\{\left[\left(p(1)+p(0)\right)c_1(1)\left(x_n^j\right)^\alpha+2c_2(1)\left(x_n^j\right)^\alpha\right.\right.\\
&+2(-1)^n\left(p(\beta)+p(0)\right)\left(x_n^j\right)^\alpha\sin n\beta^\alpha\pi-2(-1)^n c_1(\beta)\left(x_n^j\right)^\alpha\cos n\beta^\alpha\pi\\
&\left.+\left(p\left(x_n^j\right)+p(0)\right)\left(c_1(1)+2(-1)^n\sin n\beta^\alpha\pi\right)\left(x_n^j\right)^\alpha-c_4\left(x_n^j\right)\right]\cos\left(n\pi\left(x_n^j\right)^\alpha-Q\left(x_n^j\right)\right)\\
&+\left[c_1\left(x_n^j\right)(c_1(1)+2(-1)^n\sin n\beta^\alpha\pi)\left(x_n^j\right)^\alpha-(c_1(1)+2(-1)^n\sin n\beta^\alpha\pi)^2\left(x_n^j\right)^{2\alpha}\right.\\
&\left.\left.+c_3\left(x_n^j\right)\right]\sin\left(n\pi\left(x_n^j\right)^\alpha-Q\left(x_n^j\right)\right)\right\}+o\left(\frac{1}{n^2}\right)=0,|n|\to\infty.
\end{aligned}
$$

If last equality is divided by $\cos\left(n\pi\left(x_n^j\right)^\alpha-Q\left(x_n^j\right)\right)$ and necessary arrangements are made, for $|n|\to\infty$, we obtain that

$$\tan\left(n\pi\left(x_n^j\right)^\alpha - Q\left(x_n^j\right)\right) = \left\{1 + \frac{1}{2n\alpha\pi}\left[p\left(x_n^j\right) + p(0) + B_n^j\right] + \frac{1}{4n^2\alpha^2\pi^2}\left[c_1\left(x_n^j\right)\left(c_1(1) + 2(-1)^n \sin n\beta^\alpha\pi\right)\left(x_n^j\right)^\alpha\right.\right.$$
$$\left.\left. -\left(c_1(1) + 2(-1)^n \sin n\beta^\alpha\pi\right)^2\left(x_n^j\right)^{2\alpha} - c_3\left(x_n^j\right)\right]\right\}^{-1} \times \left\{-\frac{1}{2n\alpha\pi}\left[\left(c_1(1) - A_n^n + 2(-1)^n \sin n\beta^\alpha\pi\right)\left(x_n^j\right)^\alpha - c_1\left(x_n^j\right) + A_n^j\right] - \frac{1}{4n^2\alpha^2\pi^2}\left[\left(p(1) + p(0)\right)c_1(1)\left(x_n^j\right)^\alpha + 2c_2(1)\left(x_n^j\right)^\alpha + 2(-1)^n\left(p(\beta) + p(0)\right)\left(x_n^j\right)^\alpha \sin n\beta^\alpha\pi - 2(-1)^n c_1(\beta)\left(x_n^j\right)^\alpha \cos n\beta^\alpha\pi + \left(p\left(x_n^j\right) + p(0)\right)\left(c_1(1) + 2(-1)^n \sin n\beta^\alpha\pi\right)\left(x_n^j\right)^\alpha - c_4\left(x_n^j\right)\right] + o\left(\frac{1}{n^2}\right)\right\},$$

where,

$$B_n^j = \int_0^{x_n^j} \left(q(t) + p^2(t)\right)\sin\left(2n\pi t^\alpha - 2Q(t)\right)d_\alpha t + \int_0^{x_n^j} \left(T_\alpha p(t)\right)\cos\left(2n\pi t^\alpha - 2Q(t)\right)d_\alpha t.$$

Hence, if Taylor's expansion formula is taken into account for the function $\frac{1}{1+u}$ as $u \to 0$ then,

$$\tan\left(n\pi\left(x_n^j\right)^\alpha - Q\left(x_n^j\right)\right) = \frac{1}{2n\alpha\pi}\left[c_1\left(x_n^j\right) - c_1(1)\left(x_n^j\right)^\alpha - \left(A_n^j - A_n^n\left(x_n^j\right)^\alpha\right) - 2(-1)^n\left(x_n^j\right)^\alpha \sin n\beta^\alpha\pi\right]$$
$$+ \frac{1}{2n^2\alpha^2\pi^2}\left[c_2\left(x_n^j\right) - \left(c_2(1) + \frac{\left(p(1)+p(0)\right)c_1(1)}{2}\right)\left(x_n^j\right)^\alpha + (-1)^n\left(p(\beta) + p(0)\right)\left(x_n^j\right)^\alpha \sin n\beta^\alpha\pi - (-1)^n c_1(\beta)\left(x_n^j\right)^\alpha \cos n\beta^\alpha\pi\right] + o\left(\frac{1}{n^2}\right),\ |n| \to \infty$$

and if Taylor's expansion formula for Arctangent is taken into account then,

$$n\pi\left(x_n^j\right)^\alpha - Q\left(x_n^j\right) = j\pi + \frac{1}{2n\alpha\pi}\left[c_1\left(x_n^j\right) - c_1(1)\left(x_n^j\right)^\alpha - \left(A_n^j - A_n^n\left(x_n^j\right)^\alpha\right) - 2(-1)^n\left(x_n^j\right)^\alpha \sin n\beta^\alpha\pi\right] +$$
$$\frac{1}{2n^2\alpha^2\pi^2}\left[c_2\left(x_n^j\right) - \left(c_2(1) + \frac{\left(p(1)+p(0)\right)c_1(1)}{2}\right)\left(x_n^j\right)^\alpha + (-1)^n\left(p(\beta) + p(0)\right)\left(x_n^j\right)^\alpha \sin n\beta^\alpha\pi - (-1)^n c_1(\beta)\left(x_n^j\right)^\alpha \cos n\beta^\alpha\pi\right] + o\left(\frac{1}{n^2}\right),\ |n| \to \infty$$

is obtained. From the last equality, we arrive at (17).

Corollary 4.2 From (17) it is obvious that for each fixed α, the set X of all nodal points is dense in the interval $[0,1]$.

Let X be the set of nodal points and $\beta^\alpha = \frac{k}{\ell}$, $k, \ell \in \mathbb{Z}$. For each fixed $x \in [0,1]$ and $\alpha \in (0,1]$, we can choose a sequence $\{j_n\} \subset X$ so that $\lim_{|n|\to\infty} x_n^{j_n} = x$. Clearly the subsequence $\left\{x_m^{j_m}\right\}$ converges also to x for $m = 2n\ell$. Then, there exist finite limits and corresponding equalities hold:

$$\pi \lim_{|m|\to\infty}\left(m\left(x_m^{j_m}\right)^\alpha - j_m\right) := Q(x), \tag{18}$$

$$2\alpha\pi \lim_{|m|\to\infty} m\left[\pi\left(m\left(x_m^{j_m}\right)^\alpha - j_m\right) - Q\left(x_m^{j_m}\right)\right] := f(x), \tag{19}$$

$$\alpha\pi \lim_{|m|\to\infty} m\left\{2\alpha m\pi\left[\pi\left(m\left(x_m^{j_m}\right)^\alpha - j_m\right) - Q\left(x_m^{j_m}\right)\right]\right. \tag{20}$$
$$\left. -f\left(x_m^{j_m}\right) + A_m^{j_m} - A_m^m\left(x_m^{j_m}\right)^\alpha + 2(-1)^m\left(x_m^{j_m}\right)^\alpha \sin m\beta^\alpha\pi\right\} := g(x)$$

and

$$f(x) = c_1(x) - c_1(1)x^\alpha, \tag{21}$$

$$g(x) = c_2(x) - \left(c_2(1) + \frac{\left(p(1)+p(0)\right)c_1(1)}{2}\right)x^\alpha - c_1(\beta)x^\alpha. \tag{22}$$

Therefore, we can prove the following theorem for the solution of the inverse nodal problem.

Theorem 4.3 Given any dense subset of nodal points $X_0 \subset X$ uniquely determines the functions $p(x)$ and $q(x)$ a.e. on $[0,1]$. Moreover, these functions can be found by the following procedure.

Step-1. Denote $m = 2n\ell$ and for each fixed x and α, choose a sequence $\left\{x_m^{j_m}\right\} \subset X_0$ such that $\lim_{|m|\to\infty} x_m^{j_m} = x$,

Step-2. Find the function $Q(x)$ from (18) and taking into account (6) calculate

$$p(x) = T_\alpha Q(x), \tag{23}$$

Step-3. Find the function $f(x)$ from (19) and determine

$$q(x) - \alpha \int_0^1 q(t)d_\alpha t := r(x) = T_\alpha f(x) - p^2(x) + \alpha \int_0^1 p^2(t)d_\alpha t, \tag{24}$$

Step-4. $2\alpha Q(x) - (p(1) + p(0))x^\alpha - 2\beta^\alpha x^\alpha \neq 0$ and for each fixed x, α, find $g(x)$ from (20) and calculate

$$\begin{aligned}\int_0^1 q(t)d_\alpha t = \frac{2}{2\alpha Q(x) - (p(1) + p(0))x^\alpha - 2\beta^\alpha x^\alpha}\Bigg[g(x) - \int_0^x (r(t) + p^2(t))p(t)d_\alpha t \\ + x^\alpha \int_0^1 (r(t) + p^2(t))p(t)d_\alpha t + \frac{(p(1)+p(0))x^\alpha}{2}\int_0^1 (r(t) + p^2(t))d_\alpha t \\ + x^\alpha \int_0^\beta (r(t) + p^2(t))d_\alpha t\Bigg],\end{aligned} \tag{25}$$

Step-5. Calculate the function $q(x)$ via the formula

$$q(x) = r(x) + \alpha \int_0^1 q(t)d_\alpha t. \tag{26}$$

Proof. From (6), it is obvious that formula (23) is provided.

α-differentiating (21), we get

$$T_\alpha f(x) = q(x) + p^2(x) - \alpha \int_0^1 (q(t) + p^2(t))d_\alpha t.$$

If denote $r(x) := q(x) - \alpha \int_0^1 q(t)d_\alpha t$, then we obtain (24). If we substitute $q(x) = r(x) + \alpha \int_0^1 q(t)d_\alpha t$ in (22) and take (4) into account, we get formula (25).

Finally, from (24) and (25), we arrive at (26).

Conflicts of interest

There are no conflicts of interest in this work.

Acknowledgements

I would like to express his gratitude to the editor and anonymous referees for their helpful comments which significantly improved the quality of the paper.

References

[1] McLaughlin J.R., Inverse Spectral Theory Using Nodal Points as Data—a Uniqueness Result, *J. Differential Equations*, 73 (2) (1988) 354-362.

[2] Hald O.H., McLaughlin J.R., Solutions of Inverse Nodal Problems, *Inverse Problems*, 5 (1989) 307-347.

[3] Yang X.F., A Solution of the Nodal Problem, *Inverse Problems*, 13 (1997) 203-213.

[4] Browne P.J., Sleeman B.D., Inverse Nodal Problems for Sturm–Liouville Equations with Eigenparameter Dependent Boundary Conditions, *Inverse Problems*, 12 (1996) 377-381.

[5] Hald O.H., McLaughlin J.R., Inverse Problems: Recovery of BV Coefficients from Nodes, *Inverse Problems*, 14 (1998) 245-273.

[6] Law C.K., Yang C.F., Reconstructing the Potential Function and Its Derivatives Using Nodal Data, *Inverse Problems*, 14 (1998) 299-312.

[7] Shen C.L., Shieh C.T., An Inverse Nodal Problem for Vectorial Sturm–Liouville Equation, *Inverse Problems*, 16 (2000) 349-356.

[8] Yang X.F., A New Inverse Nodal Problem, *J. Differential Equations*, 169 (2001) 633-653.

[9] Law C.K., Shen C.L., Yang C.F., The Inverse Nodal Problem on the Smoothness of the Potential Function, *Inverse Problems*, 15 (1999) 253-263. Errata: *Inverse Problems*, 17 (2) (2001) 361-363.

[10] Freiling G., Yurko V.A., Inverse Sturm–Liouville Problems and Their Applications, New York: Nova Science Publishers, (2001).

[11] Shieh C.T., Yurko V.A., Inverse Nodal and Inverse Spectral Problems for Discontinuous Boundary Value Problems, *J. Math. Anal. Appl.*, 347 (2008) 266-272.

[12] Keskin B., Ozkan A.S., Inverse Nodal Problems for Impulsive Sturm–Liouville Equation with Boundary Conditions Depending on the Parameter, *Advances in Analysis*, 2 (3) (2017) 151-156.

[13] Koyunbakan H., A New Inverse Problem for the Diffusion Operator, *Appl. Math. Lett.*, 19 (2006) 995-999.

[14] Buterin S.A., Shieh C.T., Inverse Nodal Problem for Differential Pencils, *Applied Mathematics Letters*, 22 (8) (2009) 1240-1247.

[15] Yang C.F., Reconstruction of the Diffusion Operator with Nodal Data, *Z. Naturforsch A.*, 65 (2010) 100-106.

[16] Buterin S.A., Shieh C.T., Incomplete Inverse Spectral and Nodal Problems for Differential Pencils, *Results in Mathematics*, 62 (2012) 167-179.

[17] Yang C.F., An Inverse Problem for a Differential Pencil Using Nodal Points as Data, *Israel Journal of Mathematics*, 204 (2014) 431-446.

[18] Gordeziani N., On Some Non-local Problems of the Theory of Elasticity, *Bulletin of TICMI*, 4 (2000) 43-46.

[19] Yin Y.F., On Nonlinear Parabolic Equations with Nonlocal Boundary Conditions, *Journal of Mathematical Analysis and Applications*, 185 (1) (1994) 161-174.

[20] Bitsadze A.V., Samarskii A.A., Some Elementary Generalizations of Linear Elliptic Boundary Value Problems, *Doklady Akademii Nauk SSSR*, 185 (4) (1969) 739-740.

[21] Hu Y.T., Yang C.F., Xu X.C., Inverse Nodal Problems for the Sturm—Liouville Operator with Nonlocal Integral Conditions, *Journal of Inverse and Ill-Posed Problems*, 25 (6) (2017) 799-806.

[22] Keskin B., Inverse Nodal Problems for Dirac Type Integro Differential System with a Nonlocal Boundary Condition, *Turkish Journal of Mathematics*, 46 (6) (2022) 2430-2439.

[23] Ozkan A.S., Adalar İ., Inverse Nodal Problems for Sturm—Liouville Equation with Nonlocal Boundary Conditions, *Journal of Mathematical Analysis and Applications*, 520 (1) (2023) 126907.
[24] Qin X., Gao Y., Yang C., Inverse Nodal Problems for the Sturm—Liouville Operator with Some Nonlocal Integral Conditions, *Journal of Applied Mathematics and Physics*, 7 (1) (2019) 111-122.
[25] Xu X.J., Yang C.F., Inverse Nodal Problem for Nonlocal Differential Operators, *Tamkang Journal of Mathematics*, 50 (3) (2019) 337-347.
[26] Yang C.F., Inverse Nodal Problem for a Class of Nonlocal Sturm—Liouville Operator, *Mathematical Modelling and Analysis*, 15 (3) (2010) 383-392.
[27] Çakmak Y., Keskin B., Inverse Nodal Problem for the Quadratic Pencil of the Sturm—Liouville Equations with Parameter-Dependent Nonlocal Boundary Condition, *Turkish Journal of Mathematics*, 47 (2023) 397–404.
[28] Khalil R., Al Horania M., Yousefa A., et al., A New Definition of Fractional Derivative, *J. Comput. Appl. Math.*, 264 (2014) 65-70.
[29] Abdeljawad T., On Conformable Fractional Calculus, *J. Comput. Appl. Math.*, 279 (2015) 57-66.
[30] Atangana A., Baleanu D., Alsaedi A., New Properties of Conformable Derivative, *Open Math.*, 13 (2015) 889-898.
[31] Mortazaasl H., Jodayree Akbarfam A., Trace Formula and Inverse Nodal Problem for a Conformable Fractional Sturm—Liouville Problem, *Inverse Problems in Science and Engineering*, 28 (4) (2020) 524–555.
[32] Allahverdiev B.P., Tuna H., Yalçinkaya Y., Conformable Fractional Sturm—Liouville Equation, *Mathematical Methods in the Applied Sciences*, 42 (10) (2019) 3508-3526.
[33] Keskin B., Inverse Problems for one Dimentional Conformable Fractional Dirac Type Integro Differential System, *Inverse Problems*, 36 (6) (2020) 065001.
[34] Adalar I., Ozkan A.S., Inverse Problems for a Conformable Fractional Sturm—Liouville Operators, *Journal of Inverse and Ill-posed Problems*, 28 (6) (2020) 775-782.
[35] Çakmak Y., Inverse Nodal Problem for a Conformable Fractional Diffusion Operator, *Inverse Problems in Science and Engineering*, 29 (9) (2021) 1308-1322.
[36] Çakmak Y., Trace Formulae for a Conformable Fractional Diffusion Operator, Filomat, 36 (14) (2022) 4665–4674.
[37] Wang Y., Zhou J., Li Y., Fractional Sobolev's Spaces on Time Scales via Conformable Fractional Calculus and Their Application to a Fractional Differential Equation on Time Scales, *Adv. Math. Phys.*, 2016 (2016) 1-21.
[38] Buterin S.A., On Half Inverse Problem for Differential Pencils with the Spectral Parameter in the Boundary Conditions, Tamkang Journal of Mathematics, 42 (3) (2011) 355-364.

Cumhuriyet Sci. J., 44(2) (2023) 364-369
DOI: https://doi.org/10.17776/csj.1182017

Cumhuriyet Science Journal

| csj.cumhuriyet.edu.tr | Founded: 2002 ISSN: 2587-2680 e-ISSN: 2587-246X Publisher: Sivas Cumhuriyet University

Comparative Estimation of Global Solar Radiation over Two Nigerian Cities, Using Artificial Neural Network and Empirical Models

Gbadebo Ismaila Olatona [1,a,*], Emmanuel Oluwapelumi Ajilore [1,b], Fakunle Mutiu [1,c], Alani Paul Oluwadetan Olaniyi [1,d], Oluwatosin Akintunde Makinde [1,e]

[1] *Department of Physics, Osun State University, Osogbo, Osun State, Nigeria..*

**Corresponding author*

Research Article

History
Received: 04/11/2022
Accepted:16/06/2023

ABSTRACT

The estimation of solar radiation intensity has been a focus of many researchers due to the cost of setting up its actual measurements. While many of them employed empirical models, this study utilizes the artificial neural network for the analysis and estimation of global solar radiation over two Nigerian cities. The model developed using sunshine hours, temperatures and relative humidity were compared with the existing empirical models. Model performance indicators comparing the measured data and the computed data for the derived and selected models, using the same number of input meteorological parameters showed that ANN having average values of RMSE, MBE, and MPE of 0.0744 $MJm^{-2}day^{-1}$, -0.0020 $MJm^{-2}day^{-1}$, and -0.0043%, respectively, performed slightly better. When different number of input meteorological parameters were used, the ANN gave the following error indicators for RMSE, MBE, MPE of 0.0394$MJm^{-2}day^{-1}$, -0.0023$MJm^{-2}day^{-1}$ and -0.0144% respectively. Also, in the result of solar radiation in Abuja, using the same number of meteorological parameters, the model with the best performance in the estimation of solar radiation is the ANN model with average values of RMSE, MBE, MPE of 0.1301$MJm^{-2}day^{-1}$, 0.0053$MJm^{-2}day^{-1}$ and 0.0441% respectively. Hence, the models are versatile for predicting global solar radiation in locations in the same climatic zones as locations studied in this study, where direct measurements of solar radiation is scarce and widely separated but there is availability of commonly measured meteorological parameters such as sunshine duration, minimum temperature, maximum temperature and relative humidity.

Keywords: Global Solar Radiation, Empirical, Prediction, Artificial Neural Network, Model.

[a] *olatonagi@uniosun.edu.ng* *https://orcid.org/0000-0001-9415-6265*
[b] *ajilore33@gmail.com* *https://orcid.org/0000-0003-2544-0101*
[c] *mutiu.fakunle@uniosun.edu.ng* *https://orcid.org/0000-0001-7686-0216*
[d] *paul.olaniyi@yahoo.com* *https://orcid.org/0000-0002-0922-3142*
[e] *makindetosine1@gmail.com* *https://orcid.org/0000-0000-0000-0000*

Introduction

The need for improving energy mix can not be over emphasized because many households in developing nations are not connected to the National grid. The alternative is small stand alone generators powered by fossil fuels. Apart from the cost of this fuels which in most cases is beyond the reach of average householders, is the environmental prolusion resulting from the incomplete combustion of such fuels. Thus, there has been an increase in the demand for renewable and clean energies according to [1].

One of the most viable renewable energy options, particularly in Nigeria, is the abundant solar energy falling on the Earth surface. Using solar energy necessitates an exact prediction of solar energy in the proposed location(s) according to [2]. The measurements of solar radiation are important due to increasing number of various applications of solar energy in design and installation of solar energy devices. Harnessing this radiant energy from the sun is essential, due to our reliance on hydrocarbon-based energy sources which cause negative impact on human health.

Since the trend of energy utilization has shifted to solar energy, knowledge about the amount of solar radiation at a location where solar energy is needed to be harnessed is essential, according to [3]. The amount of solar radiation is measured using an instrument called Pyrheliometer. However, the cost of setup could be very expensive and delicate, according to [4]. Hence, pyrheliometers setups are scarce and widely spaced in Nigeria. Thus, alternative means have to be developed to generate solar radiation data using commonly measured meteorological parameters for locations without instrument for measuring solar radiation, [5]. In order to circumvent this draw backs, modeling techniques had been used to significantly evaluate global solar radiation using more commonly measured meteorological data.

Empirical models for predicting global solar radiation have been proposed by [6-8]. The former estimates global solar radiation from sunshine hours while the latter did so from air temperature These models enable researchers or users of solar radiation data estimate the magnitude of the global radiation from meteorological parameters that are commonly measured at all meteorological stations

because it is difficult and costly to set up instruments that measure global solar radiation directly. These models differ in the number of meteorological parameters used in correlating global solar radiation, accuracy and applicability. They can be categorized into empirical models, radiative transfer models and machine learning models. The radiative transfer models entail complex modeling of solar radiation using geographical and meteorological parameters. Hence, the aim of this study is to write an Artificial Neural Network soft code to estimate global solar radiation from commonly measured meteorological parameters, over the selected locations. The selected parameters shall be studied by ANN, which shall eventually lead to the development of a model to estimate the global solar radiation from routinely measured meteorological parameters. Such parameters include sunshine hours, minimum temperature, maximum temperature and relative humidity. The accuracy of the estimates shall be compared alongside estimates obtained from empirical models using firstly the same number of inputs and secondly with different number of inputs with measured data and the errors involved determined using error indicators.

With technological advancement, the use of artificial neural network is being acknowledged in various fields. Some previous studies have reported their assessment on the use of artificial neural network in some other studies, but it has not been fully utilized in estimating solar radiation in the locations under study and there is need to ascertain its accuracy in prediction of solar radiation. In a study, [9] used ANN to estimate monthly average daily global solar irradiation on a horizontal surface in Uganda based on weather station data (sunshine duration, maximum temperature, and cloud cover) and location parameters of (latitude, longitude, and altitude). Also, [10] who based their study on six years data, using back propagation method with tangent sigmoid as the transfer function to train the ANN model with daily values of measured sunshine duration and maximum temperature as input parameters.

Materials and Methods

The measured solar radiation, sunshine hour, minimum temperature, maximum temperature, and relative humidity data between (1999-2019) for Ibadan were obtained from the meteorological station of the International Institute of Tropical Agriculture Ibadan (IITA) while measured solar radiation, the minimum temperature and maximum temperature between (1990-1992) and (2012-2015) for Abuja were obtained from Nigerian Meteorological Agency (NIMET), Abuja. IITA is an international agricultural research institute with state-of-the-arts meteorological instrument used in measuring meteorological data while NIMET is a national agency saddled with measurement of meteorological data in the country. Data quality control was conducted on the data obtained from the meteorological stations mentioned above. The data were first examined for missing values and outliers. Missing values could be due to instrument failure or power surge. The missing values were replaced by the average of values from same week. Long arrays of missing data (a month for example) are replaced with the corresponding average of same days over the remaining years. The total number of missing data in the measured solar radiation, sunshine hour, minimum temperature, maximum temperature, and relative humidity columns did not exceed 3% of the total data points. The excessive days which are the (February 29) days in the leap years were removed, in order to have a 365-day for all the years considered in the study, to ensure uniformity of month comparison in the data.

The selected commonly measured meteorological parameters were analyzed using Mat Lab. The artificial neural network is a function in the Mat Lab tool box and it was used for the data analysis and prediction of solar radiation data. ANN is a soft computing tool and a data analysis method whose operation resembles a network of biological neurons that learn patterns which are eventually used to predict. Artificial Neural Network soft code was written and relationship between the selected parameters was studied by ANN, which eventually led to the development of a model. The model developed is capable of training and estimating the solar radiation for each month of the year as well as the mean solar radiation of each month.

The Angstrom, sunshine hour-based model is given by

$$\frac{\mathrm{H}}{\mathrm{H_o}} = a + b\,\frac{\mathrm{S}}{\mathrm{S_o}} \qquad (1)$$

where H and Ho are respectively global and extraterrestrial solar radiations, S and So are respectively the actual sunshine and maximum possible sunshine hours while a and b are geographical factors specific to the location.

On the other hand, the Hargreaves-Samani air temperature based model is given by

$$\mathrm{H} = \mathrm{Ho} \times K_r[(\Delta T)^n] \qquad (2).$$

where H and Ho are again global and extraterrestrial solar radiations respectively, ΔT is the difference between the maximum and minimum air temperature while Kr and n are geographical factors specific to the location.

[11] have determined a and b for the location under study and their modified Angstrom model is considered as model 1. [12] obtained 0.125 for Kr and their modified Hargreaves and Samani temperature is considered as model 2.

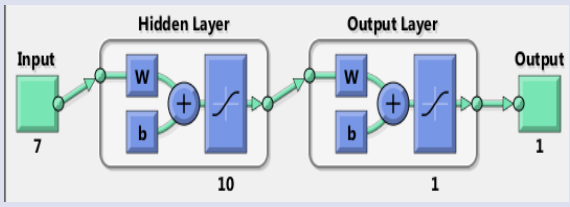

Figure 1. Pictorial representation of the artificial neural network employed in prediction of solar radiation in Ibadan.

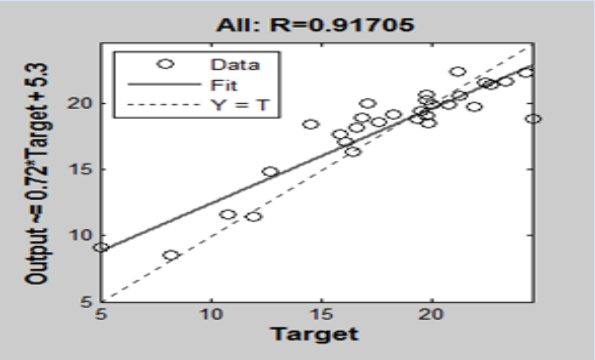

Figure 2. Post-Training regression analysis of the ANN (7-10-1) used for prediction of solar radiation in Ibadan.

The Artificial Neural Network generated model is model 3 and is given by

$$H = \Sigma\left[W_{oj}\left(\frac{2}{1-exp^{-2N}} - 1\right) + b_o\right]$$

Where H is the computed solar global solar radiation, $\frac{2}{1-exp^{-2N}} - 1$ is the activation function, N is the summed input and b_o is the bias of the output.

Hence, the three models are summarized in Table 1.

Table 1: Models used for the Comparative Estimation of Global Solar Radiation

Model Number and Name	Model Equation
1. Sunshine based model: [1]	$\frac{H}{H_o} = 0.24 + 0.35\,\frac{S}{S_o}$.....3
2. Temperature based model: [12]	$\frac{H}{H_o} = 0.125[(\Delta T)^{0.5}]$ 4
3. Artificial Neural Network model	$(H) = \Sigma\left[W_{oj}\left(\frac{2}{1-exp^{-2N}} - 1\right) + b_o\right]$ ... 5

Also, the model developed were tested by comparing its estimates derived from each model with measured data, using statistical error analysis tools such as Root Mean Squared Error (RMSE), Mean Bias Error (MBE), Mean Percentage Error (MPE).

RESULTS AND DISCUSSION

The results of the estimates of solar radiation in Ibadan when different number of meteorological parameters are employed, using the modified Angstrom-Prescott model, modified Hargreaves and Samani Model and the Artificial Neural Network model are displayed in Figure 3 below, while the Table 2 shows the results of error indicators.

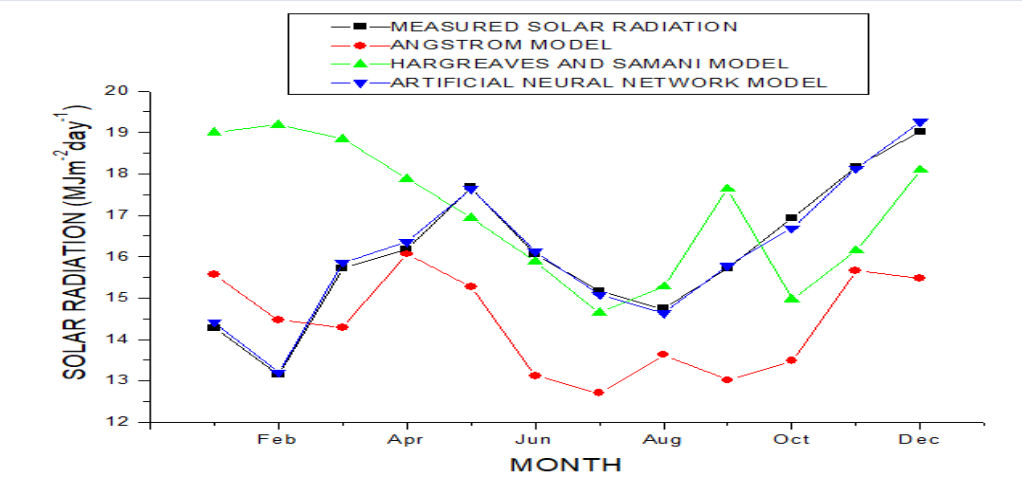

Figure 3. Comparison of the computed mean solar radiation with measured data.

Table 2: Error analysis of the result of the Prediction of solar radiation in Ibadan, when different numbers of meteorological parameters are employed.

MODEL PERFORMANCE INDICATOR			
MODELS	***RMSE***	***MBE***	***MPE (%)***
Angstrom-Prescott Model	0.6731	-0.1396	-0.8107
Hargreaves-Samani Model	0.7667	0.0801	0.6155
Artificial Neural Network Model	0.0394	-0.0023	-0.0144

It can be seen from Figure 3 that the ANN estimates matched the actual value more when compared with the estimates derived from the other two models. This might not be unconnected with more meteorological parameters used to trian the ANN because some other factors apart from sunshine hours and air temperature affect the global radiation.

Figure 3 also shows the comparison of the computed mean solar radiation with measured data. The maximum value of the solar radiation occurred in December (19.24 $MJm^{-2}day^{-1}$). The lowest solar radiation occurred in February (13.16 $MJm^{-2}day^{-1}$), this can be attributed to high turbidity of the atmosphere. This high turbidity is caused by accumulation of aerosol which arises from the prevalence of wind-blown dust of Saharan origin (north-easterly surface wind) known locally as harmattan dust, [12,13]. In addition, the low value of solar radiation recorded in February is due to prevalence of particulates such as aerosol that is being released from activities such as (bush burning) at this time of the year.

The result of the estimates of solar radiation in Ibadan when the same number of meteorological parameters are employed, using the modified Angstrom model, modified Hargreaves and Samani Model and the model derived from Artificial Neural Network model is displayed in Figure 4 below, while the error indicators are shown in Table 3.

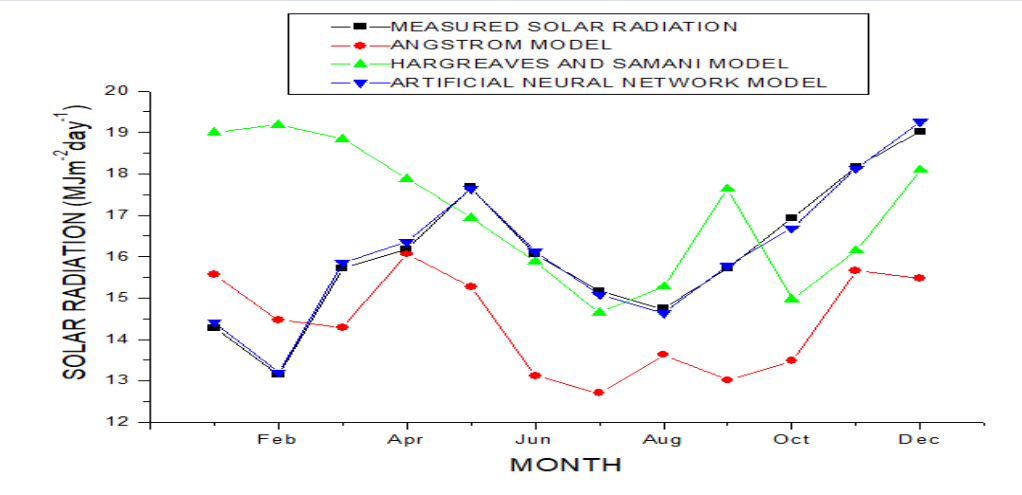

Figure 4. Comparison of the computed mean solar radiation with measured data.

Table 3: Error analysis of the result of the estimates of solar radiation in Ibadan, derived from the models, when the same numbers of meteorological parameters are employed.

MODEL PERFORMANCE INDICATOR			
MODELS	***RMSE***	***MBE***	***MPE (%)***
Angstrom-Prescott Model	0.4322	-0.1063	-0.6536
Hargreaves-Samani Model	0.3619	0.0638	0.4328
Artificial Neural Network Model	0.0744	-0.0020	-0.0043

Figure 4 shows the comparison of the computed mean solar radiation with measured data. The month with the highest solar radiation is April with solar radiation of (18.53$MJm^{-2}day^{-1}$), this can be attributed to lowering of the turbidity of the atmosphere due to the removal of aerosol particles by showers of rain in this month. As such, there is less attenuation of the incoming solar radiation and increase in the amount of direct solar radiation reaching the Earth's surface. The month with the least solar radiation is August with solar radiation of (11.98$MJm^{-2}day^{-1}$), this is due to the raining season being at its peak and it can also be attributed to the high amount of cloudiness, increase in relative humidity, precipitable water molecules in the atmosphere and frequent thunderstorm activities.

Here the root means square error, though still lower than the other two models, shows a slight over estimation of 0.035 but surprisingly a reduced under estimation by mean percentage error.

The result of the estimates of solar radiation in Abuja, when the same number of meteorological parameters are employed, using modified Hargreaves and Samani Model and the Artificial Neural Network model is displayed in Figure 5 below, while the error indicators are depicted in Table 4.

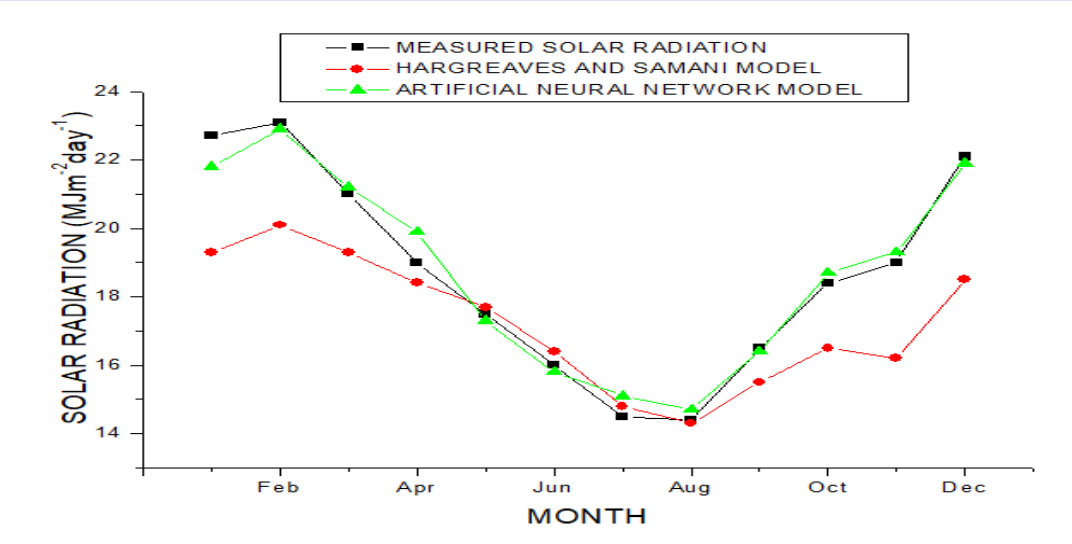

Figure 5: Comparison of the computed mean solar radiation with measured data

Table 4: Error analysis of the result of the Prediction of solar radiation in Ibadan, when different numbers of meteorological parameters are employed.

MODEL PERFORMANCE INDICATOR			
MODELS	***RMSE***	***MBE***	***MPE (%)***
Angstrom-Prescott Model	0.5876	0.1181	0.5577
Hargreaves-Samani Model	0.1301	0.0053	0.0441
Artificial Neural Network Model	0.5876	0.1181	0.5577

Figure 5 shows the comparison of the computed mean solar radiation with measured data. The month with the highest solar radiation is February with solar radiation of (23.12 $MJm^{-2}day^{-1}$), which is due to the dry season being at its peak. The month with the least solar radiation is August with solar radiation of (14.43 $MJm^{-2}day^{-1}$), this is due to the raining season being at its peak and the rain bearing clouds pervade. Also, this indicates that the month of August is characterized by overcast and cloudy condition. The variations showed by the predictive models followed the same trend but with various degrees of over and under predictions by the different models.

The computed results compared favorably with that of [9] that showed good agreement between the ANN estimated and actual values of global solar radiation. A correlation coefficient of 0.974 was obtained with MBE of 0.059 $MJm^{-2}day^{-1}$ and RMSE of 0.385 $MJm^{-2}day^{-1}$. These results confirmed the superiority of the ANN prediction model. The model used several parameters, and the data used in its development was run only for three years. Also, the results are better compared to[10], where the ANN model performed well with all inputs used, but with the MBE and RMSE values obtained were 0.12% and 5.67%, respectively which were higher than obtained in this study. This might not be unconnected with in improved capacity of ANN over time.

CONCLUSION

The result of the estimation of solar radiation in Ibadan showed that the artificial neural network model performed slightly better than the existing models when both the same and different numbers of metrological parameters were employed in the prediction. In the estimation of solar radiation in Abuja, the artificial neural network model performed slightly better than the Hargreaves-Samani model when the same numbers of metrological parameters were employed in the prediction. The performance of the ANN model is in agreement with a work done by [9], in which they used ANN to estimate monthly average daily global solar irradiation on a horizontal surface in Uganda. The data used in their research covered a period of three years in their result; a correlation coefficient of 0.974 was obtained with MBE of 0.059 $MJm^{-2}day^{-1}$ and RMSE of 0.385 $MJm^{-2}day^{-1}$. Hence, the models are versatile for predicting global solar radiation in locations in the same climatic zones as location studied in this research, where there are no direct measurements of solar radiation but there is availability of common meteorological parameters such as sunshine duration, minimum temperature, maximum temperature and relative humidity.

The computing power of Artificial Neural Networks should further be explored, since the field is very diverse, with a view to accessing more of its potentialities in solving data acquisition and analysis in mitigating climate change and bringing green energy to the populace at a relatively cheap costs. Other machine learning techniques should also be explored for estimation of global solar radiation in developing countries and the results be compared with that obtained in this study.

More importantly, government, non-governmental organizations and individuals should step up their effort in harnessing this renewable energy, among which is the solar energy, in order to boost the economy and standard of living in their countries.

Conflicts of interest

There are no conflicts of interest in this work.

Acknowledgments

The authors wish to acknowledge the management of the International Institute of Tropical Agriculture, Ibadan, and the Nigeria Meteorological Agency, Abuja, Nigeria for making the data of the global solar radiation, minimum temperature, maximum temperature and relative humidity available.

References

[1] Chineke T.C., Nwofor O.K., Okoro U.K., Optimal benefits of utilizing renewable energy technologies in Nigeria and the CIBS Quadrangle-A review, *Bayero J. Pure Appl. Sci., (* 2010) 3(1): 142-146.

[2] Chukwu S.C., Nwachukwu A.N., Analysis of Some Meteorological Parameters Using Artificial Neural Network Method for Makurdi, Nigeria, *African Journal of Environmental Science and Technology*, (2012). 6(3), 182-188.

[3] Adesola S.O., Adeniji N.O., Investigation on the Possibility of Using Available Sunshine Duration Data of a Relatively close Region to Estimate Global Solar Radiation for a Different Region, *International Journal of Advance scientific Research and Engineering (IJASRE),* (2019). ISSN: 2454-8006, Vol. 5, NO/ (2).

[4] Olatona G.I., Estimating global solar radiation from routine meteorological parameters over a Tropical City (7.23° N; 3.52° E) using quadratic models, *Ann. West Univ. Timisoara-Phys.,* (2018) 60(1): 45-55.

[5] Osinowo A.A., Okogbue E.C., Ogungbenro S.B., Fashanu.O., Analysis of Global Solar Irradiance over Climatic Zones in Nigeria for Solar Energy Applications, *Journal of Solar Energy*, (2015). Article, 9 pages.

[6] Angstrom A., Solar and terrestrial radiation, *Quarterly Journal of the Royal Meteorological Society*, (1924). 50, 121–126.

[7] Prescott J.A., Evaporation from a water surface in relation to solar radiation, *Transaction of the Royal. Society of South Australia,* (1940). 64, 114–125.

[8] Hargreaves G.H., Samani Z.A., Crop Evapotranspiration from Temperature, *Applied Engineering in Agriculture,* (1985), 1, 96-99.

[9] Mubiru J., Banda E. J. "Prediction of monthly average daily global solar irradiation using artificial neural networks," *Solar Energy*, (2008) 82 (2), 181–187.

[10] Tymvios F.S., Jacovides C.P., Michaelides S.C., Scouteli C.,. Comparative study of Angstrom's and artificial neural networks methodologies in estimating global solar radiation, *Solar Energy*, (2005) 78, 752–762.

[11] Olatona G.I., Adeleke E. A., Estimation of solar radiation over Ibadan from routine meteorological parameters, *Journal of Engineering and Sciences,* 4(3) 44-51.

[12] Tikyaaet E.V., Akinbolati, A., Shehu M., Assessment of empirical models for estimating mean monthly global solar radiation in katsina, *FUDMA Journal of Sciences (FJS)*, (2019) 3(1) 333 – 344.

[13] Okogbue, E.C., Adedokun, J.A., Holmgren, B., Hourly and daily clearness index and diffuse fraction at a tropical station, Ile-Ife, Nigeria, *Int. J. Climatol*, (2009) 29, 1035–1047.

[14] Falaiye, O.A., Babatunde, E.B., Willoughby, A.A., Atmospheric aerosol loading at Ilorin, a tropical station, *Afr. Rev. Phys*., (2014). 9 (0065), 527–535.

Cumhuriyet Sci. J., 44(2) (2023) 370-376
DOI: https://doi.org/10.17776/csj.1247286

Cumhuriyet Science Journal

| csj.cumhuriyet.edu.tr | Founded: 2002 ISSN: 2587-2680 e-ISSN: 2587-246X Publisher: Sivas Cumhuriyet University

The Energy Spectra of Electric Induced Mathieu Quantum Dot with Hydrogenic Impurity Implanted in Quantum Plasma

Mustafa Kemal Bahar [1,a,*]

[1] *Department of Physics, Faculty of Sciences, Sivas Cumhuriyet University, Sivas, Türkiye.*

**Corresponding author*

Research Article

History
Received: 03/02/2023
Accepted:04/04/2023

ABSTRACT

In this study, the energy spectra of the electric induced Mathieu quantum dot (MQD), containing the central hydrogenic impurity, fabricated by heterostructure $In_xGaAs_{1-x}/GaAs$, implanted in quantum plasma is considered. The effects of the external electric field, structural parameters and plasma screening on the energy levels of the MQD with the hydrogenic impurity are probed. The more general exponential cosine screened Coulomb (MGECSC) potential is used to depict the quantum plasma interactions. In order to solve the related Schrödinger equation, the numerical asymptotic iteration method (AIM) is employed. Achievable values of the effective potential parameters are taken into consideration, and for special purposes, the alternative to each other of these parameters is also evaluated.

Keywords: Quantum dot, Quantum plasma, Mathieu potential, Electric field, Electronic properties.

[a] *mussiv58@gmail.com* *https://orcid.org/0000-0003-4265-1402*

Introduction

Quantum dots are, in general, electron-confined systems. In these structures it is possible to confine one, two or more electrons. Quantum dots can be fabricated using various semiconductor materials. Quantum dots formed by $In_xGaAs_{1-x}/GaAs$ heterostructure will be considered in the present work, due to experimental advantages such as non-deformation of the growth material and sharp interface formation arising from reduced mixing in the formation of quantum dots [1]. The electronic and optical properties exhibited by the quantum dot are closely related to the confinement effects. A quantum dot is called as three-dimensional if the confinement effects of electrons are isotropic, but two-dimensional if one direction is more dominant than the other two in the encompassment effect [2]. Tuning the radiation frequencies of the quantum dot is possible by changing the size, shape, content and confinement effects of the quantum dot. The reason why quantum dots have technological reflections in a very important and wide area is the possibility of this frequency tuning. There are many experimental methods used in the production of quantum dots. Thanks to advanced nanofabrication methods, it is possible to synthesize quantum dots with different numbers of electrons and different surrounding geometries [3]. These types of quantum dots have been studied in detail both theoretically and experimentally [4-5]. Some experimental studies suggest that the optimal quantum dot profiles to encompass electrons should be of the well-like type [6]. Due to this experimental prediction, the Mathieu quantum dot (MQD), which exhibits a well-likeconfinement, will be considered in the present work [7-9]. Plasmas are a very important experimental argument for the experimental generation and modification of quantum dots [10,11]. Plasma environments can create a tuning mechanism on the electronic properties of quantum dots, thanks to the shielding effects caused by the complex correlation between the charged particles in them. The more general exponential cosine screened Coulomb (MGECSC) potential is predicted in a more detailed, more functional and more physical studying plasma interactions theoretically, and is expressed as [12-15]

$$V_{MGECSC}(r) = \frac{-Ze^2}{4\pi\varepsilon_0 r}(1+br)\exp\left(-\frac{r}{\lambda}\right)\cos\left(\frac{ar}{\lambda}\right), \qquad (1)$$

where a, b and λ are the plasma screening parameters. The MGECSC potential is more functional as it can be reduced to SC, ECSC and pure Coulomb (PC) potentials thanks to the parameters in its [15]. In this study, the effects of external electric field, structural factors and plasma shielding on the energy levels of the MQD with hydrogenic impurity, implanted in a quantum plasma environment modeled by the MGECSC potential are investigated. The motivation of the study is to compare the efficiency of the plasma shielding effect with the structural factors and the efficiency of the external electric field on energy levels. In this manner, it is important to do alternative parameter analysis.

The work is planned as follows: In the Section 2, the theoretical model and computation method are furnished. In Section 3, the finding are discussed. The last paragraph is allocated to the conclusions.

Theoretical Model and Computation Method

In order to obtain the energy spectra of the electric field induced MQD including the hydrogenic impurity at its centre, embedded in quantum plasma medium, the Hamiltonian operator whose eigenvalues must be found is given by

$$H = -\frac{\hbar^2\nabla^2}{2m^*} + V_{MQD}(r) + V_i(r) + V_{ef}(r), \quad (2)$$

where, $V_{MQD}(r)$ is the quantum dot confinement potential, $V_i(r)$ is the shielded impurity potential energy, $V_{ef}(r)$ is the potential energy term arising from the external electric field. They are given by

$$V_{MQD}(r) = V_0(sin^2(\eta r) - \cos(\eta r)), \quad (3)$$

$$V_i(r) = -\frac{Ze^2}{4\pi\varepsilon r}\exp(-r/\lambda)(1+br)\cos(ar/\lambda), \quad (4)$$

$$V_{ef}(r) = e\vec{\xi}.\vec{r}, \quad (5)$$

where, V_0 is the MQD depth parameter; η is the MQD width parameter; ε is the static dielectric constant in the material; a, b, and λ are the plasma screening parameters; ξ is the external electric field. Here it is assumed that $\vec{\xi}.\vec{r} = \xi r$. In this case, the wave equation to be solved to obtain the energy spectra is stated as

$$H\psi(r,\theta,\phi) = E\psi(r,\theta,\phi). \quad (6)$$

where, as the interaction system is the spherical symmetric, the angular solution is the spherical harmonics. In order to be able to find the eigenvalues of Eq.(6), the numerical asymptotic iteration method (AIM) is employed.

The AIM is a method that can provide both a numerical and, if possible, analytical solution. Here, the outline of AIM is outlined. For detail, please refer Refs.[16-18]. The AIM is a very functional and practical method to solve the following second-order differential equations.

$$y'' = \lambda_0(x)y' + s_0(x)y, \quad (7)$$

where, $\lambda_0(x) \neq 0$, ve $\lambda_0(r), s_0(r)$ are in $C_\infty(a,b)$. Also, $\lambda_0(x), s_0(x)$ are differentiable functions. The general physical solution of Eq.(7) is as follows

$$y(x) = \exp(-\int^x \upsilon dx'), \quad (8)$$

in that, for enough large n,

$$\frac{s_n(x)}{\lambda_n(x)} = \frac{s_{n-1}(x)}{\lambda_{n-1}(x)} \equiv \upsilon, \quad (9)$$

where

$$\lambda_n(x) = \lambda'_{n-1}(x) + s_{n-1}(x) + \lambda_0(x)\lambda_{n-1}(x),$$

$$s_n(x) = s'_{n-1}(x) + s_0(x)\lambda_{n-1}(x), n = 1,2,3 \ldots \quad 10)$$

The termination condition of the AIM is considered to obtain the energy spectra. This termination condition is expressed as

$$\Delta(x) = \lambda_{n-1}(x)s_n(x) - \lambda_n(x)s_{n-1}(x) = 0. \quad (11)$$

The quantum dot radius is taken as $R_{dot} = 6a_0$ throughout the study as well as $m^* = 0.067m_0$, $\varepsilon_{GaAs} = 13.18$. The effective Bohr radius are calculated as $a_0 = 103.7A^o$, respectively.

Results and Discussion

In this study, the energy spectrum of an external electric field induced MQD with central hydrogenic impurity implanted in a quantum plasma is investigated. In the study, the effect of 6 parameters, namely plasma shielding parameters (a, b ve λ), external electric field strength parameter (ξ), and structural parameters ((x, *In*-concentration and η, quantum dot width) are taken into account. The relevant range of these parameters is within the experimentally achievable limit. The effective potential profile, which includes the MQD potential for the effect of each parameter, is also examined. Here it should be pointed out that although certain quantum levels are considered for the spectrum of the MQD, it is also possible to calculate for arbitrary quantum levels. In addition, since the motivation of the study is based only on the energy spectrum, the wave functions are not examined.

In Figure 1a, when $\xi = 10$kV/cm, the energy values for some quantum levels of the MQD with $\eta = 0.25a_0^{-1}$ implanted in the quantum plasma presented by the MGECSC potential with $a = 1, b = 1a_0^{-1}$ and $\lambda = 10a_0$ are demonstrated as a function of In-concentration x. In Figure 1b, the effective potential profile with $\ell = 1$ for different In-concentrations is displayed in synchronization with the parameter set in Figure 1a.

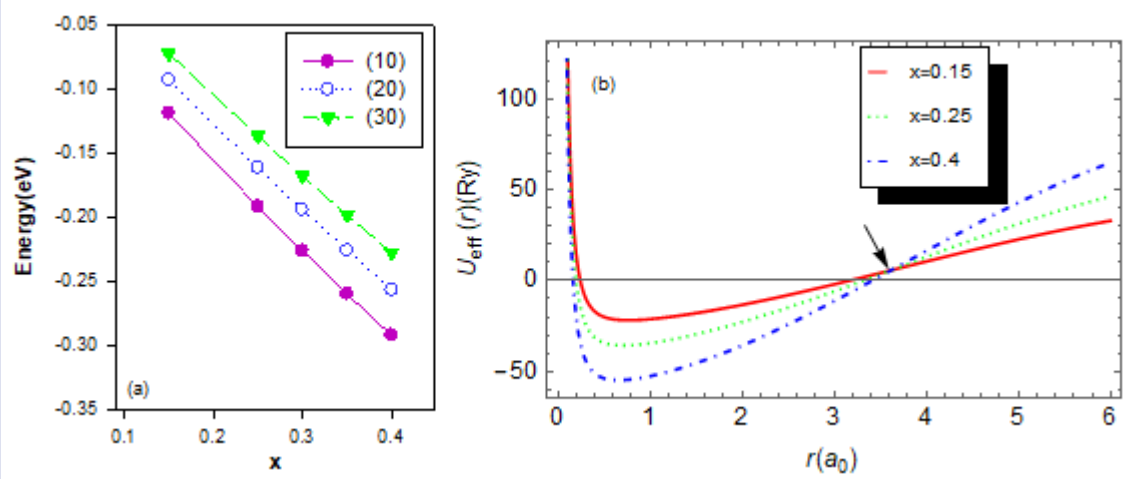

Figure 1. When $\xi = 10$kV/cm, the energy values for some quantum levels of the MQD with $\eta = 0.25a_0^{-1}$ implanted in the quantum plasma presented by the MGECSC potential including with $a = 1, b = 1a_0^{-1}$ and $\lambda = 10a_0$, as a function of x, b) the effective potential profile with $\ell = 1$ in synchronization with the parameter set in panel (a).

Figure 1a shows the energy of the first three quantum levels for only $\ell = 0$. As seen, as the *In*-concentration increases, the energies of the quantum levels decrease significantly. In Figure 1b, it is clear that the increment of *In*-concentration increases the potential strength and makes it more attractive. The bound state localizations in a more attractive potential are lowered (See Figure 1a). Here another remarkable one is that after approximately $R_{dot} \cong 3.8a_0$ of the MQD spatial limitation, the augment of *In*-concentration causes the effective potential profile having an inverse character compared to before one. However, it seems that the effective potential exhibits the character before this critical threshold. Because increasing x decreases the bound state energies. Since the energy difference between the bound state localizations will increase in a deepening potential profile, it is expected that the resonant frequencies of some nonlinear optical properties shift to blue.

In Figure 2a, when $\xi = 10$kV/cm, the energy values for some quantum levels of the MQD with $x = 0.4$ implanted in the quantum plasma presented by the MGECSC potential potential including with $a = 1, b = 1a_0^{-1}$ and $\lambda = 10a_0$, are presented as a function of MQD width parameter η.

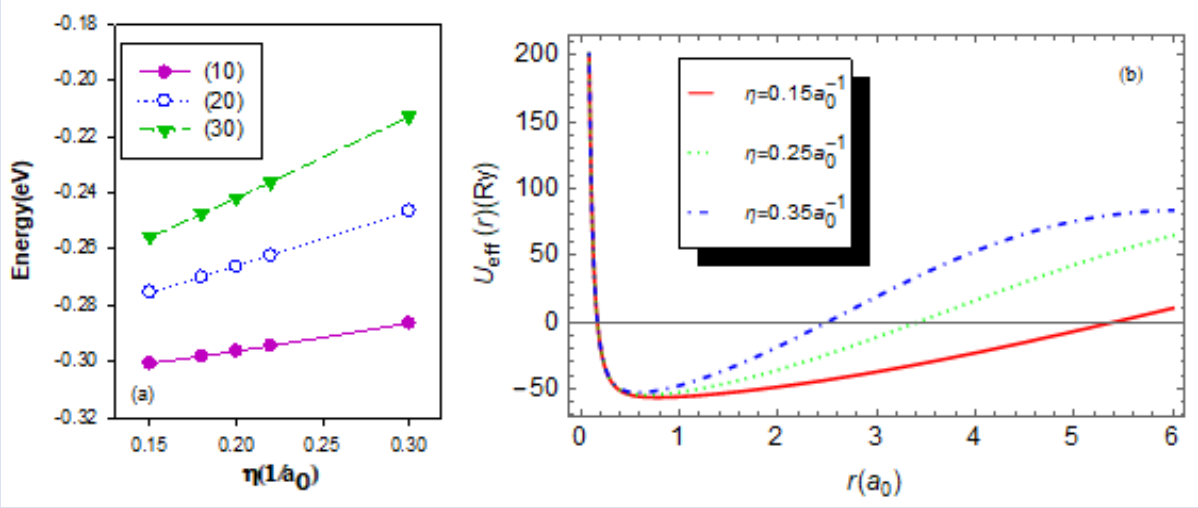

Figure 2. a) When $\xi = 10$kV/cm, the energy values for some quantum levels of the MQD with $x = 0.4$ implanted in the quantum plasma presented by the MGECSC potential potential including with $a = 1, b = 1a_0^{-1}$ and $\lambda = 10a_0$, as a function of η, b) the effective potential profile with $\ell = 1$ in synchronization with the parameter set in panel (a).

As seen in Figure 2a, increasing the MQD width parameter enhances the bound state energy values. Because the increase of the parameter η increases the repulsion of the effective potential (See Figure 2b). In the potential profile with increased repulsion, the bound state localizations increase. Also, the energy difference between the bound state localizations increases. This increase is also confirmed in Figure 2a. When considering Figure 2a, it is observed that there is an augment between the energy levels as the parameter η increases. Due to this augment, it may be said that the resonant frequencies of the nonlinear optical properties of the MQD exhibit the blue-shifting.

In Figure 3a, the energy values for some quantum levels of of the MQD with $x = 0.4, \eta = 0.25a_0^{-1}$ implanted in the quantum plasma presented by the MGECSC potential potential including with $a = 1, b = 1a_0^{-1}$ and $\lambda = 10a_0$, are represented as a function of the external electric field parameter ξ.

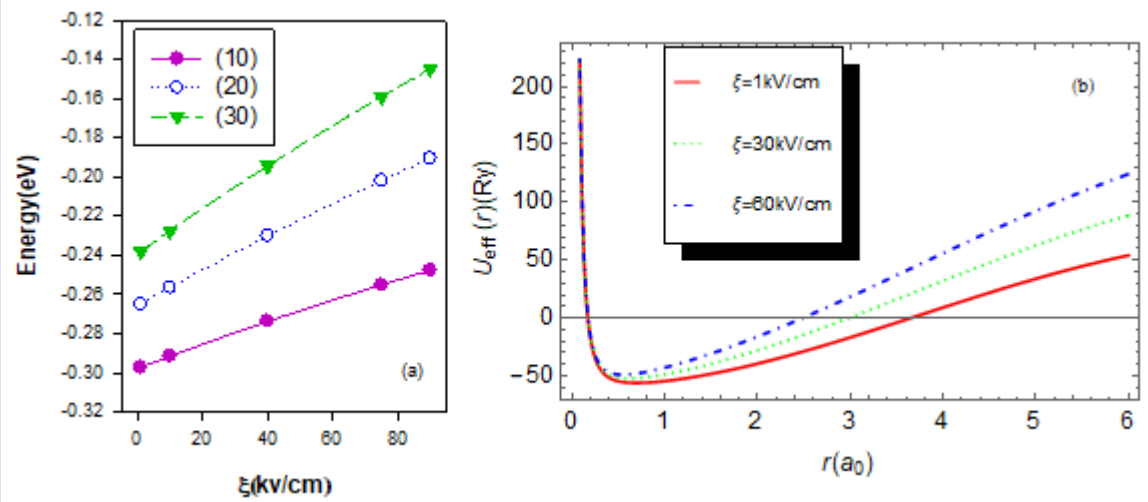

Figure 3. a)The energy values for some quantum levels of of the MQD with $x = 0.4, \eta = 0.25a_0^{-1}$ implanted in the quantum plasma presented by the MGECSC potential potential including with $a = 1, b = 1a_0^{-1}$ and $\lambda = 10a_0$, as a function of ξ, b) the effective potential profile with $\ell = 1$ in synchronization with the parameter set in panel (a).

As seen in Figure 3a, the increment in the external electric field strength increases the energy values of the respective quantum levels. Because the increase in the external electric field strength increases the repulsion of the effective potential (See Figure 3b). In this case, new localizations are expected to rise, which is confirmed in Figure 3a. In addition to the enhancement of the bound state localizations formed in the profile in Figure 3b, the energy differences between them are expected to increase.

As seen in Figure 3a, the increase in the external electric field strength increases the difference between the respective quantum levels. It can be said that this increase in difference may cause the nonlinear optical properties of MQD to shift the resonant frequencies to blue.

In Figure 4a, when $\xi = 10$kV/cm, the effective potential profile of the MQD with $x = 0.4, \eta = 0.25a_0^{-1}$ implanted in the quantum plasma presented by the MGECSC potential potential are plotted, in panel (a), when $a = 1, b = 1a_0^{-1}$, for different λ parameter values as a function of the radial direction (r); in panel (b), when $a = 1, \lambda = 10a_0$, for different b parameter values as a function of the radial direction (r); in panel (c), when$b = 1a_0^{-1}, \lambda = 10a_0$, for different a parameter values as a function of the radial direction (r). Here it is important to note that the potential profiles in Figure 4 are synchronized with Tables 1,2 and 3, respectively, in terms of parameter sets.

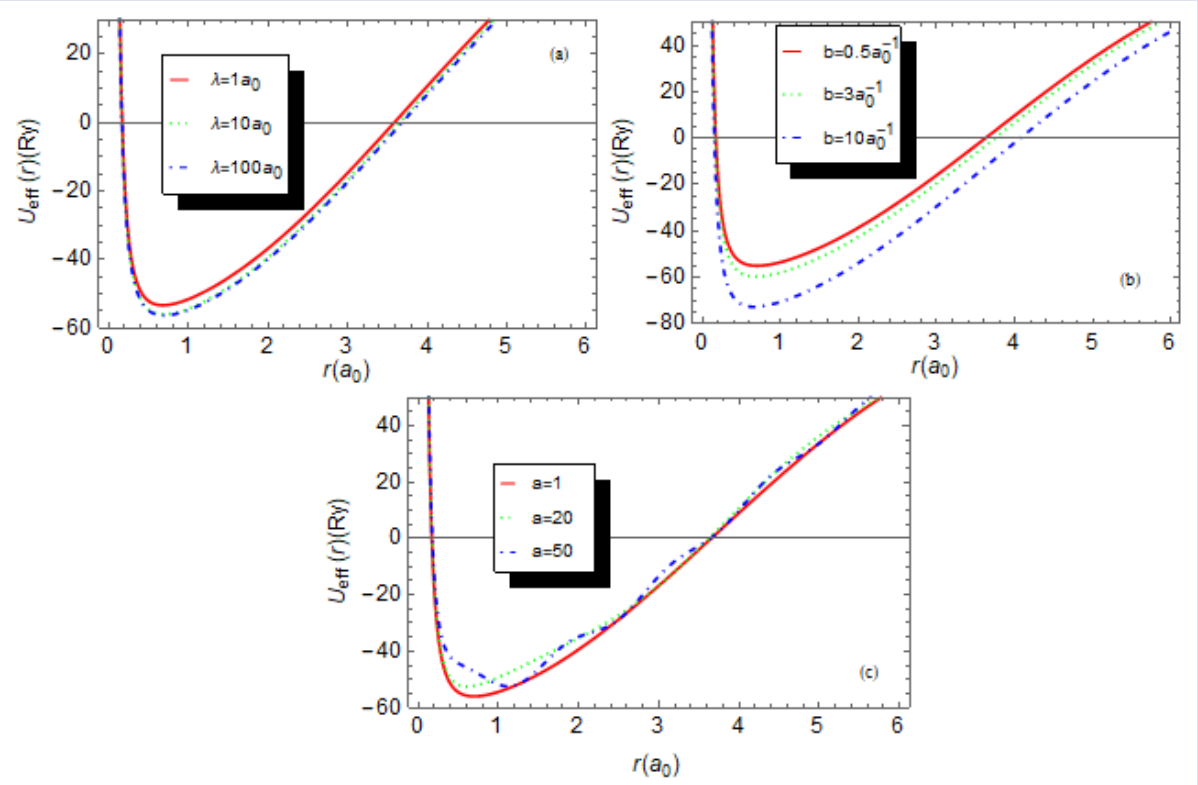

Figure 4. When $\xi = 10$kV/cm, the effective potential profile of the MQD with $x = 0.4, \eta = 0.25a_0^{-1}$ implanted in the quantum plasma presented by the MGECSC potential potential are plotted, in panel (a), when $a = 1, b = 1a_0^{-1}$, for different λ parameter values as a function of the radial direction (r); in panel (b), when $a = 1, \lambda = 10a_0$, for different b parameter values as a function of the radial direction (r); in panel (c), when$b = 1a_0^{-1}, \lambda = 10a_0$, for different a parameter values as a function of the radial direction (r).

In Table 1, when $\xi = 10$kV/cm, the energy values for some quantum levels of the MQD with $x = 0.4$ implanted in the quantum plasma presented by the MGECSC potential potential including with $a = 1, b = 1a_0^{-1}$ and $\lambda = 1 - 10 - 100 - 500a_0$, are furnished in eV unit. As seen in Table 1, the increment of λ parameter leads to decrease the energy values of the bound state. However, this decrease becomes monotonous at large values of λ. Therefore, small regimes are more suitable for the functional range of λ, which is an expected situation. Because at sufficiently large values of λ, the interaction potential exhibits Coulombic character, and the plasma shielding is less felt. Decrease in the bound state localizations (See Table 1) weakly increases the attractiveness of the effective potential due to the increase in λ (See Figure 4a).This causes their energy level to lift down faintly. Besides, it is clear that the parameter λ does not have a significant effect on the differences between energy levels. Therefore, it can be said that the parameter λ is not functional on the resonant frequencies of some nonlinear optical properties, except for the tuning that can be made with small λ regimes in systems with sensitive frequency requirements.

Table 1: When $\xi = 10$kV/cm, the energy values for some quantum levels of the MQD with $x = 0.4, \eta = 0.25a_0^{-1}$ implanted in the quantum plasma presented by the MGECSC potential potential including with $a = 1, b = 1a_0^{-1}$ and $\lambda = 1 - 10 - 100 - 500a_0$, in eV unit.

$(n\ell)$	$\lambda = 1a_0$	$\lambda = 10a_0$	$\lambda = 100a_0$	$\lambda = 500a_0$
(10)	-0.278211106611	-0.291501806989	-0.293013116151	-0.293147807383
(20)	-0.220340993620	-0.234318701486	-0.236232079492	-0.23640317908
(30)	-0.168186518338	-0.181910613646	-0.184107444614	-0.184304583361
(11)	-0.242266526524	-0.256477349404	-0.258262933377	-0.258422345642
(21)	-0.189873771657	-0.203922691933	-0.206012117004	-0.206199293668
(31)	-0.139976576236	-0.153569499145	-0.155906031947	-0.156116096074
(12)	-0.212884712082	-0.291501806989	-0.256477349404	-0.227395230788
(22)	-0.162537463664	-0.234318701486	-0.203922691933	-0.176565875165
(32)	-0.113925943360	-0.181910613646	-0.153569499145	-0.127389894947

In Table 2, when $\xi = 10$kV/cm, the energy values for some quantum levels of the MQD with $x = 0.4$ implanted in the quantum plasma presented by the MGECSC potential potential including with $a = 1, b = 0.5 - 2.5 - 5 - 10a_0^{-1}$ and $\lambda = 10a_0$, are furnished in eV unit. An increase in the b plasma parameter causes a linear decrease in the bound state energy values (See Table 2). The reason for this decrease is that the effective potential becomes more attractive due to the increase of the b parameter, as can be seen in Figure 4b. As can be seen, the increase of the b parameter has a significant function on the optical properties of the system. However, the difference between the energy levels is almost unchanged, as the increase of the b parameter creates a perfectly symmetrical attraction in the effective potential profile. From here, the following can be concluded that the b parameter is ineffective on the resonant frequencies of some nonlinear optical properties of the MQD.

Table 2: When $\xi = 10$kV/cm, the energy values for some quantum levels of the MQD with $x = 0.4, \eta = 0.25a_0^{-1}$ implanted in the quantum plasma presented by the MGECSC potential potential including with $a = 1, b = 0.5 - 2.5 - 5 - 10a_0^{-1}$ and $\lambda = 10a_0$, in eV unit.

$(n\ell)$	$b = 0.5a_0^{-1}$	$b = 2.5a_0^{-1}$	$b = 5a_0^{-1}$	$b = 10a_0^{-1}$
(10)	-0.286578039947	-0.306277296948	-0.330916740495	-0.380244358712
(20)	-0.229620036540	-0.248419869438	-0.271938800332	-0.319038468753
(30)	-0.177371320523	-0.195534105491	-0.218258396788	-0.263774521260
(11)	-0.251706812079	-0.270794451246	-0.294674227602	-0.342498483771
(21)	-0.199322802181	-0.217728063413	-0.240755746965	-0.286879354594
(31)	-0.149108855877	-0.166957413886	-0.189290303123	-0.234028118382
(12)	-0.222737268674	-0.241375143811	-0.264694745172	-0.311405530092
(22)	-0.172052900062	-0.190110922134	-0.212706120618	-0.257969901577
(32)	-0.123002784625	-0.140557572469	-0.162524590908	-0.206535031193

In Table 3, when $\xi = 10$kV/cm, the energy values for some quantum levels of the MQD with $x = 0.4$ implanted in the quantum plasma presented by the MGECSC potential potential including with $a = 1 - 5 - 10 - 30, b = 1a_0^{-1}$ and $\lambda = 10a_0$, are furnished in eV unit. The increase of the a plasma parameter causes an increase in the bound state energy values (See Table 3). The increment here has a certainty at larger values of a, due to the oscillation in the plasma potential arising from the cosine term. As the a plasma parameter increases, the stable structure of the effective potential deteriorates and a more aggressive repulsion occurs in the potential (See Figure 4c). In strong regimes of a, besides the increase in bound state levels caused by this repulsion, the energy difference between some levels decreases. In this case, it can be stated that the red-shifting can realize in the resonant frequencies of some nonlinear optical features of the MQD.

Table 3: When $\xi = 10$kV/cm, the energy values for some quantum levels of the MQD with $x = 0.4, \eta = 0.25a_0^{-1}$ implanted in the quantum plasma presented by the MGECSC potential potential including with $a = 1 - 5 - 10 - 30, b = 1a_0^{-1}$ and $\lambda = 10a_0$, in eV unit.

$(n\ell)$	$a = 1$	$a = 5$	$a=10$	$a = 30$
(10)	-0.291501806989	-0.290309932655	-0.286869363563	-0.264162803777
(20)	-0.234318701486	-0.231852530744	-0.225335545505	-0.210165328050
(30)	-0.181910613646	-0.178407132431	-0.170052579468	-0.166759219919
(11)	-0.256477349404	-0.254506904882	-0.249034187397	-0.224308352546
(21)	-0.203922691933	-0.200858425688	-0.193146676584	-0.184757937524
(31)	-0.153569499145	-0.149556480957	-0.140511711773	-0.139052137697
(12)	-0.227395230788	-0.224780394058	-0.217772080671	-0.198693456784
(22)	-0.176565875165	-0.172958960142	-0.164278012201	-0.159028236265
(32)	-0.127389894947	-0.122900343357	-0.113300885223	-0.112274549821

The results of this study can be summarized as follows: Some energy levels of electric field induced MQD with hydrogenic impurity, implanted in quantum plasma modeled by the MGECSC potential have been investigated. Structural parameters are functional and dominant over the electronic properties of the system. However, although the external electric field strength is an external factor, it is effective on energy levels. In this context, since both ξ and η parameters increase the energy levels, the ξ and η parameters may be alternative to each other. The effect of plasma shielding is quite feeble compared to structural factors and external electric

field effect. While the λ parameter, which can be considered as the most important plasma screening parameter, is effective in small regimes, it is not effective in strong regimes. Although the b parameter lowers the energy levels, it is not effective on the energy difference between the levels due to its linear effect. This means that the b parameter will not have observable effect on the resonant frequency of some nonlinear optical properties. At large values of the a plasma parameter, some levels converge due to the aggressive repulsion. To summarize, for the relevant system, the structural and external electric field effects are functional, whereas plasma shielding effects are not. For the relevant system, plasma shielding is effective on electronic properties but not on possible optical properties. Because plasma shielding has a very feeble effect on the difference between energy levels.

Conflicts of interest

There are no conflicts of interest in this work.

References

[1] Liculescu E. C., Bejan D., Nonlinear optical properties of GaAs pyramidal quantum dots: Effects of elliptically polarized radiation, impurity, and magnetic applied fields, *Physica E: Low-dimensional Systems and Nanostructures*, 74 (2015) 51-58.

[2] Harrison P., *Quantum Wells, Wires, Dots* (2. Edition). England:Wiley, (2005).

[3] Jacak L., Semiconductor quantum dots-towards a new generation of semiconductor devices, *European Physical Journal*, 21 (2000) 487-497.

[4] Xie W. F., Two interacting electrons in a Gaussian confining potential quantum dot, *Solid State Communications*, 127 (2003) 401-405.

[5] Owen J., Brus L. Chemical synthesis and luminescence applications of colloidal semiconductor quantum dots, *Journal of American Chemical Society*, 139 (2017) 10939-10943.

[6] Davies J. H., *The Physics of Low-Dimensional Semiconductors: An Introduction* (5.Edition). USA:Cambridge, (1999).

[7] Başer P, Bahar M. K., Evaluation of the external electric- and magnetic field-driven Mathieu quantum dot's optical observables, *Physica B:Condense Matter*, 639 (2022) 413991-413999.

[8] Bahar M. K, Başer P., Nonlinear optical characteristics of thermodynamic effects-and electric field-triggered Mathieu quantum dot, *Micro and Nanostructures*, 170 (2022) 207371-207382.

[9] Bahar M. K, Başer P., Tuning of nonlinear optical characteristics of Mathieu quantum dot by laser and electric field, *The European Physical Journal Plus*, 137 (2022) 1138-1148.

[10] Kortshagen U., Nonthermal plasma synthesis of semiconductor nanocrystals, *Journal of Physics D: Applied Physics*, 42 (2009) 113001-113023.

[11] Pi, X. D., Kortshagen, U., Nonthermal plasma synthesized freestanding silicon–germanium alloy nanocrystals, *Nanotechnology*, 20 (2009) 295602-295608.

[12] Bahar M. K., Soylu A., Two-electron quantum dot in plasmas under the external fields, *Physics of Plasmas*, 25 (2018) 022106-022118.

[13] Bahar M. K., Soylu A., Confinement control mechanism for two-electron Hulthen quantum dots in plasmas, *Journal of Physics B:Atomic, Molecular and Optical Physics*, 51 (2018) 105701-105715.

[14] Bahar M. K., Soylu A., Laser-driven two-electron quantum dot in plasmas, *Physics of Plasmas*, 25 (2018) 062113-062125.

[15] Bahar M. K., Plasma screening effects on the energies of hydrogen atom under the influence of velocity-dependent potential, *Physics of Plasmas*, 21 (2014) 072706-072716.

[16] Ciftci H., Hal R. L., Saad N., Asymptotic iteration method for eigenvalue problems, *Journal of Physics A: Mathematical and General*, 36 (2003) 11807-11816.

[17] Ciftci H., Hall R. L., Saad N., Construction of exact solutions to eigenvalue problems by the asymptotic iteration method, *Journal of Physics A: Mathematical and General*, 38 (2005) 1147-1155.

[18] Saad N., Ciftci H., Hall R. L., Criterion for polynomial solutions to a class of linear differential equations of second order, *Journal of Physics A: Mathematical and General*, 39 (2005) 13445-13454.

Cumhuriyet Sci. J., 44(2) (2023) 377-383
DOI: https://doi.org/10.17776/csj.1185157

Cumhuriyet Science Journal

| csj.cumhuriyet.edu.tr | Founded: 2002 ISSN: 2587-2680 e-ISSN: 2587-246X Publisher: Sivas Cumhuriyet University

Numerical Investigation of Diffraction Patterns of Small Size Apertures Using Light Sources From Xuv to The Visible Region: Simulation for The Small Size Structures

Muhammed Sayrac [1,a,*], Emine Kaynar [1,b], Fatih Ungan [2,c]

[1] *Department of Nanotechnology Engineering, Faculty of Engineering, Sivas Cumhuriyet University, Sivas, Türkiye.*
[2] *Department of Physics, Faculty of Sciences, Sivas Cumhuriyet University, Sivas, Türkiye.*
**Corresponding author*

Research Article

History
Received: 06/10/2022
Accepted: 06/06/2023

ABSTRACT

In the present work, a computer simulation program generates Fresnel diffraction patterns from small-size apertures using illumination wavelengths from extreme ultraviolet (XUV) to the visible region suggesting that it can be used to model a wide range of experimental setups. By being able to simulate diffraction patterns for such a broad range of wavelengths, the program can be used to investigate the effects of varying wavelengths and aperture size on the resulting pattern. By using a computer simulation program that can generate Fresnel diffraction patterns across a wide range of wavelengths, one can explore how different wavelengths of light interact with various aperture sizes. This allows one to investigate the effects of changing these parameters on the resulting diffraction pattern. The computer simulation program generating Fresnel diffraction patterns from square apertures by using the illumination wavelength sources from XUV to the visible region has been studied. Changing the aperture-screen distance, the illumination wavelength, and the aperture size provides a clear transition of diffraction patterns from the Fresnel to the Fraunhofer region. The diffraction patterns obtained by the Fresnel integral method have been compared with that simulated by the Fraunhofer calculation. There is a good agreement between the results. The structural similarity index (SSI) exhibits that comparing the diffraction images produced with both approaches agree.

Keywords: Diffraction. Optics. Numerical simulation. Micron/nanostructures. XUV radiation.

[a] *muhammedsayrac@cumhuriyet.edu.tr* *https://orcid.org/0000-0003-4373-6897*
[b] *emineekaynar@hotmail.com* *https://orcid.org/0000-0002-0050-348X*
[c] *fungan@cumhuriyet.edu.tr* *https://orcid.org/0000-0003-3533-4150*

Introduction

Optics is one of the important fields of physics that studies the properties of light. It plays an important role in technical applications such as communication and information sciences. In optics, the diffraction of light plays a paramount role in solving optical problems that do not usually reach an agreement with an exact solution. Therefore, numerical methods make it easy to investigate simpler cases. When the optical wave encounters an aperture, diffraction of light occurs [1]. Diffraction is classified known as Fraunhofer (far-field) and Fresnel (near-field) diffraction. The Fraunhofer diffraction pattern occurs when the aperture-observation screen distance is large. However, the Fresnel diffraction pattern appears when the aperture-screen distance is short [2, 3]. Diffraction and propagation of the optical field from an aperture were calculated by using Helmholtz-Kirchhoff [4] and Rayleigh-Sommerfeld integrals [5]. The Fresnel and Fraunhofer diffraction patterns were obtained by using the Fourier transform method [6] and the two-dimensional Fast Fourier transform method [7, 8].

The calculation of the diffraction integral is possible with minimum effort due to the personal computer and packaged mathematical software. In this paper, the diffraction patterns have been obtained by using Matlab software (R2017b 9.3.0.713579 (x64)) in the XUV and visible region. [9]. The Fresnel and Fraunhofer diffraction patterns have been simulated for a nano or micron size aperture by using the radiation source from 4nm to 600nm (corresponding to photon energy from ~310eV to 2eV) [1, 10-12]. This paper aims to study diffraction phenomena further for small-size structures by using short-wavelength radiation. The "soft x-ray region" of 4nm corresponds to the water window region in which water is transparent to extreme ultraviolet (XUV) radiations. Therefore, the wavelength region has a crucial role in viewing water-dominant biological samples, and the diffraction of light has a vital role in life science. On the other hand, this phenomenon is complex for studies in the short wavelength region, and it is not easy for laboratory experiments. For this reason, the simulation approaches facilitate viable alternatives and bring an idea for pre experiments studies. Over the last 20 years, the optics field including coherent XUV beamlines has brought opportunities that study in several disciplines from biological imaging [13-15] to material science [16, 17], and astrophysics [18] to high energy plasmas [19-21]. Also, it is useful to science and engineering students who deal with Fresnel diffraction, especially in short-wavelength regions. Therefore, the implementation of a diffraction

model for a small-size aperture by using a short-wavelength source is important.

The diffraction patterns discussed the Fraunhofer diffractions of the single slit at the visible or infrared region, however, the diffraction patterns at the XUV region were not mentioned. The paper introduces a simulation for Fraunhofer and Fresnel diffraction at a wavelength range from XUV to the visible region. The simulation program is compiled by several input parameters, namely the aperture-screen distance, the illumination wavelength, and the aperture size. The simulation program demonstrates how a diffraction pattern changes with varying input parameters from the Fraunhofer to the Fresnel region at the short wavelength region. Optical diffraction has been studied by several researchers in the visible wavelength region [12, 22-28]. In this paper, the diffraction patterns from small-size apertures (nano/micron-size objects) at the short-wavelength regions have been studied. This is the novelty of this paper for studying diffraction patterns from small-size structures illuminated by monochromatic light. In addition, diffraction patterns obtained by the Fresnel and the Fraunhofer methods have been compared by using the structural similarity index (SSI). The SSI is used for metric measure the similarity between two patterns. The concept of SSI is introduced in Section 4. Both approaches produce similar patterns for the same input parameters. The rest of the paper is organized as follows. Section 2 gives basic diffraction theory. Section 3 describes the simulation results. Section 4 compares simulation results obtained by the Fraunhofer and Fresnel diffraction methods. Finally, the conclusion is drawn in Section 5.

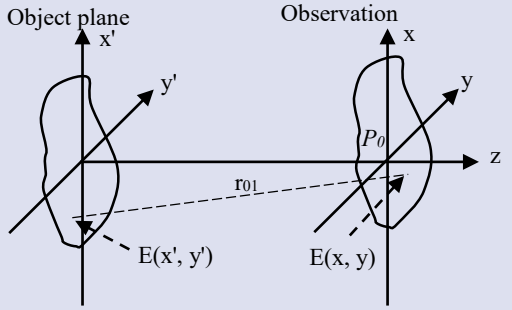

Figure 1. Schematic diagram of diffraction [1, 11]

Basic Diffraction Theory

Light propagation and diffraction have been described by using the Huygens-Fresnel principle by several researchers [4, 6-8, 10, 12]. The fundamental calculation of Fresnel diffraction from a rectangular aperture is that a light wave passes through an aperture and the total electric field at any point in the xy-plane can be obtained by the Huygens-Fresnel Principle for rectangular coordinates, Fig. 1 [1, 11]. The diffracted light is observed on the screen located at a distance. By using the Huygens-Fresnel principle, the total field in the xy-plane is integral to the fields of all the wavelets produced in each part of the aperture in the x'y'-plane [1, 10, 12] and can be described as follows

$$E = \frac{-iE_u}{2}\left[C(\mathrm{u}) + \mathrm{i}\,S(u)\right]_{\alpha_1}^{\alpha_2}\left[C(v) + \mathrm{i}\,S(v)\right]_{\beta_1}^{\beta_2} \quad (1)$$

where E_u is the unobstructed electric field at P_0. C and S are the Fresnel integrals and two-dimensional variables are defined $u = y\left[\frac{2(\mathrm{r}_{01}+\mathrm{P}_0)}{\lambda r_{o1}P_0}\right]^{0.5}$ and $v = z\left[\frac{2(\mathrm{r}_{01}+\mathrm{P}_0)}{\lambda r_{o1}P_0}\right]^{0.5}$. λ is the wavelength, and r_{01} is a vector from an aperture point to a parallel screen. $E(x', y')$ and $E(x, y)$ are electric fields on the aperture and the screen, respectively. There are two approximations: (i) the dimensions of the diffraction geometry are larger than the illumination wavelength (λ). (ii) The observation screen distance is many wavelengths from the aperture ($r_{01} >> \lambda$)

Taking the square of the electric field, Eq. 1 gives the illumination intensity I and can be written as,

$$I = \frac{I_u}{4}\left\{\left[C(\alpha_2) - C(\alpha_1)\right]^2 + \left[S(\alpha_2) - S(\alpha_1)\right]^2\right\} \times \times\left\{\left[C(\beta_2) - C(\beta_1)\right]^2 + \left[S(\beta_2) - S(\beta_1)\right]^2\right\} \quad (1)$$

I_u is unobstructed intensity corresponding to the square of E_u, and $\alpha = \sqrt{\frac{2}{\lambda z}}(x' - x)$ and $\beta = \sqrt{\frac{2}{\lambda z}}(\mathrm{y}' - \mathrm{y})$ are coefficients. α and β indicates the position of the edges of the structure in the x and y direction, respectively.

The derivation of the Fresnel integral method is given in a detailed manner [10, 12]. When the distance between the aperture to the observation screen is increased, the Fresnel diffraction region gradually approaches the Fraunhofer diffraction region. In the simulation part, the Fresnel diffraction integral has been used, Eq. 2 [10]. Input parameters namely the aperture to screen distance, the illumination wavelength, and the aperture size have been changed, and the diffraction patterns vary with changing input parameters.

Simulation results

The input parameters of the simulation program are as follows: the width of the aperture in millimeters, the wavelength in nanometers, and the aperture to screen distance in millimeters. For Fig. 2-4 (a-d), the upper figures correspond to 2D diffraction patterns, and the lower ones are for 1D normalized intensity distribution of diffraction patterns. To compare the diffraction patterns, we gradually increase the aperture to screen distance, Fig. 2. Figure 2 shows the diffraction patterns for the increasing aperture to screen distance. The illumination wavelength and the aperture size are kept constant at 32nm and 0.1mm×0.1mm, respectively. The transition of diffraction

patterns from the Fresnel regime to the Fraunhofer regime is expected, Fig.2 (a)-(d). When the aperture-screen distance is increased, the Fresnel diffraction pattern gradually changes into the Fraunhofer diffraction pattern. Aperture size is about 3100 wavelengths wide, and the screen has been placed from the aperture about 0.3million to 43million wavelengths away, Fig. 2 (a) 0.3million, (b) 2.2million, (c) 22milllion, and (d) 43million. For the case of a large aperture to screen distance, the diffraction patterns resemble a Fraunhofer diffraction pattern (Fig. 2(d)). On the other hand, for the smallest aperture to screen distance, a Fresnel diffraction pattern is obtained, (Fig 2(a)).

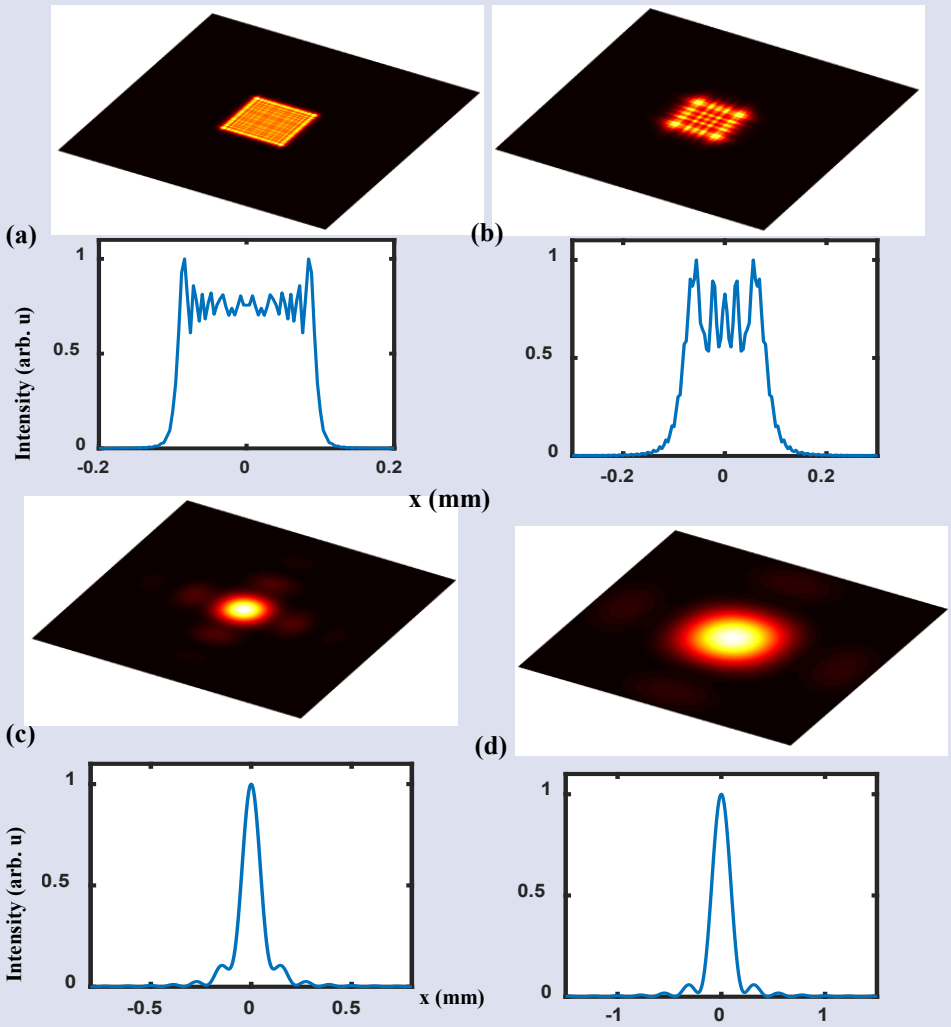

Figure 2. Diffraction patterns for increasing the aperture-screen distance. (a)10mm, (b)70mm, (c)700mm, (d)1400mm. The aperture size is 0.1mm×0.1mm, and the illumination wavelength is 32nm

Moreover, the effect of the change of wavelength on the diffraction patterns is observed, in Fig. 3. Figure 3 presents diffraction patterns (upper figures Fig. 3 (a-d)) for a fixed aperture size of 0.1mm×0.1mm and for the apertures to screen distance of 700mm. The illumination wavelength gradually increases from 4nm to 600nm wavelength. Thus, the aperture width varies from 25×10^3 to 160 wavelength size, and the distance between the aperture-observation screen changes from 175 to 1 million wavelengths away, Fig. 3 (a)-(d). When the aperture size and the aperture-to-screen distance are constant, the Fresnel diffraction patterns are generated at the short wavelength region. An increase in the illumination wavelength generates the Fraunhofer diffraction patterns, Fig. 3. A clear transition from the Fresnel regime to the Fraunhofer regime is observed with the increment of wavelength from 4nm to 600nm, Fig 3

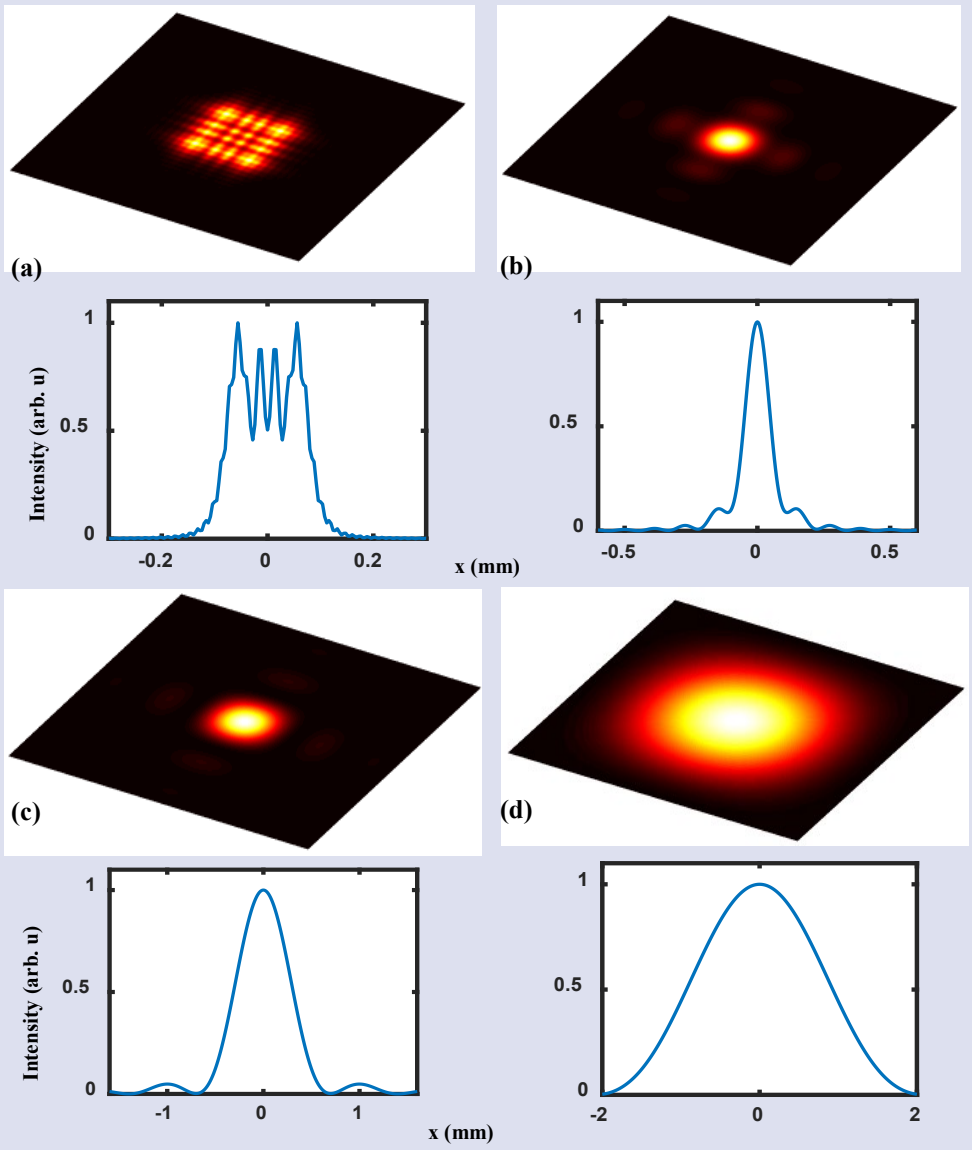

Figure 3. Diffraction patterns for increasing wavelength. (a) 4nm, (b) 32nm, (c) 200nm, (d) 600nm. The aperture size is 0.1mm×0.1mm, and the aperture-screen distance is 700mm

For a final investigation, we have studied the effects of change in the aperture sizes. The effect of a change in the aperture size is investigated. Figure 4 presents diffraction patterns of increasing aperture sizes from nano to micro size while keeping the illumination wavelength and the aperture-screen distance constant. The illumination wavelength is 4nm, and the aperture to screen distance is 700mm. The aperture size changes from 500nm to 100µm. The aperture-screen distance corresponds to about 175 million wavelengths, and the aperture size varies from 125 to 25000 wavelength size, Fig. 4 (a)-(d). For the smallest aperture size, the diffraction pattern resembles the Fraunhofer diffraction patterns (Fig. 4(a)), while the Fresnel diffraction pattern is obtained for the largest aperture size (Fig. 4(d)). Figures 2-4 agree with the rule that the aperture size, the illumination wavelength, and the aperture-screen distance have effects on the diffraction patterns [1, 11]. A practical comparison, if a satisfies the relation of $r_{01} < a^2/\lambda$, the Fresnel diffraction occurs. The relation $r_{01} > a^2/\lambda$ gives the Fraunhofer diffraction [10]. Here r_{01}, a, and λ are the aperture-screen distance, the aperture size, and the illumination wavelength, respectively. The relation for the occurrence of Fresnel and Fraunhofer diffractions can be immediately checked by using the above numerical formula. The real-time observation is obtained that the diffraction patterns change from Fresnel to Fraunhofer regime for the increasing input parameters of aperture-screen distance and the illumination wavelength, Fig. 2-3. Variations from Fraunhofer to Fresnel diffraction regime are obtained for increasing the aperture size, Fig. 4.

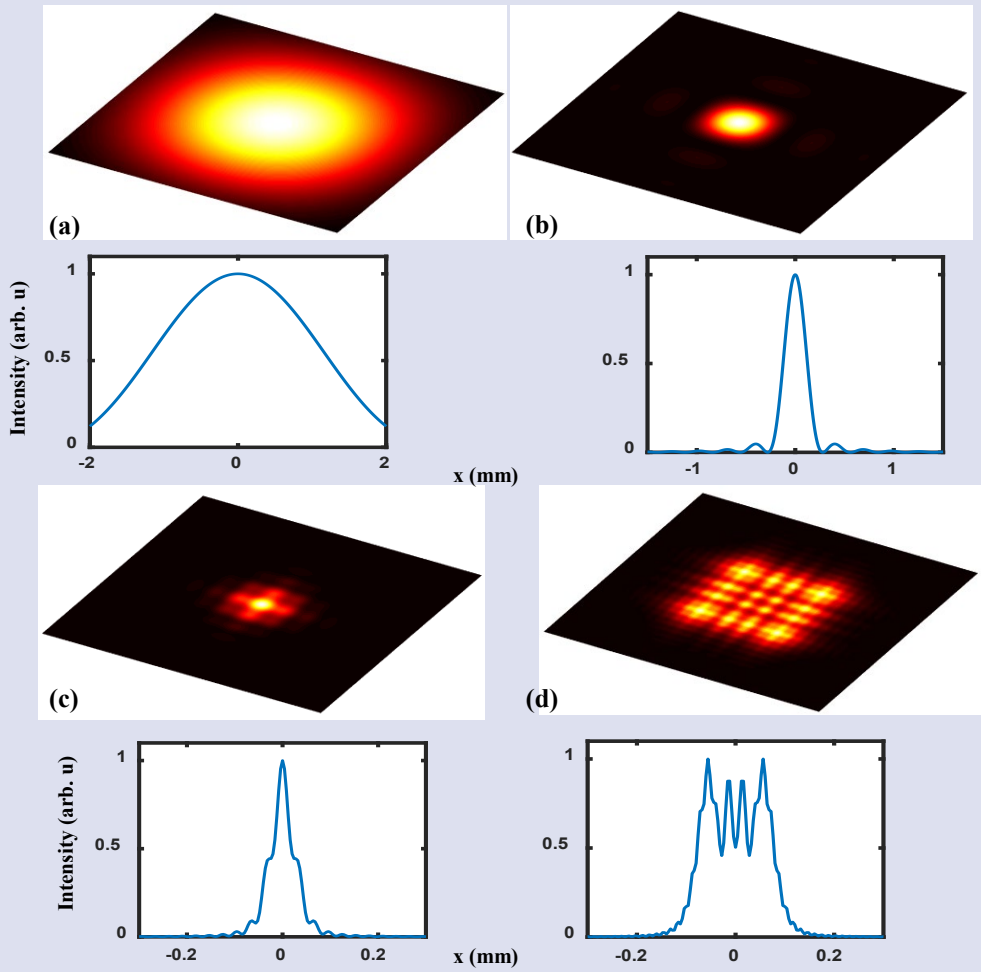

Figure 4Diffraction patterns for increasing aperture size. (a) 500nm×500nm, (b) 5000nm×5000nm, (c) 50000nm×50000nm, (d) 100000nm×100000nm. The illumination wavelength is 4nm, and the aperture-screen distance is 700mm

Figures 2-4 agree with the rule that the aperture size, the illumination wavelength, and the aperture-screen distance have effects on the diffraction patterns [1, 11]. A practical comparison, if a satisfies the relation of $r_{01} < a^2/\lambda$, the Fresnel diffraction occurs. The relation $r_{01} > a^2/\lambda$ gives the Fraunhofer diffraction [10]. Here r_{01}, a, and λ are the aperture-screen distance, the aperture size, and the illumination wavelength, respectively. The relation for the occurrence of Fresnel and Fraunhofer diffractions can be immediately checked by using the above numerical formula. The real-time observation is obtained that the diffraction patterns change from Fresnel to Fraunhofer regime for the increasing input parameters of aperture-screen distance and the illumination wavelength, Fig. 2-3. Variations from Fraunhofer to Fresnel diffraction regime are obtained for increasing the aperture size, Fig. 4.

Diffraction pattern using the Fraunhofer diffraction method

The diffraction patterns in the previous section are obtained using the Fresnel integral method [10]. In this section, the diffraction pattern obtained by using the Fraunhofer diffraction calculation is compared with that obtained by using the Fresnel integral for nano/micron size structures of the monochromatic light. The Fraunhofer diffraction studied by many researchers [2, 11, 26] is given by

$$I = I_0(\sin(\alpha)/\alpha)^2(\sin(\beta)/\beta)^2. \quad (2)$$

where I_0 is the intensity. $\alpha(=2\pi aX/R\lambda)$ and $\beta(=2\pi bY/R\lambda)$ are coefficients. *a* and *b* correspond to the aperture size, and *R* is the aperture-observation screen distance. The simulation using Eq. 3 compares the Fresnel diffraction with the Fraunhofer diffraction method. Figure 5(a) resembles the Fraunhofer diffraction image obtained by Eq. 3. Figure 5(b) is calculated by the

Fresnel integral method (Eq. 2) for the same parameters used for Fig. 5(a). Figure 5 (a)-(b) are well-known diffraction patterns of Fraunhofer diffraction [2, 11].

Figure 5 (b) obtained by the Fresnel integral method (Eq. 2) resembles that of the diffraction pattern presented in Fig. 5 (a) (Eq. 3) obtained by the Fraunhofer calculation method. This shows that the diffraction patterns produced using illumination wavelength in the XUV region are correct. In Fig. 5, the input parameters are the following: the illumination wavelength is 500nm, the aperture size is 1mm×1mm, and the aperture to observation screen distance is 1000mm.

Figure 5 proves that the diffraction images obtained by using the Fraunhofer calculation are perfectly matched with that obtained by using the Fresnel integral method. Measurements for diffraction pattern quality obtained by the Fraunhofer and Fresnel diffraction methods are presented in Fig. 5.

Structural Similarity Index (SSI)

SSI measures the similarities between two images (a reference image and a sample image) based on three features: luminance, contrast, and structure. The signals coming from the reference and the sample images are represented mathematically. The first feature of luminance is the measurement by averaging over all pixel values. Then, contrast is measured by taking the square root of the variance of all the pixels from the images. Finally, the structure is a comparison function by dividing the input signal by its square root of variance. After the three features are determined, the comparison function combines them and produces the similarity index value [31].

In the scope of this study, the calculation of SSI between the two patterns in Fig. 5 (a)-(b) is performed. Figure 5 (a) is used as a reference image, and Figure 5 (b) acts as a sample image. Figure 5 (c) shows that each calculation generates diffraction patterns in the Fraunhofer region and displays SSI. SSI index value is 0.57. Thus, the diffraction images in the XUV region obtained by using Fresnel integral method must be correct.

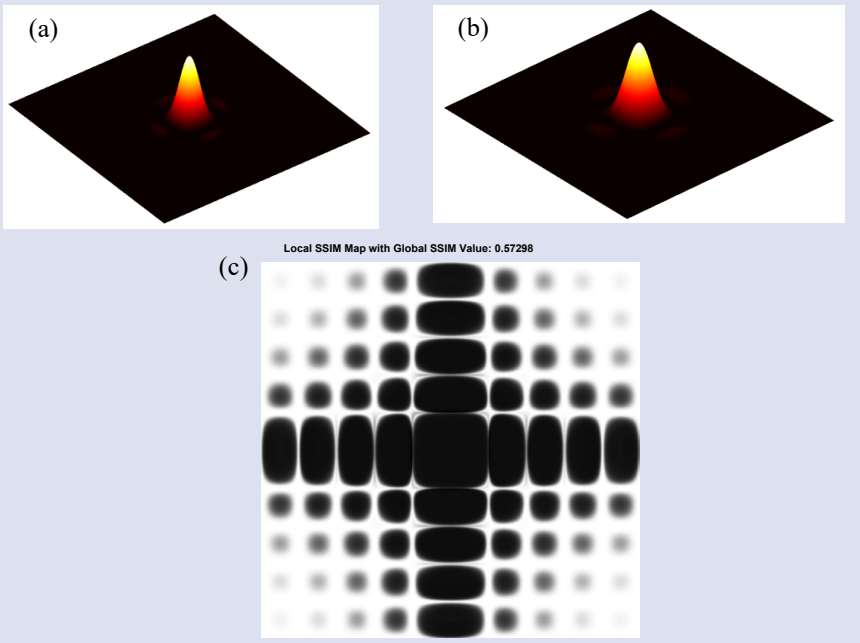

Figure 5. (a) 3D intensity distribution of the Fraunhofer diffraction image generated by using Eq. 3. (b) Simulation result of the Fresnel integral (Eq. 2) using the same simulation input parameters of Fig. 5 (a). (c) Structural similarity index (SSI) for Fig. 5 (a)-(b)

Conclusions

This paper describes that the diffraction images are generated in the Fresnel and the Fraunhofer region by using illumination wavelength from XUV to the visible region. The basic diffraction theory is described. The simulated 2D diffraction images and 1D diffraction intensity distribution for small-size apertures (nano-micron size) and different wavelength sources (from 4nm to 600nm) are presented in the results. The Matlab software simulates the diffraction patterns. The transition from the Fresnel to Fraunhofer region is observed with varying input parameters, namely the aperture-screen distance, the aperture size, and the illumination wavelength.

The diffraction images are obtained from the nano or micron-size structures at a different aperture-screen distance by using the illumination wavelength from 4nm to 600nm. The Fresnel and Fraunhofer diffraction methods produce diffraction images, and both methods generate similar diffraction patterns, Fig. 5. The structural similarity index (SSI) for comparing diffraction images obtained by the Fraunhofer and the Fresnel calculation has been performed. The diffraction patterns obtained with both approaches resemble. Thus, the Fresnel diffraction images produced by using short-wavelength sources presented in Section 3 are correct.

Acknowledgment

This work is supported by the Scientific Research Project Fund of Sivas Cumhuriyet University under project number [M-2021-819].

Conflict of interests

The authors state that did not have a conflict of interest.

References

[1] Goodman, J. W.: Introduction To Fourier Optics. McGraw-Hill Science, McGraw-Hill Science (1996).
[2] Born, M., Wolf, E.: Principles of Optics: Electromagnetic Theory of Propagation Interference and Diffraction of Light. Cambridge University (1999).
[3] Ball, C. J.: An Introduction to the Theory of diffraction. Pergamon Press, New York (1971).
[4] Rudolf, P. G., Tollett, J. J., McGowan, R. R.: Computer modeling wave propagation with a variation of the Helmholtz-Kirchhoff relation. *Appl. Opt*. 29, 998-1003 (1990).
[5] Räsänen, J., Abedin, K. M., Kawazoe, M., Tenjimbayashi, K., Eiju, T., Matsuda, K., Peiponen, K. E.: Computer simulation of the scatter plate interferometer by scalar diffraction theory. *Appl. Opt.* 36, (1997) 5335-5339.
[6] Dodds, S. A.: An optical diffraction experiment for the advanced laboratory. *Am. J. Phys*. 58, (1990) 663.
[7] Dauger, D. E.: Simulation and study of Fresnel diffraction for arbitrary two-dimensional apertures. *Comput. Phys*. 10, (1996) 591-604.
[8] Trester, S.: Computer-simulated Fresnel diffraction using the Fourier transform. *Comput. Sci. Eng.* 1, (1999) 77-83.
[9] MATLAB version 9.3.0.713579. The Mathworks, Natick, Massachusetts (2017).
[10] Abedin, K. M., Islam, M. R., Haider, A. F. M. Y.: Computer simulation of Fresnel diffraction from rectangular apertures and obstacles using the Fresnel integrals approach. *Opt. Laser Technol*. 39, (2007) 237-246.
[11] Hecht, E.: Optics. Pearson (2016).
[12] JDíaz, J. A.: Comment on "Computer simulation of Fresnel diffraction from rectangular apertures and obstacles using the Fresnel integrals approach". *Opt. Laser Technol.* 121, (2020) 105819.
[13] Seibert, M. M., Ekeberg, T., Maia, F. et al.: Single mimivirus particles intercepted and imaged with an X-ray laser. *Nature* 470, (2011) 78-81.
[14] Chapman, H., Fromme, P., Barty, A. et al.: Femtosecond X-ray protein nanocrystallography. *Nature* 470, (2011) 73-77.
[15] Helk, T., Zürch, M., Spielmann, C.: Perspective: Towards single shot time-resolved microscopy using short wavelength table-top light sources. *Struct. Dynam*. 6, (2019) 010902.
[16] Chapman, H., Barty, A., Bogan, M., et al.: Femtosecond diffractive imaging with a soft-X-ray free-electron laser. *Nature Phys*. 2, (2006) 839-843.
[17] Milathianaki, D., Boutet, S., Williams, G. J., et. al.: Femtosecond Visualization of Lattice Dynamics in Shock-Compressed *Matter. Science* 342, (2013) 220-223.
[18] Savin, D. W., Brickhouse, N. S., Cowan, J. J., et. al.: The impact of recent advances in laboratory astrophysics on our understanding of the cosmos. *Rep. Prog. Phys*. 75, (2012) 036901.
[19] Beye, M., Schreck, S., Sorgenfrei, F., Trabant, C., Pontius, N., Langeheine, C. S., Wurth, W., Föhlisch, A.: Stimulated X-ray emission for materials science. *Nature* 501, (2013) 191-194.
[20] Rudek, B., Son, SK., Foucar, L. et al.: Ultra-efficient ionization of heavy atoms by intense X-ray free-electron laser pulses. *Nat. Photonics* 6, (2012) 858-865.
[21] Lopez, M. R., Faenov, A., Pikuz, T. et. al.: Coherent X-ray beam metrology using 2D high-resolution Fresnel-diffraction analysis. *J. Synchrotron Rad.* 24, (2017) 196-204.
[22] Makris, K. G., Psaltis, D.: Huygens–Fresnel diffraction and evanescent waves. *Opt. Commun*. 284, (2011) 1686-1689.
[23] Cui, Y., Zhang, W., Wang, J., Zhang, M., Teng, S.: Fresnel diffraction of aperture with rough edge. *J. Optics* 17, (2015) 065607.
[24] Tan, J., Lu, Z., Liu, J., Jin, P., Wang, Y.: Analysis of Fraunhofer diffractive characteristics of a tilted metallic mesh for its effect on optical measurement. *Meas. Sci. Technol.* 18, (2007) 1703-1709.
[25] Abedin, K. M., Rahman, S. M. M.: Computer simulation of Fresnel diffraction from double rectangular apertures in one and two dimensions using the iterative Fresnel integrals method. *Opt. Laser Technol*. 44, (2012) 394-402.
[26] Zhang, Z., Bai, H., Yang, G., Jiang, F., Ren, Y., Li, J., Yang, K., Yang, H.: Computer simulation of Fraunhofer diffraction based on MATLAB. *Optik* 124, (2013) 4449-4451.
[27] Stevanovic, N., Markovic, V. M., Nikezic, D.: New method for determination of diffraction light pattern of the arbitrary surface. *Opt. Laser Technol*. 90, (2017) 90-95.
[28] Markovic, V. M., Stevanovic, N., Nikezic, D.: Propagation of light from dipole source and generalization of Fresnel-Kirchhoff integral. *Optik* 180, (2019) 447-454.

Cumhuriyet Sci. J., 44(2) (2023) 384-388
DOI: https://doi.org/10.17776/csj.1260686

Cumhuriyet Science Journal

| csj.cumhuriyet.edu.tr | Founded: 2002 ISSN: 2587-2680 e-ISSN: 2587-246X Publisher: Sivas Cumhuriyet University

Comparison of Single and Multiple Treatment Plans for Multiple Brain Metastases in CyberKnife® Radiosurgery System on Phantom

Kevser Sözen [1,a,*], Hasan Uysal [2,b], Nihal Büyükçizmeci [3,c], Kaan Oysul [4,d]

[1] *The Graduate School of Selçuk University, Institute of Science, 42130, Konya, Türkiye.*
[2] *Department of Radiation Oncology, CyberKnife Radiosurgery Center, Medicana International Ankara Hospital, 06510, Ankara, Türkiye.*
[3] *Department of Physics, Institute of Science , University of Selçuk, 42130, Konya, Türkiye.*
[4] *Department of Radiation Oncology, CyberKnife Radiosurgery Center, Medicana International Ankara Hospital, 06510, Ankara, Türkiye.*

**Corresponding author*

Research Article

History
Received: 20/03/2023
Accepted:08/06/2023

ABSTRACT

While the use of CyberKnife® radiosurgery systems is increasing, the choice of treatment plan is also important. In this study, it was aimed to determine the more advantageous application by comparing the irradiation of all metastases at once and the protocols of irradiation of metastases separately in multiple brain metastases. For this, on an entirely new head phantom; 6 brain metastases and 3 critical organs, including the spinal cord, brain stem, and chiasm, were determined over the spaces where the dosimeters were placed. Computed tomography (CT) images of the head phantom were taken and these 6 tumors and 3 critical organs were drawn (contouring) on the image. In the treatment planning system, the dose we wanted to give was written and irradiation plans were created to be done separately with a single irradiation. Luminescence (OSL) dosimeters with BeO optical excitation were removed from the phantom after each irradiation and the count value obtained from the dosimeter reader device was recorded. Homogeneity index (HI), conformity index (CI), new conformity index (nCI), duration of treatment, and gradient index (GI) values of irradiation at one time and separately were compared. While it was found that irradiation of tumors with a separate treatment plan was more advantageous in terms of conformity index (CI), new conformity index (nCI), homogeneity index (HI), and coverage values, it was seen that a single plan was more suitable in terms of gradient index and duration.

Keywords: Cyberknife System, Radiosurgery, Multiple brain metastases, Conformity, Dose gradient.

[a] *kevser07@gmail.com* *https://orcid.org/0009-0005-9561-4674*
[b] *uysalhasann@gmail.com* *https://orcid.org/0000-0002-4867-304X*
[c] *nihal@selcuk.edu.tr* *https://orcid.org/0000-0002-6030-9574*
[d] *kaan@oysul.com* *https://orcid.org/0000-0002-4359-318X*

Introduction

Brain metastases are the most common malignancies in the central nervous system [1]. Up to forty percent of cancer patients have brain metastases at some point in their disease. The most common cancers that metastasize to the brain are lung, breast, kidney, colorectal, and melanoma. Primary treatment options in patients with brain metastases are surgery, chemotherapy, whole brain radiotherapy (WBRT), and stereotactic radiosurgery (SRS) [2].

Today, various radiotherapy methods are used for cancer treatment. In recent years, developments in engineering and computing have led to great advances in radiotherapy methods. As a result of these developments, technologies such as intensity modulated radiotherapy (IMRT), image-guided radiotherapy (IGRT), stereotactic radiotherapy (SRT), and stereotactic radiosurgery (SRS) have been routinely used in clinical practice.

SRS is based on the fact that radiation beams intersect at a precisely placed three-dimensional target. The Gamma Knife device is the first commercially produced intracranial SRS system to prevent patient movement and minimize the risk of damage to tissues adjacent to the tumor. In this system, the stereotactic frame consisting of fixed cobalt sources is fixed to the patient's head by screwing. Thanks to advances in imaging techniques, a robot-mounted CyberKnife® device was developed in the following years that could provide SRS without requiring surgical immobilization of the skull [3]. This radiosurgery system, also called "Space Scalpel", is a robotic radiosurgery system developed for the treatment of not only intracranial cancer but also whole-body cancer [4].

SRS is a treatment method that does not need to open the skull in deep-seated small lesions surgically,and allows to reach the normal brain tissues around the target as much as possible without damaging it. It shows 1mm targeting accuracy on fixed targets, such as cranial or spinal cord tumors, and on moving targets, such as lung tumors [4]. Small and well circumscribed tumors are the most suitable targets for this method [3]. The CT images taken before the treatment of the patient are compared with the snapshots taken during the treatment by the system. According to the obtained tumor coordinates, the radiation dose is adjusted instantly on the computer. Thus, the possible small movements of the patient during the treatment are prevented from affecting the treatment [5].

Whole brain irradiation or SRS can be performed in patients with multiple metastases following the surgical

procedure. For patients with multiple metastases following the surgical procedure, it is more preferable to apply SRS alone without whole-brain irradiation due to concerns that whole brain irradiation may cause side effects such as cognitive dysfunction, hair loss, and fatigue that reduce the quality of life. Therefore, SRS has become increasingly important in the treatment of brain metastases [3]. SRS 1-3 is standard in patients with metastases and is increasingly used instead of whole-brain radiation therapy in cases with up to 10 brain metastases, as it provides local tumor control while reducing neurological side effects. [6].

The aim of our study is to determine the more advantageous aspects of treatment plans by comparing the irradiation of all metastases at once and the irradiation of metastases separately in patients with multiple brain metastases based on HI, CI, treatment duration, scope, and gradient index values.

Materials and Methods

Today, irradiation in brain metastases can be done with radiosurgery. In this study, treatment plans for 6 brain metastases were investigated in a homemade phantom to preserve neurocognitive functions and irradiate less normal tissue.

Dose Calibration

In radiation therapy, it is crucial to give the desired dose to the patient in an adequate amount. Because if the adequate dose is not given, it may not be possible to destroy the tumor tissue completely. Radiation dosimetry is a method of checking whether the dose values calculated and displayed in the planning system are actually these values. For this, 11 BeO OSL dosimeters were used in our study. The dimensions of the BeO crystal used are 4.7×4.7×0.5 mm and the sheathed dimensions are 11×11×4 mm. Calibration of these dosimeters was carried out in the PTW brand RW3 solid water phantom. For the calibration, BeO OSL dosimeters were irradiated at 50 MU with 60mm collimator and 6Mv x-ray with SAD=80cm, 30cm x 30cm phantom diameter, dmax=1.5cm. From here, the calibration coefficients obtained by dividing the average OSL number showing the sensitivity of the dosimetry crystals by the dosimetry number were calculated separately for each dosimetry.

İmaging of the Phantom on Computed Tomography

In the study, first of all, the phantom, produced with a three-dimensional printer, was taken on the GE brand Revolution Evo Model CT device with 128 sections in Medicana Ankara hospital, and an image with a 1 mm cross-section range was obtained. Before the CT image of the phantom was taken, a thermoplastic frame was placed on the phantom (figure 1) to match the imaging system coordinate system and the device coordinate system.
All obtained CT data were transferred to the multi-plan treatment planning system.

Figure 1. Fixing the phantom with a thermoplastic mask. Picture is taken during the measurements in the laboratory of Medicana Ankara hospital.

Figure 2.Head phantom produced by using 3D printer. This phantom is produced for this research by H. Uysal

On the tomography images transferred to the Phantom's Multiplan treatment planning system, 6 tumor metastasis volumes as Tumor1, Tumor2, Tumor3, Tumor4, Tumor5, and Tumor6 and is contoured volumes as Critical1 (Spinal cord), Critical2 (Brainstem), Critical3 (Chiasma). In the plans, 3 shells with 2mm, 5mm, and 10mm widths were created at the target volume planned on the phantom. Treatment planning was carried out in such a way that 100 cGy was delivered to the target with the sequential technique, using the ray tracing algorithm for each section. A 10 mm collimator was chosen among 12 different collimators with 5 to 60 mm diameters to be used in planning. Plans have been created to treat all metastases on the phantom, both separately and at once. The locations of the metastatic tumor and critical organs in the phantom were determined as follows. Tumor1 is in the posterior right part of the 4th section, Tumor2 is in the rearmost left part of the 6th section, Tumor3 is in the far right front of the 7th section, Tumor4 is in the anterior left of 7th section, Tumor5 is in the anterior of the 8th section, and Tumor6 is in the right posterior of the 15th section. Critical1 formed in the spinal cord is located in the 15th section; Critical2 formed in the brain stem, and Critical3 formed in the chiasma, are located in the 7th section. The head phantom was irradiated with 6 MV photons with CyberKnife® device and dose measurements were made with BeO dosimeters placed inside the phantom. Count values for a single measurement are given in Table-1.

Table 1. For the 1st measurement, when 1Gy dose was given to each tumor volume, the count values of all tumors and critical organs were read in BeO dosimeters.

1.Measurement	*Tumor1*	*Tumor2*	*Tumor3*	*Tumor4*	*Tumor5*	*Tumor6*	*Single Plan*
T1	429521	6590	6782	4390	5811	4292	455755
T2	4162	432902	6230	5853	2970	3437	439105
T3	10675	15247	401255	6875	33779	4418	500360
T4	4763	23533	4674	397898	14931	3187	465847
T5	3539	4784	51563	8901	516929	4284	422143
T6	3315	3446	2815	2733	3130	389236	429734
K1	3000	2897	2754	3575	3601	37340	27028
K2	5085	8345	30259	11463	13302	3868	109703
K3	3704	4284	32948	12244	108860	3542	165417

Quality Control Indices

The Dose Volume Histogram (DVH) is used to evaluate the tumor volume and the dose delivered to the surrounding healthy tissue and critical structures. From DVH, dose parameters such as maximum dose, minimum dose, and average dose delivered to the volume of interest can be derived [7]. The DVH graph of the third metastasis tumor obtained in our study is given in Figure 3.

Different indices have been defined to evaluate the quality of a treatment plan to obtain an optimal dose distribution. Thanks to these indices, it will be easier for us to choose a plan that provides maximum tumor coverage homogeneously and preserves healthy tissues [8]. Some of these indexes are HI, CI, nCI, GI, and coverage. These indices provide an easy method of quantitatively assessing the dose distribution, which represents the agreement between the predicted dose area and the planned tumor volume

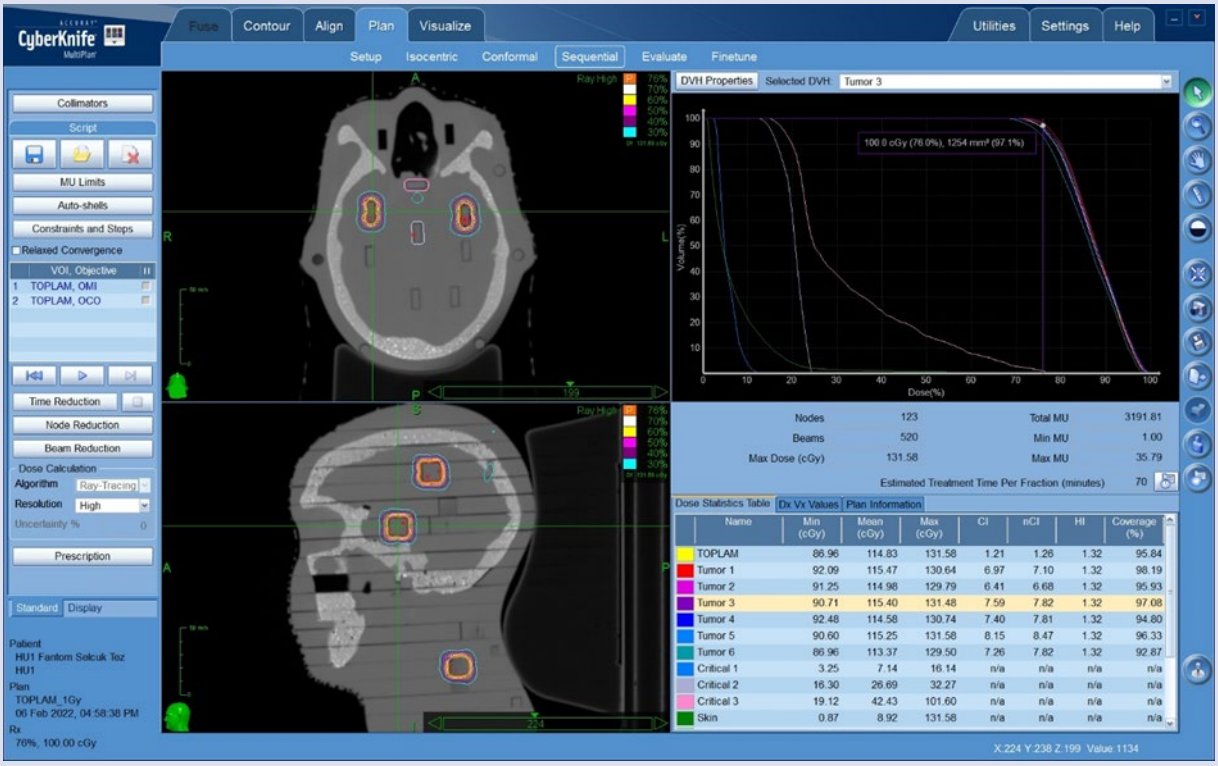

Figure 3. DVH graph of the 3rd metastasis tumor in a single treatment plan (obtained from the Multiplan treatment planning system).

Statistical Calculation

Statistical calculation was done using SPSS version V20. Paired Sample t-test was used in the analysis of all data. $0.01 \leq p < 0.05$ status statistical significance, $0.001 \leq p < 0.01$ status was accepted as high statistical significance.

Results

6 tumor volumes were determined in the HU phantom study to compare the irradiation of all metastases at once and the irradiation of each metastasis separately in patients with multiple brain metastases. The dose we wanted to give in the treatment planning system and the measurements we read in the BeO dosimeters in the HU phantom were evaluated. In addition, homogeneity index (HI), conformity index (CI), gradient index, duration of treatment, and coverage values, which show the quality of a treatment plan, were tried to determine the more advantageous application in multiple brain metastases by comparing the irradiation of all metastases at once and the irradiation of metastases separately. In our study, the durations for the planning of 6 brain metastases in the head phantom produced by the three-dimensional printer were calculated by the Multiplan treatment planning system. When we create a plan for the irradiation of each tumor separately, the irradiation time varies between 16 and 20 minutes—in total, the average irradiation time lasted 110 minutes. In a single plan, the irradiation time is 70 minutes on average. When the average times were compared, it was seen that the irradiation time in the separate planning took 40 minutes more than in the single planning. Therefore, since irradiation in a single treatment plan takes a shorter time than separate planning, it has been seen that the single plan is advantageous in terms of time.

The steep dose gradient outside the radiosurgery target is one of the factors that enable radiosurgical treatment [9,10]. The GI is an index used to evaluate off-target dose reduction and indicates the optimal off-target dose distribution [7]. The Paddick Gradient index formula, which is defined as the ratio of the volume of half of the defined isodose to the defined isodose volume, was used in our study. While the gradient index value was 4.55 in the single treatment plan, the total GI value of the separate treatment plans was 5.38. A lower GI value means a steeper dose distribution gradient outside the target and better normal tissue preservation. Therefore, the gradient index value was better when a single plan was made compared to the planning made separately.

The homogeneity index is an index that shows how homogeneously the dose given to the tumor volume is distributed in this volume. The HI will be determined as the maximum dose in the treatment volume divided by the prescribed dose. HI values close to 1.0 (the ideal value is expected to be 1) indicate higher dose homogeneity, while values greater than 1 indicate more heterogeneous dose distribution [11,13]. In this study, the homogeneity index ranged from 1.25 to 1.28 in the treatment plan made separately, and the mean value was 1.26. The HI index value was 1.32 in single plan, and a high level of statistical significance (p = 0.00) was found between the HI values of the two plans.

The RTOG conformity index formula, given as the ratio of the found isodose volume to the tumor isodose volume, was used. When each of the 6 metastases is planned separately, the conformity index varies between 1.16 and 1.20 and the mean value is 1.17. The CI index value was 1.21 in a single plan. Therefore, a statistically high level of significance (p = 0.004) was found in the conformity index between the two plans.

In addition, the nCI value ranged from 1.19 to 1.26 when treatment was planned separately, and the mean value was 1.22. In a single plan, the nCI value is 1.26. (p = 0.015), it was found to be statistically significant.

While the dose of 5% of the head volume skin dose is 24.9cGy in single plan, it is 30.7cGy in the separate plan. When we consider the coverage values, when we plan separately, coverage varies between 95.15 and 98.22. The mean value was 95.79. In single treatment planning, it varies between 92.87 and 98.19. The mean value was 95.84.

Discussion and Conclusion

Brain metastases (BM) are the most common malignant brain tumors and are a serious cause of death in cancer cases [14]. Fortunately, there is an increase in cancer survival due to advances in early detection and treatment. After successful cancer treatment, patients have to cope with the physical and psychological effects of the treatment [15]. It is essential to minimize functional and cognitive impairments after treatment.

The aim of radiotherapy is to preserve the healthy tissues and critical organs surrounding the tumor as much as possible and to deliver the entire dose to a defined volume. [16,17]. For this, treatment plans need to be prepared very carefully. While evaluating the prepared plan, it is necessary to consider clinical, biological, geometric, dosimetric, and radiological parameters simultaneously. This is an important but complex and time-consuming process. Often, several plans are prepared for the same patient, and without objective parameters, it becomes difficult to choose. Indexes such as CI, HI, GI and coverage can be used to select the best plan among available treatment options or to compare various devices and techniques [8]. In our study, treatment plans for multiple brain metastases were compared using these indices.

When we compare the irradiation of all metastases at once and the irradiation of each metastasis separately in terms of treatment time, it is seen that the irradiation of a single plan is advantageous in terms of patient comfort as it takes a shorter time. Patients treated in a much shorter time will be able to return to their everyday lives more quickly.

Ideal treatment planning is the one in which the lowest possible dose is given to normal tissues, and the entire prescribed dose is delivered to the target volume. In optimal treatment planning, isodose volume and tumor volume should overlap and be as close to CI=1 as possible [18]. If we consider the CI values in our study, it has been determined that the plans made separately are advantageous compared to a single plan. Yu et al., while finding the CI value similar for both plans, Uzel reported that the plan made separately for each metastasis is more

advantageous in terms of CI. In our result, it was found that separately treatment planning was more advantageous in terms of CI, in line with Uzel [19,20]. In our result, it was found that separately treatment planning was more advantageous in terms of CI, in line with Uzel Likewise, it was concluded that it was more appropriate to plan separately according to the nCI values.

In stereotactic radiotherapy treatments, the cases where the dose falling on the surrounding normal tissue decreases sharply while irradiating the target increases the quality of the treatment. While this value expressed by the gradient index value was found to be more appropriate in the separately treatment plan by Uzel, it was found more reasonable in terms of single-plan GI value in our study on the HU phantom.

The homogeneity index gives the ratio between the maximum and minimum dose in the target volume, and a lower value indicates a more homogeneous dose distribution within the tumor volume. It is not the right approach to try to reach the ideal value of HI at all costs. In some clinical situations, inhomogeneity (heterogeneity) may be desired [9]. However, in our study, the homogeneity index (HI) value was within the range of appropriate values in both plans, and a better homogeneity was found for the treatment plan prepared separately for each metastasis. In terms of coverage, both planes cover tumor volume very close to each other.

It has been found that a single plan is more advantageous in terms of treatment duration, gradient index and protecting organs at risk. In addition, planning separately in terms of conformity index, new conformity index and homogeneity index gave more appropriate results. All these results should be evaluated together and the patient's condition should be taken into consideration, and the most appropriate plan should be preferred for the patient.

Conflicts of interest

There are no conflicts of interest in this work.

Acknowledgments

The authors thank Medical Physics Specialist Mehmet Fazıl ENKAVI and Eng. İsmail Burak KORKUT from PHYSMART Medikal for their contributions. This research was supported by the Selçuk University. Research Grant, BAP (21111004).

References

[1] Kotecha R., Gondi V., Ahluwalia M.S., Brastianos P.K., Mehta M.P., Recent advances in managing brain metastasis. *F1000Res.,* 7 (2018) 1772.

[2] Stanley J., Breitman K., Dunscombe P., Spencer D.P., Lau H., Evaluation of stereotactic radiosurgery conformity indices for 170 target volumes in patients with brain metastases. *J Appl Clin Med Phys.*, (2011) 3449.

[3] O'Beirn M., Benghiat H., Meade S., Heyes G., Sawlani V., Kong A., Hartley A., Sanghera P., The Expanding Role of Radiosurgery for Brain Metastases. *Medicines.,* 5(3) (2018) 90.

[4] McGuinness M.C., Gottschalk A.R., Lessard E., Nakamura J.L., Pinnaduwage D., Pouliot J., Sims C., Descovich M., Investigating the clinical advantages of a robotic linac equipped with a multileaf collimator in the treatment of brain and prostate cancer patients*. Clin Med Phy.*, (2015) 16.

[5] Antypas C., Pantelis, Performance evaluation of a CyberKnife G4 image-guided robotic stereotactic radiosurgery system. *Phys Med Biol.*, 53(17) (2008) 4697-718.

[6] Acker G., Hashemi S. M., Fuellhase J., Kluge A., Conti A., Kufeld M., Kreimeier A., Loebel F., Kord M., Sladek D., Stromberger C., Budach V., Vajkoczy P., Senger C., Efficacy and safety of CyberKnife radiosurgery in elderly patients with brain metastases: a retrospective clinical evaluation. *Radiation Oncology*, 225(15) (2020) 1-10.

[7] Cao T., Dai Z., Ding Z.,- Li w., Quan H., Analysis of different evaluation indexes for prostate stereotactic body radiation therapy plans: conformity index, homogeneity index and gradient index. *Precision Radiation Oncology*, 3(3) (2019) 72-79.

[8] Kataria T., Sharma K., Subramani V., Karrthick K. P., Bisht S. S., Homogeneity Index: An objective tool for assessment of conformal radiation treatments*. J Med Phys.*, 37(4) (2012) 207-13.

[9] Paddick I., Lippitz B., A simple dose gradient measurement tool to complement the conformity index. *J. Neurosurg.*, 105 (2006) 194-201.

[10] Zhang S., Yang R. Shi C., Li J., Zhuang H., Tian S., Wang J., Noncoplanar VMAT for Brain Metastases: A Plan Quality and Delivery Efficiency Comparison with Coplanar VMAT, IMRT, and CyberKnife. *Technol Cancer Res Treat.*, 18 (2019) 1-8.

[11] Narayanasamy G., Stathakis S., Gutierrez A.N., Pappas E., Crownover R., Floyd JR 2nd., Papanikolaou N., A Systematic Analysis of 2 Monoisocentric Techniques for the Treatment of Multiple Brain Metastases. *Technol Cancer Res Treat*.,16(5) (2017) 639-644.

[12] Sio T.T., Jang S., Lee S.-W., Curran B., Pyakuryal A.P., Sternick, E.S., Comparing gamma knife and cyberknife in patients with brain metastases. *J Appl Clin Med Phys*., 15(1) (2014) 14-26.

[13] Yan L., Xu Y., Chen X., Xie X., Liang B., Dai J., A new homogeneity index definition for evaluation of radiotherapy plans. *J Appl Clin Med Phys*., 20(11) (2019) 50-56.

[14] Fares J., Cordero A., Kanojia D., Lesniak M.S., The Network of Cytokines in Brain Metastases. *Cancers.*, 13(1) (2021).

[15] Miller K.D., Nogueira L., Mariotto A.B., Rowland J.H., Yabroff K.R., Alfano C.M., Jemal A., Kramer J.L., Siegel R.L., Cancer treatment and survivorship statistics. *CA Cancer J Clin.*, 69(5) (2019) 363-385.

[16] Yoon M., Park S.Y., Shin D., Lee S.B., Pyo H.R., Kim D.Y., Cho, K.H., A new homogeneity index based on statistical analysis of the dose-volume histogram. *J Appl Clin Med Phys.,* 8(2) (2007) 9-17.

[17] Feuvret L., Noel G., Mazeron J. J., Bey P., Conformity index: a review. *Int J Radiat Oncol Biol Phys.*, 64(2) (2006) 333-421.

[18] Lomax N.J., Scheib S.G., Quantifying the degree of conformity in radiosurgery treatment planning. *Int J Radiat Oncol Biol Phys.*, 55(5) (2003) 1409-19.

[19] Yu X., Wang Y., Yuan Z., Yu H., Song Y., Zhao L., Wang P., Benefit of dosimetry distribution for patients with multiple brain metastases from non-small cell lung cancer by a Cyberknife stereotactic radiosurgery (SRS) system. *BMC Cancer.*, 20(1) (2020) 1144.

[20] Uzel E., CyberKnife Radyocerrahi sisteminde çoklu beyin metastazlarının tedavi planlamasının dozimetrik olarak iyileştirilmesi ve incelenmesi, Master thesis, Ankara Yıldırım Beyazıt University, Health Sciences Institute, (2019).

Cumhuriyet Sci. J., 44(2) (2023) 389-395
DOI: https://doi.org/10.17776/csj.1226987

Cumhuriyet Science Journal

| csj.cumhuriyet.edu.tr | Founded: 2002 ISSN: 2587-2680 e-ISSN: 2587-246X Publisher: Sivas Cumhuriyet University

Investigation of Thermal Quenching Effect for Lithium Fluoride (LiF) Type Dosimeters

Engin Aşlar [1,a,*]

[1] *Institute of Nuclear Sciences, Ankara University, 06100 Beşevler, Ankara, Türkiye.*
**Corresponding author*

Research Article

History
Received: 30/12/2022
Accepted: 10/06/2023

ABSTRACT

The thermal quenching effect was investigated for LiF:Mg,Ti (TLD-100), LiF:Mg,Cu,P (TLD-100H), ^{6}LiF:Mg,Ti(TLD-600) and ^{7}LiF:Mg,Ti (TLD-700) at two different doses (10, 1000mGy) using ^{90}Sr/^{90}Y beta source in this study. TLD-100, TLD-600 and TLD-700 showed different thermal quenching behavior according to dose values, while TLD-100H had the same characteristics for both doses. TLD-100, TLD-600, and TLD-700 showed thermal quenching based on the total area at 10mGy, while they did not show thermal quenching when ROI was used. All dosimeters were not affect thermal quenching at 1000mGy. In conclusion, it is recommended to use the lowest heating rate, to use the ROI, or to keep the same heating rate used in calibration and subsequent measurements at a low dose measurement (10mGy) for TLD-100, TLD-600, and TLD-700, while the desired heating rate can be used for high-dose measurement (1000mGy) for all LiF-type dosimeters.

Keywords: *Thermal quenching, LiF, Dosimetry, Thermoluminescence (TL), Heating rate.*

[a] *easlar@ankara.edu.tr* *https://orcid.org/0000-0002-1414-0317*

Introduction

The thermal quenching phenomenon is defined as the decrease in luminescence efficiency with an increasing measurement temperature [1-3]. The luminescence intensity decreases with increasing heating rates in the presence of thermal quenching. In such a case, the heating rate to be used in the measurements becomes important because measurements taken at high heating rates may lead to erroneous dose assessments. Therefore, thermal quenching studies are of great importance not only for candidate dosimetric materials but also for the dosimeters in luminescence dosimetry research. The existence of a thermal quenching effect can be identified by monitoring the TL glow curves obtained at different heating rates under the same amount of radiation exposure [4]. Thermal quenching can also be understood with the change in the OSL signal obtained at different reading temperatures and luminescence lifetime measurements [5-9].

Lithium fluoride (LiF) type dosimeters have been widely used for radiation dosimetry for many years. They are chemically very strong materials due to properties having their resistance to corrosion and wear, and difficulty dissolving in water [2]. As well as its chemical advantages, the effective atomic number of LiF dosimeters is accepted to be tissue equivalent (effective atomic number of 8.31 compared to 7.35-7.65 for tissue), thus the dosimeters have a low energy response [10]. The LiF:Mg,Ti (TLD-100) and LiF:Mg,Cu,P (TLD-100H) dosimeters are used mainly in personnel dosimetry applications, while ^{6}LiF:Mg,Ti(TLD-600) and ^{7}LiF:Mg,Ti (TLD-700) dosimeters are used frequently in mixed fields neutron-gamma measurements due to having different neutron cross sections [2].

The thermal quenching effect for LiF-type dosimeters has been investigated by various researchers. The thermal quenching was investigated for TLD-100 irradiated with 3.5Gy by Taylor and Lilley [11]. The peaks 2 to 5 does not show thermal quenching according to this study. Pradhan and Bhatt [12] studied the influence of three different heating rates (4.5, 10, and 33°C/s) on TLD-100 irradiated with 0.9Gy and 9Gy. The results showed that all the peaks were not affected by thermal quenching. According to another study for TLD-100 performed by Caprile et al. [13], the variation in the area of dosimetric peak (peak 5) was investigated for four heating rates (7,10,15 and 25°C/s) for the dose of 0.2, 2 and 20cGy. No significant change was observed attributable to thermal quenching, although a slight decrease in intensity was observed. In a recent study by Singh and Kainth [14], TL intensity for TLD-100 irradiated with 186cGy was investigated for heating rates between 2 and 50°C/s. It was reported that the TL intensity decreased with increasing heating rate, indicating that TLD-100 undergoes thermal quenching in this study. However, when the literature was reviewed, TLD-100 does not show thermal quenching in most studies. For TLD-100H, the thermal quenching effect was investigated by Pradhan [15] for a heating rate between 1 and 20°C/s. Thermal quenching was not observed for TLD-100H according to this study. In another study on TLD-100H performed by Luo et al. [16], TL intensity was not change for heating rates between 1 and 30°C/s, thus the dosimeters did not show a thermal quenching effect.

The thermal quenching effect has been investigated by several researchers for TLD-700 [15,17-18]. Pradhan [15] and [17] studied the influence of heating rates on various TLDs including TLD-700, for heating rates ranging from 1 to 50°C/s. The variation in the area value of the low dosimetric peak (200°C) and high temperature peak (270°C) of TLD-700 was investigated according to increasing heating rates. As a result, the area of the dosimetric peak does not change, while the area of the high-temperature peak is affected by variations in the heating rates. Therefore, thermal quenching was substantial for the high-temperature peak, while thermal quenching was not observed at the low dosimetric peak. On the other hand, it was seen that the thermal quenching studies were quite limited for TLD-600 when the literature was reviewed. A recent study performed by İflazoglu et al. [18] studied the thermal quenching for both TLD-600 and TLD-700 dosimeters. In this study, both dosimeters were irradiated with 15Gy and the variation in TL intensities was investigated considering the total area under the glow curve for heating rates ranging from 1 to 10°C/s. According to the results of this study, both dosimeters were affected by thermal quenching.

Generally, the thermal quenching studies for TLD-100 and TLD-100H were quite common in the literature, while it was quite limited for TLD-600 and TLD-700, especially TLD-600. Additionally, these studies were generally conducted on a single irradiation dose value and the heating rates used were either with relatively low heating rates (~10°C/s) or using several heating rates without a full sweep of the range used. The study aimed to investigate in detail the existence of thermal quenching effects over a wide heating rate range (1 to 50°C/s) for the TLD-100, TLD-100H, TLD-600, and TLD-700 dosimeters from the LiF family. Additionally, the behavior of the thermal quenching effect (10, 1000mGy) dosimeters will be investigated for all at two different doses (10, 1000mGy)..

Materials and Methods

Material

In this study, LiF:Mg,Ti (TLD-100), LiF:Mg,Cu,P (TLD-100H), ^{6}LiF:Mg,Ti (TLD-600) and ^{7}LiF:Mg,Ti (TLD-700) dosimeters purchased from Harshaw Chemical Company, U.S.A were used. Their dimensions were the same with of 3.2×3.2×0.9mm^3 in the chip form. The TLD-100 and TLD-100H consist of two elements of ^{6}Li (7.4%) and ^{7}Li (92.6%), respectively. On the other hand, TLD-600 and TLD-700 have ^{6}Li (95.6%) and ^{7}Li (4.4%) and ^{6}Li (0.1%) and ^{7}Li (99.9%), respectively. Dosimeters were irradiated using a ^{90}Sr/^{90}Y beta source with two doses at 10 and 1000mGy. TL measurements were performed with a Harshaw TLD-3500 reader controlled with the WinREMS program and consisted of a glass filter, a photomultiplier tube (PMT) and a heating element (planchet). A thermo theldo furnace was used for the annealing and preheat process of the dosimeters.

Calibration steps & TL measurements

Dosimeters were firstly subjected to the annealing process before starting the measurement. Annealing &preheat temperature and their duration times were given in Table 1 for each type of dosimeter. The preheat process was applied in the machine for TLD-100H, while it was applied in the oven for other dosimeters.

Table 1. Annealing and preheat temperature & time

Dosimeter Type	Annealing temperature & time	Preheat temperature & time
TLD-100H	**240°C+10min**	**135°C+10s**
TLD-100, TLD-600, TLD-700	400°C+1hour followed 100°C+2hour	100°C+10 min

The TL measurement protocol was presented in Table 2. The readout time in Table 2 was given according to 1°C/s. In other cases, the total readout time was determined according to the heating rate value.

Table 2. TL measurement protocol

Dosimeter Type	Measurement temperature (°C)	Readout time (s)
TLD-100H	240	11
TLD-100	350	300
TLD-600, TLD-700	400	350

Dosimeters were calibrated separately for both doses since there might be differences in the intensity values since two different dose values were studied. The element correction coefficient (ECC), which considers differences in the intensity between the dosimeters was obtained separately for two dose values (10 and 1000mGy) by Equation 1.

$$ECC_i = \frac{I_i}{I_{mean}} \quad (1)$$

where the I_i and I_{mean} were the luminescence intensity obtained from each dosimeter and the mean luminescence intensity obtained according to all dosimeters used, respectively. The final luminescence intensity (I_f) was determined by multiplying I_i and ECC_i values for both dose values. Calibration measurements were carried out at the lowest heating rate (1°C/s). Therefore, the measurement protocol for calibration was the same as given in Table 2.

Investigation of the thermal quenching effect

The thermal quenching effect was studied for varying heating rates (1, 2, 4, 6, 8, 10, 20, 40,and 50°C/s). For TLD-100H only, heating rates from 1 to 10 °C/s were used because higher heating rates require dosimeters to heat exceeding 240°C. The existence of thermal quenching was

determined by both the Region Of Interest (ROI) and total area value for TLD-100, TLD-600, and TLD-700 at a dose value of 10mGy. The ROI was obtained over three peaks in the dosimetric peak region, while the total area value was determined under the glow curve.

Results and Discussion

Variation in the TL glow curves

Figure 1a,b,c,d show the variation of the glow curves for TLD-100, TLD-100H, TLD-600 and TLD-700 obtained at different heating rates for the dose value of 10mGy. The maximum peak temperatures (Tmax) for TLD-100, TLD-100H, TLD-600 and TLD-700 at 1°C/s were obtained at ~205°C, ~201°C, ~204°C and ~205°C, respectively. The glow curves of all dosimeters shifted to the right, that is, the peaks were obtained at higher temperatures with increasing heating rate (1 to 50°C/s). The peak shapes in the glow curves did not change according to the increasing heating rate. The total variation in Tmax was obtained at ~106°C, ~102°C and ~101°C for TLD-100, TLD-600 and TLD-700, respectively when the heating rate increased from 1 to 50°C/s. As a result, the temperature shifts can be considered the same for all three dosimeters. On the other hand, the variation in Tmax for TLD-100H was ~39°C for heating rates between 1 and 10°C/s. Another observation was that an increase in luminescence intensity was observed in TLD-600 and TLD-700 after 350°C due to the predominance of blackbody radiation. This situation is related to due to the lower intensity of the peaks in the glow curve obtained at a lower dose (10mGy) for TLD-600 and TLD-700. As the irradiation dose value increased to 1000mGy, the peaks in the dosimetric region become more intense. Here, the increase seen after 350°C was not observed in the glow curve becoming a lower intensity, although it was still present.

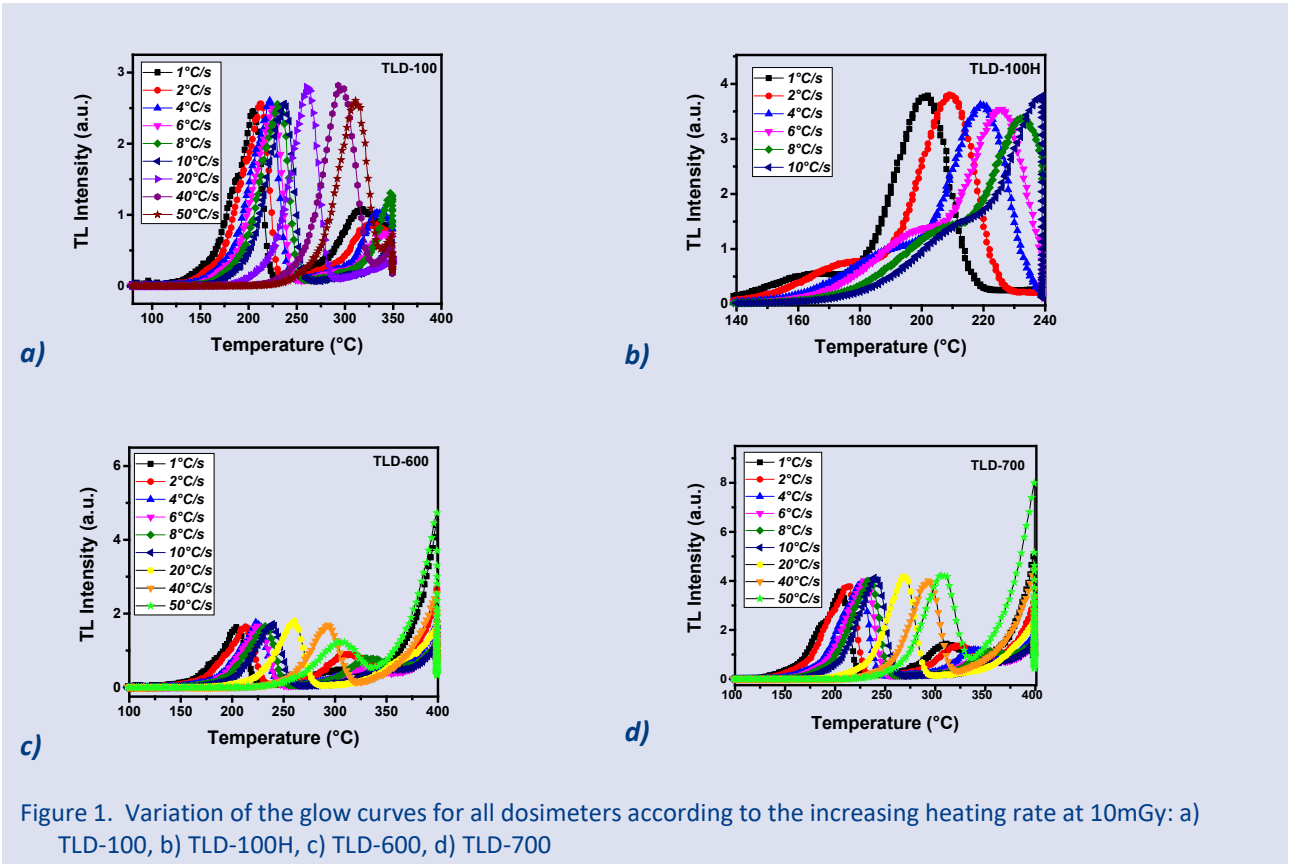

Figure 1. Variation of the glow curves for all dosimeters according to the increasing heating rate at 10mGy: a) TLD-100, b) TLD-100H, c) TLD-600, d) TLD-700

Figure 2a,b,c,d indicate the variation of the glow curves for TLD-100, 100H, TLD-600, and TLD-700 obtained at different heating rates for the dose value of 1000mGy. The Tmax of all dosimeters was around ~205°C. Therefore, the positions of the peaks did not change as the dose increased. Similar to Figure 1, the peaks shifted to higher temperatures as the heating rate increased for all dosimeters. The total variation in Tmax was observed ~110°C, ~108°C, ~102°C and ~37°C for TLD-100, TLD-600, TLD-700, and TLD-100H, respectively. Therefore, the temperature shifts in Tmax were unchanged compared to the dose value of 10mGy. Furthermore, the increase seen in high temperature for TLD-600 and TLD-700 in Figure 1c,d was not observed at high dose (1000mGy) in Figure 2c,d due to high luminescence intensity.

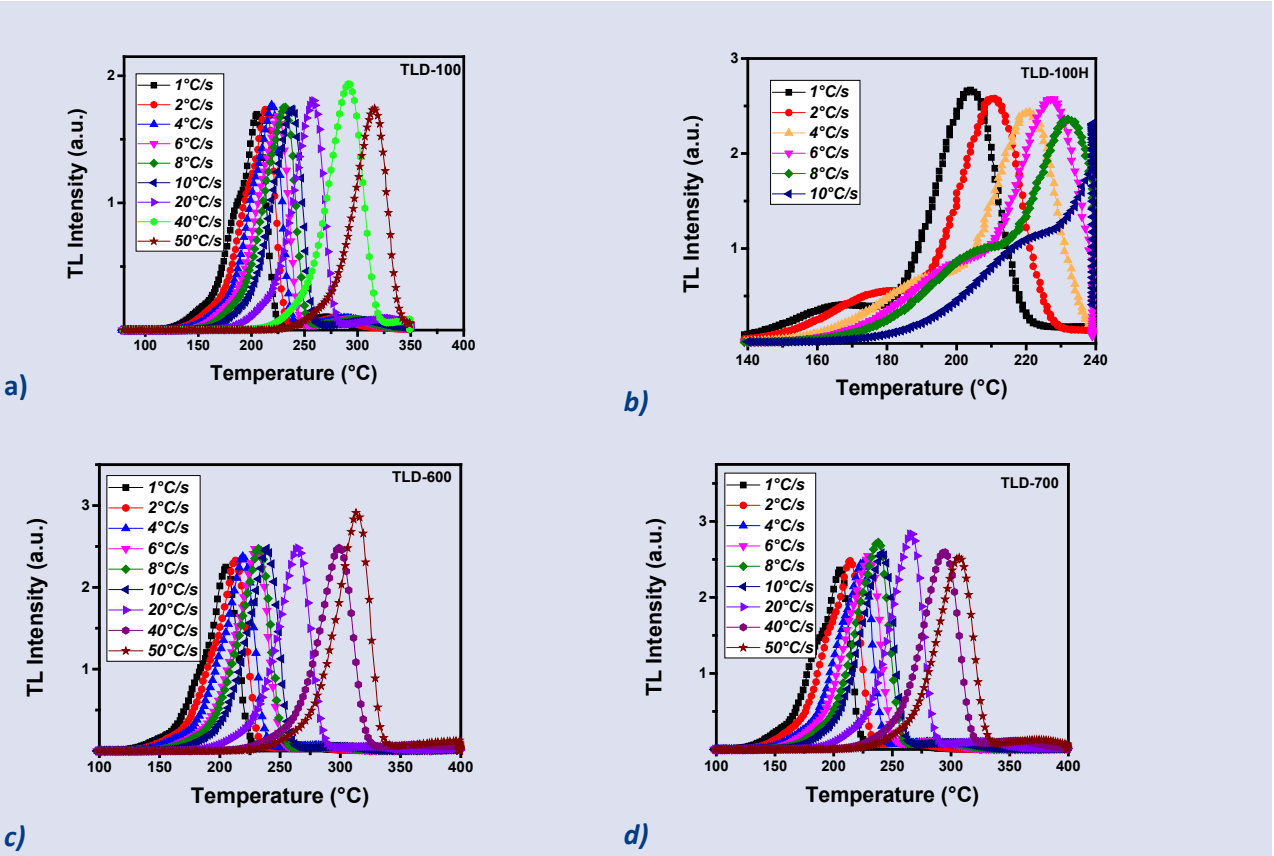

Figure 2. Variation of the glow curves for all dosimeters according to the increasing heating rate at 1000mGy: a) TLD-100, b) TLD-100H, c) TLD-600, d) TLD-700

Standard deviations in ECC values were also monitored for both dose values, taking into account the total area under the glow curve. Accordingly, the deviation in ECC values at 10mGy ranged between 10% and 15% for the TLD-100, TLD-600, and TLD-700, while it was <5% for TLD-100H. On the other hand, the deviation in ECC values obtained for 1000mGy was ~5% for each type of dosimeter. Therefore, the standard deviations in ECC values decreased significantly as the dose increased. These results showed the importance of selecting ROIs for TLD-100, TLD-600, and TLD-700 at 10mGy.

Thermal quenching results

Figure 3 indicates the variation in the area values obtained at different heating rates for all dosimeters at the 10mGy. In the figure, normalization was done according to the heating rate of 1°C/s. According to Figure 3a, TLD-100 shows thermal quenching considering the total area condition. The intensity obtained at 10°C/s showed a 30% reduction compared to 1°C/s. After 10°C/s, the area value behaved stable. Notable thermal quenching was observed in TLD-100 in the case of the total area condition. On the other hand, thermal quenching was not observed in TLD-100 when the ROI was used. As for TLD-100H, the total area value was around 1.00 for all heating rates used, thus thermal quenching was not observed (Figure 3b). According to Figure 3c,d, both TLD-600 and TLD-700 showed different behavior according to the total area and ROI similarly seen in TLD-100. Thermal quenching was observed for both dosimeters considering the total area, while thermal quenching was not seen when ROI was used. The intensity value obtained for TLD-600 at 10°C/s decreased by 35% according to 1°C/s, while no significant decrease was observed when considering the ROI. TLD-700 showed also similar behavior by showing a 35% reduction in the total area, again no thermal quenching was observed when ROI was used. On the other hand, a significant increase in intensity was observed for both TLD-600 and TLD-700 for heating rates of 40 and 50°C/s in the case of total area. This increase was thought to be due to the more pronounced increase in blackbody radiation with increasing heating rates in TLD-600 and TLD-700.

In conclusion, TLD-100, TLD-600, and TLD-700 have thermal quenching when considering the total area, while thermal quenching is not observed when ROI is used in the 10mGy. The reason for not seeing thermal quenching at 10mGy in the case of ROI could be related to dosimetric peak regions being more stable to changing heating rates than higher temperatures in the glow curve. In other words, higher peaks in TLD-100, TLD-600 and TLD-700 are more affected by thermal quenching. On the other hand, thermal quenching was not observed in TLD-100H.

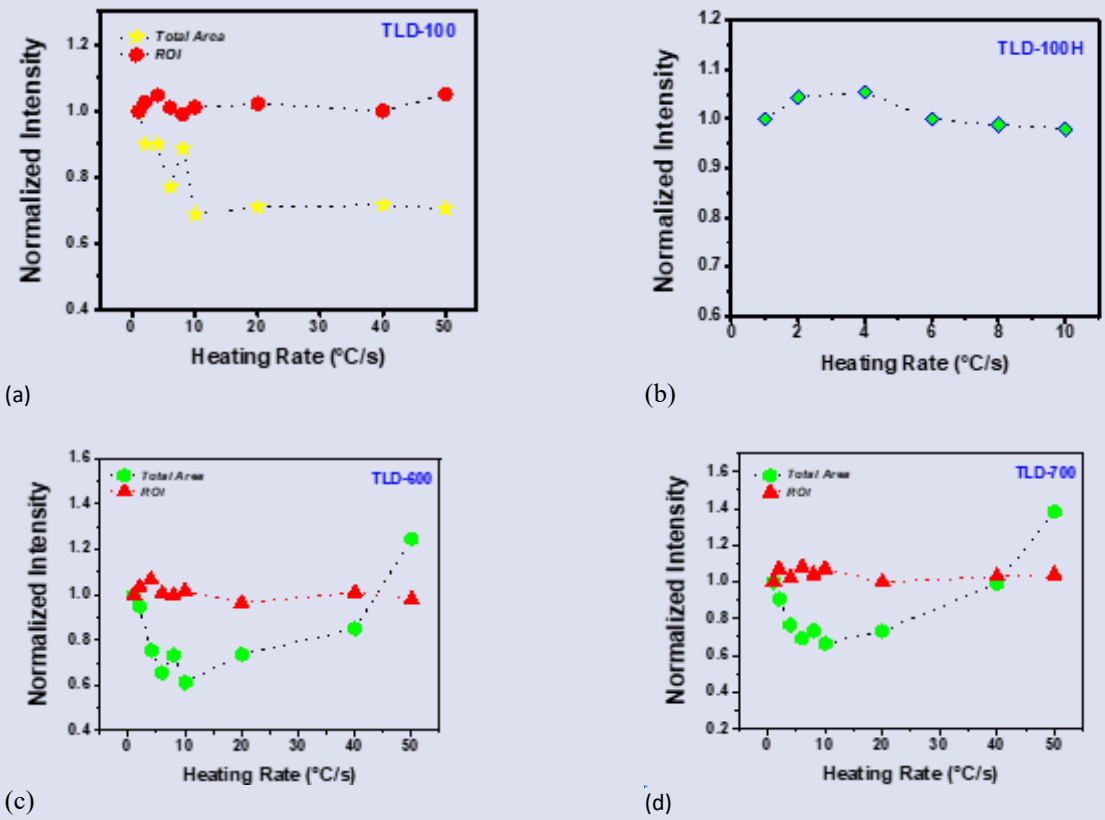

Figure 3. The variation of the area values according to the different heating rates for the 10mGy: a) TLD-100, b) TLD-100H, c) TLD-600, d) TLD-700.

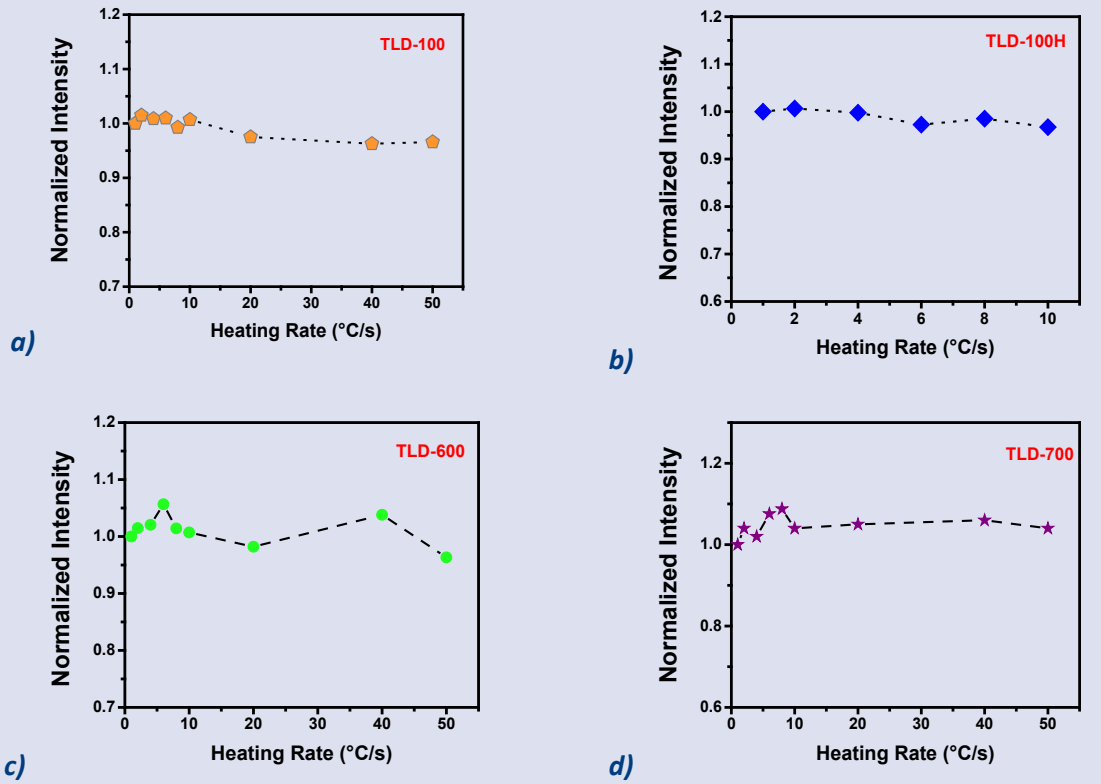

Figure 4. The variation of the area values obtained according to the different heating rates for the 1000mGy: a) TLD-100, b) TLD-100H, c) TLD-600, d) TLD-700.

Figure 4 shows the variation in the area values obtained at different heating rates of all dosimeters for 1000mGy. The normalization was performed according to 1°C/s. The area values varied from 0.95 to 1.00 for both TLD-100 and TLD-100H (Figure 4a,b). Although partial increases were observed in the initial heating rates for TLD-600 and TLD-700, the area values in general varied between 1.00 and 1.10 (Figure 4c,d). As a result, all dosimeters did not show thermal quenching effect at 1000mGy as opposed to 10mGy over the total area

Most thermal quenching studies for TLD-100 in the literature generally do not show thermal quenching for in the order of Gy [11-13]. In the study performed by Caprile et al. [13] in the order of mGy, the area of the peak did not change according to the heating rate, that there was no thermal quenching. Apart from this, there are rare studies reporting existence of thermal quenching in TLD-100 [14]. In our study, TLD-100 irradiated with 1000mGy did not show thermal quenching. Similarly, TLD-100 was not affected by thermal quenching at 10mGy when ROI was used. In this regard, the results obtained for TLD-100 were consistent with the literature of [11-13]. However, thermal quenching was observed only at the 10mGy when only the total area value was considered. The reason for thermal quenching observed in the total area condition at low dose is thought to be because the peaks after the dosimetric peak region are more affected by the increasing heating rates. TLD-100H was not shown thermal quenching for both 10 and 1000mGy. These results were compatible with studies of [15,16].

TLD-700 showed thermal quenching according to the studies of [15,17-18]. In our study, thermal quenching was observed only in the 10mGy over total area conditions for TLD-700. However, thermal quenching was not observed in both TLD-600 and TLD-700 at 1000mGy and using ROI. When the results obtained for TLD-600 and TLD-700 in our study are compared directly with the study of İflazoğlu et al. [18], thermal quenching was reported in İflazoğlu et al. [18], but no thermal quenching in our study in the order of Gy. As a conclusion, the findings obtained in the above mentioned studies [15,17-18] in the order of Gy do not seem compatible with those obtained in our study. The Tmax values for the main dosimetric peak for both TLD-600 and TLD-700 were reported at ~245°C for the heating rate of 1°C/s in these studies of [15,17-18]. However, Tmax values for the main dosimetric peak obtained in our study were obtained at ~205°C for both TLD-600 and TLD-700 for 1°C/s, which was almost same with that of TLD-100. The Tmax values were reported ~205°C for TLD-600 and TLD-700 by Oster et al. [19]. In another study, Tmax value was again ~205°C for TLD-600 by [20-21]. Therefore, the Tmax values obtained in our study for TLD-600 and TLD-700 were in agreement with the studies of [19-22]. The reason why thermal quenching is seen in the studies of [15,17-18] for TLD-600 and TLD-700, but not in our study may arise from previous use of the dosimeter depending on the thermal treatment, the readout process, irradiation and/or possible differences in the impurities during the production conditions. Therefore, these differences between the dosimeters could cause not only the change in the peak maximum temperatures but also change the behavior of the peaks under different heating rates by leading to the thermal quenching effect.

In a nutshell, TLD-100H did not show any change when considering the thermal quenching effect at low and high doses, while TLD-100, TLD-600, and TLD-700 showed differences according to the total area. This dose-related change may be related to the fact that thermal quenching is more effective at a low dose at high temperature peaks, and this effect decreases as the dose increases. In order to better understand this situation, additional experiments are required on subjects such as analyzing each peak in the glow curve doing deconvolution methods and investigating the effects of deep traps in dosimeters on the heating rates. According to the outcome of the study, it is recommended to use the lowest heating rate, to use the ROI, or to keep the same heating rate used in calibration and subsequent measurements for low dose measurement (10mGy). On the other hand, any heating rate can be preferred for high dose measurement (1000mGy) for all LiF-type dosimeters.

Conclusion

LiF-type dosimeters have been widely used for radiation dosimetry for many years. TLD-100 and TLD-100H are used mainly in personnel dosimetry, while TLD-600 and TLD-700 are preferred for the mixed fields neutron-gamma measurements. The decrease in intensity with increasing heating rate, namely thermal quenching, is of great importance for accurate dose evaluation. In this study, thermal quenching at two different dose values (10 and 1000mGy) was elaborately investigated for LiF-type dosimeters. Considering the total area values at a low dose (10mGy), thermal quenching was observed in all dosimeters except TLD-100H, whereas thermal quenching was not seen in any dosimeter at a high dose (1000mGy). According to the outcome of the study, it was recommended to use the lowest heating rate, to use the ROI, or to keep the same heating rate used in calibration and subsequent measurements for low-dose measurement (10mGy). On the other hand, all types of LiF dosimeters can be read with the desired heating rate at high-dose measurement (1000mGy), regardless of the total area and ROI.

Conflicts of interest

There are no conflicts of interest in this work.

References

[1] Bøtter-Jensen L., McKeever S.W.S., Wintle A.G., Optically stimulated luminescence dosimetry, Elsevier, (2003) 27-44.

[2] McKeever S.W.S., Thermoluminescence of solids, Cambridge University Press, (1985) 127-152.

[3] Akselrod M.S., Agersnap Larsen N., Whitley V., McKeever S.W.S., Thermal quenching of F-center luminescence in Al2O3:C, *J. Appl. Phys.,* 84(6) (1988) 3364-3373.

[4] Aşlar E., Meriç N., Şahiner E., Kitis G., Polymeris G. S., Calculation of thermal quenching parameters in BeO ceramics using solely TL measurements, *Radiat. Meas.*, 103 (2017) 13-25.

[5] Bulur E., Göksu H.Y., OSL from BeO ceramics: new observations from an old material, *Radiat. Meas.*, 29(6) (1998) 639-650.

[6] Chithambo M.L., The analysis of time-resolved optically stimulated luminescence: II. Computer simulations and experimental results, *J. Phys. D.,* 40(7) (2007) 1880-1889.

[7] Yukihara E.G., Luminescence properties of BeO optically stimulated luminescence (OSL) detectors, *Radiat. Meas.,* 46(6-7) (2011) 580-587.

[8] Bulur E., Saraç B.E., Time-resolved OSL studies on BeO ceramics, *Radiat. Meas.,* 59 (2013) 129-138.

[9] Altunal V., Guckan V., Ozdemir A., Sotelo A., Yegingil Z., Effect of sintering temperature on dosimetric properties of BeO ceramic pellets synthesized using precipitation method, *Nucl. Instrum. Methods Phys. Res. B,* 441 (2019) 46-55.

[10] Bos A.J.J., High sensitivity thermoluminescence dosimetry, *Nucl. Instrum. Methods Phys. Res. B*, 184(1-2) (2001) 3-28.

[11] Taylor G.C., Lilley E., The analysis of thermoluminescent glow peaks in LiF (TLD-100), *J. Phys. D*, 11(4) (1978) 567-581.

[12] Pradhan A.S., Bhatt R.C., Influence of heating rates on the response of TLD phosphors, *Int. J. Appl. Radiat. Isot.*, 30(8) (1979) 508-510.

[13] Caprile P.F., Sánchez-Nieto B., Pino A.M., Delgado J.F., Effects of heating rate and dose on trapping parameters of TLD-100 crystals, *Health Phys.*, 104(2) (2013) 218-223.

[14] Singh R., Kainth H.S., Effect of heating rate on thermoluminescence output of LiF:Mg,Ti (TLD-100) in dosimetric applications, *Nucl. Instrum. Methods Phys. Res. B,* 426 (2018) 22-29.

[15] Pradhan A.S., Influence of heating rate on the TL response of LiF TLD-700, LiF:Mg,Cu,P and Al_2O_3:C, *Radiat. Prot. Dosim.,* 58(3) (1995) 205-209.

[16] Luo L.Z., Velbeck K.J., Moscovitch M., Rotunda J.E. LiF:Mg,Cu,P glow curve shape dependence on heating rate. *Radiat. Prot. Dosim.*, 119(1-4) (2006) 184-190.

[17] Pradhan A.S., Thermal quenching and two peak method-influence of heating rates in TLDs, *Radiat. Prot. Dosim.*, 65(1-4) (1996) 73-78.

[18] İflazoğlu S., Kafadar V.E., Yazici B., Yazici A.N., Thermoluminescence kinetic parameters of TLD-600 and TLD-700 after 252Cf Neutron+ Gamma and 90Sr-90Y beta radiations, *Chin. Phys. Lett.*, 34(1) (2017) 017801.

[19] Oster L., Eliyahu I., Horowitz Y.S., Reshes G., Shapiro A., Garty G., Demonstration of the potential and difficulties of combined TL and OSL measurements of TLD-600 and TLD-700 for the determination of the dose components in complex neutron-gamma radiation fields, *Radiat. Prot. Dosim.*, 188(3) (2020) 383-388.

[20] Youssian D., Horowitz Y.S., Estimation of gamma dose in neutron dosimetry using peak 4 to peak 5 ratios in LiF: Mg,Ti (TLD-100/600), *Radiat. Prot. Dosim.*, 77(3) (1998) 151-158.

[21] Yasuda H., Fujitaka K., Non-linearity of the high temperature peak area ratio of 6LiF: Mg,Ti (TLD-600), *Radiat. Meas.*, 32(4) (2000) 355-360

Cumhuriyet Sci. J., 44(2) (2023) 396-402
DOI: https://doi.org/10.17776/csj.1242731

Cumhuriyet Science Journal

| csj.cumhuriyet.edu.tr | Founded: 2002 ISSN: 2587-2680 e-ISSN: 2587-246X Publisher: Sivas Cumhuriyet University

Influence of The Substrate-Target Angle and Sputter Temperature On The Properties of CIGS Thin Films Sputtered From Single Quaternary Target

Filiz Keleş [1,2,a,*], Furkan Güçlüer [2,3,b]

[1] *Department of Physics, Faculty of Arts and Sciences, Niğde Ömer Halisdemir University, Niğde, Türkiye.*
[2] *Nanotechnology Application and Research Center, Niğde Ömer Halisdemir University, Niğde, Türkiye.*
[3] *Department of Energy Science and Technologies, Niğde Ömer Halisdemir University, Niğde, Türkiye.*

**Corresponding author*

Research Article

History
Received: 31/01/2023
Accepted:06/04/2023

ABSTRACT

In this study, Copper Indium Gallium Selenide (CIGS) thin films were successfully sputtered from a single quaternary target onto soda lime glass substrates. The effect of the incident angle of target atoms and sputter temperature on the properties of the films were examined using various techniques. It was found that a higher incident angle of target atoms resulted in a columnar microstructure, while a lower angle produced a solid film. The columnar structure showed improved optical absorption compared to the solid film. The sputter temperature had a greater effect on the crystalline properties of the films, with all films except those sputtered at room temperature showing polycrystalline formation. The films displayed a chalcopyrite structure and acceptable band gaps in the range of 1.1-1.3 eV, regardless of the incident angle and sputter temperature. These results indicate that the optical properties of CIGS thin films can be improved by a small increase in the incident angle of target atoms, without adversely affecting the structural and crystalline properties.

Keywords: CIGS thin film, RF magnetron sputtering, Oblique angle, Substrate temperature, Columnar structure.

[a] *fkeles@ohu.edu.tr* *https://orcid.org/0000-0003-4548-489X* [b] *furkangucluer@hotmail.com* *https://orcid.org/0000-0002-8708-8994*

Introduction

Chalcopyrite Cu(In,Ga)Se_2 (CIGS) is one of the most preferable absorber layers in thin-film solar cells with high efficiencies due to its tunable bandgap (1.04 – 1.68 eV) [1], high absorption coefficient (~ 10^{15} cm^{-1}) [2] and high stability [3]. However, it is a challenging task to carry out a successful CIGS absorber layer deposition due to its quadruple component structure [4]. Three-stage co-evaporation process is the prominent method that is based on the simultaneous evaporation of multiple sources respectively at each stage [5, 6]. Although much progress has been made in fabrication of high-efficiency CIGS solar cell by this method [7], there are some drawbacks that limits its application in large scale devices. Since the evaporation of point sources of components (Cu, In, Ga, Se) is subjected, the CIGS film may not be uniformly coated. Besides, the difficulty of controlling the correct flux rates of the components usually results in the inhomogeneous elemental distribution through the CIGS. Another promising method for CIGS fabrication is the two-step process in which the metal precursors are sputtered followed by the post-selenization [8]. The Ga accumulation at the backside of CIGS thin film which is detrimental to the efficiency has usually been observed after the deposition of precursors. Therefore, the post-selenization process is offered as an inevitable solution [8, 9]. Although healing in the structural properties of CIGS could be achieved, the complexity and high-cost necessity of the post-selenization are the side effects. Besides, the chemical used for selenium supplement during post-selenization is hazardous for human health.

A more practical and effective way of deposition of CIGS absorber layer is the single-step sputtering by using a quaternary target [10-14]. Sputtering directly from a single target provides good uniformity of thin film and simplification of process by eliminating the post-selenization-which paves the way for mass production along with the reduced material cost [15-18]. Nevertheless, further improvements in structural, morphological, and optical properties CIGS absorber layers deposited by single-step sputtering would be beneficial via additional practical attempts. It has attracted our attention that there is not any related study on how the incident angle of target species according to the substrate normal affects the film properties although there are many reports about some other parameters such as post-annealing [19] and bandgap engineering [20].

In this study, we introduce the way of varying the properties of CIGS thin film at two different incoming angles of elements that compose the Cu(In,Ga)Se_2 thin film. As the details will be given in the experimental section, the morphology and thus the related properties have differed when the angle has changed to 60^0 from the existing incident angle of 40^0. Besides, the effect of the temperature has also been evaluated at these two

different angles. It was found that the incident angle of CIGS atoms is more effective on the morphology of the films while the structural and optical properties can be better properly controlled by the substrate temperature during the sputter.

Materials and Methods

The deposition of CIGS thin films was performed by one-step RF magnetron sputtering (Nanovak NVTS-400). Soda-lime glass (SLG) substrates with 25 mm x 25 mm x 1mm dimensions were ultrasonically cleaned sequentially in acetone for 5 minutes, isopropanol for 5 minutes, and distilled (DI) water for 10 minutes, followed by drying with N_2 gas. The clean glass substrates were placed onto the holder and transferred into the deposition chamber. 2-inch diameter and 0.25-inch-thick single quaternary $CuIn_{0.7}Ga_{0.3}Se_2$ target with 99.99% purity was preferred for sputtering. Prior to the sputtering process, the base pressure of the chamber was pumped down below 2 x 10^{-6} Torr. The working gas pressure of high-purity Argon (Ar) was set to the 8 mTorr equivalent to the 4.3 sccm flow rate. The sputtering was carried out at the power of 95 W and the substrate rotation of 8 rpm to provide the homogenous film formation during all depositions.

In our study, we mainly focused on how the CIGS films are affected under two different incident angles of the incoming target atoms. The film composed on the substrate surface may have a dense or porous microstructure based on whether the target atoms reach to the substrate directly or obliquely. The dense film is obtained in case of the low incident angles of the impinging target atoms with respect to the substrate normal because of the stacked layer-by-layer formation. On the other hand, the impinging atoms tend to form a porous film with columnar microstructure at highly oblique angles due to the cluster formation at the beginning of the deposition. When the angle of incidence is high, the incoming target atoms pile up and form randomly assembled islets on the film surface due to the phenomenon called the "shadowing effect" [21-23] which can be explained as the formerly clusters' shadowing the later atoms. These islets continue to grow and join each other during the sputtering process, and thus a porous, thin film that has a columnar type of microstructure is formed eventually. The approximate angle between target and substrate in our existing sputtering is 40^0 at which we can successfully deposit conventional thin films. We increased the angle to ~ 60^0 by simply raising the target holder little bit in the lateral position, as schematically described in Figure 1. Additionally, we investigated the effect of deposition temperature as well on the structural and optical properties of CIGS thin films grown at different angle configurations. As can be interpreted, the distance between the substrate and target would also change along with the varying angle. Therefore, we set the same thickness for all deposited films under various angles and temperatures in terms of performing a confident comparison. The same amount of deposited material because of setting the same thickness can be provided with the help of mass loading values using quartz crystal microbalance (QCM) [24]. The details of the CIGS thin films grown under different incident angles and temperatures are given in Table I.

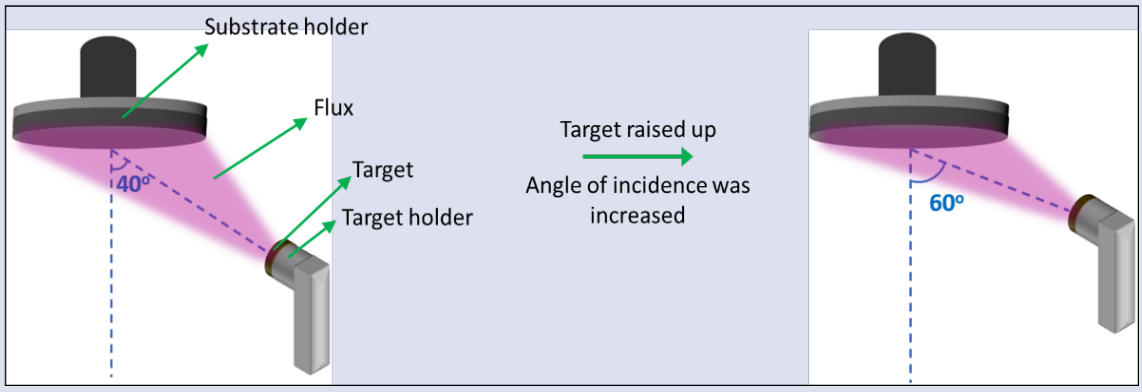

Figure 1. Schematic illustration of the 40^0 and 60^0 incident angle of target atoms towards substrate normal.

Table 1. The list of the CIGS thin films grown under various sputter parameters.

Sample Name	*Deposition Temperature (°C)*	*Incident Angle (Degrees)*
1	Room Temperature	40
2	150	40
3	300	40
4	Room Temperature	60
5	150	60
6	300	60

The morphological study of the CIGS thin films was conducted by Scanning Electron Microscope (SEM, FEI QUANTA FEG 250). The compositional properties were examined by Raman spectroscopy (Renishaw Raman-SPM/AFM) with the laser source at a wavelength of 633 nm. The crystallinity of the films was investigated by XRD Diffractometer (Malvern Panalitycal Empyrean) with Cu-Kα radiation (λ= 0.54 nm). The absorption measurements were carried out by UV-Vis-NIR (Jasco V-670) Spectrophotometer at a wavelength range of 400-2500 nm.

Results & Discussion

Cross-sectional SEM images of CIGS samples obtained under different incident angles of target atoms and deposition temperatures are shown in Figure 2. Columnar structure formation is apparent in thin films deposited at higher angle of 60^0 (Figure 1d-f) while relatively more planar and smooth thin films are formed in conventional configuration with an angle of 40^0 (Figure 2a-c). The main reason behind the difference in the microstructure formation is the shadowing effect [22] that becomes significant when the arriving atoms reach the substrate at higher oblique angles. In our case, the shadowing effect which results in columnar formation is observed at the angle of 60^0 since the target atoms have a more oblique trajectory towards the substrate. The incident angle of target atoms not only affects the microstructure but also changes the thickness of the films. The thickness of the samples grown at 40^0 and 60^0 (room temperature) is approximately 1.1 µm and 1.6 µm, respectively, as shown in Figure 2a and Figure 2d in which the difference is the most significant among all films. The difference in thicknesses can be attributed to the microstructure of the films. Since the mass loading values were set the same, the film with columnar formation would be longer compared to conventional thin film because of the gaps between the columns. Despite the difference in the morphology from the side-view, the surface of the films seems almost the same as concluded from the top-view SEM images (not shown).

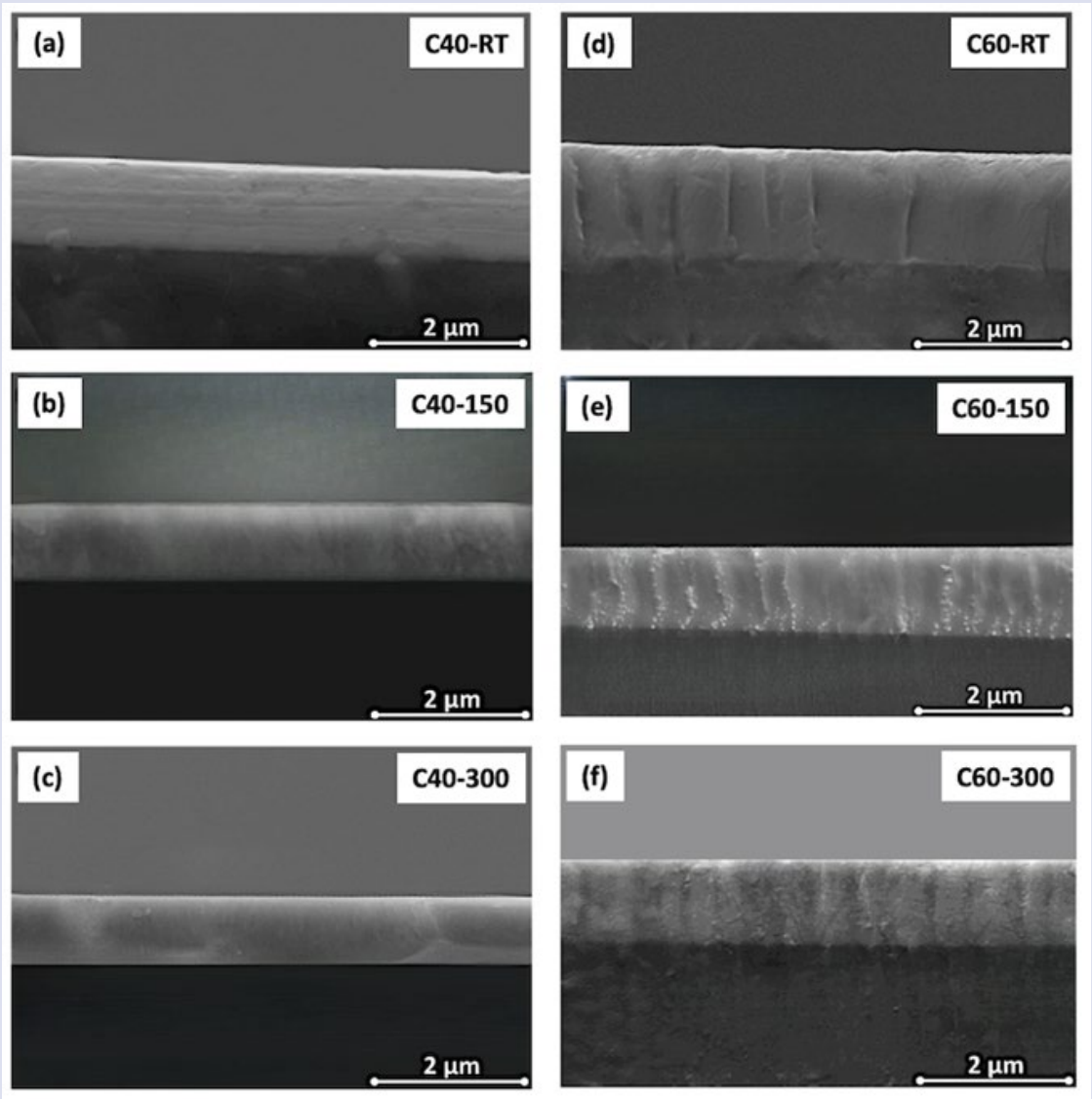

Figure 2. Cross-sectional SEM images of CIGS thin films grown under 40^0 of incident angle (a-c) and 60^0 of incident angle (d-f) at different substrate temperatures.

On the contrary, the temperature does not a have a significant effect on the morphology of the films. The thickness of the films slightly decreases at temperatures of 150^{0}C and 300^{0}C which is a well-known result from the literature [25].

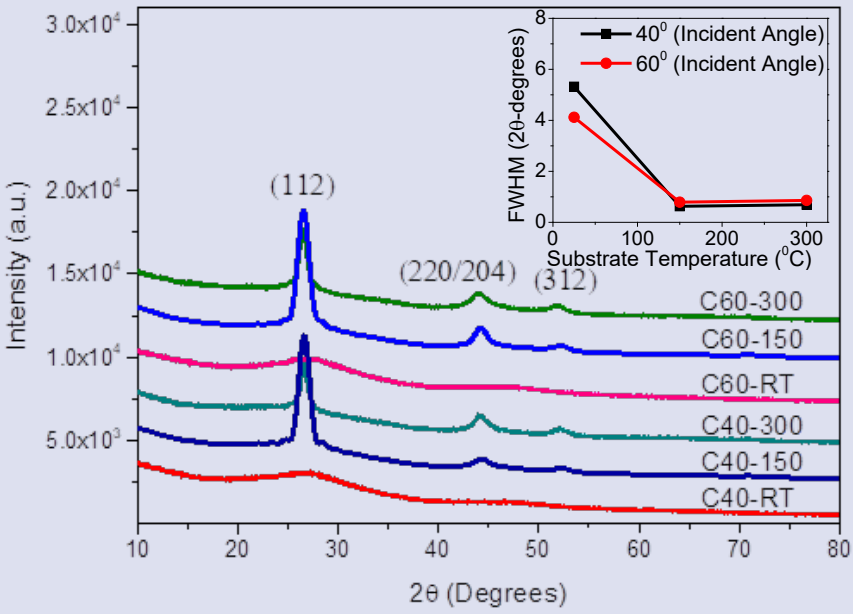

Figure 3. XRD patterns of CIGS thin films, the inset demonstrates the FWHM values of the main (112) XRD peaks belong to the CIGS films.

Figure 3 shows the XRD patterns of the samples deposited at different temperatures and the incident angle of target atoms. The most apparent fact concluded from the graph is that there is no obvious peak for the samples obtained at room temperature. While all the remaining films exhibit one strong and two weak peaks located at approximately 2-theta of 26, 44, and 52 degrees, which are correlated to the (112), (220/204), and (312) planes, respectively. It can be interpreted that the crystalline formation occurs only when the substrate temperature is applied during the sputtering process regardless of the incident angle. Indeed, the dramatic decrement in FWHM of the main peak of the films obtained even at low temperature is demonstrated in the inset of Figure 3. On the other hand, both incident angles of 40^0 and 60^0 have no significant effect on the crystalline properties. The XRD data verifies the polycrystalline structure of CIGS thin films in the form of the chalcopyrite phase [12, 13, 26]. Thus, the fact that the kinetic energy of target atoms provided by the applied temperature is the main parameter that affects the crystalline formation while the incoming trajectory of the atoms towards the substrate alters the morphology of the films without having any impact on the crystallinity.

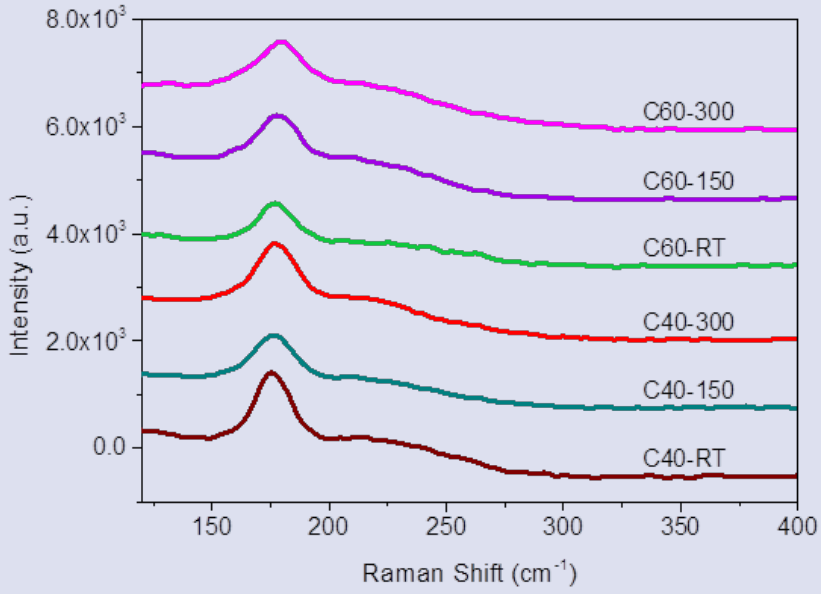

Figure 4. Raman spectra of CIGS thin films with different sputter parameters.

Raman spectra, a useful tool to investigate the chemical composition and phases of the films, are shown in Figure 4. All the films demonstrate a dominant peak located in the range of 174-179 cm^{-1} that can be correlated to the A_1 mode of the $A_IB_{III}C_2V_I$ chalcopyrite compounds [27-30]. Since there is only A_1 mode which is the most frequent and strong among all and no other obvious peak is observed in the spectra, it can be interpreted that all films obtained under different temperatures and substrate-target configurations exhibit the chalcopyrite formation. When it is recalled that the films grown at room temperature do not provide any prominent XRD peak while the A_1 Raman mode is obtained from the same samples, it can be safely stated that the films are in chalcopyrite phase with polycrystalline form regardless of the crystalline quality of the films. In addition, since no second phase peak is formed like Cu_2Se in the Raman spectrum curves, it can be said that a single-phase thin film structure was obtained [31]. FWHM values of A_1 mode of the Raman curves was also examined. Although FWHM of the films obtained from main peak, 174-179 cm^{-1}, do not differ significantly (in the range of 17-21 cm^{-1}), it was noticed that there is a slight broadening in FWHM of the samples for which temperature applied during growth. This finding may be attributed to the decay in phonon lifetime as a result of growth temperature [32].

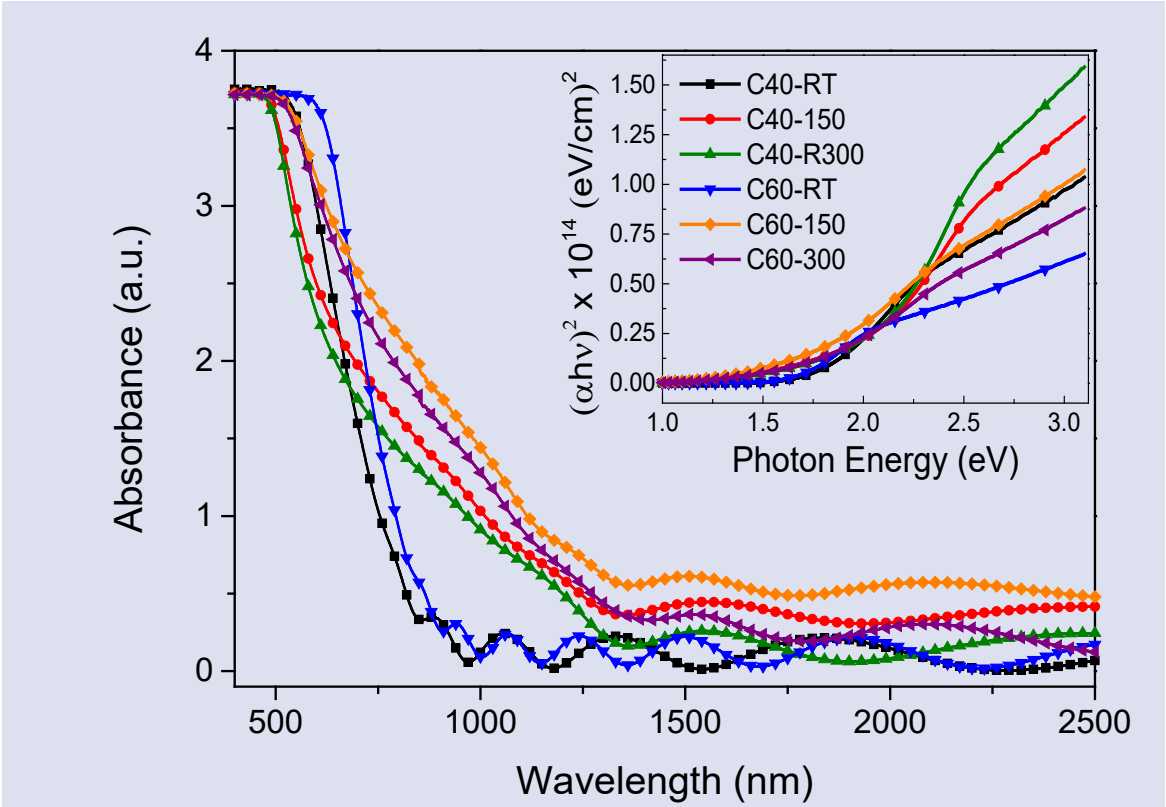

Figure 5. Absorbance spectra of CIGS thin films, the Tauc plot of the films are given in the inset graph.

The wavelength-dependent absorbance graph of the CIGS samples is demonstrated in Figure 5. The absorption enhancement in the near-infrared region (~700-2500 nm) for the samples grown with the temperature of 150^0C and 300^0C is the most remarkable observation at first glance. As compatible with the literature [33], the fact that crystallinity is improved even at low temperatures (150^0C) could be expressed as the main reason for the higher absorption. On the other hand, the slight increment in absorption for each film deposited with a higher incident angle of 60^0 compared to its counterpart film obtained with a lower angle of 40^0 is another important observation that should be evaluated. The absorption enhancement for the samples obtained at higher incident angle of 60^0 can be attributed to the columnar microstructure of the films (Figure 2), which may be attributed to the slight diminishing in bandgap. As the bandgap decreases, it is expected that there would be an increment in Urbach tail shown in absorbance spectra [34]. Since we only observe a slight increment in Urbach tail for the samples grown at higher angles, the above statement can be accepted for our case as making a true correlation between SEM images (Figure 2) and absorbance graph (Figure 5). Moreover, the ripple-like behavior at longer wavelength range for all samples regardless of temperature and incident angle is due to the thin film formation of the samples. The slightly higher thickness of the films grown at room temperature as shown in Figure 2 yields more ripples in longer wavelength range.

The optical bandgap of the films was estimated from Tauc's equation, $(\alpha h\nu)^2 = A.(h\nu - E_g)^{1/2}$ in the range of ~ 1.1-1.3 eV [34]. The inset in Figure 5 shows $(\alpha h\nu)^2$ graphs versus the frequency-dependent energy ($h\nu$),

where α is the absorption coefficient, h is Planck's constant, and ν is the frequency. The bandgap is extrapolated from the intersection of the line drawn through the linear part of the Tauc's plot with the x-axis (photon energy) [35]. Although there is not any significant trend in terms of the bandgap of the films, the bandgap increment by the temperature can be evaluated as the general interpretation from the inset graph. As the temperature increases, the thermal energy required for the deposited CIGS molecules to interact with each other is provided. Thus, more molecules interact, and the grain size is enhanced which results in the widening bandgap [37]. The slight enhancement in bandgap for the films sputtered under the incident angle of 60^0 compared to their counterparts can be attributed to the morphological and elemental differences which may result from their material densities [22].

Conclusion

In summary, we have conducted the sputtering of CIGS thin films from a single quaternary target under two different incident angles of target atoms and various substrate temperatures. The most significant observation is that the incident angle of target atoms is more effective on the microstructure formation and absorption while substrate temperature plays an important role in crystallinity. Regardless of the temperature, the columnar-like and solid films are obtained at 60^0 and 40^0 degrees of incident angle, respectively. On the other hand, the crystalline formation concluded from XRD data only shows up when the temperature is applied during sputtering. Indeed, the films obtained under both incident angles demonstrate better crystallinity even at low temperature of 150 ^{0}C. In addition, all films considered in this study have the chalcopyrite structure provided by Raman spectra. The slightly higher absorption of the films deposited with an angle of 60^0 compared to their counterparts is another significant conclusion. It was also observed that the bandgap values for all films obtained by Tauc's relation are close to each other and between 1.1-1.3 eV, although there is slight increment for the films when the temperature is applied during the growth. To sum up, we have revealed that the morphology and optical absorption of CIGS thin films can be improved by simply changing the substate-target configuration while the chalcopyrite formation and crystallinity of the films are ensured even at low substrate temperature. In this regard, it can be predicted that the optical properties of high-quality CIGS thin films can be further improved by accordingly tuning the substrate-target configuration.

Acknowledgements

The deposition and characterization of the CIGS thin films was carried out in Nanotechnology Application and Research Center at Nigde Ömer Halisdemir University. The authors would like to thank Selçuk University Physics Department for UV-Vis-NIR spectroscopy measurements.

Conflicts of interest

There are no conflicts of interest in this work.

References

[1] Dullweber T., Rau U., Contreras M. A., Noufi R., Schock H. W., Photogeneration and carrier recombination in graded gap Cu (In, Ga) Se/sub 2/solar cells, *IEEE Trans. Electron Devices*. 47 (2000) 2249–2254.

[2] Han S. H., Hermann A. M., Hasoon F. S., Al-Thani H. A., Levi D. H., Effect of Cu deficiency on the optical properties and electronic structure of CuInSe 2 and CuIn 0.8 Ga 0.2 Se 2 determined by spectroscopic ellipsometry, *Appl. Phys. Lett.* 85 (2004) 576–578.

[3] Huang Y., Tang Y., Yuan W., Wang Q., Zhang S., Influence of surface-modified Mo back contact on post-selenized Cu (In, Ga) Se2 thin films, *Mater. Sci. Semicond. Process.* 57 (2017) 227–232.

[4] Ramanujam J., Singh U. P., Copper indium gallium selenide based solar cells–a review, *Energy Environ. Sci.* 10 (2017) 1306–1319.

[5] Yin L., Zhang K., Luo H., Cheng G., Ma X., Xiong Z., Xiao X., Highly efficient graphene-based Cu (In, Ga) Se 2 solar cells with large active area, *Nanoscale.* 6 (2014) 10879–10886.

[6] Jung S., Ahn S. J., Yun J. H., Gwak J., Kim D., Yoon K., Effects of Ga contents on properties of CIGS thin films and solar cells fabricated by co-evaporation technique, *Curr. Appl. Phys.* 10 (2010) 990–996.

[7] Jackson P., Hariskos D., Wuerz R., Kiowski O., Bauer A., Friedlmeier T. M., Powalla M., Properties of Cu (In, Ga) Se2 solar cells with new record efficiencies up to 21.7%, *Phys. Status Solidi (RRL)–Rapid Res. Lett.* 9 (2015) 28–31.

[8] Huang P. C., Sung C. C., Chen J. H., Hsiao R. C., Hsu C. Y., Effect of selenization and sulfurization on the structure and performance of CIGS solar cell, *J. Mater. Sci. Mater. Electron.* 29 (2018) 1444–1450.

[9] Liang H., Avachat U., Liu W., Van Duren J., Le M., CIGS formation by high temperature selenization of metal precursors in H2Se atmosphere, *Solid. State. Electron.* 76 (2012) 95–100.

[10] Chen C. H., Lin T. Y., Hsu C. H., Wei S. Y., Lai C. H., Comprehensive characterization of Cu-rich Cu (In, Ga) Se2 absorbers prepared by one-step sputtering process, *Thin Solid Films.* 535 (2013) 122–126.

[11] Ouyang L., Zhao M., Zhuang D., Han J., Gao Z., Guo L., Li X., Sun R., Cao M., Annealing treatment of Cu (In, Ga) Se2 absorbers prepared by sputtering a quaternary target for 13.5% conversion efficiency device, *Sol. Energy.* 118 (2015) 375–383.

[12] Wang Q., Zhao Z., Li H., Zhuang J., Ma Z., Yang Y., Zhang L., Zhang Y., One-step RF magnetron sputtering method for preparing Cu (In, Ga) Se2 solar cells, *J. Mater. Sci. Mater.* Electron. 29 (2018) 11755–11762.

[13] Yan Y., Li S., Ou Y., Ji Y., Yan C., Liu L., Yu Z., Zhao Y., Structure and properties of CIGS films based on one-stage RF-sputtering process at low substrate temperature, *J. Mod. Transp.* 22 (2014) 37–44.

[14] Zhang L., Yu Y., Yu J., Wei Y., Effects of annealing atmosphere on the performance of Cu (InGa) Se2 films sputtered from quaternary targets, *R. Soc. Open Sci.* 7 (2020) 200662.

[15] Chen C. H., Shih W. C., Chien C. Y., Hsu C. H., Wu Y. H., Lai C. H., A promising sputtering route for one-step fabrication of chalcopyrite phase Cu (In, Ga) Se2 absorbers without extra Se supply, *Sol. Energy Mater. Sol. Cells.* 103 (2012) 25–29.

[16] Wang Y. H., Ho P. H., Huang W. C., Tu L. H., Chang H. F., Cai C. H., Lai C. H., Engineering a Ga-Gradient by One-Step Sputtering to Achieve Over 15% Efficiency of Cu (In, Ga) Se2 Flexible Solar Cells without Post-selenization, *ACS Appl. Mater. Interfaces.* 12 (2020) 28320–28328.

[17] Frantz J, A., Bekele R. Y., Nguyen V. Q., Sanghera J. S., Bruce A., Frolov S. V., Cyrus M., Aggarwal I. D., Cu (In, Ga) Se2 thin films and devices sputtered from a single target without additional selenization, *Thin Solid Films.* 519 (2011) 7763–7765.

[18] Lin T. Y., Lai C.H., Grading G., CIGS solar cell by one-step sputtering from a quaternary target without post-selenization, *in: 2015 IEEE 42nd Photovolt. Spec. Conf., IEEE, 2015:* pp. 1–4.

[19] Chen J., Shen H., Zhai Z., Li J., Wang W., Shang H., Li Y., Effect of substrate temperature and post-annealing on the properties of CIGS thin films deposited using e-beam evaporation, *J. Phys. D. Appl. Phys.* 49 (2016) 495601.

[20] Yan L., Bai Y., Yang B., Chen N., Tan Z., Hayat T., Alsaedi A., Extending absorption of near-infrared wavelength range for high efficiency CIGS solar cell via adjusting energy band, *Curr. Appl. Phys.* 18 (2018) 484–490.

[21] Keles F., Cansizoglu H., Badraddin E. O., Brozak M. P., Watanabe F., Karabacak T., HIPS-GLAD core shell nanorod array photodetectors with enhanced photocurrent and reduced dark current, *Mater. Res. Express.* 3 (2016) 105028.

[22] Keles F., Badradeen E., Karabacak T., Self-anti-reflective density-modulated thin films by HIPS technique, *Nanotechnology.* 28 (2017) 335703.

[23] Badradeen E., Brozak M, Keles F., Al-Mayalee K., Karabacak T., High performance flexible copper indium gallium selenide core–shell nanorod array photodetectors, *J. Vac. Sci. Technol. A Vacuum, Surfaces, Film.* 35 (2017) 03E112.

[24] Nakano T., Baba S., Gas pressure effects on thickness uniformity and circumvented deposition during sputter deposition process, *Vacuum.* 80 (2006) 647–649.

[25] Liu G. S., Li H. N., Shen X. Y., Hu Z. Q., Hao H. S., Effect of Substrate Temperature on One-Step Magnetron-Sputtered Cu (In, Ga) Se2 Thin Films for Solar Cells, *in: Appl. Mech. Mater., Trans Tech Publ, 2013:* pp. 703–707.

[26] Zhang H. X., Hong R. J., CIGS absorbing layers prepared by RF magnetron sputtering from a single quaternary target, *Ceram. Int.* 42 (2016) 14543–14547.

[27] Witte W., Kniese R., Powalla M., Raman investigations of Cu (In, Ga) Se2 thin films with various copper contents, *Thin Solid Films.* 517 (2008) 867–869.

[28] Roy S., Guha P., Kundu S. N., Hanzawa H., Chaudhuri S., Pal A. K., Characterization of Cu (In, Ga) Se2 films by Raman scattering, *Mater. Chem. Phys.* 73 (2002) 24–30.

[29] Huang X., Miao X., Yu N., Guan X., Effects of deposition profiles on RF-sputtered Cu (In, Ga)Se 2 films at low substrate temperature, *Appl. Surf. Sci.* 287 (2013) 257–262.

[30] Shi J. H., Li Z. Q., Zhang D. W., Liu Q. Q., Sun Z., Huang S. M., Fabrication of Cu (In, Ga) Se2 thin films by sputtering from a single quaternary chalcogenide target, *Prog. Photovoltaics Res. Appl.* 19 (2011) 160–164.

[31] Nagaoka A., Nose Y., Miyake H., Scarpulla M. A., Yoshino K., (2015). Solution growth of chalcopyrite compounds single crystal. Renewable Energy, 79, 127-130.

[32] Ruiz C. M., Fontané X., Fairbrother A., Izquierdo-Roca V., Broussillou C., Bodnar Bermudez V. (2012, June). Developing Raman scattering as quality control technique: Correlation with presence of electronic defects in CIGS-based devices. In 2012 38th IEEE Photovoltaic Specialists Conference (pp. 000455-000458). IEEE.

[33] Yu Z., Yan Y., Li S., Zhang Y., Yan C., Liu L., Zhang Y., Zhao Y., Significant effect of substrate temperature on the phase structure, optical and electrical properties of RF sputtered CIGS films, *Appl. Surf. Sci.* 264 (2013) 197–201.

[34] Dhanaraj A., Das K., Keller J. M., A Study of The Optical Band Gap Energy and Urbach Energy of Fullerene (C60) Doped PMMA Nanocomposites, AIP Conference Proceedings. 2270 (2020) 110040.

[35] Mankoshi M. A. K., Mustafa F. I., Hintaw N. J., Effects of Annealing Temperature on Structural and Optical Properties of CIGS Thin Films for Using in Solar Cell Applications, *in: J. Phys. Conf. Ser., IOP Publishing, 2018:* p. 12019.

[36] Chandramohan M., Velumani S., Venkatachalam T., Experimental and theoretical investigations of structural and optical properties of CIGS thin films, *Mater. Sci. Eng. B.* 174 (2010) 205–208.

[37] Wang H., Zhang Y., Kou X. L., Cai Y. A., Liu W., Yu T., Pang J. B., Li C. J., Sun Y., Effect of substrate temperature on the structural and electrical properties of CIGS films based on the one-stage co-evaporation process, *Semicond. Sci. Technol.* 25 (2010) 55007.

Cumhuriyet Sci. J., 44(2) (2023) 403-410
DOI: https://doi.org/10.17776/csj.1241984

Cumhuriyet Science Journal

| csj.cumhuriyet.edu.tr | Founded: 2002 ISSN: 2587-2680 e-ISSN: 2587-246X Publisher: Sivas Cumhuriyet University

Amazonite in Pakistan: A Comprehensive Study with XRD, XPS, SEM and PL Analyses

Eren Cihan Karsu Asal [1,a,*]

[1] *Department of Electric and Energy Technologies, Manisa Celal Bayar University, 45400 Turgutlu Manisa, Türkiye.*
**Corresponding author*

Research Article

History
Received: 25/01/2023
Accepted: 04/04/2023

ABSTRACT

Although amazonite minerals from various locations have been studied before rather less attention has been paid to the amazonite mineral from Pakistan. The present work is presented an extensive structural characterization of natural amazonite aliquots (KAlSi3O8) from Tangir Valley, Gilgit-Pakistan. The phase and elemental analysis have been characterized by both X-ray Diffraction (XRD) and X-ray Photoelectron Spectroscopy (XPS), respectively. The surface morphology and particle size have been identified by Scanning Electron Microscopy (SEM). The luminescence properties have been investigated using PhotoLuminescence (PL). In addition, the lifetime of the PL emission measurements has been estimated.

Eventually, this microcline has a triclinic phase, mainly composed of $(AlO_4)^{-5}$ ions, SiO_2, metal SiO_4, Al_2O_3 and oxygen originating from impurities. The average particle size is around 1–10 µm with a complex structure. The PL spectrum has broad emission and excitation bands (520 nm and 340 mm respectively). The average lifetime of the PL emission is 265,21 µs. For the accuracy of the results all experiments were performed with not only a single aliquot, but with three aliquots, and representative results are presented.

Keywords: *Photoluminescence, Amazonite, Characterization.*

[a] *eren.karsu@cbu.edu.tr* *https://orcid.org/0000-0001-6392-2668*

Introduction

The importance of the crystalline phase, in both the analysis of various emission characteristics and lattice parameters is a well-known subject. Furthermore, any aspect of the luminescence phenomena, (e.g., lifetime, effectiveness, emission spectra) is known to be dependent on the crystalline phase which is primarily brought about by pressure and/or temperature. Minor changes in the lattice structure caused by inclusions, impurities, substituted ions, or surface defects in ppm concentrations display changes in the intensity and wavelength location of the emission spectra [1].

Recently there has been a grooving interest in microcline, a variety of potassium-rich alkali felspar. One of these, Amazonite, has blue green color because of its structure of one aluminum and three silicon ions ($KAlSi_3O_8$). The silicone and aluminum ions occupy the centers of interlinked tetrahedrons of SiO_4 and AlO_4 compounds. These tetrahedrons are connected at each corner to other tetrahedrons forming an intricate three-dimensional negatively charged framework [2]. While the simple form of this microcline has been reported as a monoclinic crystal, the triclinic form of this mineral is also observed [3].

Given the lack of attention paid to the amazonite mineral from Tangir Valley, Gilgit-Pakistan, the current study intends to achieve the following primary contributions, which are summarized as follows:

- This, in my opinion, is the first time an amazonite mineral from the Talgir Valley in Gilgit, Pakistan, has been thoroughly examined.
- This will be a thorough evaluation that includes all phase-elemental studies, surface morphology, particle size, and luminescence properties.
- The decay character of PL emission was measured, and the emission and excitation spectrums were studied.
- Each experiment used not only one aliquot but three aliquots to ensure the accuracy of the data.

Materials and Methods

1. Sample Details and Preparation

The materials employed in the current study were natural aliquots of Amazonite crystal that were from Tangir Valley, Gilgit-Pakistan. Three aliquots of a single crystal that had been crushed in an agate mortar to a weight of 5.0±0.1 mg were utilized in each research, and representative findings were presented.

2. Apparatus and Measurement Conditions

i.Characterization:

An overlook of characterization was performed. In addition to both phase and elemental analysis by X-Ray Diffraction (XRD) and X-Ray Photoelectron Spectroscopy (XPS) technique, Scanning Electron Microscopy (SEM) patterns were also obtained to observe the particle morphology of the aliquots.

- XRD Technique:

The crystal structures and phase analysis of the natural amazonite were carried out at room temperature (RT) by using the Panalytical Emperian X-ray diffractometer with a Cu-K_α radiation source (λ=1,5406 Å). The system was operated at 45 kV voltage and 40 mA current.

For the qualitative test, XRD patterns were recorded at a speed of 2,00°/min in the interval of 10°–80° (2θ). The step size was 0,02° and the interaction time was 0,6 seconds. The detector type was fixed slits. The scanning mode was continuous. Formation parameters were obtained from Rietveld refinement through the 2.71 version of the Maud program. The outcomes were tested with those of the ICSD 98-001-6597 df card (Figure 1. and Table 1). [4]

- XPS Technique:

The excellent spatial resolution of XPS examinations allowed the sensitive detection of the contents of the amazonite mineral and prevented contaminations that might be caused by tiny inclusions. As a result, the XPS analyses' conclusions have turned out to be far more reliable than those of the other techniques. For these reasons, the XPS technique was used to characterize the data about the materials' elements and chemical states.

In the system, called Thermo-Scientific, a monochromatic Al-Kα (1486.7 eV) X-ray source and a beam size of 400 nm diameter were used. The calibration was performed concerning gold; 4f7/2. While spectral data acquisition, the pressure was held under 5×10^{-10} mbar. The scanning was performed in the range between −10 and 1350 eV. For high-resolution elemental scanning, the pass energy was 30 eV. 20 scans from a single point were recorded. By using the curve fitting method via Thermo Avantage V5.65 programs both the binding energies and the deconvolution of the spectra were achieved (Figure 2 and Table 2) [4].

- SEM Patterns:

The surface morphology was estimated by SEM patterns (Figure 3). Utilizing an electron microscope (COXEM EM-30+) and high potential (30 kV) accelerating, the microstructures of the particles were evaluated. Similar to the study of Gliozo et al., the samples were carbon coated and mounted directly on sample holders. No surface polishing was performed [5].

ii. Optical Properties:

PL technique was used to investigate the optical properties. The PL studies were utilized at Time-Correlated Single Photon Counting (TCSPC). The decay period was also measured during PL experiments in addition to the emission and excitation spectra. A 15W xenon lamp was used. During tests, to obtain the Instrument Response Function (IRF), a non-fluorescing mixture of silica aerogel (LU-DOX 30%, Sigma Aldrich) in water was used. Before decaying, 24 hrs the mineral was held inside the device in the darkness. The decay character was then immediately set. Excitation with the xenon lamp was performed for 1 minute during the readout, and the parameters were obtained using repeated convolution and a weighted, nonlinear least squares method. The reduced chi-square test was applied to correctly fit the calculated and measured decay curves [4].

Results

1. Phase analyses:

The phase purity and crystallinity of amazonite were examined by the XRD technique. The XRD pattern of the natural amazonite is shown in Figure 1 The reference XRD pattern is also stated for comparison in the figure.

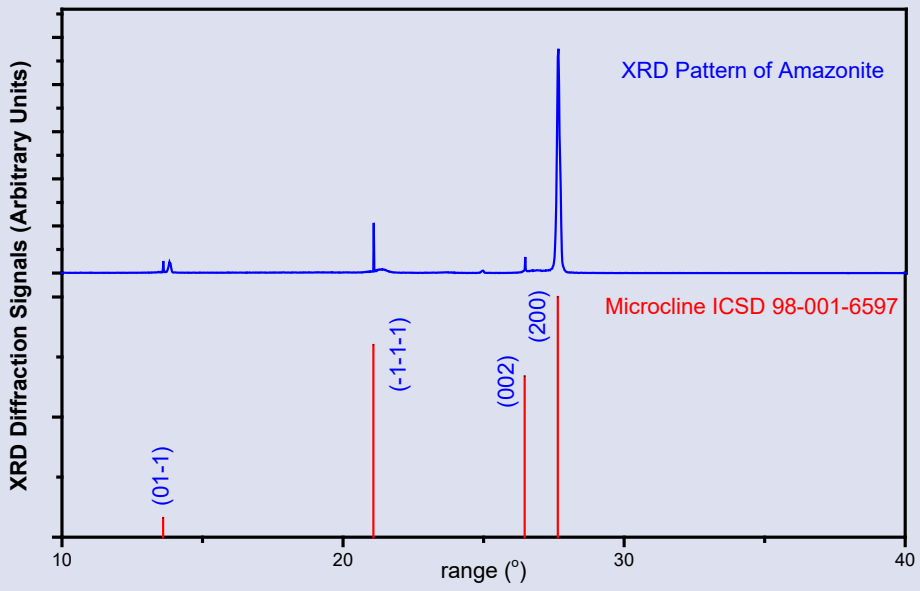

Figure 1. The basal latencies of rats before and after operation (paired student t-test, *p<0.05)

By comparing the XRD peaks with The Joint Committee on Powder Diffraction Standards (JCPDS) file, the peaks were indexed by International Centre for Diffraction Data (ICSD) and matches precisely with standard data ICSD 98-001-6597. The diffraction peaks of the amazonite are well indexed to a triclinic phase structure of amazonite (Figure 1) [6]. Structural and lattice parameters of amazonite were calculated with the Rietveld refinement using the Maud 2.71 V software. The results obtained from the patterns are indicated in Table 1 Here, it was discovered that the structural parameters a and c were quite tight to one another (8,59 and 7,22 Å respectively).

Table 1. The results of XRD patterns of the amazonite sample:

Mineral		Crystal System	Unit Cell Parameters					
Name	**Formula**		**a(Å)**	**b(Å)**	**c(Å)**	**α(°)**	**β(°)**	**γ(°)**
Microcline (amazonite)	$KAlSi_3O_8$	Triclinic	8,59	12,97	7,22	90,6	116	87,8

2. Elemental analysis:

The valence states, chemical nature and oxidation of numerous elements in the natural amazonite aliquots were characterized using XPS, as marked in Figure 2. It is a representation of the findings from the analysis and high-resolution elemental detects of the aliquot. Table 2 presents specifically the binding energies of the present elements and the weight ratios of the analyses. The observed C1s is taken as an impurity of the system. The peaks at 284 and 286 eV belong to C-C and C-O bonding respectively. These peaks were observed because of the hydrocarbon at the medium where the XPS measurements were performed. Moreover, Na1s was peeked, but with a trace amount, only 0,88%. Figure 2(a) remarks on the regular scanning of the aliquot. 531.03 eV for O1s, 102.89 eV for Si2p, 293.53 eV for K2p, and 74.71 eV for Al2p are revealed for the mineral. Figure 2(b)-(e) represents just the detailly scanning of each large amount element. Figure 2(b) shows the peaks of Al-O bonds (~74-75 eV) originating from $(AlO_4)^{-5}$ ions. In Figure 2(c), Si2p oxidation state is represented by two peaks, these originating from SiO_2 and metal SiO_4 (102,5-1.3,5 eV). K2p deconvolution with three elemental peaks (~292,5-293,5-296 eV) is given in Figure 2(d), and Figure 2(e) marks the high-resolution deconvoluted peak of O1s. Three peaks were observed at around 529,5-531-532 eV which are belongs to SiO_2, Al_2O_3, and organic oxygen originating from impurities.

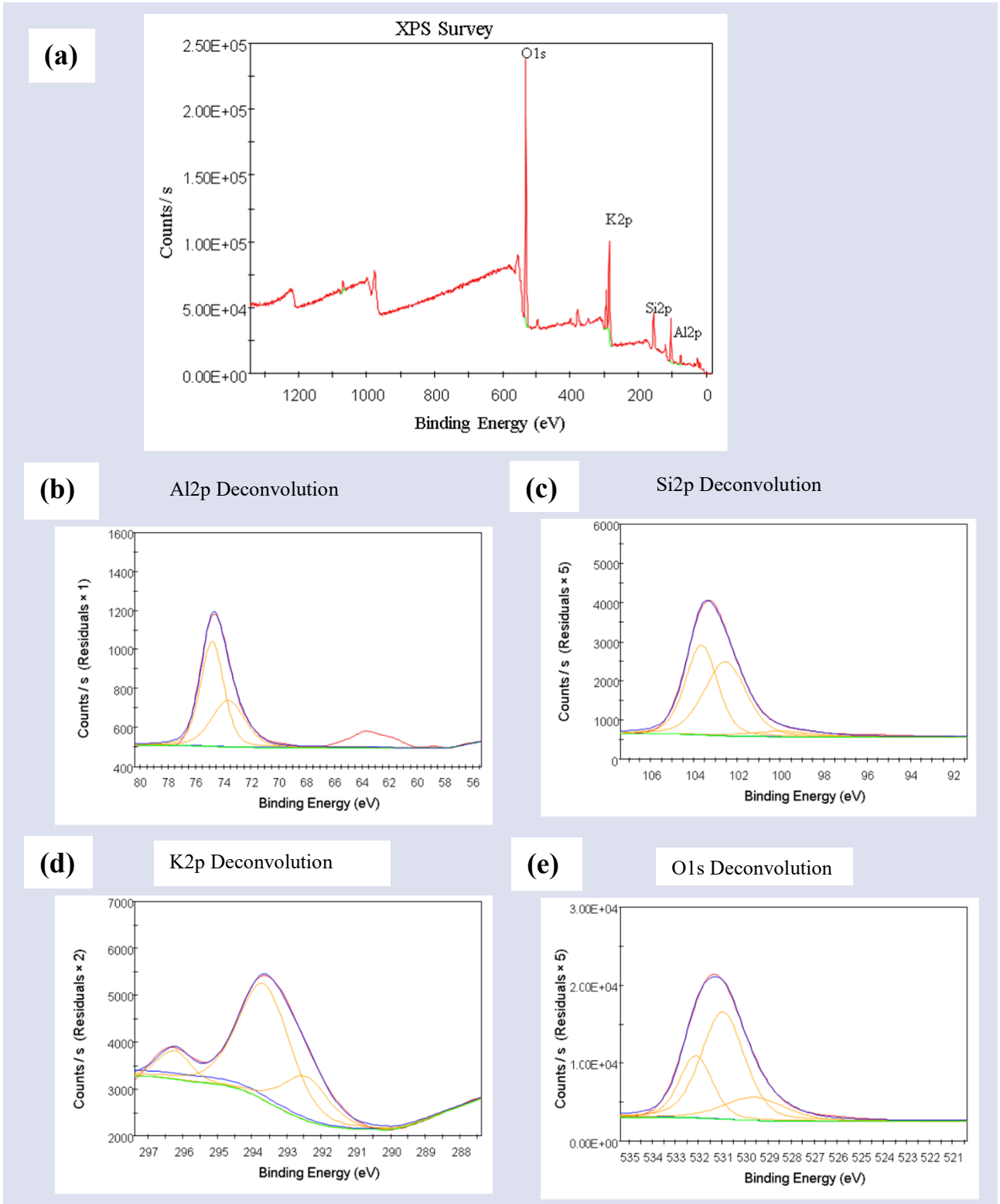

Figure 2 XPS (also known as ESCA) spectrum of amazonite. **(a)** survey and deconvoluted **(b)** Al2p, **(c)** Si2p, **(d)** K2p, **(e)** O1s

Table 2 XPS outcomes of natural amazonite aliquots

Sample	Elements	Binding Energy (eV)				Survey weight (%)
		Survey B.E.	Decay Elemental B.E.			
			1st peak	2nd peak	3rd peak	
Amazonite $KAlSi_3O_8$	O 1s	531.03	529,5	531	532	35.82
	C 1s	284.41	284	285	-	25.43
	Si 2p	102.89	102,5	103,5	-	24.49
	K 2p	293.53	292,5	293,5	296	6.80
	Al 2p	74.71	74	75	-	6.59
	Na 1s	1068.75	1071	1072	-	0.88

Surface Morphology & Particle Size:

Regarding the imaging purpose and morphology of the mineral, there are smooth micro monolithic surfaces with tiny hollows (pore diameter is ~ 0,2-1 µm) on the surface and small pieces (~ 0,2-3,5 µm) all around. The average particle size of amazonite was found to be 1-10 µm (Figure 3). The given α and γ crystallographic angles are very close to 90° (Table 1).

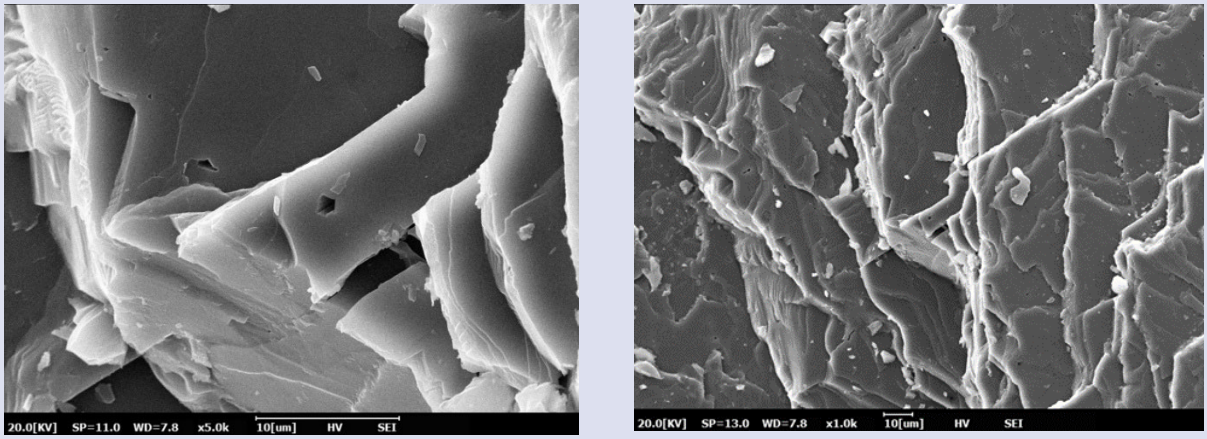

(a) **(b)**

Figure 3. SEM images of the surface of the amazonite aliquots.

Optical Analysis

Figure 4 represents not only the excitation and emission bands but also the PL decay curves of amazonite aliquots. Figure 4(a) states the excitation and emission spectrum at RT of the mineral. The excitation spectrum of emission has a wide band (250- 500 nm) making a peak around 340 nm, corresponding to the host lattice transition. The excitation range is noted in the UV-blue region of the electromagnetic spectrum. The emission peak under excitation launches from 360 nm and gives broadband that lasts at around 650 nm. The summit of the emission peak was detected at around 520 nm which is attributed to the blue-green colour of the amazonite. A long afterglow is observed (Figure 4(b))

The decaying duration of the amazonite mineral at RT was also tested (Table 3 and Figure 4(b)). The decay data was monitored afterward the excitation was ended and the decaying duration was calculated using the exponential formula's principle. [4]. In Figure 4(b) it is marked that, the decay curves and the long-lasting phosphorescence of the amazonite mineral consist of two main sections: the fast-decaying section and the slow-decaying section, which is given in detail with empirical equations by Gultekin et al. [4].

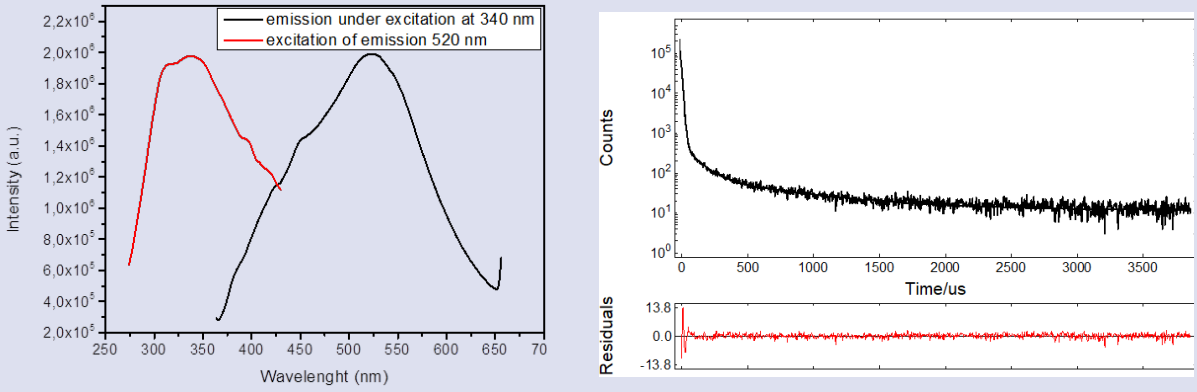

Figure 3. SEM images of the surface of the amazonite aliquots.

In Table 3. τ_1, τ_2 and τ_3 are the decaying durations. The amazonite aliquot showed three exponential decaying durations. The short lifetime (9.13 µs), the middle lifetime (103.76 µs), and the long lifetime (682,75 µs) components were noted.

Table 3 Excitation and emission wavelength and decay time measurement results of amazonite aliquots with standard deviation and percentage distribution

Sample	Excitation wavelength (nm)	Emission wavelength (nm)	X^2		Decay Period (µs)	Standard Deviation	Rel.%
$KAlSi_3O_8$	340	520	1.765	ζ_1	9.13	318.4296	85.25
				ζ_2	103.76	16.6616	7.09
				ζ_3	682.75	4.1549	7.66
				ζ_{avr}	265,21		

Discussion

The initial step of the study included structural phase analysis, elemental analyses, structure morphology, and particle size since both the formation and crystallinity have a significant impact on the luminescence curves. It has long been understood that all the features of the luminescence phenomena, including lifetime, efficiency, and emission spectra, are dependent on the crystalline phase, which is primarily induced by temperature and pressure [1]. The second step was the PL characteristics.

Amazonite has been the subject of numerous studies regarding its luminescence properties, but it is well known that changes in the intensity and wavelength position at emission spectra can be caused by even minute variations in the lattice structure caused by inclusions, impurities, substituted ions, or surface defects in ppm concentrations [1]. For this reason, the amazonite mineral sample from Tangir Valley, Pakistan, was carefully examined. Below is a detailed explanation of the collected results.

1. Phase & Elemental Properties:

The diffraction pattern of the amazonite observed in this study is compatible with the results in the literature [6]. Furthermore, while most feldspars have monoclinic structures, the amazonite investigated possesses a triclinic structure. The formation of triclinic microcline is possible by the transformation of monoclinic K-feldspar upon cooling [7] or by K-replacement of Na/Ca feldspar [6]. The study by Deer et al. explains this circumstance by providing a detailed explanation of the microcline framework [8]. As they indicated, the K(Al,Si)O4 tetrahedra that make up the crystal lattice of K-feldspars, known as amazonite, are joined to four other tetrahedra at their edges by shared or bridging O-1, providing a continuous and interconnected structure [9]. The framework contains four tetrahedral locations. The two of each are referred to as T1 and T2 sites and are occupied by Si4+ or Al3+. The structure also includes a net negative charge that is balanced by massive K+ cations that are in gaps called M-sites [8, 9]. Al3+ has an equal chance of occupying any of the four tetrahedral places at the framework of amazonite in high temperatures [8]. During gradual cooling, as the framework shrinks, Al3+ diffuses to occupy one of the two T1-sites and monoclinic low sanidine develops [8]. With continuous slow cooling, Al3+ diffuses into the other T1-site, causing a symmetry change from monoclinic to triclinic, which is the structure of the amazonite examined in this work [8, 9]. For more information, the authors refer to Deer et al. 's book [8].

As the weight % values of elements given by the XPS technique are defined in Table 2 Na1s with 0,88% noted. This small amount is an impurity at KAlSi3O8 which may cause emission. The potential of this emission has already been emphasized by many scientists. The other observing impurity is C1s with 25,43 %. Inside the XPS system, there

were hydrocarbon impurities, for this reason, 284 and 286 eV peaks, which are indicating C-C and C-O bindings were observed, respectively. As both C-C and C-O bonds are not related to KAlSi3O8 and just because of the pollution of the system C1s deconvolution is not given in Figure 2

2. Surface Morphology & Particle Size:

While in the literature it has been reported that (a) K-feldspar contains macropores of 0.1-1 µm diameter [10] and (b) it has been common to see symmetrical intergrowth with a triclinic microcline because of the triclinic structure in feldspars [10, 11]; In the current study (a) the average particle size of amazonite was found to be 1-10 µm (Figure 3) and (b) the given α and γ crystallographic angles are very close to 90° (see Table 1), therefore it is tough to detect symmetrical intergrowth structures in SEM patterns since the surface would need to be slightly tilted. Similar to the findings of Welti et al. [6], both the obtained SEM and XRD patterns in the current study are in good agreement with the patterns of amazonite from Namibya [6], where height above sea level and geographic conditions are similar. Furthermore, for K-feldspars Hodson emphasized that the contribution of pores to the total particle surface increases with decreasing particle sizes [6, 12].

Related to the obtained results, it can be remarked that amazonite aliquots display a complex structure due to the complexity of their geological origin. This result is in line with earlier research, which revealed that this mineral's structure has several planar defects, including twinning and exsolution interphases [1, 6]. These defects can hold both hydroxyl groups and water molecules. In addition to planner defects, point defects that behave as luminescence centres may also occur. Considering this circumstance, structural defects can be the cause of the detected blue-green emission (it can be concluded that structural defects are one of the causes of the detected blue-green emission). Furthermore, Correcher and Garcia-Guinea underlined that the structure defect associated with emission can occur at the twin-domain boundaries, where ionic alkali self-diffusion, irreversible water losses, and irreversible dihydroxylation processes occur [1].

3. Optical Properties:

The achieved PL emission under excitation of 340 nm is broadband (from 360 to 650 nm) with a peak at 520 nm. This emission determines the blue-green colour of the microcline aliquot. The literature has also reported the presence of this emission, particularly for samples of amazonite from the Transbaikal, Ploskaia Mountain (Slovenia), Kola Peninsula, Urals, Kazakhstan, and Transbaikal [1, 3]. I now have this emission peak for amazonite samples from Tangir Valley in Gilgit-Pakistan.

Riedesel et al. found that the emission at 520 nm is brighter than the other dimmer-disclosed emissions at 300, 400, and 700 nm [9] and stated that this emission is disclosed at about 170 °C [9]. The results of this study involving the PL results are well consistent with their findings.

The examined amazonite is thought to be nonvolcanic [13] because it has been noted that volcanic feldspars fade more quickly than those formed by nonvolcanic processes [14]. Regarding the system of the long afterglow, the long lifetime components are attributed to afterglow properties [4] The first decay process results from the short survival time of the electron while the slow decay process could be attributed to the deep trap energy centre of the host lattice. The "hole-trapped-transported-retrapped" process has already been known as the reason for the phosphor's long afterglow [4]. Besides, long-lasting PL can be attributed to hole mobility, e-hole recombination, and a low rate of hole mobility, all of which rise the possibility of re-trapping and slowing down the decaying process [15]. Moreover, the mineral's fluorophore property could be caused by (1) structural defects located in the twin-domain borders, which could include ionic alkali-self-diffusion, irreversible water losses, and irreversible de-hydroxylation processes, (2) the intricate structure of amazonite, which contains several points and planar impurities (Na, Table 2) that can function as luminescence centres, (3) any continuity in the distribution of traps [1]. Although Gomez-Gonzales et al. stressed that, the blue-green colour of amazonite is related to the amount of lead or rubidium contents, this is not always the case, as demonstrated by this study [16].

Conclusion

Up to now, the partially investigated amazonite mineral from Talgir Valley Pakistan is studied in detail on both crystal morphology and luminescence properties. The present conclusions can be summarized as follows:

1. Surface Morphology, Particle Size, Phase and Elemental Properties:

It is observed that both the crystal's structural state and the kind of its interfaces play a great role in determining the mineral's luminescence qualities [9].

The analysed amazonite has a triclinic structure. A trace amount of Na, 0.88 wt%, was found by XPS studies in addition to the components O, C, Si, K, and Al. This impurity is a type of point defect that can act as a luminescence centre. However, the characteristic UV emission of Na was not observed in the current investigation, and this might be caused by the minute levels of Na. The emission might also be moved to the blue. Amazonite aliquots have a complex structure, as evidenced by SEM micrographs. The size of macropores ranges from 0.1 to 1 µm.

2. Optical Properties:

Blue-green emission spectra (λmax = 520 nm) were observed when the material was stimulated with 340 nm UV light. For the current microcline, this emission is thought to be caused by defects originating from a hole in the middle of an Al-O1- bridge (Al3+-O1--Al3+) [9, 17]. The study of Krbetschek et al. is a comprehensive review of emission centers associated with crystal defects in

feldspars, hence I offer this publication for further studies on emission centers of feldspars [18].

In the current study, the afterglow properties of amazonite have been reported, and three different decay times were observed. It has been thought that the longest decay duration is due to deep traps formed during host lattice transitions.

Acknowledgment

The author would like to acknowledge Associated Professor Serdar Yıldırım for his valuable technical assistance.

Conflicts of interest

There are no conflicts of interest in this work.

References

[1] Correcher V., and Garcia-Guinea J., Study of The Luminescence Properties of a Natural Amazonite, Radiation Measurements, 46 (2011) 971-974.

[2] Mittani J., Cano N., and Watanabe S., Use of [Pb–Pb]3+ Center of The Amazonite for Dating, Applied Radiation and Isotopes, 62 (2005) 251-254.

[3] Ostroouumov M., Amazonite: Mineralogy, Crystal Chemistry, and Typomorphism, Amsterdam, Boston, Heidelberg, London, New York, Oxford, Paris, San Diego, San Francisco, Singapore, Sydney, Tokyo: Elsevier (2008).

[4] Gultekin S., Yıldırım S., Yılmaz O., Keskin I., and Katı M., Structural and Optical Properties of SrAl2O4: Eu2+/Dy3+ Phosphors Synthesized by Flame Spray Pyrolysis Technique, Journal of Luminescence, 206 (2019) 59-69.

[5] Gliozzo E., Mattingly D., Cole F., and Artioli G., In the Footsteps of Pliny: Tracing the Sources of Garamantian Carnelian from Fazzan, South-West Libya, Journal of Archaeological Science, 52 (2014) 218-241.

[6] Welti A., Lohmann U., and Kanji Z., Ice Nucleation Properties of K-Feldspar Polymorphs and Plagioclase Feldspars, Atmospheric Chemistry and Physics Discussions, 19 (16) (2019) 10901-10918.

[7] Waldron K., and Parsons I., Solution-Redeposition and the Orthoclase Microcline Transformation: Evidence from Granulites and Relevance to 18O Exchange, Mineralogical Magazine, 57 (1993) 687-695.

[8] Deer W., Howie R., and Zussman J., An Introduction to the Rock-Forming Minerals, 3rd edition, London: The Mineralogical Society, 2013.

[9] Riedesel S., Bell A., Duller G., Finch A., Jain M., King G., Pearce N., and Roberts M., Exploring Sources of Variation in Thermoluminescence Emissions and Anomalous Fading in Alkali Feldspars," Radiation Measurements, p. 06541, 2021.

[10] David F., Walker F.D.L., Lee M. R., and Parsons I., Micropores and Micropermeable Texture in Alkali Feldspars: Geochemical and Geophysical Implications, Mineralogical Magazine, vol 59, pp. 505-534, 1995.

[11] Whale T., Holden M., Kulak A., Kim Y., Meldrum F., Christ H., and Murray B., The Role of Phase Separation and Related Topography in The Exceptional Ice-Nucleating Ability of Alkali Feldspars, Royal Society of Chemistry, vol. 19, pp. 31186- 31193, 2017.

[12] Hodson M., Micropore Surface Area Variation with Grain Size in Unweathered Alkali Feldspars: Implications for Surface Roughness and Dissolution Studies, Geochimica et Cosmochimica Acta, vol. 17, pp. 3429-3435, 2017.
Huntley D., and Olav B., Some Observations on Tunnelling of Trapped Electrons in Feldspars and Their Implications for Dating, Quaternary Science Reviews, vol. 25, pp. 2503-2512, 2006.

[13] Aitken M., Thermoluminescence Dating, Quaternary Research, vol. 26, pp. 280-281, 1986.

[14] Weiyi J., Huabiao Y., Lizhu L., Huimin L., and Yen W., Phosphorescent Dynamics in SrAl2O4: Eu2+, Dy3+ Single Crystal Fibers, Journal of Luminescence, vol. 76-77, pp. 424-428, 1998.

[15] Gomez-Gonzalez M. A., Garcia-Guinea J., Garrido F., Townsend P., and Marco J., Thallium and Magnesium Complex Involved in The Luminescence Emission of Potassium-Bearing Aluminosilicates, Journal of Luminescence, pp. 197-206, 2015.

[16] Finch A., and Klein J., The Causes and Petrological Significance of Chathodoluminescence emissions from Alkali Feldspars, Contributions to Mineralogy and Petrology, vol. 135, p. 234–243 , 1999.

[17] Krbetschek K., Gütze J., Dietrich J.A., and Trautmann T., Spectral Information from Minerals Relevant for Luminescence Dating, Radiation Measurements, vol. 27, pp. 695-748, 1997.

Cumhuriyet Sci. J., 44(2) (2023) 411-417
DOI: https://doi.org/10.17776/csj.1139858

Cumhuriyet Science Journal

| csj.cumhuriyet.edu.tr | Founded: 2002 ISSN: 2587-2680 e-ISSN: 2587-246X Publisher: Sivas Cumhuriyet University

Determination of Impact Size by Canonic Correlation Analysis of the Factors Affecting the Buying or Selling Agricultural Lands

İsmail Gök [1,a,*], Mustafa Şahin [2,b], Tolga Tolun [1,c]

[1] Department of Bioengineering, Faculty of Agriculture, Kahramanmaraş Sütçü İmam University, 46100, Kahramanmaraş, Türkiye.
[2] Department of Agricultural Biotechnology, , Faculty of Agriculture, Kahramanmaraş Sütçü İmam University 46100, Kahramanmaraş, Türkiye.
*Corresponding author

Research Article

History
Received: 02/07/2022
Accepted: 12/06/2023

ABSTRACT

The aim of this study is to determine the relationship between the influencing factors in the data set created with the help of canonical correlation in the factors affecting the purchase or sale of agricultural lands in certain neighborhoods in the Dulkadiroğlu district of Kahramanmaraş province and the most effective factor or factors compared to the others. For this, a survey was conducted with the parcel owners in the determined neighborhoods and a data set of 1000 people was created. As a result of the data obtained, the first data set of the study, in which the canonical correlation method was used, was the slope and irrigation status of the land, the average productivity rate of the land, and the presence of tractors and equipment used in the land, among the factors affecting the purchase or sale of agricultural lands; land parcel size, land purchase or sale price and for what purpose the land was bought or sold were also the second data set. The rate of canonical correlation coefficient in the data sets created according to the estimation results was found to be 40.32%. In the data set we compared, the average productivity of the land was determined in the first data set with the highest effect, while in the second data set it was determined as the purpose for which the land was bought or sold.

Keywords: Agricultural land, Factor, Survey and Land trading.

[a] gkisoo1995@gmail.com https://orcid.org/0000-0002-0759-1187
[b] ms66@ksu.edu.tr https://orcid.org/0000-0003-3622-4543
[c] tolga_tolun@hotmail.com https://orcid.org/0000-0003-4081-1222

Introduction

Land within the factors of production; It is the part of the earth that affects the climate, soil, topography and living things in various sizes. The land, which is only a means of production without the possibility of increasing, as well as the plant production area; It is a source of livelihood for people in various fields such as beekeeping, greenhouse cultivation, sheep and cattle breeding. It is also known as the security guarantee and investment area of most people [1]. Due to the infrastructure and superstructure investments implemented by private and public areas in Turkey, the expropriation work is in the first place, and various areas such as consolidation works, the irrigation planning project of the land and making the land open to the zoning area are closely related to the determination of the current price of the land. However, the fact that studies such as taxation and guarantees in banks are related to the current market prices of the land increases the importance of the research applied to determine the land precedent value. Valuation; It is the real and complete presentation of the prices of business area parcels, agricultural enterprises and other rural goods and rights [2].

In this study, considering the geographical shape of the lands in the determined neighborhoods, it can be possible to scientifically analyze which degree of influence is dominant when buying or selling land in the survey conducted for our farmers. For this reason, the factors that have had an impact on the sale or purchase of land and the effect sizes of these factors have been classified with each other, and it is necessary to determine the degree of impact of these factors in the sale or purchase of land. It is thought that what are the factors affecting the sale or purchase of land for various targets and it will be beneficial to reduce these factors.

The study is expected to be a guide in determining the current value in the sale or purchase of the land of the landowners in the selected areas and determining the extent of the effect of the factors affecting this activity. As a result of the results obtained in this study, the real and scientific appraisal of the valuation taken by the landowners in the land acquisition or sale of the land in the region, taking into account the factors such as the structure of the land, its roughness, wet-dry state, its location, productivity rate, and the distance to the nearest settlement area. will determine whether it is based on fundamentals. It is foreseen that it will also contribute to the investment planning in the region where the research is carried out.

The aim of the research is to try to determine the effect sizes of the factors affecting the sale or purchase of agricultural lands in the determined neighborhoods in the Dulkadiroğlu district of Kahramanmaraş province. For this, the effect sizes of the factors were classified from most to least with the help of the canonical correlation

method using the data obtained through the survey study.

Materials and Methods

Material

This research refers to the 27-year period when the land was sold or bought with the land owners in nine determined neighborhoods in the Dulkadiroğlu district of Kahramanmaraş between the years 1995-2021. The most important factor in determining the places where the research is applied is to consider that the general data on the purchase or sale of agricultural land in the region will be met.

In this research, a questionnaire was applied with a total of 1000 participants who sold or bought land in 9 neighborhoods, whose sole purpose of participation was determined. In the survey conducted with the land owners in question, it was determined that there is a total of 15913,000 m2 of land that has been subject to purchase and sale. The total land parcel sizes of the neighborhoods are given in Table 1.

Table 1. The total parcel size of the lands in the determined neighborhoods in Dulkadiroğlu district.

Neighbourhood	1995-2021 In Trading Parcel Size
Çınarlı	1395.000 m²
Çiğli	2838.000 m²
Sivricehüyük	1100.000 m²
Kapıçam	1964.000 m²
Abbaslar	1241.000 m²
Alibeyuşağı	2680.000 m²
Kocalar	936.000 m²
Yeniyurt	2266.000 m²
Tevekkeli	1493.000 m²
Total	15913.000 m²

A survey was conducted randomly and by reaching as many people as possible and it was determined that 91.07% of the people who participated in the survey were male and 8.93% were female. In addition, the average number of children in the family was determined as 4, and their education level was determined to be 97.48% primary school or literate.

Table 2. Wet and dry parcel sizes of the lands in the determined neighborhoods in Dulkadiroğlu district.

Neighbourhood	AQUEOUS Land Size	ANHYDROUS Land Size
Çınarlı	1286.000 m²	109.000 m²
Çiğli	2486.000 m²	352.000 m²
Sivricehüyük	1100.000 m²	0 m²
Kapıçam	1964.000 m²	0 m²
Abbaslar	1241.000 m²	0 m²
Alibeyuşağı	2680.000 m²	0 m²
Kocalar	936.000 m²	0 m²
Yeniyurt	1866.000 m²	400.000 m²
Tevekkeli	1493.000 m²	0 m²
Total	15052.000 m²	861.000 m²

As a result of the answers given by the land owners whose lands were the subject of the survey between 1995-2021, it was determined that there were 15052.000 m2 of irrigated land and 861.000 m2 of non-watery land. In addition, while Yeniyurt has the highest amount of waterless land in the determined neighborhoods, Alibeyuşağı District has the highest amount of wet land. The products planted in this region; barley, cotton, beet, wheat, cucumber, corn, watermelon, pepper and chickpea. In addition, per 1000 m2 in neighborhoods: The average productivity of irrigated lands in Çınarlı District; beet=7000-12000 kg, corn=1000-1500 kg, cotton=500-700 kg, wheat=500-600 kg, barley=400-500 kg, cucumber=350-400 kg, pepper=400-500 kg and chickpeas =300-400 kg of land productivity without water; wheat=300-400 kg, barley=250-300 kg and chickpeas=200-300 kg; Average productivity of irrigated lands in Çiğli District; beet=6000-12000 kg, corn=1000-1500 kg, cotton=500-700 kg, wheat=500-600 kg, barley=400-500 kg and chickpeas=300-400 kg, while the land productivity without water; wheat=300-400 kg, barley=250-300 kg and chickpeas=200-300 kg; Average productivity of irrigated lands in Sivricehüyük District; beet=4000-7000 kg, corn=800-1000 kg, cotton=300-500 kg, wheat=500-600 kg, barley=400-500 kg, cucumber=300-400 kg and pepper=250-400 kg; Kapicam District average irrigated land productivity; beet=4000-8000 kg, corn=700-1000 kg, cotton=300-500 kg, wheat=400-500 kg barley=300-400 kg and cucumber=300-500 kg; Average productivity of irrigated lands in Abbaslar District; beet=10000-13000 kg, corn=1000-1700 kg, cotton=400-600 kg, wheat=700-800, barley=400-500 kg and chickpeas=300-400 kg; Average productivity of irrigated lands in Alibeyuşağı Mahallesi; beet=6000-12000 kg, corn=1000-1500 kg, cotton=500-700 kg, wheat=500-600 kg, barley=400-500 kg, cucumber=300-400 kg and pepper= 450-500 kg; Average productivity of irrigated lands in Kocalar Mahallesi; beet=6000-12000 kg, corn=1000-1500 kg, cotton=500-900 kg, wheat=600-700 kg, barley=500-600 kg, cucumber=400-700 kg and pepper=300-500 kg; Average productivity of irrigated lands in Yeniyurt Mahallesi; beet=4000-8000 kg, corn=800-1000 kg, cotton=400-600 kg, wheat=400-500 kg, barley=300-400 kg, cucumber=300-500 kg, pepper=250-300 kg and chickpeas = 250-300 kg, while the average productivity of the lands without water; wheat=300-400 kg, barley=200-300 kg and chickpeas=200-300 kg and average productivity of irrigated lands in Tevekkeli District; beet=4000-8000 kg, corn=700-1000 kg, cotton=300-500 kg, wheat=400-500 kg, barley=300-400 kg and cucumber=300-500 kg.

While it is possible to produce all of them in irrigated agricultural lands, wheat, barley and chickpea production is common in non-irrigated agricultural lands. In line with the answers given by the landowners who participated in the survey, there is a production of once a year in the irrigated lands, while this production is carried out twice in the irrigated agricultural lands. Since the structural

shape is not uneven in the region where the land is located, it was determined that the soil is stony in lands without water and normal in wet lands. In addition, the distance range to the nearest residential area; Average 19-21 km in Tevekkeli district, 19-22 km in Çınarlı district on average, 16-18 km in Kapıçam district, 20-22 km in Kocalar district on average, 16-18 km in Çiğli district on average, 25-27 km in Abbaslar district on average, Yeniyurt district on average It has been determined as a result of the answers given by the landowners in the survey that it is 19-20 km on average, 20-23 km on average in the Sivricehüyük district and 24-25 km on the Alibeyuşağı district.

Table 3. The presence of tractors and equipment in the designated neighborhoods in Dulkadiroğlu district.

Region	Number of People Who Participated in the Survey	Number of Own Tractors and Equipment	Number of Those Without Tractors and Equipment
Çınarlı	179	113	66
Çiğli	138	90	48
Sivricehüyük	40	40	0
Kapıçam	178	104	74
Abbaslar	71	71	0
Alibeyuşağı	110	100	10
Kocalar	44	34	10
Yeniyurt	120	80	40
Tevekkeli	120	60	60
Total	1000	692	308

As a result of the survey conducted with the landowners in the sale or purchase of land between 1995-2021, it was determined that 69.20% of the land owners included in the survey had tractors and equipment, while 30.80% did not have tractors and equipment.

While the factors affecting the land owners who were included in the survey by buying or selling land within the specified years were investigated with the help of the survey, 19.23% of them became landowners in Çınarlı Mahallesi with the aim of animal husbandry activities and 80.77% of them with the aim of having an investment relationship; 83.02% of them sold their lands due to expropriation of the land, 1.30% of them quitting agriculture, 2.61% of them due to migration and 13.07% of them due to financial insufficiency. In Çiğli Neighborhood, 12% becomes land owner with the aim of relations between heirs, 4% of the transfer of the land from the treasury to private property, 12% of livestock activities and 72% of investment relations; , 52.30% of them sold their lands due to expropriation of the land, 6.81% due to relations between heirs, 6.81% due to migration, 4.54% to quit agriculture and 29.54% due to financial insufficiency. In Sivricehüyük Neighborhood, 30% becomes the owner of land with the aim of relations between heirs, 10% of livestock activities and 60% of investment relations; 50% of them sold their lands due to relations between heirs, 10% due to immigration and 40% due to financial insufficiency. In Kapıçam Neighborhood, 48.07% becomes land owner with the aim of transferring the land from the treasury to private property, 13.47% with the aim of relations between heirs, 1.93% with livestock activities and 36.53% with the aim of investment relationship; 8.10% of them sold their lands due to relations between heirs, 21.62% due to expropriation of the land, 2.70% due to migration and 67.56% due to financial insufficiency. In Abbaslar Neighborhood, 11.42% becomes land owner with the aim of relations between heirs, 5.71% of livestock activities and 82.87% of investment relations; 8.33% of them left the agriculture, 11.11% of them sold their lands due to relations between heirs, 16.16% due to changes in land productivity and 63.90% due to financial insufficiency. While 26.67% of them become landowners in Alibeyuşağı Mahallesi with livestock activities and 73.33% with the target of investment relationship; 13.21% of them sold their lands due to quitting agriculture, 13.21% due to immigration and 73.58% due to financial insufficiency. While 36.37% of them become landowners in Kocalar Mahallesi with the aim of animal husbandry activities and 63.63% of them with the aim of investment relationship; 9.10% of them left the agriculture, 27.27% of them migrated and 63.63% of them sold their lands due to financial insufficiency. In Yeniyurt Mahallesi, 17.85% becomes land owner with the aim of relations between heirs, 17.85% of livestock activities and 64.30% of investment relations; 14.25% of them sold their lands due to relations between heirs, 12.50% due to immigration, 12.53% due to quitting agriculture and 60.72% due to financial insufficiency. In Tevekkeli Neighborhood, 50% will become landowners with the aim of relations between heirs, 5.88% with livestock activities and 44.12% with the aim of investment relations; 23.12% of them sold their lands due to relations between heirs, 15.35% to quit agriculture, 15.38% to immigration and 46.15% to financial insufficiency reasons.

The survey was applied in 9 neighborhoods determined in Dulkadiroğlu District of Kahramanmaraş Province in 2021. Dulkadiroglu District; A survey was conducted with 1000 landowners whose only condition of participation was the purchase or sale of agricultural lands in the neighborhoods of Çınarlı, Çiğli, Sivricehüyük, Kapıçam, Abbaslar, Alibeyuşağı, Kocalar, Yeniyurt and Tevekkeli between the years 1995-2021 and for all parcels where the survey was conducted in the periods covering this research. It is assumed that agricultural technology does not change.

Methods

The aim of this study is to determine the factors that are effective in the region and the degree of impact of these factors, in line with the information obtained from the land owners who were included in the survey by purchasing or selling land between the years 1995-2021 in 9 selected neighborhoods in the Dulkadiroğlu district of Kahramanmaraş province. In this, the canonical

correlation method, which is a statistical analysis method, was used.

Canonical Correlation Analysis

Canonical correlation analysis, which is the most basic and most complex interaction analysis, deals with the connections between two-way datasets taken from a multi-dimensional population. A method related to the general problems of the connection between the two-way dataset taken from it is envisaged. In this method, which is called canonical correlation analysis, the highest level correlation of the variables in each class and combination pairs with unit variances are found at the beginning, and the process continues by finding the second linear combination pair. Canonical correlation analysis is a special part of multiple regression analysis [3]. While multiple regression analysis examines the relationship between one dependent and more than one independent variable, canonical correlation analysis examines the relationship between p dependent and q independent variables [4]. In canonical correlation analysis, the goal is not to develop or derive a model for the variables, but to analyze the connection between the variable sets [5].

Canonical correlation analysis can be shown in general as follows [6]:

$$Y_1 + Y_2 + \cdots + Y_p = X_1 + X_2 + \cdots + X_k \quad (1)$$

In the above equation, the variables can take measured or unmeasured values. in the first group (Y_p) p(1-p)/2 among the variables, whereas in the second group (X_k) there are q(1-q)/2 correlations between the variables and p.q correlations between the two variable groups. When the number is large, it is very difficult to analyze the correlation coefficients one by one. For this, canonical correlation analysis aims to minimize these correlation coefficients [7].

If there is only one dependent variable in canonical correlation analysis, multiple regression analysis is used instead of canonical correlation analysis. Since ANOVA and two-class dicirminant analysis are special cases of multiple regression analysis, these two methods are also special cases of canonical correlation analysis. If the dependent variable is a versatile nominal variable, canonical correlation analysis refers to multiple discriminant analysis [8].

In canonical correlation analysis, one of the variable groups can be called the independent variable group and the other the dependent variable group. If it is a group of independent and dependent variables, the goal in canonical correlation is to analyze whether and to what extent the independent variable group affects the dependent variable group [9]. However, there is no obligation to define this in variable groups. In this analysis, it is aimed to maximize the correlation between variable groups, and towards this goal, canonical variable dichotomies are derived from linear combinations of variables in both variable groups [10].

The objectives of canonical correlation analysis are as follows [11]:

a) Testing that two classes of variables obtained from identical individuals are statistically free from each other,
b) Identifying the variables in both variable classes that provide the greatest benefit among the classes,
c) Determining the linear combination that maximizes the correlation in the classes of dependent and independent variables,
d) Determining the extent to which variable sets can explain each other among themselves,
e) Determining how much a canonical variable benefits the explanatory power of its class in the variable class,
f) Determining the relative power of various canonical factors to predict or explain relationship size.

Canonical Correlation Analysis Assumptions

Results of canonical correlation analysis; covariance, multiple normal distribution, multiple linear relationship assumptions and linearity should be analyzed. The linear assumption affects canonical correlation analysis in two ways. First, the link between the two variables is assumed to be linear, and if the link between the two variables is nonlinear, analysis is performed until it becomes linear. Second, the canonical correlation coefficients show the linear relationship of the two canonical variables. For this reason, nonlinear connections between variables cannot be explained [12]. The multiple normal distribution condition must be minimized or provided, the variables must meet a normal distribution condition and there must be no multicollinearity problem. The minimum number of data variables is 20

It should be solid and the data should not have extreme values [13]. There should be no unnecessary variables in variable groups [14]. Since identical variance reduces the covariance between variables, it should also be analyzed in canonical correlation analysis [15].

Significance of Canonical Correlation Coefficients

As a result of canonical correlation analysis, it should be decided how important the canonical variable dichotomies are [16]. In this method, the goal is to analyze how many of the obtained canonical correlation binaries are significant. While it is predicted that all canonical correlations are equal to zero in Wilk's Lambda method, the H_0 hypothesis is analyzed against the H_1 hypothesis, which predicts that the lowest canonical correlation coefficient is different from zero [17]. The hypotheses to be written to determine the meaning levels of the coefficients are as follows [18].

$$H_0 : P_1 = P_2 = P_3 = \cdots P_n = 0 \quad (2)$$
$$H_1 : P_1 \neq P_2 \neq P_3 \neq \cdots P_n \neq 0 \quad (3)$$

Wilk's Lambda analyzes canonical correlation coefficients together and in identical time. Failure to accept the null hypothesis suggests that the lowest first canonical correlation coefficient is significant, while the remaining n-1 canonical correlation coefficients may be meaningless or significant. The significance of the second canonical correlation coefficient can be analyzed independently of the first. In the calculation of the first canonical correlation coefficient, the significance level of Wilk's Lambda statistic conforms to the p×q degrees of freedom χ^2 distribution. Secondly, $(p \times q) \times (q-1)$ degrees of freedom χ^2 distribution and i. Inside $(p \times i) \times (q-i)$ degrees of freedom χ^2 fits the distribution. If the probability value is less than 0.05 at the 5% confidence level, the null hypothesis is rejected. That is, the correlation coefficients are found to be significant and significant. The second canonical correlation coefficient is analyzed independently of the first canonical correlation coefficient. This process is continued until we find the insignificant one in the canonical correlation coefficient [19].

Results

The purpose of this research is to determine the land that is thought to affect the landowners while buying or selling land in line with the answers given by the landowners as a result of the data obtained from the survey, where the only participation condition was the sale or purchase of land within the specified period in 9 neighborhoods determined in the Dulkadiroğlu district of Kahramanmaraş province. The aim of this study is to analyze the relationship and effect sizes between the factors that affect the slope and roughness of the land, the average productivity of the land, the presence of tractors and equipment of the land owners, the size of the land parcel and the reason why the land owners sell or sell the land, with the help of the canonical correlation method.

The main goal is to determine the degree of influence and size of the factors that affect the land owners while buying or selling land, by scientific methods, within the specified period. The sample of the research was obtained with the help of a questionnaire, which was the purchase or sale of land by landowners between the years 1995-2021 in 9 neighborhoods in the Dulkadiroğlu district of Kahramanmaraş province, where the only participation condition was determined. As a result of the data obtained from the questionnaire, the canonical correlation method was used to indicate the relationships between the factors and their degree of influence. According to the estimation results obtained in the research, the average productivity of the land in the first data set, which is thought to be under the influence of the landowners while purchasing or selling the land within the specified years and the degree of impact was determined as the purpose for which the land was bought or sold in the second data set. The rate of canonical correlation coefficient in the data sets created according to the estimation results was found to be 40.32%. It has been determined by the scientific analysis that the impact factors obtained with the help of the survey covering the years 1995-2021 and the only participation condition is the purchase or sale of land by the landowners during these years.

[20], [21], [22], [23], [24], [25], [26], [27], [28], ' is in harmony with their work.

In 9 neighborhoods selected from the Dulkadiroğlu district of Kahramanmaraş, the only condition of participation was specified. The fact that landowners do not buy or sell land each year has led to disruptions in the analysis. In future articles or thesis research, in order to avoid these and similar problems, villages or neighborhoods that have been subject to land sales or purchases every year or where there are land owners who bought or sold land in the same years should be preferred, land expropriation and transition assets from treasury to private property should be considered. should not be overlooked.

Discussion and Conclusion

In this research, first of all, data groups were created as a result of the data obtained from the land owners who bought or sold land between the years 1995-2021 with the sole participation condition in 9 determined neighborhoods in the Dulkadiroğlu district of Kahramanmaraş province. Ranking in the obtained data set;

X1: The slope and unevenness of the lands of the surveyed landowners

X2: Average productivity of the lands of the surveyed landowners involved in the land purchase and sale between 1995-2021.

X3: Tractor and equipment availability of surveyed landowners between 1995-2021. X4: Parcel sizes of the lands of the surveyed land owners that were included in the land purchase and sale between 1995-2021.

X5: The current value of the land purchase and sale of the land owners included in the survey between the years 1995-2021.

X6: The reason why the land owners included in the survey sold or bought land.

is in the form.

Table 4. Spss pearson correlation probability value.

	X1	X2	X3	X4	X5	X6
X1	1	-0,40	-0 0,946	0,03 0,39	0,098 0,002	0,004 0,893
X2	-0,40	1	0,163 0	0 0,95	0,232 0	-0,16 0
X3	-0 0,946	0,163 0	1	0,15 0	-0,01 0,729	0,246 0
X4	0,027 0,394	0,002 0,953	0,15 0	1	-0,01 0,764	-0,08 0,011
X5	0,098 0,002	0,232 0	-0,01 0,729	-0,01 0,76	1	-0,15 0
X6	0,004 0,893	-0,16 0	0,246 0	-0,08 0,01	-0,15 0	1

However, for the canonical correlation analysis, the first data set was X1, X2 and X3, while the second data set was analyzed as X4, X5, X6.

In Table 4., the pearson probability values are given between the determined values.

Table 5. Spss canonical correlation result.

	1	2	3
Correlation	,403	,250	,012
Eigenvalue	,194	,067	,000
Wilk's statistic	,785	,937	1,000
F	28,113	16,363	,139
Number D.F.	9,000	4,000	1,000
Name D.F.	2419,285	1990,000	996,000
Probability	,000	,000	,710

Table5. In addition, 3 different correlational relationships were determined. Among them, it was found that the correlational relationship of the first and second in probability values was significant and the third was insignificant. It was determined that the first correlation in the eigenvalues was probably higher than the others. In Wilk's statistics, the relationship of the first correlation is closer to 0.05, so it is probably more significant than the others. It can be said that two of the three correlation scores that occur together are statistically significant. Canonical correlation value is 40.3%.

Table 6. Standardized canonical correlation coefficient in the spss first dataset.

Values	1	2	3
X1	,466	-,601	-,787
X2	,906	-,549	,330
X3	-,715	-,693	,204

Since the first correlation scores are found to be more significant, a model can be written over the first scores that are significant in Table 6 and more statistically significant models can be established.

$$0.466 \times X1 + 0.906 \times X2 - 0.715 \times X3 \quad (4)$$

form a meaningful model.

Table 7. Standardized canonical correlation coefficient in the spss second dataset.

Values	1	2	3
X4	-,283	-,531	,803
X5	,540	-,798	-,310
X6	-,733	-,505	-,489

Since the first correlation scores are found to be more significant, a model can be written over the first scores that are significant in Table 7 and more statistically significant models can be established.

$$-0.283 \times X4 + 0.540 \times X5 - 0.733 \times X6 \quad (5)$$

form a meaningful model.

Table 8. Result of canonical loads in spss first dataset.

Values	1	2	3
X1	,105	-,380	-,919
X2	,602	-,421	,679
X3	-,568	-,781	,260

In the first data set in Table 8., it was determined that the perceived safety was 0.602, which has the highest effect among the first canonical scores values. Therefore, in the first data set, X2 (the average productivity of the land owners included in the survey included in the land purchase and sale between the years 1995-2021) is the perceived reliability, which has the strongest explanatory power.

Table 9. Result of canonical loads in spss second dataset.

Values	1	2	3
X4	-,230	-,483	,845
X5	,655	-,715	-,242
X6	-,793	-,341	-,505

In the second data set in Table 9, it was determined that the perceived security was the highest with -0.793 among the first canonical scores values. Therefore, in the second data set, X6 (the reason why the land owners in the survey sell or buy land) is the perceived reliability, which is negative but has the strongest explanatory power.

Table 10. Cross-correlation result in spss first dataset.

Values	1	2	3
X1	,042	-,095	-,011
X2	,243	-,105	,008
X3	-,229	-,195	,003

The variable showing the strongest canonical effect in the first data set in Table 10. was X2 with -0.243. In other words, the variable X2 (the average productivity of the land owners involved in the land purchase and sale between the years 1995-2021) that established the strongest relationship with the second data set in the first data set.

Table 11. Cross-correlation result in spss second dataset.

Values	1	2	3
X4	-,093	-,121	,010
X5	,264	-,179	-,003
X6	-,320	-,085	-,006

The variable showing the strongest canonical effect in the second data set in Table 11 was -0.320 to X6. In other words, the variable X6 (the reason why the land owners included in the survey sold or bought land) had the strongest relationship with the first data set in the second data set.

In Table 12., the strongest explanation value for the first data set was 0.458, the second data set for the first data set was found to be 0.038, the second data set for

the first data set was found to be 0.370, and the first data set for the second data set was found to be 0.060

Table 12. Explained rate of variance of canonical correlation in spss.

Canonical Variable	Set 1 to set 1	Set 1 to set 2	Set 2 sets to 2	Set 2 sets to 1
1	,232	,038	,370	,060
2	,310	,019	,287	,018
3	,458	,000	,343	,000

Acknowledgment

This study was presented at the "III. International Applied Statistics Conference (UYIK 2022)".

Conflicts of interest

The authors of the article declare that there is no conflict of interest between them

References

[1] Başer U., Determination of the factors affecting the land price in Lâdik district of Samsun province, Master's thesis, Ondokuz Mayıs University, Institute of Science and Technology, 2015.

[2] Guide E., Agricultural valuation and expertise, Bursa, Third Edition, Ekin Publishing House, (2012).

[3] Çemrek F., Investigation of the Relationship Between Income and Welfare Level Variables of Provinces in Turkey with Canonical Correlation Analysis, Eskişehir Osmangazi University *Journal of Economics and Administrative Sciences*, 7 (2) (2012) 197-215.

[4] Özçomak MS., Demirci A., Investigation of the Relationship Between Social and Economic Indicators of African Union Countries by Canonical Correlation Analysis, Atatürk University *Journal of Economics and Administrative Sciences*, 14 (1) (2010) 261-274.

[5] Sümbüloğlu K., Akdağ B., Advanced biostatistical methods, Hatipoğlu Publications, Ankara, (2009) 330.

[6] Albayrak S., Applied multivariate statistical techniques, Asil Publications Edition, Ankara, (2006) 500.

[7] Özçomak MS., Gündüz M., Demirci A., Yakut E., Investigation of the Relationship Between Various Climate and Crop Data with Canonical Correlation Analysis and Data Envelopment Analysis Methods, *Atatürk University Journal of the Faculty of Economics and Administrative Sciences,* 26 (1) (2012) 111-131.

[8] Albayrak S., Applied multivariate statistical techniques, Asil Publications Edition, Ankara, (2006) 500.

[9] Dillon WR., Goldstein M., Multivariate analysis methods and applications, John Wiley and Sons Inc., New York, (1984).

[10] Keskin S., Özsoy A.N., Canonical Correlation Analysis and an Application, *Journal of Agricultural Sciences*, 10(1) (2004) 67-71.

[11] Çemrek F., Investigation of the Relationship Between Income and Welfare Level Variables of Provinces in Turkey with Canonical Correlation Analysis, Eskişehir Osmangazi University *Journal of Economics and Administrative Sciences*, 7 (2) (2012) 197-215.

[12] Kalaycı Ş., SPSS applied multivariate statistical techniques, Asil Publications Edition, Ankara, (2006).

[13] Karagöz Y., SPSS Applied biostatistics-for medicine, pharmacy, Dentistry and Health Sciences, Nobel Publications Edition, 2nd ed. Ankara (2014) 760.

[14] Mr. A., Koğar H., Çakan M., Examination of Relationships Between Graded Courses with Canonical Correlation Technique: The Example of Classroom Teaching, *Journal of Measurement and Evaluation in Education and Psychology*, 3(1) (2012) 210- 220.

[15] Har J.F., Anderson R.E., Tatham R.L., Black W.C., Multivariate data analysis, Prentice Hall, New Jersey, (1998).

[16] Tatlıdil H., Applied multivariate statistical methods, Cem Web Ofset, Ankara, (1996).

[17] Oktay E., Kaynak S., Investigation of Canonical Relationship Between Information Economy Input and Output Variables of Turkey and European Union Countries, *Atatürk University Journal of Social Sciences Institute*, 2(10) (2007) 419-440.

[18] Özçomak M.S., Gündüz M., Demirci A., Yakut E., Investigation of the Relationship Between Various Climate and Crop Data with Canonical Correlation Analysis and Data Envelopment Analysis Methods, *Atatürk University Journal of the Faculty of Economics and Administrative Sciences*, 26 (1) (2012) 111-131.

[19] Karagöz Y., SPSS Applied biostatistics-for medicine, pharmacy, Dentistry and Health Sciences, Nobel Publications Edition, 2nd ed. Ankara (2014) 760.

[20] Açıl A.F., The values of various agricultural land types in Turkey between 1950-1974 and their changes, Ankara University Faculty of Agriculture Publications, (1976) 619.

[21] Chicoine D.L., Farmland Values at the Urban Fringe, an Analysis of Sale Prices, Land Econ, 57(3) (1981) 353 -362.

[22] First A., A Research on the Factors Affecting the Values of Field Lands in Erzurum and Erzincan Provinces, PhD Thesis, Atatürk University, Institute of Science, 1997.

[23] Öztürk K.C., Engindeniz S., Hedonic Analysis of Agricultural Land Values: The Example of Menemen District of İzmir, *Ege University Faculty of Agriculture Journal*, 50(3) (2013) 241-250.

[24] Başer U., Kılıç O., Determination of factors affecting land price, Samsun Province Lâdik District Example, Turkey XII. National Agricultural Economics Congress, 25-27 May, (2016) 273-280, Isparta, Turkey.

[25] Karaca D., İbraimi S., Engindeniz S., Akyüz Y., Çınar G., Analysis of Factors Affecting the Land Purchase-Sale Decisions of Producers in Rural Areas: The Example of Kemalpaşa District of İzmir, *Journal of Ege University Faculty of Agriculture*, 53(4) (2016) 481-489 .

[26] Engindeniz S., Bayraktar Ö., Örük G., Analysis of Factors Affecting the Value of Irrigable Agricultural Lands in İzmir: İzmir Case, Selçuk Journal of Agriculture and Food Sciences, 31(3) (2017) 75-87.

[27] Çınar G., Altınok A.C., Özcan H., Aslan F., Estimation of factors affecting agricultural land value in Aydın province with hedonic pricing model, Ahtamara I. International Multidisciplinary Studies Congress, 25-26 August, (2018) Van, Turkey.

[28] Başer U., Kılıç O., Abacı H., Determination of Direct and Indirect Effects of Factors Affecting Land Price by Path Analysis, Samsun Province Lâdik District Example, *Turkish Journal of Agricultural Research*, 6(1) (2019) 50-56.

AUTHOR GUIDELINES

Thank you for choosing to submit your paper to Cumhuriyet Science Journal. The following instructions will ensure we have everything required so your paper can move through pre-evaluating, peer review, production and publication smoothly. Please take the time to read and follow them as closely as possible, as doing so will ensure your paper matches the journal's requirements.

Submission

Cumhuriyet Science Journal is an international, peer-reviewed, free of charge journal covering the full scope of both natural and engineering sciences. Manuscripts should be submitted by one of the authors of the manuscript as online submission after registration to the Cumhuriyet Sciences Journal. Microsoft Word (.doc, .docx, .rtf), files can be submitted. There is no page limit. If there is a problem while uploading the files of manuscript, please try to reduce their file size, especially manuscripts including embedded figures. Submissions by anyone other than one of the authors will not be accepted. The submitting author takes responsibility for the paper during submission and peer review. If for some technical reason submission through the online submission systme is not possible, the author can contact csj@cumhuriyet.edu.tr for support.

Submission or processing charges

Cumhuriyet Science Journal does not charge any article submission, processing charges, and printing charge from the authors.

Terms of Submission

Papers must be submitted on the understanding that they have not been published elsewhere (except in the form of an abstract or as part of a published lecture, review, or thesis) and are not currently under consideration by another journal. The submitting author is responsible for ensuring that the article's publication has been approved by all the other coauthors. It is also the authors' responsibility to ensure that the articles emanating from a particular institution are submitted with the approval of the necessary institution. Only an acknowledgment from the editorial office officially establishes the date of receipt. Further correspondence and proofs will be sent to the author(s) before publication unless otherwise indicated. It is a condition of submission of a paper that the corresponding author permit editing of the paper for readability. All enquiries concerning the publication of accepted papers should be addressed to csj@cumhuriyet.edu.tr. Please note that Cumhuriyet Science Journal uses iThenticate software to screen papers for unoriginal material. By submitting your paper to Cumhuriyet Science Journal are agreeing to any necessary originality checks your paper may have to undergo during the peer review and production processes. Upon receiving a new manuscript, the Editorial office conducts initial pre-refereeing checks to ensure the article is legible, complete, correctly formatted, original, within the scope of the journal in question, in the style of a scientific article and written in clear English. Any article that has problems with any of the journal criteria may be rejected at this stage.

Peer Review

This journal operates a single blind review process. All contributions will be initially assessed by the editor for suitability for the journal. Papers deemed suitable are then typically sent to a minimum of two independent expert reviewer to assess the scientific quality of the paper. The author is required to upload the revised article to the system within 15 days by making the corrections suggested by the referee. The article will be rejected if there are no fixes in it. The Editor is responsible for the final decision regarding acceptance or rejection of articles. The Editor's decision is final

Title and Authorship Information

The following information should be included

Paper title

Full author names

Full institutional mailing addresses

Corresponding address

Email address

Abstract

The manuscript should contain an abstract. The researchers who are native speakers of Turkish have to add Turkish title and abstract as well. The abstract should be self-contained and citation-free and should be 250-300 words.

Keywords

Keywords of the scientific articles should be selected from the web address of www.bilimadresleri.com

Introduction

This section should be succinct, with no subheadings.

Materials and Methods

This part should contain sufficient detail so that all procedures can be repeated. It can be divided into subsections if required.

Conflicts of interest

Sample sentence if there is no conflict of interest: The authors stated that did not have conflict of interests.

Acknowledgements

Sample sentences for acknowledgements: The work was supported by grants from CUBAP (T-11111). We would like to acknowledge Prof. Mehmet Sözer, MD, for his precious technical and editorial assistance. We would like to thank

References

References to cited literature should be identified by number in the text in square brackets and grouped at the end of the paper in numerical order of appearance. Each reference must be cited in the text. Always give inclusive page numbers for references to journal articles and a page range or chapter number for books. References should be styled and punctuated according to the following examples

[1] Karaca E., Ulusoy S., Morgül Ü., Ulusoy H.I., Development of Analytical Method for Sensitive Determination of Streptozotocin based on Solid Phase Extraction, Cumhuriyet Sci. J., 41 (4) (2020) 826-831. (sample reference for journals)

[2] Keskin B., Ozkan A.S., Inverse Spectral Problems for Dirac Operator with Eigenvalue Dependent Boundary and Jump Conditions, Acta Math. Hungar., 130 (2011) 150-159(sample reference for journals)

[3] Mazur M.T., Kurman R.J., Dysfunctional Uterine Bleeding. In: Mazur M.T., Kurman R.J., (Eds). Diagnosis of endometrial biopsies and curettings, A practical approach. 2nd ed. Berlin: Springer, (2005) 100-120. (sample reference for book chapters)

[4] Mazur M.T., Kurman R.J.,Diagnosis of endometrial biopsies and curettings, A practical approach. 2nd ed. Berlin, (2005) 100-120. (sample reference for book)

[5] National Cancer Institute, Surveillance Epidemiology and End Results. Cancer of the Corpus and Uterus, NOS. Available at: http://seer.cancer.gov/statfacts/html/corp.html?statfacts_page=corp. Retrieved March 2, 2008. (sample reference for websites)

[6] Surname N., Title of thesis, PD or master thesis, Name of university, name of institue, year. (sample reference for thesis)

[7] Surname N., Title of fulltext conference paper, name of conference, city, year, pages. (sample reference for Abstratcs in conferences are not accepted as a valid reference except full text)

Preparation of Figures

Each figure can be integrated in the paper body or separately uploaded and should be cited in a consecutive order. Figure widths can be 4-6 inch as 300 dpi. The labels of the figures should be clear and informative. The name and the subtitles of the figures must be 9-point font.

Preparation of Tables

Tables should be cited consecutively in the text. Every table must have a descriptive title and if numerical measurements are given, the units should be included in the column heading. Tables should be simple with simple borders and text written as left text. The name and the subtitle of the tables must be 9-point font

Proofs

Corrected proofs must be returned to the publisher within 2 weeks of receipt. The publisher will do everything possible to ensure prompt publication. It will therefore be appreciated if the manuscripts and figures conform from the outset to the style of the journal.

Copyright

Ethical Guidelines

New methods and ethically relevant aspects must be described in detail, bearing in mind the following:

Human Experiments. All work must be conducted in accordance with the Declaration of Helsinki (1964). Papers describing experimental work on human subjects who carry a risk of harm must include:

A statement that the experiment was conducted with the understanding and the consent of the human subject.

A statement that the responsible Ethical Committee has approved the experiments.

Animal Experiments. Papers describing experiments on living animals should provide:

A full description of any anaesthetic and surgical procedure used.

Evidence that all possible steps were taken to avoid animal suffering at each stage of the experiment. Papers describing experiments on isolated tissues must indicate precisely how the donor tissues were obtained.

Submission Preparation Checklist

As part of the submission process, authors are required to check off their submission's compliance with all of the following items, and submissions may be rejected that do not adhere to these guidelines.

The submission has not been previously published, nor is it before another journal for consideration (or an explanation has been provided in Comments to the Editor).

The submission file is in Microsoft Word document file (Times New Roman) format.

Where available, URLs for the references have been provided.

The text is single-spaced; uses a 11-point font; employs italics, rather than underlining (except with URL addresses); and all illustrations, figures, and tables are placed within the text at the appropriate points, rather than at the end.

The text adheres to the stylistic and bibliographic requirements outlined in the Author Guidelines, which is found in About the Journal.

If submitting to a peer-reviewed section of the journal, the instructions in Ensuring a Double-Blind Review have been followed.